5-2021

Towards Neutron Transformation Searches

Joshua L. Barrow
The Univeristy of Tennessee, jbarrow3@vols.utk.edu

To the Graduate Council:

I am submitting herewith a dissertation written by Joshua L. Barrow entitled "Towards Neutron Transformation Searches." I have examined the final electronic copy of this dissertation for form and content and recommend that it be accepted in partial fulfillment of the requirements for the degree of Doctor of Philosophy, with a major in Physics.

Yuri A. Kamyshkov, Major Professor

We have read this dissertation and recommend its acceptance:

Nadia Fomin, Sowjanya Gollapinni, Yuri Efremenko, Lawrence Townsend

Accepted for the Council:

Dixie L. Thompson

Vice Provost and Dean of the Graduate School

(Original signatures are on file with official student records.)

Towards Neutron Transformation Searches

A Dissertation Presented for the

Doctor of Philosophy

Degree

The University of Tennessee, Knoxville

Joshua Lawrence Barrow

May 2021

To my family and friends, advisors, instructors and colleagues, past and present, in thanks to all they have given me, with no thought of remuneration.

But, especially, to my grandfather.

In questions of sciences, the authority of a thousand is not worth the humble reasoning of a single individual.

-Galileo

The pursuit of knowledge is hopeless and eternal.

-Hubert J. Farnsworth

The first gulp from the glass of natural sciences will turn you into an atheist, but at the bottom of the glass, God is waiting for you.

-Werner Heisenberg

Professional Acknowledgments

First, I would like to thank my advisor, Professor Yuri Kamyshkov, for pushing me along this amazing journey; he knew just when I needed his instruction, and just when to set me free. I set out to study experimental and phenomenological beyond Standard Model physics toward the end of my college career, and have had the privilege and pleasure of doing so through his leadership. I will miss our times together as I move forward, especially our 3+ hour arguments at the whiteboard. I am indebted to him far beyond his knowledge.

Second, I would like to thank my close colleague and partner in crime, Elena Golubeva. She, without any need of her own, took me under her wing and taught me much of what marks her as a world-expert in nuclear interaction Monte Carlo simulation. I continue to treasure our discussions and work together, and hope that it continues. Much of our work together will be highlighted in this thesis.

Third, I would similarly like to thank my Fermilab-affiliated colleagues for their immense support over the last two years. I am particularly indebted to my GENIE and DUNE (High-Energy Physics Working Group) colleagues, including Steven Gardiner, Saori Pastore, Ivan Martinez-Soler, Yeon-jae Jwa, Viktor Pěč, Ben Rybolt, Christoph Alt, Robert Hatcher, Carlos Sarasty, Jeremy Hewes, Gianluca Petrillo, Ken Herner, Lisa Whitehead Koerner, Vitaly Kudryavtsev, Yun-Tse Tsai, Gregory Pawloski, Georgia Karagiorgi, Ed Kearns, Aaron Higuera, Afrodite Papadopoulou, Adi Ashkenazi, Noemi Rocco, Alessandro Lovato, Michael Wagman, Maury Goodman, Steve Dytman, Erica Snider, Thomas Junk, Stephen Mrenna, Marco Roda, Minerba Betancourt, Geralyn "Sam" Zeller, Teppei Katori, and Pedro Machado. I could not have completed this work without all of your robust discussion, active long-term collaboration and leadership. I treasure also the near constant physics (and life) discussions I have had the pleasure of sharing with my Fermilab family, including among Albert Stebbins, Filippo "Pippo" Varanini, Jason

Crnkovic, Steve Dennis, Chris and Kimberly Polly, Karie Badgley, Douglas Tuckler, Laura Kelton, Manuel Blanco Valentin, Dante Totani, Federico Spiranza, Luisa Lucie-Smith, Juan Hererro Garcia, Samuel Hedges, Salvador Rosauro Alcaraz, Rene Padilla Dieppa, Brendan Kiburg, and the incomparable Tania Claudette Brown. Thank-you for your welcoming spirits, your constant belief in, support of, and challenging of me and my work, your advice and arguments, and each of your friendships; I cherish them.

Fourth, I would like to thank my fellow UTK, ORNL, Swedish and ESS-affiliated, and many other colleagues for their leadership, awesome collaborative work with me, and recognition of my potential; thank-you to Jean-Marc Richard, Charles "Garrett" Ladd, Eduard Paryev, Alexander Botvina, Bernhard Meirose, Katherine Dunne, Matthew Frost, Leah Broussard, Zurab Berezhiani, Lisa Debeer-Schmidt, Albert Young, William "Mike" Snow, David Milstead, Sze Chun "Billy" Yiu, Valentina Santoro, Anders Oskarsson, Gustaaf Brooijmans, Valery Nesvizhevsky, Lawrence Heilbronn, Jordy de Vries, Robert Shrock, Bhupal Dev, Kaladi Babu, Rabindra Mohaptra, Goran Senjanovic, and Marcel Demarteau. Thanks are also in order for my close friends and study partners Jimmy Caylor, Andrew Mogan, Gray Yarborough, Charles Hughes, Chloe Keeling-Sandoval, Michael Sandoval, Nathan Traynor, and Kyle Noordhoek; thanks for keeping me sane, and helping me to learn so much about both physics and myself. I would also like to thank Associate Professor Nadia Fomin for her great support and mentorship through some of my most uncertain times.

Fifth, a thank-you is absolutely necessary to Chrisanne Romeo, Showni Medlin-Crump, and Chair Hanno Weitering for constantly keeping me on the right track, grounded, and supported throughout my career here at the University of Tennessee (UTK). I am grateful to you all.

Sixth, I would also like to thank the Department of Energy Office of Science Graduate Student Research (SCGSR) Program and the Universities Research Association Visiting Scholar Program for their support of my work over these past two years. Thanks is also deserved by Alan Stone and his office for provision of housing support while at Fermilab. Thank-you for the opportunity, and your belief in me throughout. Other support for this work includes the Department of Energy High Energy Physics Grant DE-SC0014558, the UTK Chancellor's Fund, the UTK Department of Physics and Astronomy Birkhoff Fellowship, the UTK Faculty Senate Research Council Summer Graduate Research Assistantship, the UTK Fellowship for Graduate Excellence, and the UTK

Department of Physics and Astronomy Paul H. Stelson Fellowship for Professional Promise. I would also like to thank the Neutrino Theory Network and the FRIB Theory Alliance award DE-SC0013617, the Nordic Institute for Theoretical Physics, the American Physical Society, and the UTK Graduate Student Senate for travel support throughout my graduate work. I also appreciate my colleagues, mentors, and supporters at Los Alamos National Laboratory, where I served as a Computational Physics Student Summer Workshop Fellow.

Finally, I would like to thank Professor Emeritus Ray Hefferlin (now deceased), his wife and wonderful travel companion Inelda, and his family from the bottom of my heart. While a student at my alma mater, Southern Adventist University, he brought me into this scientific world, and without him, I would not have pursued any of this as far as I have. Rest in peace, Doc.

Abstract

To probe the origins of the baryon asymmetry, baryon number violation, the last unconfirmed Sakharov condition, must be definitively observed experimentally. Similarly, the nature of dark matter is currently unknown, and calls out for new candidates to be investigated. Each of these issues can be considered through the study of neutron transformations.

Some rare baryon number violating processes, such as neutron-antineutron transformations, are expected to probe baryogenesis. Here, I show progress on this discovery target through construction of more accurate Monte Carlo models, the design of future detectors, creation of more complete atmospheric neutrino background simulations, and use of automated analysis techniques within the the NNBAR/HIBEAM experimental program at the European Spallation Source (ESS) and the Deep Underground Neutrino Experiment (DUNE). First simulation-based sensitivities for these experiments will be discussed. Modeling of rare neutron-antineutron transformation and subsequent annihilation will be discussed at length for multiple nuclei useful to these and other collaborations. To go along with this work, more comprehensive lepton-scattering nuclear models must be integrated into neutrino event generators for proper atmospheric neutrino background simulations. I discuss the first furnishing of these backgrounds for DUNE, and I highlight a potential path forward for the community in this vein using precision electron scattering modeling as a facsimile.

Aspects of other potentially related neutron–mirror-neutron oscillations pertinent to dark matter and the neutron lifetime anomaly will also be considered for the ESS HIBEAM experiment. Here, I will present the first experimental sensitivity calculations for a broad range of modular experimental setups which will serve as research and design stepping stones toward NNBAR while producing a multitude of physics results over short time scales.

Table of Contents

List of Tables

List of Figures

Chapter 1

Introduction and Physics Overviews

To study rare processes requires an attack plan on multiple fronts. First, one must properly conceive of and constrain the potential beyond Standard Model phenomena at a theoretical level, employing quantum mechanical formalisms. Following this, one must consider the phenomenological modeling, potentially via simulation, of the rare process, along with any associated backgrounds. The precision of these simulations in many ways will dictate the potential sensitivity of a given experiment, as it's interpretation is based by default on the rare process' modeling. Thus, to discover new physics, one must consider both the particle and nuclear physics at play within a given process carefully, beyond of course the difficulties of a proper detector simulation. In this thesis, I work toward these developments within the Deep Underground Neutrino Experiment and the NNBAR/HIBEAM experimental program at the European Spallation source, principally considering Monte Carlo simulation modeling to assess the viability of searches for rare processes such as neutron transformations.

In this first chapter, I begin by summarizing the problems and enumerate some theoretical aspects of baryogenesis and dark matter, as well as give an overview of lepton scattering physics. In the former cases, neutron oscillations will be discussed as a potential solution; the latter is an important consideration for improving background estimations for future intranuclear baryon number violation searches. The design of experimental tests and uses of these theoretics in simulation, along with validation and associated data comparisons where possible will be the focus of the chapters hereafter[1].

1.1 The Standard Model

One of the central accomplishments of the Standard Model is the supremely simple way in which it is constructed at its most fundamental levels. Though the Model is known to be incomplete (as will soon be discussed), it's beauty can be holistically encapsulated by the gauge group structure

$$\mathcal{G}_{SM} = SU(3)_C \times SU(2)_L \times U(1)_Y, \tag{1.1}$$

containing three fermion generations experiencing some of all or the strong (color, $SU(3)_c$), left-handed (L) weak ($SU(2)_L$), and electric ($U(1)_Y$) (hypercharge) interactions. Following Wigner, particles are identified as the irreducible representations of this global gauge symmetry group, with quarks in one fermionic representation and leptons in another. With this gauge symmetry and the SM's particle content, one may construct the *accidental* apparent global symmetry

$$\mathcal{G}_{SM} = U(1)_{\mathcal{B}} \times \prod_{\mathcal{L}}^{e,\mu,\tau} U(1)_{\mathcal{L}}, \tag{1.2}$$

at perturbative levels; here, $U(1)_{\mathcal{B}}$ is the baryon ($\mathcal{B}$) number symmetry, and $\prod_{\mathcal{L}}^{e,\mu,\tau} U(1)_{\mathcal{L}}$ are the three lepton flavor symmetries with total lepton number $\mathcal{L} = \mathcal{L}_e + \mathcal{L}_\mu + \mathcal{L}_\tau$. Fermions (though not necessarily neutrinos without some arguably simple extensions) gain masses through Yukawa interactions after spontaneous symmetry breaking [231]. Embracing an overarching and collective view, the theory is decisively beautiful, though some inherent flaws remain.

The successes of the Standard Model of particle physics (SM) cannot be understated. The injection of field theories and Lagrangian formalism into quantum mechanics (QM) has yielded an impressive list of well defined, precisely calculable physical observables across a multitude of electromagnetic, weak, and strongly interacting systems. To date, no high statistics data (outside

[1]Note here that for *all* proceeding chapters, all figures without any specific caption detailing their provenance are of my own design and making. My contributions to the many fields of study detailed throughout this thesis stem primarily from these many figures. All code, simulations, and details of their production are available upon reasonable request.

of the neutrino, ν, sector) has shown any definitive deviation from the SM's robust predictions at high energy ($\sim$TeV) scales: there has been no sighting of sparticles, extra dimensions, or other exotic, beyond Standard Model (BSM) phenomena thus far.

None-the-less, the problems that many of the concepts mentioned above were designed to rectify, remain, stubborn as ever. In my opinion, chief among the most important problems in physics today are the baryon asymmetry of the universe (the BAU, also known as the matter-antimatter asymmetry of the universe, or the baryon abundance), and the unknown nature of dark matter (DM). Each represents a possibly fundamental disability of the SM (see Eq. 1.2), and they remain some of the toughest quandaries for scientists to resolve within the great structures of nature.

In order to explain such quandaries, the SM must be extended, but the question remains as to how. Previously, within extensions such as supersymmetry (SUSY, which had promised a rich landscape of new and exciting particles and phenomena to be observed and studied), scientists focused on reaching higher and higher energy scales; this is known as the energy frontier. Today, another set of perspectives is beginning to take hold: the low energy and intensity frontiers are now being sought out within the high precision era in order to uncover any potentially new signals drowned out by the noise. It is this philosophy, and its many crossovers, which drives much of my and others' work on baryogenesis, lepton scattering, and DM today, where long time scale and or precision measurements of SM observables aim to find any lurking, previously hidden physics above SM backgrounds (such as those from atmospheric neutrinos, to be discussed later). I will discuss prospects for these over the coming chapters across several experiments, including the NNBAR/HIBEAM two-stage experimental program at the European Spallation Source (ESS), and the Deep Underground Neutrino Experiment (DUNE). All studies have required ample simulation developments to assess their experimental viabilities.

1.2 The Baryon Asymmetry of the Universe, the Sakharov Conditions, and Baryogenesis

Given what is known of the big bang and the plausible mechanisms by which it arose, physicists have found the universe today to be flat (zero net energy density), expanding, and made principally of matter [20]. Most scientists believe that the universe began from a charge (C) symmetric state, wherein all masses of particles and antiparticles were balanced, the decay widths of those particles identical, and their electric charges opposite. However, while such a symmetric state would require equivalent number densities of particles and their antiparticles, it is instead seen (albeit only in the local cosmic neighborhood) that the universe is predominately made of matter rather than antimatter. Here, electrons, protons, and neutrons dominate the density of their respective antiparticle cousins. This fact is solidified by the observation of little to no flux of energetic γ-radiation due to annihilation events (for example, in a $p\bar{p}$ collision, production of π^0's can occur, which can subsequently decay into 2γ). This observation, along with data showing the near perfect isotropy of the CMB [20] radiation allows one to calculate a convenient, dimensionless number characterizing the magnitude of the BAU [171, 173, 172]:

$$\beta = \frac{n_{\mathcal{B}} - n_{\bar{\mathcal{B}}}}{n_\gamma} \approx 10^{-10}, \tag{1.3}$$

where β is the BAU, $n_{\mathcal{B}}$ the number density of baryonic charge, $n_{\bar{\mathcal{B}}}$ the number density of antibaryonic charge, and n_γ the number density of cosmic-microwave background photons [20]. Accurate estimates of β, which is (assumed to be) constant in time, are confirmed by the astronomical observation of light elements (nuclei) throughout the universe. These elements include ${}^4_2$He, ${}^3_2$He, ${}^7_3$Li, and especially ${}^2_1$H, all thought to be made during the first few minutes following the big bang. In models of such nucleosynthesis, these observations are key and sensitive inputs, and offer a good understanding of the baryonic number density during this epoch.

It should be noted that in the case of a pure, symmetric state of the universe, one would expect for there to be effectively no baryons (or antibaryons) at all due to mutual annihilation occurring down to a temperature of roughly 1 GeV (where they would "freeze" out), giving rise to a surviving BAU of [173, 171, 172]

$$n_{\mathcal{B}} = n_{\bar{\mathcal{B}}} \approx \frac{n_\gamma}{\sigma_{ann} m_{\mathcal{B}} M_{Pl}} \approx 10^{-19} n_\gamma. \tag{1.4}$$

Here, σ_{ann} is the cross-section of nucleon-antinucleon annihilation, $m_{\mathcal{B}}$ is the baryon mass, and M_{Pl} is the Planck mass. This quantity, of course, is far too small compared to Eq. 1.3, showing an effective nine orders of magnitude overabundance when considering the universe today [172]; an understanding of this asymmetry could hold important clues to BSM physics [50, 47], as it seems a clear violation of Eq. 1.2.

To help explain this incredible discrepancy, in the 1967, Andrei Sakharov proposed his famed conditions. These can be nicely summarized in the following example. Let the universe be created from a C-symmetric vacuum state with total baryon and lepton numbers of zero. Consider an arbitrarily heavy particle that existed close to the beginnings of the universe, X, and its antiparticle, $\bar{X}$. Recall by consequence of the charge-parity-time reversal symmetry (CPT) theorem that, for any quantum field theory, all decay rates of particles and antiparticles contained within that theory are identical. If X were to decay with a branching fraction f into a state with baryon number $\mathcal{B}_1$, and into another possible state $\mathcal{B}_2$ with branching $(1-f)$ (and vice versa for $\bar{X}$), then it is seen that the change in the baryon number before and after the decays is

$$\begin{aligned}
|\Delta\mathcal{B}| &= \mathcal{B}_F - \mathcal{B}_O = \mathcal{B}_F - (0) = \mathcal{B}_{F_X} - \mathcal{B}_{F_{\bar{X}}} \\
&= [f\mathcal{B}_1 + (1-f)\mathcal{B}_2] - [\bar{f}\mathcal{B}_1 + (1-\bar{f})\mathcal{B}_2] \\
&= (f-\bar{f})\mathcal{B}_1 + [(1-f) - (1-\bar{f})]\mathcal{B}_2 \\
&= (f-\bar{f})(\mathcal{B}_1 - \mathcal{B}_2) \neq 0.
\end{aligned} \tag{1.5}$$

From this simple example, and the plain observation of the existence of the universe, one must conclude that 1) $f \neq \bar{f}$, which means there is CP non-conservation within nature, and 2) $\mathcal{B}_1 \neq \mathcal{B}_2$ implies that $\mathcal{B}$ non-conservation has at some point occurred. These are two of the three Sakharov conditions, which, in full, are:

1. CP non-conservation implies the interactions of particles and antiparticles in physical processes are different.

2. $\mathcal{B}$ non-conservation implies that baryon number (alone) is not a good quantum number.

3. Departure from thermal equilibrium (not discussed directly within the context of Eqs. 1.5) implies that the original configuration of the universe was not perfectly symmetric.

All three of these arguments are central to any understanding of the evolution of the universe, and act as key boundary conditions upon any permissible model which claims to be consistent with its existence [172, 263, 349, 352]. This was the first hint of the need for BSM physics. Two of the three of these conditions have been empirically demonstrated: CP violation, as observed in K^0 and $\bar{K}^0$ decays [148], and departure from thermal equilibrium in the early universe, as observed in temperature data from the cosmic microwave background (CMB) radiation[2] [20]. Only one of Sakharov's conditions has yet to be definitively observed: *baryon number violation*.

1.2.1 $\mathcal{B} - \mathcal{L}$ Conservation in the Electroweak Sector

Fermions interact via vector minus axial-vector ($V - A$) terms present in the lagrangian density of the electroweak sector within the SM; this leads to the fact that the axial-vector current is not generally conserved for massive particles. Due to this, the Bell-Adler-Jackiw (also known as the axial) anomaly develops at non-perturbative scales [156]. This led t'Hooft and Veltman [156, 387] to his renormalization of the SM, requiring that the SM have equal numbers of lepton and quark families. Simultaneously, it was shown that the baryonic and leptonic currents were conserved over all flavors for Dirac fermions:

$$3\partial_\mu J^\mu_{quark} = \partial_\mu J^\mu_{lepton} \to \partial_\mu J^\mu_{baryon} = \partial_\mu J^\mu_{lepton} \to \Delta\mathcal{B} = \Delta\mathcal{L}. \tag{1.6}$$

This led to the creation of a new, "good" quantum number for non-perturbative regimes: the combined form $\mathcal{B} - \mathcal{L}$, which is always conserved in SM processes, to all orders. This is rather different than the "good" individual $\mathcal{B}$ or $\mathcal{L}$ quantum numbers present at perturbative regimes within the SM (and are thus representable by Feynman diagrams; see again Eq. 1.2).

[2] This effect is broadly illustrated by the CMB, as it is evidence of an out of equilibrium phase transition between ionized and atomized phases of nucleons and electrons, and was only smoothed out by the expansion rate of space in the early universe.

1.2.2 Electroweak Baryogenesis and the Sphaleron

It can be shown from such baryonic and fermionic currents that a respective topological number exists which effectively separates different possible vacuum state configurations for leptons and baryons. These different configurations can be illustrated by the blue and red outlined circles in Fig. 1.1, each of independent topological numbers $n = 1$ and $n = 2$. It was thought that topological tunneling through an energy "barrier" (the periodic function shown in black) separating these states could, be emblematic of simultaneous baryon and lepton number violation, accounting for the matter-antimatter asymmetry (this process is being illustrated in cartoon fashion in light green); classical motion over the barrier is also possible. At energies above the electroweak phase transition in the early universe, it has been suggested that the rates of processes with $\Delta\mathcal{B} \neq 0$ are faster than the expansion rate of the universe, meaning that any asymmetry between baryons and antibaryons would be removed. To be clear, it could be the case that in electroweak interactions at high temperature, one may conserve $\mathcal{B} - \mathcal{L}$, but instead $\mathcal{B} + \mathcal{L}$ is erased. Cognizant of these facts, they can be shown to be ineffective at reproducing the observed BAU [173, 171, 349]. Some recent progress is also discussed in [341], and other reviews include [54].

If this is the case, then the anomalies of the SM, especially in the electroweak sector, while capable of rendering the model renormalizable, are ineffective at generating any asymmetry (they would, in fact, act as a terminator of any asymmetry [173, 171, 172]). Precisely, if the electroweak phase transition is of second order and thermal equilibrium is not disturbed, then the asymmetry is not generated. This turns out to depend critically on the mass of the Higgs boson, where for a high mass ($\gtrsim 100\,\mathrm{GeV}$) the transition will be of second order, while for a low mass ($\lesssim 50\,\mathrm{GeV}$), it will be of first order, and regions of asymmetry could be generated. However, considering the Higgs is heavy, it is now known that the transition must have been second order, resulting in effectively no asymmetry whatsoever [156, 173, 171, 172, 185, 246, 387, 263].

The electroweak phase transition and its ability to generate the BAU is recognized to create far too weak of an effect to act as an adequate explanation of the BAU as observed today. In order to mitigate these facts, the sphaleron mechanism was proposed [387, 386]. Speaking roughly, it is known that processes with a non-zero change in baryonic charge are, at high temperatures, accompanied by changes in the structure of the Higgs field. It is possible to deduce that the

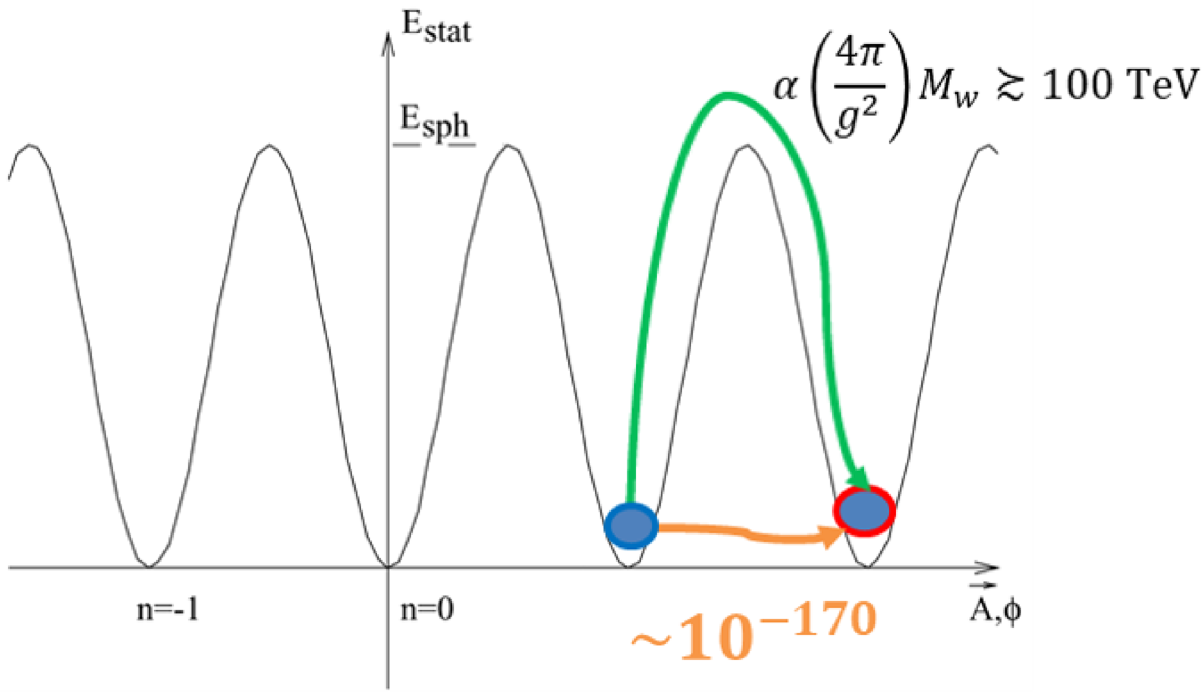

Figure 1.1: A simplified schematic plot (taken from Dolgov's discussions throughout [171, 172, 173], Kuzmin *et al.* [277], and Rubakov and Shaposhnikov [349]) of potential mechanisms of baryon number violation between different topologial vacuum states. The continuous, periodic barrier represents the Higgs field at early time, and minima of this potential represent classical vacua. (Green) The sphaleron mechanism is illustrated, likely active at high temperatures (~ 10 TeV), and represented by classical motion over the potential barrier. (Orange) Topological tunneling between topological states through the potential barrier is illustrated. Figure adapted from [349].

sphalerons are objects that, if assumed to be in thermal equilibrium with one another (and so described by a Boltzmann exponent dependent upon the Gibbs free energy) at TeV scales, then baryon number violating process again may not be suppressed at high temperatures (see again the dark green of Fig 1.1). However, the rate of production of these classical field states is not known and one cannot say if they would even be in thermal equilibrium or not. From these configurations, it is thought that one would need to create quite a special coherent field, which is quite improbable in the early universe. If such is the case, once again, yet another SM process apparently does not produce any appreciable baryon asymmetry due to washout [171]. This would imply that the quantum number of $\mathcal{B} - \mathcal{L}$ is itself not a good quantum number, and so must too be violated at some point in the early universe in order to generate the BAU. This points to the plausible need of a new extension to the SM. It should be noted that these conclusions are not from analytical solutions to this problem (as none exist), but instead stem from numerical lattice calculations. Considering such effects are non-perturbative and multi-particle, this leads to many different results from different groups [173, 171, 172, 185, 387, 348, 349].

1.3 Classic Baryon Number Violation: $|\Delta\mathcal{B}| = 1$ Proton Decay

Proceeding by contradiction, in the preceding, some reasons have been discussed why it appears important for nature to employ deliberately asymmetric processes which violation baryon (lepton) number in order to generate the BAU; these could be accomplished by violating $\mathcal{B} - \mathcal{L}$ itself. This implies the existence of specific $\Delta\mathcal{B}$ ($\Delta\mathcal{L}$) operators in the extended SM lagrangian density. Forays into grand unification theories (GUTs) at high energy scales include extensions to the SM (usually, but not always, in the form of supersymmetric theories) in which low dimension operators are added that can generate these kinds of $\mathcal{B}$ ($\mathcal{L}$) violation, though not always with $\mathcal{B} - \mathcal{L}$-violating character; one such extension, and quite a popular one historically, is proton decay. Such an operator is usually of dimension six, and could take the form of

$$\mathcal{O}_p \propto \lambda_p \frac{qqql}{M_{GUT}^2}, \tag{1.7}$$

where q's represent quarks, and l a lepton, as shown in Fig. 1.2. Thus, such proton decays violate $\mathcal{B}$ by one unit, while technically $\mathcal{L}$ can be violated by any odd unit (if these operators take different forms) [43]; most do not violate $\mathcal{B} - \mathcal{L}$.

Due to the connection between proton decay and the GUT mass scale (seen in the denominator of Eq. 1.7), proton decay has historically been placed on a pedestal of sorts by the particle physics community. While it is an important process to search for in and of itself, other than this connection, it should be noted that its existence (or lack thereof) solves no great fallacy underlying some of the larger questions surrounding baryogenesis.

On the whole, proton decay in its many forms, such as the reaction $p \to e^+\pi^0$ or $p \to \mu^+\pi^0$ (Fig. 1.2), can be severely constrained given very strong experimental lower limits at some of the largest detectors currently operating; sources of background (predominately atmospheric neutrinos) make this difficult even despite the impressive $\gtrsim 10^{32}$ protons available for decay within the fiducial volume at Super-Kamiokande [388].

Lack of experimental evidence for proton decay has been a setback of sorts for the particle physics community; this, presently coupled with lack of any viable candidates for SUSY at the LHC, has prompted some physicists to abandon the theoretical aspects of proton decay entirely. For purposes focusing on the discussion of the BAU, it should be further noted that the so called "golden channel" of observation of proton decay (thought to be more distinguishable from background candidates in large mass detectors such as DUNE), where again $p \to K^+\bar{\nu}$, similarly does not violate $\mathcal{B} - \mathcal{L}$, and so cannot help account for the BAU.

1.4 A General $|\Delta\mathcal{B}| = 2$ Theoretical Overview and Opportunities

In many BSM theories, the origins of the BAU can be extrapolated from the observation of several potentially related $|\Delta\mathcal{B}| = 2$ modes, including but not limited to neutron-antineutron transformations ($n \to \bar{n}$), and more generally dinucleon decays[3]. Observation of $n \to \bar{n}$ [299, 219, 326] would be clear evidence for baryon number ($\mathcal{B}$) violation (BNV), one of the three Sakharov conditions [352] that has yet to be experimentally confirmed, and which together

[3]Thanks to my many Snowmass 2021 colleagues for their collaboration and discussions on this work [66, 63, 3].

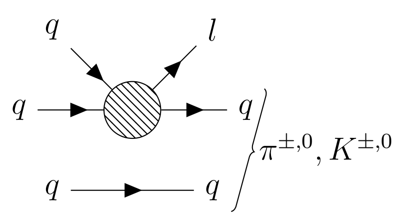

Figure 1.2: A simplified Feynman diagram of classic, general proton decay to a meson (through the spectator quark) and a lepton (typically an e^+, μ^+, or $n\bar{u}$). Examples can include $p \rightarrow e^+\pi^0$ or $p \rightarrow K^+\bar{\nu}$, important for searches at Super-Kamiokande and DUNE.

can explain the dynamical generation of the BAU. As discussed, $(\mathcal{B}-\mathcal{L})$-violation is a prerequisite for any pre-existing $\mathcal{B}$ or $\mathcal{L}$ asymmetry to dynamically develop and survive; the latter is the case in classic leptogenesis [207]. With the effective impossibility of a definitive, "on shell" test for classic leptogenesis, similar to the confirmations of the $W^{\pm}$, Z^0, and Higgs, other potentially observable baryogenesis alternatives become attractive to consider. Since $\Delta(\mathcal{B}-\mathcal{L}) \neq 0$ for $n \to \bar{n}$, the fundamental physics behind $n \to \bar{n}$ may well underlie the origin of the $\mathcal{B}$-asymmetry surviving until the current epoch. This contrasts with the ephemeral $\mathcal{B}$-asymmetry generated in grand unified theories via $\Delta(\mathcal{B}-\mathcal{L}) = 0$ processes, which can be diluted (washed-out) by sphaleron effects.

Continuing, many BSM theories of baryogenesis predict $n \to \bar{n}$ in an observable range. One example is the compelling [304] post-sphaleron baryogenesis (PSB) model [50, 48, 47] where baryogenesis occurs after the electroweak phase transition, predicting an upper limit on the $n \to \bar{n}$ oscillation period $\tau_{n\bar{n}}$, and which may be within reach of forthcoming experiments. More generally, "Majorana baryogenesis" [147, 55, 234], effective at low energy scales, can also lead to observable $n \to \bar{n}$; these mediating Majorana fermions could be the gluinos or neutralinos of supersymmetric models with R-parity violation, or can be involved in neutrino (ν) mass generation [168]. In some cases, if certain colored scalars remain light at the TeV scale [49], GUT scale BNV interactions can lead to successful baryogenesis and observable $n \to \bar{n}$. It has been shown that $n \to \bar{n}$ can also result in models where baryogenesis proceeds through the related process of particle-antiparticle oscillations of heavy flavor baryons [293, 24]. This possibility points towards new physics at the scale of a few TeV, and its ingredients (heavy neutral fermions and colored scalars) could be within the reach of the Large Hadron Collider (LHC).

All this being said, as a brief review, some generic points to keep in mind include[4]:

1. Physicists have, as yet, no evidence confirming the correctness of any given baryogenesis model, and so the field remains very open

2. What can be said with confidence is that baryogenesis models must satisfy the Sakharov conditions (of which BNV is one)

3. From both of these points, is important that experiments look for many different $\Delta\mathcal{B}$ (and $\Delta\mathcal{L}$) selection rules

[4]Thanks to D. Milstead [133] for discussions on these points.

1.4.1 Some Details

In a low-energy effective field theory (EFT) analysis, the leading operators contributing to proton (and bound n) decay are four-fermion operators, which have dimension $d = 6$, and hence coefficients of the form $1/M_{Nd}^2$, where M_{Nd} denotes the mass scale characterizing the physics responsible for nucleon decay. However, these operators conserve $(\mathcal{B} - \mathcal{L})$, and are thus not useful for understanding the BAU.

It is known that $n \to \bar{n}$ can occur naturally at observable rates in a model with a left-right-symmetric gauge group $G_{LRS} = SU(3)_c \times SU(2)_L \times SU(2)_R \times U(1)_{B-L}$ [298, 362, 299]. Here, $\mathcal{B}$ and $\mathcal{L}$ are connected via the $(\mathcal{B} - \mathcal{L})$ gauge generator, and the breaking of $\mathcal{L}$ leads to Majorana ν's via the seesaw mechanism. This, in turn, can lead naturally to $n \to \bar{n}$ in a quark-lepton unified theory, while proton decay is absent in minimal versions of such models.

Another class of models with $n \to \bar{n}$ are those with extra spatial dimensions, where SM fermions can retain localized wave functions within these extra dimensions [311, 215, 217]. In such models, it is trivial to suppress nucleon decays well below experimental limits by separating the wave function centers of quarks and leptons sufficiently; $n \to \bar{n}$ transitions are not suppressed because the six-quark operators do not involve leptons. In these cases, $n \to \bar{n}$ oscillations can occur at rates comparable to existing experimental limits [311, 215, 217], and there are many explicit model examples [299, 311, 215] in which nucleon decay is absent or highly suppressed. Thus, $n \to \bar{n}$ would remain the primary manifestation of BNV for forseeable terrestrial experiments. Other examples of models without proton decay but with $n \to \bar{n}$ have been discussed in [334, 43, 30, 211].

Predictions for $\tau_{n\bar{n}}$ and dinucleon decay rates start with quark-level amplitudes for $\Delta\mathcal{B} = 2$ six-quark operators, which are then matched to the hadronic level by calculations combining lattice QCD and chiral effective field theory (χEFT). Depending on the quark-level operator, different hadronic-level operators are induced. Typically, the most important are one-body $n \to \bar{n}$ operators, giving rise to both $n \to \bar{n}$ as well as dinucleon decays at leading order in χEFT [314, 239]. The $n \to \bar{n}$ transition matrix elements of these operators have recently been calculated in exploratory lattice QCD calculations which directly connect the low-energy $n \to \bar{n}$ oscillation period to the parameters of BSM theories of $(\mathcal{B} - \mathcal{L})$-violation [340, 339]. In χEFT, $n \to \bar{n}$ is described by a Majorana n mass whose coupling can be fixed by matching to lattice QCD results. The same coupling can be used to calculate the deuteron lifetime [314] at leading order in χEFT, but at higher-order there are additional contributions from two-body operators encoding the strength of $\Delta\mathcal{B} = 2$ nuclear interactions. The presence of these relatively unexplored interactions currently gives rise to uncertainties in determinations of BNV decays of nuclei. With improvements in the hadronic and nuclear theory, this difference could instead be turned into a feature for eventually discriminating between different BSM explanations of $(\mathcal{B} - \mathcal{L})$-violation after observing *both* free and bound $n \to \bar{n}$ in experiments. Capitalizing on recent progress in lattice QCD calculations of nuclear matrix elements [166, 162] and *ab initio* nuclear theory calculations [241, 209] which include high-order nucleon-nucleon and nucleon-antinucleon chiral interactions, the lifetimes of some heavier nuclei of experimental interest, such as ^{16}O, could be reliably calculated using similar EFT methods, relying on controlled approximations to the SM to compute the required nuclear matrix elements. BSM physics parameters can be related to the lifetimes of even heavier nuclei using well-known existing nuclear models [176, 201, 71], themselves offering excellent phenomenologies to be probed.

1.5 Experimental $n \to \bar{n}$ Signals and Possible Backgrounds

Whether in a free beam or in a bound nucleus, the definitive observation of neutron to antineutron oscillation has yet to occur. Because of this, the oscillation time $\tau_{n\bar{n}}$ is now of order 10^8 s (approximately three yrs), both from free neutron beam searches at the Institut Laue-Langevin (ILL) [56], and in bound neutron searches, such as in oxygen at Super-Kamiokande [4, 6], or in deuterium at SNO+ [23]. Whether in a free or bound system, such a transformation, implying the effective conversion of matter into antimatter, leads to quite unique physical observables.

If a free, cold (low momentum) neutron beam is used to search for $n \to \bar{n}$, one usually employs a thin target of carbon for the beam to pass through before entering a beam dump. Due to the effective transparency (low cross-section) of carbon to normal neutrons, most pass through with little to no effect, and then are absorbed by a beam dump downrange. However, if a neutron was to spontaneously transform into an antineutron, annihilation on the target nucleus would occur near the surface to first order [180, 227], producing a fantastic, semi-spherical star of 2-7 mesons (most annihilation events are thought to create ~ 5 pions), reconstructable with little to no total momentum, and an excess of $\sim 1.9\,\mathrm{GeV}$ of invariant mass energy released for the annihilation of two nucleons. However, this is only a first order approximation of the true signal, as nuclear transport must occur for some (or all) of the mesons, leading to rescattering, absorption, evaporation and fragmentation of smaller excited remnant nuclei, and possibly knockout of constituent nucleons, making the signal less clean. Quite similarly, if the transformation were to occur within the nuclear environment (as shown for an $^{40}_{18}\mathrm{Ar}$ nucleus in Fig. 1.3), again producing multiple mesons in a roughly isotropic fashion before nuclear transport, possibly leading to knockout of protons or other nuclear remnants.

Differently from a thin annihilation target, when considering bound neutron searches for $n \to \bar{n}$ in large exposure (mass), underground detectors, one cannot immediately claim a clean, backgroundless search due to ever present cosmic ray muons or neutrons, and atmospheric neutrinos (atmospherics). In the case of *very* deep underground experiments, cosmics can largely be ignored for rare process searches such as $n \to \bar{n}$, but (primarily neutral current, NC) atmospherics most definitely cannot. In Fig. 1.4, a similar cartoon to the pion star of Fig. 1.3 can be seen, where an incoming atmospheric interacts with an $^{40}_{18}\mathrm{Ar}$ nucleus and undergoes deep inelastic scattering through a neutral weak current, similarly causing the creation of mesons, evaporation nuclei, and nucleon knockout after nuclear transport. However, unlike the signal for $n \to \bar{n}$, where to first order one expects a signal with $\sim 1.9\,\mathrm{GeV}$ of invariant mass and low momentum, atmospherics come in a wide variety of incoming energies and momenta, meaning that one would expect a spectrum of possible event topologies and kinematic observables. Secondarily, observation of correlation in the directionality (momentum) of the outgoing final state products is expected, which could be traced back to the incoming ν momentum, again theoretically allowing for separation of signal from atmospheric background.

1.5.1 Previous $n \to \bar{n}$ Searches

As illustrated in Fig. 1.5, free (or extranuclear) searches consist of a beam of focused free neutrons propagating in field-free (or quasifree [107, 360]) regions to an annihilation detector at which any antineutrons would annihilate with a thin target, giving rise to a final state dominated by charged pions, photons from π^0 decays, and nucleons (see again Fig. 1.3). Searches for free $n \to \bar{n}$

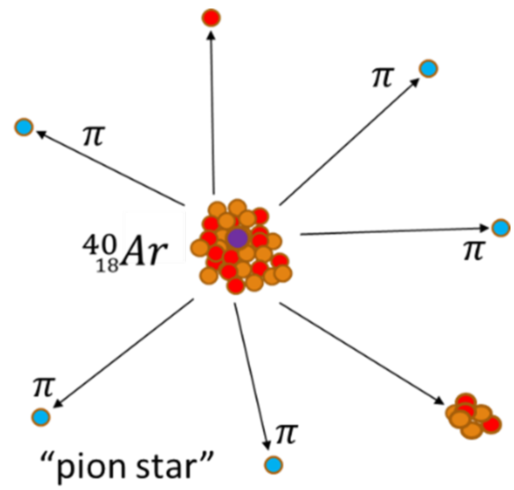

Figure 1.3: A simple "ideal" intranuclear $n \to \bar{n}$ topology is shown for $^{40}_{18}$Ar, also known as a "pion star", where pions are blue, protons red, neutrons orange, and the previously transitioned, pre-annihilation $\bar{n}$ is shown in purple for illustration. Here, a low amount of total momentum (due only to Fermi motion) yields a mostly spherical topology. With absence of final state interactions (intranuclear rescattering, meson absorption), one would expect to attain ~ 4-5 pions in the final state carrying ~ 1.9 GeV of total invariant mass. One should expect a similar topology and physical quantities for extranuclear oscillation (and subsequent annihilation) searches.

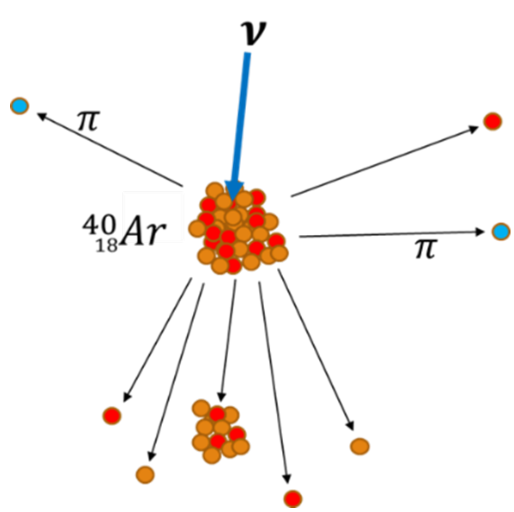

Figure 1.4: The predominant competing intranuclear $n \to \bar{n}$ background, shown in a simplified topology generated by an atmospheric neutrino, is shown for $^{40}_{18}$Ar. Again, pions are blue, protons red, neutrons orange. One should expect a wide range of total momentum and invariant masses from such signals, leading to a correlated directionality within the topology. It is these visual differences which permit visual machine learning to be used, to be discussed later in 4. Similar topologies are also possible for terrestrial extranuclear searches via cosmic ray interactions within the annihilation detector volume.

oscillation have taken place at the Pavia Triga Mark II reactor [117, 118] and at the ILL [189, 56]. The latter ILL search [56] provides the most competitive limit for the free neutron oscillation time: $\sim 8.6 \times 10^7$s.

The figure of merit (FOM) of sensitivity for a free $n \to \bar{n}$ search is best estimated not by the oscillation time sensitivity but by the quantity:

$$\mathrm{FOM} = \sum_i N_{n_i} \cdot t_{n_i}^2 \sim \langle N_n \cdot t_n^2 \rangle, \tag{1.8}$$

where N_{n_i} is the population of neutrons per unit time reaching the annihilation detector after t_{n_i} seconds of flight through a magnetically protected, quasifree conditioned [107, 360] vacuum region. As will be discussed later in this Chapter, the probability of a conversion is proportional to the (transit time)^2. Thus FOM $= \langle N_n \cdot t_n^2 \rangle$ is proportional to the approximate number of the conversions per unit time in a neutron beam which impinge on a target. Thus, a high precision free neutron search therefore requires a large flux of slow neutrons produced at a low emission temperature which are then allowed to propagate over a long time to allow conversions to occur.[5]

The experiment performed at the Institut Laue Langevin, completed in 1994, was the most sensitive to date, producing a limit of $\tau_{n\bar{n}} > 0.86 \times 10^9$ s [56]. The layout of this experiment is depicted in Fig. 1.6. The cold neutron beam emerged from curved guide system, effectively removing high energy backgrounds from the beam, and entered a conical reflector system 33.6 m in length, followed by the drift region and then a $100\,\mu$m thick, 1.1 m diameter, graphite target, and finally on into a beam dump. The target was surrounded by a tracking calorimeter with dimensions of about 4 m on a side, with an estimated signal efficiency of $52 \pm 2\%$. The performance of this experiment has set the standard to date, with no candidate annihilation events detected with one calendar year of operation at an integrated beam intensity on target of 1.25×10^{11} n/s. The ILL experiment demonstrates that cold neutron beam experiments can be designed to be background free, making them effectively limited by the drift time and the integrated intensity. Opportunities to increase both parameters exist in next generation experiments with neutron beams, leveraging the

[5] Summarizing, the basic strategy of a cold neutron beam experiment is to prepare an experimental region in which the neutrons move with freely (free from perturbing magnetic fields, material walls, and ambient gasses) for a length ℓ. After propagation through this "drift" region, the $\bar{n}$ amplitude will be approximately $(t_d/\tau_{n\bar{n}})$ now with $t_d = \ell/v$, where v is the velocity of the cold neutrons.

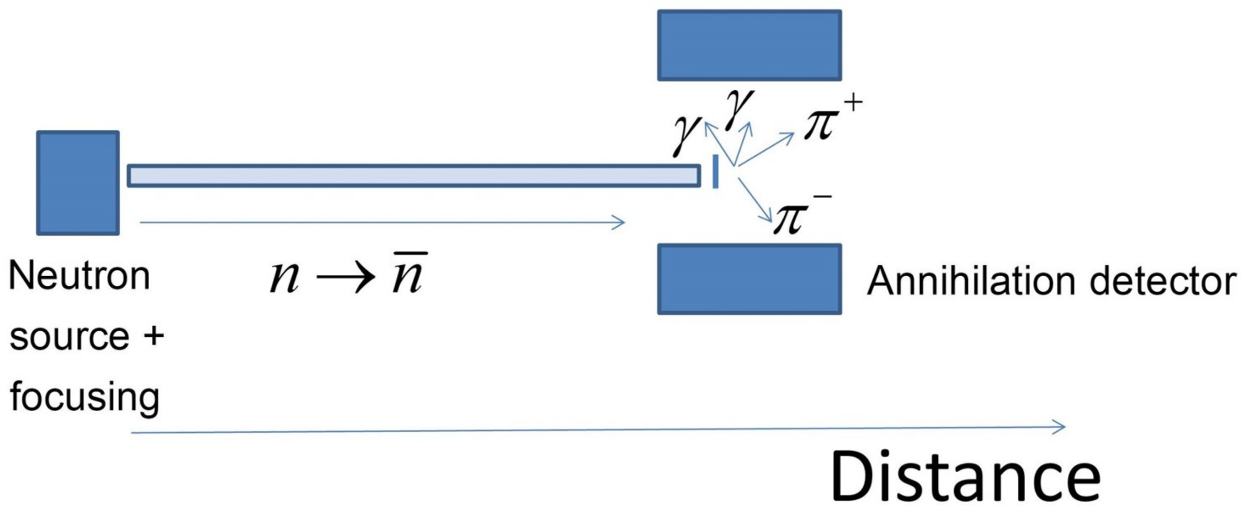

Figure 1.5: Illustration of the principles of free extranuclear $n \rightarrow \bar{n}$ searches, each producing semi-spherical topologies of pions and photons (from heavy mesonic resonance and pi^0 decays) for the signal. Courtesy of D. Milstead.

increased intensity available from modern neutron guide and optics technology and the potential availability of larger area beams with much greater intensity at next generation neutron facilities, such as the ESS.

Searches for $n \to \bar{n}$ using bound neutrons in large volume detectors look for a signature of pions and photons consistent with a $\bar{n}N$ annihilation event inside a nucleus, as illustrated in Fig. 1.3. Searches have taken place at Homestake [143], KGF [276], NUSEX [73], IMB [259], Kamiokande [390], Frejus [103], Soudan-2 [150], the Sudbury Neutrino Observatory [23], and Super-Kamiokande [4, 6, 237]; see Tab. 1.1. With Super-Kamiokande provides the most competitive search, for which an inferred free neutron oscillation time lower limit of $\sim 4.7 \times 10^8$s was obtained. Super-Kamiokande has also searched for dinucleon decays to specific hadronic final states, such as $nn \to 2\pi^0$ and $np \to \pi^+\pi^0$, as well as dinucleon decays into purely leptonic and lepton+photon final states [125, 389, 385]. Further limits on BNV decays have been obtained by relating these types of decays [214, 312, 216, 217].

Extranuclear and intranuclear $n \to \bar{n}$ experiments are complementary both in their sensitivity to new physics and the interpretability of their results [326, 421]. On a fundamental level, dimension $d = 9$, 6-quark operators can produce intranuclear transformations through a broader range of processes and with potential enhancement or suppression relative to free neutron experiments (see references in [326], especially [84]. As such, free neutron experiments provide a very precise and sensitive probe for neutron-antineutron transformations, and intranuclear experiments provide a "broadband" sensitivity to related dinucleon processes. Because free neutron experiments can be designed to be "background free" [56], they provide unambiguous discovery potential. Free neutron experiments also have (by controlling the magnetic field along the neutron trajectory) the ability to identify false positive results. This is in contrast to large underground experiments, for which a component of (irreduceable) background due to atmospherics is expected. A key question in this regard is to what degree the remarkable advances in tagging the interaction products in underground experiments such as DUNE (to be discussed later) can be supported by detailed models of the nuclear dynamics (for example pion scattering and absorption) in target nuclei.

The primary searches for baryon violating processes have been completed in large detectors deep underground, and each has a potentially significant associated background of atmospheric

Table 1.1: Experimental lifetime lower limits (90% CL) for $\tau_{n\bar{n}}$; note all limits appear as published. New, more accurate suppression factors for nuclei such as ^{16}O and ^{56}Fe have become available [201] which are generally a factor of two lower than initially *estimated* as $R^{\text{O}}_{\text{old}} \sim 1.0 \times 10^{23}\text{s}^{-1}$ and $R^{\text{Fe}}_{\text{old}} \sim 1.4 \times 10^{23}\text{s}^{-1}$ within prior publications; this effectively increases the hypothesized lower limits, which is illustrated by the $>$ symbols below. Also note that a newly computed suppression factor for ^{16}O will soon be available [70] using similar techniques to those discussed in [71], and will detailed in Chap. 2. There is also recent work using Super-Kamiokande I-IV data [409, 410, 6] which raises the prospective lower limit to $\tau_{n\bar{n}} \geq 4.7 \times 10^8$ s using machine learning techniques [6], though at great cost to signal efficiency. These techniques are similar to those to be discussed later in Chap. 4.

Experiment	Exposure (10^{32} n-yr)	τ_m (10^{32} yr)	$R\,(10^{23}\,\text{s}^{-1})$	$\tau_{n\bar{n}}(10^8\text{ s})$
ILL (free n) [56]	—	—	—	0.86
IMB (^{16}O) [259]	3.0	0.24	< 1.0	> 0.88
Kamiokande (^{16}O) [390]	3.0	0.43	< 1.0	< 1.2
Frejus (^{56}Fe) [103]	5.0	0.65	< 1.4	> 1.2
Soudan-2 (^{56}Fe) [150]	21.9	0.72	< 1.4	> 1.3
SNO (^{2}H) [104]	0.54	0.30	0.25	1.96
Super-K I (^{16}O) [4]	245	1.89	0.517	2.7
Super-K I-IV (^{16}O) [6]	1979	3.6	0.517	4.7

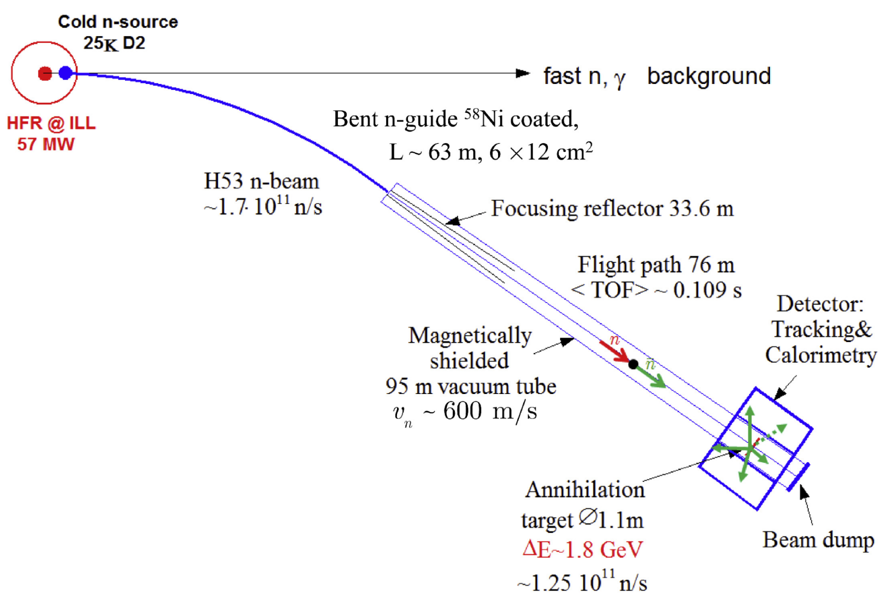

Figure 1.6: A schematic of the cold neutron beam experiment at the 58 MW research reactor at the Institut Laue Langevin in Grenoble [56] is shown. This experiment set the most stringent limits to date for $n \to \bar{n}$ using free neutrons at 0.86×10^8 s, and was backgroundless with a signal efficiency of $\sim 50\%$ thanks to a requirement of at least two charged reconstructed tracks. Improvements are expected through the NNBAR/HIBEAM experimental program at the ESS. Courtesy of W. M. Snow.

neutrinos where, respectively, electroweak neutral (and charge) current event topologies from large swaths of the atmospherics spectrum can obscure their true BSM signal. For example, in the search for intranuclear $n \to \bar{n}$ in the water-Cherenkov detector of Super-Kamiokande [4, 6], a considerable background from an expected 9.3 atmospheric neutirno interactions effectively removed any statistical significance from the observed 11 candidate events. None-the-less, the search remains the most far reaching of its kind, producing a lower limit for the intranuclear n lifetime in oxygen of $\tau_M = 3.6 \times 10^{32}$ yr; when converted into a free mean $n \to \bar{n}$ time, $\tau_{n\bar{n}}$, through the conventional theoretical nuclear physics formalism [175, 176, 178, 201, 71], wherein

$$\tau_M = R\tau_{n\bar{n}}^2. \tag{1.9}$$

and with an appropriately calculated *suppression factor*, R, this lower limit becomes 4.7×10^8 s ≈ 10 yr. This value can be contrasted with the predictions for the free mean $n \to \bar{n}$ time in [47], making it clear that a new landmark, sea-changing experiment(s) is necessary to further explore the pertinent parameter space for these phenomena. The value and derivation of R will be discussed in Sec. 2.5.

Historically, as shown in Fig. 1.7, it should be noted that as detector mass has increased it can be seen that the background rejection rate has not remained entirely constant, but instead, has proportionally decreased. This implies that the rate at which improvements are made upon limits of $\tau_{n\bar{n}}$ over time are actually less than linear or square root in rate, a highly dissatisfying notion. This implies that, in order to continue to probe higher and higher limits on $\tau_{n\bar{n}}$ in bound systems, new detector technology must be exploited and reconstruction improved for better particle identification, momentum and invariant mass reconstruction.

1.6 Post-Sphaleron Baryogenesis

Some compelling [304] and well motivated models of baryon number violation have been formulated wherein the proton decay plays little to no role (and similarly for a bound neutron). Importantly, models such as these utilize decays of new, high mass, colored, Higgs-like, (diquark) scalar fields which couple to quark (and possibly lepton) bilinear terms within the extended SM

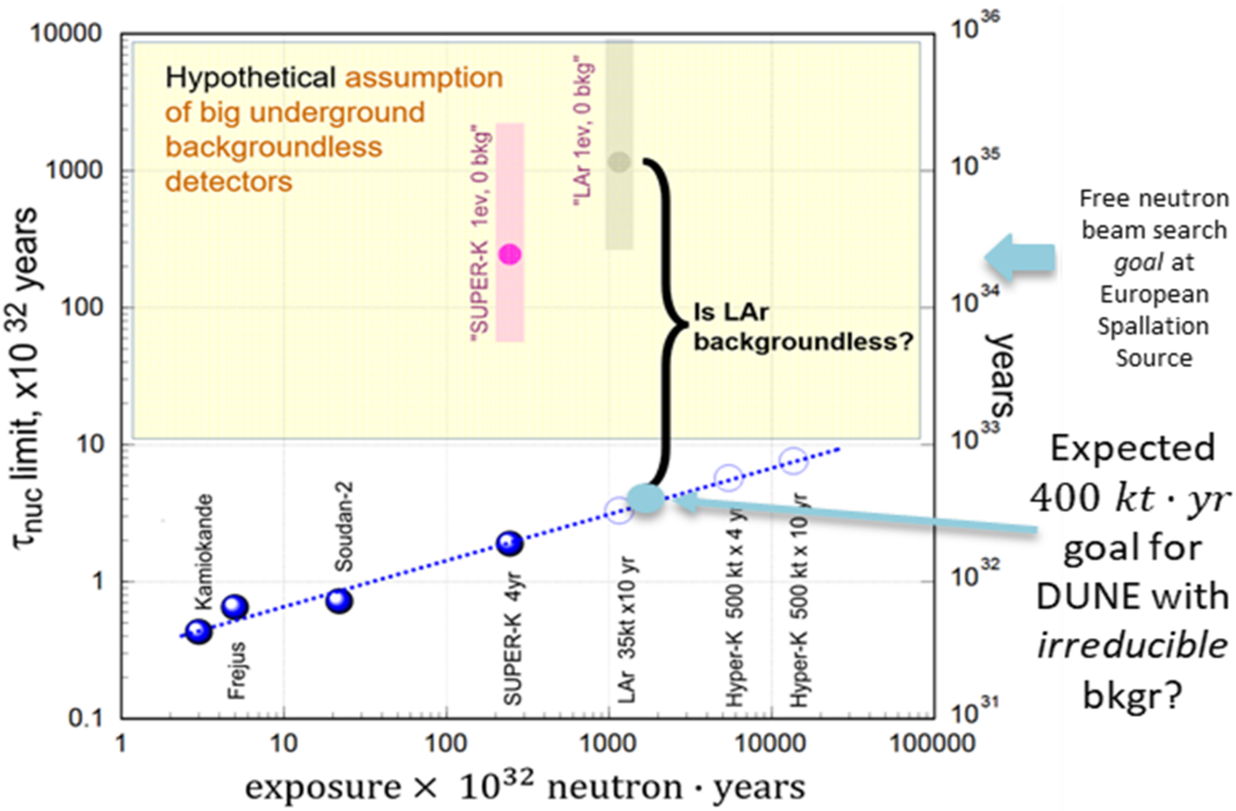

Figure 1.7: A simplified plot of $n \to \bar{n}$ searches within heavier nuclei, showing the nonlinear relationship between measured intranuclear lifetime limits vs. neutron exposure. This implies the likely irreducible nature of background as a function of detector mass, meaning that detection technology must improve greatly to attain any definitive discovery. Edited from original figure of Y. Kamyshkov.

lagrangian. These new fields can lead to baryon number violation through trilinear or quartic scalar interactions [43, 50, 47]. It should be noted that, while these models are not explicitly supersymmetric (though they can be), the cubic scalar interaction is similar to renormalizable terms in the superpotential that gives rise to $\mathcal{B}-\mathcal{L}$ violation in supersymmetric extensions to the SM [43]. This decaying scalar field S couples to the SM via a high-dimensional operator $\mathcal{O}$, which can take the form of

$$\mathcal{O} \propto \lambda \frac{qqqqqq}{M^5_{\sim EWPT}}, \tag{1.10}$$

and can be seen to be of dimension nine ($d = 9$). Unlike the immense mass scale seen in the proton decay operator, this one is far more manageable, and is potentially visible, given it would be closer to that of the electroweak phase transition temperature. A simplified Feynman diagram of a neutron-antineutron-like process, governed by a nine-dimensional operator, is shown in Fig. 1.8; the mixing parameter, α, represents the strength, or amplitude, of the process.

To account for the BAU and lack of matter-antimatter symmetry breaking ability of the sphaleron mechanism given conservation of $\mathcal{B}-\mathcal{L}$, new extensions to the SM can make use of post-sphaleron baryogenesis (PSB), wherein the dynamics occur at or below the TeV scale, critically following the epoch of the electroweak phase transition, and when any sphalerons have gone out of thermal equilibrium. One PSB model makes use of higher-order gauge groups which utilize spontaneous symmetry breaking at various scales down to the current SM group. The leading candidate for such a theory is due to Mohapatra et al. [50, 47], where PSB is realized through an upper limit symmetry group of

$$SU(2)_L \times SU(2)_R \times SU(4)_C, \tag{1.11}$$

utilizing a quark-lepton unified field theory generalization of the seesaw mechanism at the TeV scale; from here, this representation has its symmetries broken by a Higgs field—which splits the $SU(4)_C$ mass scale from the remaining ones above $\gtrsim 1000\,\text{TeV}$ (satisfying constraints from kaon decay)—down to the gauge group

$$SU(2)_L \times SU(2)_R \times U(1)_{\mathcal{B}-\mathcal{L}} \times SU(3)_C, \tag{1.12}$$

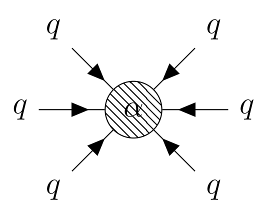

Figure 1.8: A simplified Feynman diagram of a general matter-to-antimatter, $d = 9$, six-quark operator. Quarks and antiquarks can be collected into valence triplets to form baryons, such as a neutron and antineutron, and so represents a transformational process.

This surviving group is then broken down again by another Higgs field to, which in turn eventually breaks once more to the group of the SM [13]. The $d = 9$ operator $\mathcal{O}$ from this model couples to a TeV-scale scalar field S from the exchange of color-sextet fields; $\mathcal{O}$ also leads to baryon violation through neutron-antineutron oscillation.

The S scalar field is contained within a complex field as a real, physical Higgs particle, and therefore can decay into six quarks or antiquarks (or, with appropriate crossing symmetries, a mixture of both), violating baryon number by two units with no associated change in the lepton number of the universe. These same interactions, upon insertion of a vacuum expectation value (VEV) for S, leads to neutron-antineutron oscillations.

Considering Fig. 1.9, if the diquarks Δ_{qq} have TeV range masses, then they will lead to large rates for baryon violating processes, allowing $n \to \bar{n}$ to remain in equilibrium until the TeV scale (near the electroweak phase transition). Thus, as previously discussed, this would only continually erase any pre-existing matter-antimatter asymmetry through the sphaleron process; therefore, a new process (the PSB) must be commissioned, which can simultaneously satisfy all of Sakharov's conditions. If one assumes that S is light, then it will go out of equilibrium and decay after the electroweak phase transition, producing six quarks (antiquarks), and so asymmetrically generate the baryon asymmetry.

In closing this rather narrow and simplified discussion of baryogenesis, an overview of the theoretical landscape seems pertinent, as seen in Fig. 1.10. Of course, such a theoretical landscape can include leptogenesis [207, 149]. PSB is a leading and highly complimentary candidate to explain the BAU in a testable way due to the lower energy scales needed to probe it (and possible to do so with low energies and long time scales with such phenomena as $n \to \bar{n}$).

Over the past several pages, some detail has been discussed of the inability for popular BSM theories and searches (such as proton decay) to explain the BAU. Exciting new methods, such as PSB, can be instead used to attain all of Sakharov's conditions, along with a plausible BAU ratio (and even primordial CP asymmetry). The extension to the SM is both simple and elegant, providing rich physics for experimental study at current or soon-to-be visible energy ranges on the order of $\sim$ 10-100 TeV. Such testability is arguably vital to the future of particle physics. It is with these motivations in mind that searches for $n \to \bar{n}$ using two experimental methodologies

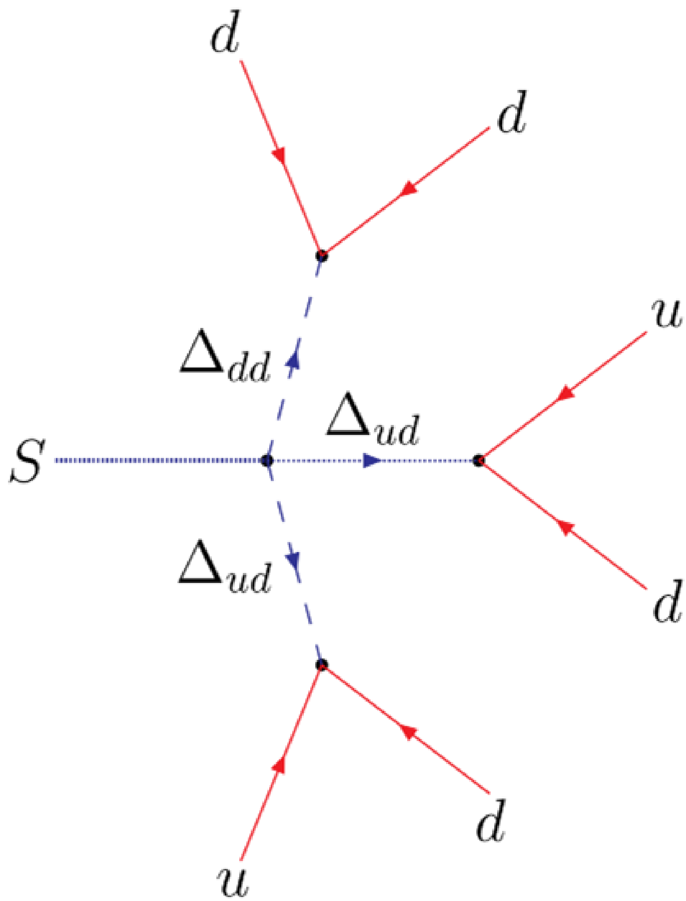

Figure 1.9: A proposed Feynman diagram for $n \to \bar{n}$ (upon inversion), fully derived in the leading PSB model [50, 47]. Such a diagram, along with accompanying loop diagrams, can explain the BAU through a new scalar field S, which decays into heavy diquarks.

(utilizing free or *extranuclear*, and bound or *intranuclear* neutrons) will be discussed throughout this thesis.

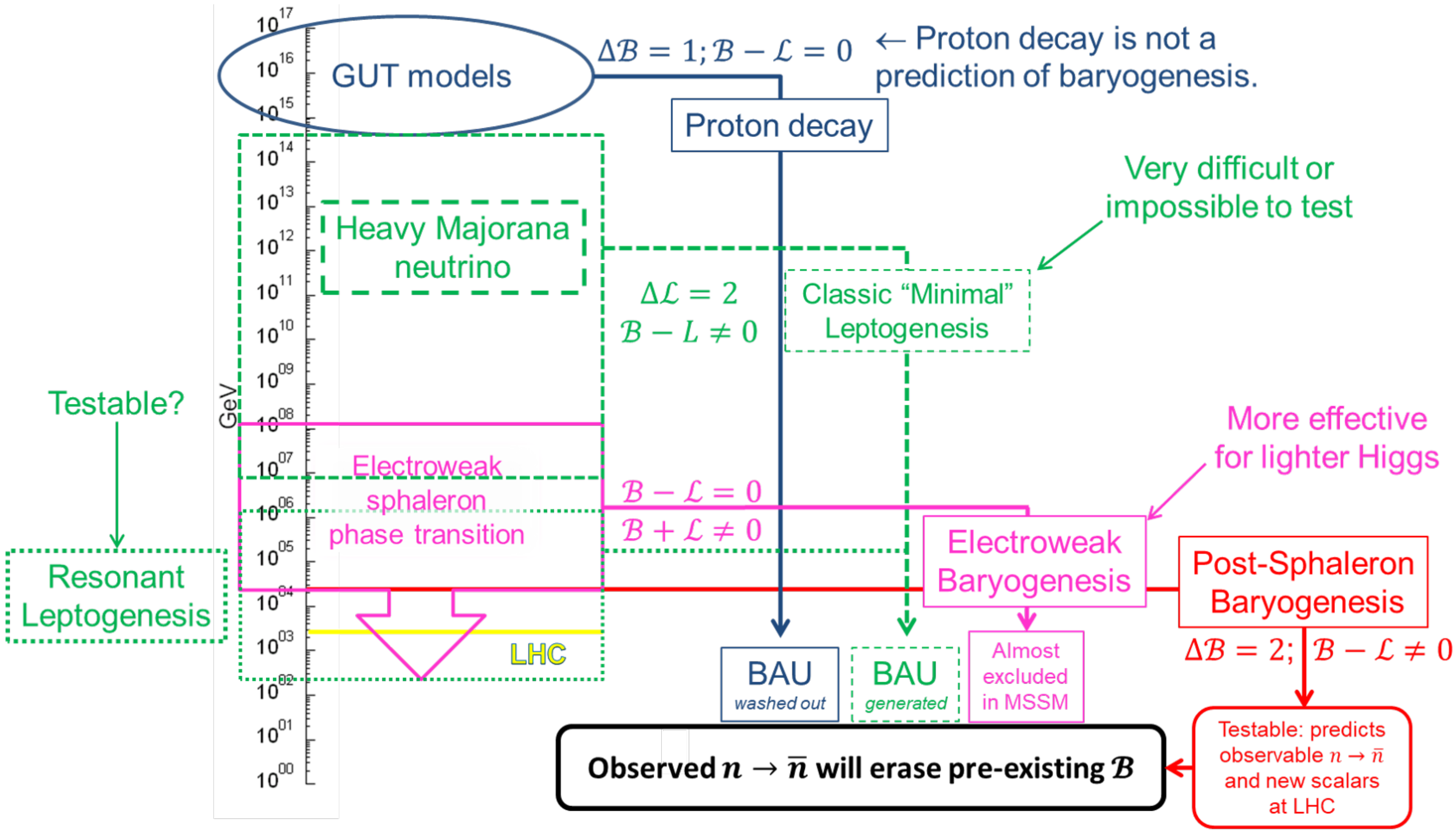

Figure 1.10: A simplified overview of hypothetical new physics' testability by prospective energy regimes. Approximate scales or scale ranges are shown; post-sphaleron baryogenesis is given in red, leptogenesis models in green, electroweak baryogenesis in pink, and grand unification in dark blue. For post-sphaleron baryogenesis, consider [50, 47]; for minimal leptogenesis [207]; for resonant leptogenesis [106]. Note that minimal leptogenesis can have a lowered (slightly fine-tuned) scale of $\sim 10^6$ GeV by taking account of effects such as neutrino flavor within the expanding plasma in the early universe [297]. Remade in collaboration with Y. Kamyshkov.

1.6.1 Pertinent PSB Parameter Space

It should be noted that PSB has a remarkable property not shared by most BSM theories: though compelling, it can in principle be invalidated given that it predicts an absolute maximum for $\tau_{n\bar{n}}$. This can be seen via the abrupt cutoff of the probability density shown in Fig. 1.11, describing all permissible values of $\tau_{n\bar{n}}$. The methodology to derive this distribution involves a calculation of parameters allowed by constraints put upon couplings within the extended lagrangian density given the new terms' contribution to various observed processes, and then randomly sampling from the range of these parameters in Monte Carlo in order to devise an optimal oscillation time [47].

Overlaid on top of Fig. 1.11's green probability distribution[6] are the various limits that DUNE and ESS could reach in principle, assuming a single event is observed above any background. Not all too dissimilar from the design of the original ILL beam search, in red one sees the reach of the baseline ESS NNBAR collaboration design, which would probe $\gtrsim 1000$X the original ILL sensitivity with only three years of beamtime, assuming zero background and $\sim 50\%$detector efficiency (a la ILL [56], though this is expected to increase). The blue line to the right shows the absolute reach of $400\,$kt·yrs of exposure time for the DUNE far detector to be ~ 13500X the limit of ILL, presuming a zero background and a 25% signal efficiency. Obviously, this differs greatly from the dark blue line to the far left, showing the reach of Super-Kamiokande I-IV [6], which contains significant background. Of course, the truth is somewhere in the middle, with quasifree (or potentially free) background searches seeming possible at the cost of efficiency; these backgrounds will be discussed in more detail Sec. 4.2[7]. A full scale, detailed recalculation of the possible reach of ESS given recent political developments has been completed [204], and detector design, simulation, and optimization is underway [19, 67]. Some new developments in assessing DUNE's capabilities will be discussed in Chap. 4.

[6]There is active developing work by Dev *et al.* to update the $\tau_{n\bar{n}}$ probability distribution in consideration of recent work [407, 340, 339].

[7]Considering Fig. 1.11, the question becomes: can the DUNE intranuclear search be improved? What is the error bar on this search? How can one estimate the error band as it relates to theoretical uncertainties in the modeling of the rare process? This is part of the subject of this thesis and forthcoming publications.

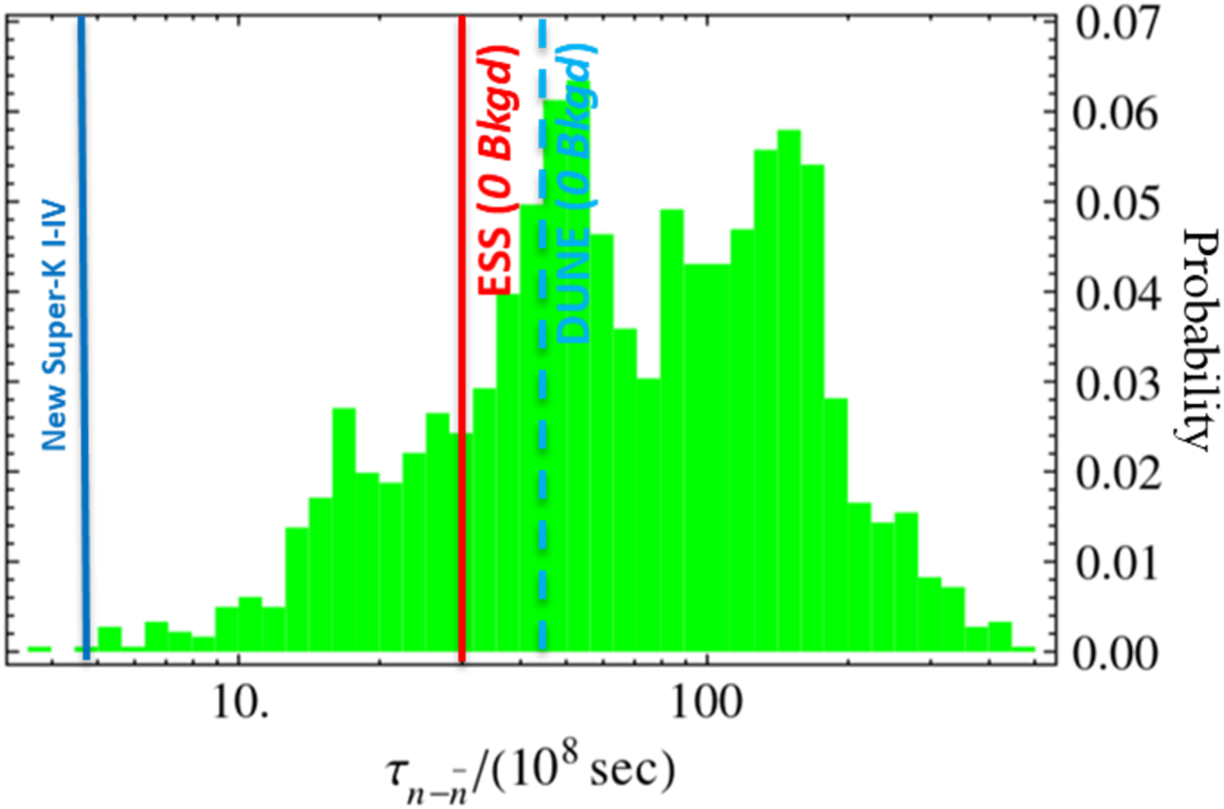

Figure 1.11: Expected *converted* $\tau_{n\bar{n}}$ lower limits are shown compared to expected theoretical values of $\tau_{n\bar{n}}$ within post-sphaleron baryogenesis [47]. For an idealized DUNE detector, shown in blue, a 25% signal efficiency and zero background has been assumed; previous DUNE simulation studies [257] using automated boosted decision tree analysis methods are not shown here, but will be discussed later in Chap. 4; these have lower efficiencies and are not backgroundless. For the NNBAR experiment at the ESS, one assumes a 1000-fold increase in the sensitivity or figure of merit ($\langle Nt^2 \rangle$) [56, 204, 271, 19] with an implicit assumption of a similar signal efficiency and backgroundless search, as in ILL [56]. These are also compared to measured lower limits from Super-Kamiokande I-IV [409, 410, 6], while Super-Kamiokande I [4] is too low to be shown. Adapted from [47].

1.7 $n \to \bar{n}$ Phenomenology

That Nature must violate baryon number is a statement that can be made with confidence. However, should Nature have chosen BNV-only processes, then not only does this imply that the channels which are available for high precision study are limited, but also that a BNV signal is *fragile*. Each channel can require special experimental conditions and apparatuses in order for BNV to manifest itself.

1.7.1 Extranuclear $n \to \bar{n}$

To review briefly, in the SM the neutron has only the Dirac Mass term $m\overline{n}n$ which conserves $\mathcal{B}$. However, as mentioned, $n \to \bar{n}$ can proceed by effective six-quark operators. These involve light quarks u and d and violate $\mathcal{B}$ by two units,

$$\mathcal{O}_{\Delta\mathcal{B}=2} = \frac{1}{\mathcal{M}^5}(udd)^2 + \text{h.c.}\,, \tag{1.13}$$

where $\mathcal{M}$ is a large cutoff scale originating from new physics beyond the Standard Model, and so can induce a Majorana mass term

$$\frac{\alpha}{2}(n^T C n + \bar{n} C \bar{n}^T) = \frac{\alpha}{2}(\overline{n_c} n + \overline{n} n_c)\,, \tag{1.14}$$

where C is the charge conjugation matrix and $n_c = C\overline{n}^T$ stands for the antineutron field.[8] Thus, the $n \to \bar{n}$ matrix element/mixing mass term α depends on the scale of new physics:

$$\alpha = \frac{C\Lambda_{\text{QCD}}^6}{\mathcal{M}^5} = C\left(\frac{500\text{ TeV}}{\mathcal{M}}\right)^5 \times 7.7\cdot 10^{-24}\text{ eV}\,, \tag{1.15}$$

with $C = O(1)$ being the model dependent factor in the determination of matrix element $\langle\bar{n}|\,\mathcal{O}_{\Delta\mathcal{B}=2}\,|n\rangle$. The direct bound on $n \to \bar{n}$ oscillation time $\alpha^{-1} = \tau_{n\bar{n}} > 0.86 \times 10^8$ s [56], i.e. $\alpha < 7.7 \times 10^{-24}$ eV, corresponds to $\mathcal{M} \gtrsim 500$ TeV. By improving the experimental sensitivity by three orders of magnitude, one could test for new physics above the PeV scale.

[8] Generically these operators induce four bilinear terms $\overline{n}n_c$, $\overline{n}\gamma^5 n_c$, $\overline{n_c}n$ and $\overline{n_c}\gamma^5 n$, with complex coefficients. However, by proper redefinition of fields, these terms can be reduced to just one combination (Eq. 1.14) with a real α which is explicitly invariant under transformations of the charge conjugation ($n \to n_c$) and parity ($n \to i\gamma^0 n$, $n_c \to i\gamma^0 n_c$) [101, 100].

Free conversion of $n \rightarrow \bar{n}$ can be understood as the evolution of a beam of initially pure neutrons

$$|\Psi(t)\rangle = \begin{pmatrix} \psi_n(t) \\ \psi_{\bar{n}}(t) \end{pmatrix} = e^{-i\hat{\mathcal{H}}t}\,|\Psi(t=0)\rangle\,, \qquad |\Psi(t=0)\rangle = |n\rangle = \begin{pmatrix} 1 \\ 0 \end{pmatrix}, \tag{1.16}$$

described by 2×2 Hamiltonian

$$\hat{\mathcal{H}} = \begin{pmatrix} E_n & \alpha \\ \alpha & E_{\bar{n}} \end{pmatrix}, \tag{1.17}$$

where E_n and $E_{\bar{n}}$ are the neutron and antineutron energies, respectively. While the neutron and antineutron masses are equal by CPT invariance, E_n and $E_{\bar{n}}$ are not generically equal due to the environmental effects which act on the neutron and antineutron states differently; these include the presence of matter or nuclear potentials, magnetic fields, or perhaps some hypothetical fifth forces [18, 51].

The probability to find an antineutron at a time t is given by $P_{n\bar{n}}(t) = |\psi_{\bar{n}}(t)|^2$, or explicitly

$$P_{n\bar{n}}(t) = \frac{\alpha^2}{(\Delta E/2)^2 + \alpha^2} \sin^2\left[t\,\sqrt{(\Delta E/2)^2 + \alpha^2}\right] e^{-t/\tau_\beta}, \tag{1.18}$$

where $\Delta E = E_n - E_{\bar{n}}$ and τ_β denotes the mean decay time of the free neutron. It thus becomes immediately clear that the probability of a conversion is suppressed when the energy degeneracy between neutron and antineutron is broken. In particular, for free neutrons suppression occurs due to the interaction of the magnetic field ($B \simeq 0.5\,\mathrm{G}$ at the Earth) with the neutron and antineutron's magnetic dipole moments ($\vec{\mu}_n = -\vec{\mu}_{\bar{n}}$), equivalent to $\Delta E/2 = |\vec{\mu}_n \vec{B}| \approx (B/1\text{ G}) \times 10^{-11}\,\mathrm{eV}$ in Eq. 1.18. To prevent significant suppression of $n \rightarrow \bar{n}$ conversion, one must maintain so called quasifree regime $|\Delta E|t \ll 1$ which can be realized in vacuum in nearly zero magnetic field [107, 360, 161]. In this case Eq. 1.18 reduces to

$$P_{n\bar{n}}(t) = \alpha^2 t^2 = \frac{t^2}{\tau_{n\bar{n}}^2} = \left(\frac{t}{0.1\text{ s}}\right)^2 \left(\frac{10^8\,\mathrm{s}}{\tau_{n\bar{n}}}\right)^2 \times 10^{-18}, \tag{1.19}$$

where $\tau_{n\bar{n}} = 1/\alpha$ is characteristic oscillation time. Since in real experimental situations the free neutron flight time is small, $t \sim 0.1\,\mathrm{s}$ or so, the exponential factor related to the neutron decay can be neglected in Eq. 1.18. This necessitates magnetic shielding for searches utilizing a neutron beam [117, 118, 189, 56], and so HIBEAM and NNBAR must employ such shielding. Note that in the experiment [56] performed at the ILL, the magnetic field was suppressed below $\sim 10\,\mathrm{mG}$. The effects of imperfect vacuum (residual gas pressure) on the observation of neutron to antineutron transformation were similarly discussed with respect to their effects upon the quasifree condition in [155, 56, 266, 235].

1.7.2 Some Details on New Matrix Element Results

Within the framework of an assumed ultraviolet extension of the Standard Model that features $n \to \bar{n}$ transitions, one has a prediction for the coefficients of the various types of six-quark operators in the resultant low-energy effective Lagrangian, and the next step in obtaining a prediction for the $n \to \bar{n}$ transition rate of free neutrons is to estimate the matrix elements of these six-quark operators between $|n\rangle$ and $|\bar{n}\rangle$ states. Since the six-quark operators have dimension 6, their matrix elements are of the form Λ_{eff}^6. The relevant scale is set by the QCD confinement scale, $\Lambda_{QCD} \sim 0.25$ GeV, so one expects, roughly speaking, that the matrix elements are of order $\sim \Lambda_{QCD}^6 \simeq 2.4 \times 10^{-4}$ GeV^6, and this expectation is borne out by both early estimates using the MIT bag model [333, 334] and recent calculations using lattice QCD (LQCD) [407, 340, 339, 127, 126], including approximate assessments of modeling uncertainties. The LQCD results in [340, 339] indicate that for most operators the corresponding Λ_{eff} is larger by $\sim$ 10-40$\%$ over the Λ_{eff} characterizing the MIT bag model results, i.e., a factor $\sim$ 2-8 for Λ_{eff}^6, and thus for the matrix elements themselves. This suggests that overall experimental sensitivities may reach higher than previously expected [407]. This being said, direct constraint of PSB and its predicted upper bound on $\tau_{n\bar{n}}$ [47] (consider again Fig. 1.11) is slightly different, as this limit is derived not from tree level amplitudes but instead from loop diagrams involving W-boson exchange. In [47], larger MIT bag-model estimates are used, and so the LQCD matrix element for this particular amplitude appears smaller by some $\sim 15\%$ [339]; this leads to an expectation that the upper limit for $\tau_{n\to\bar{n}}$ will be shifted slightly up by roughly the same proportion. The community's integration of this new knowledge is continuing, and still more accurate predictions are being actively discussed and developed [167]. Similar computational methods may eventually advance peripheral modeling of secondary processes, such as the annihilation itself and background interactions.

1.7.3 Intranuclear $n \to \bar{n}$

Consider a nucleus, large enough to be considered spherical, of some diameter. Modeling the constituent nucleons within this nucleus as a Fermi gas, they can be thought to bounce around a spherical well with some momentum. From this momentum, an average speed can be extracted, and from this, a free flight time across the diameter of the nucleus. From such simple considerations, a bound "experimental" flight time can be derived, where $t_A \sim 10^{-23}\,\mathrm{s}$. Thus, one can apply the above equation for the free oscillation probability to this simplified situation, although treating the experimental time as $t \equiv t_{exp} \sim t_A$. Thus, when approximating the transition probability as a decay width Γ, one derives:

$$\frac{P_A[n(t)=\bar{n}]}{t_{exp}} \propto R \sim \Gamma = \frac{1}{\tau_A} \to P_{free}[n(t_{exp} \sim 10^{-23}\,\mathrm{s}) = \bar{n}] \approx \left(\frac{10^{-23}\,\mathrm{s}}{\tau_{n\bar{n}}}\right)^2 \tag{1.20}$$

$$\to \tau_A \approx R\tau_{n\bar{n}}^2 \sim \left(\frac{10^{8}\,\mathrm{s}}{\tau_{n\bar{n}}}\right)^2 \times 10^{31}\,\mathrm{yr}, \tag{1.21}$$

where the need for a suppression factor, $R = [\mathrm{s}^{-1}]$, has been recognized to be the reciprocal of the square of the bound flight time, which thus relates the bound oscillation time to the free oscillation time. One can also estimate this by considering the effective energy difference in the nuclear potential well for neutrons and antineutrons:

$$\tau_A = \frac{\Delta V_{nvs.\bar{n}}}{\hbar}\tau_{n\bar{n}}^2 = R\tau_{n\bar{n}}^2. \tag{1.22}$$

It turns out that both of these simple methods are good, *approximate* ways to estimate the suppression factor *to within an order of magnitude*, wherein

$$R \sim \frac{1}{10^{-23}\,\mathrm{s}} \sim 10^{22}\mathrm{s}^{-1}. \tag{1.23}$$

This is quite close to the more rigorously calculated values seen in [175, 176, 179, 201, 71], and a short synopsis of the calculation techniques is available in section of [243, 71]. For instance, for $^{16}_{8}\mathrm{O}$ (within water molecules used by Cherenkov detectors like Super-Kamiokande [201]) and $^{40}_{18}\mathrm{Ar}$ nuclei (DUNE) [71], it has been calculated that

$$R_{^{16}\mathrm{O}} \approx 5.2 \times 10^{22}\,\mathrm{s}^{-1} \pm 15\%\,, \quad \text{and} \quad R_{^{40}\mathrm{Ar}} \approx 5.6 \times 10^{22} \pm 15\%\,. \tag{1.24}$$

This might lead one, possibly, to discount the notion of searching for the transformation in matter; however, with large mass (large neutron density), underground, and hopefully low background detectors, it is possible to attain highly competitive lower limit results for the mean oscillation time, $\tau_{n\bar{n}}$. However, it is important to stress the usefulness of both techniques due to the possibility that if such a phenomena were to exist, any discrepancy between the oscillation time measurements made using free or bound neutrons could highlight key misunderstandings in nuclear theory and structure, possibly pointing to yet more BSM physics. Details of the computation of new intranuclear suppression factors will be detailed in Chap. 2.

Caution is required when comparing limits and sensitivities for free and bound neutron searches. Calculations relating τ_A and $\tau_{n\bar{n}}$ rely on underlying model assumptions, such as a point-like conversion process, while the physics behind $n \to \bar{n}$ conversion is *a priori* unknown[9]. The visibility of a signal in a bound neutron search could therefore be arbitrarily suppressed compared to a free search, or vice-versa. For example, a recently proposed model of low scale BNV contains the possibility of a suppressed (or even enhanced) bound neutron conversion probability [84]. There can also exist environmental effects which can affect free $n \to \bar{n}$, even if the magnetic field is properly shielded. These effects can be related, e.g. with long range fifth-forces induced by very light $\mathcal{B} - \mathcal{L}$ baryophotons. Present high-sensitivity limits on such forces [408] with Yukawa radius comparable to the Earth radius or to sun-Earth distance still allow significant contribution to the neutron-antineutron energy level splitting, which in fact can be as large as $\Delta E \sim 10^{-11}\,\mathrm{eV}$ or so [18, 51]. Consideration of free and bound neutron searches is thus complementary: neither makes the other redundant, and indeed they require one another to help constrain the underlying physical process.

[9]This being said, there has been great progress in a broad program of intranuclear suppression factor calculations across many nuclei which show rather remarkable similarity despite their quite disparate theoretical origins[71, 314, 239, 175]. One should also note that intranuclear experiments like SNO [23] have chosen specific targets (deuterium) and techniques to minimize contamination from these and other potentially model dependent nuclear effects, including avoiding excessive final state interactions.

1.8 Summary of $|\Delta\mathcal{B}| = 2$ Experimental Opportunities

Future facilities will provide compelling and complementary opportunities to further explore both BNV and dark sector candidates using free n's alongside more traditional intranuclear searches for $n \to \bar{n}$ and dinucleon decays. Searches for free and intranuclear $n \to \bar{n}$ are both needed to determine the source(s) of BSM physics. The European Spallation Source (ESS), currently under construction, will be the world's most powerful pulsed source of cold n's. Current and future large underground detectors such as Super-Kamiokande [6], DUNE [257], and Hyper-Kamiokande [5] offer substantial increases in mass, exposure, and reconstruction capabilities, and thus hypothetically higher sensitivities to rare processes (see again Fig. 1.7). It should be noted that existing US-based Basic Energy Science facilities, including but not limited to the Spallation Neutron Source (SNS) and High Flux Isotope Reactor (HFIR) at ORNL [121, 120], can also be leveraged for research and development for complementary science on short time scales, and are also interesting possibilities to consider with their planned future upgrades. Examples include an optimized future $100\,$MW HFIR and the planned Second Target Station at the SNS [165, 3].

In the intervening period since the last free neutron search at the ILL [56], there has been substantial progress in both development of advanced neutron optics and annihilation-generated particle detection capabilities. By taking advantage of the current state of the art at future neutron sources, an improvement in sensitivity of $\gtrsim 1000\times$ILL [205, 272, 356, 326] becomes possible, reaching $\tau_{n\bar{n}} \sim 10^{9-10}\,$s [305, 19, 235]. The most promising opportunity for a future free $n \to \bar{n}$ search comes from an ambitious proposal by the NNBAR Collaboration [326, 19] at the ESS. The ESS has included an important design accommodation for NNBAR to achieve the high neutron intensities needed for this search, the Large Beam Port (LBP), which has now been constructed. Optimization of the cold source for NNBAR is underway via the Horizon2020 HighNESS project[10] [19, 356]. As the ESS is expected to run at $5\,$MW operation after $\gtrsim 2030$, a staged program accessing the physics questions of dark sectors through sterile n' searches such as $n \to n'$, $n \to n' \to n$ [121] and $n \to n' \to \bar{n}$ has been developed, taking advantage of the existing neutron scattering facilities at ORNL, and continuing with an optimized experimental setup on the

[10]Thanks to my many ESS NNBAR/HIBEAM colleagues for their collaboration on this work.

lower intensity fundamental physics ANNI beamline [379] as part of the HIBEAM program [19]. Much of this will be discussed later as a part of the HIBEAM/ANNI experiment in Sec. 3.1.

Another proposed approach to the free search for $n \to \bar{n}$ utilizes a material trap for the long-term storage of ultracold neutrons. With a UCN source production of $10^8\,n$/s, the increase of the experimental sensitivity can be about 10-40×ILL, and so reaching $\tau_{n\bar{n}} \sim 10^{8-9}$ s, depending on the model of n reflection from the material trap walls [366, 196, 192, 193, 195, 194]. The sensitivity of the experiment with UCN is lower than in the baseline NNBAR beam experiment at the ESS; however, realization of the experiment with UCN is less expensive and much more compact. In addition, this approach presents an important opportunity to perform a free search in an independent experiment using a very different methodology.

In similarity to free n searches, observable rates for intranuclear dinucleon processes, including $n \to \bar{n}$, show great complementary experimental reach across large underground experiments such as Super-Kamiokande [4, 409, 6], DUNE [257], and Hyper-Kamiokande [5]. Prodigious amounts of neutrons in these large mass detectors provide the capacity to overcome expected intranuclear suppression of $n \to \bar{n}$ rates [71, 314], though irreducible atmospheric ν backgrounds seem to persist at great cost to signal efficiency [409]. Similarly, when comparing to background, intranuclear final state interactions of annihilation-generated mesons can lead to some uncertainty surrounding the region of interest when investigating reconstructed total momentum and total invariant mass [71, 4, 409]. Better modeling of the annihilation location, process, transport, and differences across many nuclear model configurations are all currently being investigated. Given the special expected topological aspects of $\bar{n}$ annihilation within nuclei, there has been much progress to date in applications of deep learning and other automated analysis techniques such as boosted decision trees to the separation of these rare process signals from background. When converting through the traditional intranuclear suppression factor formalism [176, 71], intranuclear searches are expected to probe $\tau_{n\bar{n}} \gtrsim 10^{8-9}$ s.

TeV-scale colored scalars responsible for dinucleon decay, $n \to \bar{n}$, and low-scale baryogenesis can be searched for at the LHC via dijet resonances. Current LHC limits on heavy scalar diquarks are already very stringent: $M_{qq} \gtrsim 7.5$ TeV [377]. This could be further improved at the future HL-LHC, and provide a complementary probe of $\Delta\mathcal{B} = 2$ processes. In the context of a given model with specific flavor structures, such as PSB [47], the LHC limit could be somewhat relaxed, especially if there is a sizable branching ratio to final state quarks involving the third generation. These channels, like tj and tb, are directly relevant for $n \to \bar{n}$ and should be searched for in future dijet analyses; such future collider constraints are expected to close portions of interesting parameter space to future free $n \to \bar{n}$ searches. A future $100\,$TeV collider could in principle probe the *entire* allowed parameter space of compelling PSB models.

1.8.1 Sensitivities of NNBAR, DUNE, and Other Experiments

Limits on the free $n \to \bar{n}$ oscillation time, together with the potential sensitivities of HIBEAM (Sec. 3.4) (assuming three years of running at $1\,$MW) and NNBAR (assuming three years of running at $5\,$MW, and so too a three orders of magnitude improvement in ILL units [204, 271, 17]) are shown in Fig. 1.12. Also shown is a projected *converted* free oscillation time lower limit for bound neutron conversions within ^{40}Ar nuclei within the future DUNE experiment [257], where $\tau_{n\bar{n}} \geq 5.53 \times 10^8\,$s for an assumed exposure of $400\,$kt·years[11]; There is as yet no estimate for the expected $n \to \bar{n}$ sensitivity for Hyper-Kamiokande. Simulation studies of modeling systematics[12] for intranuclear $n \to \bar{n}$ within ^{40}Ar continue within the DUNE High Energy Physics Working Group, and some progress will be featured in this thesis (Chap. 4) and in a future publication [72].

As discussed in [19, 204], consideration of limits or sensitivities on the free neutron oscillation time for free and bound neutron searches is, to a certain extent, an *apples and oranges* comparison. There is overlap in physics potential, but neither renders the other redundant [421]. Indeed, both would play essential and complementary roles in both the definitive establishment of and cross reference for any future discovery.

1.9 Dark Matter, Mirror Matter, and Connections to $n \to n'$

The question of the origin of the BAU may be related to that of the nature of dark matter, such as via a cobaryogenesis between ordinary and dark sectors [85]. The mirror sector, a hypothetical dark

[11] This limit increases to $\sim 6.0 \times 10^8\,$s with the inclusion of a recently computed suppression factor for ^{40}Ar [71], which will be discussed at length in Chap. 2.

[12] Automated analysis improvements eventually hope to eliminate most all atmospheric neutrino backgrounds, and the effects of the responses of these machine learning techniques to various model inputs are being considered, some of which will be shown in Chap. 4.

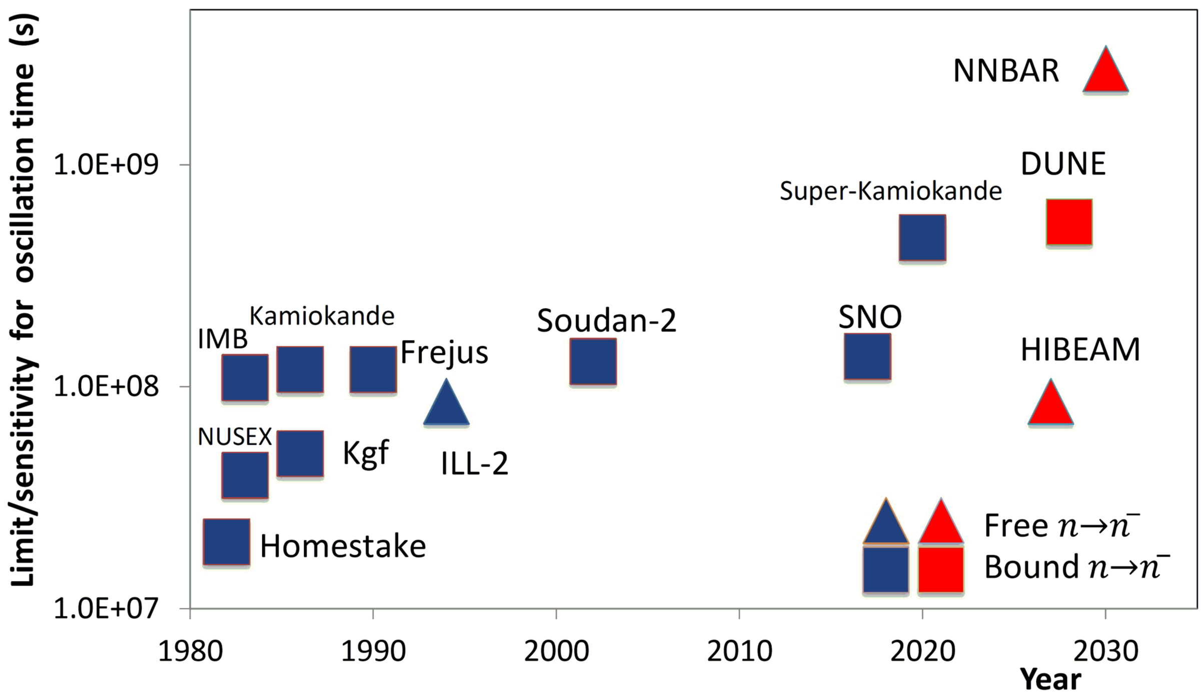

Figure 1.12: Lower limits on the free neutron oscillation time from past (blue) experiments on free and bound neutrons. Projected future (red) sensitivities from HIBEAM and NNBAR are shown together with the expected sensitivity for DUNE [257]. The most recent and competitive result from the ILL is also shown [56]. Limits from bound neutron searches are given from Homestake [143], KGF [276], NUSEX [73], IMB [259], Kamiokande [390], Frejus [103], Soudan-2 [150], SNO [23], and the most recent Super-Kamiokande analysis [6]. For the bound neutron experiments, various model-dependent intranuclear suppression factors [201, 175, 177, 275] are used to estimate a free neutron transformation time lower limit. Courtesy of D. Milstead.

sector populated by cold atomic or baryonic matter originating from a sterile parallel gauge sector (a replica of the ordinary Standard Model's *active* sector), is a viable dark matter candidate [80, 94]. Such a sterile sector may provide another experimental portal onto $n \to \bar{n}$ physics, as well as motivate synergistic research and design initiatives. $\Delta(\mathcal{B} - \mathcal{L}) = 1$ interactions between ordinary and dark sectors may be at the origin of ordinary (active) and mirror (sterile) ν mixing [102] or neutron–mirror neutron mixing, leading to neutron–mirror neutron transitions ($n \to n'$) [90, 82]. In the early universe, such mixing can cogenerate both ordinary and mirror $\mathcal{B}$ asymmetries [78, 85] giving a common origin to the observed baryonic and dark matter fractions of the universe, $\Omega_{\mathrm{DM}}/\Omega_{\mathrm{B}} \simeq 5$ [80, 81]. In contrast to $n \to \bar{n}$, $n \to n'$ could be a fast process with an oscillation period of $\sim$ 10-100 seconds, and thus contain rich astrophysical implications, e.g. for the neutron lifetime, as well as ultra-high energy cosmic rays [89, 97].

Some deviations from the null-hypothesis have been reported in $n \to n'$ disappearance searches using ultracold neutrons (UCN) [99, 91]. The phenomena of $n \to \bar{n}$ ($|\Delta\mathcal{B}| = 2$) and $n \to n'$ ($\Delta\mathcal{B} = 1$) can be interrelated in unified theoretical frameworks, becoming components of one common picture [84, 85, 88]. It can also provide a novel mechanism of $n \to \overline{n}$ via an $n \to n' \to \overline{n}$ transition, whose effect can be ten orders of magnitude larger than the one induced by direct $n \to \bar{n}$ mixing [87]. Similarly, as will be discussed in Sec. 1.15, there are tensions within the neutron lifetime community, and these disparities could be explained by this physics.

As a first foray into this physics, it is useful to conduct a brief overview of each of these topics.

1.9.1 Overview of Dark Matter as Particles, and Constraints Therein

As Einstein, Hubble, and Zwicky (along with the quantum revolutionaries of Bohr, Heisenberg, and Schrödinger, separately) showed in the early 1900's, the age of Newtonian physics was nothing short of blissful ignorance. Einstein nearly single-handedly united Riemannian geometry with mechanics [188], showing an untold and inextricable connectedness between the nature of space and time, mass and energy, acceleration and gravitation, wholly revolutionizing the field of astrophysics with his seminal general relativity (GR) [183]. Following after him, and causing him to abandon his later work on static solutions to his field equations by addition of a cosmological constant, Hubble showed there was evidence of a universal, accelerating expansion of the cosmos, pushing all points away from one another via some unknown energy density (now known as dark energy, or Ω_Λ). The story only continued to deepen with Zwicky's definitive arguments about the nature of the material makeup of the Coma Cluster, where, upon application of the virial theorem, he attained evidence of what he called *dunkle* (dark) matter due to a slight discrepancy in the amounts of invisible and visible mass (at a ratio of $\sim 400:1$) [424]. However, on a historical note, this estimate was off by more than an order of magnitude, though the main findings of his work still show great prescience for their time and place. Confirming these inferences further was work done by Babcock [46], and eventually, Rubin [350, 351], showing that spiral galaxy velocity of rotation curves were flat at higher radii, implying yet again that the unseen dominated the motions of the stars.

Obviously, these two cannot be resolved, and so more matter (dark matter, DM) must be postulated to permit the observed galaxy rotation curves to stubbornly resist decline, as shown in Fig. 1.13. However, DM is known to be far more than a local, galactic phenomenon, as entire galaxy clusters and the entire universe itself are known in one way or another to contain it. The main studies supporting these findings can be summarized quite nicely by three key observations: the weak gravitational lensing of large-scale cosmic structures [335], the merger of galaxy clusters [151], and in the structures of the CMB [20].

The collection of all these theories and astronomical data make up what is today called the standard model of cosmology, also known as the lambda cold dark matter (ΛCDM) model. This model requires that the big bang be the originating event kickstarting the cosmos from nothingness, permits the universe to cool, and eventually decouple from the photons now making up the CMB, and can be parametrized such that the universe today is observably flat (no mean curvature). It can be extended using models of inflation or quintessence (wherein the universe's expansion rate could be time dependent). The name, of course, involves the letter Λ, representing the vacuum/dark energy of empty space (a cosmological constant, perhaps) responsible for the expansion of the universe; similarly, it allows for a form of extra matter, cold and dark (sterile), to explain galaxy rotation curves and the many other cosmic quandaries already mentioned. Altogether, it forms the leading, modern cosmological model, challenged by only modified GR or modified Newtonian dynamics (MoND), but these suffer theoretically due to what many scientists perceive as an *ad hoc* attempt to reparametrize the laws of nature with little or no underlying physical arguments.

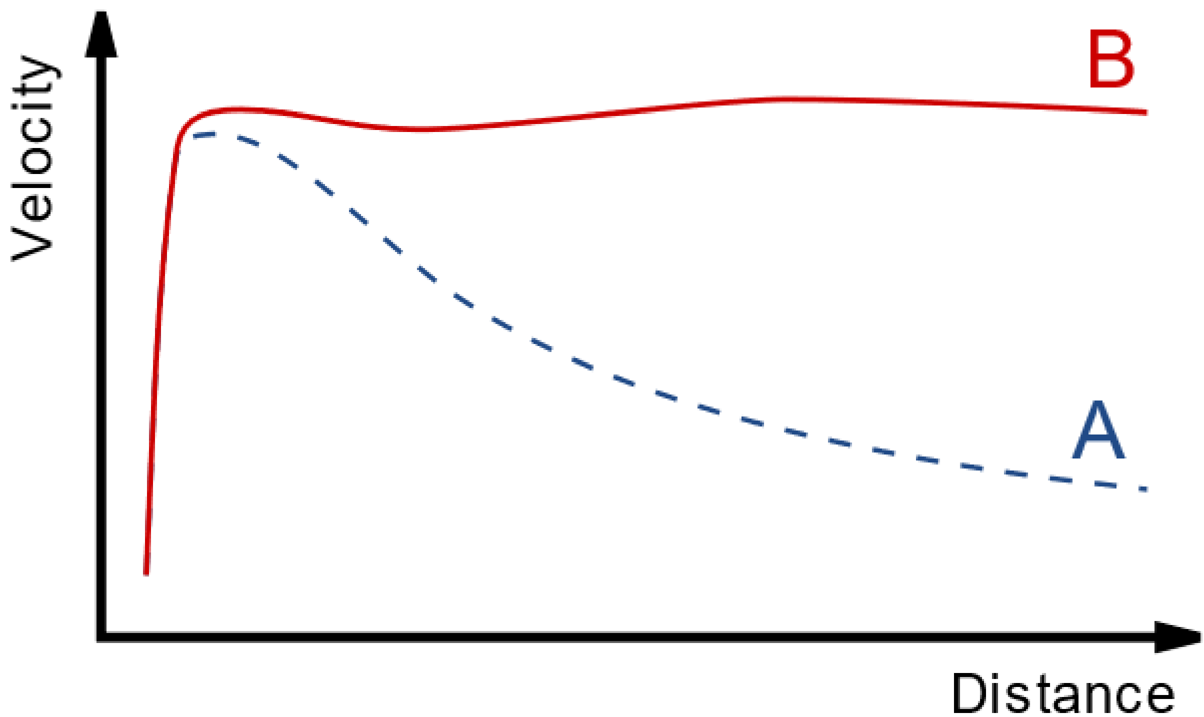

Figure 1.13: A generalization of a galactic rotation curve is seen, with the expected velocity distribution shown in blue (A), and the measured distribution shown in red (B). The expected curve follows a Keplerian decline, assuming that the observable (luminous) matter makes up the vast majority of total matter within a galaxy. Taken from [262].

Due to the vast success of QM and the SM, many believe that the ultimate nature of DM must, similarly, be that of elementary particulate. Using this assumption, it is today quite conventional to write down a small number of extension terms to the SM lagrangian and attempt to parametrize the astronomical data within a quantum field theory; this data, of course, constrains the parameters of the theory. A great overview of this process can be seen in [392], where one also gains an understanding of the great rate of diminishing parameter space available to most theories. Many of these theories, historically, have been focused either upon the idea of SUSY sparticles (supersymmetric-partner particles), which were postulated to be high-mass weakly interacting massive particles (WIMPs), or pertain to axions, a super-light pseudoscalar particle meant to solve the strong-CP problem. In Fig. 1.14, the limit plots on cross sections are shown (normalized to a single nucleon) for spin-independent couplings versus DM-candidate WIMP masses. Shown at the bottom is the neutrino floor, which some regard as an irreducible background below which no DM signal would be resolvable. However, as seen in the direct measurement of coherent elastic neutrino-nucleus scattering [26], in time, one may be able to subtract such a background. It should be noted that these curves (representing exclusions and neglecting apparently positive results) are all somewhat model dependent, but none-the-less, show a tendency to avoid low mass regions which some scientists see as critical the the understanding of DM; this is mainly due to the use of heavy target nuclei, whose recoils in these regions become difficult to reconstruct[13].

To date, the only experiment with significant, *seemingly* positive data indicating the existence of a DM particle(s) is DAMA, based in Gran Sasso, Italy, and using highly radiochemically pure sodium-iodide crystals (note that sodium is rather light). From 1995-2002, DAMA/NaI data showed an annular cycle in low energy bins (2-6 keV), very similar to that predicted from models of the galactic halo and the streaming of DM into the solar system; this was confirmed by the second run in DAMA/LIBRA, with supposedly model-independent results, yielding a total of $1.04\,$t·yrs of data. Altogether, their model independent results show a 9.3σ deviation from the null hypothesis, indicating that there could be strong evidence for dark matter in the galactic halo; so far, no suggested systematic effect or process (other than non-random noise) can eliminate the signal [152]. Some of the best signal regions that DAMA/LIBRA claims is with a WIMP mass

[13]Thus, this motivates searches for lighter DM candidates with either lighter nuclei, or doping current detectors, such as those of liquid xenon, with light species such as hydrogen.

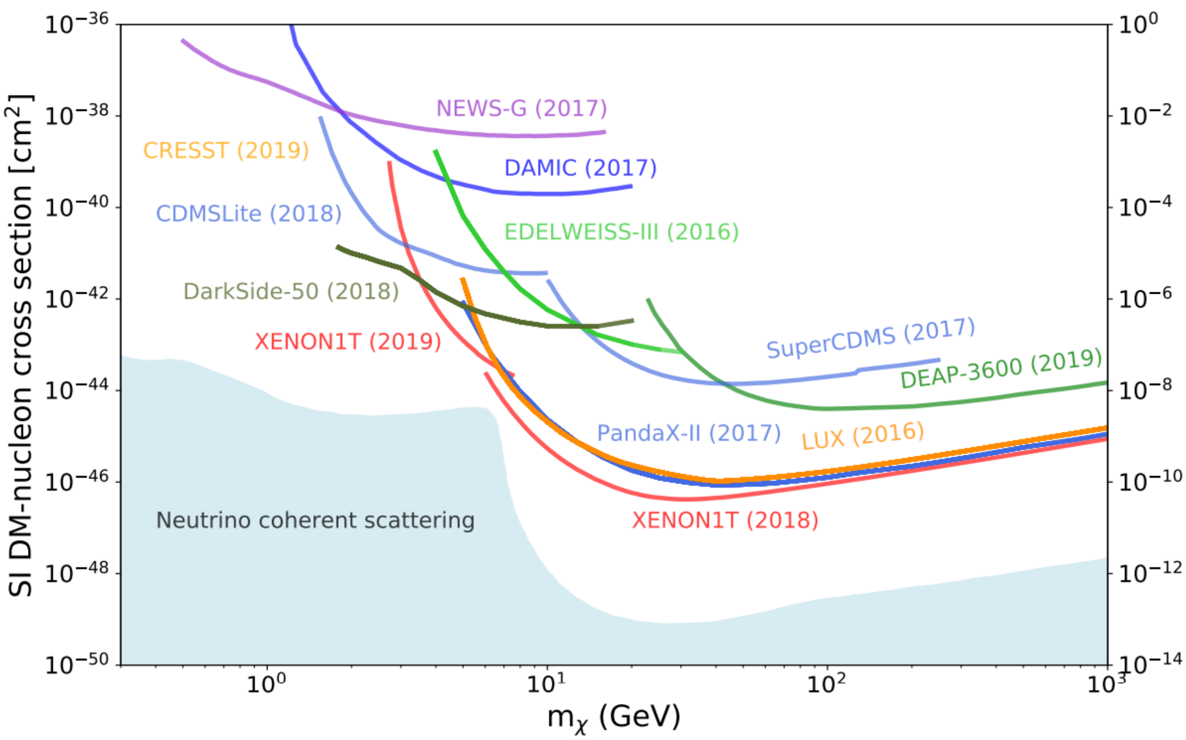

Figure 1.14: The available parameter space of potential spin-independent dark matter cross sections (such as those for a WIMP) has significantly shrunk. This pushes the overall relevant search areas toward lower, nucleon-order mass regimes toward the upper left of the plot. Taken from [392].

of $50\,\text{GeV}$ and a rather small cross section $\sim 10^{-6}\,\text{pb}$, or in the mass range of 6-$10\,\text{GeV}$, and a cross section of $\sim 10^{-3}\,\text{pb}$. However, these results have been challenged recently by the ANAIS collaboration [35, 376].

A hypothetical dark matter candidate is mostly sterile *mirror matter*, which will be discussed in Sec. 1.11; its rich phenomenology allows for many possible tests using the neutron, which will be the focus of later discussions in Chap. 3.

1.10 The Neutron Lifetime Anomaly

The neutron lifetime τ_β is the outcome of the semileptonic weak decay (β-decay) [411] of a neutron into a proton, electron, and electron antineutrino:

$$n \to p + e + \bar{\nu}_e, \tag{1.25}$$

which is energetically favorable due to the larger mass of the neutron compared to the proton resulting from Coloumb corrections and isospin symmetry breaking (from nonidentical quark masses); these interactions are relatively small at the quark level, and so one may approximate the decay amplitude with a four-fermion (nucleon-level) interaction as:

$$\mathcal{A} = [g_V \bar{p}\gamma_\mu n - g_A \bar{p}\gamma_5\gamma_\mu n][\bar{e}\gamma_\mu(1+\gamma_5)\nu], \tag{1.26}$$

where $g_{V,A}$ are the weak vector and axial coupling constants. From this, one may compute τ_β as:

$$\tau_\beta = \frac{2\pi^3\hbar^7}{m_e^5 c^4 f_R}\frac{1}{g_V^2 + 3g_A^2}, \tag{1.27}$$

where one assumes that f_R is a phase space factor which accounts for any final state interactions and all radiative corrections [411]. Microscopically, β-decay occurs by a change of a d-quark into a u-quark through a weak current; thus, the lifetime can be related to the CKM matrix element V_{ud} as [411, 290, 394]:

$$\tau_\beta = \frac{4908.7 \pm 1.9\,\text{s}}{|V_{ud}|^2(1+3\lambda^2)} = \frac{5024.7\,\text{s}}{|V_{ud}|^2(1+3g_A^2)(1+\Delta_R^V)}, \tag{1.28}$$

where $\lambda = \frac{g_A}{g_V} = \frac{g_A}{G_F V_{ud}}$, G_F is Fermi's constant, Δ_R^V represents the electroweak radiative corrections, and the numerical value of the numerator is derived from inclusion of all necessary constants, Fermi coupling constants (from muon decay), and the theoretical uncertainty of any radiative corrections. Current averages yield

$$\tau_\beta^{\text{avg.}} = 879.6 \pm 6\,\mathrm{s}\,,\; g_A^{\text{avg.}} 1.2762 \pm 5\,, \tag{1.29}$$

but there remains much tension within the experimental community upon the true lifetime, as different experimental techniques lead to significantly disparate results, potentially pointing to BSM physics.

All published data on past searches for $n \to n'$ has been focused on neutron bottling methods used within the ultracold neutron (UCN) community. The various apparatuses used generally take a cold neutron (CN, of energies in the low meV range) beam, and then cool them further to even lower energies (usually in the neV), before bottling them in traps where their properties can be studied. These include but are not limited to the neutron static electric dipole moment [330] and the neutron lifetime [384, 324, 368, 412, 422]; each of these have great importance to BSM searches and big bang nucleosynthesis predictions [279], respectively.

As seen in Figs. 1.15, there exists a strong discrepancy between the measured values of τ_β for CN beam (red) methods [422] and UCN bottle (blue) methods [364, 324]. The lone purple measurement is a preliminary assessment of JPARC data using an independent TPC technique [384]. Work done between the 1990's and early 2010's by the CN beam collaboration has been a monumental endeavor, with some incredibly robust gains in understanding what many believe to be all possible systematics [422]. The tension between these methods is further deepened by Figs. 1.16, which show various separations of experimental techniques and each experimental class' apparent consistency with other data coming from experiments to measure V_{ud} and the axial coupling constant, though over different eras. Formerly, many physicists have disbelieved some of the claims of bottle methods, as loss mechanisms on the bottle walls can be difficult to assess [331]. However, new methods using magneto-gravitational trapping [353] have been a game changer for the bottling of UCN's, as there are effectively no collisions with the trap walls, and instead the UCN's merely bounce about the chamber via magnetic levitation (thanks to their magnetic

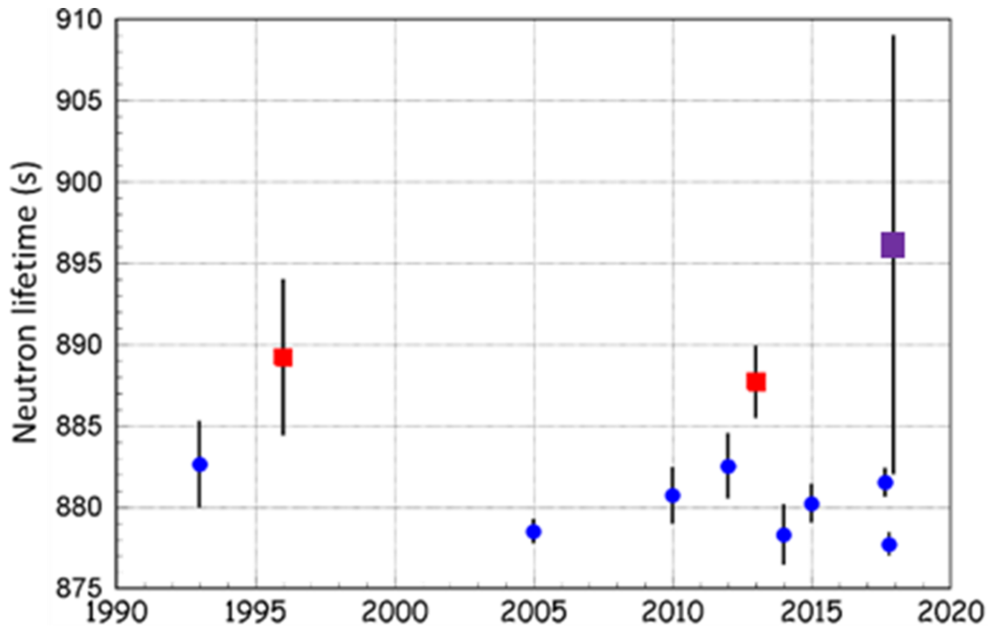

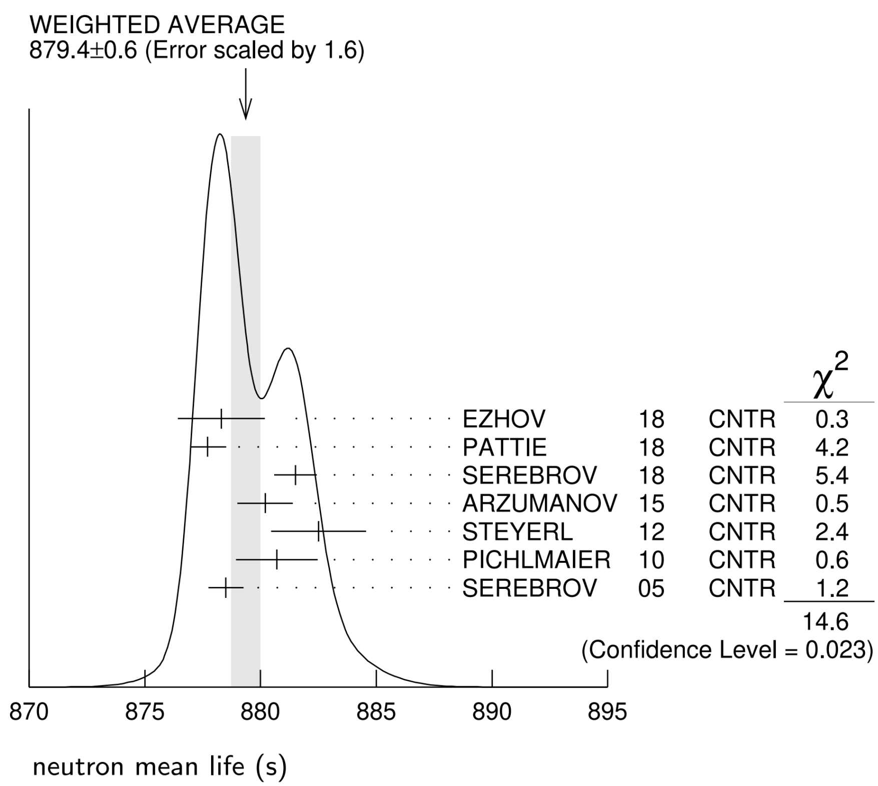

Figure 1.15: Top: A collection of measurements made between CN beam (red) and UCN bottle (blue) techniques is at odds with one another by $\sim 4\sigma$. A new TPC technique (purple) using beams of CNs will increase its precision in the coming years. The x-axis shows publication year. Courtesy of Y. Kamyshkov. Bottom: An ideogram of several of the same CN and UCN measurements is shown; the y-axis is arbitrary, but illustrates the relative probability of a given measurement's certainty via addition of gaussians. The Taken from [393].

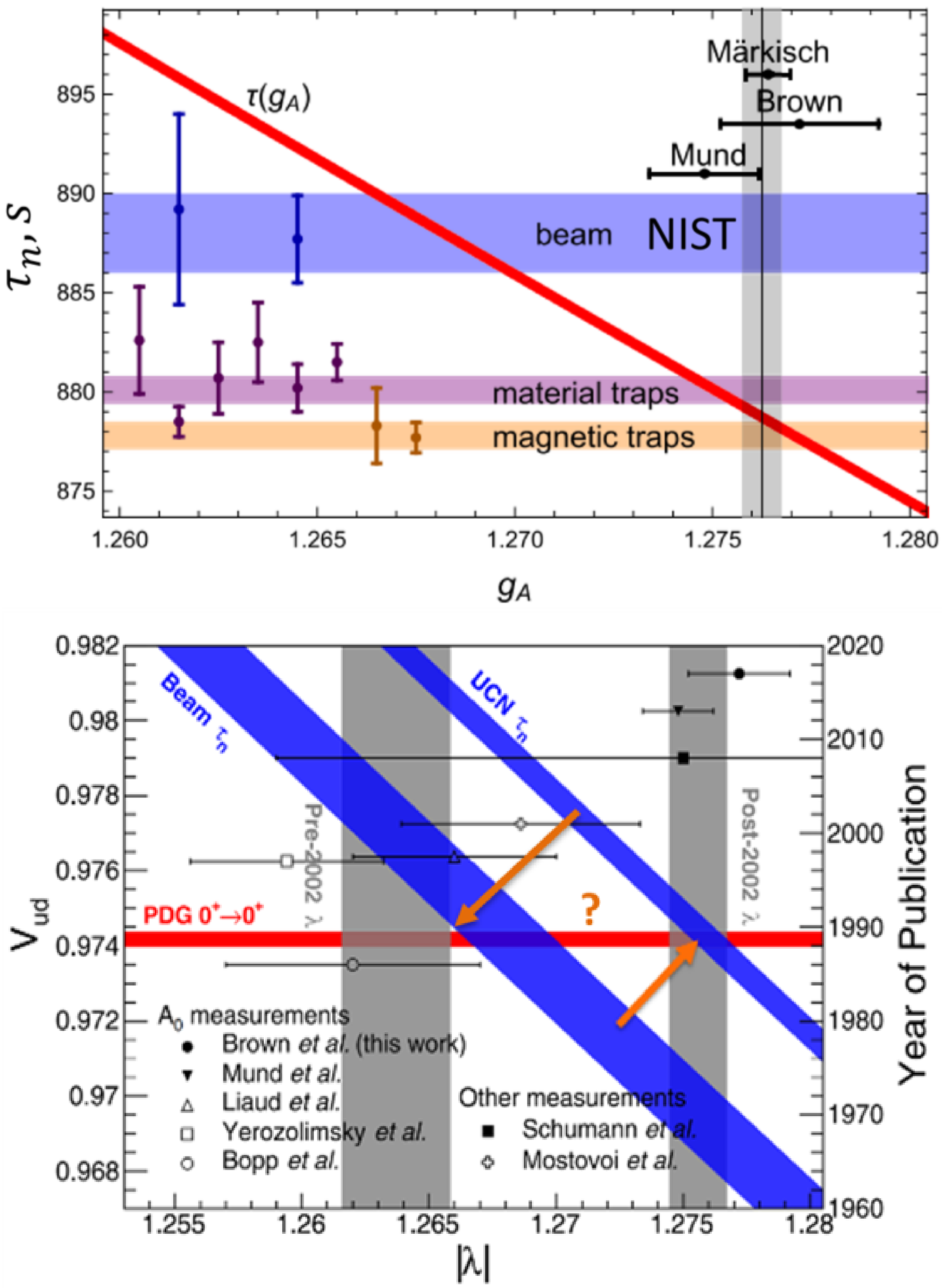

Figure 1.16: Further separation of τ_n experimental techniques is possible, and can be correlated with their consistency among different values of of the CKM matrix element V_{ud} [122, 86, 264] and the weak coupling constant g_A (note that $|\lambda| = \left|\frac{g_A}{g_V}\right|$. Modern values of V_{ud} and g_A seem to agree well with expected values of UCN bottle experiments, though material gravitational traps [365] and magnetogravitational traps [324] do appear to separate from one another even after data corrections for known phenomena such as neutron absorption against the material walls. Depending on the particular flavor of BSM physics, the beam or bottle lines could move, becoming consistent; each is possible with particular sterile (mirror) neutral particle oscillation phenomena. Top courtesy of Z. Berezhiani and Y. Kamyshkov, taken from [86]. Bottom taken from [122].

moments). Even with this new technique, a $\sim 4\sigma$ discrepancy in the neutron lifetime, is seen between the two techniques, with thus far no proper systematic being suggested as a means to explain this significant difference; further consistency issues with measurements of V_{ud} and g_A also persist, as shown in Fig. 1.16.

With this in mind, some physicists have begun to speculate upon the mechanism by which such a lifetime could be changed due to some new physical process; chief among the possibilities considered are DM upscattering, along with the possibility of $n \to n'$ disappearance from the trap. As previously mentioned, many of the same apparatuses used for neutron electric dipole moment measurements have been utilized for a search for $n \to n'$. For a discussion of these searches, see Altarev (Fig. 1.17), Serebrov, and Berezhiani [32, 364, 89]. The main point to draw attention to is that such searches have yielded lingering and persistent anomalies in the data when analysis is completed while permitting the magnetic field of the mirror sector to vary, in that $|\vec{B}_{n'}| \neq 0$. Original and redone analyses points to a $\sim 5\sigma$ signal region where $|\vec{B}_{n'}| \sim 100$ mG and $\tau_{nn'} \gtrsim 10$ s, although the χ^2 fit is weak and only slightly less consistent from assuming no signal fitting at all [32]. Fig. 1.17 shows a disappearance signal fit, but note that the disappearance (loss of neutron counts) lie conspicuously between the chosen magnetic field values. In order to corroborate these findings, more finely grained magnetic field controls must be implemented in both bottle and *beam* techniques, the latter of which will be the focus of searches at the European Spallation Source's HIBEAM/ANNI beamline [19] and discussed in detail throughout Chap. 3.

1.11 The Mirror Matter Hypothesis

One of the many candidates which fit within the constraints [200, 199] of plausible DM candidates, satisfying (or avoiding) constraints from ΛCDM, and which also offers a potential avenue of explanation for the neutron lifetime puzzle is the mirror matter (MM) hypothesis. Originally formulated as an aside by Lee and Yang [280] in 1956 as a means to restore a global parity symmetry to weak interactions, MM is a theory that conceives of two parallel sectors of particles: the mirror sector filled with mirror matter, and the ordinary sector (OS) filled with ordinary matter (that which makes up the observable universe). As it stands in its modern form, a sterile mirror sector has the ability to solve many quandaries in cosmology and particle physics, from CP

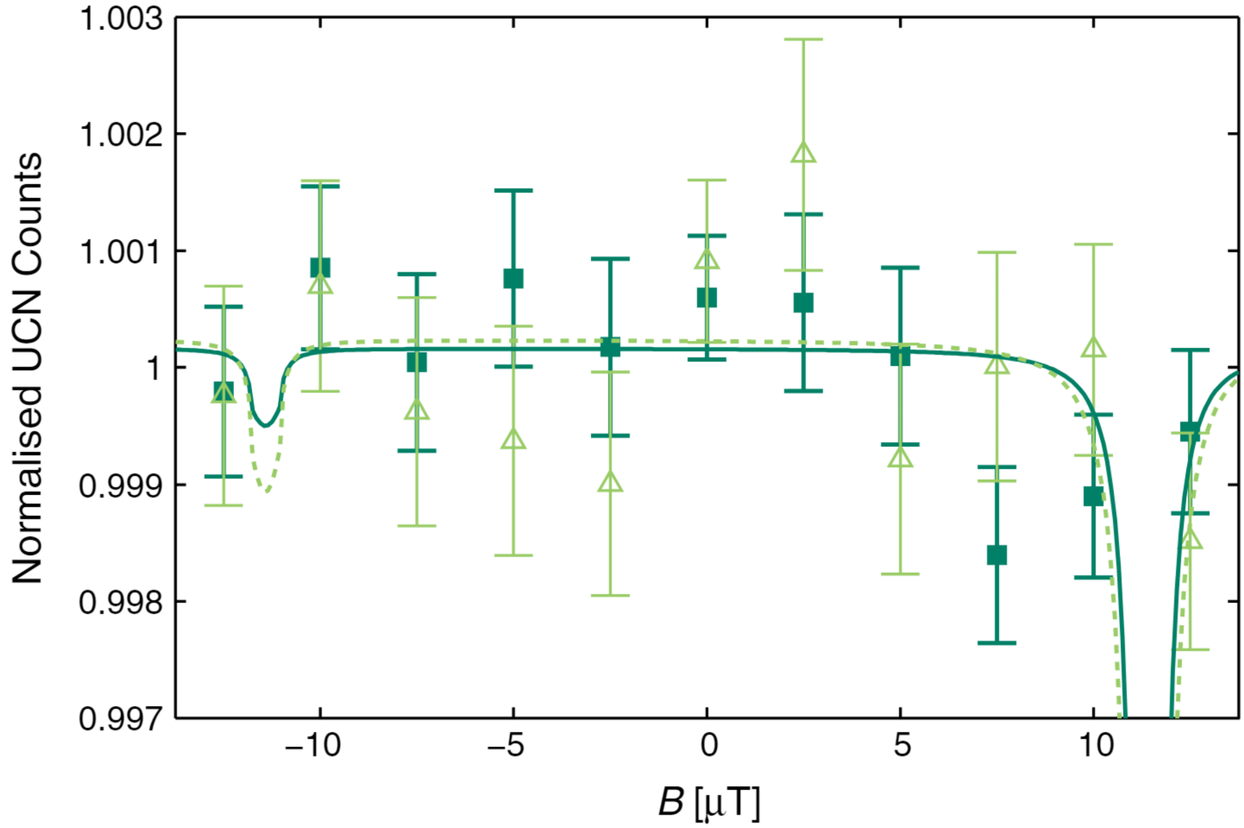

Figure 1.17: "Combined fit to the normalized UCN counts as a function of applied magnetic field $\vec{B}$ for $75\,\mathrm{s}$ (dark green solid squares and solid line) and $150\,\mathrm{s}$ (light green open triangles and dashed line). Positive (negative) $\vec{B}$ values correspond to $\vec{B}$ field up (down)." The granularity of this $n \to n'$ disappearance measurement leaves much to be desired, as several potential resonance points (around $\sim\ \pm 12\,\mu\mathrm{T}$) at each storage time have gone unresolved and cannot confirm the valleys hypothesized best fit, requiring further measurements with more precise methods, as will be discussed within Chap. 3. Figure and caption taken from [32].

asymmetry to baryogenesis (cobaryogenesis), the GZK limit [89] to DM [17]. For a robust review, see [313].

As briefly illustrated in Fig. 1.18, the main ideas of the MM hypothesis consist of extending the SM by at least one whole SM symmetry group, doubling the particle content with the addition of mirror leptons, quarks, and gauge bosons. This can be nicely expressed in a simple (yet global) way as:

$$\mathcal{G}_{global} \approx \mathcal{G}_{SM} \times \mathcal{G}'_{SM} = [SU(3) \times SU(2) \times U(1)] \times [SU'(3) \times SU'(2) \times U'(1)] \, , \tag{1.30}$$

where the primes ($'$) illustrate that the particle content of the gauge groups comes from the mirror sector. Note that the global gauge group may only be approximately equal to this, as the formulation in Eq. 1.30 ignores some of the richer structure within the full lagrangian

$$\mathcal{L}_{global} = \mathcal{L}_{SM} + \mathcal{L}'_{SM} + \mathcal{L}_{mix} \tag{1.31}$$

and so would take the term consolidating any mixing interactions between the sectors as zero. Of course, considering that otherwise the two sectors would only interact gravitationally (allowing it to be a DM candidate), experimentalists and theorists prefer to suppose that $\mathcal{L}_{mix} \neq 0$ so that experimental searches may be considered in the first place; this assumption is indeed common all other DM searches. This does however differ from many other, mostly non-SUSY DM theories, where a new, simple $U(1)$ gauge group is hypothesized, yielding a dark photon which can interact with the SM, and possibly decay into SM particles. So far, these searches have had no observations of any extraneous signal, and cannot corroborate the DAMA data; this has lead some to independently propose that one must add extra groups to the DM gauge group, as in $\mathcal{G}_{DM} = U(1) \times \cdots ??? \cdots \times \cdots$ [186]. Unless other compelling evidence is found, one will eventually arrive at a total global gauge group potentially just as complex as the one proposed by MM combined with the SM (or, possibly, beyond).

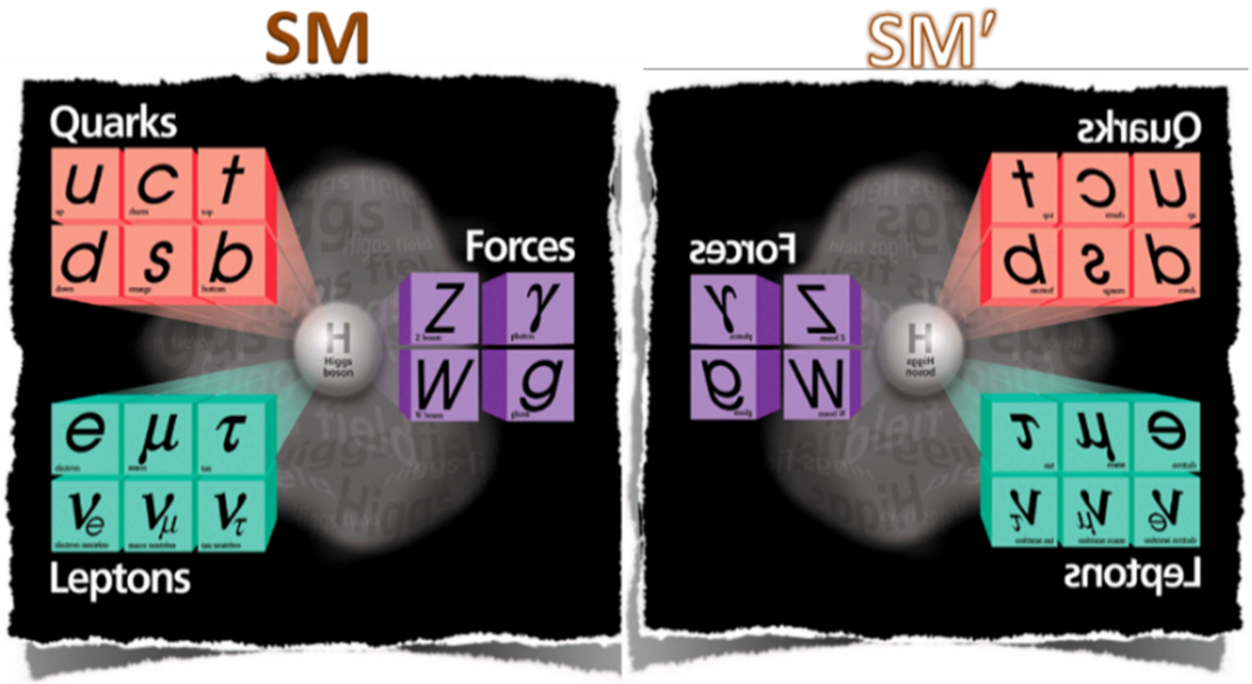

Figure 1.18: A pictorial representation of the SM and SM′ sectors, where a mirror Z_2 symmetry is shown. Gravitational interactions (expected for any DM candidate) are not depicted, nor the hypothetical very weak interactions between the sectors mediated by new heavy gauge bosons. All particles and interactions within each separate sector can be assumed to be identical, though instantonic processes during each sectors' parallel dynamics following the big bang could have lead to vastly different final states (temperatures, helium abundances, etc.) on cosmic scales [199, 200]. Courtesy of B. Rybolt.

1.11.1 Basics of Neutron–Mirror-Neutron Oscillations

If one allows for certain terms to arise within $\mathcal{L}_{mix}$, one easily arrives at dimension nine operators which similarly characterize $n \to \bar{n}$, but now instead yield neutral particles oscillations, such as $n \to n'$. In Fig. 1.19, the Feynman diagram of the proposed process is shown, again with the involvement of heavy scalars fields as mediators. The fundamentals of the theory are not all too dissimilar from that of $n \to \bar{n}$, and many key contributors have worked across both subfields; see [89, 90] for more details.

A basic effective Hamiltonian can be constructed which allows a two-component wave vector $\Psi \sim \begin{pmatrix} n \\ n' \end{pmatrix}$ to oscillate between states. If one considers oscillations in free space, this can be seen to take the form

$$\mathcal{H} = \begin{pmatrix} E_n & \epsilon \\ \epsilon & E_{n'} \end{pmatrix}, \tag{1.32}$$

where simplistically $\epsilon = \frac{1}{\tau_{nn'}}$ can also include cross terms, but is a somewhat small mixing parameter inversely proportional to a possibly short ($\gtrsim 10\,\mathrm{s}$) oscillation lifetime $\tau_{nn'}$, and where the simplest terms along the diagonal

$$E_{n,n'} \approx m_{n,n'} - \frac{i}{2}\Gamma_{n,n'} + \vec{\mu}_{n,n'} \cdot \vec{B}_{n,n'}\,, \tag{1.33}$$

represent the energies of either a neutron or mirror-neutron. Note that, in principle, the masses, decay widths, magnetic moments, and magnetic fields (which each type interacts with) need not be equivalent. However, for simplicity, via an exact (or near exact) Z_2 symmetry, one may assume that $m_n = m_{n'}$, $\Gamma_n = \Gamma_{n'}$, and $|\vec{\mu}_n| = |\vec{\mu}_{n'}|$; here one has made an implicit assumption of inherent similarities between the mathematical structures and coefficients of the various operators within the appended $\mathcal{L}'_{SM}$ and the original $\mathcal{L}_{SM}$. This leaves one free parameter to consider: the environmental magnetic field of the ordinary, Standard matter sector. Historically, this was not considered important, as one could presume that within the mirror sector the ambient magnetic field would be zero [364]. However, given the richness of the ordinary sector, one knows that cosmic magnetic fields, although tiny, abound throughout the universe, created when small amounts of

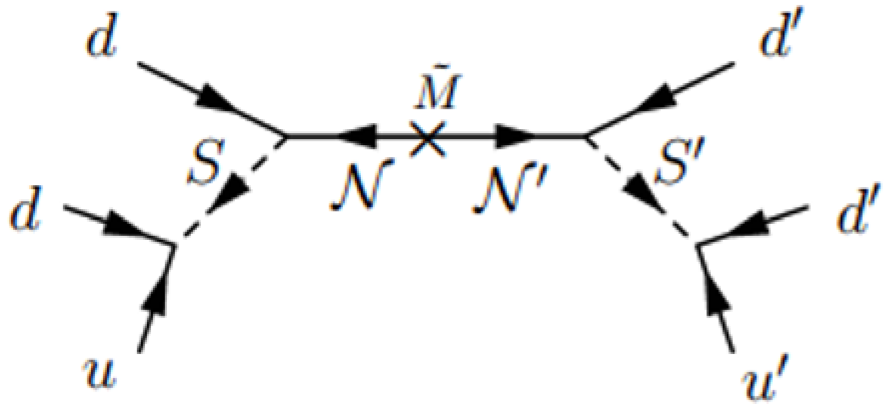

Figure 1.19: Diagram showing the mirror mixing of a neutron (udd) through heavy scalars and additional gauge singlets to a sterile dark neutron ($u'd'd'$). Taken from [90].

ionized gas and dust circulate throughout the heavens. If one makes a similar presumption with respect to the mirror sector, then with the addition of gravitational binding between the sectors, one can easily conceive of MM being trapped gravitationally within the earth or solar system, whereby, similarly, small amounts of it could become ionized throughout time, and produce small magnetic fields just as well [82]. When this process is considered within a calculation of the probability of the oscillation occurring, and ordinary sector neutron state of $\Psi_n = \begin{pmatrix} n \\ 0 \end{pmatrix}$ can then transform into a mirror-neutron, $\Psi_{n'} = \begin{pmatrix} 0 \\ n' \end{pmatrix}$, via:

$$P_{n\to n'}(t) = \frac{\sin^2[(\omega-\omega')t]}{2(\omega-\omega')^2\tau_{nn'}^2} + \frac{\sin^2(\omega+\omega')t}{2(\omega+\omega')^2\tau^2} + \cos\beta\cdot[\frac{\sin^2[(\omega-\omega')t]}{2(\omega-\omega')^2\tau^2} + \frac{\sin^2(\omega+\omega')t}{2(\omega+\omega')^2\tau_{nn'}^2}], \quad (1.34)$$

where the simplifications $\omega = \frac{1}{2}|\vec{\mu}_n \cdot \vec{B}_n|$ and $\omega' = \frac{1}{2}|\vec{\mu}_{n'} \cdot \vec{B}_{n'}|$ have been employed, $\tau_{nn'} = \frac{1}{\epsilon}$, and β represents the angle between the environmental magnetic field of each sector. Note that, similarly, the overall behavior of the probability goes as

$$P_{n\to n'} \approx \left(\frac{\epsilon t}{\hbar}\right)^2 = \left(\frac{t}{\tau_{nn'}}\right)^2. \quad (1.35)$$

It can be seen from Eq. 1.34 that resonances can occur when $\omega \Longleftrightarrow \omega'$, i.e., if $|\vec{\mu}_n| = |\vec{\mu}_{n'}|$ and the magnetic fields of the two sectors are aligned. Thus, the primary difference between the search for $n \to \bar{n}$ and $n \to n'$ is that the former requires the elimination of any ambient magnetic field during a free beam search (a quasifree condition), while the other requires magnetic field control in order to reach the resonance condition.

Two basic phenomena can be investigated in the searches for a mirror sector using neutron mixing: disappearance and regeneration. Disappearance implies that one can search for a net loss of neutrons in a neutron beam with adequate monitoring, magnetic field control and shielding, or, after the ordinary neutron beam is absorbed by a beam stop, one can search for a net gain in previously nonexistent neutrons (above background levels) downbeam due to $n \to n' \to n$. The latter, of course, is a second order process, where

$$P_{n\to n'\to n} \propto \left(\frac{t_{dis.}}{\tau_{n\to n'}}\right)^2 \left(\frac{t_{reg.}}{\tau_{n'\to n}}\right)^2 \equiv \left(\frac{t}{\tau_{nn'}}\right)^4 = P^2_{n\to n'} \equiv P^2_{nn'}\,. \tag{1.36}$$

It should be noted that the disappearance requires incredible precision in a neutron detector/monitor's ability to count neutrons within an incredibly high flux beam, while the regeneration must be able to perceive a large enough rate of regeneration in order to avoid detector backgrounds and say anything definitive. Each require rather similar magnetic field control, in and of itself an impressive technical challenge.

1.11.2 Some Details of $n \to n'$ Phenomenology

Having sketched a few basics, one can now investigate the rich textures of more complete and complex $n \to n'$ phenomenologies.

In addition to external fields and interactions in the standard sector, the possibility of equivalent fields in the sterile sector must be taken into consideration. There can exist also some hypothetical forces between ordinary and sterile sector particles which can be induced e.g. by the photon kinetic mixing with dark photon [245, 220, 135, 221], or by new gauge bosons interacting with particles of both sectors as e.g. common $\mathcal{B}-\mathcal{L}$ gauge bosons [18] or common flavor gauge bosons of family symmetry [79, 75, 74]. The respective forces can provide portals for direct detection of dark matter components from a parallel sterile sector and give a possibility for the identification of their interactive nature [199, 17, 141]. In addition, flavor gauge bosons can induce mixing between neutral ordinary particles and their dark sterile partners and induce other oscillations, e.g., between kaons and mirror kaons, conversion of muonium into mirror muonium, etc. [75, 74].

The possibility of neutron-mirror neutron mass mixing $\epsilon\overline{n}n' + \mathrm{h.c.}$was proposed in [90].It can be induced by six-fermion effective operators $\frac{1}{M^5}(\overline{u}\bar{d}\bar{d})(u'd'd')$, similar to Eq. 1.13, but involving three ordinary quarks and three quarks of the sterile (mirror) sector. This mixing violates conservation of both ordinary $\mathcal{B}$ and mirror $\mathcal{B}'$ ($\Delta\mathcal{B} = 1$, $\Delta\mathcal{B}' = -1$), but conserves the combination $\mathcal{B}+\mathcal{B}'$. The mixing coefficient ϵ can be estimated as

$$\epsilon = \frac{C\Lambda^6_{\rm QCD}}{M^5} = C^2\left(\frac{10\ \mathrm{TeV}}{M}\right)^5 \times 2.5\cdot 10^{-15}\ \mathrm{eV}\,. \tag{1.37}$$

It has been shown that no direct, astrophysical or cosmological effects currently forbid that $n \to n'$ oscillation time $\tau_{nn'} = 1/\epsilon$ can be smaller than the neutron decay time, and in fact it can be as small as a second [90]; thus, rapid $n \to n'$ oscillations could have interesting implications for the propagation of ultra-high cosmic rays [89, 97] or for neutrons from solar flares [300], as well as neutron stars [93]. Thus, the effective scale M of underlying new physics can be ∼TeV, with direct implications for the search at the LHC and future accelerators. Effects of $n \to n'$ oscillation can be directly observed in experiments searching for anomalous neutron disappearance ($n \to n'$) and/or regeneration ($n \to n' \to n$) processes [90], and experimental sensitivities of such searches with UCN and CN were discussed in [331, 96].

A Hamiltonian for $n \to n'$ is given in Eq. 1.38; the presence of a (mirror) neutron static magnetic moment $\mu_{\{n,n'\}}$ shifts the (mirror) neutron's total energy, and so is expressed for the general case of neutrons propagating in magnetic fields $\vec{B}$ (of the standard sector) and $\vec{B}'$ (of the sterile sector); the former of these is generated by the magnetic poles of the Earth, the latter by hypothetical ionization and flow of gravitationally captured dark material in and around the Earth [82]. Such an accumulation could occur due to ionized gas clouds of sterile dark ions captured by the Earth, e.g., due to photon–sterile photon kinetic mixing; present experimental and cosmological limits on such mixing [98, 404] and geophysical limits [251] still allow the presence of a relevant amount of sterile dark material captured within the Earth [83]. Thus, a mirror magnetic field can be induced by the drag of dark electrons due to the Earth rotation via mechanism described in [95], and can be enhanced through the dynamo effect [82].

$$\hat{\mathcal{H}} = \begin{pmatrix} m_n + \vec{\mu}_n \vec{B} & \epsilon + \kappa \vec{\mu}_n \vec{B} + \kappa' \vec{\mu}_n \vec{B}' \\ \epsilon + \kappa \vec{\mu}_n \vec{B} + \kappa' \vec{\mu}_n \vec{B}' & m_{n'} + \vec{\mu}_{n'} \vec{B}' \end{pmatrix}. \tag{1.38}$$

In addition to $\vec{\mu}_{\{n,n'\}}$ and unlike for the $n \to \bar{n}$ transition[14], transition magnetic moments (TMMs) [85], as shown in Fig. 1.20 may also be present in the off-diagonal as $\kappa\vec{\mu_n}$ for both the neutron and sterile neutron.[15] As analogous contributions to the Hamiltonian, it can be seen that TMMs are quantities which are as fundamental as the more familiar static magnetic moments.

[14]A non-zero TMM between the neutron and antineutron is forbidden by Lorentz invariance [101, 100]. Moreover, any transition $n \to \bar{n}\gamma^*$ with an external virtual photon connected to a proton would destabilize nuclei even in the absence of $n \to \bar{n}$ mixing.

[15]TMMs play a role both in understanding SM processes, e.g. hadronic decays [370], and the development of BSM physics models, such as those predicting neutrino flavour changing processes [119].

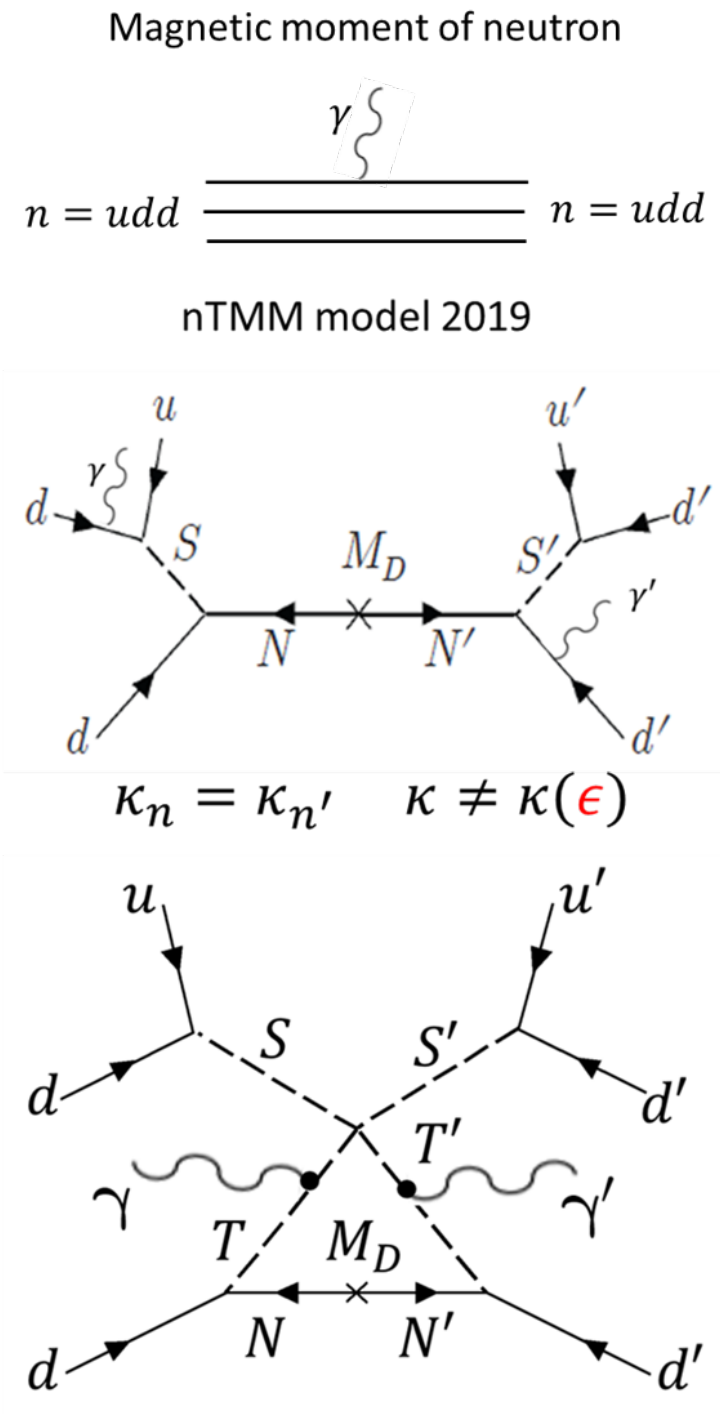

Figure 1.20: Feynman diagrams for various magnetic moments. Top: The magnetic moment of the neutron involves lines and loops (not shown) dressing udd quarks. Middle: A simple extension of this though can be applied to a diagram of nominal $n \to n'$ mixing [90], where now ordinary and mirror photons dress constituent quarks, inducing a *transitional* magnetic moment, TMM. Bottom: A more general TMM mechanism can be seen at loop level with photon dressings. Note that though the for a TMM $\kappa = \kappa'$ it is generally assumed that κ and ϵ are independent parameters within the phenomenology. Courtesy of Y. Kamyshkov and Z. Berezhiani.

The TMMs contribute to the mixing via the interaction of new physics processes with the external magnetic fields, leading to terms $\kappa\vec{\mu}_n\vec{B}$ and $\kappa'\vec{\mu}_n\vec{B}'$, where the dimensionless parameter $\kappa \ll 1$ represents the magnitude of the TMM in units of the neutron magnetic moment μ_n.

Beyond suppressing the nominal neutron decay as in Eq. 1.33, a number of simplifications can be made to $n \to n'$ mixing described by Eq.1.38. In the simplest model, it is assumed that n and n' share degeneracies such as $m_n = m_{n'}$, $|\vec{\mu_n}| = |\vec{\mu_n'}|$ and $\kappa = \kappa'$. The magnitude, direction, and time dependence of the mirror magnetic field $\vec{B}'$ is *a priori* unknown. If only $n \to n'$ mass mixing ϵ is present, i.e. taking $\kappa = 0$, then the probability of $n \to n'$ oscillation at a time t is given previously in Eq. 1.34 [82, 99]. Not that if $|\omega - \omega'|\, t \gg 1$, the oscillations can be averaged in time and one obtains

$$\overline{P}_{nn'} = \frac{\cos^2 \frac{\beta}{2}}{2(\omega - \omega')^2 \tau_{nn'}^2} + \frac{\sin^2 \frac{\beta}{2}}{2(\omega + \omega')^2 \tau_{nn'}^2}. \tag{1.39}$$

In particular, if $\vec{B}' = 0$ (i.e. $\omega' = 0$), from Eq. 1.34 the expression

$$P_{nn'}(t) < (\epsilon/\omega)^2 \tag{1.40}$$

is obtained if $\omega t > 1$, and

$$P_{nn'}(t) \approx (\epsilon t)^2 \tag{1.41}$$

if $\omega t \ll 1$.

When $\vec{B}$ approaches $\vec{B}'$, $|\omega - \omega'|$ decreases, and so the probability $P_{nn'}(t)$ resonantly increases. In a quasifree regime, when $|\omega - \omega'|\, t \gg 1$, it takes on values

$$P_{nn'}(t) \approx \frac{1}{2}(\epsilon t)^2 \cos^2 \frac{\beta}{2} = \cos^2 \frac{\beta}{2} \left(\frac{t}{0.1\,\mathrm{s}}\right)^2 \left(\frac{1\,\mathrm{s}}{\tau_{nn'}}\right)^2 \times 5 \cdot 10^{-3} \tag{1.42}$$

where $\tau_{nn'} = 1/\epsilon$ is the characteristic $n \to n'$ transition time for free neutrons in a field-free vacuum. Therefore, this leads to a situation when $n \to n'$ oscillation probability non-trivially depends on the value (and direction) of magnetic field; this effect can be observed in experiments searching for anomalous neutron disappearance ($n \to n'$) and regeneration ($n \to n' \to n$) [90]. Experimental sensitivities of such searches with CN and UCNs are discussed in [331].

Several dedicated experiments searching for $n \to n'$ oscillation with UCNs were performed in last decade [57, 367, 32, 110, 369, 99, 91]. Under the hypothesis that there is no mirror magnetic field at the Earth, i.e. $|\vec{B}'| = 0$ yields the strongest lower limit $\tau_{nn'} \geq 414\,\mathrm{s}$ at a 90 % C.L., which was obtained by comparing UCN losses in zero ($|\vec{B}| < 10^{-3}\,\mathrm{G}$) and non-zero ($|\vec{B}| = 0.02\,\mathrm{G}$) magnetic fields [367]. However, this limit becomes invalid in the presence of $\vec{B}'$. Lower limits on $\tau_{nn'}$ (and $\tau_{nn'}/\sqrt{\cos\beta}$) in the presence of a non-vanishing $\vec{B}'$ follow from experiments [57, 367, 32, 110, 369, 99, 91], and are summarized in [91]. Some experiments show deviations from null-hypothesis, which may point towards $\tau_{nn'} \gtrsim 10\,\mathrm{s}$ and $|\vec{B}'| \sim 0.1\,\mathrm{G}$. For $|\vec{B}'| > 0.5\,\mathrm{G}$ or so, a transition time as small as ~ 1 second is still allowed [91].

In the case of a TMM induced $n \to n'$ transition, the average oscillation probability becomes [92]:

$$\overline{P}_{nn'} = \frac{2\kappa^2(\omega+\omega')^2\cos^2\frac{\beta}{2}}{(\omega-\omega')^2} + \frac{2\kappa^2(\omega-\omega')^2\cos^2\frac{\beta}{2}}{(\omega+\omega')^2}. \tag{1.43}$$

Upper limits on κ can be obtained by analysis of experiments [57, 367, 32, 110, 369, 99, 91], and are given in [92]. In a case when ϵ and κ are both present, the average probability of $n \to n'$ transition is given just by a sum of terms between Eqs. 1.39 and 1.43.

If one chooses $\vec{B}' = 0$, there remain three parameters determining the probability of the $n \to n'$ process: ϵ, κ and $\vec{B}$. Fig. 1.21 illustrates the interplay between these parameters and their impact on the oscillation, assuming $\epsilon = 5.68 \times 10^{-18}\,\mathrm{eV}$ ($\tau = 500\,\mathrm{s}$). Note that for *only* TMM transitions, when $\epsilon = 0$, one obtains

$$P_{nn'} = 2\kappa^2\,. \tag{1.44}$$

and so has constant transitions. Fig. 1.21 (right panel) compares the fraction of converted neutrons after travelling $25\,\mathrm{m}$ in a vacuum for the case of a TMM $\kappa \neq 0$ term and $\epsilon \neq 0$, compared to $\epsilon = 0$.

The TMM can also lead to an enhanced $n \to n'$ transformation in a gas atmosphere due to the creation of a positive Fermi potential along the neutron path [92]. A constant magnetic field $\vec{B}$ in the flight volume can be chosen such that for a single neutron polarization a negative magnetic provides potential compensation to the positive Fermi potential of the gas: $V_F = \vec{\mu}\cdot\vec{B}$. Thus, the Fermi potential of air at Normal Temperature and Pressure corresponds to the constant magnetic

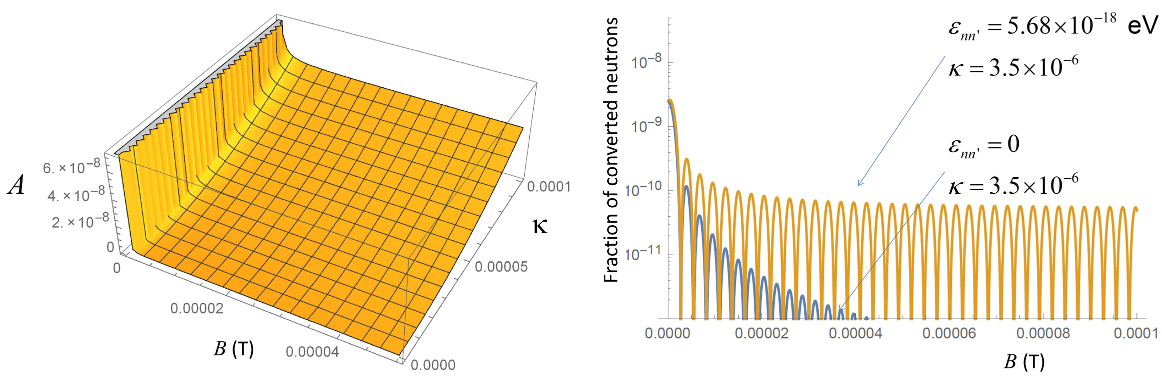

Figure 1.21: Left: amplitude of the probability function for $n \to n'$ as a function of $|\vec{B}|$ and κ for a value of $\tau \equiv \tau_{nn'} = \frac{1}{\epsilon_{nn'}} = \frac{1}{\epsilon} = 500\,\text{s}$. Right: fraction of neutrons which have been converted as a function of $|\vec{B}|$ travelling 25 m in a vacuum at a velocity of $1000\,\text{m/s}$. Predictions are shown jointly for conversions induced by mass mixing and a TMM ($\tau = 500\,\text{s}$ and $\kappa = 3.5 \times 10^{-6}$, orange), and for mass mixing alone ($\tau = 500\,\text{s}$, blue) alone. Courtesy of D. Milstead.

field of $\sim 10\,\mathrm{G}$. Continuing to assume that $|\vec{B}'| = 0$, the oscillation Hamiltonian becomes

$$\mathcal{H} = \begin{pmatrix} V_F - \mu B & \alpha_{nn'} + \kappa\mu B \\ \alpha_{nn'} + \kappa\mu B & 0 \end{pmatrix}, \tag{1.45}$$

where the zero diagonal term (in the resonance) corresponds to pure oscillation with the probability:

$$P_{nn'} = (\epsilon + \kappa\mu B)^2 t^2 \,, \tag{1.46}$$

and so the oscillation due to ϵ is here enhanced by κ proportionally to the field $\vec{B}$.

In addition to the sterile sector quantities, there are other notable differences between $n \to n'$ and $n - \bar{n}$ mixing. A non-zero TMM is possible for the former but forbidden for the latter case due to rotational symmetry. Furthermore, despite its suppression, $n \to \bar{n}$ in nuclei plays as experimentally significant a role in searches as do free neutrons. Decays due to the process $n \to n'$ would, however, be unobservable due to backgrounds from non-sterile neutron-induced decays [89].

1.11.3 $n \to \bar{n}$ via $n \to n' \to \bar{n}$

Should a sterile mirror sector exist, and within it sterile mirror neutrons, processes connecting the ordinary and sterile sectors need not be restricted to the preceding processes [85, 87]. It is essential to test the full range of conversions between the sectors: $n \to \{n', \bar{n}'\}$, $\bar{n} \to \{n', \bar{n}'\}$, $n' \to \{n, \bar{n}\}$ and $\bar{n}' \to \{n, \bar{n}\}$.

In principle, a transformation to four states can be admixed within $\{n, \bar{n}, n', \bar{n}'\}$. In free space, without any fields, these transformations can be described by the symmetric Hamiltonian

$$\hat{\mathcal{H}} = \begin{pmatrix} m_n + \vec{\mu}_n \vec{B} & \alpha & \epsilon & \beta_{n\bar{n}'} \\ \alpha & m_n - \vec{\mu}_n \vec{B} & \beta_{n\bar{n}'} & \epsilon \\ \epsilon & \beta_{n\bar{n}'} & m_{n'} + \vec{\mu}_{n'} \vec{B}' & \alpha \\ \beta_{n\bar{n}'} & \epsilon & \alpha & m_{n'} - \vec{\mu}_{n'} \vec{B}' \end{pmatrix} \tag{1.47}$$

Here, α is the $n\bar{n}$ Majorana mass mixing parameter, and ϵ and $\beta_{n\bar{n}'}$ are the respective mass mixing parameters for nn' and for $n\bar{n}'$ components. Here, possible TMM terms between $\{n, \bar{n}, n', \bar{n}'\}$ states have been neglected, and one may assume that $m_{n'} = m_n$ and $\mu_{n'} = \mu_n$.

Thus, in this case, the final state antineutron can be a result of the classical $n \to \bar{n}$ with mixing mass amplitude α and $\Delta\mathcal{B} = -2$ via $P_{n\to\bar{n}} = \alpha^2 t^2$. It can also arise via second order regeneration-like oscillation processes: $n \to n' \to \bar{n}$ with amplitude $\epsilon\beta_{n\bar{n}'}$, or $n \to \bar{n}' \to \bar{n}$ with amplitude $(\beta_{n\bar{n}'}\epsilon)$. If α is very small while ϵ and $\beta_{n\bar{n}'}$ are comparatively large, then $n \to \bar{n}$ could be observed for a non-zero sterile magnetic field. Note that neither previous limits on free $n \to \bar{n}$ from experiments in which the magnetic field was suppressed [56] nor nuclear stability limits from $n \to \bar{n}$ conversion in nuclei [4] would be valid for this scenario, since a fixed field $\vec{B}$ compensating for the magnetic field in the sterile sector would be needed to allow the full process $n \to \{n', \bar{n}'\} \to \bar{n}$ to proceed. Existing limits allow the oscillation times $\tau_{nn'}$ and $\tau_{n\bar{n}'}$ to be as small as $\sim 10\,\mathrm{s}$; see [91] for a summary of the present experimental situation. Therefore, by properly tuning the value of the ordinary magnetic field $\vec{B}$ resonantly close to the mirror field $\vec{B}'$ (with precision of mG or so) and thus achieving the quasifree regime, the probability of induced $n \to \bar{n}$ oscillation can be rendered as large as

$$P_{n\bar{n}}(t) = \frac{1}{4}\beta^2_{n\bar{n}'}\epsilon^2 t^4 \sin^2\beta = \frac{\sin^2\beta}{4}\left(\frac{t}{0.1\,\mathrm{s}}\right)^4 \left(\frac{10^2\,\mathrm{s}^2}{\tau_{nn'}\tau_{n\bar{n}'}}\right)^2 \times 10^{-8} \tag{1.48}$$

where again β is the (unknown) angle between the directions of $\vec{B}$ and $\vec{B}'$ [87]. Hence, the probability of an induced $n \to \bar{n}$ can be be several orders of magnitude larger than the present sensitivity in direct $n \to \bar{n}$ conversion (see again Eq. 1.19). Thus, the magnetic field is not suppressed, and so instead one can scan over its values and directions to find resonances when magnitudes $\vec{B} \approx \vec{B}'$ and the angle is non-zero. In addition, different from direct $n\bar{n}$ mixing, $n \to \bar{n}$ transitions induced via $n \to n'$ and $n \to n'$ mixings has a tiny effect on the stability of nuclei [87].

1.12 Experimental Concepts, Review of Previous $n \to n'$ Searches, and Looking Forward

Two main experimental approaches are used to search for $n \to n'$: measurements of neutrons trapped in a UCN bottle, as well as in CN beams. The principles behind these approaches are illustrated in Fig. 1.22. If a $n \to n'$ process exists, there would be anomalous loss of neutrons for a UCN trap (left panel (a) of Fig. 1.22); with CN beams, experiments can look for the regeneration of neutrons following a beam stop (left panel (b) of Fig. 1.22), an unexplained disappearance of neutron flux (left panel (c) of Fig. 1.22), and $n \to \bar{n}$ via $n \to \{n', \bar{n}'\} \to \bar{n}$ (left panel (d) of Fig. 1.22) which can then generate final state annihilation products on a target. For a comprehensive set of searches with both UCN and beam neutrons, disappearance and regeneration experiments should scan as wide a range of magnetic fields as possible, as illustrated in the right panels [96].

Early searches for $n \to n'$ were performed using UCN gravitational storage traps to correlate the possible disappearance of neutrons with the variation of the laboratory magnetic fields [391, 57, 367, 369, 110, 364], assuming the Earth's magnetic field should be compensated to near zero (to satisfy the quasifree condition) and to permit the $n \to n'$ process to occur. With this assumption, the best limit for a free oscillation time $\tau_{nn'}$was obtained by [369], where $\tau_{nn'} \geq 448$ s (90 % CL). More recent measurements and analyses [99, 32] (see again Fig. 1.17) have accounted for the possibility of a modest sterile sector magnetic field by including a wider variation of the laboratory magnetic field $\vec{B}$ in the UCN traps.

From the analysis of all existing UCN experimental data, the lower limits on $\tau_{n\to n'}$ as a function of $|\vec{B}'|$ were obtained [91] in the range of ~ 10 s for dark sector magnetic fields $\lesssim 0.3$ G. However, one UCN experiment [367, 369], reanalyzed in [99], has reported a non-zero asymmetry with a significance of $\sim 5\sigma$ in the storage time of unpolarized neutrons within a beryllium-coated trap when a laboratory magnetic field was regularly changed from +0.2 G to -0.2 G. This anomalous result was interpreted [99] as a $n \to n'$ signal, with the asymmetry caused by the time-dependent variation of the angle β between vectors of magnetic fields of sterile and laboratory fields, $\vec{B}'$ and $\pm\vec{B}'$. Thus, $n \to n'$ transitions with $\tau_{nn'} \sim 30$ s are not excluded for a region of $|\vec{B}'| \sim 0.25$ G.

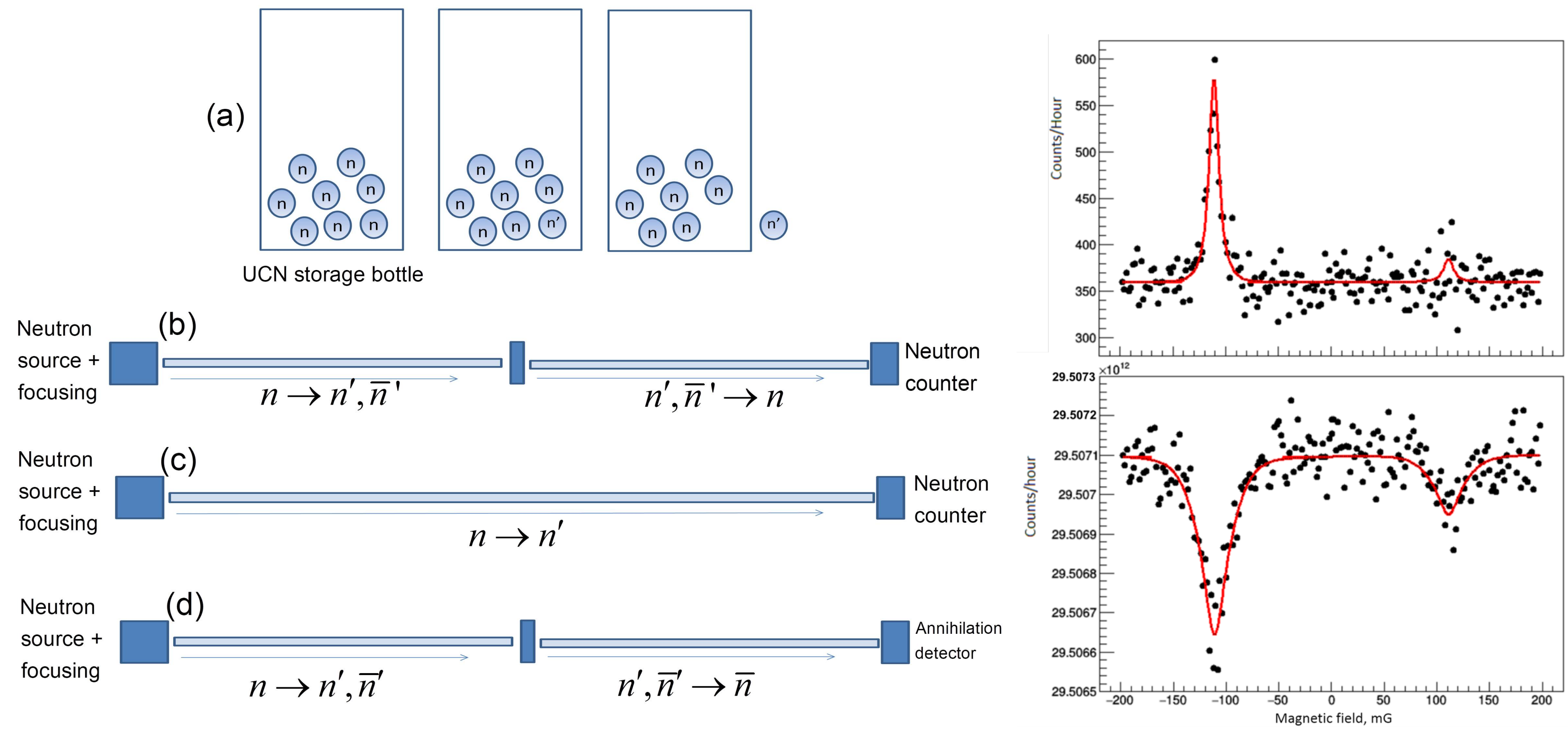

Figure 1.22: Left panels: Illustration of the principles of searches for mirror neutron mixing in a UCN trap (a) and for beam neutrons. Regeneration, disappearance and $n \to \{\bar{n}, n'\} \to \bar{n}$ modes for neutrons along a beamline are shown in (b),(c), and (d) respectively. Courtesy of D. Milstead. Right panels: Examples of $n \to n' \to n$ regeneration (top) and $n \to n'$ disappearance (bottom) style searches are shown with gaussian noise in neutron monitors/detectors; resonances occur at appropriate magnetic field values. If the transition amplitude is strong, the data can be easily fitted according to formulations such as Eq. 1.34. Taken from [96].

Fig. 1.23 shows the current best lower limit from neutron trap experiments together with the expected sensitivity of the HIBEAM experiment (in a disappearance mode) after one year of running at the ESS ANNI beamline at 1 MW of operating power (to be discussed in detail throughout Chap. 3). Increases in sensitivity of greater than an order of magnitude are possible depending on the value of the magnetic field used. It can be seen that HIBEAM covers a wide range of oscillation times for a given magnetic field value (though the uniform distribution shown here is for effect only), most of which are unexplored by current UCN-based experiments, implying the sensitivity can increase quadratically with the observation time. However, the possible contribution of a neutron TMM complicates this picture. For simplicity, the figure of merit of "sensitivity" when comparing experiments is here taken to be the lower limit on the oscillation time.

It should be noted that the interpretations of these lower limits rely on experimental assumptions, which may be poorly understood; for instance, consider neutron collisions on UCN material trap walls [331]. This source of systematic uncertainty can be removed by performing dedicated searches with propagating cold neutrons [96] in a magnetic field, as planned for the HIBEAM experiment.

High precision searches for $n \to n'$ using UCN are also being pursued currently at PSI by the nEDM collaboration [7], albeit for a magnetic field largely over regions of $|\vec{B}| < 0.2\,$G. A series of searches for $n \to n'$ due to various processes along a beamline (e.g. Fig. 1.22) are also planned at the High Flux Isotope Reactor at Oak Ridge National Laboratory [120, 121]; the higher beam intensities of the ESS, and the longer available flight paths, will permit still higher sensitivities.

1.13 Lepton Scattering

Leptons, like their baryonic counterparts, are similarly indelible yet indivisible players on the stage of Standard Model. Indeed, together with baryons, as shown in Sec. 1.2.1, they permit the interdependent renormalization of the Standard Model through anomaly cancellation [386, 21].

Thanks to their lack of strong interaction, leptons provide the primary testing grounds for electroweak interactions of the γ, $W^{\pm}$, and Z^0 gauge bosons. Because of these, and with half of them containing electric charge, they are ideal for probing the structure of the nucleus with both its charged and neutral constituents at incredibly high precision. Electrons are of course the lightest of

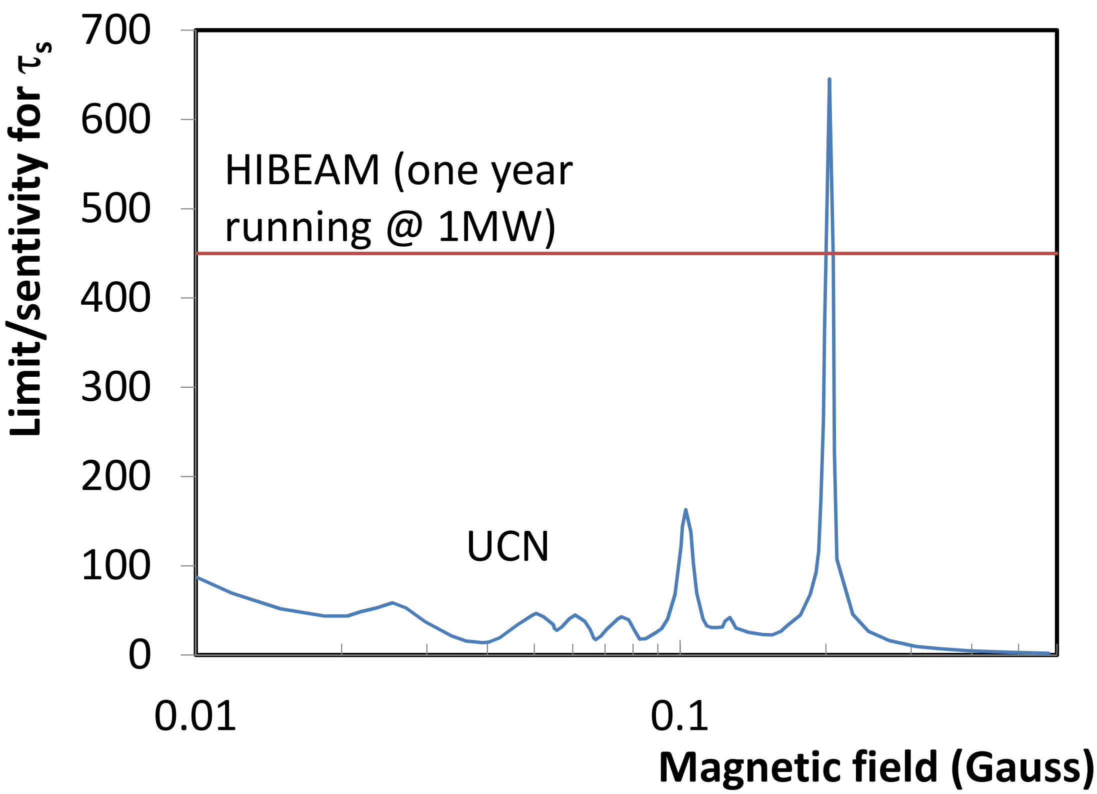

Figure 1.23: Excluded neutron oscillation times in blue for $n \rightarrow n'$ disappearance from UCN experiments [57, 364, 32, 99, 91, 8] as a function of the magnetic field $\vec{B}'$. The projected sensitivity for HIBEAM (disappearance mode) is also shown in magenta for one year of running at the ESS ANNI beamline, assuming a low 1 MW operating power, and will be discussed at length in Chap. 3. Courtesy of D. Milstead and Z. Berezhiani.

the charged leptons (thus they should never decay), and are easily produced by heating materials or exposing them to strong electric fields; their charge allows them to be accelerated and collimated into beams of precise (low and high, ~ 0.01-$10\,\mathrm{GeV}$) energies ideal to study elastic, quasielastic, resonant production, and deep-inelastic scattering processes on nuclei. Such scattering permits one to ascertain the underlying structure and dynamics of the nucleus in detail.

Assuming lepton universality holds true (which is today becoming a contentious statement [115, 248]), one may generally construct all lepton interactions and their relevant cross sections semi-identically (save for the particles' presence or absence of electric charge and the mass differences present in the propagators of their gauge bosons). Thus, one may consider electron scattering as a veritable test-bed for the interaction of their neutral cousins, the prodigious neutrino. Through studying electron interactions, one may draw many useful conclusions as to what types of processes are expected in neutrino scattering.

Neutrinos of course have their own rich phenomenologies beyond their seemingly simplified interaction processes. Their light masses leave potentially much to be discovered [362, 301, 363, 418, 207]. Together with their masses and neutral character, this allows them to oscillate [231, 206], where three flavor states exchange among three single mass states [31, 132]. However, these particles, when produced in the atmosphere, can create irreducible backgrounds for large underground experiments searching for rare signals. The imprecise modeling of the cosmological, astrological, geographical, geological, and meteorological processes which generate the conditions for the production for these atmospheric neutrinos [247] are difficult to contend with; further, the nuclear modeling within experiments of their interactions is somewhat underdeveloped [62, 34, 39]. Thus, in order to better understand the viability of rare searches, one must too understand and model these macroscopic and microscopic processes as precisely and accurately as possible.

The great commonality of the leptons allows many of their processes to be discussed simultaneously via the example of the electron without too much loss of generality. Here I will review some of the basic tenets of lepton scattering theory, their modeling and simulation.

1.13.1 Leptonic & Hadronic Tensors, and Generalized Scattering

Any lepton scattering process can be considered to emanate from two fundamental objects: the lepton and hadron tensor, $L_{\mu\nu}$ and $W^{\mu\nu}$ [342]. One may construct a total inclusive lepton scattering cross section of any process where the hadron remains undetected as

$$\frac{d^2\sigma}{dEd\Omega} \propto L_{\mu\nu}W^{\mu\nu}. \tag{1.49}$$

The hadronic tensor contains all information pertaining to the nuclear target's response:

$$W^{\mu\nu} = \sum_f \langle 0| J^{\mu\,\dagger}(q) |f\rangle \langle f| J^{\nu\,\dagger}(q) |0\rangle \, \delta^4(p_o + q - p_f), \tag{1.50}$$

where J's parametrize the electroweak currents coupling the electron and proton, and an energy conserving δ-function is shown. For a process of high momentum transfer, this object is in principle only calculable numerically, and super-computers today take on such computations [318, 343, 282]. However, the leptonic tensor is known to have a near universal[16] structure of

$$L_{\mu\nu} = k_\mu k'_\nu + k'_\mu k_\nu - g_{\mu\nu}(kk'), \tag{1.51}$$

analytically at energy scales where $Q^< < m_W^2$, where k_μ is the initial and k'_μ the final momentum.

We find that the *most general* scattering amplitude of two particles of different masses exchanging a single massless photon from quantum electrodynamics yields [402, 233]:

$$\langle|M_{fi}|^2\rangle = \frac{8e^4}{(p_1 - p_3)^4}[(p_1{\cdot}p_2)(p_3{\cdot}p_4)+(p_1{\cdot}p_4)(p_2{\cdot}p_3)-(p_1{\cdot}p_3)M^2-(p_1{\cdot}p_4)m^2+2m^2M^2]. \tag{1.52}$$

where $e^2 = 4\pi\alpha$, $m \equiv m_e$ the mass of the electron, $M \equiv M_p$ is the mass of the proton, and α is the fine structure (electromagnetic coupling) constant.

[16] This is not entirely the case, as the leptonic tensor *can* in principle be channel dependent. For instance, in neutrino scattering, there are extra terms involving Levi-Civita tensors. However, neglecting Coulomb corrections, the leptonic tensor is analytically calculable from straightforward traces over Dirac matrices and spinors.

1.13.2 Elastic and Quasielastic Scattering

The most basic of lepton scattering interactions on nuclei is that of an electron scattering on the motionless proton, wherein the proton is idealized as a point particle and the effectively massless electron scatters off with little to no deviation in its total momentum (and so *elastically*). In general, this process can be shown as in 1.25 [402], though with certain conditions.

If one works in the low energy limit, ignoring the scattered proton's recoil energy (i.e. $M \to \infty$ [197]) when considering a nonrelativistic electron, and treats both particles as spinless, one recovers the classical Rutherford scattering cross section from a quantum description [197]. This leads to the differential cross section in the laboratory frame:

$$\left(\frac{d\sigma}{d\Omega}\right)_{\text{Rutherford}} = \frac{\alpha^2 m^2}{4|\vec{p}|^4 \sin^4 \frac{\theta}{2}} \ , \tag{1.53}$$

where p is the initial three-momentum of the electron and θ the scattered angle. It should be noted that this expression can be more simply derived by considering the nonrelativistic electron to scatter from a static Coulomb potential while ignoring the magnetic moments of either the electron or proton, implying that only the total electric charges of the two particles play a significant role within these energy regimes.

One can progress beyond the simplistic assumption of a nonrelativistic electron to a relativistic one, yet continue to ignore the electron mass, then arriving at the Mott scattering cross section [402, 260, 197] where

$$\left(\frac{d\sigma}{d\Omega}\right)_{\text{Mott}} = \left(\frac{\alpha \cos \frac{\theta}{2}}{2E \sin^2 \frac{\theta}{2}}\right)^2 = \frac{\alpha^2}{4E^2 \sin^4 \frac{\theta}{2}} \cos^2 \frac{\theta}{2}, \tag{1.54}$$

where the first factor of the far right hand side of this equation can be identified with the Rutherford formula 1.53 where $E >> m$, and the second factor therein represents an overlap between initial and final state electron spins, i.e. a correction from the electron's magnetic moment. It should again be noted that one could have derived 1.54 from electrons scattering on a static electric potential. One may also properly account for the recoil motion of the proton via a new factor [139], where

$$f_{rec} = 1 + \frac{E_{e_f} - E_{e_i} \cos \theta}{E_{p_f}} \approx 1 + \frac{2E_{e_i}}{m_e} \sin^2 \frac{\theta}{2} \tag{1.55}$$

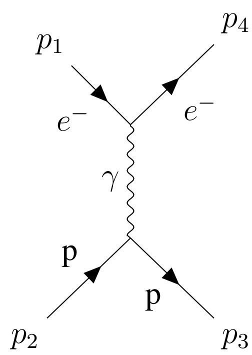

Figure 1.24: A single generalized electron (e^-, mass m) scattering Feynman diagram where the proton (p, mass M) is considered as pointlike, interacting via the exchange of a single gauge boson (photon, γ).

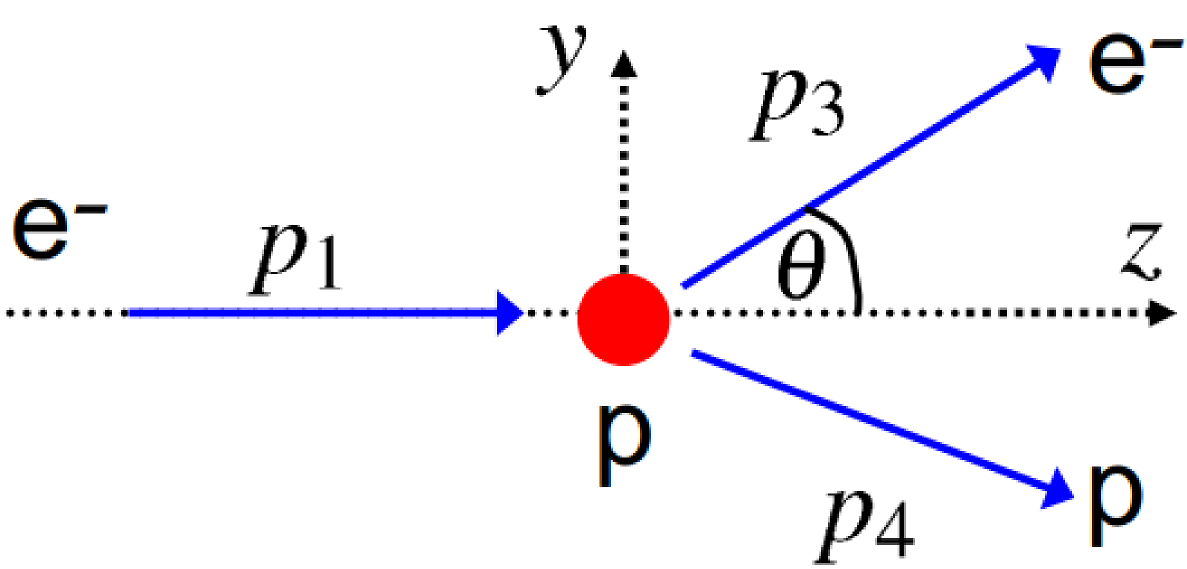

Figure 1.25: A general momentum conservation diagram for the same process, consisting of a frame (y, z) in which the proton is initially motionless. Taken from [402]

enters inversely.

When neglecting the scattered proton (perhaps it cannot be detected), one may instead speak of momentum transfer, $|\vec{q}|$, implied from the momentum difference of the incoming and outgoing electron. In doing so, one can rewrite Eq. 1.54 [402] to find that

$$\frac{d\sigma}{d\Omega} = \frac{\alpha^2}{4E_1^2 \sin^4 \frac{\theta}{2}} \frac{E_3}{E_1} \left(\cos^2 \frac{\theta}{2} - \frac{q^2}{2M^2} \sin^2 \frac{\theta}{2} \right), \tag{1.56}$$

where the ratio E_3/E_1 is seen to be due to the proton recoil, and the last term proportional to $\sin^2 \frac{\theta}{2}$ contains the magnetic interaction due to spin-spin coupling. Note that for a given value of θ, one can see that both q^2 and the outgoing energy of the electron E_3 are fixed by kinematics.

Of course, when dealing with more complicated nuclear targets of many nucleon systems or particular interactions on those nucleons (such as a neutrino with a charged current via $W^{\pm}$), one must appropriate and recast these relations for quasielastic scattering with mostly minor changes. Overall, the quasielastic regime can be thought of as an extension of the elastic one, though marked by the emission of a single nucleon and or a charged lepton (in the case of charged-current neutrino interactions) from the nuclear target. Beyond this point, other dynamics, such as those of meson exchange currents, short-range correlations, and resonant production play a critical role, taking over before entering the inelastic regime. These contributions complicate the cross section still more, especially when double counting is not properly taken account of. These will be covered more completely in Chap. 5.

1.13.3 Form Factors

We can consider the possibility of an electron scattering on a static potential representing an extended charge distribution [402] where

$$V(\vec{r}) = \int d^3\vec{r} \frac{\tilde{Q}\rho\left(\vec{r'}\right)}{4\pi\left|\vec{r} - \vec{r'}\right|}, \tag{1.57}$$

where Q is the total charge and ρ is a unit normalized charge distribution. Then pertubative calculation of scattering matrix elements yields

$$M_{fi} = \int d^3\left(\vec{r} - \vec{r'}\right) e^{i\vec{q}\cdot\left(\vec{r}-\vec{r'}\right)} \frac{\tilde{Q}}{4\pi\left|\vec{r} - \vec{r'}\right|} \cdot \int d^3\vec{r'}\rho\left(\vec{r'}\right) e^{i\vec{q}\cdot\vec{r'}}, \tag{1.58}$$

where $\vec{q} = \vec{p}_1 - \vec{p}_3$. The first integral factor of this equation can be identified with classical scattering from a point source of total charge $\tilde{Q}$. Thus, the second factor can be identified as the *form factor* taking on the integral of the charge distribution:

$$F\left(\vec{q}^2\right) = \int d^3\vec{r}\rho\left(\vec{r}\right) e^{i\vec{q}\cdot\vec{r}}, \tag{1.59}$$

which can be thought of as a Fourier transform of the charge distribution (for a spin-0 target [197]). For a point charge, the form factor is unity [402]. Thus, one may rewrite the Mott cross section as

$$\left(\frac{d\sigma}{d\Omega}\right)^{\text{w/recoil}}_{\text{Mott}} = f_{rec}^{-1}\left|F\left(\vec{q}^2\right)\right|^2 \cdot \frac{\alpha^2}{4E^2\sin^4\frac{\theta}{2}}\cos^2\frac{\theta}{2}\ . \tag{1.60}$$

Thus, such calculations take on a great semblance with classical optics via the diffraction of plane waves through a nonabsorptive medium.

Given this new ability to illuminate the inner structure of the proton (or indeed any nucleon), one can consider the charge distribution and magnetic moment of the proton (nucleon) using the electric (G_E) and magnetic (G_M) form factors in the Rosenbluth cross section [402, 197] as

$$\frac{d\sigma}{d\Omega} = \frac{\alpha^2}{4E_1^2\sin^4\frac{\theta}{2}}\frac{E_3}{E_1}\left(\frac{G_E^2 + \tau G_M^2}{1+\tau}\cos^2\frac{\theta}{2} + 2\tau G_M^2\sin^2\frac{\theta}{2}\right), \tag{1.61}$$

with $\tau = -\frac{q^2}{4M^2} > 0$ and where q is instead the four-momentum transfer, and so $q^2 = (E_1 - E_3)^2 - \vec{q}^2$. Note that for $\frac{q^2}{4M^2} << 1$ one sees that $q^2 \approx \vec{q}^2$, and so $G(q^2) \approx G(\vec{q}^2)$. Thus, in this limit, one attains direct access to the charge and magnetic moment distributions of nucleons via

$$G_E\left(q^2\right) \approx G_E\left(\vec{q}^2\right) = \int d^3\vec{r}e^{i\vec{q}\cdot\vec{r}}\rho\left(\vec{r}\right), \text{ and } G_M\left(q^2\right) \approx G_M\left(\vec{q}^2\right) = \int d^3\vec{r}e^{i\vec{q}\cdot\vec{r}}\mu\left(\vec{r}\right). \tag{1.62}$$

Here, for a spin-$\frac{1}{2}$ proton with $\mu = 2.79\frac{e}{M}\vec{S}$, one expects $G_E(0) = 1$ and $G_M(0) = 2.79 = \mu_p$; this anomalous ($\neq 1$) magnetic moment of the proton implies that the proton is not pointlike.

In scattering experiments, these form factors can be measured separately through a fixed value of q^2 at various outgoing electron angles, i.e., a Rosenbluth separation technique. A good fit to the data for these is the "dipole" form [402, 197], where

$$G_E^p(q^2) \approx \frac{G_M^p(q^2)}{2.79} \approx \frac{1}{\left(1 + \frac{q^2}{0.71\,\mathrm{GeV}^2}\right)^2}, \tag{1.63}$$

and similarly

$$G_E^p(q^2) \approx \frac{G_M^p(q^2)}{\mu_p/\mu_N} \approx \frac{G_M^n(q^2)}{\mu_n/\mu_N}, \text{ while } G_E^n = -\frac{\mu_N}{1+5.6\tau} G_E^p, \tag{1.64}$$

where the neutron's electric form factor instead follows an altered form [208]. After taking the Fourier transform, one may solve for the spatial charge and magnetic moment distributions, implying that the charge radius of the proton is $\sim 1\,\mathrm{fm}$ in size. Note that at high values of q^2, say for $\tau >> 1$ [401], the Rosenbluth expression becomes

$$\frac{d\sigma}{d\Omega} = \frac{\alpha^2}{4E_1^2 \sin^4\frac{\theta}{2}} \frac{E_3}{E_1} \left(\frac{q^2}{2M^2} G_M^2 \sin^2\frac{\theta}{2}\right) \propto q^{-6}, \tag{1.65}$$

However, due to the finite size of the proton (nucleon), it is expected that elastic or quasielastic interactions at high values of q^2 are unlikely (one reason why short-range correlations are difficult to illuminate, [198]). Though these points are *suggestive*, the evidence for the *composite* nature of the nucleon comes from deep inelastic scattering and proton breakup [402].

1.13.4 Inelastic and Deep Inelastic Scattering

We can generally consider elastic or even quasielastic scattering to pertain to those cases in which the initial and final state of the target are relatively unchanged. For inelastic and deep inelastic scattering, there exist much richer possibilities, potentially with many final state particles following a nuclear target's breakup or excitation (to a Δ baryon, perhaps).

The fact that cross section data do not follow a Mott curve ($\propto q^{-6}$) at high values of q^2 requires further study and explanation [116]. For an inelastic scattering, one can consider the possibilities of Fig. 1.26, where the final state of the hadronic system is no longer the proton mass, M, but instead can be much higher in principle due to high momentum transfers breaking up the proton.

From baryon number conservation, it is known that this system must maintain at least one total baryon in the final state, and so $M_X > M$ where $M_X = p_4^2 = E_4^2 - |\vec{p}_4^2|$; thus, M_X can include new states such as mesons.

The transition between elastic or quasielastic scattering and deep inelastic scattering can be nicely illustrated by several new kinematic variables, including the Lorentz invariant quantity Bjorken-x:

$$x = \frac{Q^2}{2p_2 \cdot q}, \tag{1.66}$$

where the negative square of four-momentum is $Q^2 \equiv -q^2 > 0$. Note that the final state baryonic system with mass $M_X \equiv W$ follows

$$M_X^2 = p_4^2 = W^2 = (q + p_2)^2 = -Q^2 + 2p_2 \cdot q + M^2, \tag{1.67}$$

where the traditional total energy W has been used for clarification. Thus:

$$Q^2 = 2p_2 \cdot q + M^2 - M_X^2. \tag{1.68}$$

From this, one sees that that $Q^2 \leq 2p_2 \cdot q$; rearranging, this allows one to easily define Bjorken-x (see again Eq. 1.66). One can thus interpret here that Bjorken-x effectively represents a kind scale parameter, where ranges of $0 < x < 1$ represent inelastic scattering while $x \geq 1$ represents quasielastic and elastic interactions [401]; indeed, high values of Bjorken-x can probe larger scales of interaction, for instance, those of short-range correlations [198]. An x-value of at least unity implies that the proton has remained intact, and so has not interacted inelastically[17]. Another way to conceive of this same range is when $W = M_X = M$, one recovers elastic or quasielastic interactions, while, for instance, if $W = M_X = M_\Delta$, instead some form of excitation process has begun via, e.g., $p \to \Delta^+(1232)$; if instead $W >> \{M, M_\Delta\}$, one may consider these processes to be deeply inelastic. One also has that the Lorentz invariant Bjorken-y takes the form:

$$y = \frac{p_2 \cdot q}{p_2 \cdot p_1}, \tag{1.69}$$

[17] Of course, it will later be found that Bjorken-x can be thought of as the fraction of the proton momentum carried by the struck quark.

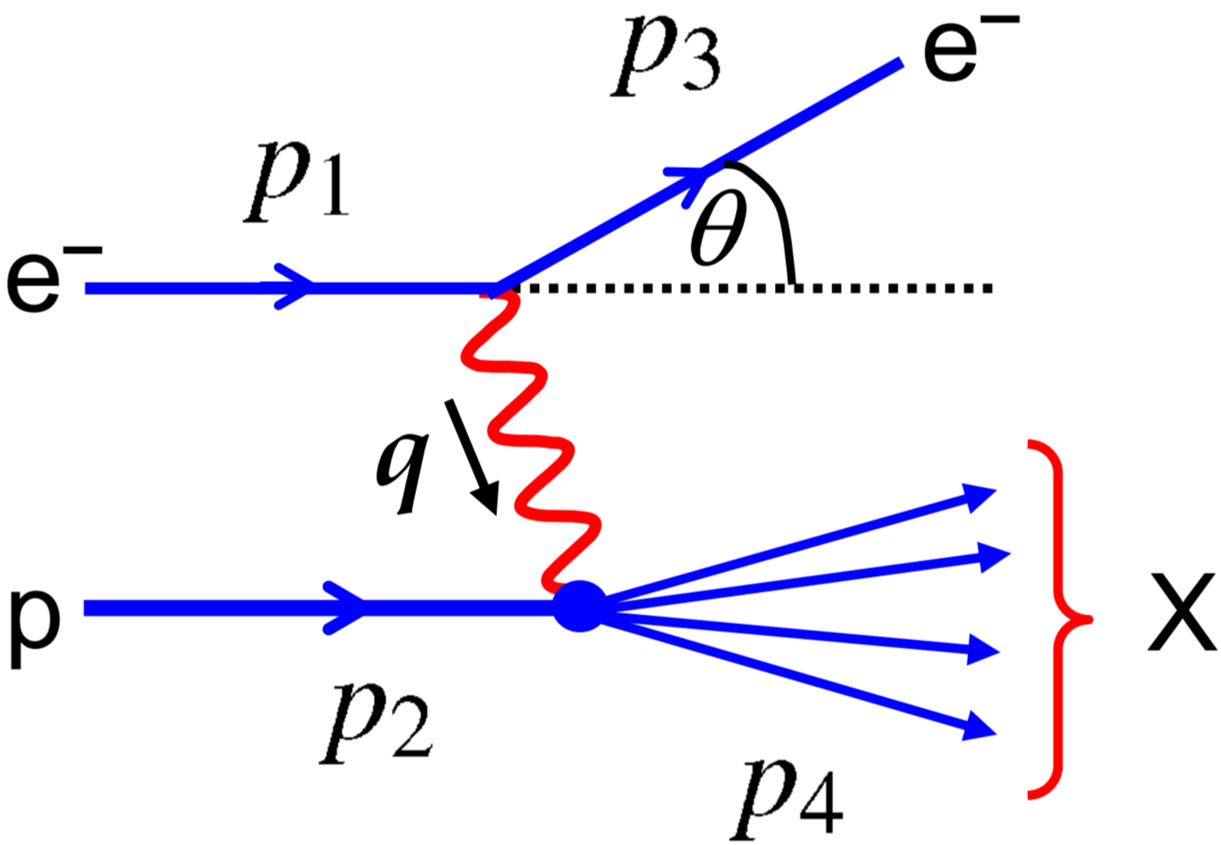

Figure 1.26: A generalized diagram of deep inelastic scattering, showing the breakup of the pointlike proton through a momentum transfer. Taken from [401].

representing the fractional loss of momentum and energy of the incoming particle.

Inelastic cross section data can be seen to weakly depend on q^2, while it has been shown that deep inelastic scattering is effectively independent of q^2. Taking heed of the previous discussion of form factors, this implies that $F \to 1$ at appropriate kinematics, and can be interpreted as a new kind of scattering from point-like objects *within* the proton [401], allowing for a most interesting connection to be made between elastic and deep inelastic scattering; in this case, one may recast the previously described form factors as *structure functions*. As discussed already, one only requires a single independent variable to describe elastic scattering; however, due to nucleon breakup, and differences between the initial and final state, one now requires two independent variables to describe deep inelastic scattering. One may rewrite both elastic and inelastic scattering cross sections using a similar form; in terms of Lorentz-invariant kinematic variables, one now finds that the single-differential elastic scattering cross section (Eq. 1.61) can be written as

$$\frac{d\sigma}{dQ^2} = \frac{4\pi\alpha^2}{Q^4}\left[\left(1 - y - \frac{M^2y^2}{Q^2}\right) f_2(Q^2) + \frac{1}{2}y^2 f_1(Q^2)\right], \tag{1.70}$$

and that the new double differential deep inelastic scattering cross section takes a similar form in

$$\frac{d^2\sigma}{dxdQ^2} = \frac{4\pi\alpha^2}{Q^4}\left[\left(1 - y - \frac{M^2y^2}{Q^2}\right) \frac{F_2(x,Q^2)}{x} + y^2 F_1(x,Q^2)\right]. \tag{1.71}$$

Note here that these structure functions F_i, unlike their form factor cousins, cannot necessarily be interpreted as Fourier transforms of magnetic moment or charge distributions; however, they can be thought of as a momentum distribution of constituent particles moving within the nucleon. In the lab frame, one can define

$$\frac{d^2\sigma}{dE_3 d\Omega} = \frac{\alpha^2}{4E_1^2 \sin^4\frac{\theta}{2}}\left[\frac{F_2(x,Q^2)}{E_1 - E_3}\cos^2\frac{\theta}{2} + \frac{2F_1(x,Q^2)}{M}\sin^2\frac{\theta}{2}\right], \tag{1.72}$$

where $Q^2 = 4E_1E_3\sin^2\frac{\theta}{2}$ and $x = \frac{Q^2}{2M(E_1-E_3)}$ have been employed. The F_2 term, containing the electromagnetic structure function, can be considered similar to the previous elastic form factor synonymous with the electric charge distribution, where, ignoring angular dependencies, $F_2(x,Q^2) \sim f_2(Q^2) \sim \frac{G_E^2+\tau G_M^2}{1+\tau}$. Similarly, the F_1 term is known as the (pure) magnetic structure function. Each have been experimentally measured to be almost entirely independent of Q^2 [401, 203].

Given the independence of the structure functions on Q^2, one can then see that $F_i(x, Q^2) \sim F_i(Q^2)$, which again is emblematic of scattering on point-like sources within the nucleon. One also sees that F_1 and F_2 are related via the Callan-Gross relation [134, 401], where

$$F_2(x) = 2xF_2(x), \tag{1.73}$$

implying that pointlike constituents of the nucleon substructure are spin-$\frac{1}{2}$ particles.

1.13.5 The Quark (Parton) Model

Historically called "partons", it is now known that the pointlike constituents of the nucleon are quarks and gluons. As seen in Fig. 1.27, one can now consider *elastic* interactions on a (quasi-)free quark. If one works in the "infinite momentum frame" where the proton (and thus its constituent quarks) has a very high energy, its mass can be neglected, and one assumes that each of the three valence quarks carry a particular fraction ξ_i^μ of the total four-momentum of the proton such that $\sum_{i=1}^{3} \xi_i^\mu = p_2^\mu$. Considering Fig. 1.27 and suppressing tensorial indices, one then sees that

$$(\xi p_2 + q)^2 = m_q \approx 0, \tag{1.74}$$

$$\therefore \xi^2 p^2 + 2\xi p_2 \cdot q \approx 2\xi p_2 \cdot q = 0, \tag{1.75}$$

and so

$$\xi = \frac{Q^2}{2p_2 \cdot q} = x. \tag{1.76}$$

Thus, Bjorken-x can be thought of as the fraction of momentum carried by the struck quark within the proton. It can be shown that, in this frame, scattering on the partons is elastic, and thus electron scattering on a *motionless* quark takes the form

$$\frac{d\sigma}{dQ^2} = \frac{4\alpha^2 e_q^2}{Q^4}\left[(1-y) + \frac{y^2}{2}\right]. \tag{1.77}$$

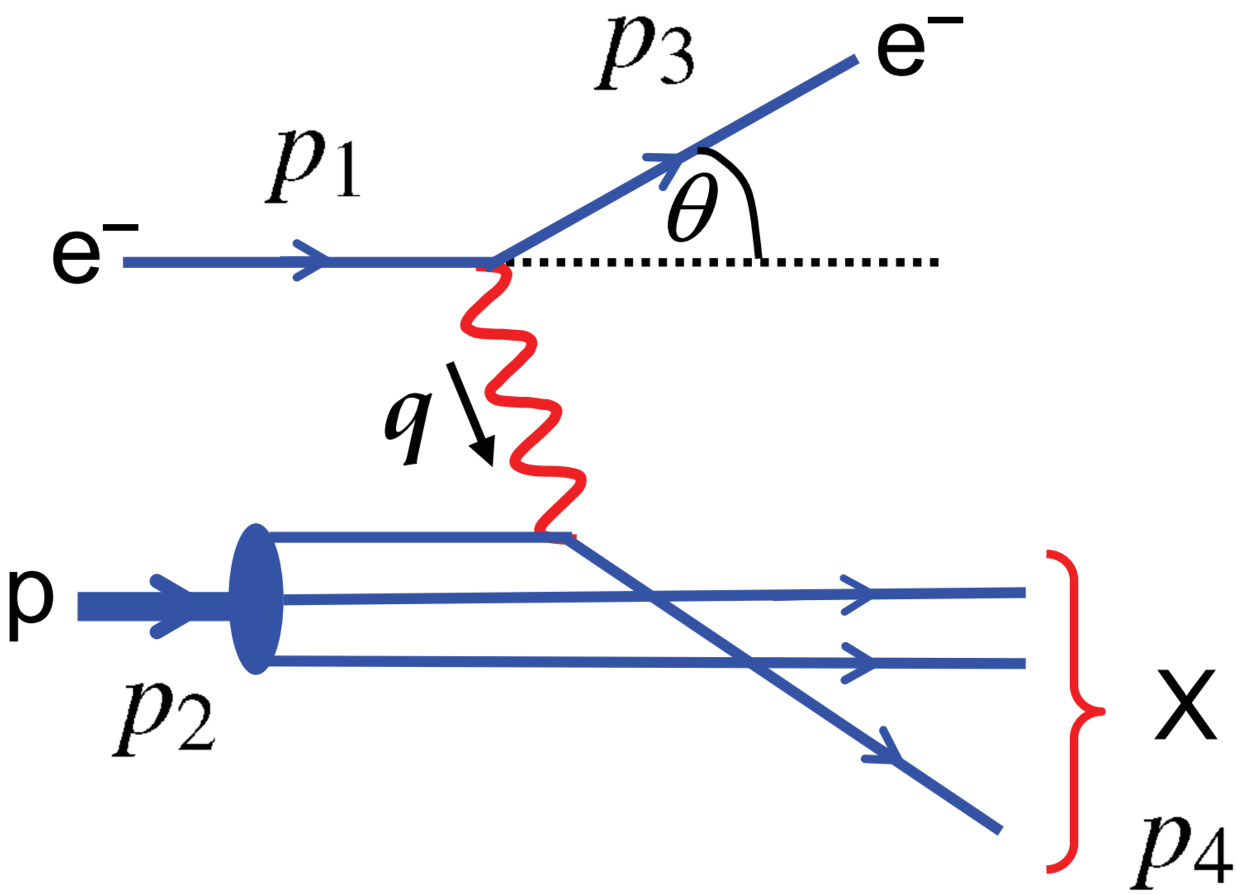

Figure 1.27: A generalized diagram of deep inelastic scattering, showing the breakup of the proton through a momentum transfer to a single valence quark carrying some fraction of the total proton momentum. Taken from [401].

In order to understand the motion of quark inside the nucleon, N, one must take account of the *parton distribution functions*, $q^N(x)$, where, after summing over all quark types within the proton [401] one finds the total inclusive electron-proton scattering cross section:

$$\frac{d^2\sigma^{\mathrm{ep}}}{dQ^2} = \frac{4\pi\alpha^2}{Q^4}\left[(1-y)+\frac{y^2}{2}\right]\sum_q e_q^2 q^{\mathrm{p}}(x). \tag{1.78}$$

This bears a fantastic resemblance to the previous finding in Eq. 1.71 at high values of Q^2, and so one may relate the structure functions to these parton distribution functions for the proton via

$$F_2^{\mathrm{p}}(x,Q^2) = 2xF_1^{\mathrm{p}}(x,Q^2) = x\sum_q e_q^2 q^{\mathrm{p}}(x). \tag{1.79}$$

Thus, at high energies, measurements of the structure functions allows for a determination of the parton distribution functions, as well as determine the mean fraction of u and d quarks within the proton [401].

1.13.6 Short-Range Correlations

So far, only interactions on a single nucleon (proton) struck by a lepton (electron) have been considered through the exchange of a single gauge boson (photon). However, most nuclear targets are far more complex, and multiple scales of interaction can effect (and potentially *enhance*) the total inclusive cross section. Thus, not only must one consider the scattering process on the nucleon, but also the initial state of the struck nucleon which is itself interacting with the nuclear environment throughout the scattering process.

At short to intermediate distances ($\lesssim$ 1.2 fm), it is possible for nucleons to pair together in pairs and triplets through Yukawa interactions utilizing virtual meson exchanges [198] which mediate the strong interaction between constituent nucleons; these can be considered within a many-body Hamiltonian [318]. Such interaction introduce *correlations* between the nucleons; these were initially added in an *ad hoc* manner to nucleon-nucleon interactions to avoid issues with calculations of the ground state energy of nuclei [198, 255]; their dynamical origin would not become clear for some time. It is now known that such correlations lie visible predominately within the high Bjorken-x quasielastic scattering regime, and have been measured directly [383, 198] via $(eA, e'NNX)$ coincidence experiments at facilities such as Jefferson Laboratory [256].

Effectively, the existence of short-range correlations imply that a given lepton may electroweakly scatter on more than a single, primary nucleon. Indeed, scattering may now occur on pairs of correlated nucleons[18]; speaking purely phenomenologically and using geometric inference, such a pair thus enhances the effective total inclusive cross section. The scattering on single and paired nucleons is nicely illustrated in Fig. 1.28, and will be the subject of further discussions in Chap. 5.

The interactions which mediate these correlations are two-and-three nucleon operators. In a χEFT which uses fitted coefficients to expansion terms which maintain underlying QCD dynamics and symmetries, contact terms officiate the short-range interactions, while one and two pion exchanges mediate the long range ($r \propto m_\pi^{-1}$) and intermediate range ($r \propto (2m_\pi)^{-1}$) interactions [318, 69]. These can be used to construct a full Hamiltonian of a given nucleus (in principle; these are calculated in the context of super-computing quantum Monte Carlo within [343, 345, 344, 282, 284, 318, 69, 414, 413]); see later discussions within Chap. 5 for a more complete discussion. Thus, these in turn inform the methodology of calculating lepton scattering from one-and-two bodies.

In a χEFT, one-and-two body scattering is mediated by one-and-two-body currents, the latter being a manifestation of two-nucleon correlations. For electromagnetic scattering, the two body currents satisfy the current conservation law

$$\mathbf{q} \cdot \mathbf{j} = [H, \rho] = [t_i + v_{ij} + V_{ijk}, \rho] \,, \tag{1.80}$$

where the Hamiltonian's terms represent one body, two body, and three body operators, respectively. Here, the nuclear charge operator takes the form

$$\rho = \sum_{i=1}^{A} \rho_i + \sum_{i<j} \rho_{ij} + \cdots \,, \tag{1.81}$$

[18]Scattering on triplets is of course possible as well, though this cross section is very small [198].

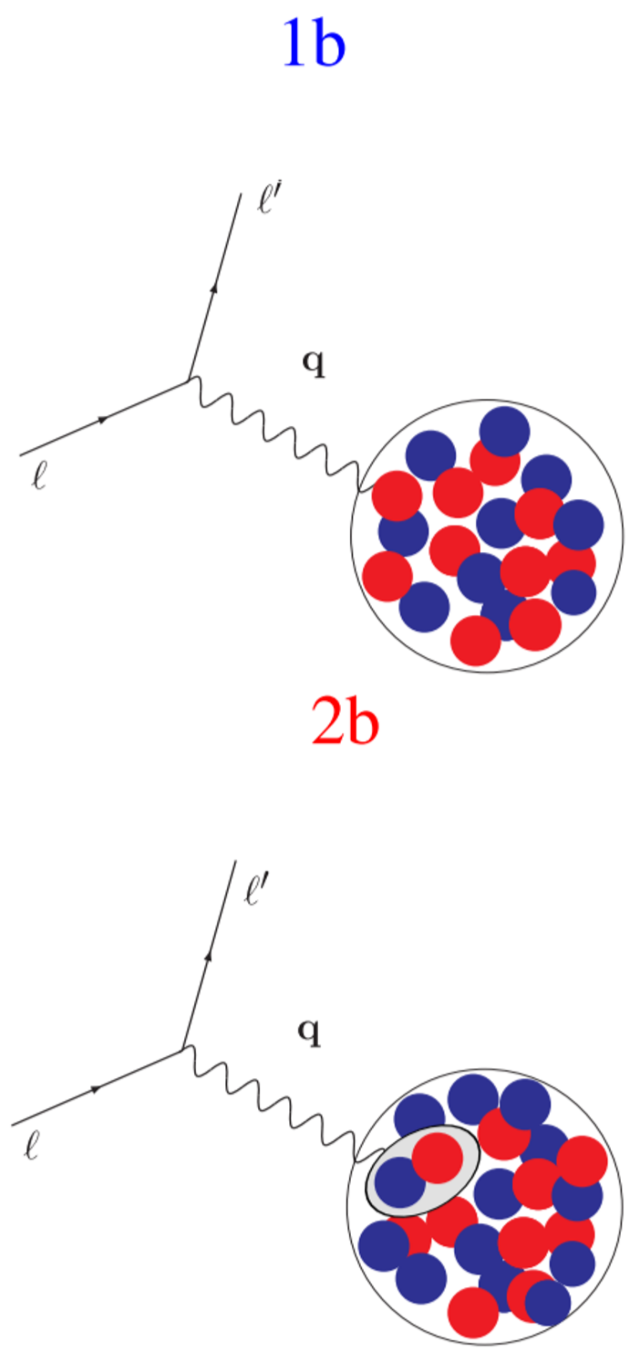

Figure 1.28: Generalized quasielastic scattering on single and correlated pairs of nucleons within the nucleus. Courtesy of S. Pastore.

and the nuclear (vector) current operator takes the form

$$\mathbf{j} = \sum_{i=1}^{A} \mathbf{j}_i + \sum_{i<j} \mathbf{j}_{ij} + \cdots . \tag{1.82}$$

From here, one can surmise for electromagnetic scattering that the longitudinal nuclear response function will be encoded within the charge operator, while the transverse response will come from the current operator. Similarly, this confirms measured back-to-back-like two-body final states [383]. The currents terms of leading one-body and interference terms can be nicely viewed as Feynman diagrams in Fig. 1.29. The details of the nuclear response [260, 69], along with how experimental simulation frameworks such as the `GENIE` Monte Carlo Event Generator work will be detailed in Chap. 5.

1.14 Conclusions and Following Chapters

A review of all critical theory discussions and formulations have been made throughout this chapter, including the physics of baryogenesis, dark matter, and the neutron lifetime. Avenues toward resolution of these issues were also discussed, including via neutron oscillation physics of various types; these will be discussed further throughout Chaps. 2, 3, and 4. In the last section of this chapter, some pertinent theoretical points of electron scattering have been discussed; similar to neutrino scattering in many ways, I hope it serves as a brief yet instructive overview. Current developments in this area will be discussed further in Chap. 5, which could greatly affect future work on neutrino oscillation measurements and atmospheric neutrino background calculations, as pursued in Chap. 4.

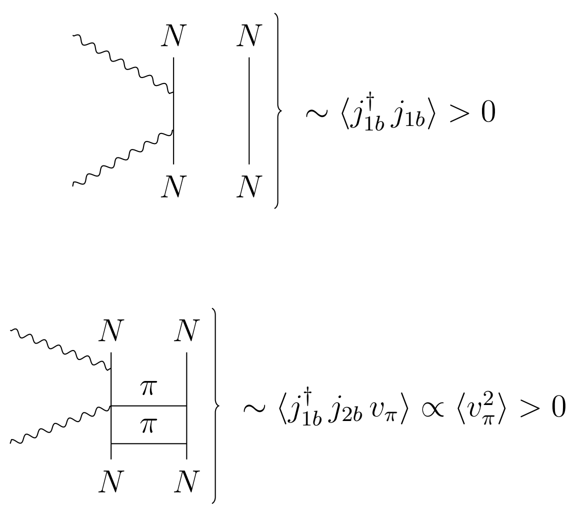

Figure 1.29: Top: The leading one-body current term showing scattering on two uncorrelated nucleons. Bottom: An interference term is shown with a two pion exchange between two correlated nucleons; the vertex of the scattering lepton's virtual photon can connect with one of the pion legs. Of course, each additional new diagram progressively changes the total inclusive cross section perturbatively up to any order, but most quantum Monte Carlo calculations take account only of one-and-two body scattering.

Chapter 2

Modeling $n \to \bar{n}$ Annihilation via an Independent Monte Carlo Simulation

2.1 A Brief $n \to \bar{n}$ Review and Goals

Searches for baryon number violation, including searches for proton decay and neutron-antineutron transformation ($n \to \bar{n}$), are expected to play an important role in the evolution of the physics community's collective understanding of beyond Standard Model physics. $n \to \bar{n}$ is a key prediction of certain popular theories of baryogenesis [50, 47], and experiments such as the Deep Underground Neutrino Experiment (DUNE), the European Spallation Source (ESS), and Hyper-and-Super-Kamiokande plan to or already are searching for this process with bound- and free-neutron systems. Accurate simulation of this process in Monte Carlo will be important to understand the signal's properties for the proper reconstruction with a high signal efficiency and improved separation of these rare events from background.

In this chapter, I present universal developments[1] [229, 71, 70] towards accurate simulation of extranuclear and intranuclear $\bar{n}$ annihilation processes. These simulations are designed for experimental research and design preparation uses in a cold, free neutron beam for $n \to \bar{n}$ searches using $\bar{n}$C annihilation for ESS's NNBAR collaboration, as well as intranuclear searches for $\bar{n}^{15}$O

[1]Many thanks to E. S. Golubeva, J-M. Richard, E. Paryev, A. Botvina, and C. G. Ladd for their collaboration on this work.

and $\bar{n}^{39}$Ar for Super-Kamiokande and the Deep Underground Neutrino Experiment (DUNE), respectively. Experimental validation is made on available $\bar{p}p$ and $\bar{p}^{12}$C data [229], and other comparisons follow against `GENIE` [40, 39] for the case of ^{40}Ar [71]; some progress will also be briefly discussed throughout pertaining to a forthcoming publication [70] on ^{16}O.

2.2 Past Simulations for Free and Bound $n \to \bar{n}$ Searches

It is critical to recognize the interdependency of the computational modeling of BSM signals *and* backgrounds in the estimation of detectors' signal efficiencies and background rates within the context of large modern experiments. Thus, it becomes crucially important that one should take care to model BSM signals and backgrounds as completely, consistently, and rigorously as necessary by employing limited approximations which attempt to preserve as much microphysics as possible. This is especially true given nontrivial automated triggering and analysis schemes[2] planned for future rare event searches, to be discussed in Chap. 4. Unfortunately, for many previous $n \to \bar{n}$ studies, this has not altogether been the case, yet MCs have been an integral part of all past experiments. Sadly, the descriptions of these MCs are not always complete or seemingly consistent, and are not easily accessible.

Intranuclear searches have been completed far more times than free neutron experiments, and so their accompanying generators are similarly abundant. Never-the-less, many of their descriptions are scattered throughout a multitude of dissertations and have been historically poorly defended within published works[3]. Similarly, open access to these simulations is lacking. For instance, the original $n \to \bar{n}$ Super-Kamiokande publication [4] cites only three works in reference to their generator, one of which is a previous work of my chief collaborator, E. S. Golubeva, and two of which contain rather ancient antiproton annihilation data; how exactly these are implemented within their model is not available, and was not discussed with Golubeva.

Previous work in ^{40}Ar (though applicable to all nuclei) by Hewes [243] and others from the DUNE High-Energy Physics (formerly the Nucleon Decay and Atmospheric Neutrinos) [68, 395] Working Group is best document. While implementing new generator modules within the

[2]Note the successful use of a boosted decision tree in [6], and use of a convolutional neural network within [243], which has greatly influenced the work of the DUNE High-Energy Physics Working group along with this thesis.

[3]Luckily, these tendencies have slightly improved across the community [243, 39, 6].

GENIE [39] Monte Carlo (MC) event generator represents excellent progress and motivated the development of technically fantastic analysis schemes using convolutional neural networks and boosted decision trees, many of the underlying physics assumptions of a hypothesized $n \to \bar{n}$ signal within the GENIE *default* model are not entirely correct. Some approximate notions include:

1. The assumption that the annihilation occurs along the nuclear density distribution of the nucleus, as discussed in [243] and other works, even while the outcomes of [201] are referenced openly and often used; this ignores the surface dominance of the transformation and subsequent annihilation [180, 201].

2. Employing a single nucleon momentum distribution described by a *nonlocal*, relativistic Bodek-Ritchie [109, 39] Fermi gas (the radial dependence of the annihilating (anti)nucleons' momenta are ignored).

3. Only $\sim$ 10 annihilation channels (a la [4]) are assumed to be necessary to describe the annihilation products. This seems low, as ~ 100 are known [229], many of them containing heavier resonances; these heavier species can be responsible for $\sim 40\%$ of all pion ($\pi^{0,\pm}$) production.

4. A fully stochastic intranuclear cascade model has not yet been employed, and instead has been approximated as a single effective interaction (GENIE's Intranuke hA2015 [39] was used for previous results [243]).

5. There also exists no de-excitation model(s) (nucleon evaporation, etc.) within current publicly available builds of GENIE for all nuclei (though ^{16}O is handled)

6. No comparison tests against antinucleon annihilation data have yet been considered.

7. Only an rough estimation of the nuclear suppression factor of ^{40}Ar has thus far been used to approximate lower limits on the transformation time.

It is no doubt that some of these current technicalities proceed directly from the secondary nature of the GENIE $n \to \bar{n}$ module's genesis, a consequence of GENIE's top-down structure and first-and-foremost focus on neutrino interactions. This being said, similar issues or inconsistencies are known to exist in other work [238], and detailed explanations of past simulation's internal processes are quite lacking [212, 4], but to individually contend these here is not the goal of this thesis.

2.3 Independent Monte Carlo Model Simulation Stages (Factorization)

My goal alongside my collaborator E. S. Golubeva has been to create an adequately accurate generator, one which can serve as a platform to be used within all free and intranuclear $n \to \bar{n}$ experiments. In this chapter, I will present the main framework and approaches underlying the MC model, wherein the annihilation of an antineutron on or in the target nucleus is considered to consist of several sequential and independent (factorized) stages. The approach used here was originally undertaken in [224, 227].

In the first stage of this approach, one defines the absorption point of an antineutron by the nucleus in the framework of the optical model. Extranuclear annihilation simulations were performed for $10\,\mathrm{meV}$ antineutrons incident upon a ^{12}C nucleus [224, 227, 229] and show that the annihilation has radial dependence; intranuclear annihilations take account of these now as well [71, 70]. All of the following stages of the simulation for ^{12}C, ^{16}O, and ^{40}Ar do not differ and are considered within a unified approach.

The second stage in this factorization is the actual annihilation of the antineutron with one of the constituent intranuclear nucleons. In contrast to [224, 227], where a statistical model for nucleon-antinucleon annihilation into pions was used, the present model instead uses a combined approach first proposed in [226] and will be described in Sec. 2.6.3 along with corresponding available experimental data to be discussed in Sec. 2.7.

The third stage is the intranuclear cascade (INC), initiated by the emergence and nuclear transport of mesons from the annihilation; decays of short-lived heavy mesonic resonances are also handled. The model which takes account of the nonlinear effect of decreasing the nuclear density, along with a time coordinate [228], which is necessary for the correct description of the passage of resonances through the nucleus.

The final stage is the de-excitation and fragmentation of the residual nucleus into nuclear remnants of various masses, which may themselved evaporate nucleons of emit photons.

Throughout this chapter, I present a general description of the model and results obtained for extranuclear $\bar{n}$C (for the NNBAR/HIBEAM experimental program at the ESS), intranuclear $\bar{n}$Ar (for DUNE), as well as first (unpublished) results for $\bar{n}$O (for Hyper-and-Super-Kamiokande).

2.4 Absorption of a Slow $\bar{n}$ by a ^{12}C Nucleus

The approach used here to describe the interaction between the nucleus and the incoming slow (cold) antineutron[4] resulting from $n \to \bar{n}$ is based on the integration of optical and cascade models[5]. In the optical-cascade model, the initial conditions for the INC are formulated within an optical model. This approach was first applied in [226] to describe the annihilation of stopping antiprotons on nuclei when the antiproton is absorbed from the bound state made by the antiproton orbiting the atom. The same approach was used for the antineutron and presented in great detail by Kondratyuk [224, 227] in the discussion of future $n \to \bar{n}$ search experiments. The radial (r) distribution of the absorption probability density $P_{abs}\,(r)$ is directly related to the radial nuclear density $\rho(r)$ and the radial wave function $\phi(r)$, and is derived from the wave equation for a slow antineutron:

$$P_{abs}(r) \sim 4\pi r^2 \rho(r) |\phi(r)|^2 \,. \tag{2.1}$$

In order to define the annihilation point in the MC simulation, it is desirable to use a simple analytic function. Therefore, an solution is for $P_{abs}(r)$ as obtained in [224, 227], a Gaussian function with a maximum situated at $r = c + 1.2\,\text{fm}$, where c is the radius of half density (with $c(^{12}_{6})\text{C}) = 2.0403\,\text{fm}$) with a width of $\sigma = 1\,\text{fm}$. This approximated function is presented in Fig. 2.1 as the solid orange curve with arbitrary units to demonstrate the penetration depth of the antineutron inside the nucleus.

[4]The calculation of the total annihilation cross section of an $\bar{n}$ on ^{12}C is a separate problem that is not considered within the scope of this model, and instead the annihilation event itself is the starting point.

[5]The interaction of a slow antineutron with the nucleus cannot be considered within an INC framework, as is usually done for antinucleon energies above several tens of MeV. Such an interaction also cannot be legitimately modeled using antineutron-nucleon cross sections.

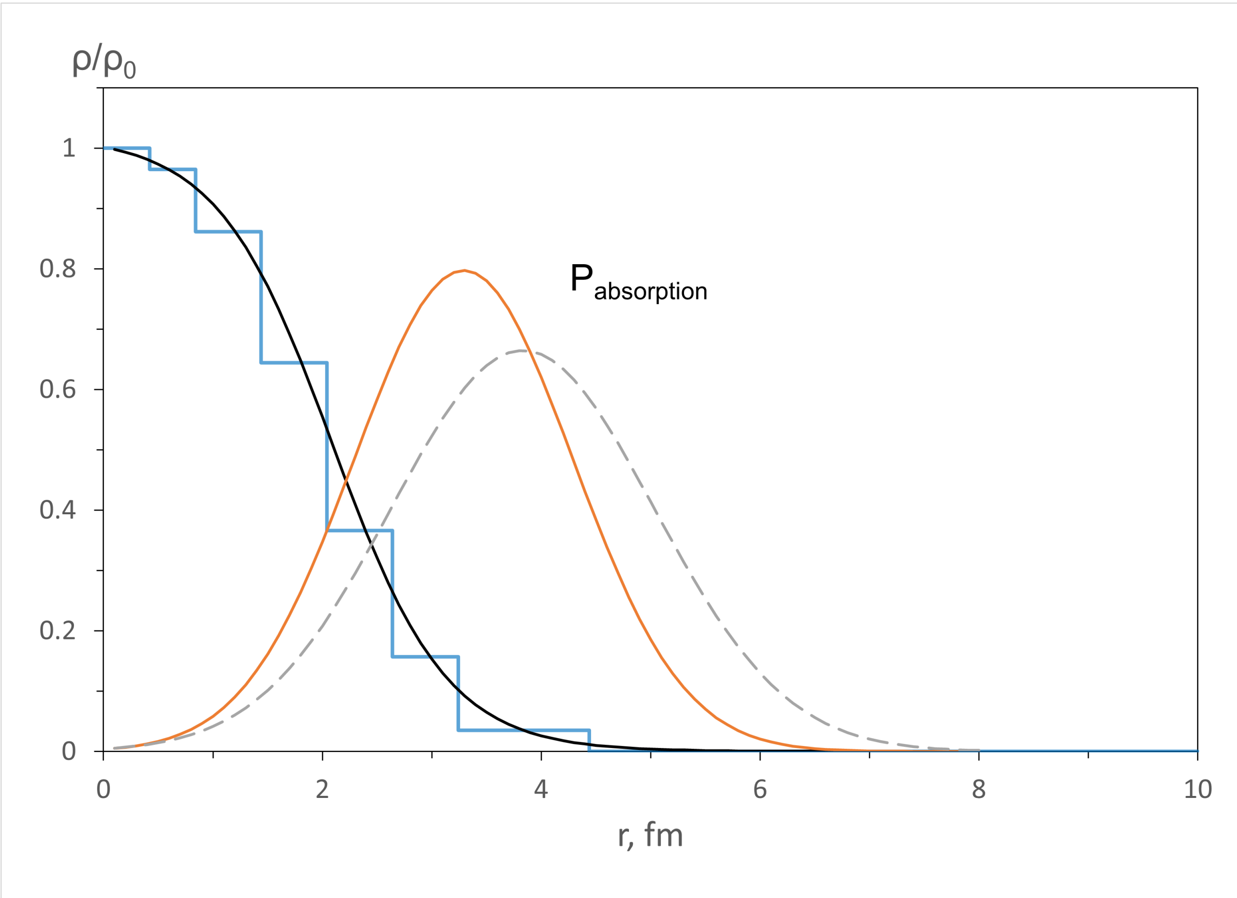

Figure 2.1: The radial distribution of the relative density of protons and neutrons throughout the ^{12}C nucleus (they are identical). The solid black line is a Woods-Saxon density distribution, while the blue step function is an approximation used to divide the nucleus into seven zones of constant density. Right: The radial dependence of the absorption probabilities P_{abs} for the ^{12}C are shown for an antineutron (solid orange) and an antiproton (dashed grey) [252]. Note that an eighth, highly diffuse zone extends from the end of zone seven at $r = 4.44$ fm to $r = 10$ fm.

The model assumes that the proton density within the nucleus $\rho(r)$ is described as an electrical charge distribution, similar to those obtained in high-energy electron scattering experiments. The function $\rho(r)$ is assumed to obey a Woods-Saxon distribution:

$$\frac{\rho(r)}{\rho(0)} = \left[1 + e^{\frac{r-c}{a}}\right]^{-1}, \tag{2.2}$$

where $a = 0.5227\,\mathrm{fm}$ is the diffuseness parameter for the ^{12}C nucleus, and c its radius of half density [59]. For practical reasons within the modeling process, the nucleus is split into seven concentric zones, within which the nucleon density is considered to be constant. Fig. 2.1 shows the density distribution of the nucleons for ^{12}C, calculated by Eq. 2.2, along with a step approximation. It is seen that although an antineutron penetrates more deeply compared to an antiproton (the dotted line in the Fig. 2.1), the absorption of the antineutron still occurs about the periphery of the nucleus [180]. Since an antineutron could be strongly absorbed even within the diffuse (radially exponentially decaying) periphery of the nucleus, another eighth zone with density $\rho_{out} = 0.001 \cdot \rho(7)$ is added which extends far beyond the nominal nuclear envelope.

2.5 Nuclear Effects of Intranuclear Transformations

Similar to the preceding section, one must take account of radial position correlations in the intranuclear annihilation process as well. This is accomplished in a shell model approach, and is pursued for $^2_1$D (a historical, explanatory calculation) and ^{40}Ar [71], and soon for ^{16}O, which will be discussed in [70]. A wonderful outgrowth of these calculations is the computation of the intranuclear suppression factor for $n \to \bar{n}$, which can be seen to be a *reduced lifetime*.

2.5.1 Concepts and Pertinent Questions

Assuming that the $n \to \bar{n}$ transformation does occur in a vacuum, an interesting question arises: what are the consequences for an intranuclear transformation[6]? Can calculations of suppression factors be trusted? What are the model dependencies, and can they lead to instabilities in the results that disallow any comparisons between extranuclear and intranuclear $n \to \bar{n}$? Of course,

[6] Many thanks to J-M. Richard for his collaboration and many discussions on this work [71].

if an intranuclear n becomes an $\bar{n}$, an annihilation will eventually take place within the nucleus, releasing $\sim 2\,\mathrm{GeV}$ of rest-mass energy, from which ~ 4-5 mesons are emitted on average (to be discussed soon). After this point, the wounded nucleus will evaporate several nucleons and perhaps break into unstable daughter nuclei.

Several more parallel questions are immediately raised:

1. When a n tentatively becomes an $\bar{n}$, it ceases feeling a smooth potential of $\lesssim 50\,\mathrm{MeV}$ and instead experiences a (complex) potential whose magnitude is $\gtrsim 100\,\mathrm{MeV}$. How much is such a transformation *suppressed* by this change in potential?

2. A deep annihilation could produce multiple fragments with the primary mesons ultimately being absorbed. Alternatively, a peripheral annihilation [180] would probably release a large fraction of the primary mesons and at most rip out only a few nucleons, albeit with a more asymmetric topology. So, where, *preferentially*, does the annihilation take place?

3. Many measurements were accumulated at Brookhaven throughout the 1960-70s, and later at CERN thanks to the LEAR facility (1982-1996), which benefited from a pure, intense, and cooled antiproton ($\bar{p}$) beam. For a review, see, e.g., [38, 270]. However, LEAR was shared by many experiments with various aims dealing with fundamental symmetries, strangeness physics, exotic mesons, etc., and experiments providing knowledge of vital systematics for antinucleon-nucleon and antinucleon-nucleus measurements were not given top priority. With this in mind, *is* the current knowledge of antinucleon-nucleon and antinucleon-nucleus interactions *sufficient* to carry out such an investigation?

4. Some concerns have been expressed about the reliability of the estimate of the $n \to \bar{n}$ lifetime inside nuclei within a straightforward nuclear-physics approach; see, e.g., [155, 314]. Can one face these criticisms and demonstrate stable and consistent results?

In this section, a review of these questions are discussed with methods based on the Sternheimer equation (see, e.g., [381], and refs. therein), as used by Dover *et al.* and Friedman *et al.* [175, 176, 177, 201] throughout past discussions of these topics. Such methods are then applied to the ^{40}Ar and briefly to the ^{16}O isotopes, which comprise the main component of the DUNE and Super-Kamiokande detectors. For completeness, the main steps of these calculations are repeated.

2.5.2 The $\bar{n}$ Lifetime in the Deuteron

As a *brief warm-up*, consider a simplified deuteron, consisting of a pure s-wave bound state of a proton (p) and neutron (n). One may adopt the wave function by Hulthen [249, 21]:

$$\begin{aligned}
\Psi_n &= \frac{1}{\sqrt{4\,\pi}}\,\frac{u_n(r)}{r}\,, \qquad \int_0^\infty u_n(r)^2 dr = 1\,, \\
u_n(r) &= N_n\,\left[\exp(-\lambda_1\, r) - \exp(-\lambda_2\, r)\right]\,,
\end{aligned} \tag{2.3}$$

which has been tuned to reproduce the correct binding energy and spatial extension of the deuteron; here, N_n is a normalizing factor, r is in GeV^{-1}, $\lambda_1 = 0.2316\,\hbar c$, and $\lambda_2 = 5.98\,\lambda_1$. It has been checked that using another wave function does not change the following results significantly, provided it fits the deuteron energy and radius.

In the presence of $n \to \bar{n}$ transformations, the wave function becomes

$$\frac{1}{\sqrt{4\,\pi}}\left[\frac{u_n(r)}{r}\,|pn\rangle + \frac{w(r)}{r}\,|p\bar{n}\rangle\right]\,. \tag{2.4}$$

Assuming an arbitrary (and unknown) strength $\gamma \equiv \alpha = 1/\tau_{n\bar{n}}$ for the $n \to \bar{n}$ transition (see again 1.7.1), the induced $\bar{n}$ component, w, is given by the Sternheimer equation

$$-\frac{w''(r)}{m} + V\,w(r) - E\,w(r) = -\gamma\,u_n(r)\,. \tag{2.5}$$

This gives an exact estimate of the first-order correction to the wave function and, hence, of the second order correction to the energy without involving a summation over the unperturbed states. Here, E is the unperturbed energy and V the antineutron-proton optical potential, resulting in a width

$$\Gamma = -\,2\int_0^\infty |w(r)|^2\;\mathrm{Im}\,V(r)\,dr \tag{2.6}$$

$$= -\,2\gamma\int_0^\infty u_n(r)\;\mathrm{Im}\,w(r)\,dr\,. \tag{2.7}$$

This immediately implies the scaling law $\Gamma \propto \gamma^2$, or for the lifetime $T = \Gamma^{-1}$ of the deuteron

$$T = T_R\, \tau_{n\bar{n}}^2\,, \tag{2.8}$$

where $T_R \equiv R$, sometimes called the intranuclear suppression factor (as discussed in Sec. 1.7.3), is actually seen to be interpreted as a *reduced lifetime*. Models for the optical potential $V(r)$ have been constructed, and are tuned to reproduce the main features of low-energy antinucleon-nucleon scattering and have predicted the shift and broadening of the low-lying levels of the protonium atom.

A method to solve Eq. 2.5 is discussed in [201], which is similar to the one used in the earlier studies [175, 176], and involves the matching of several independent solutions corresponding to various limiting conditions. The alternative below directly provides the desired solution. First, to get the neutron wave function from the neutron potential $V_n(r)$, one should solve the radial equation

$$-\frac{1}{\mu}{u_n}'' + V_n(r)\, u_n(r) = E\, u_n(r)\,, \tag{2.9}$$

subject to $u_n(0) = u_n(\infty) = 0$. A method adapted from aircraft engineering [302] consists of the change of variables $r = r_0\, x/(1-x)$, where r_0 is a typical distance, and, for the wave function $u_n(r) = \tilde{u}_n(x)$, of an expansion

$$\tilde{u}_n(x) = \sum_{j=1}^{N} a_j\, \sin(j\,\pi\, x)\,, \tag{2.10}$$

in which the coefficients a_j are closely related to the values of the function at the points $x_i = i\,/(N+1)$, for $i = 1, 2, \ldots N$. This results in a $N \times N$ eigenvalue equation $A\, U_n = E\, U_n$, where A is the discretized Hamiltonian and U_n is the vector of the $(1-x_i)\, \tilde{u}_n(x_i)$. See [336] for an application to quarkonium in potential models. For the Sternheimer equation (Eq. 2.5), one then constructs a simple matrix equation

$$(\bar{A} - E\, \mathbb{1})\, W = \gamma\, U_n\,, \tag{2.11}$$

where the $N \times N$ matrix $\bar{A}$ is the discretized Hamiltonian for the $\bar{n}$, E the n energy, and $W = \{(1-x_i)\,\tilde{w}(x_i)\}$ is the vector containing the $\bar{n}$ wave function. This calculation is fast and robust.

Besides the deuteron energy $E_0 = -0.0022\,\mathrm{GeV}$ and the wave function u_n, solving Eq. 2.5 requires a model for the antineutron-proton potential V. As shown by Fermi and Yang [187], the long-range part of the $\bar{n}N$ potential in isospin I is deduced from the NN interaction in isospin I by the G-parity rule: if a meson (or set of mesons) with $G = +1$ is exchanged, it gives the same contribution, while under $G = -1$ exchange, the sign is flipped. The complex short-range part of V is fitted as to reproduce the low-energy data on $\bar{p}$ scattering and protonium. The so-called DR2 model [178, 337] has been adopted, and it was checked that variants such as the Kohno-Weise potential [274] produce very similar results. Of course, the isospin $I = 1$ of the potential is used for the full calculation of the deuteron lifetime.

For the deuteron, the reduced lifetime is estimated to be about $T_R^D \simeq 3 \times 10^{22}\,\mathrm{s}^{-1}$. This result shows great consistency with other recent calculations such as [275]. A calculation by Oosterhof *et al.* [314], based of chiral effective field theory, is in some disagreement, but it has been revisited very recently by Haidenbauer *et al.* [239] who found a perfect agreement with the old estimate by Dover et al. [175].

This estimate is *remarkably stable*. For instance, increasing the core of the $\bar{n}p$ interaction *by an unphysical order of magnitude* results in only a 20% increase of R. Even with a large $|V|$, the transformation is more suppressed, but it actually annihilates more efficiently. Remarkably, there is an almost exact cancellation between these two effects. It can also be seen that the calculation is sensitive mainly to the value of $V(r)$ near $0.8 - 1\,\mathrm{fm}$. This is fortunate, as low-energy $\bar{p}$ scattering on nucleons and the shift of the antiprotonic hydrogen atom probes essentially this region and so one cannot determine the interaction at closer distances[7]. It is shown in [175] that adding a realistic D-wave component, and a Sternheimer equation attached to it, does not modify the result significantly.

2.5.3 The $\bar{n}$ Lifetime in ^{40}Ar

In [175, 201] there are estimates of the lifetimes (suppression factors) of nuclei that were important to analyze for some past underground experiments, particularly those of ^{16}O [4, 6] and ^{56}Fe [150].

[7] Thanks to Femke Oosterhof for discussions on this point.

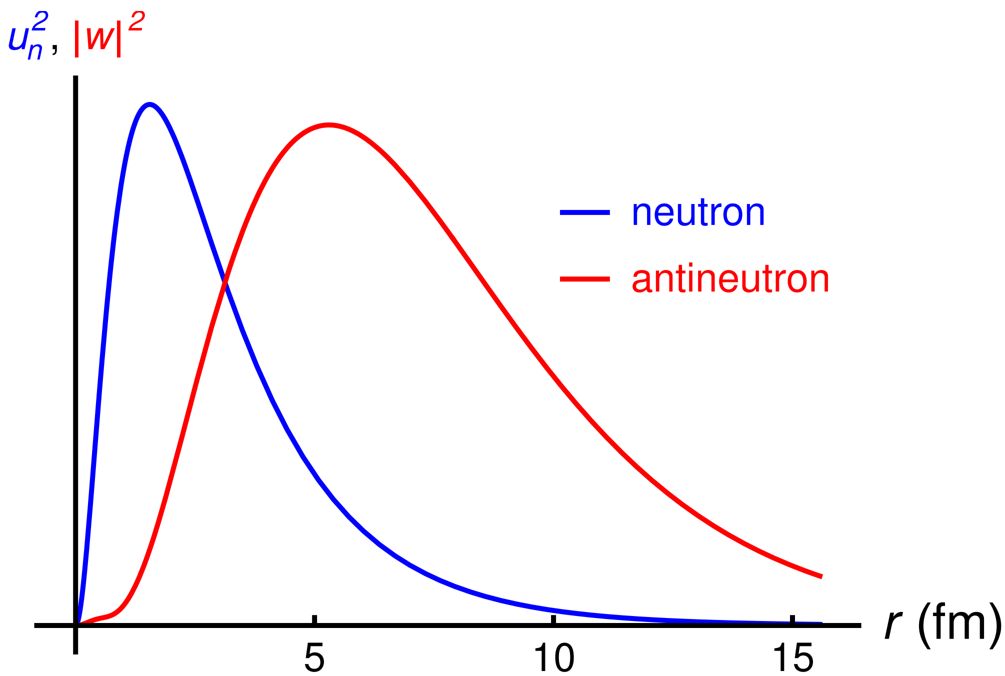

Figure 2.2: (Anti)nucleon densities are shown for deuterium. The $\bar{n}$ radial distribution (red), arbitrarily rescaled to fit the figure, is compared to the nominal neutron distribution (blue). Courtesy of J-M. Richard.

The tools developed in the precending section can now be applied for a study of ^{40}Ar, relevant for DUNE.

The detailed properties of atomic nuclei are well accounted for by sophisticated Hartree-Fock calculations. For many applications, it turns out to be rather convenient to use *ad-hoc* shell-model wave functions that are tuned to reproduce the main properties of the nuclei, in particular the spatial distribution of p's and n's. This was done in connection with the compilation of nuclear data [25]. For ^{40}Ar, besides a more efficient handling of the Sternheimer equation, the variant discussed here consists in using the strategy outlined within and neutron wave functions from [111]; these wave functions correspond to a fit of the main static properties of ^{40}Ar. The p and n wave functions have been calculated by Karim Bennaceur in the so-called "filling approximation": the nucleus is supposed to be spherical, implying that the states of each shell are populated with the same (integer or fractional) occupation number.

The second ingredient necessary for a proper intranuclear annihilation is knowledge of the $\bar{n}$-nucleus potential. With the noticeable exception of the OBELIX collaboration having studied antineutron scattering [13, 250], most data deals with the $\bar{p}$-nucleus interaction, either via $\bar{p}$ scattering or antiprotonic atom formation. The question is whether one can reasonably assume that the $\bar{n}$- and $\bar{p}$-nucleus potentials are nearly equal.

The most striking feature of $\bar{n}N$ cross-sections is the smallness of the charge-exchange component, already stressed by the team having discovered the antiproton [142], and confirmed in further measurements [270]. Indeed, a one-pion-exchange alone would make the charge-exchange the largest contribution to the total cross section. This implies a large cancellation of the isospin $I = 0$ and $I = 1$ amplitudes, resulting in a somewhat isospin-independent $\bar{n}N$ interaction, and is confirmed by the available experimental data. If one compares the $\bar{p}p$ and $\bar{n}p$ total cross sections, they almost coincide, and differ only in tentative extrapolations towards lower energies [250, 128]. This is confirmed by a comparison of the angular distribution of $\bar{p}$ scattering on the isotopes ^{16}O and $^{18}_{8}$O at the same energy by the PS184 collaboration, with practically no differences [123]. Considering this, it will soon be seen that changes in the $\bar{n}$-nucleus interaction, such as its departure from understood $\bar{p}$-nucleus interactions, results in only very small modifications of the estimated lifetimes. Of course, the $\bar{p}$-nucleus potential fitting scattering experiments and antiprotonic-atom data is the strong-interaction part, and Coulomb effects have been adequately removed.

For each n shell, there is an induced $\bar{n}$ wave function governed by an equation analogous to Sternheimer 2.5, with a centrifugal term for p, d and f states, where V is now the $\bar{n}$-$^{39}_{18}$Ar potential, and m the corresponding reduced mass. In Fig. 2.3, some details are given for one of the external shells which contributes most to the instability, namely $1d_{5/2}$. It is seen that $\bar{n}$ are produced in the tail of the n distribution, with subsequent annihilation at the surface of the matter distribution; the pattern is similar for all other shells.

For comparison, the distribution of the $1f_{7/2}$ shell are shown in Fig. 2.4; the peripheral character of the antineutron component is even more pronounced, though still decays exponentially as in all other shells[8]. The resulting radial $\bar{n}$ distributions for all shells are shown in Fig. 2.5. If one now adds up the contributions of each neutron to the width, calculates the average width per n, and estimates the corresponding reduced lifetime, one gets a value of $T_R^{Ar} \sim 5.6 \times 10^{22}\,\mathrm{s}^{-1}$. As in the case of the deuteron, this value is remarkably stable against changes in the parameters of the $\bar{n}$-nucleon interaction. Thus, a similar uncertainty of $\sim 20\,\%$ is estimated.

This stability in the width can be understood: if one increases the absorptive potential, $n \to \bar{n}$ is more suppressed, but, on the other hand, the antineutron annihilates more efficiently. In Fig. 2.6 the factor γ is shown, by which the width of the $1d_{5/2}$ level is modified when the real $\bar{n}$-nucleus potential is multiplied by f_r and its imaginary part by f_i. If one changes these values by $\pm 20\%$, far beyond what can be admitted to keep a good fit to the antinucleon-nucleus data, modifications to the width are less than 10%. The same pattern is observed for the other levels. A consequence of this stability is that the estimated suppression factor R keeps the same order of magnitude from one nucleus to the other, even from the deuteron to ^{40}Ar.

One can also illustrate how intranuclear $n \to \bar{n}$ transformation and subsequent annihilation is a surface phenomenon. In Fig. 2.7, the absorptive potential is modified near $r = r_c$ by applying as a factor a "glitch" function with the form

$$g = 1 + 0.4\, e^{-20\cdot(r-r_c)^2} \tag{2.12}$$

[8]Some questions have arisen from colleagues regarding the possibility of an annihilation occurring on *another* nucleus within the larger (detector) medium; this is not permitted due to the exponential decay of the $\bar{n}$ density distribution over *inter*nuclear distances, just as a n of one nucleus is not found inside another.

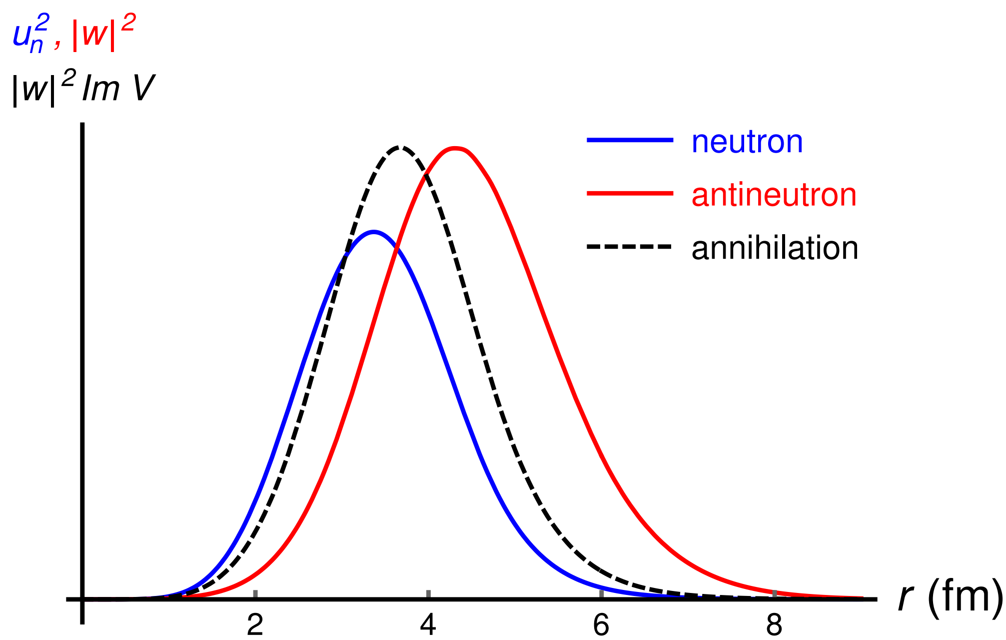

Figure 2.3: (Anti)nucleon densities for the $1d_{5/2}$ shell of ^{40}Ar. The $\bar{n}$ radial distribution (red), arbitrarily rescaled to fit the figure, as compared to the nominal neutron distribution (blue), and the annihilation density of Eq. 2.7, also arbitrarily rescaled (dashed black). Courtesy of J-M. Richard.

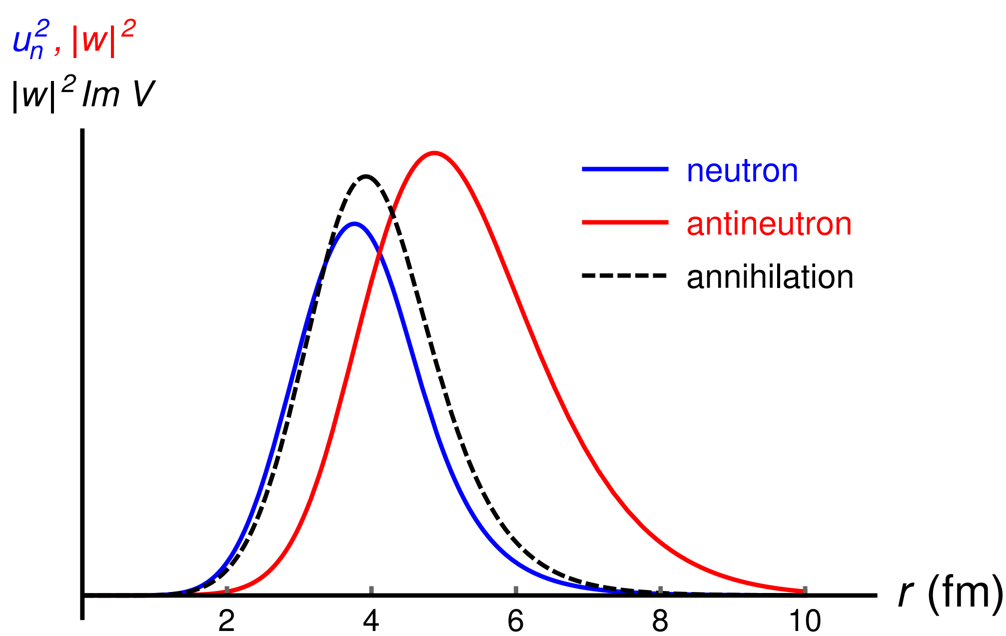

Figure 2.4: The same (anti)nucleon densities for Figs. 2.3, but now for the $1f_{7/2}$ shell of ^{40}Ar. Courtesy of J-M. Richard.

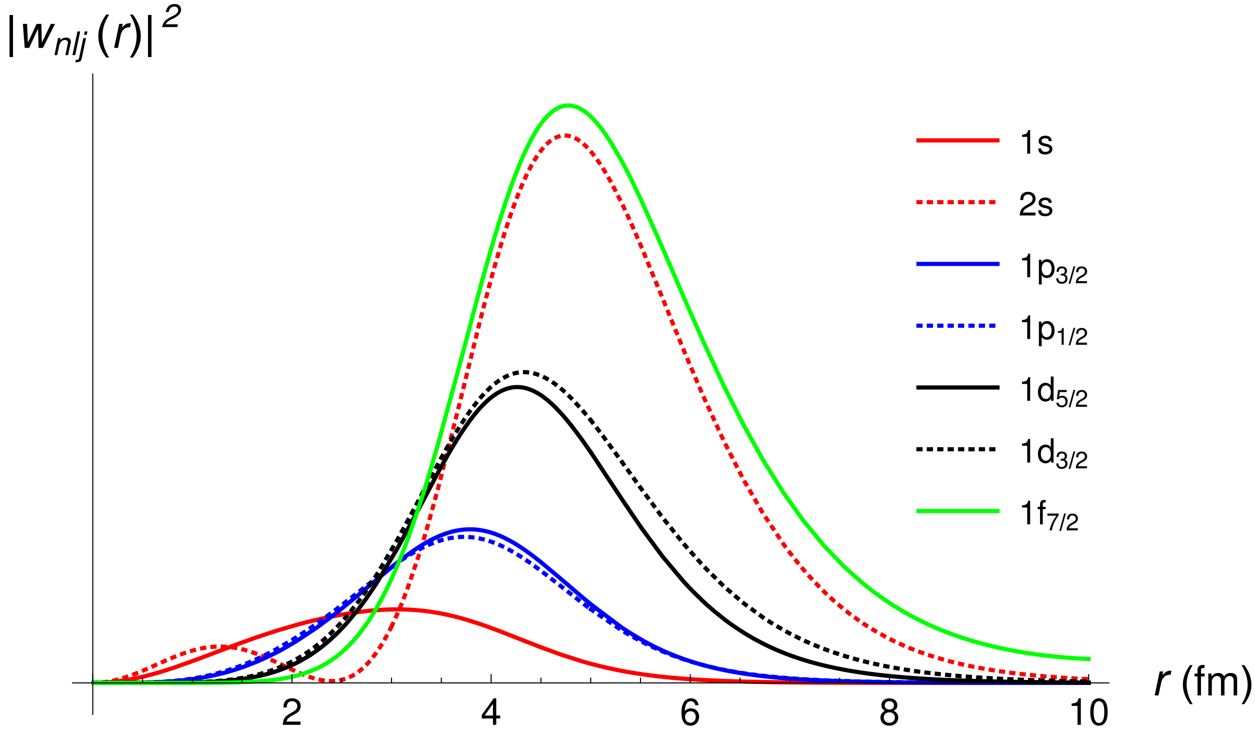

Figure 2.5: Antineutron densities for the shells of ^{40}Ar. Courtesy of J-M. Richard.

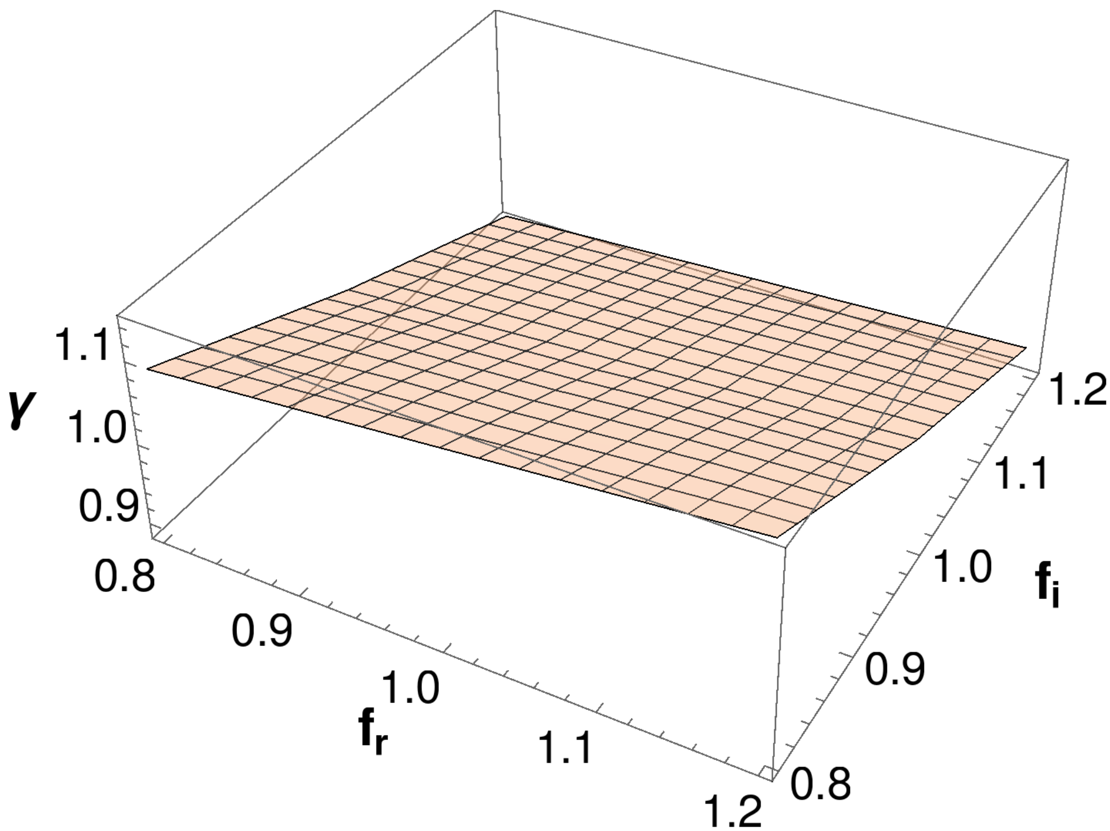

Figure 2.6: The relative change to the width of the $1d_{5/2}$ shell is shown when a factor f_r is applied to the real potential, and f_i to the imaginary part. Courtesy of J-M. Richard.

where r_c is varied. The width is seen to be modified only near the surface, and is insensitive to what happens in the center of the nucleus. Again, the example shown is for the $1d_{5/2}$ shell, but the other levels exhibit a similar behavior.

To end this section, it is instructive to compare the method based on an exact solution using perturbation for Eq. 2.5 in the approximation where the n and $\bar{n}$ spatial distributions are not distinguished. If the n- and $\bar{n}$-nucleus do not differ too much in their real part, then the width is given by (see, e.g., [145]):

$$\Gamma \approx -2/\bar{W} \ , \qquad \bar{W} = \int_0^\infty |u_n(r)|^2 \, W(r) \, dr \, . \tag{2.13}$$

For the low-lying shells of ^{40}Ar, the difference is small with respect to this estimate. For the most external shell, the width is *overestimated* by a factor of about 3.5, overemphasizing the suppression of the process.

2.5.4 Brief Overview of Ongoing Work Considering the $\bar{n}$ Lifetime in ^{16}O

Work has begun on simulation of intranuclear $n \to \bar{n}$ in ^{16}O [70], and preliminary unpublished results will be briefly summarized (in bits and pieces) throughout this chapter.

Shortly, the formalism laid down over the preceding sections can be similarly applied to ^{16}O to determine the radial densities of nucleons, antineutrons, and so too of annihilation, which in turn inform the calculation of the reduced lifetime (intranuclear suppression factor, R). Fig. 2.8 shows the radial distributions of pertinent (anti)nucleon components (similar to Figs. 2.3 and 2.4 for ^{40}Ar) within the $1P_{1/2}$ shell of ^{16}O. From this, one can contrast behavior of the radial position annihilation densities between each species, shown in Fig. 2.9.

2.6 The Nuclear Model of these Independent Simulations

With the initial radial positions now known for extranuclear and intranuclear annihilations, one can begin to discuss the underlying physics contained within the MC simulation which informs the expected final states of $n \to \bar{n}$ within various experiments.

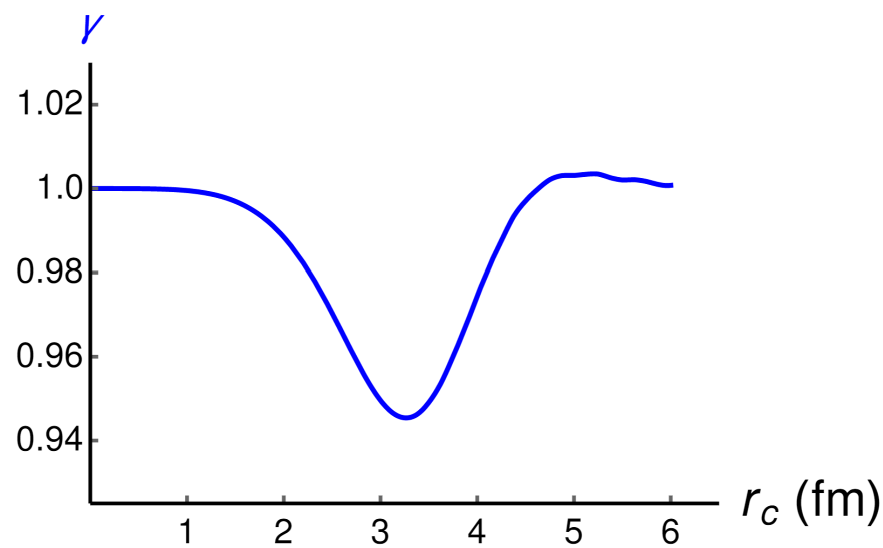

Figure 2.7: The factor γ multiplying the width of the $1d_{5/2}$ shell when a factor $1+0.4\,\exp(-20(r-r_c))$ (r is in fm) is applied to the absorptive potential. Courtesy of J-M. Richard.

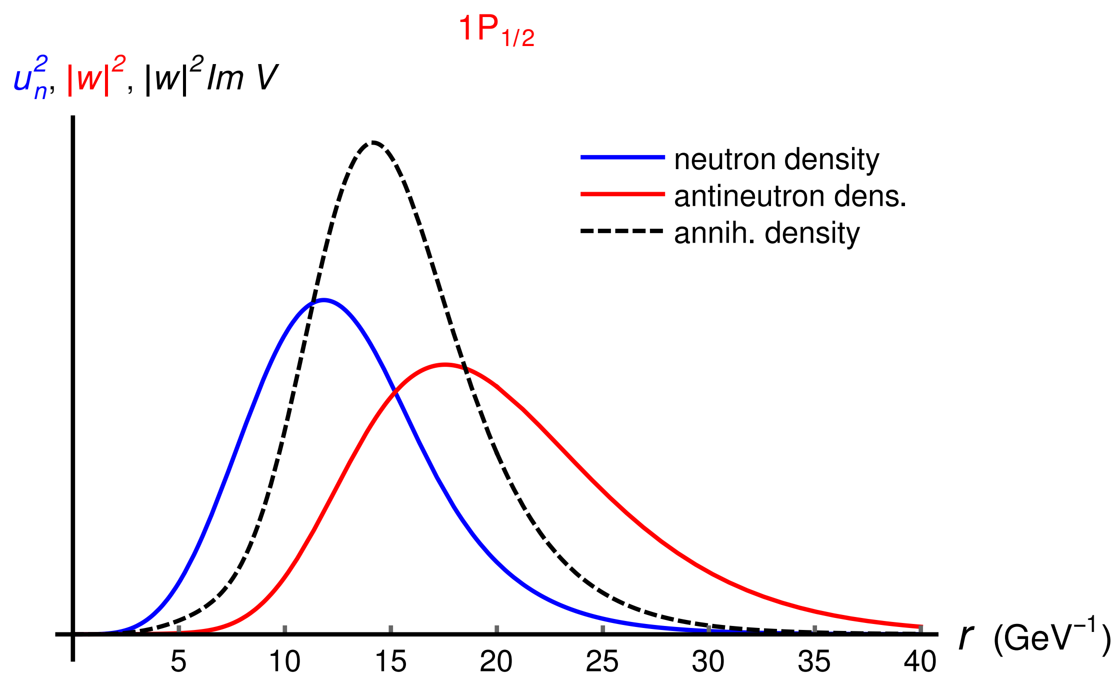

Figure 2.8: Radial distributions for the $1P_{1/2}$ shell of ^{16}O: neutron, antineutron, and annihilation. The units are arbitrary for the vertical axis. The annihilation density shown in dashed black is the same as shown in Fig. 2.9 for ^{16}O. Courtesy of J-M. Richard.

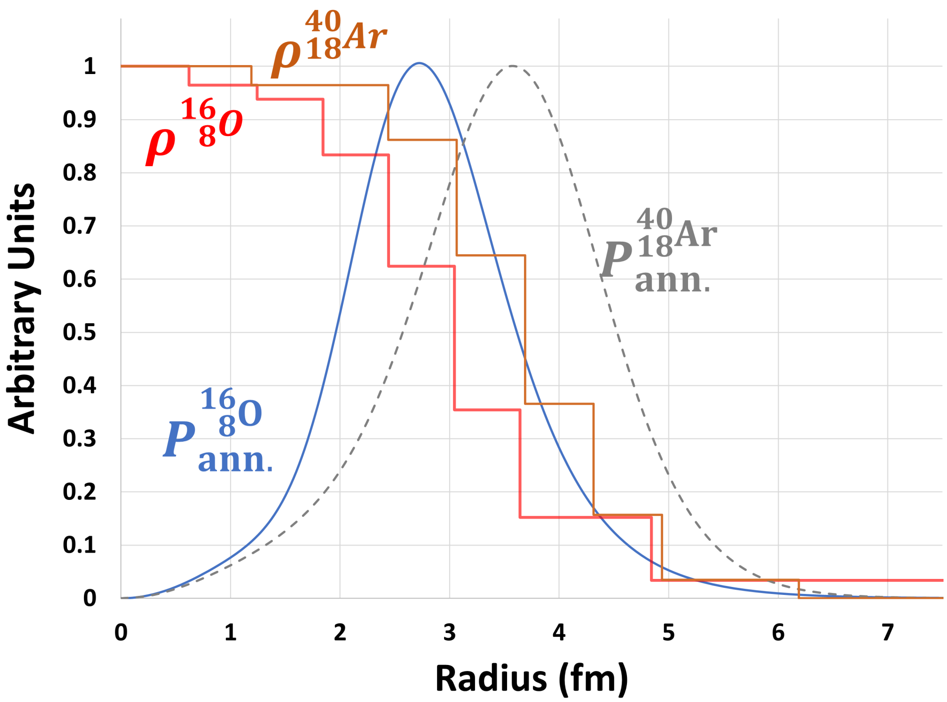

Figure 2.9: Radial position annihilation probability distributions are shown for two nuclei, ^{16}O in solid blue and ^{40}Ar in dashed gray, using an arbitrary vertical axis. These are compared to the fitted, eight-zoned nuclear density distribution of ^{16}O in solid orange, and ^{40}Ar in dotted purple. For context, one may reduce the mean nuclear radius of the ^{40}Ar curve, moving leftward to nearly overlap with the curve describing ^{16}O [70], though this should not and is not perfect due to a larger range of states widening the total distribution [71].

2.6.1 Nucleon Potentials and Momentum Distributions

Within the MC model, the nucleus is considered to be a degenerate, free Fermi gas of nucleons, enclosed within a spherical potential well with a radius equal to the nuclear radius. Nucleons fill all energy levels of the potential well, from the lowest, when a nucleon can have the largest negative potential energy and ~ 0 momentum, to the highest echelons of the Fermi level, where the nucleon moves with Fermi momentum p_{FN}, and is retained within the nucleus only because of the binding energy ε (where $\varepsilon \approx 7\,\mathrm{MeV}$ per nucleon).

In the interval $p \in [0, p_{FN}]$, the three-momentum of the nucleon can take all permissible values. The differential probability distribution of the nucleons with respect to the total momentum and kinetic energy [59] takes the form:

$$W(p) = \frac{3p^2}{p_{FN}^3}, \quad p \leq p_{FN}\,, \tag{2.14}$$

$$W(T) = \frac{3T^{\frac{1}{2}}}{2T_{FN}^{\frac{3}{2}}}, \quad T \leq T_{FN}\,. \tag{2.15}$$

Here, T is the kinetic energy of a nucleon within the nucleus, and $T_{FN} = (p_{FN}^2)/(2m_N)$ represents the boundary Fermi kinetic energy, while m_N is the mass of the nucleon. If the nucleons are distributed evenly throughout the spherical well having a radius $R = r_0 A^{1/3}$ (where r_0 is 1.2-$1.4\,\mathrm{fm}$ for the case of ^{12}C), then their Fermi momentum and energy are easily expressed in terms of the radius (and so, creating a *local* model). Because every cell in phase space $d^3x d^3p$ contains a number of states

$$\frac{2s+1}{(2\pi\hbar)^3} d^3x d^3p\,, \tag{2.16}$$

where s is the spin of the nucleon, and the total number of protons or neutrons in the nucleus being equal to n_N, it then follows from the normalization condition that

$$\frac{2s+1}{(2\pi\hbar)^3} \int d^3x d^3p = \frac{V p_{FN}^3}{3\pi^2\hbar^3} = n_N\,, \tag{2.17}$$

and one finally obtains

$$p_{FN} = \hbar \left(\frac{3\pi^2 n_N}{V} \right)^{\frac{1}{3}} , \tag{2.18}$$

$$T_{FN} = \frac{p_{FN}^2}{2m_N} = \frac{\hbar^2}{2m_N} \left(\frac{3\pi^2 n_N}{V} \right)^{\frac{2}{3}} , \tag{2.19}$$

where $V = \frac{4}{3}\pi R^3$ is the volume of the nucleus, and m_N remains the nucleon mass.

If the nucleus is subdivided into concentric spherical zones of constant density, the values of p_{FN} and T_{FN} for each zone are calculated similarly to equations 2.18 and 2.19, but with an i-th radius, and the density of the nucleons within this i-th zone. Fig. 2.10 shows the spatial distribution of the potential $V_N = -(T_{FN} + \varepsilon)$ for protons and neutrons in ^{12}C, ^{16}O, and ^{40}Ar nuclei.

The momentum distribution of the nucleons in individual zones will be the same as for a degenerate Fermi gas, and the probability of a nucleon to have momentum p in the i-th zone will continue to be determined by Eq. 2.18, although corresponding to i-th zone's boundary Fermi momentum value. Figs. 2.11 shows the momentum distributions of nucleons for both ^{12}C, ^{16}O, and ^{40}Ar nuclei, obtained by summing all the momentum distributions for all individual zones. From both Figs. 2.10 and 2.11, one can see that the nucleons located in the central zone of the nucleus can attain the highest values of T_{FN}, and, accordingly, the maximum value of the Fermi momentum p_{FN}. Therefore, the contribution to the total momentum distribution from the nucleons located in the central ($i = 1$) zone gives the high-momentum part which extends up to 250-270 MeV/c. Conversely, the nucleons located within the peripheral zone of the nucleus ($i = 7$) have momenta up to 80-100 MeV/c. Moreover, the contribution to the overall momentum distribution of a particular zone is greater the more nucleons within it. Expanding, in this model, there is a correlation of the momentum with the density and, respectively, with the radius (again, a *local* model).

Thus, for the first stage of this approach, just before the annihilation occurs, the nucleon annihilation partners are spatially distributed within a given nucleus according to its step density function (see Figs. 2.1 and 2.9). Next, according to the radial distribution of the antineutron absorption or annihilation for a given nucleus (also Figs. 2.1 and 2.9), the point of annihilation is taken randomly. The radius of this point determines the ith number of the zone in which the nucleon partner (neutron or proton) is located, and with which the antineutron annihilates.

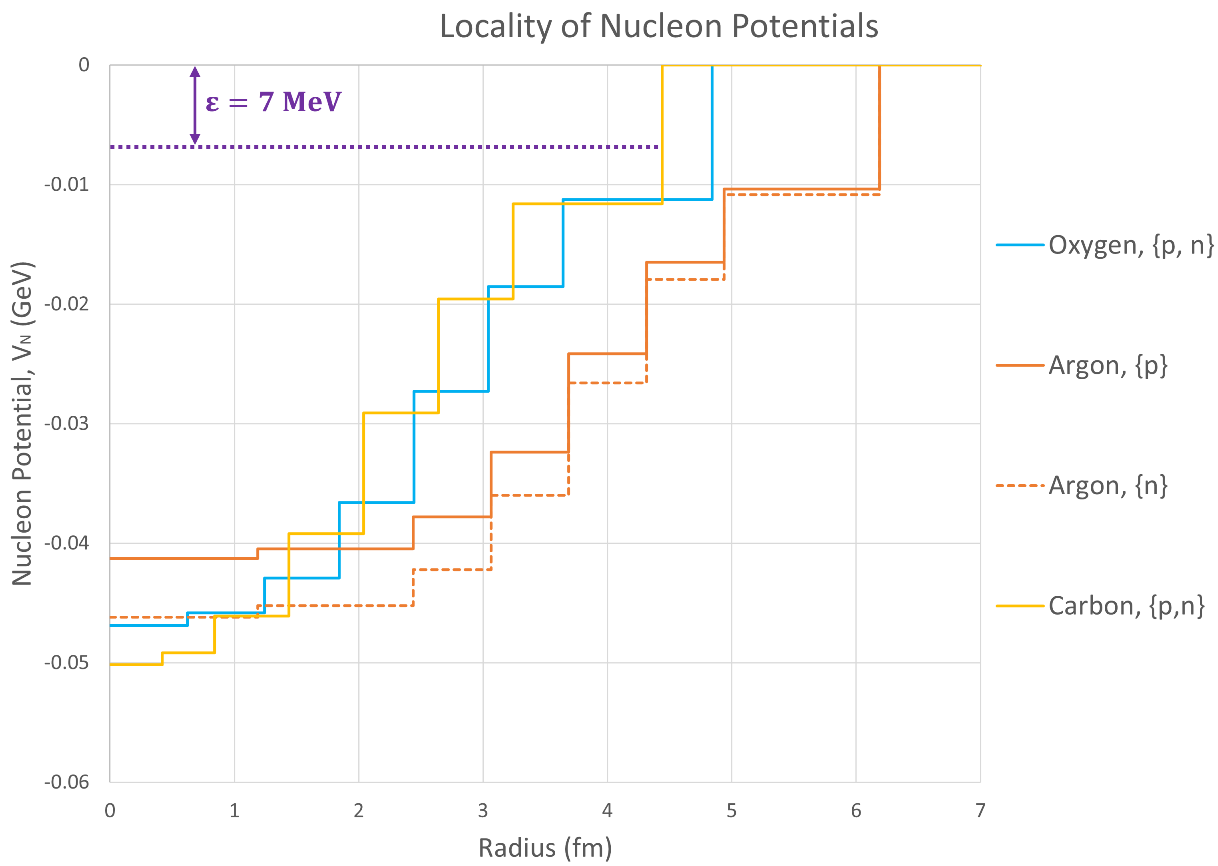

Figure 2.10: The spatial distribution of the nucleon potentials $V_N = -(T_{FN} + \varepsilon)$, with appropriate partitioning of the nucleus into seven zones for protons (solid histograms) and neutrons (dotted histogram for non-symmetric ^{40}Ar) for ^{12}C (yellow), ^{16}O (blue), and ^{40}Ar (orange) nuclei. For symmetric nuclei, the solid and dotted histograms lay atop one another. ε is the average nuclear binding energy of 7 MeV per nucleon. Remade in collaboration with E. S. Golubeva from [229].

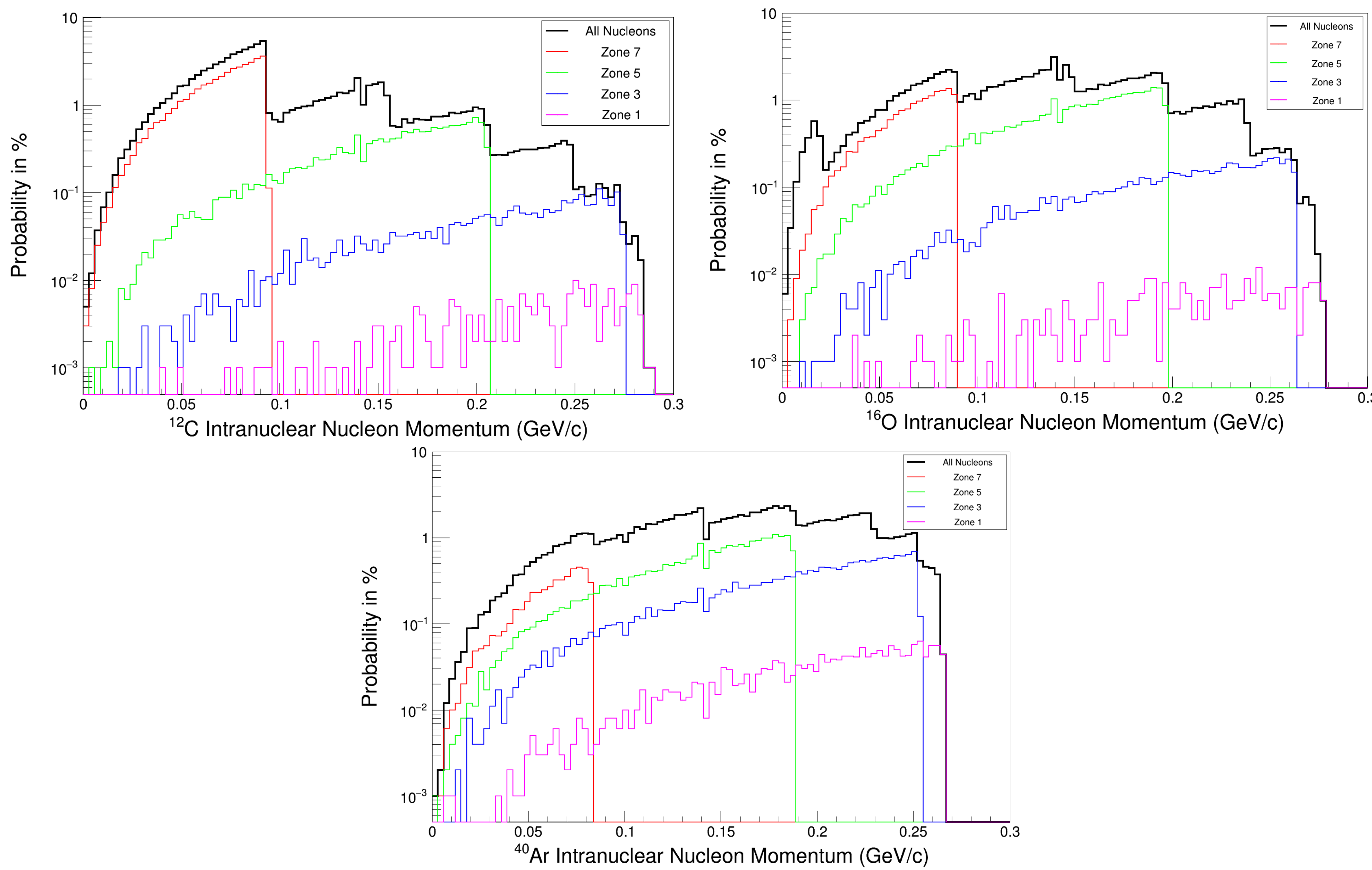

Figure 2.11: The black histograms shows the momentum distribution of intranuclear nucleons in both ^{12}C, ^{16}O, and ^{40}Ar nuclei, summed over all zones. The thinner colored lines show histograms which correspond to contributions from individual zones of the nucleus to the total momentum distribution (only odd-numbered zone distributions are shown so that the picture is not indecipherable). Probabilities inferred from samples of 100,000 events. Remade from [229].

2.6.2 The $\bar{n}A$ Intranuclear Potential and How an $\bar{n}$ Modifies the Nuclear Medium

The influence of the nuclear environment on an incoming extranuclear or intranuclear $\bar{n}$ leads to the modification of the $\bar{n}$'s vacuum four-momentum $\tilde{p}_{\bar{n}} = (E_{\bar{n}}, \mathbf{p}_{\bar{n}})$ (where $\tilde{p}_{\bar{n}}^2 = E_{\bar{n}}^2 - \mathbf{p}_{\bar{n}}^2 = m_n^2 = m_{\bar{n}}^2$) *inside* the target nucleus due to an effective scalar *attractive* nuclear potential of the form [140]

$$U_{\bar{n}}(r) = V_0 \, \frac{\rho(r)}{\rho_0} \,, \tag{2.20}$$

where $\rho(r)$ the local nucleon density (normalized to the atomic mass number A of the nucleus), ρ_0 is the saturation density, V_0 is the $\bar{n}$ potential depth at this density, and r is the distance between the $\bar{n}$ and the center of the nucleus.

Using inferences (from Fig. 2.6), one may *assume* that the $\bar{n}A$ and $\bar{p}A$ nuclear potentials are effectively the same. With this potential, a parameter of the model, the total $\bar{n}$ energy $E'_{\bar{n}}$ in the nuclear interior of ordinary nuclei can be expressed in terms of its in-medium mass $m^*_{\bar{n}}$ [140, 375, 140][9], defined as

$$m^*_{\bar{n}}(r) = m_{\bar{n}} + U_{\bar{n}}(r) \,, \tag{2.21}$$

and its in-medium three-momentum $\mathbf{p}'_{\bar{n}}$, as in the free particle case [375, 140], is

$$E'_{\bar{n}} = \sqrt{m^{*2}_{\bar{n}} + \mathbf{p}'^2_{\bar{n}}} \,. \tag{2.22}$$

Analysis of $\bar{p}$ production in proton–nucleus and nucleus–nucleus collisions at kinetic energies of a several GeV [375, 140] showed that the $\bar{p}$ potential at normal nuclear matter density is in the range of -100 to -150 MeV for outgoing $\bar{p}$ momenta below 2.5 GeV$/c$. Studies of $\bar{p}$ production at AGS energies [273, 380] suggest $\bar{p}$ potentials of $\simeq -250$ MeV and $\simeq -170$ MeV at density ρ_0 for $\bar{p}$ annihilation events at rest with respect to the nuclear matter and for $\bar{p}$ with momentum of 1 GeV$/c$, respectively. The real parts of an $\bar{p}$ optical potential in the center of the nucleus of $-(150\pm30)$ MeV

[9]The potential $U_{\bar{n}}$ is the effective $\bar{n}A$ scalar potential. The value of this potential in the center of the nucleus, V_0, is actually a free parameter of the model. This determines the total *in-medium* $\bar{n}$ energy through the "free space" dispersion relation of Eq. 2.22, and is not the usual Lorentz scalar potential $U_S^{\bar{n}}$, determining along with the Lorentz vector potential $U_V^{\bar{n}}$ the total in-medium antinucleon energy $E'_{\bar{n}}$ via the dispersion relation $E'_{\bar{n}} = \sqrt{(m_N - U_S^{\bar{n}})^2 + \mathbf{p}'^2_{\bar{n}}} - U_V^{\bar{n}}$ [296].

and of $-(220 \pm 70)$ MeV were extracted in [278] from the data on $\bar{p}$ absorption cross sections on nuclei and on the annihilation spectra of π^+'s and p's, correspondingly. Combined analysis [202] of data on antiprotonic x-rays and of radiochemical data showed that at the center of the nucleus the $\bar{p}$ potential is approximately -110 MeV in depth. So, in spite of various attempts to fix this potential, its depth at density ρ_0 *still* remains rather uncertain presently. For the sake of definiteness, in the subsequent calculations, a realistic value of $V_0 = -150$ MeV will be used within Eq. 2.20.

The in-medium momentum $\mathbf{p}'_{\bar{n}}$ is related to the vacuum momentum $\mathbf{p}_{\bar{n}}$ by the following expression:

$$E'_{\bar{n}} = \sqrt{m^{*2}_{\bar{n}} + \mathbf{p}'^2_{\bar{n}}} = \sqrt{m^2_{\bar{n}} + \mathbf{p}^2_{\bar{n}}} = E_{\bar{n}} \,. \tag{2.23}$$

For example, with $V_0 = -150$ MeV, this shows that for $\bar{n}$ annihilation at rest, i.e., when $\mathbf{p}_{\bar{n}} = 0$, the $\bar{n}$ momentum $|\mathbf{p}'_{\bar{n}}|$ in the center of the nucleus and at its periphery, corresponding to 10% of the central density, is equal to 510 and 167 MeV/c, respectively.

Within the non-interacting local Fermi gas model used in these MC simulations [229, 71, 70], for the bound target nucleon total energy E'_N in the medium at the annihilation point r the formula [288, 182]

$$E'_N = \sqrt{m^2_N + \mathbf{p}'^2_N} + V_N(r) \approx m_N + \frac{\mathbf{p}'^2_N}{2m_N} + V_N(r) \,, \tag{2.24}$$

is used, where for every ith concentric zone of a spherical nucleus the same formulations shown in Eqs. 2.18 and 2.19 are used. One can briefly recast these as

$$V^i_N(r) = -\frac{P^i_{FN}(r)^2}{2m_N} - \varepsilon_N \,, \tag{2.25}$$

with

$$P^i_{FN}(r) = \left[\frac{3\pi^2\rho(r)}{2}\right]^{1/3} \,. \tag{2.26}$$

In Eq. 2.24, $\mathbf{p}'_N$ is the momentum of the nucleon N ($N = \{p, n\}$) in the Fermi sea, $P_{FN}(r)$ is the boundary Fermi momentum at the local point r, and again the quantity $\varepsilon_N \approx 7$ MeV is the average binding energy per nucleon; at this point, $0 \leq |\mathbf{p}'_N| \leq P_{FN}(r)$. Within the representation of Eqs. 2.22–2.24, the invariant collision energy s for the interaction of an $\bar{n}$ with a nucleon bound in the nucleus at the point r is

$$s = (E'_{\bar{n}} + E'_N)^2 - (\mathbf{p}'_{\bar{n}} + \mathbf{p}'_N)^2 \approx (E_{\bar{n}} + E'_N)^2 - (\mathbf{p}'_{\bar{n}} + \mathbf{p}'_N)^2 \,. \tag{2.27}$$

The total collision energy $E_{\bar{n}} + E'_N$ entering into the right-hand side of Eq. 2.27 in the non-relativistic limit, appropriate to this case, and can be calculated as

$$E_{\bar{n}} + E'_N = m_{\bar{n}} + m_N + \frac{\mathbf{p}^2_{\bar{n}}}{2m_{\bar{n}}} + \frac{\mathbf{p}'^2_N}{2m_N} + V_N(r)\,. \tag{2.28}$$

Contrary to the on-shell interaction, for $\bar{n}$ annihilation at rest, from Eq. 2.28 it is seen that this energy is always less than $m_n + m_N$ and its maximum value is $m_n + m_N - \varepsilon_N$. If a bound target neutron is transformed into an $\bar{n}$ (for the intranuclear case), one can assume that its total energy E'_n, defined by Eq. 2.24, is equal to that $E'_{\bar{n}}$ of the $\bar{n}$, determined by Eq. 2.22 above. Namely:

$$E'_n = \sqrt{m^2_n + \mathbf{p}'^2_n} + V_N(r) = \sqrt{m^{*2}_{\bar{n}} + \mathbf{p}'^2_{\bar{n}}} = E'_{\bar{n}}\,. \tag{2.29}$$

It is interesting to note that, for $p_F(0) = 250\,\mathrm{MeV}/c$, Eq. 2.29 gives for the $\bar{n}$ momentum $|\mathbf{p}'_{\bar{n}}|$ the values of 430 and 40 MeV/c if the transition $n \to \bar{n}$ of the target n at rest occurs in the center of the nucleus and at its periphery, respectively (corresponding to 10% of the central density). The value of s for the intranuclear case is given by the first relation of Eq. 2.27.

2.6.3 The Annihilation Model of these Independent Simulations

Unlike [224, 227] where a statistical model for nucleon-antinucleon annihilation into pions was used, the current model uses a combined approach first proposed in [226]. The phenomena of $N\bar{N}$ annihilation can lead to the creation of many particles through many possible (at times $\sim$ 200) exclusive reaction channels; many neutral particles may be present, which can make experimental study and confirmation difficult. Thus, experimental information for exclusive channels is known only for a small fraction of possible annihilation channels, and therefore a statistical model based on $SU(3)$ symmetry [105] has been chosen to describe the $N\bar{N}$ annihilation. Work to generalize the unitary-symmetric model for $N\bar{N}$ annihilations, along with the development of methods for calculating the characteristics of mesons produced from the annihilation, was performed by

Pshenichnov [332]. According to the model, the $N\bar{N}$ annihilation allows for the production of between two and six *intermediate* particles, including heavy resonances. Given the estimates of the phase space volume at low momenta, the production of a larger number of intermediate particles is unlikely. Intermediate particles, such as π, ρ, ω, and η mesons, are all possible; the channels with strangeness production are not considered within this version of the model, but are possible in future iterations. This unitary-symmetric statistical model predicts 106 $p\bar{p}$ annihilation channels, and 88 $n\bar{p}$ annihilation channels, but this differs from experiments, which effectively measure only ~ 40 channels for $p\bar{p}$ and ~ 10 channels for $n\bar{p}$ annihilation [229]. However, neither the statistical model, nor the experimental data, can provide a complete and exclusive description of the elementary nucleon-antinucleon annihilation processes. For this reason, semi-empirical Tables I and II of [229] (not reproduced here for brevity) for all annihilation channels are employed for use in the annihilation simulation. These are obtained as follows: First, all experimentally measured channels were included (as seen in Tables I and II of [229]); then, by using isotopic relations, probabilities were found for those channels that have the same configurations but different particle charges. Finally, the predictions of the statistical model with $SU(3)$ symmetry were entered for the remaining intermediate channels. Sometimes, the probabilities of intermediate channels measured in different experiments differ significantly; in this case, the data in the semi-empirical tables were corrected within experimental accuracies in order to describe the cross sections and other relevant experimental data for $p\bar{p}$ and $n\bar{p}$ in a consistent way. In this approach, a substantively large collection of experimental data were used: multi-particle topologies, inclusive spectra, pion cross sections, and branching ratios of various resonance channels were all considered. It is assumed that channels for $n\bar{n}$ are identical to $p\bar{p}$ channels, and that annihilation channels for $p\bar{n}$ are charge conjugated to $n\bar{p}$ channels.

Considering the laws of energy and momentum conservation for each annihilation, the procedure for simulating the characteristics of both the intermediate particles and their various decay products consists of the following: first, a single channel from Tables I and II from [229] is randomly selected as the initial state, with all necessary momenta of all annihilation products determined according to the pertinent phase-space volume. This takes into account the Breit-Wigner mass distribution for meson resonances, while all charged and neutral pions are assumed to have a simplified mass value of 0.14 GeV/c^2. The subsequent disintegration of unstable mesons is modeled according to experimentally known branching ratios. All major decay modes for meson resonances have been considered, such as in Table III of [229].

2.6.4 Improvements to Branching Fractions from Recent OBELIX and Crystal Barrel Analyses

Analysis of experimental data from $\bar{p}p$ annihilation at rest obtained from the LEAR (CERN) $\bar{p}$ beam by the OBELIX [354] and Crystal Barrel [37] collaborations are now recently integrated [71] into the internal annihilation model. In Tabs. I and II of [71], some of the the absolute changes in several branching fractions of individual annihilation channels in accordance with this newer experimental data and compared to branchings used in [229]. With this in mind, Tab. 2.1 shows the average multiplicities of mesons produced in $\bar{p}p$ annihilation at rest. The first column re-presents the simulation results from Table IV in [229], while the second column presents the results of modeling when taking into account data from [354, 37]. The third column also re-presents the experimental data itself [269, 295, 281, 240, 229] for ease of comparison. It follows from Tab. 2.1 that the average multiplicities of annihilation mesons with changes in the branching ratios of some individual channels do not change significantly and the differences between the older and newer versions of the model are within the uncertainty of the experimental data. Nevertheless, in all simulations presented here, these new branchings (along with all others present in Tabs. I and II of [229]) will be used for modeling all annihilations. See Sec. 2.7 for further comparisons to data.

2.6.5 The Intranuclear Cascade Model of these Independent Simulations

Inelastic intranuclear interactions are clearly statistical (stochastic) in nature, as they can be realized in many possible states. A statistical approach is key to describing such systems, and replaces the evolution of a system's wave function with the description of the evolution of an ensemble of the many possible states of the system. There are two dramatically different stages of a deeply inelastic interaction: 1) a fast, out-of-equilibrium stage in which energy is redistributed between the various degrees of freedom within the nucleus as a finite open system, and 2) the slow equilibrium stage of the evaporation or decay (fragmentation) of the thermalized residual nuclear remnants (remnants are the result of the fragmentation).

Table 2.1: Meson multiplicity comparisons from previous work [229] and this model, which include experimental integration of some more recent OBELIX [354] and Crystal Barrel [37] data sets.

Multiplicity	$\bar{p}p$ Simulation [229]	$\bar{p}p$ Simulation w/New Model	$\bar{p}p$ Experiment
$M(\pi)$	4.91	4.95	4.98 ± 0.35 [269], 4.94 ± 0.14 [295]
$M(\pi^{\pm})$	3.11	3.09	3.14 ± 0.28 [269], 3.05 ± 0.04 [269], 3.04 ± 0.08 [295]
$M(\pi^0)$	1.80	1.86	1.83 ± 0.21 [269], 1.93 ± 0.12 [269], 1.90 ± 0.12 [295]
$M(\eta)$	0.09	0.09	0.10 ± 0.09 [281], 0.07 ± 0.01 [269]
$M(\omega)$	0.20	0.27	0.28 ± 0.16 [281], 0.22 ± 0.01 [240]
$M(\rho^+)$	0.19	0.19	—
$M(\rho^-)$	0.19	0.18	—
$M(\rho^0)$	0.19	0.18	0.26 ± 0.01 [240]

The INC model is a phenomenological model describing the out-of-equilibrium stage of inelastic interactions and operates under the notion that the nuclear system has a certain probability of being in a given state. Transitions between different states are caused by two-body interactions, leading to secondary particles exiting the nucleus, and dissipating excitation energy in the process. However, this phenomenological model is linked to fundamental microscopic theory. It was shown in [129] that it is possible to transform a non-stationary Schrödinger equation for a many body system into kinetic equations, if large energy (and so short time) wave packet formulations are used. To explain, if the duration of the wave packet's individual collisions are shorter than the interval of time between consecutive collisions, then the amplitudes of these collisions will not interfere. This condition is essentially analogous to the condition of a free gas approximation: $\tau_0 < \tau_{FP}$, where τ_0 is the duration time of the collision, and τ_{FP} is the mean-free-path time. This condition allows for the consideration of a particle's motion as in a dilute gas with independent particle motion on free path trajectories perturbed by binary collisions. Under these conditions, in a quasi-classical way, one can use a local momentum approximation by assigning a particle a momentum $\vec{P}\,(\vec{r})$ between consecutive collisions. In this case, the quantum kinetic equation is transformed into a kinetic equation of Boltzmann-type describing the transport of particles within nuclear media; this differs from the conventional Boltzmann equation only by accounting for the Pauli exclusion principle. Thus, the INC model is a numerical solution of the quasi-classical kinetic equation of motion for a multi-particle distribution function using the Monte Carlo method.

Consider now the scope of the INC model and the possibility of generalizing its use, such as in the intranuclear transport of mesons resulting from an extranuclear or intranuclear antineutron annihilation. The principles underlying the model are altogether justified if the following conditions [59, 129, 58] are met:

a. The wavelengths, λ, of the majority of moving particles should be less than the mean distance between nucleons within the nucleus, i.e. $\lambda < \Delta$, where

$$\Delta \approx \left[\frac{4\pi R^3}{3A}\right]^{\frac{1}{3}} \approx r_0 \approx 1.3\,\text{fm}\,. \tag{2.30}$$

In this case, the system acquires quasi-classical characteristics, and one can speak of the trajectories of particles and two-body interactions within the nucleus. For individual nucleons, this corresponds to an energy of $\gtrsim 10\,\text{MeV}$[10]

b. The interaction time should be less than the time between successive interactions $\tau_{int} \leq \tau_{FP}$, where $\tau_{int} \approx \frac{r_N}{c} \approx 10^{-23}\,\text{s}$, and r_N is the nucleon radius. The mean-free-path-length time is

$$\tau_{FP} = \frac{l}{c} = \frac{1}{\rho\sigma c} \approx \frac{4\pi R^3}{3A\sigma c} \approx \frac{3\times 10^{-22}\,\text{s}}{\sigma}\,, \tag{2.31}$$

where σ is the cross section in mB. This requirement is equivalent to the condition of requiring sufficiently small cross sections of elementary interactions and proves problematic for pions produced from the annihilation and lying within the energy range of the Δ-resonance, where $\sigma > 100\,\text{mB}$. However, it should be kept in mind that the effective mean-free-path-length within the nucleus is increased by the Pauli exclusion principle; secondarily, because the uptake of the antineutron is predominately on the periphery of the nucleus, where the nuclear density and Fermi momentum are low while the distance between the nucleons is large, one can expect that the INC model would work in this case. Never-the-less, the comparison of the simulation results with experimental data is the main criterion for the applicability of the model, and will be discussed in Sec. 2.7.

The standard INC model is based on a numerical solution of the kinetic equation using a linearized approximation, which implies that the density of the media does not change in the development of the cascade, i.e. $N_c << A_t$ (where N_c is the number of cascading particles, and A_t is the number of nucleons making up the target nucleus). Such an approximation is violated in the case of multi-pion production in pA and πA interactions at $E_{p,\pi} \geq$ 3-5 GeV, and also in the case of annihilation, especially when considering light nuclei such as ^{12}C.

This version of the model considers the nucleus as consisting of separate nucleons, the position of their centers computed randomly according to the prescribed density distribution $\rho(R)$ such that the distance between their centers is no less than $2r_c$, where $r_c = 0.2\,\text{fm}$ is the nucleon core radius. A cascading particle may interact with any intranuclear nucleon which lies inside the cylinder of

[10]Of course, this condition cannot be met in the case of a slow antineutron, and therefore, its absorption is described in the framework of the optical model described in Sec. 2.4.

diameter $2r_{int} + \lambda$ extending along the particle's velocity vector (here, r_{int} is the interaction radius, while λ is the deBroglie wavelength of the particle). The r_{int} is a parameter of the model and is chosen for better agreement with the experimental data. The key point to understand here is the ability to determine the probability of the cascading particle interacting with another constituent nucleon. One now consider this process in more detail.

Within the standard cascade model, the randomly chosen interaction point is computed from a Poisson distribution for the mean-free-path-length. In this case, the probability $\omega(k)$ of the particle experiencing k collisions along the path-length L in nuclear media with density ρ, where the particle has a total cross section σ, is defined as:

$$\omega(k) = e^{-\rho\sigma L} \cdot \frac{(\rho\sigma L)^k}{k!}\,. \tag{2.32}$$

If on the path-length L there lie n individual particle centers, each has an equal collision probability p for the particle to collide on k of n centers, and so $q = 1 - p$; this probability is described by a binomial distribution:

$$\omega(k, n, p) = \frac{n!}{k!(n-k)!} p^k q^{n-k}\,. \tag{2.33}$$

From the Poisson distribution 2.32, it follows directly that the probability of a particle experiencing no collisions along L is simply:

$$\omega(0) = e^{-\rho\sigma L}\,. \tag{2.34}$$

The same probability for this process can be obtained from the binomial distribution in 2.33:

$$\omega(0, n, p) = (1 - p)^n = q^n\,, \tag{2.35}$$

If one takes $\omega(0) = \omega(0, n, p)$, and when considering that $n = \rho\pi L(r_{int} + \lambda/2)^2$, then:

$$q = 1 - p = e^{-\frac{\rho\sigma L}{n}} = e^{-\frac{\sigma}{\pi(r_{int}+\lambda/2)^2}}\,. \tag{2.36}$$

An essential feature of present version of the INC model is the fact that after interactions occur inside the nucleus, the nucleon is considered to be cascade particle and not a constituent part of the nuclear system. Thus, a reduction in nuclear density takes place during the cascade development[11]. In order to describe the evolution of the cascade and the decays of unstable meson resonances over time, an explicit time-coordinate has been incorporated into the model.

Elementary processes, such as those seen in the channels of Tab. 2.2 are described by empirical approximations from analysis of experimental data on NN and πN interactions at kinetic energies $T < 20\,\mathrm{GeV}$ [59, 58]. Now consider some of the features of the INC model related to the introduction of unstable meson resonances into the model. It is assumed within the model that ρ-mesons produced by annihilation decay quickly enough to avoid interacting with any intranuclear nucleons; in contrast, ω-mesons produced by annihilation can both interact with other intranuclear nucleons and decay within or outside the nucleus. The competition between the decay of the ω-meson and its interaction with intranuclear nucleons is determined by the expression for the mean-free-path:

$$\frac{1}{\lambda} = \frac{1}{\lambda_{decay}} + \frac{1}{\lambda_{int}}\,, \tag{2.37}$$

where $\lambda_{int} = \left(\rho_n \sigma^{tot}_{\omega N}\right)^{-1}$, $\lambda_{decay} = \gamma\beta\left(h\Gamma_\omega\right)^{-1}$, ρ_n is the nuclear density, and γ is the Lorentz factor. The mean lifetime of the η-meson is large enough for the particle to be considered stable within the nucleus, which can then decay upon exit. The model uses the experimentally measured decay modes of the meson resonances described in Table III of [229] and references therein. When the annihilation products are allowed to disintegrate, their three-body decay is simulated by evaluation of the permissible phase-space volume.

To accommodate the passage of η-and-ω-mesons through nuclear material, in addition to channels listed in Tab. 2.2, other pertinent interactions are also considered in Tab. 2.3. Along with the creation of η- and ω-mesons by annihilation, the model also accounts for the creation of mesons through interactions between annihilation pions and nucleons, such as

$$\pi N \to \eta N\ , \pi N \to \omega N\,. \tag{2.38}$$

For cross sections of reactions in Tab. 2.3, estimates given in [226] were employed. For those few reactions shown in Eq. 2.38, experimental cross sections were taken from compilation [191]. As these interactions are considered at relatively low energy, the angular distributions for reactions

[11] This version of the model was first proposed in [58].

Table 2.2: The various nucleonic and pionic interaction modes available to the intranuclear cascade model.

$NN \to NN$	$NN \to \pi NN$	$NN \to i\pi NN (i \geq 2)$
$\pi N \to \pi N$	$\pi + (NN) \to NN$	$\pi N \to \pi\pi N$

Table 2.3: The various η and ω-meson interaction modes on nucleons available to the intranuclear cascade model.

$\eta N \to \eta N$	$\eta N \to \pi N$	$\eta N \to \pi\pi N$	$\eta + (NN) \to NN$	$\eta + (NN) \to \pi NN$
$\omega N \to \omega N$	$\omega N \to \pi N$	$\omega N \to \pi\pi N$	$\omega + (NN) \to NN$	$\omega + (NN) \to \pi NN$

shown in Tab. 2.3 and Eq. 2.38 are assumed to be isotropic in the center of mass of the system. Reactions with three particles in the final state are simulated via their pertinent phase-space volume.

From the preceding discussions, a summary of the physical considerations underlying the INC model can be made as follows:

- The nuclear target is a degenerate Fermi gas of protons and neutrons within a spherical potential well with a diffuse nuclear boundary. The real nuclear potentials for nucleons ($V_N \neq 0$ [229, 71]), antinucleons ($V_{\bar{N}} \neq 0$ [71]), and mesons (V_π, V_η, V_ω) effectively takes into account the influence on the particle of all intranuclear nucleons. The depth of the potential well for the antinucleon and mesons within the nucleus remains a free-parameter of the model (see again Sec. 2.6.2). Recognizing that the annihilation process usually occurs on the periphery of the nucleus, a good approximation for mesons is considered to be $V_{\pi,\eta,\omega} \approx 0$.

- Hadrons (nucleons, annihilation generated mesons, and mesons produced via secondary interactions on nucleons) can be involved in collisions, and are treated as classical particles. A hadron can initiate a cascade of consecutive, independent collisions upon nucleons within the target nucleus. The interactions between cascading particles are not taken into account.

- The cross sections of hadron-nucleon interactions are considered within the nucleus to be identical to those in vacuum, except that Pauli's exclusion principle explicitly prohibits transitions of cascade nucleons into states already occupied by other nucleons.

2.6.6 De-excitation of the Residual Nucleus

For inelastic nuclear reactions, after the rapid stage of the intranuclear cascade ($\tau_{cas} \approx \tau_0$) and once statistical equilibrium ($\tau_{eq} \approx (5\text{-}10)\tau_0$) is established inside the residual nucleus, a slow stage begins ($\tau_{ev} >> \tau_0$) involving the disintegration of the highly excited residual nucleus (note that $\tau_0 \leq 10^{-22}$ s, which is the average time required for a particle to pass completely through the nucleus). The INC model is able to describe the dissipation of energy throughout the nucleus. At the end of the cascade stage, the nuclear degenerate Fermi gas contains a number of "holes" N_h, which is equal to the number of collisions of cascade particles with nucleons within the nucleus.

Also, there exists some number of excited particles N_p, which is equal to the number of slow cascade nucleons trapped by the nuclear potential well. The excitation energy of the residual nucleus E^*, is the sum of the energy of all such quasiparticles calculated from the Fermi energies ϵ_i:

$$E^* = \sum_{i=1}^{N_h} \epsilon_i^h + \sum_{j=1}^{N_p} \epsilon_j^p \,. \tag{2.39}$$

The resulting residual nuclei have a broad distribution on the excitation energies E^*, momenta, masses, and charges. The INC model correctly accounts for the fluctuations of the cascade particles, and reliably defines the entire set of characteristics for residual nuclei.

The de-excitation mechanism for a residual nucleus is determined from the accumulated excitation energy of the nucleus [45]. Under low excitation energies (where $E^* \leq$ 2-3 $\frac{\text{MeV}}{\text{nucleon}}$), the primary de-excitation mechanism is the consecutive emission (evaporation) of particles from the compound nucleus [400]. When the excitation energy of the nucleus is approaching the total binding energy (where $E^* \geq 5\,\frac{\text{MeV}}{\text{nucleon}}$), the prevalent mechanism is explosive decay [113]. For intermediate energies, both mechanisms coexist.

Further implementations of nuclear breakup and de-excitation via photons are currently being pursued within ^{16}O [70] with input[12] from works such as [112, 114, 357, 158, 76, 44, 328, 159][13].

2.7 Comparisons Between the Independent Model and Experimental Data

Now that the MC model has been rather completely described, one can compare simulation outputs to various data sets, particularly from $p\bar{p}$ and $\bar{p}^{12}$C annihilation; data for $\bar{p}$O and $\bar{p}$Ar are not known to exist. This exercise will legitimize the use of the model for $\bar{n}A$ extranuclear and intranuclear annihilations on many nuclei in ways not completely discussed within other works [4, 6, 243, 238,

[12] Many thanks to A. Botvina for his ongoing collaboration on this work.

[13] Some recent results will be shown later in Fig. 2.32 showing the population distribution of nuclear remnants following an intranuclear $\bar{n}$ annihilation, as well as the single photon spectra emitted from those nuclear remnants (with $A \geq 2$) as they de-excite in Fig. 2.33.

237], as the basic microscopic physics described over the preceding pages does not change from nucleus to nucleus.

All experimental data used for comparison with the annihilation model are described in great detail in [226, 37, 354]. Tab. 2.1, reproduced and updated from [229], shows the average multiplicity of mesons formed in $p\bar{p}$ annihilations at rest. The simulation results are within the range of experimental uncertainties. From these simulation results, it follows that more than 35% of all pions have been formed by the decay of heavy meson resonances. Fig. 2.12 shows the pion multiplicity distribution generated by $p\bar{p}$ annihilation, while Fig. 2.13 shows the charged pion momentum distribution. From considering Tab. 2.1 and Figs. 2.12 and 2.13, it follows that the Monte Carlo and available experimental data are in general agreement with the main features of $p\bar{p}$ annihilation. In all, the annihilation model utilizes a complex series of tables [229] with a much larger number of predicted and pertinent channels than [4, 6, 243]. As this approach demonstrates a good description of the experimental data for $p\bar{p}$ annihilation at rest, it is also adequate for an accurate description of $n\bar{p}$ annihilation at rest, and so too can be implemented within the $\bar{n}A$ annihilation simulations described throughout this chapter.

The model has also been used to analyze experimental data taken from antiproton annihilation at rest on ^{12}C target nuclei. Tab. 2.4 shows the average multiplicity of emitted pions and nucleons from simulation and experiment (if available). Experimental data on average pion multiplicities are taken from [295]. The third to last column of Tab. 2.4 shows the average truth energy of pions and photons (resulting from the decay of η- and ω-mesons) emitted from the nucleus. Calculated values for the average multiplicities of pions are within uncertainties of the data. Since the antiproton primarily annihilates on the surface of the nucleus, many of the mesons produced fly out of the nucleus without any interaction. In the case of a light nucleus such as ^{12}C, absorption of annihilation mesons is not large and the average multiplicity of pions emitted appears to be quite similar to the multiplicities in $p\bar{p}$ annihilation[14].

[14] A comparison shown in Tab. V of [229] shows that the average pion multiplicity for an $\bar{n}$C annihilation is somewhat lower than that of $\bar{p}$C, and that the average multiplicity for exiting nucleons is slightly higher than the case of a stopped antiproton. This is due to the fact that the antineutron penetrates more deeply into the nucleus (seen in the solid line shown in Fig. 2.1) compared to an antiproton (seen in the dashed line shown in Fig. 2.1), and so there are more intranuclear interactions between annihilation mesons and constituent nucleons. Thus, the number of mesons emitted from the nucleus and their total energy E_{tot} are reduced, while instead the number of nucleons that were kicked from the original nucleus during the fast cascading stage (and then emitted from the nucleus during the de-excitation process) is increased.

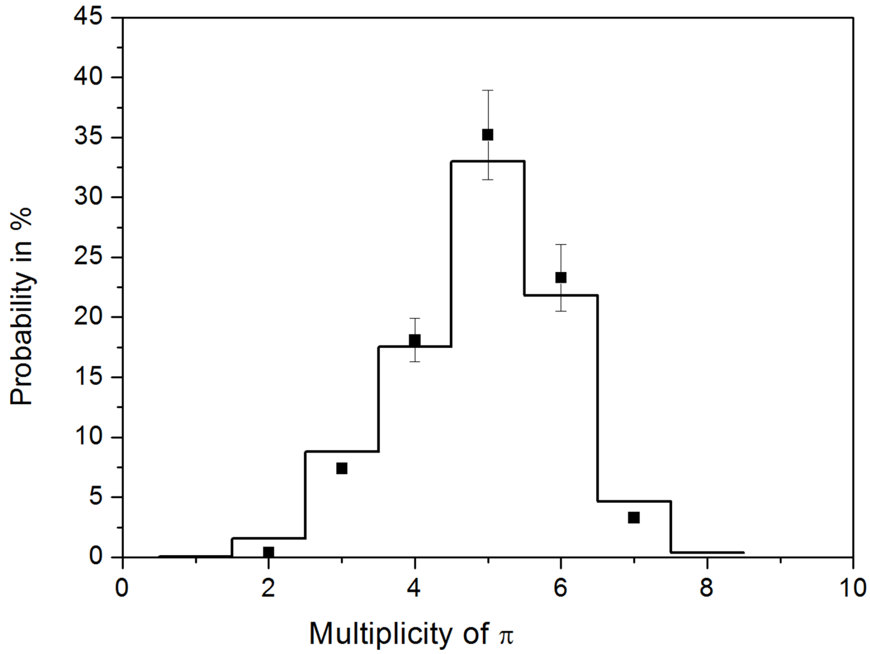

Figure 2.12: The pion multiplicity distribution for $p\bar{p}$ annihilation at rest (taking into account the decay of meson resonances). The solid histogram shows the model, with the points showing experimental data [269]. Courtesy of E. S. Golubeva [229].

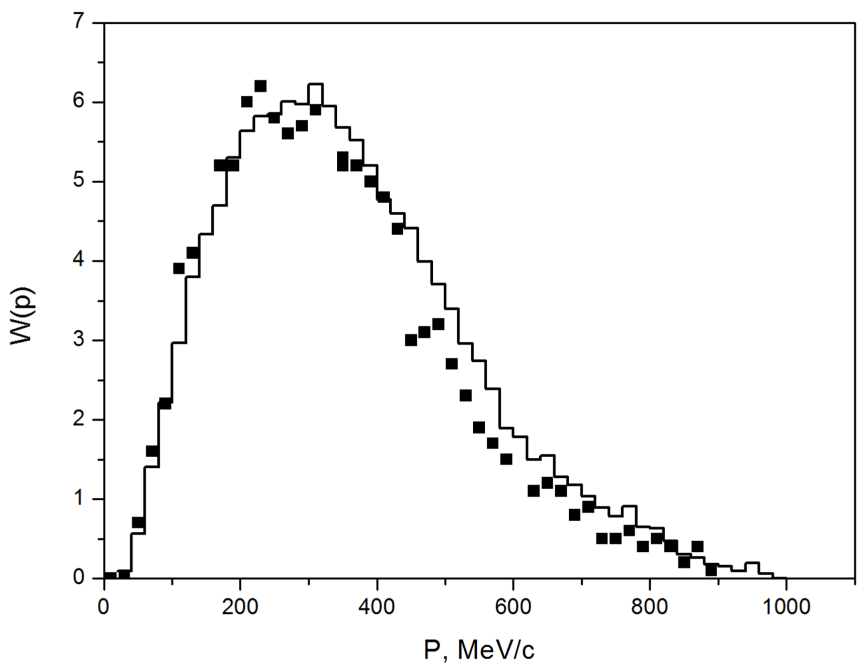

Figure 2.13: The momentum distribution of charged pions produced in $p\bar{p}$ annihilation at rest (taking into account the decay of meson resonances). The solid histogram shows the model, with the points showing experimental data [347]. Courtesy of E. S. Golubeva [229].

Table 2.4: A list of updated multiplicities from experimental data [295] and the model discussed here for $\bar{p}^{12}$C [229, 71], taking into account all annihilation branching ratios, the intranuclear antinucleon potential, and an associated nuclear medium response.

Data Type	$M(\pi)$	$M(\pi^+)$	$M(\pi^-)$	$M(\pi^0)$	E_{tot} (MeV)	$M(p)$	$M(n)$
$\bar{p}$C Experiment	4.57 ± 0.15	1.25 ± 0.06	1.59 ± 0.09	1.73 ± 0.10	1758 ± 59	—	—
$\bar{p}$C Simulation	4.60	1.22	1.65	1.73	1762	0.96	1.03

Now, consider and compare the MC simulation to other available experimental data and features for $\bar{p}$C annihilation at rest. Fig. 2.14 shows the charged pion multiplicity distribution emitted from the nucleus due to $\bar{p}$C annihilation (shown as the solid histogram). As was expected, the differences in these distributions, as with the mean number of emitted pions, are not too significant[15].

Fig. 2.15 shows the distribution of charge Q carried out by pions event-by-event. For the $\bar{p}$C annihilation, the maxima of the distribution are $Q = -1$ and $Q = 0$, which practically corresponds to mesons exiting the nucleus without any interaction with nucleons. The optical-cascade model demonstrates relatively good agreement with the experimental trends[16].

Fig. 2.16 shows the distribution of the number of emitted protons, including those of evaporative origin. The analysis of experimental data and simulation results show that a significant number of events do not have any exiting protons[17].

Fig. 2.17 shows the energy spectrum of protons exiting the nucleus from $\bar{p}$C annihilation at rest. In the low energy regime (up to $50\,\mathrm{MeV}$), evaporative protons provide a significant contribution to the spectrum. The model again shows good agreement with the available experimental data.

Fig. 2.18 shows the momentum distribution for π^+ exiting the nucleus, which is rather similar to the momentum distribution of pions created by $p\bar{p}$ annihilation (as seen in Fig. 2.13). To understand the uncertainty of the model, calculations were done 1) without any nuclear potential for the antineutron, and, as an option, 2) with a model where the antineutron nuclear potential is introduced similarly to [226]. For mesons propagating inside the nucleus, no nuclear potentials have been assumed. Both model calculations are presented in Fig. 2.18, and show rather good agreement with the experimental data from [295] (green triangles), and [292] (blue squares), although there is some exaggerated absorption behavior corresponding to the Δ-resonance region ($\sim 260\,\mathrm{MeV/c}$). The difference between experimental measurements appears to be of the same order as the uncertainty in the calculation.

[15]Similar distributions [229] appear to show some bias towards a smaller number of pions for $\bar{n}$C and a larger number for $\bar{n}$Ar.

[16]In the case of an annihilation with an $\bar{n}$ [229], the distribution has maxima which are shifted to $Q = 0$ and $Q = +1$, respectively. In the case of a peripheral annihilation for $\bar{n}$Ar, the distribution has a narrower maximum than $\bar{n}$C due to stronger final state interactions.

[17]These values are $\sim 40\%$ for $\bar{n}$C, to $\sim 60\%$ for $\bar{n}$Ar [229].

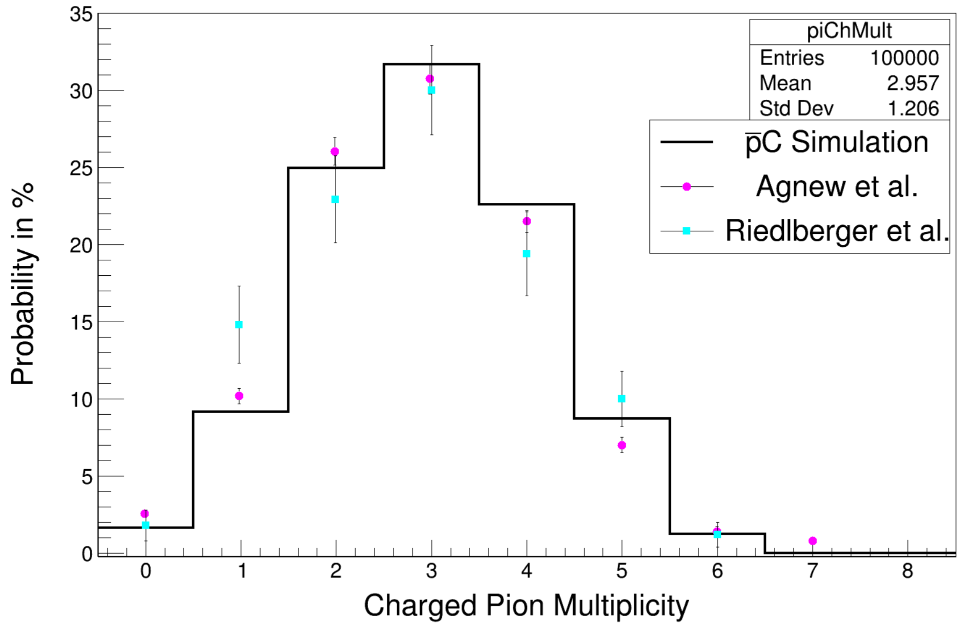

Figure 2.14: The probability (%) of formation of a given number of charged pions for $\bar{p}$C annihilation simulation. Experimental data: pink circles-[22], light blue squares-[338]. Made in collaboration with E. S. Golubeva, and redone from [229].

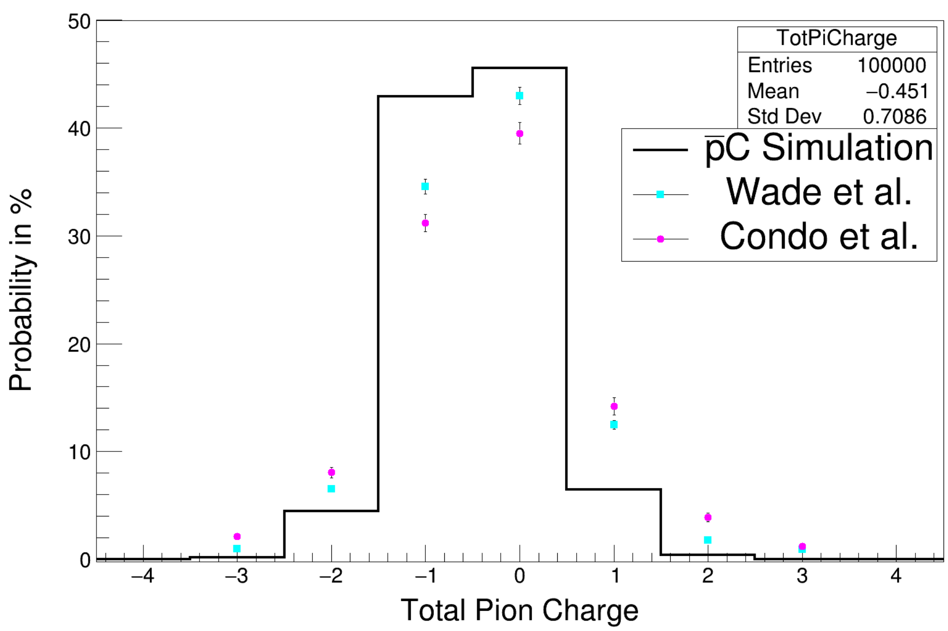

Figure 2.15: The probability (%) of particular values of total charge Q carried away by pions emitted from the nucleus. The solid histogram shows a $\bar{p}$C annihilation simulation. Experimental data: light blue squares-[406], pink circles-[154]. Made in collaboration with E. S. Golubeva, and redone from [229].

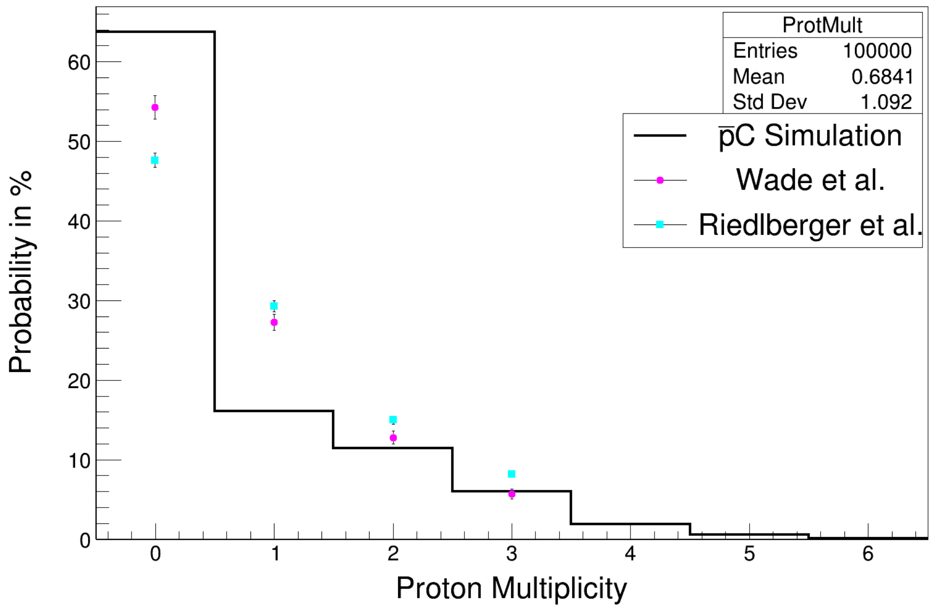

Figure 2.16: The probability (%) of the events with a given number of exiting protons. The solid histogram shows a $\bar{p}$C calculation, including all evaporative protons. Experimental data: light blue squares-[338], pink circles-[406]. Made in collaboration with E. S. Golubeva, and redone from [229].

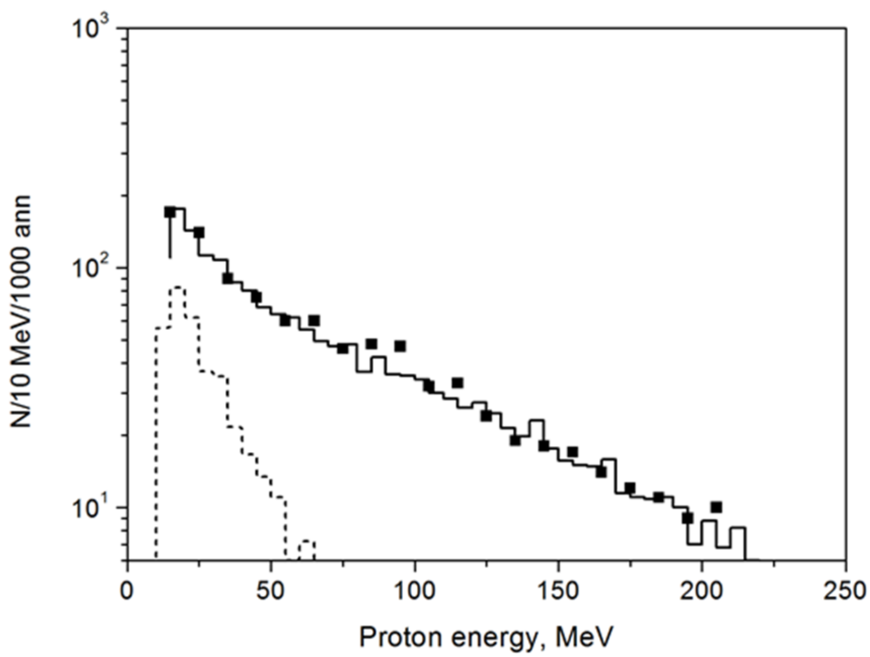

Figure 2.17: The exiting proton kinetic energy spectrum due to antiproton annihilation at rest on ^{12}C nuclei. The solid histogram shows the simulation result. The dotted histogram shows the contribution which evaporative protons impart to the whole distribution. The points show the experimental data taken in [292]. Courtesy of E. S. Golubeva [229].

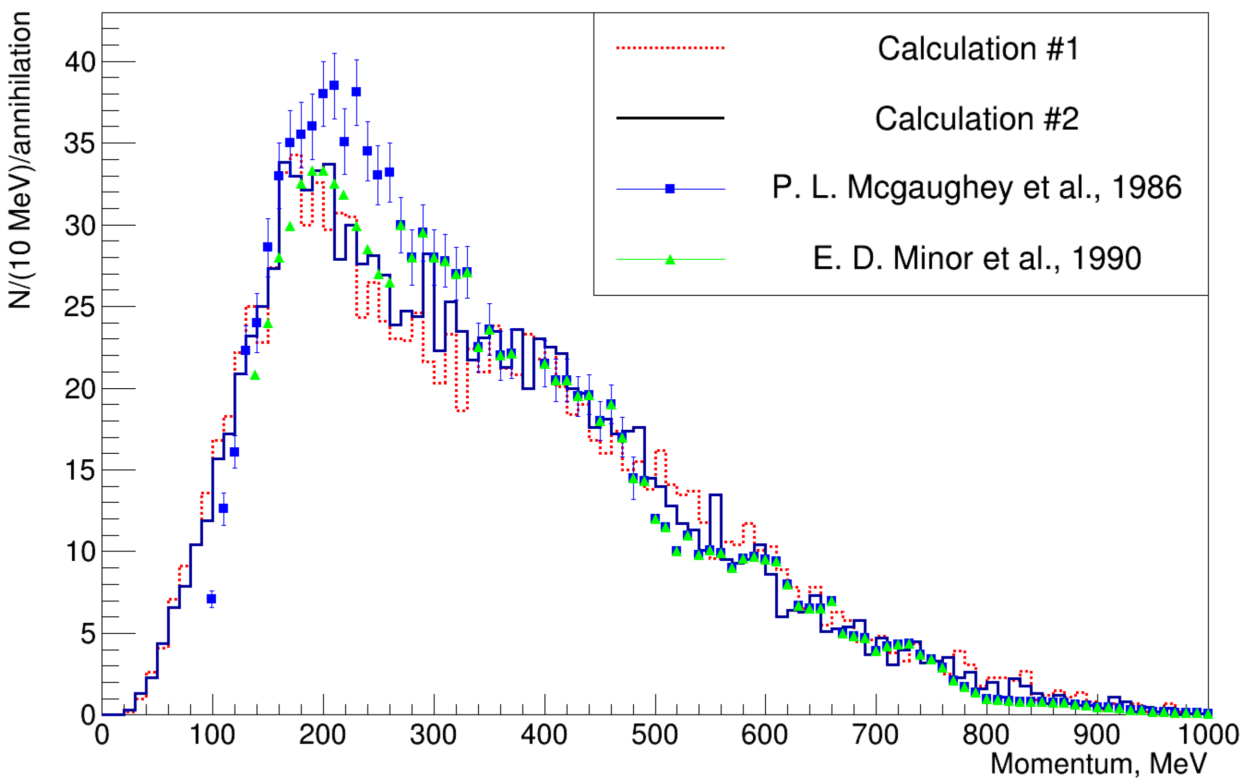

Figure 2.18: The momentum distribution for π^+ emitted from $\bar{p}$C annihilation at rest. The dashed red histogram shows the distribution generated from simulations without an antinucleon potential (Calculation #1), while the solid black shows simulation with an antinucleon potential (Calculation #2). All experimental data points are taken from [295, 292].

From these comparisons, it follows that the model as a whole describes experiments well, thus accurately reflecting the dynamics of the annihilation process and the propagation of annihilation mesons throughout the nucleus.

2.8 Simulations of $\bar{n}A$ Annihilation

Given the above validation of the model with respect to available $p\bar{p}$ and $\bar{p}$C data, one may now speculate on and discuss hypothetical signals arising from $\bar{n}A$ annihilation in an extranuclear or intranuclear context across several nuclei. Some of these have already been mentioned briefly in the preceding section, but will be fleshed out more completely here. Though many of the plots discussed here could be made similarly for each nucleus, this would be highly repetitive (many looking quite identical for the final state pions and photons of key interest), and so I will discuss as many different kinds as possible for brevity.

The generators for all discussed nuclei have been shown to conserve charge, energy, momentum, baryon number, etc., through all stages of the simulation. Outputted .txt files, formatted in such a way as to easily separate the particle content and their respective physical variables through the stages. Analysis of the output has been completed by ESS colleagues using C++ and the CERN ROOT scientific software framework [124]. 100,000+ simulated annihilation events are available for each nucleus upon reasonable request of the authors [229, 71, 70].

2.8.1 Extranuclear $\bar{n}^{12}$C Annihilation Simulations Using the Independent Model

Considering discussion in Sec. 2.6.2, for the intranuclear cascade the operating energy conservation law for the annihilation process of an *extranuclear* neutron is written as

$$E_{ann} + E^* = E^{'}_{\bar{n}} + E^{'}_{N}, \tag{2.40}$$

where $E^{'}_{\bar{n}}$ is the total energy of the $\bar{n}$ inside the nucleus at the point of annihilation, $E^{'}_{N}$ is the total energy of the nucleon annihilation partner at the same point, and E^* is the excitation energy of the nucleus after the annihilation. In the degenerate Fermi gas model, this is defined as

$$E^* = T^i_{FN} - T^i_N, \tag{2.41}$$

varying from 0 to T^i_{FN}, where i is the zone number in which the annihilation takes place, T^i_{FN} is the boundary Fermi energy of the i-th zone, and T^i_N is the Fermi energy of the annihilation partner in the same zone. If one takes into account Eqs. 2.23–2.25 and 2.28, it follows that

$$E_{ann} + E^* = m_{\bar{n}} + m_N - \varepsilon_N, \tag{2.42}$$

where again $\varepsilon_N = 7$ MeV/nucleon. Similar formulations pertain to the intranuclear annihilation as well, again following from Sec. 2.6.2.

With the above in mind, an important characteristic for any relativistic many particle system is the invariant mass. One may analyze the invariant mass distribution for annihilation mesons at the annihilation point, and then see how it distorts due to final state interactions (the intranuclear cascade) throughout the nucleus; detector performance might affect the invariant mass further [67, 61]. Fig. 2.19 shows how the distribution of invariant mass changes for all outgoing pions and photons generated by $\bar{n}$C annihilation products (solid), a result of interactions with nuclear media. The dotted line shows the original distribution of invariant mass of the initial $\bar{n}N$ annihilation products within the ^{12}C nucleus. The intranuclear interactions of annihilation mesons with nucleons have resulted in a significant redistribution of energy between mesons and other nuclear constituents, shifting and smearing the initial distribution of M_{inv} down to values of even $\lesssim 1$ GeV/c^2. Note that the higher the initial value of M_{inv}, or the deeper the penetration of the antineutron into the nucleus, the larger the number of mesons which will interact with the nuclear environment, quickly devouring this particular part of the distribution. The spread of the original invariant mass down to values ~ 1.7 GeV/c is due to the off-shell mass defect caused by the (anti)nucleon potentials.

Similarly, for Fig. 2.20, see that the momentum distribution reconstructed from initial annihilation mesons is perturbed and expanded by transport through the intranuclear environment. The structure shown in the dotted histogram illustrates a similar distribution as in Fig. 2.11, though implicitly convolved with Fig. 2.1, and considerate of different scales. After intranuclear transport, this distribution distorts as particles cascade through the nucleus, shifting values up $\gtrsim 0.8$ GeV/c. Again, the large amount of Fermi motion this plot implies is due to the disproportionate acceleration of the extranuclear antineutron due to the antineutron potential. By conservation, Fig. 2.20 also considers the dynamical (position-correlated) momentum of the initial annihilation pair. The $\bar{n}$ is always assumed to come from a transformation down-range of a cold neutron source with a mean energy of only ~meV; in an old variant of the model [229], the $\bar{n}$-potential was ignored until [71]. Thus, the original momentum distribution of the annihilation products was effectively a direct observation of the non-interacting zoned local Fermi gas single nucleon momentum distribution folded with the radial annihilation probability distribution. In the initial state of the model described here (dashed line), the mass of the $\bar{n}$ is defined by Eq. 2.21 and the momentum of the $\bar{n}$ follows from Eq. 2.23. The direction of the momentum of the nucleons are isotropically distributed, and thus the total momentum of the annihilation products varies from $|P'_{\bar{n}} - P'_N|$ to $|P'_{\bar{n}} + P'_N|$, smoothing and spreading out the structure associated with the presence of zones in the target nucleus. The peak in the histogram in the region just below $100\,\mathrm{MeV}/c$ corresponds to annihilations on the outside of the nucleus (within the diffuse eighth zone), where the $\bar{n}$-potential is taken to be zero with no associated off-shell mass accounted for, and so the momentum of the annihilating pairs is equal only to the momentum of the nucleon partner.

Following the preceding one-dimensional projective figures, he most impressive figures in consideration of $\bar{n}$C extranuclear annihilation are likely Figs. 2.21 and 2.22. Here, see that the event-by-event correlated total available initial and final mesonic/pionic and photonic parameter space for an $n \to \bar{n}$ signal, most commonly shown via total momentum versus invariant mass plots (*similar* to Fig. 2 in [4]) at the annihilation point before any nuclear transport is completed. In Fig. 2.21, the effect of the antineutron potential and off-shell nature of nucleon masses are clearly seen[18].

Fig. 2.22 show the same variables after transport, but re-scattering, Δ-resonance, and absorption of annihilation mesons leads to an overall decrease in the observed invariant mass, lessening the apparent final state differences between the two simulation variants.

[18]Otherwise, there would be a small momentum range due to the effective absence of additional antineutron momentum [71]. Also, there would be a rightward instead of leftward inclination of initial mesonic parameter space as a consequence of the on-shell mass' effects on the overall kinematics of the annihilation. Thus, ignoring (anti)nucleon potentials can create significantly different *initial* conditions for the transport of annihilation mesons through the nucleus, and so similarly final state topologies identifiable within a detector.

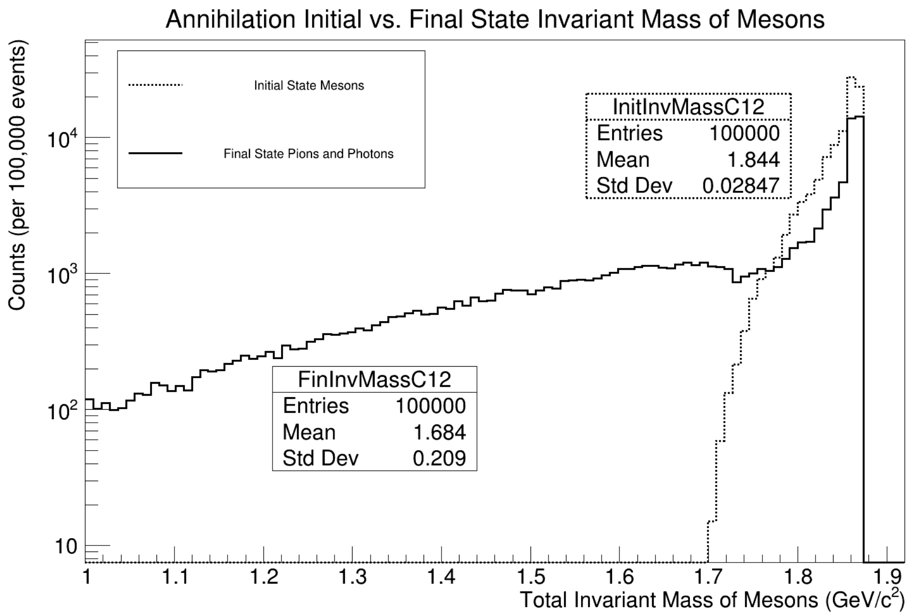

Figure 2.19: The distribution of total invariant mass of $\bar{n}$C annihilation products. The dotted histogram shows the distribution of invariant mass due only to original annihilation mesons at the annihilation point. The solid histogram shows the invariant mass of pions and photons emanating from the nucleus after intranuclear transport.

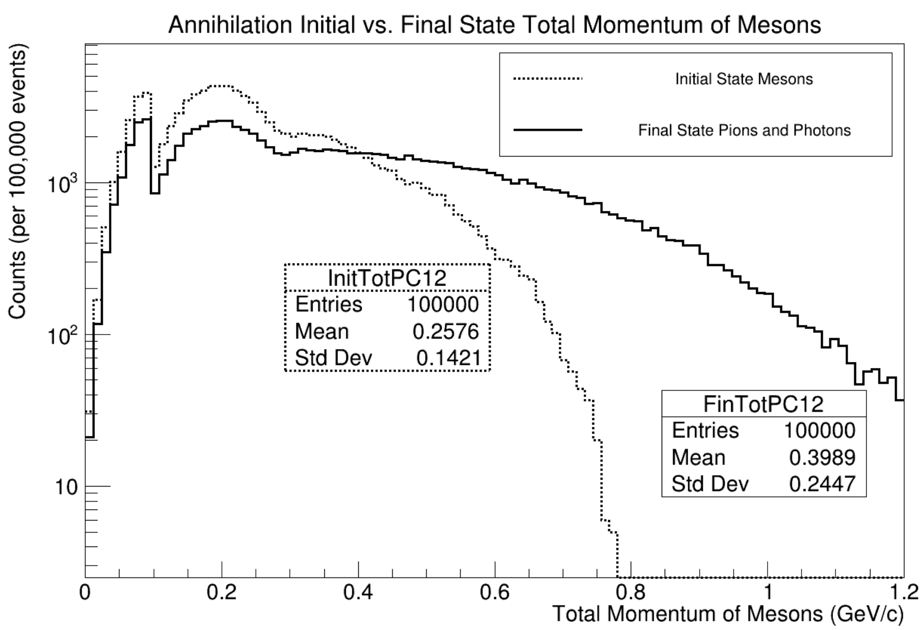

Figure 2.20: The distribution of total momentum of $\bar{n}$C annihilation products. The dotted histogram shows the distribution of total momentum of all original annihilation mesons. The solid histogram shows the distribution of total momentum of pions and photons emanating from the nucleus after intranuclear transport.

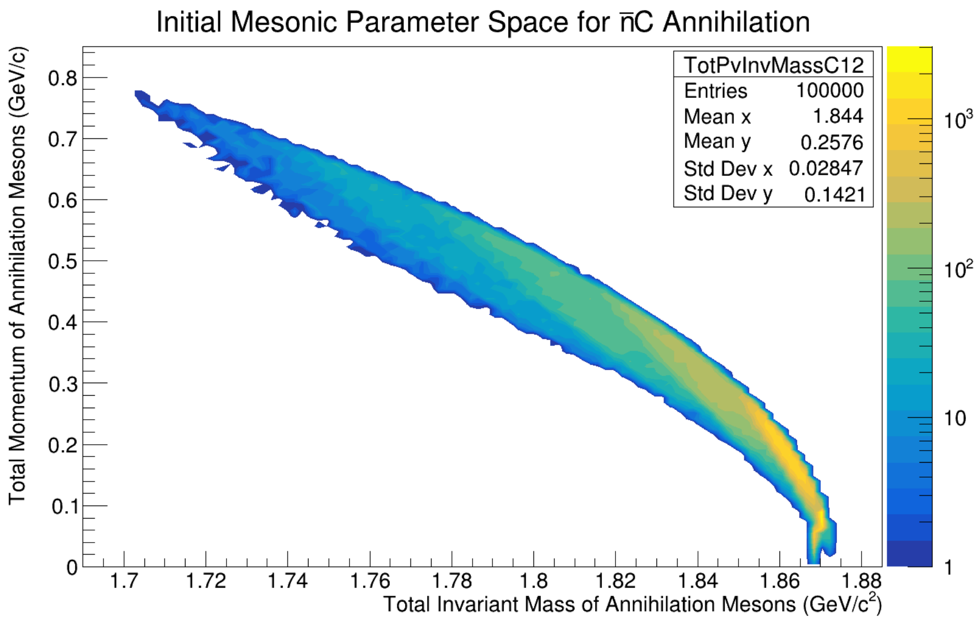

Figure 2.21: The total mesonic initial state parameter space is shown for extranuclear $\bar{n}$C annihilation.

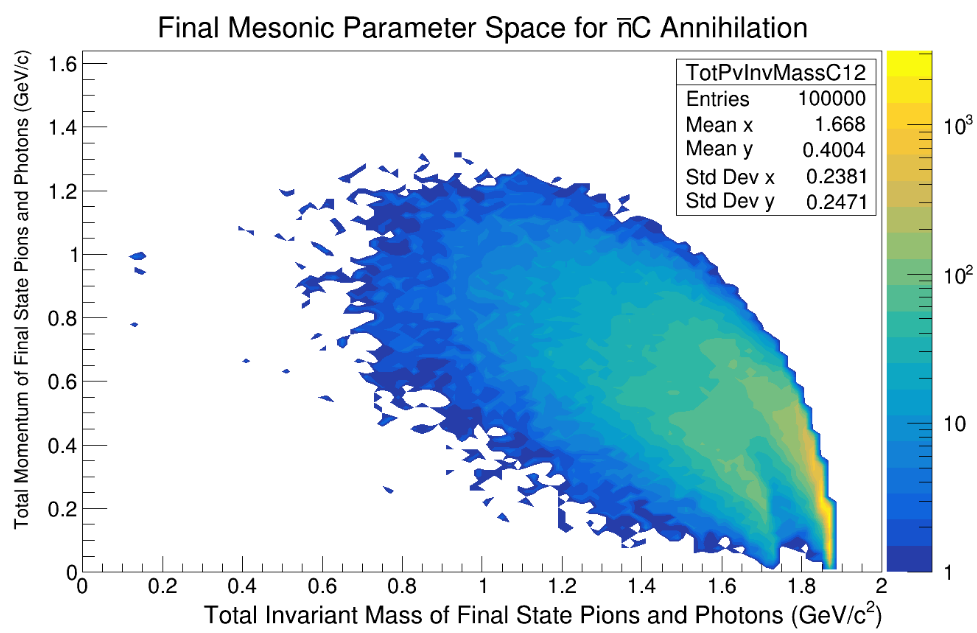

Figure 2.22: The total pionic/photonic final state parameter space is shown for extranuclear $\bar{n}$C annihilation.

Overall, the mesonic/pionic/photonic parameter space is rather spatially if not statistically constrained, which could lead to high hypothetical signal efficiencies for future experiments [67, 61].

2.8.2 Intranuclear $\bar{n}^{39}$Ar Annihilation Simulations, and **GENIE** Comparisons

As mentioned, there now exist some public generators for $n \to \bar{n}$ within the particle physics community, notably developed in [243] using `GENIE` [39]. As discussed throughout this chapter, while the demonstration of this independent MC generator's capabilities in the reproduction of antinucleon data is well-established for ^{12}C [229], such a *complete* set of physical observables does not readily exist to constrain the model for larger nuclei, especially not for ^{40}Ar. Thus, out of a need for ample comparisons, one may endeavor to show the commonalities and differences between each of these $n \to \bar{n}$ generators for intranuclear $\bar{n}\,^{39}_{18}Ar$ annihilation, useful to DUNE. This is accomplished by attempting to make some of the same assumptions (roughly) as `GENIE`, and vice-versa. For instance, one can generate events by simulating the annihilation position sourced from a Woods-Saxon distribution within this independent generator; similarly, with little work, one may perturb the default settings of the `GENIE` $n \to \bar{n}$ generator module to utilize a noninteracting local Fermi gas nuclear model along with a full (stochastic) intranuclear cascade. The inclusion of an $\bar{n}$-potential within `GENIE` has not yet been investigated; implementation of the modern annihilation position probability distribution (Sec. 2.5.3) is currently underway. While none of these comparisons across generators are ever to be *exact*, their approximately equivalent formalism can serve to inform one on the stability of quantities which characterize the possible final state topologies of a true $n \to \bar{n}$ signal event with respect to their associated backgrounds. This stability across models, and their interplay with model detector reconstruction, will be studied in detail in future work with DUNE collaborators, as well as within Chap. 4.

Two of the probability distributions of intranuclear radial position upon annihilation for these generators are shown in Fig. 2.23 in orange and blue, and are surprisingly similar even with quite different physical assumptions. The quantum mechanical, shell-by-shell distributions discussed in Fig. 2.5 are all taken in a weighted average to create the final orange curve, from which this generator can source its initial annihilation positions in a binned fashion; this position is thrown, a nearest neighbor nucleon found within a given zone (and then "moved" to the annihilation position), a Fermi momentum computed for each of the pair given their initial positions, and then a total phase space calculated. All GENIEv3.0.6 events source their annihilation positions from a smooth Woods-Saxon (nuclear density) distribution [39] incredibly similar to the continuous parameterization for the nuclear density, and from which one can derive the eight local zone densities discussed within this model:

$$\rho_{WS}^{Ar} = (1 + \exp(\frac{r - 3.6894}{0.5227}))^{-1} \ . \tag{2.43}$$

GENIE also similarly throws momenta from (non)local single nucleon momentum distributions. When this curve is multiplied by r^2, one generates the blue annihilation probability distribution. These curves effectively demonstrate how even the most simple of assumptions, some only quasi-classical, can lead to quite good approximations; however, note the preponderance of events *even further* toward or beyond the surface [180] of the nucleus using a quantum-mechanical formalism. The increased likelihood of such surface annihilations, along with their associated correlation with lower momenta and higher final state meson multiplicity, will be shown in the coming figures to be an arguably critical part in the proper evaluation of future experimental efficiencies and possible lower limits on mean intranuclear $n \to \bar{n}$ transformation time; the interplay of these quantities and any changes in the final state π-star topology observable in the DUNE detectors has not yet been completely investigated. For similar plots and discussions, see [226, 224, 225, 227, 229].

Some of the differences between this work and GENIEv3.0.6's generator pertain to the initial dynamics of the intranuclear annihilation. An example of this can be seen in Fig. 2.24, showing the initial annihilation mesons' total energy for this work (using the orange curve in Fig. 2.23) and GENIE (using the blue curve in Fig. 2.23), each using a version of a local Fermi gas nuclear model. Like the extranuclear $\bar{n}$ annihilation described on ^{12}C in preceding sections, energy balance in the annihilation point is given as $E_{ann} + E^* = E_{\bar{n}}^{'} + E_{N}^{'}$; taking into account that $E_{\bar{n}}^{'} = E_{n}^{'}$, and that

$$E^* = T_{Fn}^{i} - T_{Fn}^{i} + T_{FN}^{i} - T_{N}^{i} \tag{2.44}$$

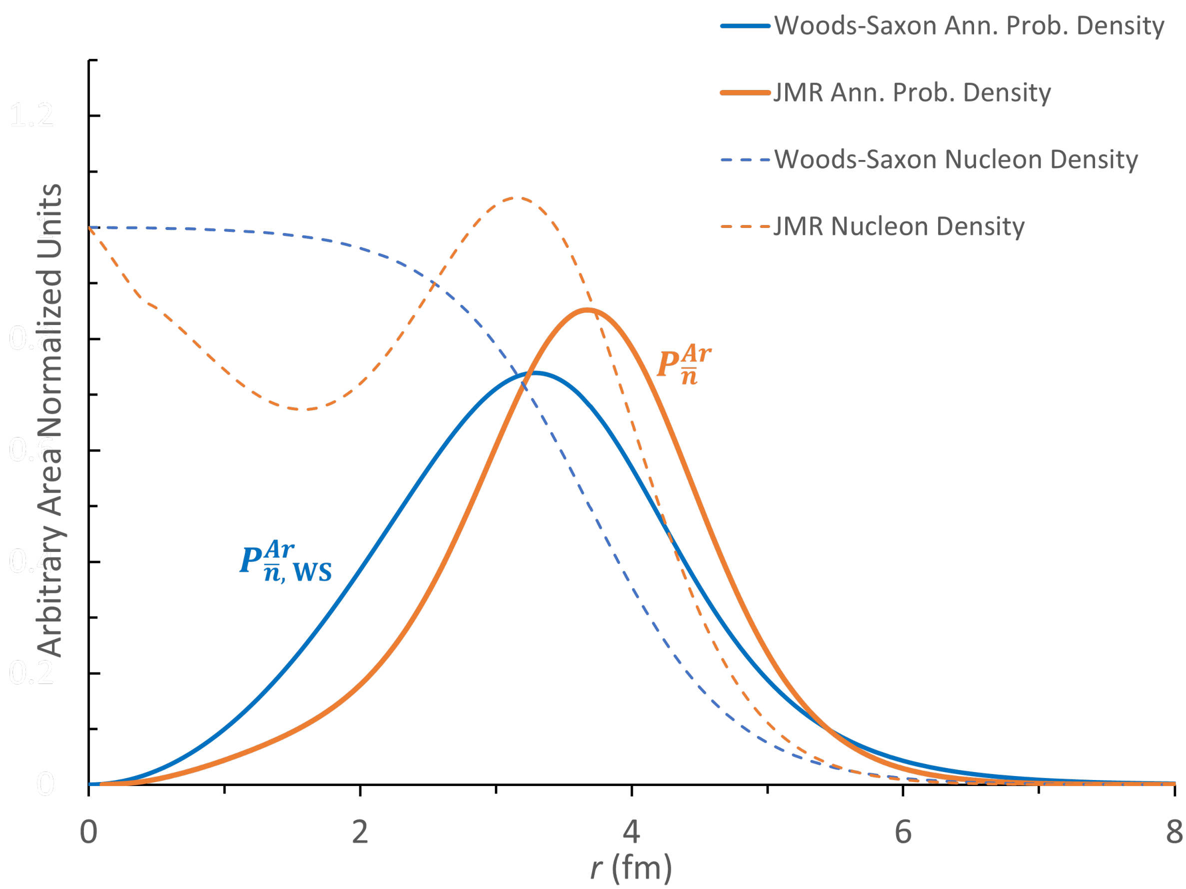

Figure 2.23: Several plots are shown for various generator assumptions. In solid blue, it is seen that the naive intranuclear radial position of annihilation probability distribution generated by a Woods-Saxon (abbreviated "WS"), as presented in `GENIE`; the relevant nuclear density is also shown in dashed blue (see Eq. 2.43. In orange, the modern, quantum-mechanically derived, shell-averaged, true intranuclear radial position of annihilation probability distribution as developed in Sec. 2.5 is shown, present in the independent generator described here; the effective "nuclear density" is shown in dashed orange. Distributions are normalized to the same arbitrary integral for a direct comparison, and the scale is arbitrary.

and so one constructs the total energy

$$E_{ann} + E^* = m_{\bar{n}} + m_N - 2\varepsilon = 1.866\,\text{GeV}\,. \tag{2.45}$$

Note that these relations are legitimate for all intranuclear simulations to follow.

It can be seen in Fig. 2.24 that the distribution of energies available to an annihilation in this model is always less than $1.866\,$GeV. GENIE's distribution (which assumes a similar binding energy per nucleon as the independent model) can be explained simply by considering the minimum/maximum potential magnitudes of annihilation pair momentum (corresponding to an anti/co-parallel intranuclear collision) while assuming an approximately constant intranuclear defect nucleon mass of $\sim 910\,$MeV/c^2. The sharp rise of the GENIE distribution around $1.82\,$GeV can be seen to correspond to the addition of momentum distribution shapes around zero momentum (see Fig. 2.25).

One can see the different initial single nucleon momentum assumptions in Figs. 2.25. The GENIE nonlocal Bodek-Ritchie or local Fermi gas nuclear models mentioned here serve effectively as a set of initial conditions which enable certain nucleon momentum and radial position correlations (or lack thereof). The nonlocal Bodek-Ritchie [109, 39] has been considered the default operating model within GENIE for $n \to \bar{n}$ and neutrino scattering simulations; however, for most of the rest of this section, comparisons to local Fermi gas models will be considered against each other for simplicity. Note the different characteristic ranges of momenta; in general, the shapes and ranges of each nucleon local Fermi gas model (solid lines, top and bottom figure) are incredibly similar, while the nonlocal Bodek-Ritchie is quite unique (dashed lines), especially with its phenomenological, short-range "correlation" tail. For GENIE, one sees that the *shapes* of all distributions are identical: $p_f(\bar{n}) = p_f(n) \approx p_f(p)$; this is not the case for the independent model, where $p_f(\bar{n}) \neq p_f(n) \approx p_f(p)$ due to the $\bar{n}$-potential[19].

The most important aspect of correlated behavior which has been previously unaccounted for in GENIE-affiliated work on $n \to \bar{n}$ is that of initial (anti)nucleon momentum and radius. In

[19]For simplicity, throughout this section, I have labeled certain plots with "Golubeva-Richard-Paryev" (for original work done with the modern shell model-derived annihilation position probability distribution and modification of the nuclear medium due to $\bar{n}$ interactions), "Golubeva-WS-Paryev" (for original work done with a Woods-Saxon-derived annihilation position probability distribution and nuclear medium modification), and then the various GENIEv3.0.6 model identifiers [39].

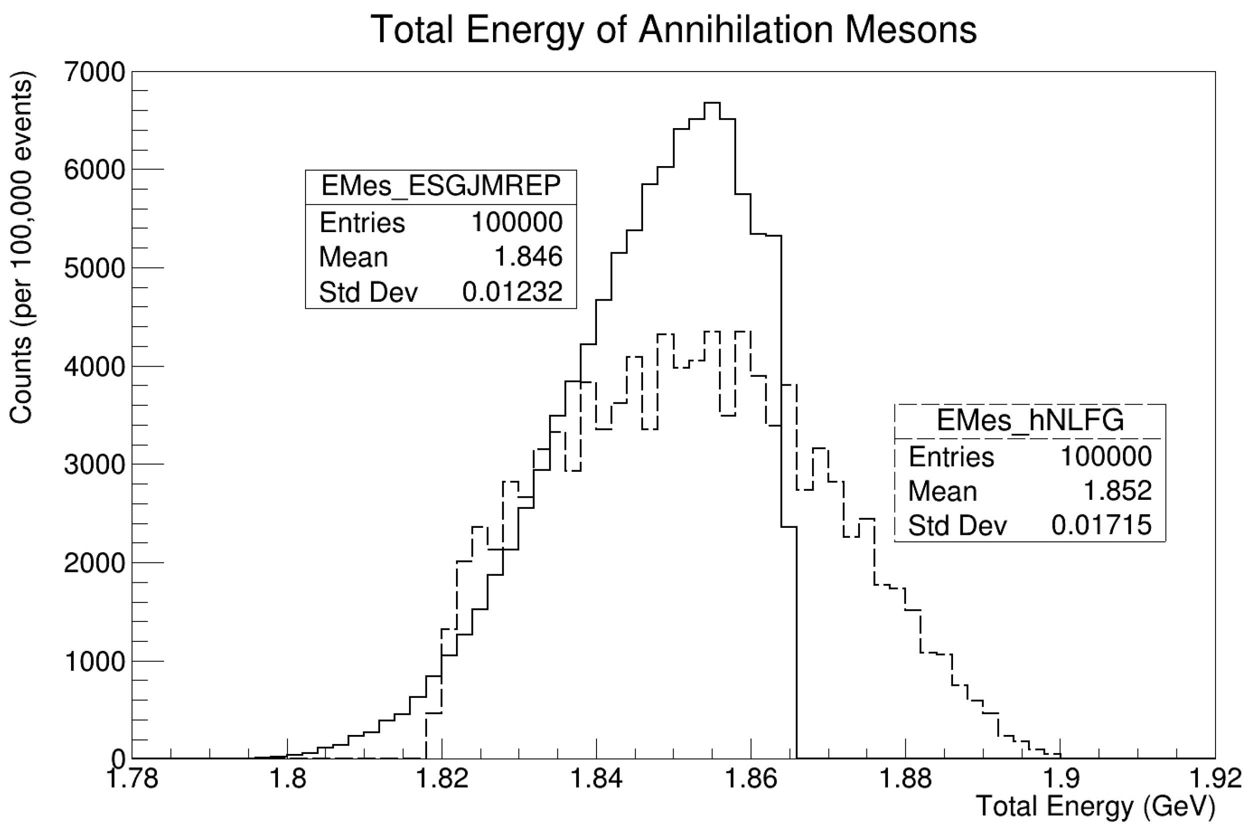

Figure 2.24: The distributions of total initial annihilation meson energy are shown for this work (solid line) and GENIEv3.0.6 (dashed line) using local Fermi gas models. Via conservation, each of these is equivalent to the distributions of the annihilating $\bar{n}N$ pair.

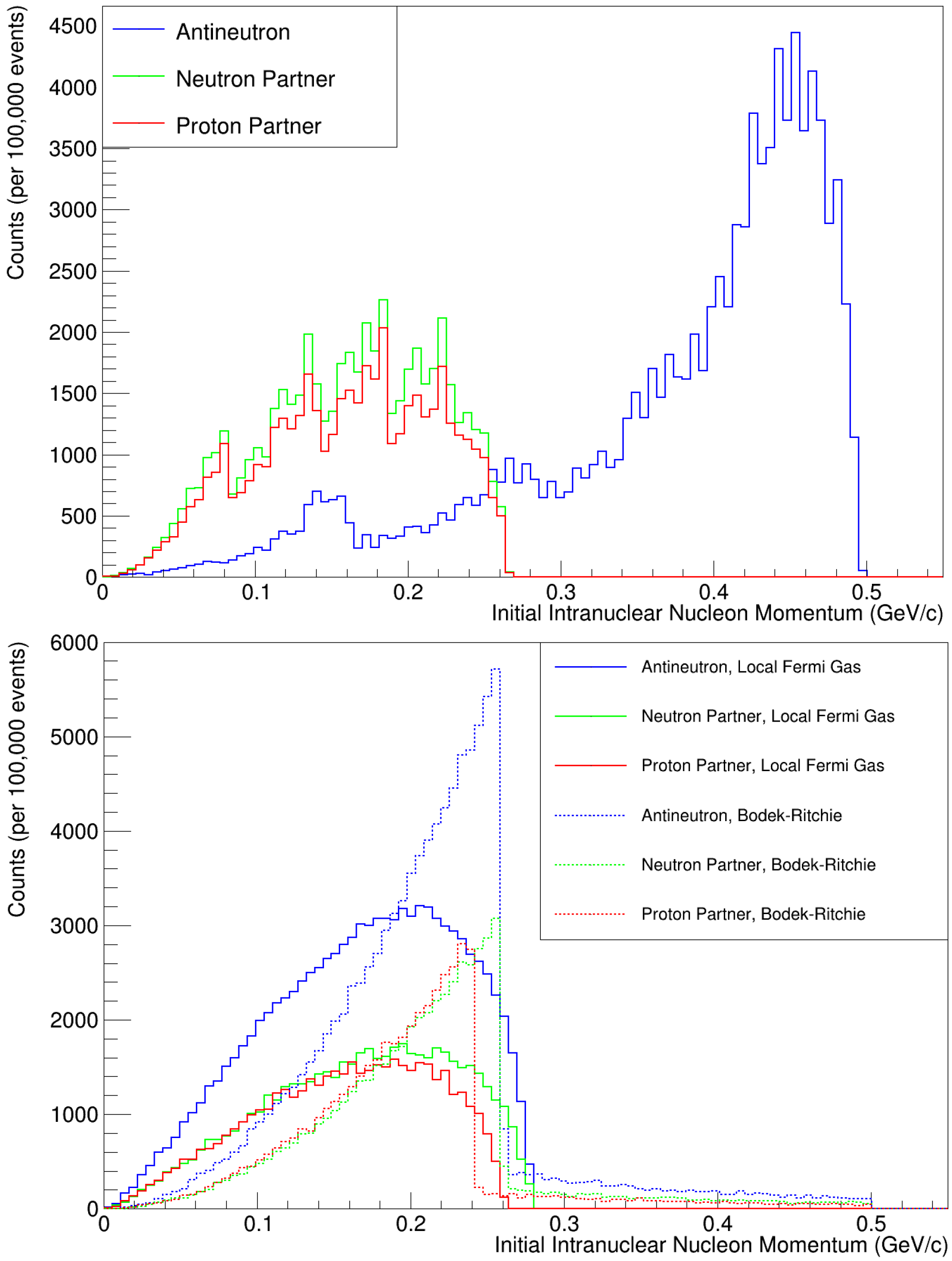

Figure 2.25: Top: This work, showing the initial (anti)nucleon momentum distributions, using a *zoned* local Fermi gas model with an additional $\bar{n}$ potential. Bottom: the same for the GENIEv3.0.6, showing a local Fermi gas model and the default nonlocal Bodek-Ritchie model.

Figs. 2.26, comparisons between the independent model described here and GENIE's local Fermi gas nuclear models are shown, which by definition preserve these radial correlations, alongside the inherently *nonlocal* Bodek-Ritchie nuclear model. All figures assume a (zoned or smooth) Woods-Saxon-like annihilation position probability distribution for easier direct comparisons; all outputs from the independent simulations using the modern annihilation probability distribution from Sec. 2.5 appear somewhat similar when graphed in these coordinates, and so are not shown here to conserve space. The $\bar{n}$-potential is apparent in the top right plot, which appears smoothed and lacking of any zoned discontinuities due to the strength of the interaction (as seen in the top left plot, showing correlations for $\bar{n}$ annihilation partners). All *local* models correctly predict a falling-off of nucleon momentum at higher radii, a key consideration for event reconstruction and background rejection. This behavior is not present within GENIE when using the default *nonlocal* Bodek-Ritchie nuclear model, shown at the bottom right; the asymmetry present in this plot is due to the Fermi momentum cutoff, above which only phenomenologically "short-range correlated" $\bar{n}$'s populate.

The initial annihilation meson total momentum distribution is seen for the independent and GENIE models in Fig. 2.27; these distributions are equivalent to the initial two-body annihilation pair momentum distributions by conservation. Each histogram shares a Gaussian-like shape due to the randomized momentum selection from underlying distributions, though the independent model's output shows much higher available momentum due to the interaction of the $\bar{n}$ with the modified nuclear medium.

All of this leads one to consider the available initial (and final) mesonic parameter space, again à la Fig. 2 of [4]. As seen in Figs. 2.28, this serves as an initial condition of the annihilation-generated mesons before intranuclear transport; thus, for GENIE, hA/hN2018 models (see Secs. 2.5.4 and 2.5.5 of the GENIE v3.0 manual [39] for full discussions) are at this stage equivalent. Due to the *non-dynamical* off-shell masses of annihilation pairs, GENIE predicts higher invariant masses, while the independent model shows them decrease due to off-shell mass defects in correlation with radial position. Overall, the space is quite differently filled for each model, though considering this is *before* the intranuclear cascade, one cannot necessarily predict much about the final state. The follow-up to these figures can be studied in the comparison of Figs. 2.29, where the independent model and GENIE generated events proceed through a full intranuclear cascade (hN2018 only is shown here). Note that the independent model includes photons in the final state from high-mass resonance decays, while GENIE does not. The disconnected regions toward the left of the plots are signs of single π emission after at least one or more meson absorptions. While *overall* the distribution of events is rather consistent, critically, the high density of events with large invariant mass and low momentum (bottom right of plots) among these local Fermi gas models shows the importance of modeling correlations between position and momentum as they imply a comparatively large number of escaping (and possibly visible) π's in the final state. It is with these areas that one may hope to find a significant rejection of background events, possibly allowing for an observation of $n \to \bar{n}$[20].

One may close a comparison of these generators with Tab. 2.5 and Figs. 2.30 and 2.31, which show many similarities and some differences across them. Multiplicities in Tab. 2.5 are seen to be most different between the independent model and GENIE in the realm of outgoing nucleons (resulting from nucleon knock-out or evaporative de-excitation); this should not be surprising, as GENIE does not currently contain a public version of an evaporation model[21] within either its hN2018 (full intranuclear cascade) or hA2018 (single effective interaction) models. Small differences can also be seen in the $\pi^{0,\pm}$ multiplicities, which are partially due to the fact that more $n \to \bar{n}$ events are predicted toward or beyond the surface of the nucleus (see again Fig. 2.23), but there are also nontrivial dependencies given the larger number of possible branching channels simulated in this model [229] compared to GENIE [243, 39].

To give a more complete context to Tab. 2.5, several (absolute magnitude) final state momentum spectra can be plotted for π^+ and p species, two key constituents in the eventual experimental search for $n \to \bar{n}$ in DUNE; note that the $\pi^{0,-}$ distributions are quite similar. In Fig. 2.30, one sees that the independent generator models agree quite well with the full intranuclear cascade simulation from GENIE (using hN2018) in both multiplicity and shape; there is some lack of structure around the Δ-resonance within the hA2018 simulation (recall this models the cascade as a *single effective interaction* using tabulated reaction rates), a sign of the competition between cross-sections (or rates) of processes such as Δ decay and pion absorption.

[20] A full characterization of these effects across many nuclear model configurations within the DUNE detectors is continuing within the DUNE High-Energy Physics Working Group, and will be discussed some in Chap. 4.

[21] Exciting work by GENIE developers in this regime is expected to be completed soon, and the community looks forward to being able to compare these results.

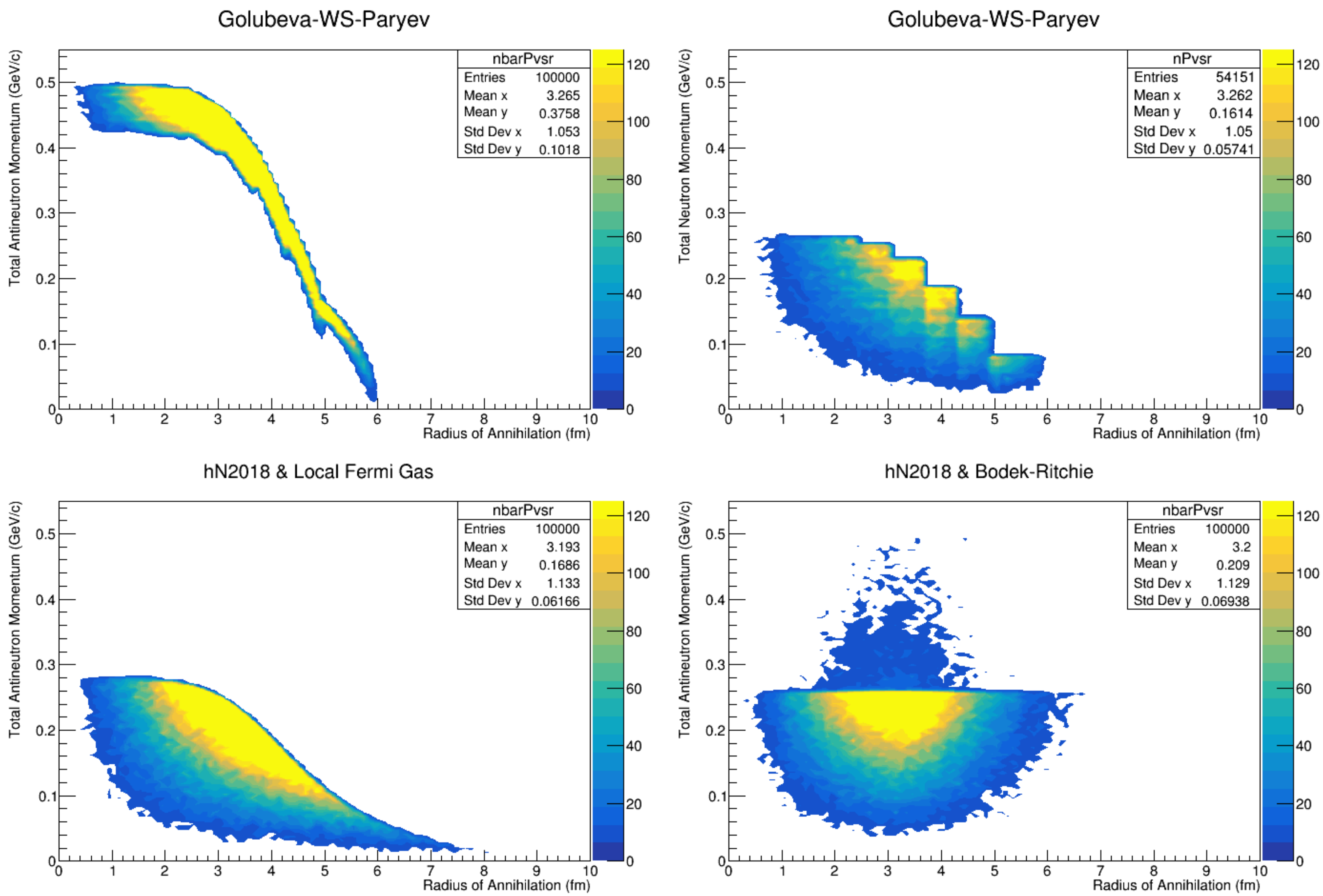

Figure 2.26: Two dimensional $\bar{n}$ and n momentum-radius correlation plots for this work (top two plots, using a *zoned* local Fermi gas and *zoned* Woods-Saxon annihilation position distribution) alongside `GENIE`v3.0.6's *local* Fermi gas and *nonlocal* Bodek-Ritchie single (anti)nucleon momentum nuclear models (bottom two plots, also with a smooth Woods-Saxon initial $\bar{n}$ annihilation position distribution).

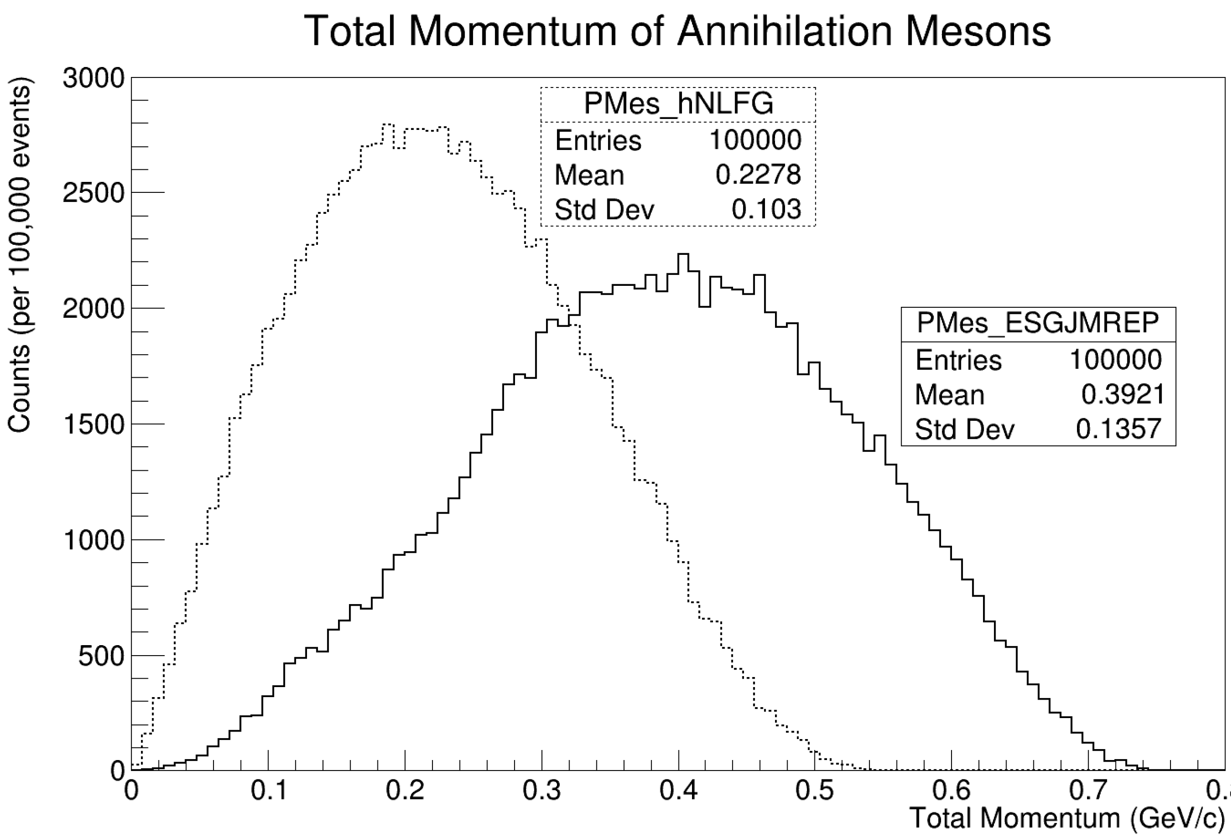

Figure 2.27: The distributions of total initial annihilation meson momentum are shown for this work (solid line) and `GENIE`v3.0.6 (dashed line) using local Fermi gas models.

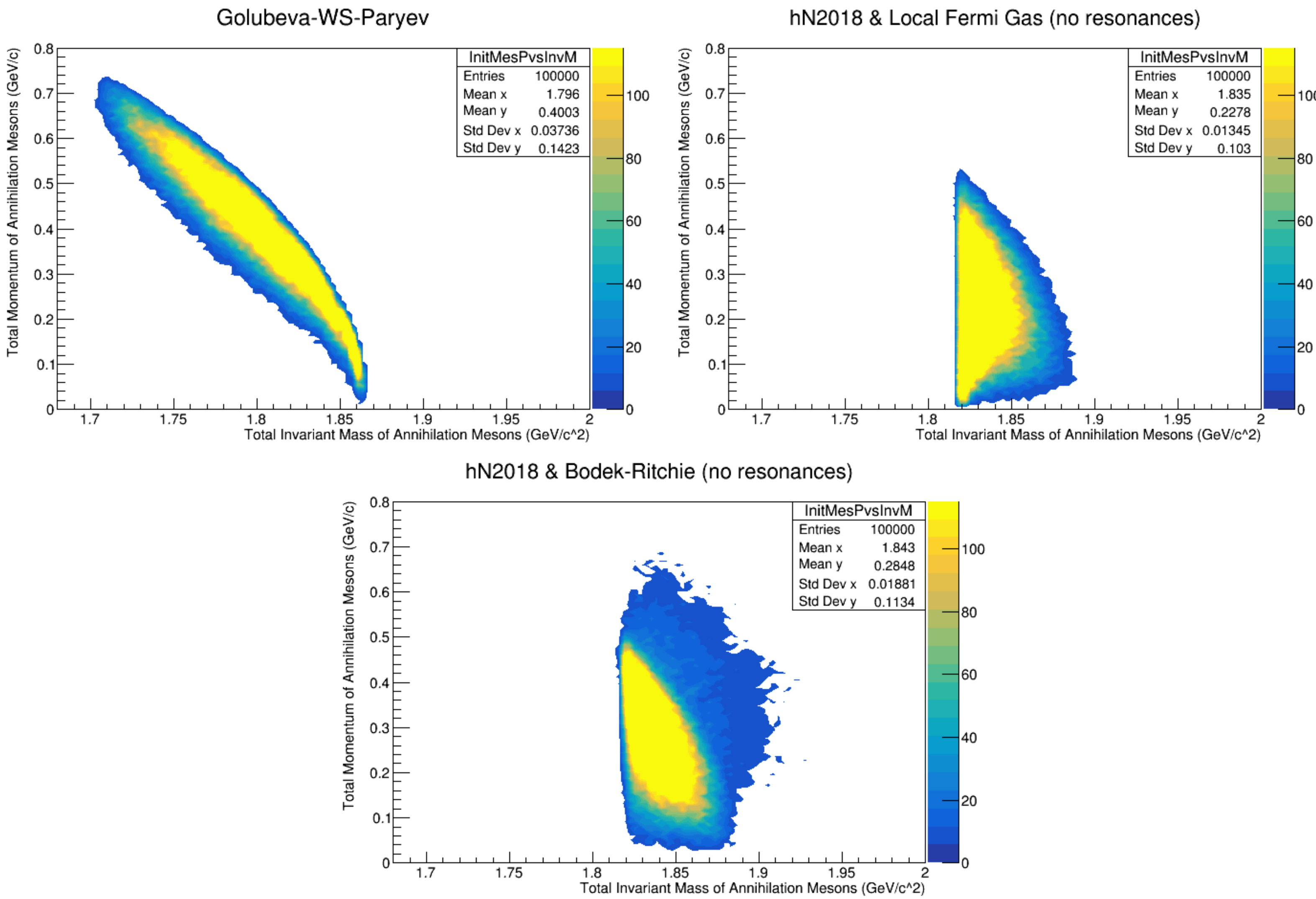

Figure 2.28: The initial mesonic parameter space (total momentum versus invariant mass) is compared for multiple generators; top, this work; bottom, GENIEv3.0.6. The "no resonances" phrase refers to a GENIE Mother particle status code cut which removes virtual contributions to invariant mass.

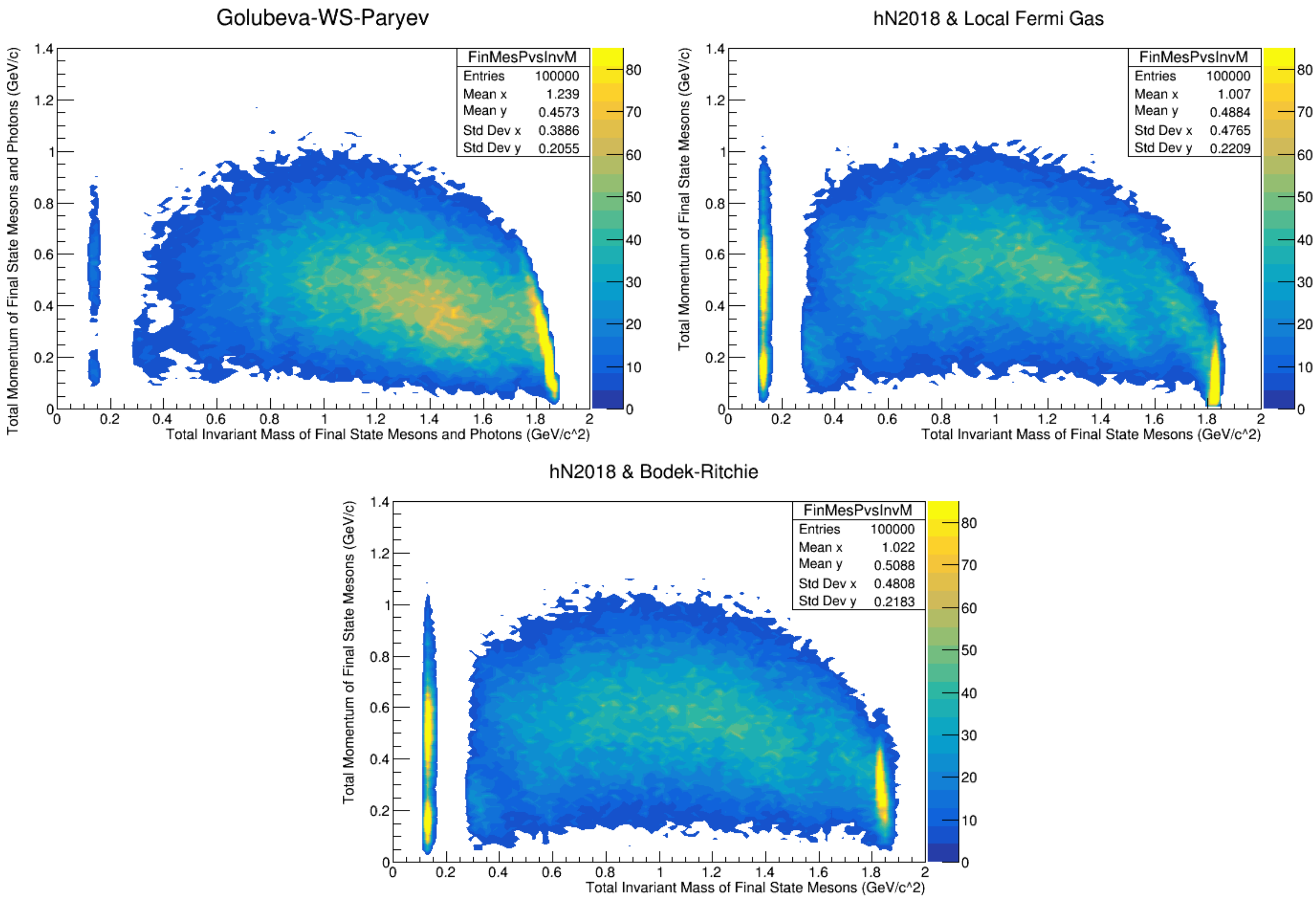

Figure 2.29: The final state mesonic/pionic parameter space (total momentum versus invariant mass) after intranuclear transport is compared for multiple generators; top, this work; middle and bottom, GENIEv3.0.6 local Fermi gas and nonlocal Bodek-Ritchie, respectivley. Differences in these may lead to different detector signal efficiencies.

Table 2.5: Final state average stable particle multiplicities for several 10,000 event samples across multiple $\bar{n}Ar$ annihilation MCs. Also included is the initial total annihilation energy. See [229] for a full description of the zoned local Fermi gas and the intranuclear cascade used in this work. See the `GENIE` v3.0 manual [39] for discussions of nuclear models and intranuclear cascades.

Model Description	$M(\pi)$	$M(\pi^+)$	$M(\pi^-)$	$M(\pi^0)$	$M(p)$	$M(n)$	E_o^{tot} (MeV)
$\bar{n}^{39}_{18}$Ar Golubeva-Richard-Paryev (*Zoned* Local Fermi Gas, INC)	3.813	1.239	1.008	1.566	3.459	4.823	1.846
$\bar{n}^{39}_{18}$Ar Golubeva-Woods-Saxon-Paryev (*Zoned* Local Fermi Gas, INC)	3.781	1.22	0.998	1.563	3.63	4.896	1.845
$\bar{n}^{39}_{18}$Ar `GENIE`v3.0.6 (*Default* Bodek-Ritchie, hA2018)	3.610	1.183	0.991	1.436	3.021	3.151	1.925
$\bar{n}^{39}_{18}$Ar `GENIE`v3.0.6 (*Default* Bodek-Ritchie, hN2018)	3.280	1.159	0.968	1.153	6.192	6.654	1.922
$\bar{n}^{39}_{18}$Ar `GENIE`v3.0.6 (Local Fermi Gas, hA2018)	3.594	1.173	0.9776	1.444	3.045	3.174	1.908
$\bar{n}^{39}_{18}$Ar `GENIE`v3.0.6 (Local Fermi Gas, hN2018)	3.24	1.155	0.956	1.129	6.269	6.718	1.905

In Fig. 2.31, one sees the outgoing proton spectra. Here, the independent model described here and GENIE differ greatly (and GENIE even among itself) across lower momenta. Though there is a full intranuclear cascade model within GENIE (hN2018), it can be directly seen that it does not yet include any nucleon evaporation *currently*. In some respect, these differences should be expected due to the novel nature of the phenomena modeled (transporting $\sim$ 4-5 mesons is no easy business), and the fact that the independent generator was comparatively purpose-built to reproduce antinucleon annihilation data. Note, however, that if one takes a more experimental viewpoint, these are not actually so disparate; indeed, if one considers an *approximate, conservative, minimum* proton kinetic energy detectability threshold in liquid ^{40}Ar to be $\gtrsim\ 100\,\mathrm{MeV}$ (i.e., $\gtrsim\ 450\,\mathrm{MeV}/c$) [153], one observes that above this value much of the shape and magnitude of *all* distributions are quite similar. Thus, in some respect, one expects these models to appear rather degenerate for protons when taking detector response into account.

2.8.3 Preliminary Intranuclear $\bar{n}^{15}$O Annihilation Simulations in the Independent Model

Though a publication concerning intranuclear $\bar{n}$O annihilation is still in development and hopes to be useful to Super-and-Hyper-Kamiokande, a few short discussions are worth considering here, and of course are similarly relevant for all other nuclei.

Fig. 2.32 shows the nuclear remnants arising from an annihilation as a function of their size and charge. This greatly informs the validation of the nuclear disintegration[22] model [112, 114, 357, 158, 76, 44, 328, 159] now being introduced for ^{16}O [70] (also see again Sec. 2.6.6); this new nuclear disintegration model will soon become available for other nuclei discussed throughout this chapter. These nuclear remnants can be highly excited, and so can do many things to equilibrate over short times ($\sim 10^{-21}$-10^{-23} s), including evaporating whole nucleons as well as emitting de-excitation photons, as shown in Figs. 2.33. Here, the single photon spectrum alone is shown, and most all nuclear fragments (labeled) within Fig. 2.32 are represented (if only with very low statistics).

[22]For smaller nuclei such as ^{16}O, this is best described as a Fermi break-up process rather than multifragmentation which is works best for medium and larger-sized nuclei. Each are at work within the new model.

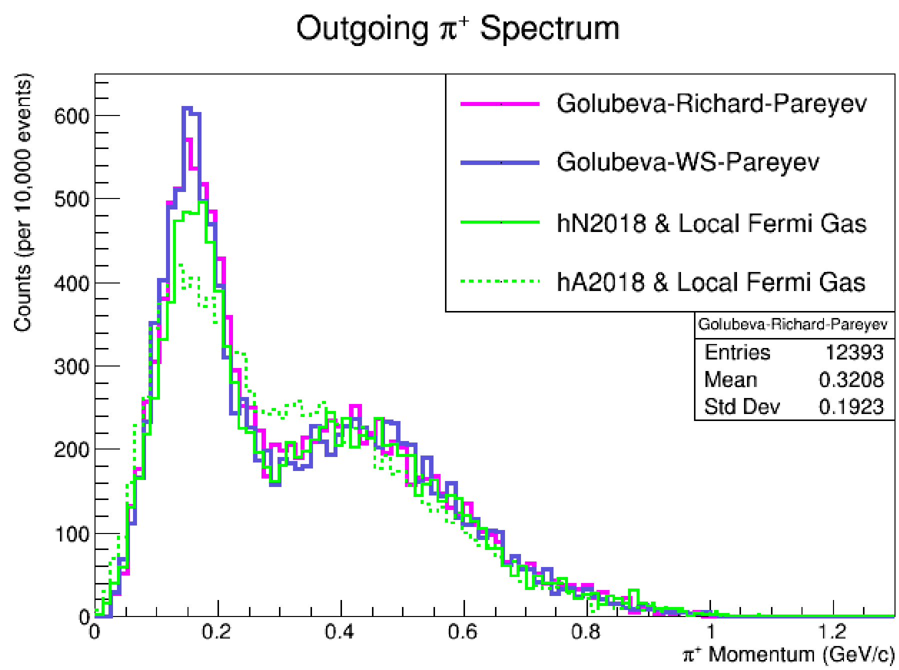

Figure 2.30: The outgoing π^+ momentum spectrum is shown for several local Fermi gas models.

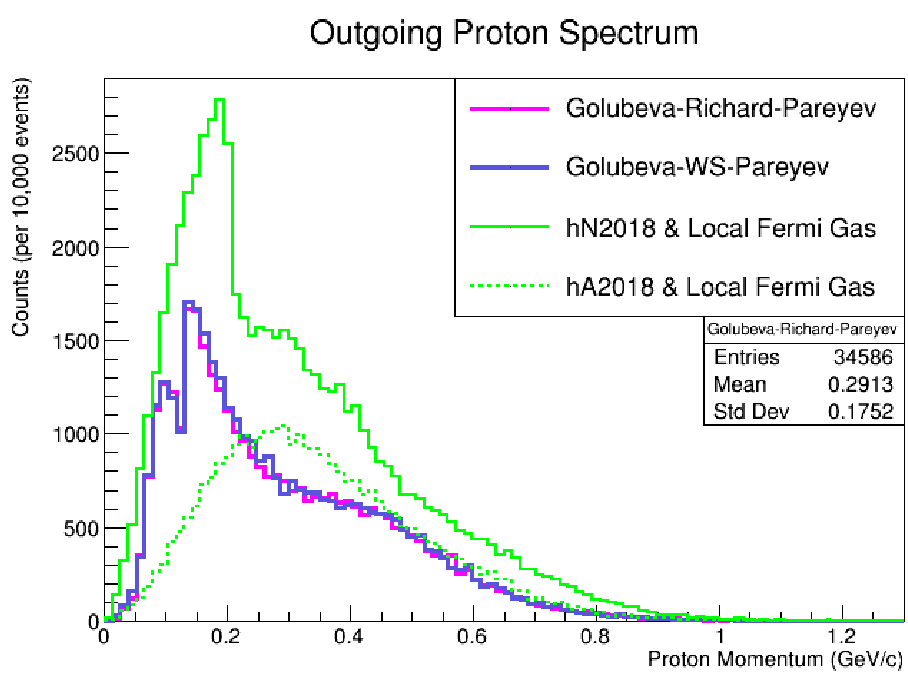

Figure 2.31: The outgoing p momentum spectrum is shown for several local Fermi gas models.

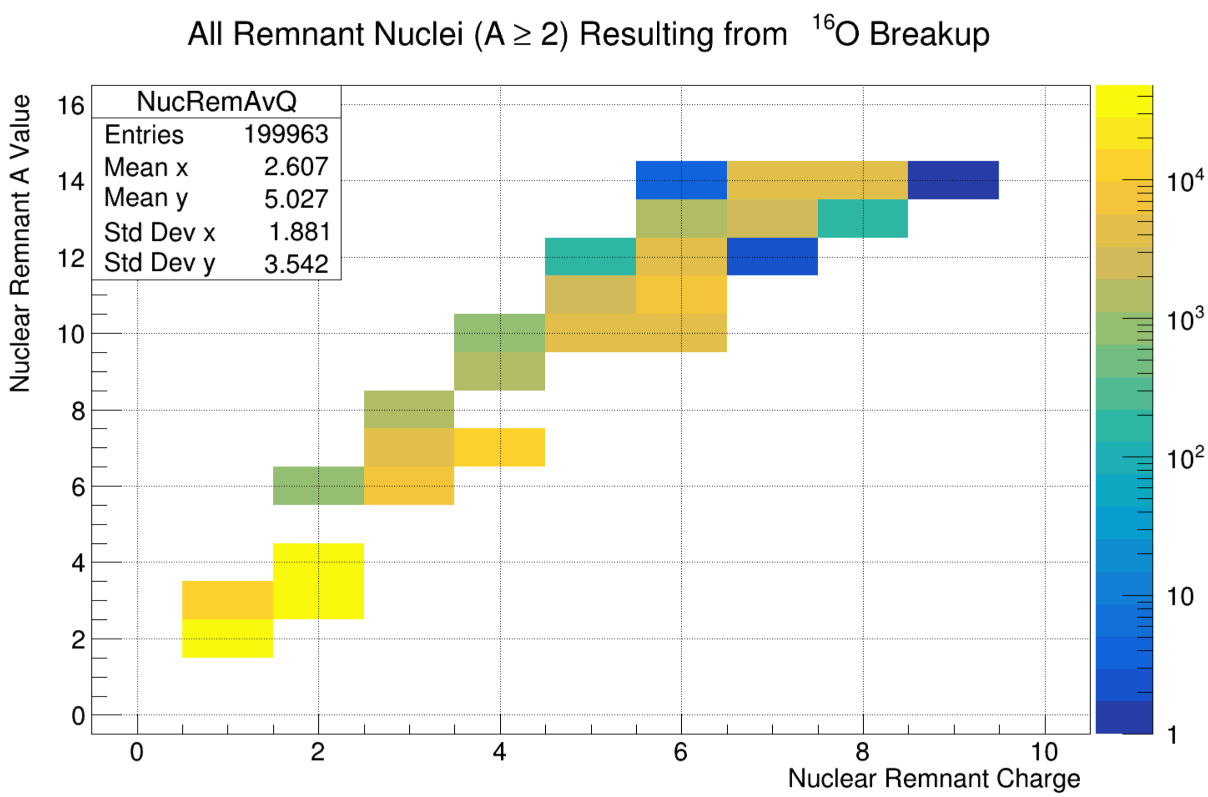

Figure 2.32: A correlation plot showing all intranuclear $n \rightarrow \bar{n}$ derived remnant nuclei with $A \geq 2$ is shown following the breakup of the ^{16}O nucleus. When ignoring evaporative particles with $A < 2$, there are on average two residual nuclei per annihilation event.

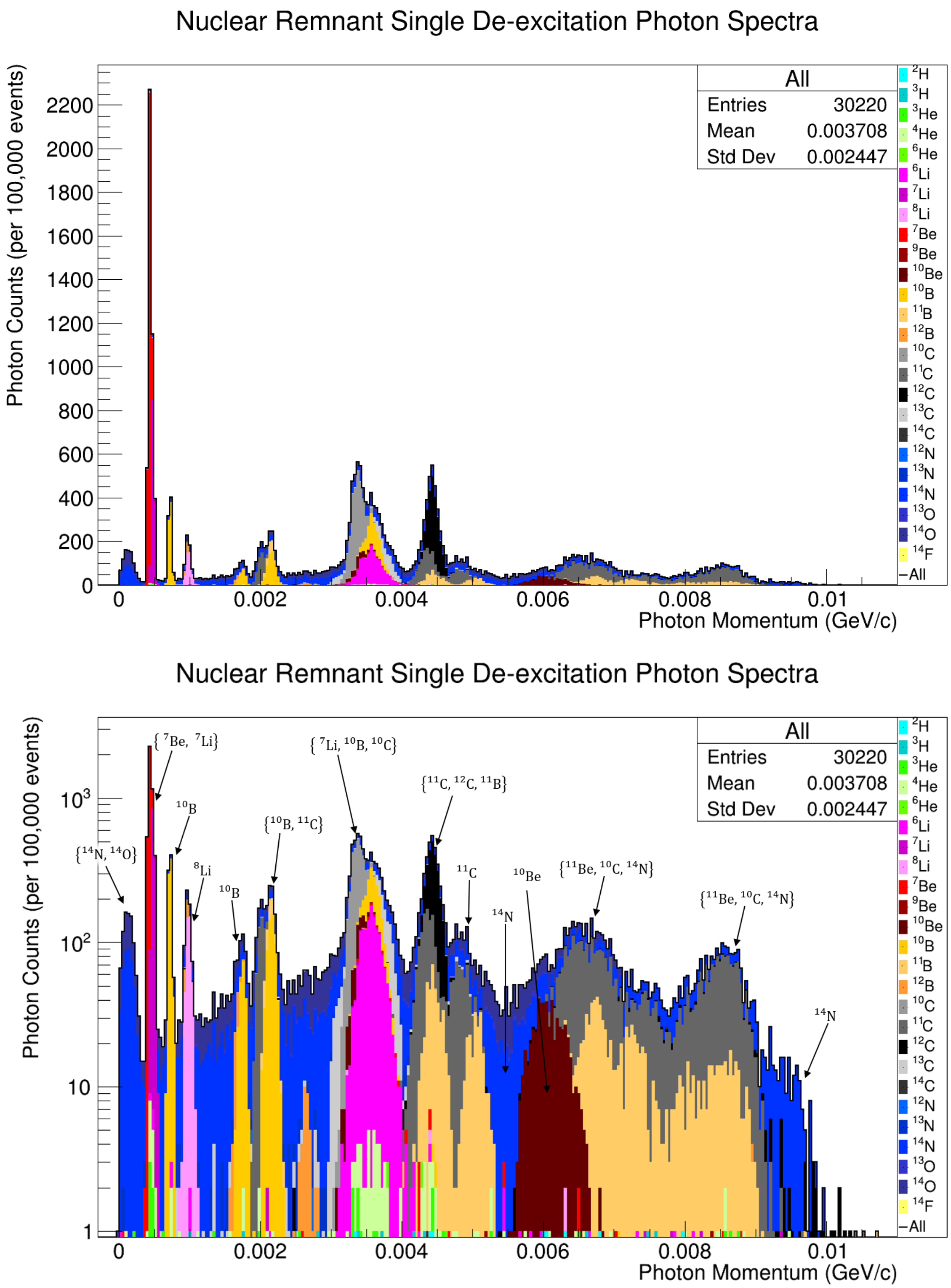

Figure 2.33: The de-excitation single emission photon spectrum of remnant nuclei arising from the nuclear decay and evaporative process following intranuclear $n \to \bar{n}$ in ^{16}O, shown in linear and logarithmic scales (labeled with predominant nuclear isotopes for clarity). There are events where two photons are emitted, though these are produced exceedingly rarely and are not included here for simplicity.

In a similar vein to photons generated from de-excitation (which may allow for timing searches within experiments), another observable to consider for a smaller proportion of signal events is the photon spectrum from the decay of heavy mesonic resonances arising from the the annihilation process, as shown in Fig. 2.34. These high energy photons, in coincidence with low energy photons and many pions in the final state, could be a BSM smoking gun.

Other phenomenology to consider within the simulation includes the locality of the annihilating pair of (anti)nucleons, as shown in Fig. 2.35. The projection of the momentum distribution from the y-axis is broadly consistent with that shown for the initial state of $\bar{n}$C annihilation in Fig. 2.20, as should be expected from the fact that the (anti)nucleon potentials do not vary much from nucleus to nucleus (see again Fig. 2.10). The gradually decreasing value of total momentum as a function of the radial position confirms the local nature of the modeling; the color gradient is due to convolution with the radial annihilation density, as partially shown for one shell in Fig. 2.8.

Of course, all pertinent physical quantities can be seen to be local, including the initial and final state invariant masses of mesons and photons. As shown in Figs. 2.36, the higher the radius, the higher the initial (top) invariant mass of all annihilation-generated mesons; this is due to the smallness of the intranuclear (anti)nucleon potentials at these higher radii. Similarly, this correlation is preserved within the final state (bottom) pions and photons, as fewer final state interactions occur at this higher radii; this can significantly effect the topological characteristics of the final state. Note that in the absence of any local (anti)nucleon potential, the shape of the final state invariant mass vs. radius would be quite hemispherical, rather than shifted.

2.9 Conclusions

In this chapter, I have endeavored to give an update to the community on recent developments in the modeling of $\bar{n}A$ annihilation events in service of future BSM $n \to \bar{n}$ searches, primarily using an independently developed MC simulation. This approach is universal, and can be used for simulating antineutron annihilation on many different nuclei. It is quite important that the radial dependence of the annihilation probability is used within the initial stage of the simulation. A combination of experimental data with the results of a statistical model employing $SU(3)$ symmetry is used to describe the annihilation process. The propagation of annihilation-produced

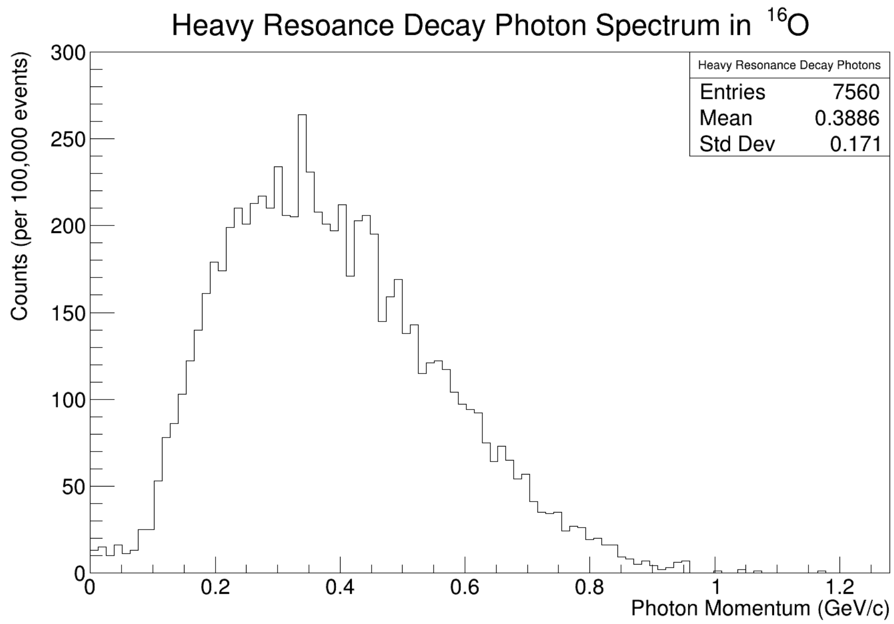

Figure 2.34: Heavy mesonic resonances can arise following an $\bar{n}N$ annihilation within the nucleus, some of which may decay into γs; see [229] for branching fractions. This holds for only around $\lesssim 10\%$ of events.

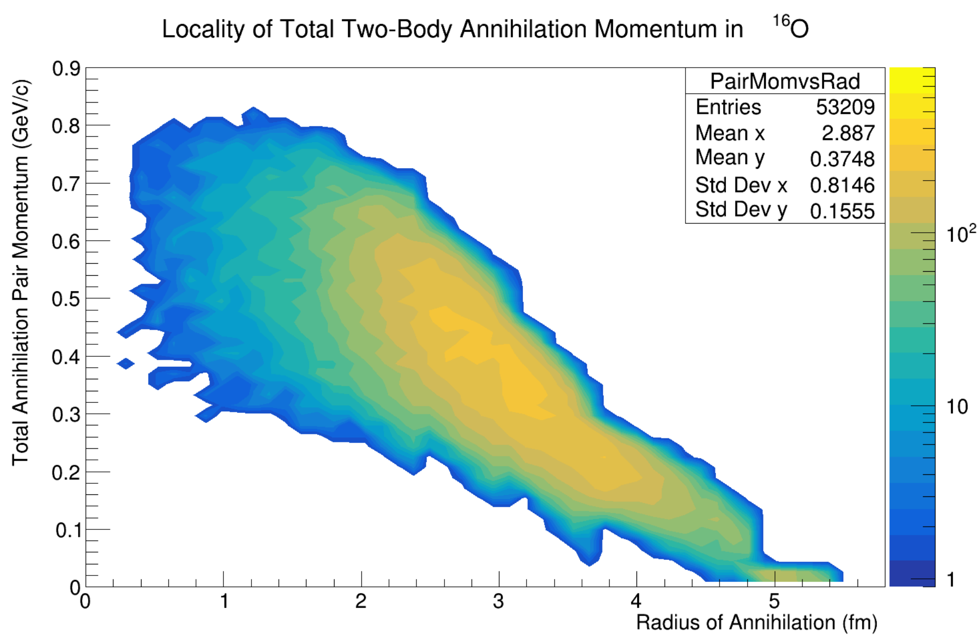

Figure 2.35: The local nature of the annihilation pair ($\bar{n}p$) momentum is shown. Other than counts, the behavior is very similar for $\bar{n}n$ pairs.

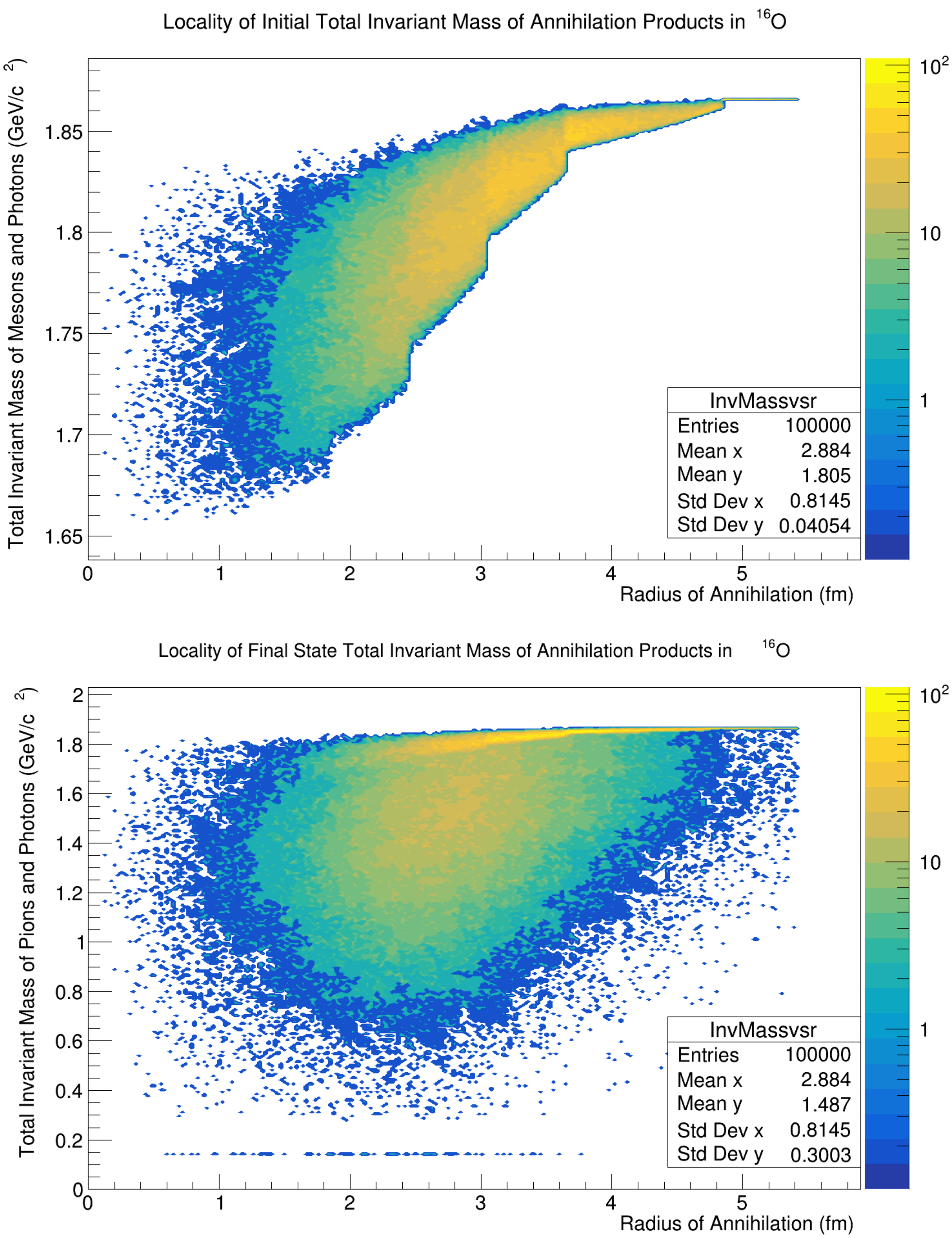

Figure 2.36: Top: The initial state's truth invariant mass of annihilation-generated mesons and photons vs. radius is seen before FSIs, showing the local effects of the (anti)nucleon potential and associated mass defects. The stepping shape seen here derives from the zoned nature of the nuclear density (see again Fig. 2.9). Bottom: The same for the final state's truth invariant mass of all pions and photons following FSIs, showing the importance of taking account of both the (anti)nucleon potential and radial position of the annihilation to avoid excessive final state interactions.

pions and heavier meson resonances within the nucleus is described by the intranuclear cascade model, which takes into account the nonlinear effect of decreasing nuclear density. The process of de-excitation of residual nuclei is described by a combination of the evaporation model and the Fermi model of explosive disintegration.

Critical among the findings of within this chapter is the calculation of a new intranuclear suppression factor for ^{40}Ar, $R^{Ar} \sim 5.6 \times 10^{22}\,\mathrm{s}^{-1}$, along with a new and associated calculation of the ^{40}Ar intranuclear radial annihilation probability distribution [71][23]; similar distributions are being developed now for ^{16}O. Also, efforts have been described throughout this chapter on implementing this and other important $\bar{n}N$ annihilation dynamics into an independently developed, antinucleon-data-driven MC generator to service both the ESS NNBAR collaboration [19] and DUNE [243, 257], as well as Super-and-Hyper-Kamiokande [6] in the future. Comparisons and discussions of differences and similarities have been made to data where available and other publicly available event generators such as `GENIE` [229, 71].

Within this chapter, a kind of forward path has been illuminated for the BSM community, showing the importance of *some* initial physical correlations in the modeling of BSM signals, most importantly that of the event constituent's momenta and intranuclear position. However, the effects of final state interactions cannot be understated. It is with these findings, and the associated event generators for various nuclei described here, that future experiments will be empowered to better understand probable signal topologies for rare decays. Another future step elucidated particularly by Sec. 2.5 is the critical nature of current and future collaborations' endeavors to holistically evaluate and compare various $\bar{n}A$ interactions using common formalisms for the calculation of (anti)nucleon wave functions, radial annihilation probability distributions, and intranuclear suppression factors for all pertinent nuclei. This is a rather monumental task, but one which should be completed in the same way as for other rare decay searches, such as within the $0\nu\beta\beta$ community.

[23] Again, many, many thanks to J-M. Richard for his collaboration on this work.

Chapter 3

Physics Opportunities at the European Spallation Source

3.1 The European Spallation Source

The European Spallation Source[1] (ESS), currently under construction in Lund [325], will be the world's most powerful facility for research using neutrons. It will have a higher useful flux of neutrons than any research reactor, and its neutron beams will have a brightness that is up to two orders of magnitude higher than at any existing neutron source [356]. The project has been driven by the neutron-scattering community, and the construction budget includes 15 instruments covering a wide range of topics in neutron science. ESS will also offer opportunities for fundamental physics with neutrons, for instance, as described in this chapter.

Most existing spallation neutron sources use a linear accelerator to propel protons to high energy, storing them in an accumulator ring before extraction in short pulses to the spallation target. However, ESS will use a linear accelerator without an accumulator ring, and will thus obtain longer neutron pulses, allowing proportionally more neutrons to be produced. For experiments in fundamental physics (such as neutron oscillations) where the total integrated flux is a main component in any given figure of merit, the ESS concept is clearly beneficial. The ESS will have the world's most powerful particle accelerator in terms of MW of beam on target. A proton beam

[1]Thanks to my many ESS NNBAR/HIBEAM colleagues for their collaboration on this work.

will be accelerated to $2\,\mathrm{GeV}$ with a $14\,\mathrm{Hz}$ pulse structure; thus, with each pulse being $2.86\,\mathrm{ms}$ long, this yields a $5\,\mathrm{MW}$ average power.

Neutrons are produced when the accelerated protons hit a rotating tungsten target. The target wheel consists of sectors of tungsten blocks inside a stainless-steel disk. It is cooled by helium gas, and it rotates at approximately $0.4\,\mathrm{Hz}$, such that successive beam pulses hit adjacent sectors, thus allowing adequate heat dissipation and limiting radiation damage. The top sketch of Figs. 3.1 show a cut-out of the target monolith with the tungsten wheel in the center. High-energy spallation neutrons are slowed via an adjacent CN moderator surrounded by a beryllium reflector, eventually exiting the moderator-reflector system to be fed to beam extraction points placed within the monolith wall. The monolith extends to a radius of $5.5\,\mathrm{m}$ and contains $3.5\,\mathrm{m}$ of steel shielding extending from the beamline openings located $2\,\mathrm{m}$ after the moderator's center point.

The neutron radiation dose coming out of the monolith is substantial, and further shielding is needed within the structure, and is referred to as "the bunker", as seen in the bottom sketch of Figs. 3.1. Within the bunker, neutron beams are distributed across two wide angle regions on both sides of the target area. Neutrons from the monolith are fed into neutron guides in the bunker, pass through the bunker wall, and, ultimately, on to ESS instruments. In addition to the shielding, the bunker contains components related to the instruments such as guides, choppers, shutters and collimators [355].

In Fig. 3.2, an overview of the ESS beamlines and instruments is shown. There are 15 instruments currently under construction at ESS, representing only a subset of the full 22-instrument suite. In addition to the 15 instruments, a test beamline will be installed which will serve to characterize the target-reflector-moderator system, verifying the performance of the neutron source at the start of operations. Regarding instruments 16-22, an ESS analysis of the facility's scientific diversity has identified that the addition of a fundamental physics beamline is of the highest priority [1]. The location of the foreseen ESS fundamental physics beamline, HIBEAM/ANNI at beamport E5, is shown. The prospective beamline from the Large Beamport (LBP) leading to NNBAR [204, 271, 326, 19] is also shown, though would extend far beyond the radii of other instruments.

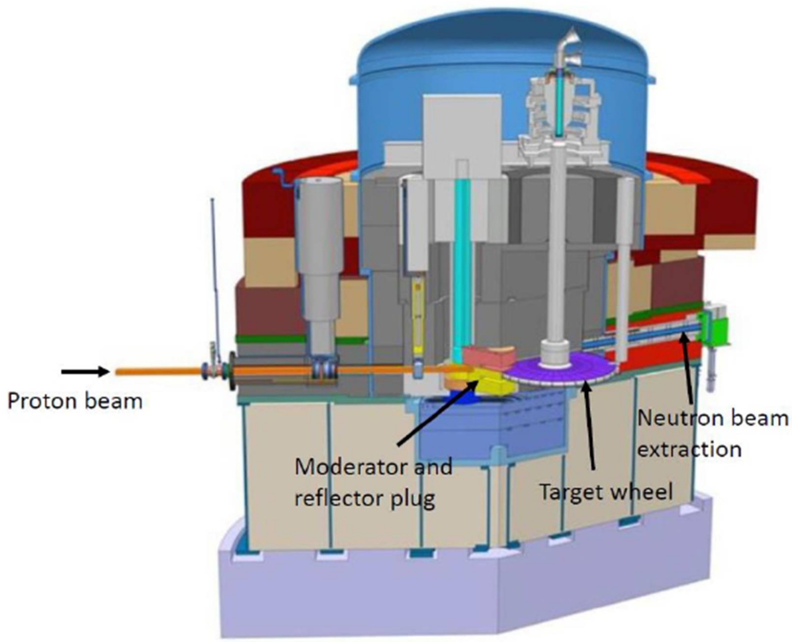

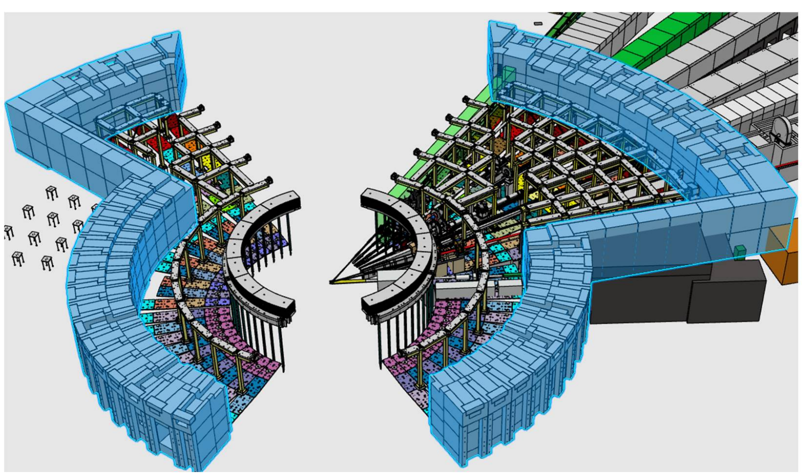

Figure 3.1: Top: Cross section view of the ESS target monolith. Bottom: the ESS target monolith housing and bunker (outlined in blue), viewed from above. Courtesy of V. Santoro and L. Zanini.

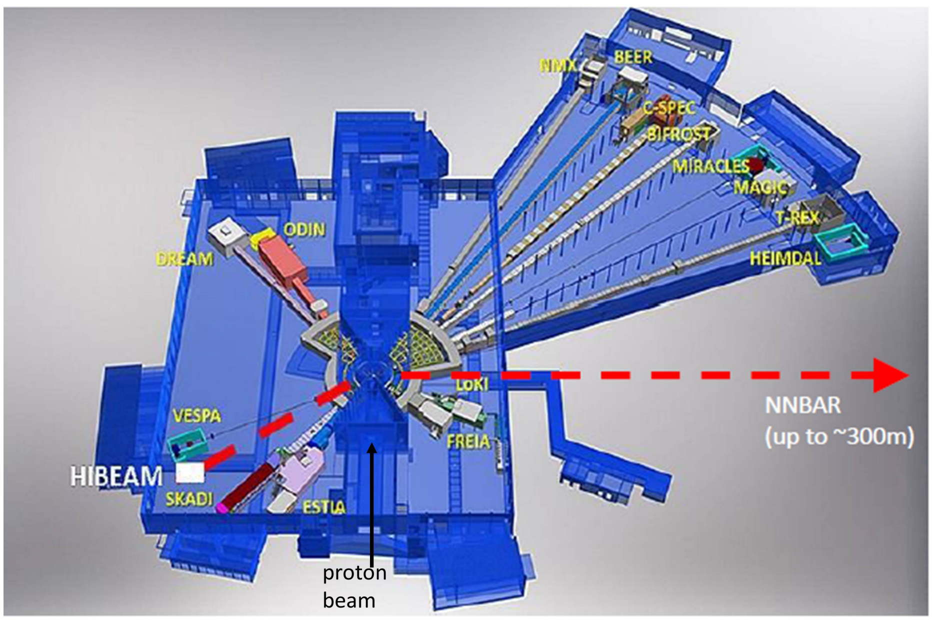

Figure 3.2: Overview of the ESS, beamlines and instruments. The locations for the proposed HIBEAM and NNBAR experiments are also shown. Courtesy of the NNBAR collaboration.

3.2 The HIBEAM Experimental Program at the ANNI Beamline

The search for $n \rightarrow \bar{n}$ with a sensitivity $\sim$ 1000X higher than in the previous ILL-based experiments [56] remains the ultimate goal of the NNBAR collaboration [19]. Due to the commissioning schedule of ESS, the minimum start time for the construction of an $n \rightarrow \bar{n}$ experiment would be no earlier than 2026 and the designed power of $5\,\mathrm{MW}$ obtainable only after 2030. The NNBAR collaboration would exploit the opportunity of low-power beam operation and commissioning times of the ESS over the intervening years to exploit opportunities for dark mirror neutron searches. The first experimental stage, known as HIBEAM, would utilize the ESS beamline developed by ANNI collaboration [379] at early times and low power. The physics of $n \rightarrow n'$ is close to and possibly generically related to the $n \rightarrow \bar{n}$ process, and so several smaller scale and relatively inexpensive experiments can be made in this area. A parallel, further goal of HIBEAM is to complete research and design for a full $n \rightarrow \bar{n}$ search at NNBAR; $n \rightarrow \bar{n}$ searches can also be done at HIBEAM, though sensitivity is expected to be lower than the ILL experiment. Such a pilot experiment will enable detector research and development together with background mitigation techniques necessary for the full NNBAR experiment [204, 271, 326, 19].

3.2.1 ANNI Beamline and Beam Properties

Ample discussion of the properties and usage of the ANNI beamline for fundamental physics searches has been considered in [379]; HIBEAM will extend this list. Fig. 3.3 gives a schematic outline of the proposed ANNI fundamental physics beamline, where neutrons emerging from the moderator pass through a guide system (shown in Fig. 3.4) and then into an experimental area with a length of around $54\,\mathrm{m}$ and a width of around $5\,\mathrm{m}$ (visualized here without other experimental apparatuses throughout the hall). Due to the beam hall size constraints, there would be very limited room to use focusing CN reflectors to increase sensitivity for neutron transformation searches (to be discussed briefly later in Sec. 3.5.2).

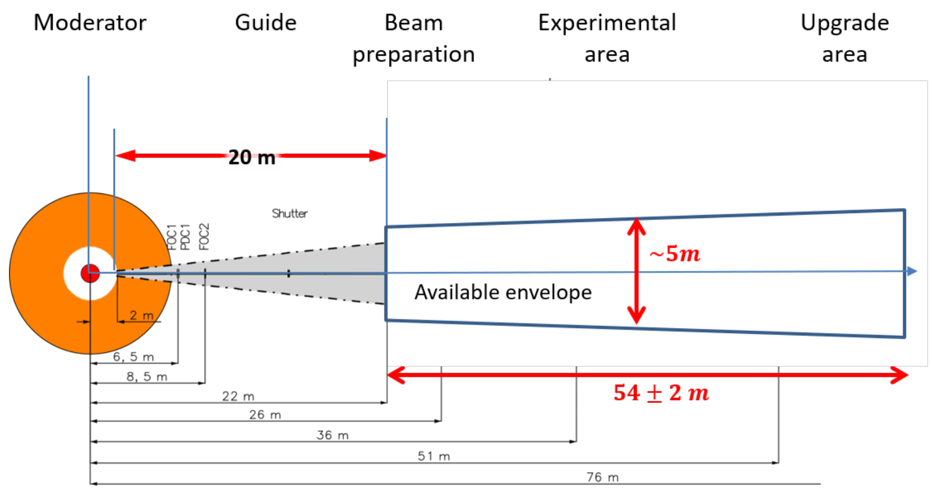

Figure 3.3: A schematic overview of the ANNI fundamental physics beamline floor plan which would be used in HIBEAM. The figure is adapted from [379]. Courtesy of the NNBAR collaboration.

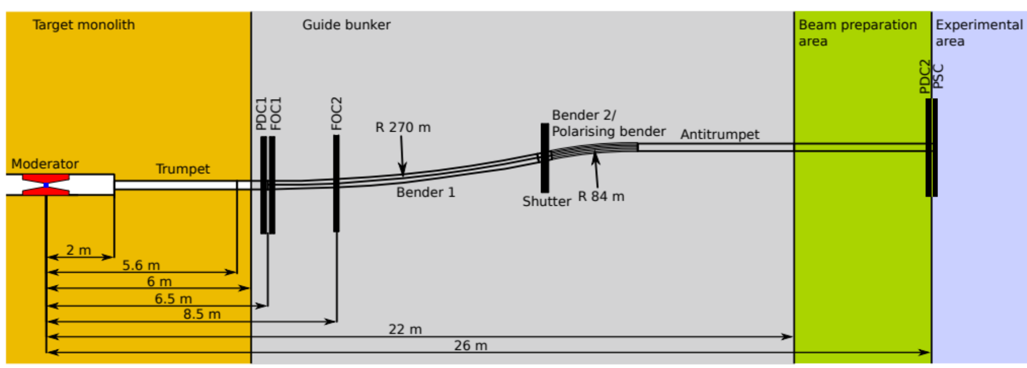

Figure 3.4: A basic schematic overview of the optimized vertically-curved S-shaped neutron guide system used in the ANNI design, preventing direct sight of the cold moderator, and so reducing backgrounds. Taken from [379].

Simulations using the ESS moderator design in McStas2.4 [309] have been performed by the ANNI collaboration, fully modeling the S-shaped curved neutron guide in a background-reduced, cold-spectrum selected, beam-shape-optimized way [379]. McStas outputs a file with coordinates, momenta (velocities), and weights (the full phase space) of the neutron trajectories, normalized to an initial spallation proton beam energy of $2\,\text{GeV}$ incident upon the ESS tungsten target before being transported through the ANNI beam optics to the collimator exit at $z = 22\,\text{m}$. A full $1\,\text{s}$ of simulated operation time is available for analysis. Fig. 3.5 shows the initial spectrum of neutron velocities from this simulation at the end of the S-shaped curved guide before flying through ANNI beamline; the average velocity is ~ 1000m/s.

As seen in Figs. 3.6, initial beam characterizations with gravity show a large swath of slow neutrons over a beam length of $\sim\, 50\,\text{m}$, having larger divergence at lower velocities[2]. Most neutrons do not fall outside a $1.5\,\text{m}$ radius ($\theta \lesssim 1.7°$), though even this would constitute an enormous and financially untenable detector size. Thus, without reflectors, there is a sacrifice of a large fraction of the valuable slowest neutrons within this baseline design by choosing a detector with a practical radius of 0.25-$0.50\,\text{m}$. Assuming a low initial operating power of $1\,\text{MW}$, simulations show an absolute beam normalization of $1.5 \times 10^{11}\, n$/s (at the beamport exit). For a conservatively designed $1\,\text{m}$ *diameter* detector downstream of the $50\,\text{m}$ propagation length, this flux becomes $6.4 \times 10^{10}\, n$/s. This is without the installation of any further beam optimization components upstream or neutron optics downstream, no lowering of the detector due to gravitational drop, reconfiguration of the beampipe shape, and effectively assuming a perfect detector efficiency.

Fig. 3.7 shows a top-view of the neutron tracks estimated by Phits for the ANNI neutron beam impinging upon a thin ^{12}C annihilation target (foil). Most of the neutrons pass directly through the target; a few are scattered by it, and a smaller fraction are absorbed (given its relatively lower cross section), a process which induces the emission of MeV-scale photons. The origin of the coordinate system is in the experimental area, after ANNI's curved guide extraction, i.e., it is located in the so-called "available envelope" shown in Fig. 3.3. Similarly, Fig. 3.8 shows a cross-sectional view of the ANNI beam at the annihilation target. The observed neutron interference

[2] Proprietary gravitational and stochastic gravitational reflector transport calculations mentioned throughout this thesis were developed independently in C++, and do not rely on McStas or other software frameworks unless otherwise mentioned.

pattern is caused by the different bounce distances the ANNI neutrons take when being transported through the S-shaped curved guide. Of course, these represent all neutrons, and so a circular geometric cut of, say, $r = 0.5\,\mathrm{m}$ can be made. These capabilities as a function of the geometry of the detector can be further contextualized when the full final flux is considered as a function of a detector radius, as seen in Fig. 3.9. This hints at the need for greater beam control via neutron reflectors; however, space constraints will limit this prospect.

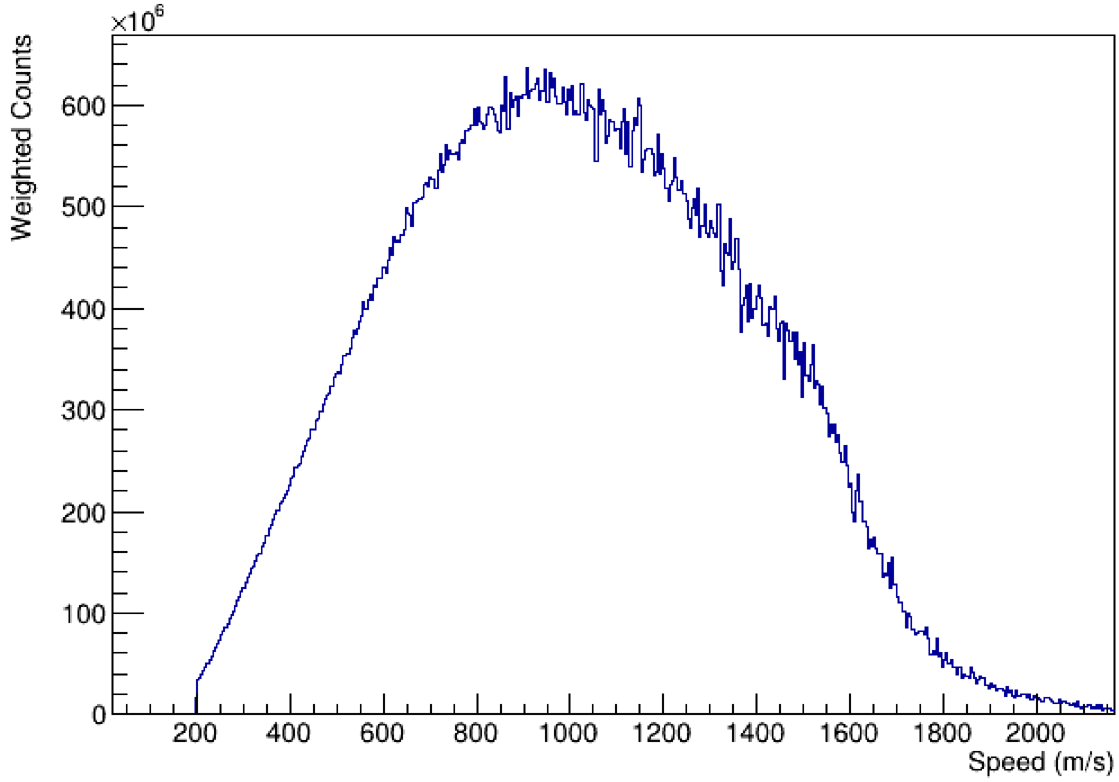

Figure 3.5: The *incident* beam velocity spectrum coming from the ANNI/HIBEAM beamport. The results use a simulation event file provided by the authors of [379].

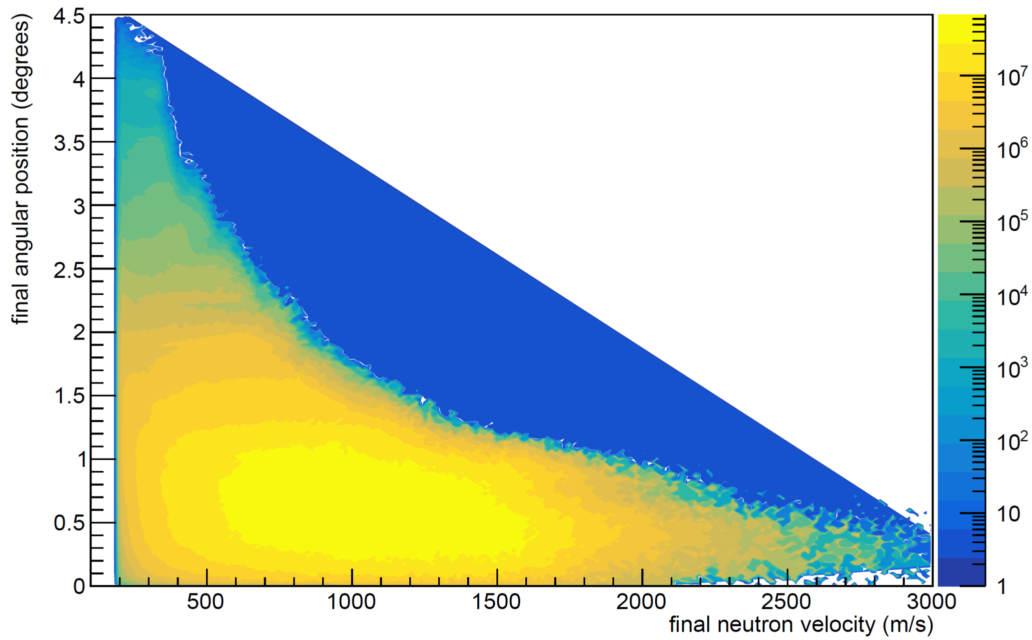

Figure 3.6: The ANNI beam divergence as a function of velocity at a distance of $50\,\mathrm{m}$ from the beamport is shown; gravity is taken into account, and the *entire flux* (irrespective of any virtual detector's effectively $\sim\infty$ size) is considered. The results use a simulation event file provided by the authors of [379].

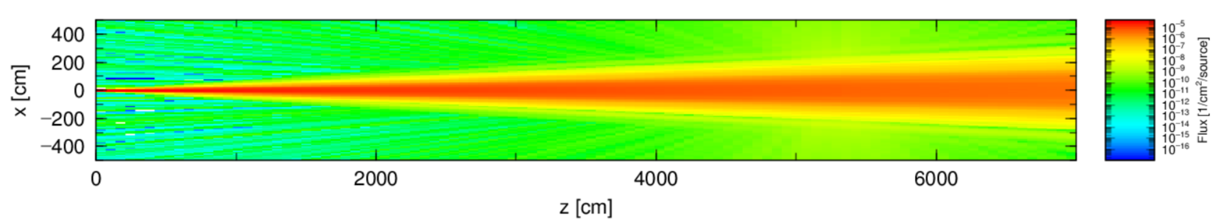

Figure 3.7: A top view of the the ANNI neutron beam tracks obtained by `Phits`. The origin of the coordinate system is in the experimental area, after ANNI's curved guide extraction. Gravitational effects are *not* taken into account in this plot, but do little to effect this top view. The results use a simulation event file provided by the authors of [379]. Courtesy of B. Meirose.

3.3 Searches for Mirror Neutron Mixing at HIBEAM

The envisaged HIBEAM physics program is based on the previously discussed theoretical possibilities for neutron oscillations, primarily $n \to n'$, and will include, but will not be limited to several experiments, each able to be performed over relatively short times at the ANNI/HIBEAM beamline. By employing complementary configurations for $n \to n'$ style searches, a characterization of the mixing between the ordinary and sterile mirror sector can be made in the event of a discovery. Recall also that one may consider $n \to \bar{n}$ via a $n \to \{n', \bar{n}'\} \to \bar{n}$ in a regeneration-style experiment, and so provides a well-motivated opportunity to refine the technical approach to the high efficiency detection of antineutron annihilation events with small backgrounds. Taken together, the range of experiments envisaged enables many discoveries with a single experimental set-up, though each with a different experimental configuration.

3.3.1 Search for $n \to n'$ via Disappearance

This discussion considers $n \to \{n', \bar{n}'\}$, and is sensitive to a scenario in which at least one of the mass mixing parameters ϵ and $\beta_{n\bar{n}'}$ (see Eq. 1.47) is non-zero. The search assumes the presence of an unknown sterile magnetic field, $\vec{B}'$, which would be compensated for, at least in magnitude, by a laboratory-generated magnetic field, $\vec{B}$.

A schematic overview of the experiment is shown in the Figs. 3.10, highlighting some details of all relevant parts of the apparatus together with a simpler schematic picture illustrating the basic principles of the search. Neutrons propagate along an aluminum vacuum tube with a length $\sim 50\,$m, and the neutron rates at the start and the end of the propagation zone are monitored. The symbol M represents a current-integrating beam monitor with an efficiency of $\sim$ 20–30%; the symbol C represents a current-integrating beam absorption counter with an efficiency of $\sim 100\%$. The assumed beam intensity used here and for subsequent HIBEAM projections is 6.4×10^{10} n/s at the end of the beamline. Measurements of any change in the neutron flux will be made for a range of laboratory magnetic field values across various directions for a range of $(-0.5, +0.5)$ G with a step of a few mG[3], a few times less than the expected resonance width [96]. Thus, the counting

[3]This speaks of the ultimate experimental plan. Sensitivity calculations completed as a part of this thesis consider a range of $(-0.2, +0.2)$ G,

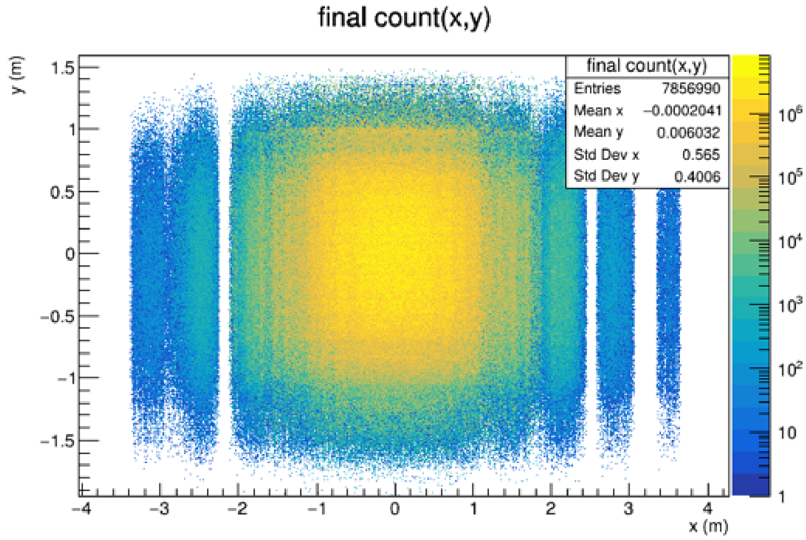

Figure 3.8: A cross section view of the target region showing the ANNI neutron beam trajectories [379] obtained after gravitational transport over $\sim$ 50 m of vacuum. The observed interference-like pattern is due to bounce-to-detector distances along ANNI's S-shaped curved guide.

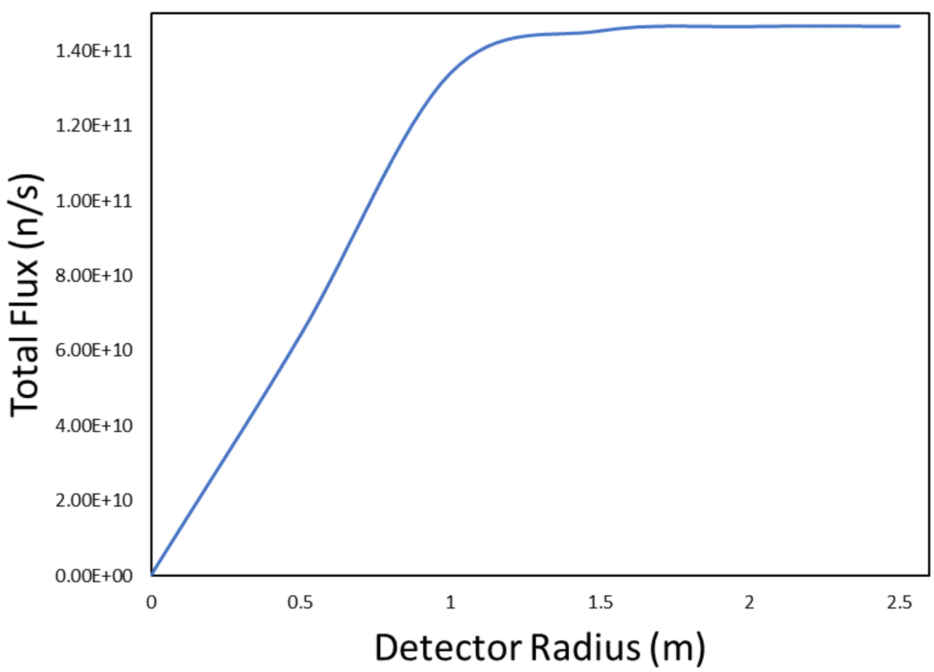

Figure 3.9: The smoothed total unreflected flux per 1 MW of spallation power for the ANNI beamline is shown as a function of final detector radius assuming $\sim$ 50 m of flight.

rate (determined by charge integration) within the counter C in Figs. 3.10 will be controlled by the magnitude of magnetic field. The charge integrating counter M will monitor variations of the beam intensity independent of variations of magnetic field.

The detection of a resonance would appear as a reduction of the overall counting rate in the C/M ratio as a function of $\vec{B}$ (and so too $|\vec{B} - \vec{B}'|$). From this measurement, a limit on the mass mixing parameter ϵ can be extracted, and so too the $n \to n'$ oscillation time, $\tau_{nn'}$. A positive signal would indicate not only the existence of the sterile state n', but also the existence of sterile photons γ', required for the transformation to occur at non-zero $\vec{B}'$ (see again Feynman diagrams in Figs. 1.20). With more detailed scans, the three-dimensional direction and potential time-variation of the mirror magnetic field $\vec{B}'$ can be established. As shown in [96, 120], the disappearance method is the most statistically sensitive approach for setting a limit on ϵ.

Measurements of $n \to n'$ disappearance with a CN beam will require full magnetic control in the flight volume of the vacuum tube shown in Figs. 3.10. The three-dimensional magnetic field should be uniform and be preset to the desired vectorial value[4] in any direction with accuracy better than $2\,\mathrm{mG}$ over a range of field magnitudes from $(0, \sim 500)\,\mathrm{mG}$, presenting a technical challenge for the experiment. Another challenge will be the construction of the charge-integrating counters which can achieve a measured charge proportional to the neutron flux with high accuracy, typically 10^{-7}. It has been recently shown [378] that such stability and accuracy can be achieved with a ^{3}He detector in charge-integration mode. Measurements for positive and negative $|\vec{B}|$-field magnitudes would allow the determination of $\tau_{nn'}$ independently of the value of the unknown angle β between the vectors $\vec{B}$ and $\vec{B}'$, as well as an estimate of the angle β itself.

[4]This should be done using four non-Cartesian, trigonal pyramidal axes to most efficiently search the potential $\vec{B}'$ configurations via component projections of $\vec{B}$.

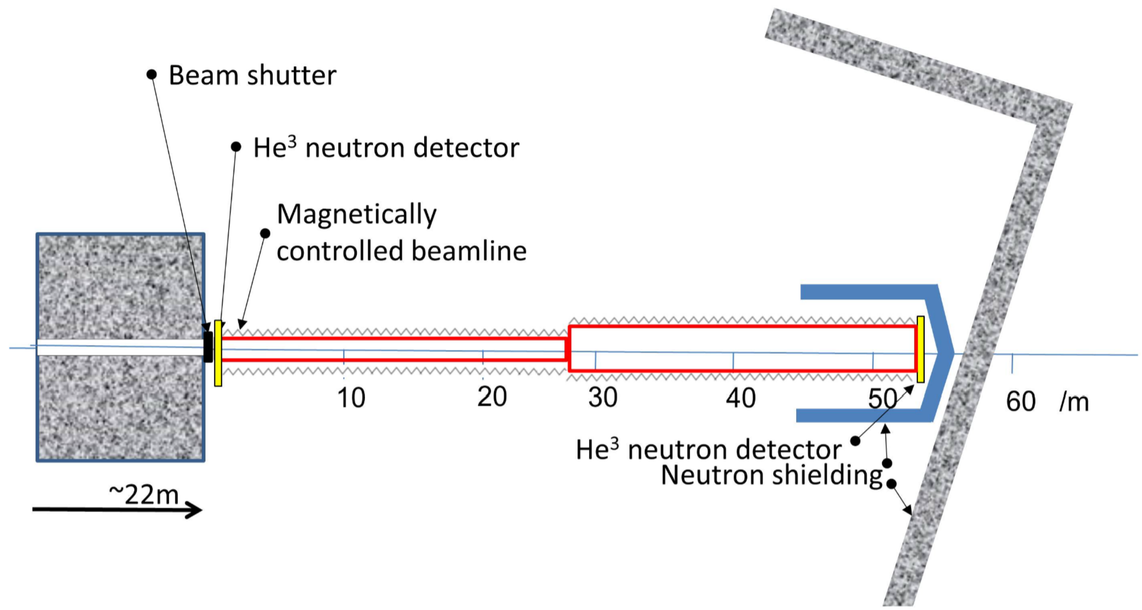

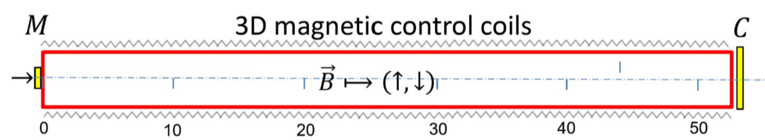

Figure 3.10: Schematic overviews of a $n \to n'$ disappearance-style search at HIBEAM/ANNI. Top: diagram showing apparatus components; fluxes at the beam shutter position are expected to be $\sim 1.5 \times 10^{11}$ n/s, and $\sim 6.4 \times 10^{10}$ n/s at the detector downstream. Bottom: A simplified schematic illustrating the basic principles of the $n \to n'$ search. The symbol M represents a current-integrating beam monitor with an efficiency of ~ 20–30%. The symbol C represents a current-integrating beam absorption counter with an efficiency of $\sim$100 %. A magnetic field is applied in the same direction in the two tubes (shown by the up and down arrows within the parentheses). Top courtesy of M. Frost, Y. Kamyshkov, and D. Milstead.

The sensitivity of $n \to n'$ searches depends on the properties of the CN beam and apparatus, and can be rather complex given the regenerative nature of the oscillation under certain magnetic field conditions, neutron monitor efficiencies, and environmental background rates. The sensitivity for a low magnetic field disappearance search in the absence of a visible resonance signal was best (if briefly) discussed in [96], but are reiterated here. For disappearance, the main dependencies concern the bare and square-normalized integrals of the neutron velocity spectrum, $S(v)$:

$$J_0 = \int S(v)dv, \quad \& \quad J_2 = \int \frac{S(v)}{v^2}dv\,, \tag{3.1}$$

which are then used to calculate the lower limit for the $n \to n'$ oscillation time, $\tau_{nn'}$:

$$\tau_{nn'} \geq \left(\frac{J_2\sqrt{J_0 T\varepsilon}}{J_0} \cdot \frac{L^2}{2} \cdot \frac{1 - 1.7\varepsilon + 0.76\varepsilon^2}{g\sqrt{1-\varepsilon}} \cdot \frac{\sqrt{2K}}{\sqrt{2+K}} \right)^{\frac{1}{2}}, \tag{3.2}$$

where T is the accumulated time in seconds for each individual magnetic field measurement point, ε is the neutron monitor efficiency (taken to be 30%), L is the length of magnetically controlled flight path, the g-factor parametrizes the confidence level (for instance, $g_{95\%} = 3.283$) obtained from statistical simulations, and K is the number of "zero-effect" measurements (at a magnetic field $|\vec{B}| = 0$). This calculation is based on the single maximum deviation of one of the $+|\vec{B}|$ and $-|\vec{B}$ measurements, which are then folded together to attain mean values of 200 individual measurements of C/M. With appropriate calculation of J_0 and J_2 (Eqs. 3.1), Eq. 3.2 can be used for scaling different measurements and configurations at the same beamline. However, better limits can be obtained with more detailed analyses based on line shape fits to experimental magnetic field scan data (see again the right plots of Figs. 1.22, and [96]).

The structure of Eq. 3.2 is mainly analytical in origin, though its dependence upon factors such as g was ascertained by thousands of independent Monte Carlo experiments. To obtain a signal sensitivity to a 95% C.L. with 200 separate magnetic field point measurements and an additional 25 background "zero-effect" runs with equidistributed run folding over a finite magnetic field range (say $(-200, 200)$ mG), a 30% neutron monitor efficiency, and two $25\,$m magnetically controlled sections of beamline, the lower limit on $\tau_{nn'}$ via disappearance can be calculated for various detector radii over different periods of running without any exploitation of the pulsed beam time-structure. One ESS operating year is considered to be approximately 200 days when discounting for routine maintenance and seasonal shutdowns. The sensitivity of the disappearance method as a function of detector radius for $\tau_{nn'}$ is shown in Fig. 3.11 together with sensitivities for regeneration modes (to be discussed in Secs. 3.3.2 and 3.3.3).

3.3.2 Search for $n \to n' \to n$ via Regeneration

The regeneration search derives from a similar theoretical basis as the disappearance search [96, 120] but corresponds to a two-stage process with a correspondingly quadratically suppressed probability. In the first stage, $n \to n'$ takes place in an intense CN beam under quasifree conditions corresponding to $|\vec{B} - \vec{B}'| \sim 0$. The neutron beam is then blocked by a high suppression beam absorber; however, the sterile mirror neutron will continue unabated through the absorber. In a second experimental volume behind the absorber (stage two), under the same condition of $|\vec{B}-\vec{B}'| \sim 0$, an $n' \to n$ process can then produce detectable neutrons with a conserved momentum as if the totally-absorbing wall were not present. The resonance-behaviour depends primarily on the magnitude of the laboratory $\vec{B}$; if the vectors of $\vec{B}$ and $\vec{B}'$ are not well aligned, i.e. the angle $\beta \neq 0$, the oscillation can still occur with somewhat reduced amplitude [82]. This feature provides a robust systematic check for the experiment: oscillations can be turned off simply by changing the magnitude of $\vec{B}$ throughout the volume before and/or after absorber. Taking measurements at the positive and negative magnitudes of the field $\vec{B}$ in both volumes (four combinations) thus allows for a determination of the oscillation time independent of the angle β[5].

A schematic overview of the principles behind the generalized regeneration experiment are shown in Fig. 3.12. Maintaining a lowest possible neutron background count rate in the detector R will be important for a high sensitivity regeneration search across many $\vec{B}$-scans, and sufficiently shielding the detector (with a possible veto system) represents an important challenge for this measurement; currently, a (conservative) background of $1\,n$/s is assumed for regeneration sensitivities projected in Fig. 3.11. In order to absorb the full ordinary neutron beam and keep backgrounds low, a highly-absorbing beam stop S must be constructed, potentially made out of boron carbide, boron nitride, or cadmium, each only requiring a depth of several mm; these

[5]This permits searches of $n \to \bar{n}' \to n$ as well.

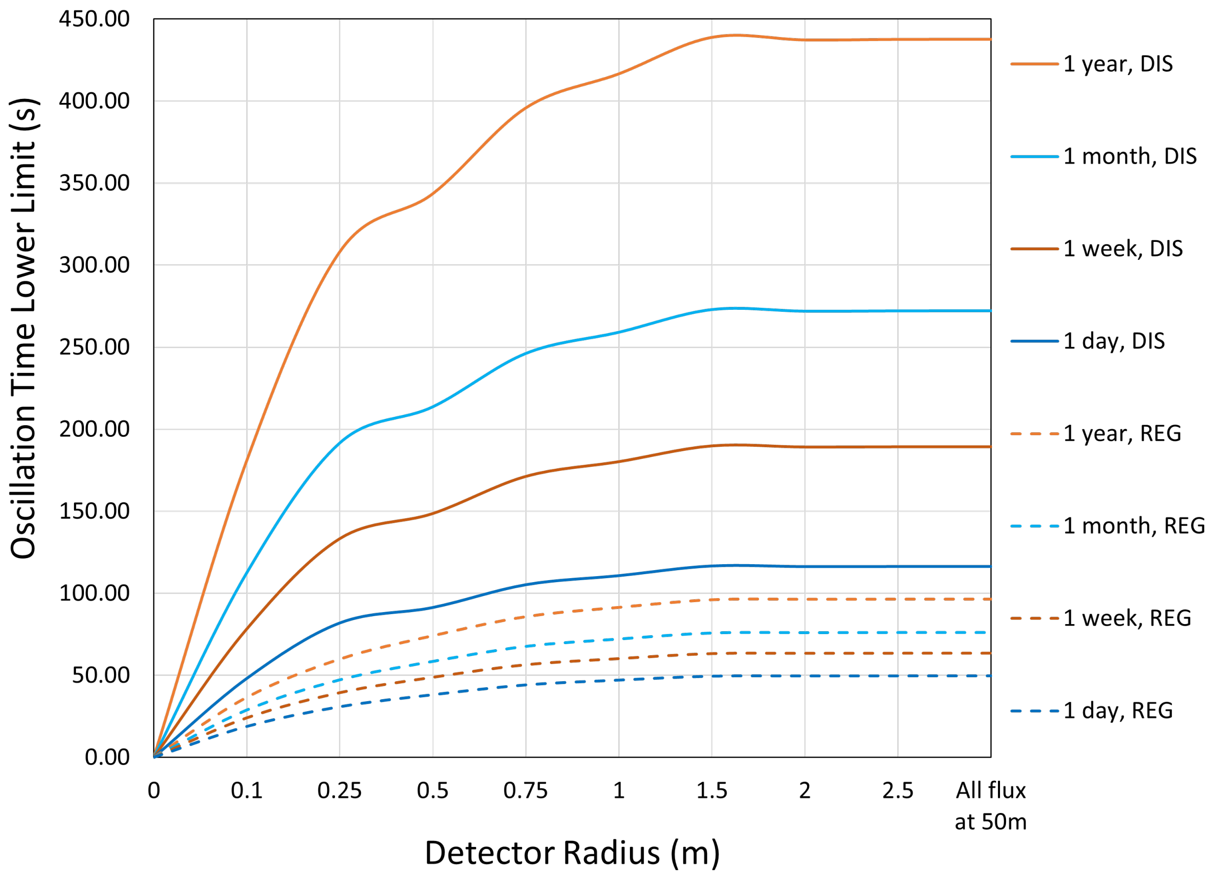

Figure 3.11: Sensitivity at 95% C.L. for the discovery of $\tau_{nn'}$ via disappearance ("DIS") and $\tau_{nn'}$ via regeneration ("REG") for various detector radii for the nominal 1MW HIBEAM/ANNI flux at $\sim 50\,$m. A background rate of $1\,n$/s is assumed for the regeneration search. Plots have been smoothed. Discussions of a regeneration search are contained in Sec. 3.3.2.

can each achieve transmission coefficients of $< 10^{-12}$, which should be sufficient to stop all neutrons within the beam assuming a 1 MW operating power[6]. The observation of the resonance during a $\vec{B}$-scan would be defined by a sudden appearance of regenerated neutrons when the $\vec{B} - \vec{B}' = 0$ condition in both volumes is met. Like with disappearance, a positive signal would be a demonstration of the $n' \to n$ transformation as well as the existence of the dark n' and γ'. The requirement of matching field conditions in both volumes for a regeneration experiment ensures this type of measurement is significantly more robust to any systematic uncertainties of disappearance, which could cause a false signal to be observed, and provides an unambiguous test of the Mirror Matter hypothesis.

For the regeneration experiments, in the absence of an observed signal above a known background level, a lower limit on the oscillation time $\tau_{nn'}$ can be established from a statistical analysis. This limit was parameterized in [96] through the quartic-normalized integral of the velocity spectrum

$$J_4 = \int \frac{S(v)}{v^4} dv \,, \tag{3.3}$$

providing the following estimate for the oscillation time:

$$\tau_{nn'} > \left(\sqrt{4T} \cdot \frac{L^4}{4g\sqrt{\bar{n}_b}} \cdot J_4 \right)^{\frac{1}{4}} , \tag{3.4}$$

where $\bar{n}_b$ is the average background rate in the detector R (see again Fig. 3.12) in n/s. This calculation is again based on the single maximum deviation of one folded magnetic scan over 200 measurements, and T is time for one individual measurement at a particular field vector value. Running over possible values of this background rate for a given detector size, the behavior of the oscillation lower limit can be constructed as shown in Fig. 3.13. From Eq. 3.4, it can be seen that the symmetric length L of each of the two vacuum tubes in the regeneration scheme is the only parameter that can essentially increase the limit for $\tau_{nn'}$. Given its second order nature, the regeneration experiment's oscillation time sensitivity is lower for the same running time compared to a disappearance configuration (see again Fig. 3.11). However, both processes are complementary across different experimental configurations, with neither sharing the exact same

[6]It is critically important to assess whether such a beam stop could lead to other backgrounds, such as photon emission via nuclear absorption. Also, there are theories [86] which can lead to further oscillations within the beam absorber materials. Thanks to Y. Kamyshkov, J. Ternullo, L. Broussard, and E. Iverson for discussions on these points.

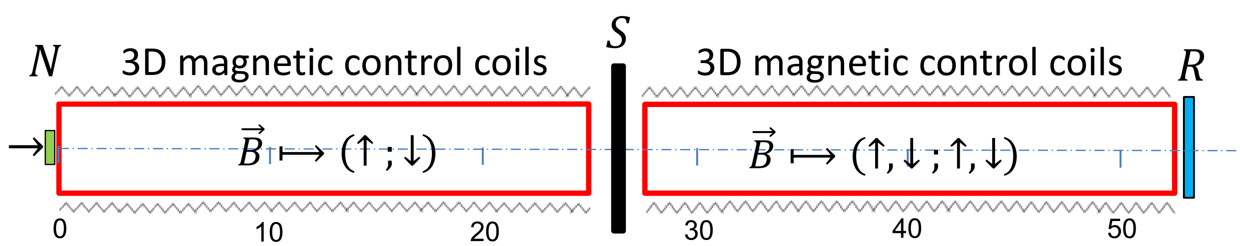

Figure 3.12: A simplified schematic of the $n \to n' \to n$ and $n \to \bar{n}' \to n$ regeneration searches. Two vacuum aluminum tubes with symmetric lengths of $25\,\mathrm{m}$ are shown. The symbol N represents a low efficiency beam monitor, R shows a high-efficiency ^{3}He low-background detector, and S is a very high efficiency beam absorber. A magnetic field is applied in different directions (shown by up and down arrows within parentheses) within the two vacuum tubes, and the configurations can be alternated to choose between hypothetically identical (opposite) magnetic moments of n and n' ($\bar{n}'$). Original figure, edited for publication [19] by D. Milstead and Y. Kamyshkov.

sets of experimental uncertainties (beyond the use of the same HIBEAM/ANNI beamline). From this discussion, any observation of disappearance could be rather easily verified by a regeneration experiment running for a longer period of time.

3.3.3 Search for $n \to \bar{n}' \to n$

As discussed, the hypothetical symmetry between ordinary matter and mirror matter (Eqs. 1.30 and 1.47) generally allows for a range of potential neutral particle transformation processes to occur between the visible and mirror sectors, beyond the simple $n \to n'$. A neutron can in principle also be transformed into a mirror antineutron, which could then regenerate back to a detectable neutron state, i.e. $n \to \bar{n}' \to n$. Due to the mirror CPT theorem, the magnetic moment of the mirror antineutron will be oppositely aligned to the magnetic moment of the mirror neutron; therefore, since the angular momentum of the process is conserved, a resonance could be observed when magnetic fields in the first and second flight tubes are *opposite* in direction; this configuration is also shown in Fig. 3.12. A $n \to \bar{n}' \to n$ search can therefore be made to complement any $n \to n' \to n$ venture and with a similar sensitivity.

3.3.4 Search for $n \to \bar{n}$ via Regeneration Through Mirror States

Classic searches for $n \to \bar{n}$ assume that the transformation occurs via mass mixing with a non-zero amplitude α term. This requires adequate magnetic shielding, as well as active and passive field components for a sensitive experiment. However, $n \to \bar{n}$ can also arise due to other potential second order mixing processes: $n \to n' \to \bar{n}$ and $n \to \bar{n}' \to \bar{n}$, each with an amplitude comprised of $\propto \beta_{n\bar{n}'}\epsilon$.

A schematic layout of a $n \to \bar{n}$ search through regeneration is shown in Fig. 3.14. Construction of the $\bar{n}$ annihilation detector at the end of second vacuum volume will be required for this experiment. This would serve as a complement to the classic $n \to \bar{n}$ search which of course assumes no sterile neutron mixing. Discussion of the details of the annihilation detector which could be used here in a prototype form will be deferred to Sec. 3.4.2, where it is described predominately in the context of the classic $n \to \bar{n}$ search.

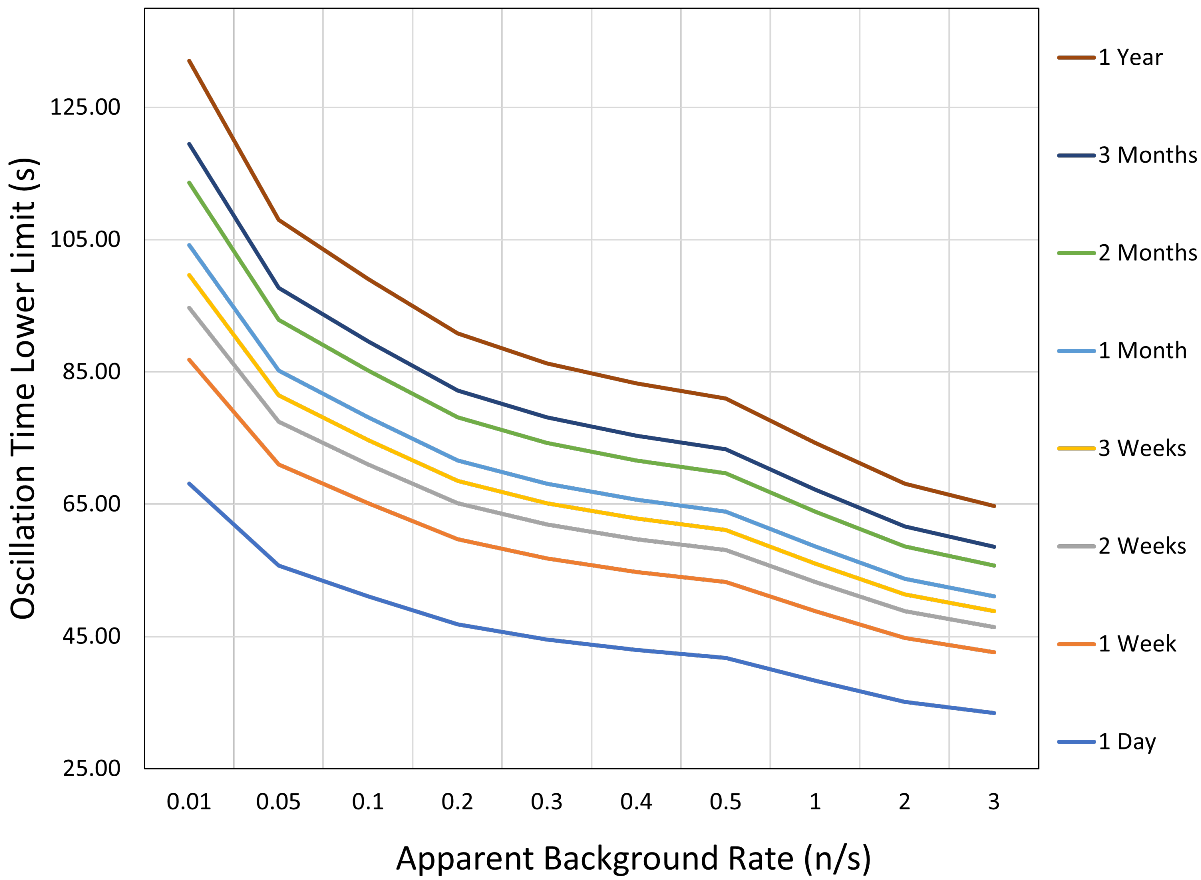

Figure 3.13: 95% C.L. sensitivities for the oscillation time as a function of the apparent background count for regeneration-style searches of $\tau_{n\to n'\to n}$ and $\tau_{n\to\bar{n}'\to n}$ in a low magnetic field configuration after $\sim 50\,\mathrm{m}$ of flight. These plots assume a $0.5\,\mathrm{m}$ radius detector for the nominal $1\,\mathrm{MW}$ HIBEAM/ANNI flux. See again Figs. 3.8, 3.9, and 3.11 for additional context.

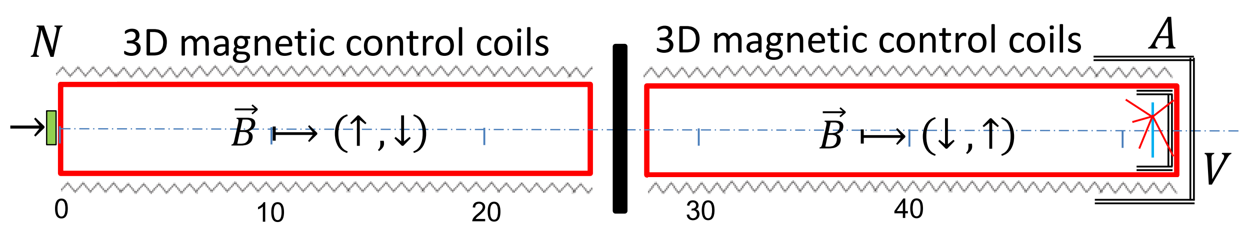

Figure 3.14: A $n \to \{n', \bar{n}'\} \to \bar{n}$ regeneration search schematic. Two aluminum vacuum tubes with a $1\,\mathrm{m}$ diameter can be used. The symbol N represents a low efficiency beam monitor, A shows an annihilation tracking detector enclosing a carbon foil target to capture the $\bar{n}$C annihilation event, and all of this can be surrounded by V, a cosmic veto system. A magnetic field is applied in different directions in each of the two tubes. Original figure, edited for publication [17] by D. Milstead and Y. Kamyshkov.

3.3.5 Complementarity of Neutron Mixing Searches

This program of searches has the potential to make both a fundamental discovery of a dark sector, and to quantify the processes underpinning any signal observations. For example, if a signal would be detected in disappearance mode, this could imply a disappearance for all possible final states of the oscillating neutrons. Since the magnetic moment of a neutron is oppositely aligned to that of an antineutron due to the CPT theorem (just as for sterile neutron and antineutrons), it will be advantageous to use non-polarized beams. Here, the compensation $\vec{B} = \vec{B}'$ would permit transformations to $\bar{n}, n'$, and $\bar{n}'$ for different initial polarization states of neutrons. In regeneration searches, all four magnetic field combinations in two flight volumes would be possible, with $\pm\vec{B}_1$ versus $\pm\vec{B}_2$ used to detect all possible channels of $n \to \{n', \bar{n}'\} \to \{n, \bar{n}\}$ regenerative processes due to mixing amplitudes ϵ and $\beta_{n\bar{n}'}$.

3.3.6 Search for Regeneration Through a Neutron TMM

As shown in Eq. 1.44 and discussed therein, the probability of the process $n \to n'$ due to a neutron transition magnetic moment (TMM) with magnitude κ for sufficiently large magnetic fields is approximately constant, where $P_{nn'} \propto \kappa^2$. Due to the relative independence of $P_{nn'}$ on the magnitude of magnetic fields surrounding the hypothetically oscillating (n, n') system, it can travel through strong magnetic fields with large gradients while retaining approximately the same probability of transformation. However, the gradients of the magnetic field potential, $\frac{\partial}{\partial r}\left(\mu \cdot \vec{B}(r)\right)$, cause a classical force which acts *only* upon the ordinary neutron part of the (n, n') system. Thus, the components of the (n, n') system become spatially separated, just as two spin states in a Stern-Gerlach experiment. When passing through a spatially varying magnetic potential, the difference in kinetic energies of the (n, n') components can become larger than the deBroglie wavelength of the wave packet for the system; this can be thought to "measure" the system by collapsing it into either a pure n state or pure n' state. The required magnetic field gradient corresponding to a "measurement" event can be found [92] according to

$$\frac{\Delta B}{\Delta x} > \frac{1}{\mu v (\Delta t)^2} = \frac{v}{\mu (\Delta x)^2}\,, \tag{3.5}$$

where Δx is the distance traveled in the magnetic field for time Δt, μ is neutron magnetic moment, and v is the neutron velocity.

A surprising consequence is that as the system continues through the gradient and has its initial state repeatedly reset by a "measurement", this creates additional opportunities for the transformations $n \rightarrow n'$ or $n' \rightarrow n$, effectively increasing the transformation rate. This mechanism was suggested [92] as an explanation for the neutron lifetime anomaly [412], where the disappearance of neutrons due to the magnetic gradients present in UCN trap experiments could account for the $\sim 1\%$ lower value of the measured neutron lifetime in bottle experiments compared to beam methods. This explanation of the neutron lifetime anomaly, together with existing limits from past experimental $n \rightarrow n'$ searches implies that $\kappa \sim 10^{-4}$-10^{-5} [92].

To test this hypothesis, solenoidal field configurations made from alternating currents in each coil can be implemented around the two vacuum tubes to create a magnetic field along the beam axis with a "zig-zag" (or saw-tooth-like) shape, providing an almost constant gradient along the vacuum tube length. These coils can be applied in a scheme as shown in Fig. 3.12 to search for a neutron TMM-induced $n \rightarrow n' \rightarrow n$ regeneration.

Also described in [92], an enhanced $n \rightarrow n'$ transformation rate can be produced in a gas atmosphere filling one of the tube volumes due to a neutron TMM. A constant magnetic field $\vec{B}$ can be applied in the flight volume to give rise to a negative magnetic potential, and can thus compensate the positive Fermi potential of the gas. The gas density can be sufficiently low to avoid incoherent scattering or absorption of the neutrons, resulting in a pure oscillation with probability (from Eq. 1.46)

$$P_{nn'} = (\epsilon + \kappa\mu B)^2 t^2 \,. \tag{3.6}$$

The magnetic field can then be scanned in order to search for a resonance condition resulting in a regeneration signal. The magnitude of the laboratory magnetic field at which the resonance might occur of course depends on the magnitude of the neglected hypothetical sterile magnetic field, and so can also determine the magnitude of $\vec{B}'$ independently by setting the laboratory magnetic field to zero and instead scanning over gas pressures in the flight tube. In this scenario, the probability is described by the corresponding equation:

$$P_{nn'} = (\epsilon_{nn'} \pm \kappa\mu B')^2 t^2 \,, \tag{3.7}$$

where $\pm$ is due to the different possible parities of the sterile magnetic field. This scenario, again, permits many new cross checks in the event of a discovery.

3.3.7 Neutron Detection for Sterile Mirror Neutron Searches

All forms of dark neutron mixing searches rely on measurements of ordinary neutrons, which of course is a major capability within the neutron scattering community of ESS. A standard solution for neutron detection uses gas detectors based on ^{3}He in a single wire proportional chamber which can be operated at low gain since the $n + {}^3\text{He} \rightarrow t + p$ reaction produces a very large ionization signal. While this is the baseline technology assumed for HIBEAM, it is also possible that modern readout solutions from high energy physics can improve the performance of such a neutron detection scheme still further. As an example, the most ideal yet challenging readout scenario can be considered, where each neutron in the beam could be individually detected. Assuming a neutron flux of 10^{11} n/s evenly spread out over a $2\,\text{m}$ diameter circular detector surface, and assuming each detector element to be about $1\,\text{cm}^2$ in area, one could expect $30,000$ readout channels with a singleton counting rate in each channel of about $3\,\text{MHz}$. This rate is not trivial to deal with, but it can in principle be accommodated by the schemes such as the ATLAS TRT detector[7], where each detector element is a single wire proportional chamber (operated at high avalanche gain) read out on the wire. Typical singleton counting rates in the ATLAS TRT are in the range of 6-$20\,\text{MHz}$, so $3\,\text{MHz}$ seems quite feasible in comparison. The ATLAS TRT electronics will be removed from the ATLAS setup in 2024, presenting a timely and interesting opportunity for HIBEAM. The energy of the reaction products do not provide any useful information about the originating neutron, therefore only the number of neutrons detected would be recorded in the data stream. The use of coincidence criteria with neighbouring detector cells can also be investigated to avoid double counting when nuclear fragments may leak into neighboring cells.

If the individual counting of neutrons is not necessary, an integration of the released charge in the detector material can yield a measurement proportional to the number of incoming neutrons. However, even upon proper calibration, such current integration is expected to be less sensitive to the actual rate of neutrons. It should also be mentioned that in view in the shortage of ^{3}He, much research and design is being done for scattering experiments pertaining to other methods for CN

[7]Thanks to D. Milstead and B. Meirose for considering these possibilities.

detection. Synergies with readout systems developed for high energy experiments are expected and neutron detection in HIBEAM is a good example of an application with a specific scientific use as motivation for exploration.

3.4 Detector Components for $n \to \bar{n}$ for the NNBAR/HIBEAM Experimental Program

In addition to the suite of dark neutron searches described previously, a major aim of HIBEAM is to act as a pilot experimental program during the early, developmental stages of the ESS, and aims to serve as a research and design space, at first without exploiting the planned full beam power of the facility. Beyond research and design via $n \to n'$-style searches, a small $n \to \bar{n}$ experiment is also possible. While this search will likely not surpass past free neutron sensitivities [56], HIBEAM can be used for ample design and prototyping of technologies necessary for the second stage NNBAR program, dedicated to world-leading, complementary, high precision searches for $n \to \bar{n}$ at the Large Beam Port. As described in Sec. 3.3.4, the HIBEAM experiment will also perform searches for $n \to \bar{n}$ via regeneration from a mirror sector, for which the target and annihilation detector described here can also be used. Since HIBEAM is a pilot experiment ahead of the NNBAR stage, it would be expected that the experience of designing and operating HIBEAM would greatly inform the final design of the NNBAR annihilation detector.

3.4.1 Magnetic Shielding and Vacuum Requirements

For a quasifree condition, neutrons must be transported in a magnetically shielded vacuum [360, 107] corresponding to a pressure of $\leq 10^{-5}$ mbar and a magnetic field of $\lesssim 10$ nT along the neutron flight path [161]. The target vacuum can be achieved with a vacuum chamber comprised of highly non-magnetic materials, e.g. aluminum, with turbo molecular pumps mounted outside of the magnetically shielded area. Magnetic fields of < 10 nT have been achieved over large volumes [33]. As shown in Fig. 3.15, for a $n \to \bar{n}$ run at HIBEAM, the shielding concept includes an aluminium vacuum chamber, a two layer passive μ-metal shield made from magnetizable alloy for transverse shielding, and end sections made from passive and active components for longitudinal shielding.

3.4.2 Detector Components for $n \to \bar{n}$ Searches

A key experimental task of any $n \to \bar{n}$ search is to isolate and detect the annihilation of $\bar{n}$'s from a beam of free neutrons. The transformation has an extremely low probability, and although an ESS experiment could have by far the longest experimental observation time of any free neutron beam, it is probable that any experiment would measure only $\mathcal{O}(1)$ candidates. Thus, the overarching goal for the detector system is to provide the highest possible sensitivity for detecting an $\bar{n}$ annihilation. These ambitions go beyond a statistical significance analysis, and should allow for a claim of discovery from even only a few observed annihilation events; in the case of non-observation, a robust lower limit can be imposed, and multiple compelling theories of baryogenesis potentially eliminated or severely constrained [50, 47].

As much as possible, the detector system[8] must provide a reliable and complete reconstruction of each annihilation event. Statistical correction of experimental shortcomings cannot be performed on the individual event level; thus, the design goal must be to record as many observable parameters as possible, taking in all available information about the annihilation generated daughter products, and, if possible, compensate directly for detector effects that are statistical in nature via over-sampling. From this, one understands immediately that special attention must also be paid to maintain a $\sim 4\pi$ detector coverage, and similarly must avoid permanently and temporarily dead detection areas due either to support structures or failing detector components, respectively. Serviceability and modularity, too, must then be a key design feature.

An important detector constraint is that a magnetic field cannot be used. Thus, momentum cannot be directly measured, and so only the kinetic energy deposited in the detector and the directionality of the particles inferred. A sensitive $n \to \bar{n}$ experiment should therefore be capable of:

1. Identifying all charged and neutral pions, properly reconstructing their energy and direction

[8] Many thanks to the NNBAR Collaboration Detector and Computing Group for their collaboration on this developing work.

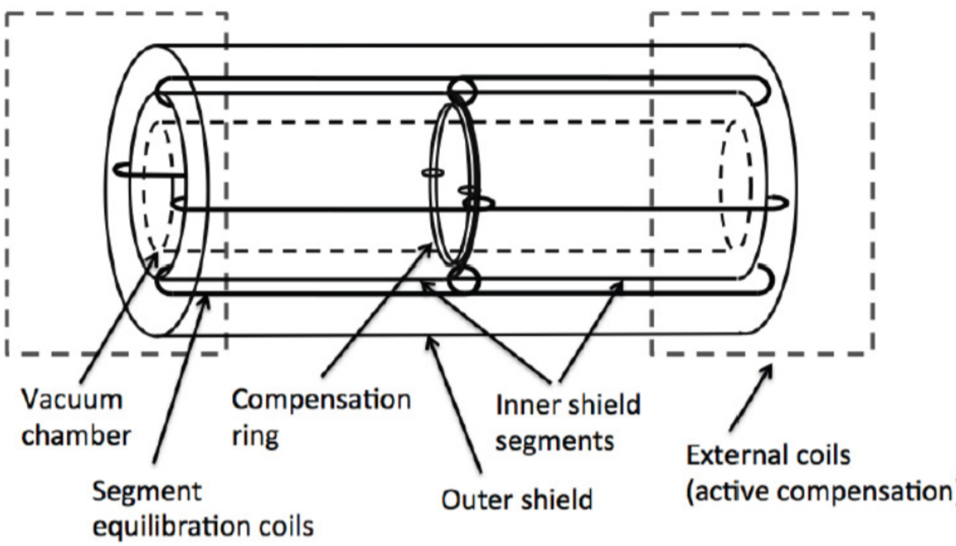

Figure 3.15: Generalized schematic overview of the planned magnetic shielding scheme. Courtesy of the NNBAR collaboration.

2. Reconstructing the energy and direction of most higher energy, charged nuclear fragments (mostly protons; fast neutrons and heavier nuclear remnants will likely not be trackable)

The positive identification of an annihilation event would *ideally* comprise the identity and momentum of all pions, a total invariant mass which amounts to two bound nucleons ($\sim 1.9\,\mathrm{GeV}$)[9], and a reconstructed common point of origin in space and time of all emitted particles (including nuclear fragments where possible) from the plane of the annihilation foil. The directionality of an event can be verified with fast timing by checking that the particles move outwards, acting as an important discriminant against backgrounds from cosmic rays and atmospheric neutrinos. A generic detector must thus include tracking, energy loss, calorimetry, timing, and cosmic ray veto systems, as illustrated in Fig. 3.16.

3.4.3 Overall Detector Geometry

The optimization of the area of the annihilation foil is a balance between a large diameter, which maximizes the visible neutron flux, and overall manufacturing cost, which is expected to grow dramatically with diameter. The baseline design assumes a $2\,\mathrm{m}$ diameter for NNBAR, and a substantially lower one for HIBEAM (perhaps, at maximum, $1\,\mathrm{m}$ in diameter). The discussion below is guided by NNBAR, while HIBEAM is understood to become a first stage research and design platform for the full experiment while also still conducting other cutting-edge BSM searches. During the long time of flight, the beam will be affected by gravitation significantly, such that the flux incident upon the annihilation foil is not expected be regular and uniform but rather elongated vertically, containing a vertical gradient in observation time due to the slowest neutrons of the velocity spectrum passing through the bottom of the foil; see Fig. 3.17. Since the oscillation probability (and so too the annihilation probability) grows as t^2, the largest number of annihilations will hypothetically take place at the bottom of the foil. Similarly, radiation load can increase at lower vertical positions.

The geometry of the detection system must also be optimized balancing practical considerations for event reconstruction. A consequence of the broad spread of annihilation positions in the foil disc is that there is no strong argument for having a cylindrical detector layout. A rectangular

[9] This is a simplification for the purposes of discussion; final state interactions have critical effects on this observable.

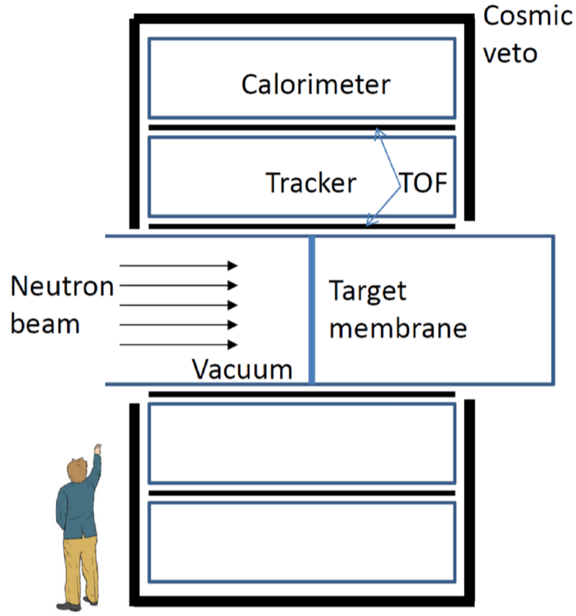

Figure 3.16: Generalized schematic overview of the NNBAR detector. See later Figs. 3.18 for more context. A smaller prototype version is possible for HIBEAM for $n \to \bar{n}$ and $n \to \{n', \bar{n}'\} \to \bar{n}$ searches and general research and design purposes for the second stage NNBAR experiment. Courtesy of the NNBAR collaboration.

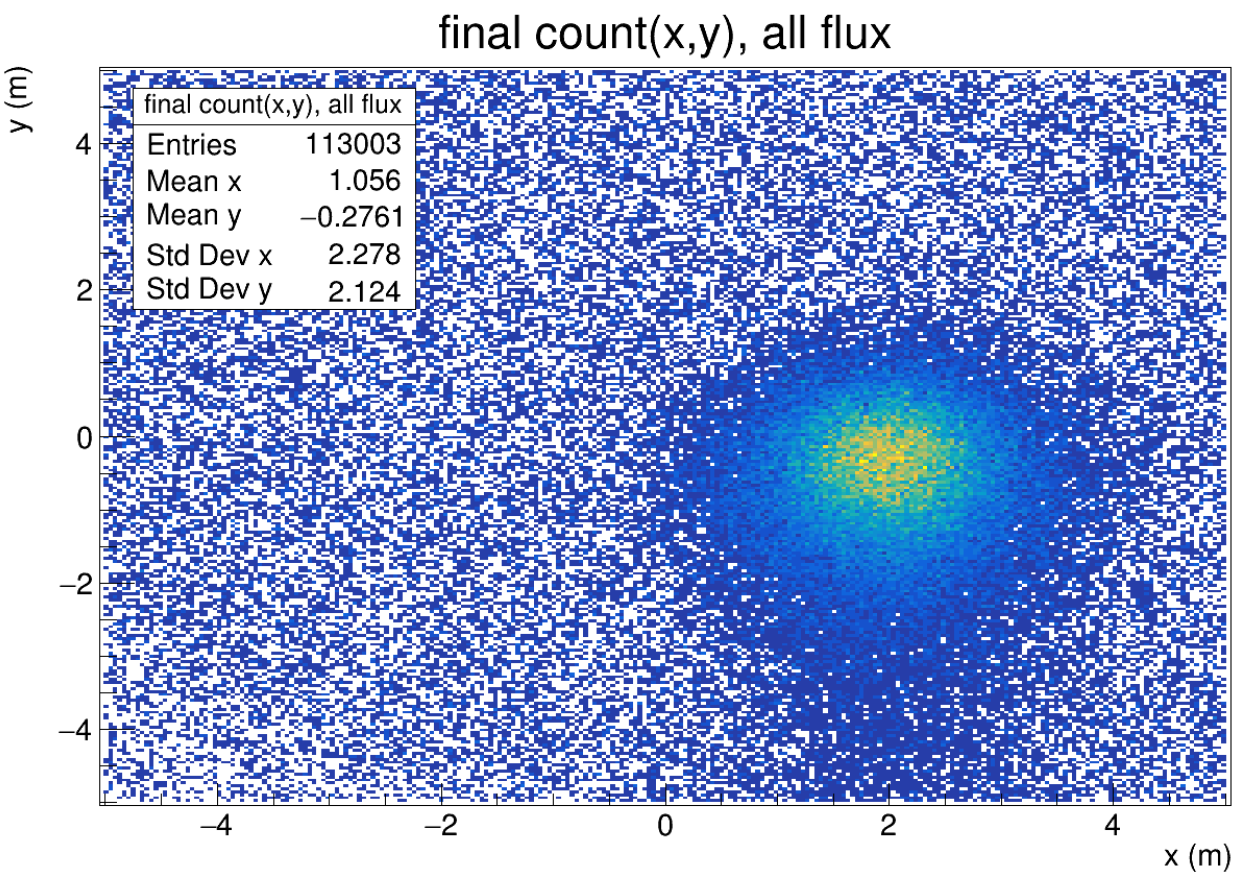

Figure 3.17: Final expected (anti)neutron positions at the detector position ($\sim$ 200 m) for the NNBAR flux [204, 19]; vertical drop of the hotspot is seen due to gravity, which most effect the slowest and most important velocity components of the neutron spectrum; the rightward offset is intentional to avoid potential backgrounds on a direct line of sight from the moderator, and is not expected to be an issue with HIBEAM given ANNI's S-shaped curved guide. Event file courtesy of M. Frost [204].

layout is likely to be cheaper, more serviceable, modular, and so will serve these purposes equally well, if not even better than a circular cross-section setup; see Figs. 3.18. A common vertex for a number of secondaries in a large area becomes a strong constraint for an annihilation event; these events must contain *at least* two tracks [56], which appears to be the case in the majority of simulated events [229], as seen in Chap. 2.

The momentum for each particle can be reconstructed if they are properly identified and their direction and kinetic energies measured. If the missing momentum (higher than the Fermi momentum) points toward any uninstrumented areas of the detector, one can in principle still have a good understanding of the event, even though the topology would not be as well characterized as signal as in the ideal case of all daughters being observed. While full efficiency and 4π coverage for tracking and reconstruction of annihilation products is impossible due to the neutron beam path, very high coverage should be achievable. A $\sim 10\,\mathrm{m}$ long detector with a $1\,\mathrm{m}$ inner radius and full coverage in azimuth would result in a geometrical acceptance of $\sim 90\%$[10]. Even with excellent geometric efficiency, loss of information about the total energy (or similarly the invariant mass) is unavoidable. Following final state interactions, pion can be absorbed or rescattered within the nucleus, and heavier nuclear remnants are generated which may be easily stopped by interior detector components; thus, the energy carried away by nuclear fragments may in most cases go unrecorded. Similarly, for momentum balance, the loss of nuclear fragments can be more significant due to their higher mass.

3.4.4 The ^{12}C Annihilation Foil

The annihilation cross section is very large (kilobarns compared to millibarns) for cold antineutron captures on carbon. A very thin carbon foil is thus sufficient to provide a high probability for the $\bar{n}$ to annihilate. However, the very large CN flux will produce nuclear reactions emitting many $\sim 1\,\mathrm{MeV}$ photons, and so will be a source of backgrounds which contribute to the singleton counting rates in the detector; however, it is not expected to be a severe background to the annihilation signal itself. The pileup of many gammas is therefore a potential problem to consider in the detector design, in particular for its required granularity to avoid said pileup. Similarly, for differentiation

[10] About half of all annihilation events are thus expected be fully reconstructed.

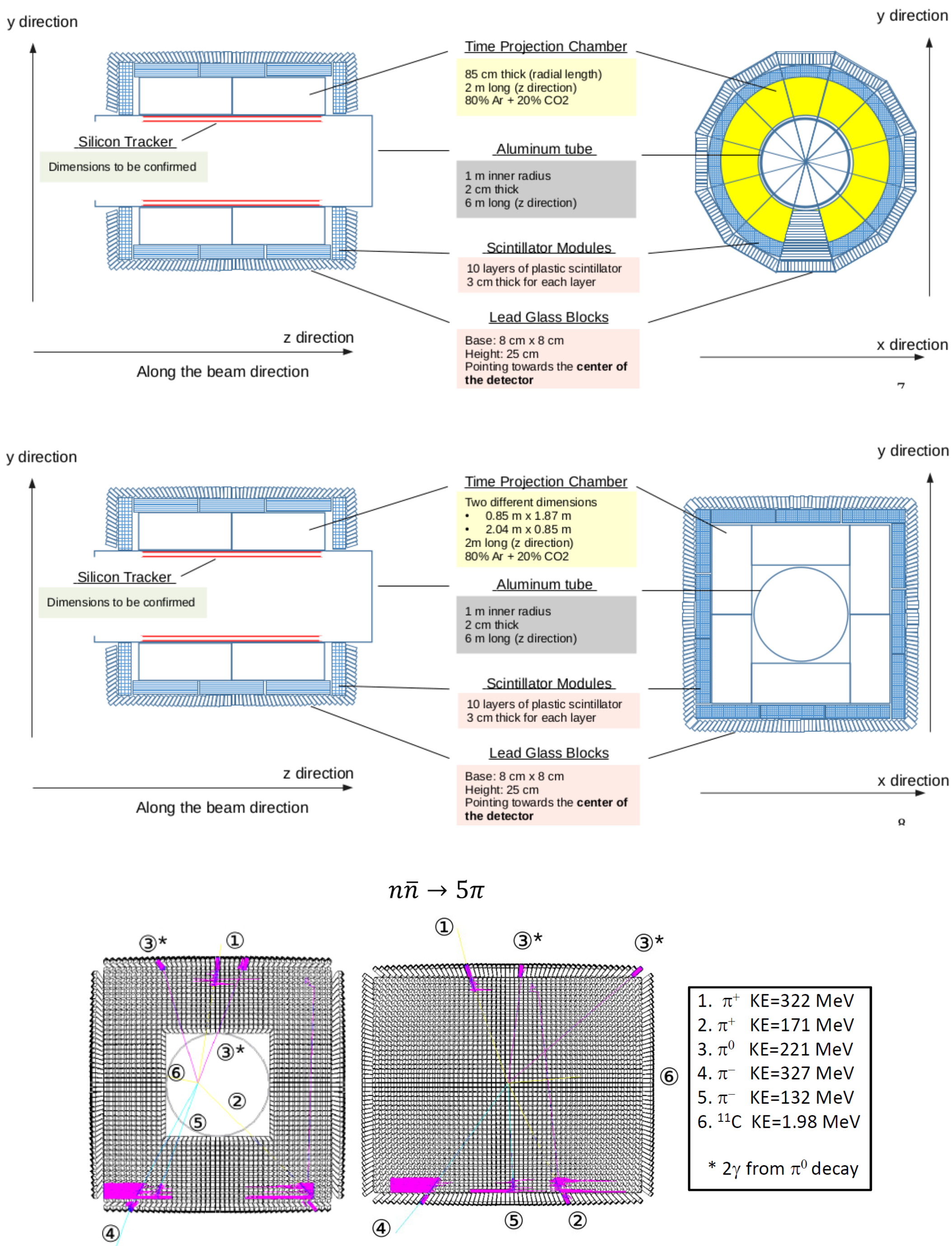

Figure 3.18: Top: The cylindrical detector design with side and front views. Middle: The box detector design with side and front views. Bottom: An event display using GEANT4 of a $\bar{n}$C annihilation [229, 71] within the box NNBAR detector design using components described in this section. Front (left) and side (center) views are shown. The identities and kinematic energies of the outgoing particles are given in the box to the right. Smaller versions of these detector concepts can be tested with HIBEAM; detector components are intended to be tested as an outgrowth of the ongoing HighNESS project [356], of which the NNBAR conceptual design report is a part. Courtesy of S-C. Yiu, B. Meirose, A. Oskarsson and D. Milstead [67], and the HIBEAM/NNBAR Detector Simulation and Computing Working Group [61].

of particularly low energy $\bar{n}A$-generated products, such as nuclear remnants' de-excitations via photons, this can be quite difficult.

A claim of discovery for $n \rightarrow \bar{n}$ should be supported by non-observation under conditions where no $\bar{n}$ is expected to arise. Thus, one strategy is to switch off the magnetic shielding throughout the beamline, effectively prohibiting transformations. However, this approach requires excessive additional running time to verify that the signal vanishes. An attractive alternative is to install two identical foils, separated by a distance of less than roughly a meter [118]. True $\bar{n}$ annihilations would then occur only in the first foil, while false annihilation signals should occur with nearly equal abundance across both, as they do not significantly attenuate the beam. A downside to this approach is that the photon background is also doubled from neutron capture processes in the foils, requiring an increase in the background rejection capability of the setup; another is potential loss (absorption) or redirecting (scattering) of annihilation products, though this is likely a small effect.

3.4.5 The Vacuum Vessel

A cylindrical vacuum chamber is envisioned with a $\geq 2\,\mathrm{m}$ diameter using $2\,\mathrm{cm}$ thick aluminum walls, and must achieve a vacuum pressure less than $10^{-5}\,\mathrm{mbar}$. The final engineering design and material choice will be informed by engineering models as well as simulations of particle transport and background calculations. Some materials and design choices have advantages within various experimental approaches, but other effects may motivate locating some tracking detectors inside the vacuum vessel[11]. Advantages of thick vacuum vessel walls include 1) stopping electrons resulting from neutron β-decay in flight, 2) shielding, to some extent, nuclear-generated photon backgrounds, and 3) providing a means for pair production for γs resulting from signal-generated π^0 decays for improved tracking and calorimetry. Drawbacks of thick vacuum vessel walls of course include a) energy losses in the material, creating higher thresholds for detection outside the wall, and b) multiple scattering leading to a worsened spatial resolution when attempting to point back to the annihilation vertex.

[11] This is the current baseline illustrated in Figs. 3.18.

3.4.6 Background Considerations for Higher Sensitivity $n \to \bar{n}$ Searches

The ILL experiment [56] was shown to be background free after a year of running due to cuts on the number of reconstructed tracks and prolific hand-scanning of events; the NNBAR experiment aims to achieve a factor of 1000X higher sensitivity in $\langle Nt^2 \rangle$ comparatively, and in a much more robust fashion. In the ILL experiment, cosmic rays produced the dominant contributions to potential backgrounds, with the total number of these events naively scaling with the exposure time and the detector volume. These backgrounds will of course be present at the ESS as well, and will ultimately place similar if not greater demands on background rejection rates compared to ILL in order to achieve higher signal to background ratios. Because the planned sensitivity increase at the ESS relies on an increase of several orders of magnitude in the CN flux, the small yet present probability for false annihilation signals due to CN beam-induced background will increase accordingly as well.

A major new difficulty compared to ILL (a reactor facility) is the presence of high energy backgrounds induced by the spallating proton beam at ESS, as the LBP has a direct view of the moderator and so too the source. The contribution from this high energy background to the annihilation signal is very hard to estimate. However, given the beam's pulsed structure, it should occur only in rather narrow time windows, making it possible to ignore events when these fast components reach the detector. The large spread of neutron velocities around $\sim 800\,$m/s for NNBAR [204] ($\sim 1000\,$m/s for HIBEAM, see again Fig. 3.5) largely implies that the arrival of CNs to the detector area at $200\,$m from the moderator will be quite uncorrelated with the cycles of the ESS linac. Based on the experience at the ILL, backgrounds to the annihilation signal are expected to be very low, but since the aim is for substantially higher sensitivity, the background discrimination should be improved as much as one can to allow for a discovery with a minimum number of events. Thus, having the best possible resolution in total energy and vertex reconstruction is the major design goal. A very strong constraint is the location of the reconstructed vertex in three dimensions. For charged particles, three-dimensional tracking is fairly straightforward to introduce. For annihilation generated π^0s, pointing back to a vertex while reconstructing their rest mass via

$$m_{\gamma\gamma}^{\text{inv.}} = 2E_{\gamma_1}E_{\gamma_2}\left(1-\cos\theta_{\gamma\gamma}\right)\,, \tag{3.8}$$

is a key development task for the calorimetry, where E_{γ_i} is the reconstructed energy of each of decay photon, and $\theta_{\gamma\gamma}$ is their opening angle. Preliminary work on this reconstruction is underway within the HIBEAM/NNBAR Detector Simulation and Computing Working Group, and some recent progress can be seen in Fig. 3.19.

3.4.7 Tracking Outside the Vacuum with Time Projection Chambers

Well over 90% of the annihilation events will have two or more charged pions (see again Chap. 2), many of which will be visible above any detector thresholds ($\sim 25\,$MeV for charged pions, and ~ 200MeV for protons), as seen in Fig. 3.20 and discussed within [67, 61]. The full reconstruction is based on these tracks, which must be reliably extrapolated through space, inwards to the annihilation vertex, and outwards to the calorimeter. The tracking of these charged particles must thus be highly reliable. A Time Projection Chamber (TPC) is ideal for this purpose, having 1) three dimensional tracking, 2) nearly identical position response independent of track direction with each ionization event recorded via space points with 3) at least one space point per cm of gas thickness to form a continuous track image such that tracks can be reconstructed with very few combinatorial mistakes to achieve an excellent $\frac{dE}{dx}$ with an eliminated Landau tail, and also 4) excellent granularity in time. A TPC tracking detector can thus record the kinematic information of each track most reliably by using both the space and time dimension to achieve a high granularity, where the TPC could effectively divide up the sensitive volume into independent voxels of $\sim 1\,\text{cm}^3$ each. A drawback is that doing so will create a poor time resolution, and so requires a trigger limited to a $\sim$kHz trigger rate.

Particle identification is incredibly important since a large fraction of the annihilation energy is bound-up in the rest masses of pions. Identifying the pions would constrain the requirement on the energy and momentum balance considerably. Measurement of $\frac{dE}{dx}$[12], together with an associated

[12]Preliminary simulations of this quantity and associated particle identification in the full NNBAR detector concept are still developing and are highly preliminary within the HIBEAM/NNBAR Detector Simulation and Computing Working Group.

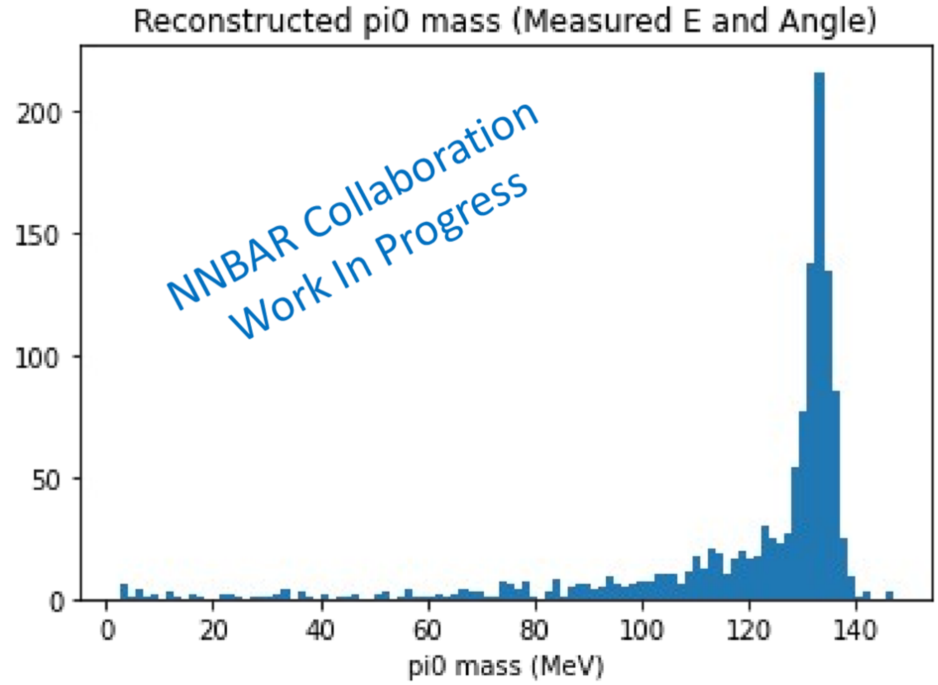

Figure 3.19: *Preliminary* reconstructed invariant masses of a 250 MeV π^0 beam entering the center of the full NNBAR detector within GEANT4 simulations (still developing). This simulation utilizes all of the detector components described in this section. Courtesy of S-C. Yiu [419].

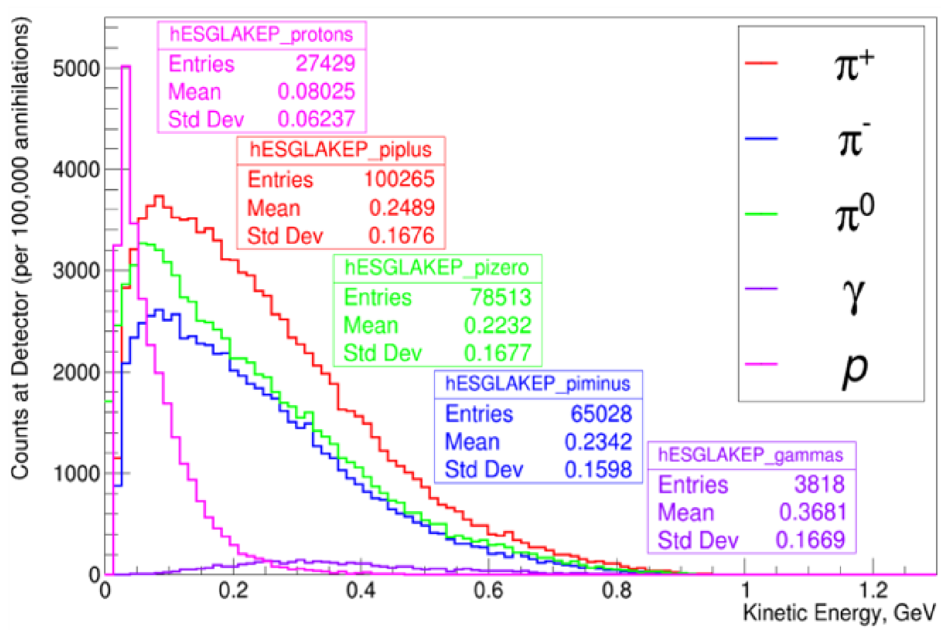

Figure 3.20: $\bar{n}$C annihilation-generated daughter particle spectra for $100,000$ events. De-excitation photons emitted from nuclear remnants are not shown; all photons shown here are due to heavy resonance decays. It is expected that charged pions with $\gtrsim 25$ MeV of energy are trackable, while protons will require $\gtrsim 200$ MeV to pass through the 2 cm of aluminum.

reconstructed kinetic energy for charged particles, can in principal provide particle identification. For a robust $\frac{dE}{dx}$ measurement the track length should be reasonably long ($> 50\,\text{cm}$). Since the track in the TPC reliably points in three dimensions, inwards and outwards, information about the track from different detectors can be assembled with minimum risk of combinatorial mistakes; this is essential since statistical correction for such combinatorial mistakes cannot be performed on individual events.

3.4.8 Tracking Inside the Vacuum Chamber

The thick wall of the vacuum vessel will cause multiple scattering such that the track direction measured outside may lose some pointing resolution. Since the charged pions have fairly low mass, and since low kinetic energies are of interest, this is a considerable effect, and so the vertex resolution is an important discriminating parameter for claiming discovery. Including track coordinates on the vacuum side of the wall resolves this situation. Two space points on each track should be sufficient since the pointing from outside is good enough for the track definition.

The detector inside the vacuum will face heavy background from both neutron β-decay in flight and photons from neutron capture reactions, thus requiring high granularity. Two silicon strip stations, with a stereo angle between strips to allow for a space point from each station, would serve this purpose well. Arranged as a cylinder with $1\,\text{m}$ radius and $10\,\text{m}$ length, this would be a very costly detector, and one may have to consider cheaper options with gas detectors or scintillating fibers. Possibly, one could compromise on the z-coordinate for the inner detectors if multiple scattering does not prohibit determination of the vertex position on the annihilation foil[13]. In that case, more options for inner detectors may be considered, as long as the issue of high singleton rates from backgrounds can be avoided, again calling for a high granularity. With silicon detectors, this could be realized, but is a matter of cost; evading these constraints is likely to be more difficult to accomplish with other detector types.

Cases where no charged pion goes through the wall cannot be handled. At least one charged particle must give a track in the tracking outside to enable a search for a potential annihilation, hypothesizing an emission point at the intercept of the extrapolated track and the annihilation foil.

[13] Simulations studying these effects are currently underway within the HIBEAM/NNBAR Detector Simulation and Computing Working Group.

Rather than pions, it is more likely that heavy, charged nuclear remnants will stop in the chamber wall. For stopping particles, a maximum energy corresponding to the range in the wall material can be set from developing GEANT4 simulations [67, 61].

3.4.9 Calorimetry

The energy measurement by the calorimeters will be a crucial part of the evidence that an annihilation event has been observed. The calorimeter can identify neutral pions, occurring in $\sim 90\%$ of the annihilations, and also ensure that the sum of absorbed energy (from kinetic energy and pion rest masses) acquires that of nearly two nucleon masses, or less. In addition, the calorimeter can provide the kinetic energy of the charged pions and any visible charged nuclear fragments. Energy measurements at these low momenta are notoriously difficult (see again Fig. 3.20), and so several processes will be considered over the following subsections.

3.4.10 Charged Hadronic Particles

As long as the incoming particle is stopped by ionization energy loss only, its kinetic energy can be measured with good resolution. However, at pion energies around $100\,\mathrm{MeV}$, this means traversing quite a bit of ionizable material, and so the probability for nuclear reactions becomes sizeable at such distances. The energy can still be correctly measured as long as secondaries are charged and all energy is absorbed in a sensitive detector material. Energy carried away by fast neutrons will not be absorbed and remain unmeasured; for this reason, a low-Z material is preferred. For the actual annihilation products, protons will be mostly stopped by ionization energy loss while the bulk part of the charged pions cause nuclear interactions resulting in an energy deficit. Other effects that obscure the energy measurement of charged pions are their weak decays, where an undetected neutrino carries away some of its total energy; however, if the charged pion identification is effective, this will be a small effect. A larger effect is when negative pions moving through the material can be captured by nuclei, where energy can then carried away by fast neutrons, and so go undetected; this can give an uncertainty in the reconstructed energy by at least a full pion mass.

All these unavoidable effects can normally be corrected for by averages based on simulations. For the purposes of the NNBAR/HIBEAM experimental program, where the energy must be measured as accurately as possible for each individual particle, one cannot correct these easily, and so the calorimeter design must be optimized differently. In some sense, these fundamentally unavoidable problems are arguments against expensive materials with very good energy resolution; possibly, simply measuring $\frac{dE}{dx}$ and the range of particles can give the most reliable information[14].

3.4.11 Photons from π^0 Decay

The two photons resulting from a (stopped) neutral pion decay have on mean kinetic energy value of $\gtrsim 67.5\,\text{MeV}$[15] each (see Fig. 3.21), far above the energy of any natural sources of particles except those of cosmic origin. Some $\gtrsim 90\%$ of all annihilations are expected to have at least one neutral pion, and so a single photon energy threshold can be a simple and reliable trigger on annihilation events. The calorimetry of photons thus serves three purposes: 1) triggering on annihilation events, 2) identifying neutral pions, and 3) the determination of the pion kinetic energy. A pointing ability towards the annihilation vertex would verify the neutral pion as having the same origin as any charged particles and so adds to the constraints on the annihilation event. Since $\gtrsim 90\%$ of the annihilation events have at least two charged pions, a vertex based on these should be identified for all events one would analyze. With this vertex known (which is also the effective decay point of the neutral pion), and the impact positions on the calorimeter measured, one can reconstruct the invariant mass of any pair of photons from the opening angle between photons and the measured photon energies (see again Eq. 3.8). The invariant mass resolution is key to a firm, particle by particle statement about the potential neutral pion, since 1) a narrow cut on invariant mass minimizes combinatorial background, and 2) the more accurately the invariant mass is measured, the better the photon origin position at the vertex of the charged particles is known. The way to improve position resolution is to choose materials with a small Moliere radius. Moving the calorimeter to a larger radial distance from the CN beam axis improves the opening angle resolution as well.

[14]This is a very active area of discussion within the HIBEAM/NNBAR Detector Simulation and Computing Working Group

[15]A stopped neutral pion of course equally shares its $\sim 135\,\text{MeV/c}^2$ rest mass between its two decay photons. However, boosts due to the non-zero momentum of the annihilation generated pions skew this.

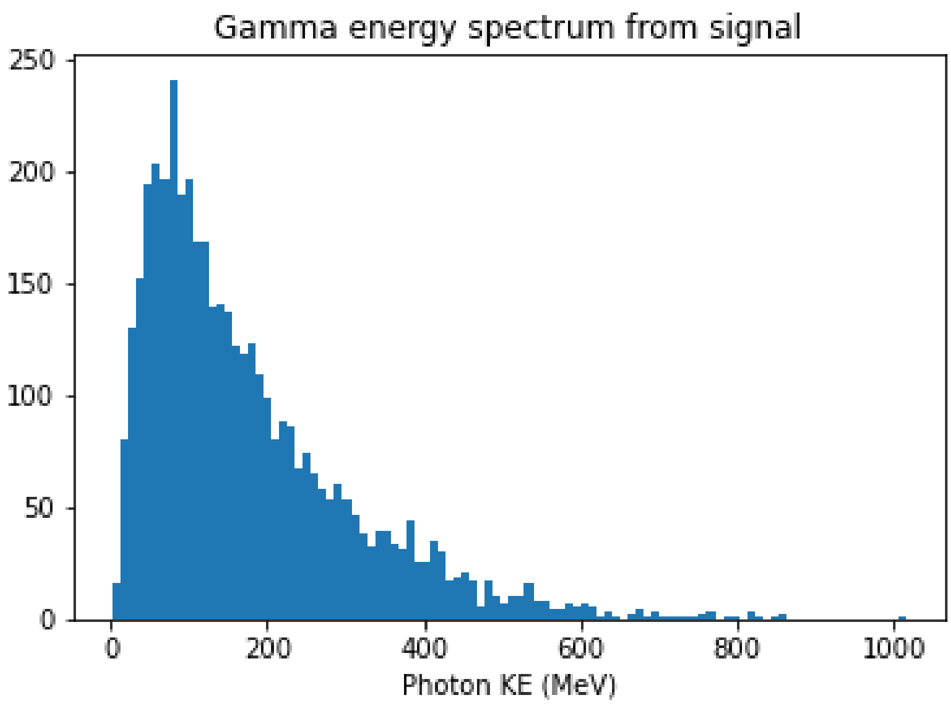

Figure 3.21: The decaying $\pi^0 \to \gamma\gamma$ spectrum is shown for π^0's generated via $\bar{n}$C annihilation (see again Chap. 2); all events have been decayed within a truth-level `GEANT4` simulation, and NNBAR/HIBEAM detector effects are not present. A small selection of 2193 events are shown, with a *mean* value of $177\,$MeV of kinetic energy; the peak value is $\sim\,100\,$MeV. Thus, very few events would be missed with a $67.5\,$MeV trigger cut. Courtesy of S-C. Yiu.

Uniformly sensitive crystals can be either based on scintillation light (several high Z materials exist) or Cherenkov light (lead glass[16] being most popularly used). Both types share the ability to measure the total energy as deposited by electrons and positrons, and from a fundamental point of view, they can have equally good resolution for photons. In the readout stage, one can expect to have more light from a scintillator, and thus somewhat better energy resolution; however, scintillators will give a signal corresponding to all deposited energy, while lead glass is basically blind to nuclear fragments due to the Cherenkov threshold; charged pions of $\sim 30\,\mathrm{MeV}$ can produce Cherenkov light. The energy calibration of lead glass for charged pions in the actual energy range desired for NNBAR is not trivial, as most beam facilities run at higher energies.

Motivated by the arguments discussed in this section, a `GEANT4` study [67, 61] of the response of a calorimeter module to charged hadrons and photons is being conducted ahead of a detailed study of a physical prototype for an *in-situ* ESS neutron test beam in 2023, and test beams at other facilities. The module is based on lead glass and scintillators, and exploits the Cherenkov signature for electromagnetic energy caused by the interaction of photons, charged hadrons (mainly via $\frac{dE}{dx}$), and hadronic energy. A charged particle range telescope comprising ten layers of plastic scintillator lies in front of the lead glass; see again Figs. 3.18.

3.4.12 Cosmic Veto, Timing, and Triggering Schemes

The sum of two nucleon masses represents a high energy, and can be produced by background sources such as cosmic rays[17]; therefore, an active veto system against charged cosmic ray particles must surround the detector. It can consist of two layers of active material such as plastic scintillators which in coincidence can reject induced backgrounds in order to avoid false vetoes. The cosmic veto is expected to be a part of the hardware trigger logic, and vetoed events will not be stored; however, it may prove possible to postpone the rejection from the cosmic veto to the offline analysis. Thus, the cosmic veto should be designed with sufficient timing resolution to determine the direction, inwards or outwards, of the particles associated with the signal.

[16] This serves as the current detector baseline design.

[17] Oscillated atmospheric neutrinos are not yet considered in NNBAR/HIBEAM studies due to their comparatively low cross section (rates are expected to be especially low for those which will interact on the ^{12}C foil). However, as will be described in Chap. 4, atmospherics can be rather easily included in these studies in the future if the NNBAR collaboration wishes to do so.

Charged cosmic rays producing high energy deposits and tracks in the NNBAR or HIBEAM detectors are rather straightforward to discriminate, but it can be much more problematic if the deposit is induced by energetic neutral particles (γs or neutrons). A geometrically long sampling calorimeter opens the possibility to measure the direction of the electromagnetic showers using a Cherenkov based calorimeter, and so could be made essentially blind to showers directed inwards. Finally, $\frac{dE}{dx}$ measurements may be helpful for an additional layer of veto for fast neutrons.

For charged particles in the tracking system, it is desirable to verify that particles of interest travel outwards. Over a $1\,\mathrm{m}$ distance, there can be $\sim$ns timing differences between relativistic particles; such timing resolution is not very demanding and detectors for this purpose can be placed at the inner and outer areas of the tracking system. Plastic scintillators are adequate to accommodate this timing resolution, and background signals from neutron induced photo-nuclear processes can be discriminated similarly as described for the cosmic veto with a double layer for each station and several centimeters of scintillator thickness.

A trigger to catch energy deposits of $\gtrsim 67.5\,\mathrm{MeV}$ for one of the photons from a neutral pion decay is straightforward to implement in hardware as a signal threshold. If taken in anticoincidence with the cosmic ray shield, the trigger should be easy to handle using modern data acquisition systems. With modern computational approaches and signal processing on the detector, online data-reduction can identify interesting activity above thresholds with hardware triggering (a potentially "self-triggered" or "trigger-less" setup). In addition to a trigger on electromagnetic energy in the calorimeter, a track trigger can be implemented with the timing detectors (plastic scintillators) as described.

3.5 Generalities of $n \to \bar{n}$ Searches within the NNBAR/HIBEAM Experimental Program

For $n \to \bar{n}$ via (non-mirror sector) mass mixing, the quasifree condition is needed, implying magnetic field-free transmission of neutrons. Any antineutrons which are produced would then annihilate within a target surrounded by a detector. The detector would reconstruct the characteristic multi-pion signal to infer the existence of $n \to \bar{n}$.

As shown previously, the figure of merit (FOM) for a free $n \rightarrow \bar{n}$ search is given by $\langle N_n\, t_n^2 \rangle$, proportional to the rate of converted neutrons impinging on a target. To achieve a high FOM, the following criteria must be met:

1. The neutron source must deliver a beam of slow CNs at high intensity, maximising both t_n and N_n, respectively, for a given beamline length
2. For a full second stage NNBAR experiment, the (Large) beamport must correspond to a large opening angle for neutron emission
3. A long beamline is needed to maximize t_n
4. A long overall running time is needed due to the rareness of the process

Note that neutron beams with lower average energies have higher transport efficiencies when supermirror reflectors are utilized, as will be the case in the second stage NNBAR experiment.

3.5.1 ILL-like Sensitivity of HIBEAM for $n \rightarrow \bar{n}$

Considering Fig. 3.14, if the central neutron absorber were to be removed, and two vacuum tubes were be combined into one with a common magnetic compensation and shielding system, one would recover the essential elements of a $n \rightarrow \bar{n}$ experiment at the HIBEAM/ANNI beamline, although with a shorter neutron flight path and lower flux compared to a full stage two NNBAR experiment[18]. Fig. 3.22 shows the sensitivity in ILL units per year normalized to the ESS running year, i.e.

$$\text{ILL units per year} = \frac{\langle N_n\, t_n^2 \rangle_{ESS}}{\langle N_n\, t_n^2 \rangle_{ILL} \cdot \text{ (Operational Factor)}} = \frac{\langle N_n\, t_n^2 \rangle_{ESS}}{(1.5 \times 10^9) \cdot (1.2)}\,, \tag{3.9}$$

for a HIBEAM/ANNI $n \rightarrow \bar{n}$ search as a function of the radius of the detector, assuming a 1MW operating power. One ILL unit is defined using the FOM, flux, and running time discussed in [56] as an observable for the number of conversion events for a given mass mixing term value. The operational factor shown in Eq. 3.9 is a correction factor for the different annual running times expected at the ESS compared to the ILL for the latter's total running period. The sensitivity

[18] For ample discussion of the full NNBAR experiment, see [204, 19].

estimate given by this approach conservatively assumes that the detection efficiency at HIBEAM would be the same as at the ILL experiment ($\sim 50\%$); as discussed throughout the previous sections on signal reconstruction and background rejection within the detector, this is expected to be improvable with modern components.

The sensitivity shown in Fig. 3.22 reaches a plateau for a detector radius of $\sim 2\,\mathrm{m}$. It can be seen that an ILL-level sensitivity can be achieved after running for several (~ 3) years with an appropriately sized detector at this low $\sim 1\,\mathrm{MW}$ power, but this should be considered a generous possibility, as cost considerations may lead to a smaller detector. These can be only linearly offset by a longer running period and higher operating power. $\bar{n}^{12}$C annihilation and outgoing product tracking efficiencies, along with their associated cosmic, atmospheric and fast neutron backgrounds, have not yet been considered entirely, though state of the art simulations of the underlying microscopic processes are being completed [229, 71, 67, 419, 61].

Nonlinear, though fractional, increases in sensitivity can be achieved with the design and construction of focusing (pseudo-)ellipsoidal supermirrors [204] starting near the beamport to increase (anti[19])neutron flux on the ^{12}C annihilation target. Highly preliminary computations using $0.25\,\mathrm{m}$ minor-axes and major-axis lengths of 27-$50\,\mathrm{m}$ for half-ellipsoidal reflector geometries assuming perfect neutron reflectivity (see next section) have shown some increase in overall sensitivity. More realistic configurations and reflectivity modeling must be completed and geometrically optimized.

3.5.2 First Ellipsoidal Reflector Studies and Potential $n \to \bar{n}$ Improvement

The $n \to \bar{n}$ sensitivity studies considered for HIBEAM over the preceding pages take account only of the $\sim 9.2\%$ of the neutron beam which enters the detector volume without any reflector present. This could greatly decrease the expected lower limits attainable for the experiment.

As a first pass at investigating any potential increase in sensitivity for an $n \to \bar{n}$ search using the HIBEAM/ANNI beamline at the ESS, a brute force method was utilized to study the maximum effectiveness of an *ideal* reflector[20]; to do so, a gravitational Monte Carlo transport code with

[19] See Sec. 3.5.3 and [306].

[20] Here, for simplicity, an effective $m \to \infty$ was taken; thus, all neutrons reflect from the surface of the ellipsoid. Lower values of m can be rather easily integrated within the simulation if the NNBAR collaboration chooses to pursue this idea further. This is currently a proprietary simulation, but may also be considered within McStas.

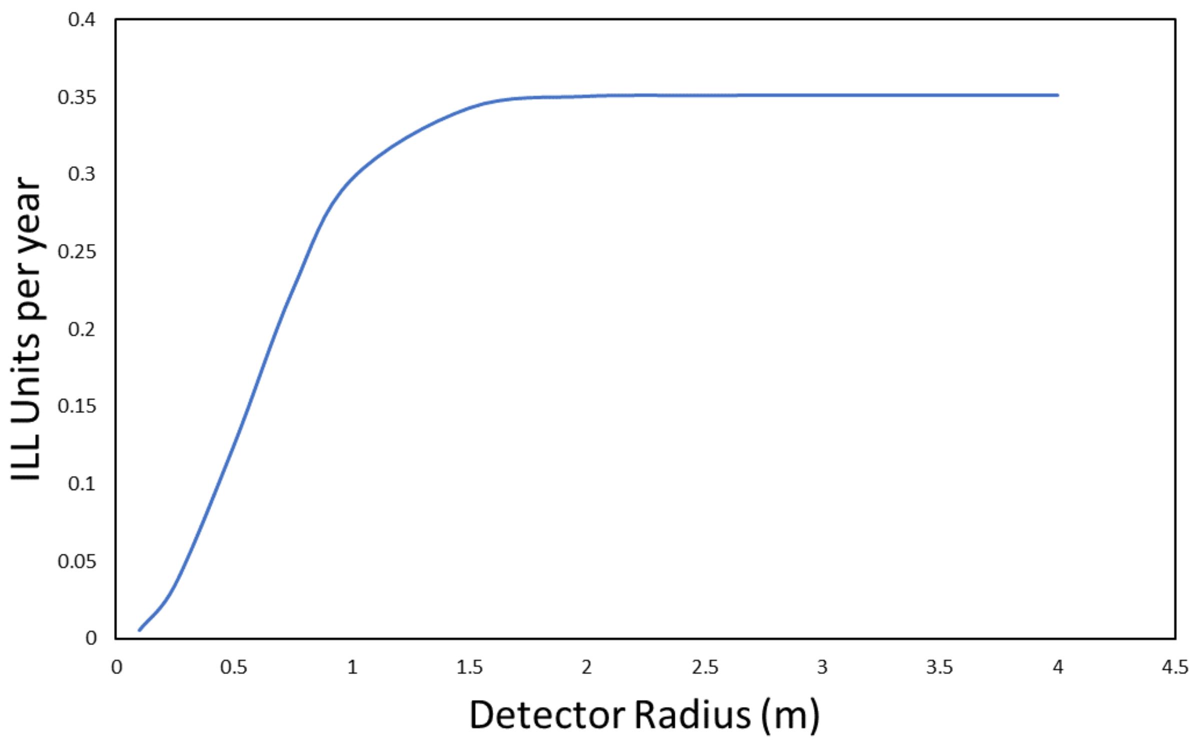

Figure 3.22: Sensitivity (in ILL units) for a $n \rightarrow \bar{n}$ search at HIBEAM/ANNI as a function of the radius of the annihilation target, assuming 1 MW of operating power. Given the usage of the ILL unit, this figure assumes comparable levels of reconstruction, background levels and rejection rates, signal efficiency, etc.; however, these will likely improve through the use of newer detector technologies and the potential installation of ellipsoidal-style supermirror reflectors. Plot has been smoothed.

an axially symmetric[21] ellipsoidal reflector was developed. A source developed by the ANNI collaboration [379] was utilized, as previously discussed in Sec. 3.2.1; the initial source consists of a 7×11 cm rectangle with a total flux of $\sim 1.5 \times 10^{11}$ n/s at a conservative 1 MW of operating power.

Taking heed of the top of Figs. 3.23, the geometrical constraints of the ellipsoid reflector are as follows:

- Consider a fully encapsulated source with a location at $z = 0$; thus, take a slightly larger area than the nominal one, say 8×12 cm. From this assumption, the minimum radius of any circumscribing circle lying tangent to the ellipsoid at $z = 0$ is $r_{\text{min}} = \sqrt{0.06^2 + 0.04^2} = 7.211$ cm.

- Use a cut-off "half" ellipsoid spanning the full half-length of the HIBEAM/ANNI beamline, and so $z_0 = 26.5$ m; the source must lie at the first focus position, and so $f = z_0$, and by syllogism $a - f \geq 0$ such that $a > 26.5$ m.

- Axial symmetry, and so the two semi-minor axes take values $b = c$.

- The maximum radius of a circumscribing circle at the center of the ellipsoid (also its cutoff plane) is taken to be the semi-minor axis, where $c = b = 25$ cm[22], and so has a total diameter of 0.5 m.

- From the above, one may then derive that focality is preserved when the semi-major axis a takes on values $a^2 = c^2 + f^2 = c^2 + z_0^2$.

The analytical definition of the interior volume of a candidate ellipsoid as considered at the top of Figs. 3.23 thus follows

$$\frac{(z - z_0)^2}{a^2} + \frac{x^2 + y^2}{c^2} \leq 1\,. \tag{3.10}$$

[21]Axially symmetric ellipsoids resulting from a single surface of revolution are the only basic geometric constructions which allow rays to pass from one focus to another upon a single reflection; general ellipsoids do not have this most important focal property. Of course, with the application of gravity on a spatially distributed source, these are merely approximations. See [204] for a robust discussion on differential reflector concepts.

[22]This could be expanded, given enough space for vacuum and magnetic shielding instrumentation in the guide hall.

For any transport with gravity, one can then consider when and where any neutron would cross this boundary surface; with small enough steps over the z-direction, the exact reflection point becomes known. From these reflection points, one can then track any neutrons flight time to the detector to calculate the sensitivity via $\langle Nt^2\rangle$ (i.e., it is assumed that at each bounce a "reset" occurs). In order to compute the reflection of the particle, one must calculate the normal vector at the reflection point (x_r, y_r, z_r) via

$$\hat{n} = \frac{\nabla f\left(\vec{x}_r\right)}{\left|\nabla f\left(\vec{x}_r\right)\right|} = \frac{\left(\frac{2x_r}{c^2}, \frac{2y_r}{c^2}, \frac{2z_r}{a^2}\right)}{\sqrt{\left(\frac{2x_r}{c^2}\right)^2 + \left(\frac{2y_r}{c^2}\right)^2 + \left(\frac{2z_r}{c^2}\right)^2}}\,, \tag{3.11}$$

from which one can then easily calculate the velocity vector of the reflected neutron via

$$\vec{v}_f = \vec{v}_o - 2\left(\vec{v}_o \cdot \hat{n}\right)\hat{n}\,. \tag{3.12}$$

In the presence of gravity and with a spatially distributed source, one easily posits that no one ellipsoidal configuration is by default the optimum one. Thus, the brute force Monte Carlo method adopted here throws all possible ellipsoidal configurations across all relevant geometric variables $\{a, b = c, f\}$ using uniform distributions, and then checks for consistency against the above listed geometric constraints. Those configurations which pass these cuts with an assumed value of $f = z_0 = 26.5\,\mathrm{m}$ are shown in Fig. 3.24; of the nearly 5 million thrown configurations, only about 15% pass.

With these configurations in mind, one can then begin the gravitational transport within the reflector. Though highly preliminary, these initial studies have shown some configurations[23] can reach sensitivities of ~ 0.55X ILL-equivalent units per year of running at $1\,\mathrm{MW}$. A large series of runs has not yet been completed, but can be easily pursued with enough computational time. Further optimizations for cost per area of the reflector can also be completed. However, many other potentially cheaper and highly effective reflector configurations are possible [372].

[23]Only about ~ 10 configurations were considered for this initial study.

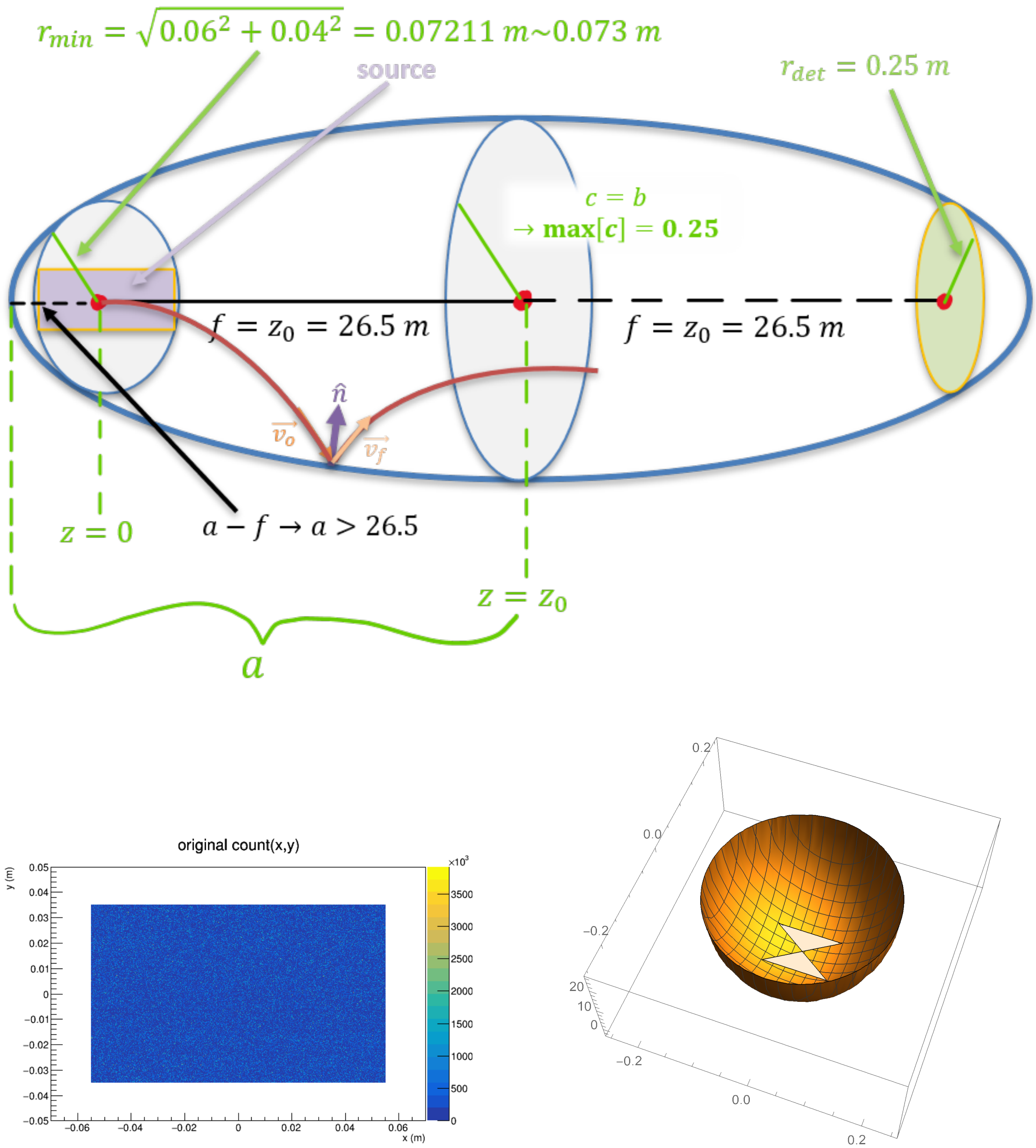

Figure 3.23: Top: A simple geometric overview of considerations for neutron transport with an ellipsoidal mirror. For these computations, only a "half"-ellipsoid spanning the space between the left-most and central tangentially circumscribed circles has been considered, though the full cross sectional curve is shown for effect. Bottom left: The dimensions ($\sim 7 \times 11$ cm) of the ANNI source are shown before entering the beamline; the vertices of this rectangle constrains the geometry of the ellipsoid. Bottom right: A representation of a possible ellipsoid is shown with a polygon inset whose vertices represent those of the ANNI source. The length of the half-ellipsoid is taken to be roughly half of the available beamline length at $a \sim 26.5$ m, and so is not shown to scale.

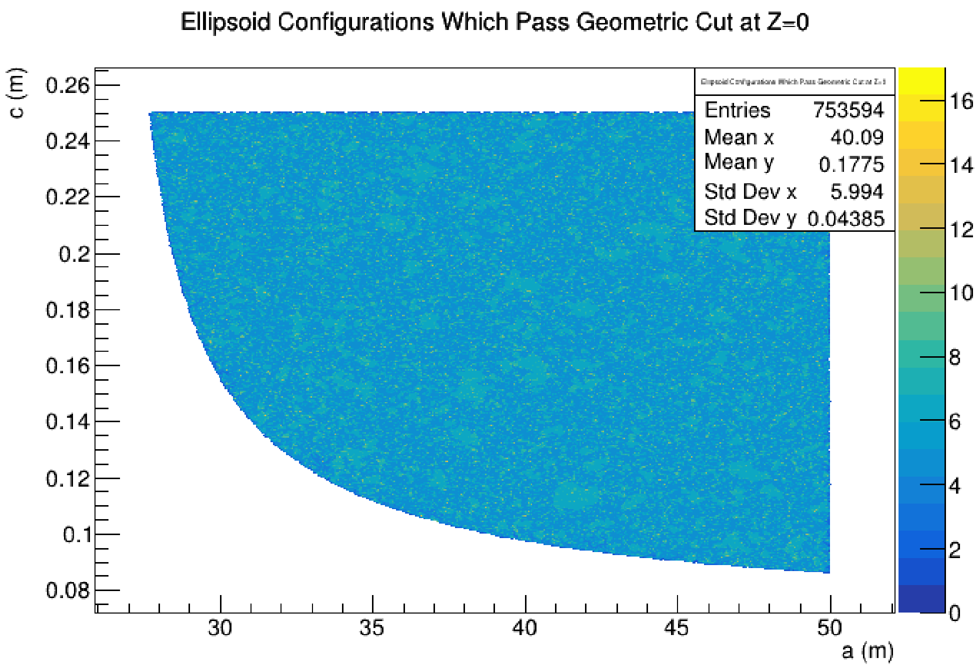

Figure 3.24: A two-dimensional correlation plot of viable axially symmetric ellipsoidal reflector geometries which can fit within the allotted space of the HIBEAM/ANNI beamline, assuming a ~ 26.5 m total length. This sampling was done via random number generation of 5 million potential values for both the foci positions, along with the semi-major and semi-minor axes; thus, only $\sim 15\%$ pass the requisite geometric constraints from the containment of the source and the instrumentation space for the beamline with an assumed 0.5 m-diameter $\bar{n}$ detector.

3.5.3 $\bar{n}$ Phase Shift Suppression

A key attribute of a traditional free $n \rightarrow \bar{n}$ conversion search is a neutron beam optically focused [326, 204, 56] onto an annihilation target to minimize interactions with, e.g, a vacuum vessel or neutron guide wall. The difference in neutron and antineutron interactions with wall material have been assumed to act as a large potential difference, suppressing the oscillation; thus, the interaction can be seen as destroying any wave function component, which effectively "resets the clock" for the oscillation time measurement. With this assumption, only the neutron's free flight time since the last wall or mirror interaction contributes to the probability to find an antineutron, necessitating a large area experimental apparatus in practice.

An *almost* free $n \rightarrow \bar{n}$ oscillation search has recently been proposed [307, 267] in which one allows slow, CNs (and antineutrons) (with energies of $< 10^{-2}$ eV) to reflect from effective $n/\bar{n}$ optical mirrors. Although the reflection of $n/\bar{n}$ had been considered in the 1980's for UCNs [144, 146, 223, 420] and recently in [267] for proposed experiments to constrain $\tau_{n\bar{n}}$, the authors have extended this approach to higher energies, namely where nominally cold, initially collimated neutrons can be reflected from neutron guides when their transverse velocities with respect to the wall are similarly very or ultra-cold. Conditions for suppressing the phase difference for neutron and antineutron were studied, and the required low transverse momenta of the $\{n,\bar{n}\}$ system was quantified, leading to new suggestions for specific nuclei composing the reflective guide material. It was shown that, over a broad fraction of phase space, the relative phase shift of the neutron and antineutron wave function components upon reflection can be small, while the probability of coherent reflection of the $\{n,\bar{n}\}$ system from the guide walls can remain high. The theoretical uncertainties associated with a calculation of the experimental sensitivity, even in the absence of direct measurements of low energy $\bar{n}$ scattering amplitudes, can be small.

An important consequence from this work could be that the conversion probability depends now on the neutron's *total* flight time, as wall interactions on these specific combinations of nuclei no longer reset the clock. Such an experimental mode relaxes some of the constraints on free neutron oscillation searches, and in principle allows a much higher sensitivity (potentially several orders of magnitude above the baseline NNBAR plan [204, 19]) to be achieved at reduced complexity and costs. It represents a new idea from within the community which requires a program of simulation and experimental verification. While this doesn't form part of the *current* core plan for the HIBEAM/NNBAR experimental program, it is considered as a promising future research direction, and experimental verification of this concept is under investigation. Full simulations and necessary beam studies of quantum mechanical facsimiles of this phase (such as spin) have yet to be completed.

3.6 Overview of Sensitivities and Conclusions

To summarize the findings of this chapter, see Tab. 3.1. Given the power of the new ESS source, even at only $1\,\mathrm{MW}$, one can achieve great strides in lower limits on $\tau_{nn'}$ with a mere month of running in a disappearance mode (see again Sec. 3.3.1). Note here as well that past experiments using UCN do not sample the magnetic field parameter space uniformly, while it is assumed throughout these calculations that HIBEAM's intended design can achieve this distinction. The low sensitivity to $n \to \bar{n}$ can improve approximately linearly only by increasing the time of running or the operating power; otherwise, ellipsoidal reflectors are needed to increase this sensitivity nonlinearly (see again Sec. 3.5.2.

In this chapter, I have detailed the main thrusts of the HIBEAM experiment at the European Spallation Source, the first stage of a research and design trajectory moving toward the full NNBAR experiment which aims to achieve a factor of ≥ 1000X $\langle Nt^2 \rangle$ figure of merit sensitivity increase over the previous ILL experiment. All initial beam simulations for this experimental program were completed by myself with the recently optimized ANNI beamline source [379]. All initial sensitivity calculations for $n \to \bar{n}$ and $n \to n'$ searches are my own, and use the full beam simulation; schematic designs of the experimental apparatuses to be used were also co-developed through my work with the NNBAR/HIBEAM collaboration. I have also incorporated $\bar{n}$C annihilation signal events generated by the independent generator discussed in Chap. 2 into the developing NNBAR detector simulation framework, and am actively involved in continuing discussions on how best to reconstruct these above any background going forward. Otherwise, I developed a first exploratory simulation on the use of potential ellipsoidal reflectors for an increase sensitivity for an $n \to \bar{n}$ experiment at HIBEAM.

Table 3.1: A comparison table between lower limit sensitivities for $n \to n'$ and $n \to \bar{n}$ achievable at HIBEAM under $1\,\text{MW}$ of power for 1 month and 1 year of running (within an ESS operating year of 200 days), respectively, at various detector radii and associated background levels (if pertinent). Experimental lower limits of $\tau_{nn'}$ are shown for ventures using UCN, primarily from re-purposed neutron electric dipole moment apparatuses. See again Fig. 1.23 for further context. Note that the experimental sensitivities of UCN experiments do not have uniform sampling over the magnetic field regimes, while HIBEAM will largely probe such parameter space quite uniformly. Simulations of small $r = 0.25$ detectors using a low background count rate were not completed.

HIBEAM Detector Radii (m)	$n \to \bar{n}$ (ILL Units)	$\tau_{nn'}$ ($n \to n'$, s)	$\tau_{nn'}$ ($n \to n' \to n$ w/1 n/s bkgr., s)	$\tau_{nn'}$ ($n \to n' \to n$ w/0.1 n/s bkgr., s)
$r = 1.0$, $\lvert(0, 0.2)\rvert$G	0.297	246	72.2	96.3
$r = 0.5$, $\lvert(0, 0.2)\rvert$G	0.125	192	58.6	78.1
$r = 0.25$, $\lvert(0, 0.2)\rvert$G	0.035	112.6	47.3	—
UCN, $\lvert(0.08, 0.17)\rvert$G [91]	—	17	—	—
UCN, $\lvert(0.15, 0.25)\rvert$G [99]	—	3	—	—
UCN, $\lvert(0.025, 0.125)\rvert$G [32]	—	12	—	—
UCN, $\lvert(0.05, 0.25)\rvert$G [8]	—	9	—	—

Chapter 4

$n \to \bar{n}$ and Atmospheric Neutrinos at the Deep Underground Neutrino Experiment and Future Directions

The forthcoming Deep Underground Neutrino Experiment (DUNE) offers a rich experimental program, including beam-derived long-baseline neutrino oscillation studies, ν_τ appearance and reconstruction, the constraining of non-standard neutrino interactions, and of course many avenues toward BSM searches for processes such as baryon number violation (BNV). DUNE will have one of the largest proton and neutron abundances of any future experiment, and so plans to include searches for proton decay ($p \to K^+\nu$) and neutron–antineutron transformation ($n \to \bar{n}$) among many other possible beyond Standard Model (BSM) processes. In this chapter, I seek to understand the prominence of atmospheric ν's by investigating their overall expected rates, interactions types, and reconstruction in the DUNE far detector using fully-oscillated three-flavor Honda atmospheric ν fluxes as inputs to the `GENIE` event generator; these will serve as backgrounds for many BSM searches such as $n \to \bar{n}$. Using fully reconstructed signal and background samples, the simulated response of a $10\,$kt detector module is able to be studied across a wide range of $n \to \bar{n}$ signal topologies, as well as background atmospheric ν flavors, energies, entry angles, topologies, and interaction types. These analyses use a now standardized automated (deep) learning technique utilizing both convolutional neural network (CNN) and boosted decision tree

(BDT) schemes [243, 257, 12] to separate signal from background and produce lower limits for $\tau_{n\bar{n}}$. Beyond rare process identification, these techniques have been used to inform triggering schemes for both μBooNE and DUNE. The MC samples developed for the work described here are now available to the broader community, and currently serve as the preeminent sources of BSM signal and background events within the DUNE High-Energy Physics Working Group. Work continues today on the $n \to \bar{n}$ and atmospherics analyses, including studies of proton decay in parallel. Some of the work described in this chapter is being prepared for publication [72] with higher statistics samples compared to past analyses [257, 12], and is somewhat preliminary[1].

The overarching goal of this work is to understand potential theoretical model uncertainties as a function of a given *signal* nuclear model configuration of Fermi motion and intranuclear cascades[2]. Disparities between these models can cause topological differences in the final state for both signal and background, and so automated analyses can yield different results for signal efficiencies, background rejection rates, and so too $\tau_{n\bar{n}}$ lower limits. By iterating across these configurations (which are not in principle reweightable to one another), a kind of model uncertainty can be assessed for a given rare signal. If many of the MC model configurations agree amongst themselves and cluster around a particularly narrow band of values for $\tau_{n\bar{n}}$, then the future experimental analysis of rare signals like $n \to \bar{n}$ can be interpreted to be safe from potentially underdeveloped simulation; an opposite outcome requires much future work to identify and correct aspects of the nuclear model to refine the signal[3] and background predictions. Similarly, this latter potentiality requires further development of reconstruction and deep learning techniques for signal identification going forward; some paths toward these goals will be highlighted.

[1]Many thanks to Y-J. Jwa, V. Pec, C. Sarasty, J. Hewes, and C. Alt for their collaboration on this work. Thanks as well to the leadership team of the DUNE High-Energy Physics Working Group.

[2]The work described in this chapter on atmospheric neutrino backgrounds for rare signals *should not be interpreted* as being able to assess uncertainties regarding atmospheric neutrino oscillation analyses and associated extraction of oscillation parameters. However, the work done in this vein and the MC samples produced will greatly inform parallel efforts such as CAFAna [53], and work with these collaborators will continue.

[3]See again discussions throughout Chap. 2.

4.1 The Deep Underground Neutrino Experiment and Liquid Argon Time Projection Chambers

Nearly a mile underground [14], the gigantic liquid argon time projection chambers (LArTPCs) of DUNE offer unique capabilities in charged particle tracking and energy reconstruction, making it a wonderful detector for intranuclear rare event searches. An overview of the full experiment and one of the four planned detector modules (each with a $10\,\mathrm{kt}$ fiducial volume) can be seen in Fig. 4.1.

Originally developed by Rubbia in 1977, LArTPCs show great promise for particle physics discovery. To have bubble chamber quality images with well defined three dimensional topological and time-zero information, photon-electron (γ-e) discrimination power, and direct access to $\frac{dE}{dx} \propto \frac{dQ}{dx}$ data via charge collection offers physicists a profound view onto fundamental interactions, both in the context of the SM and beyond. As illustrated in Fig. 4.2, this is accomplished via the ionization of the LAr following an interaction which produces charged particles[4]; as the charged particles move through the medium, electrons are displaced. With an application of an electric field, these are then drifted toward sense wire planes of $\sim$mm wire spacings. The pitches of these wires permit the reconstruction of two-dimensional projections of the full three-dimensional event topology, and the collected charge at each point informs the energy deposition across the topology. Of course, the precision of these techniques for track and physical quantity reconstruction is subject to wire noise [11] and LAr purity [16].

Currently, DUNE plans to run with two single phase LArTPCs, a dual phase LArTPC, along with a fourth "module" opportunity. Single phase implies that the whole of the detector medium is in a liquid phase and uses a horizontal drift, while a dual phase setup utilizes both liquid and gaseous argon with a vertical drift to allow passage and avalanching of ionization electrons through the gas phase, increasing the signal-to-noise ratio in the process. Each of these detector types are being investigated by the DUNE collaboration with ProtoDUNE-SP and ProtoDUNE-DP detectors currently running at CERN [9, 403, 157].

[4]Neutral particle detection is possible, especially for unstable particles such as π^0's via their photon decay products which can then pair-produce. Other species, such as neutrons, can in principle be detected via their absorption on other nuclei, which can then de-excite via photons [15].

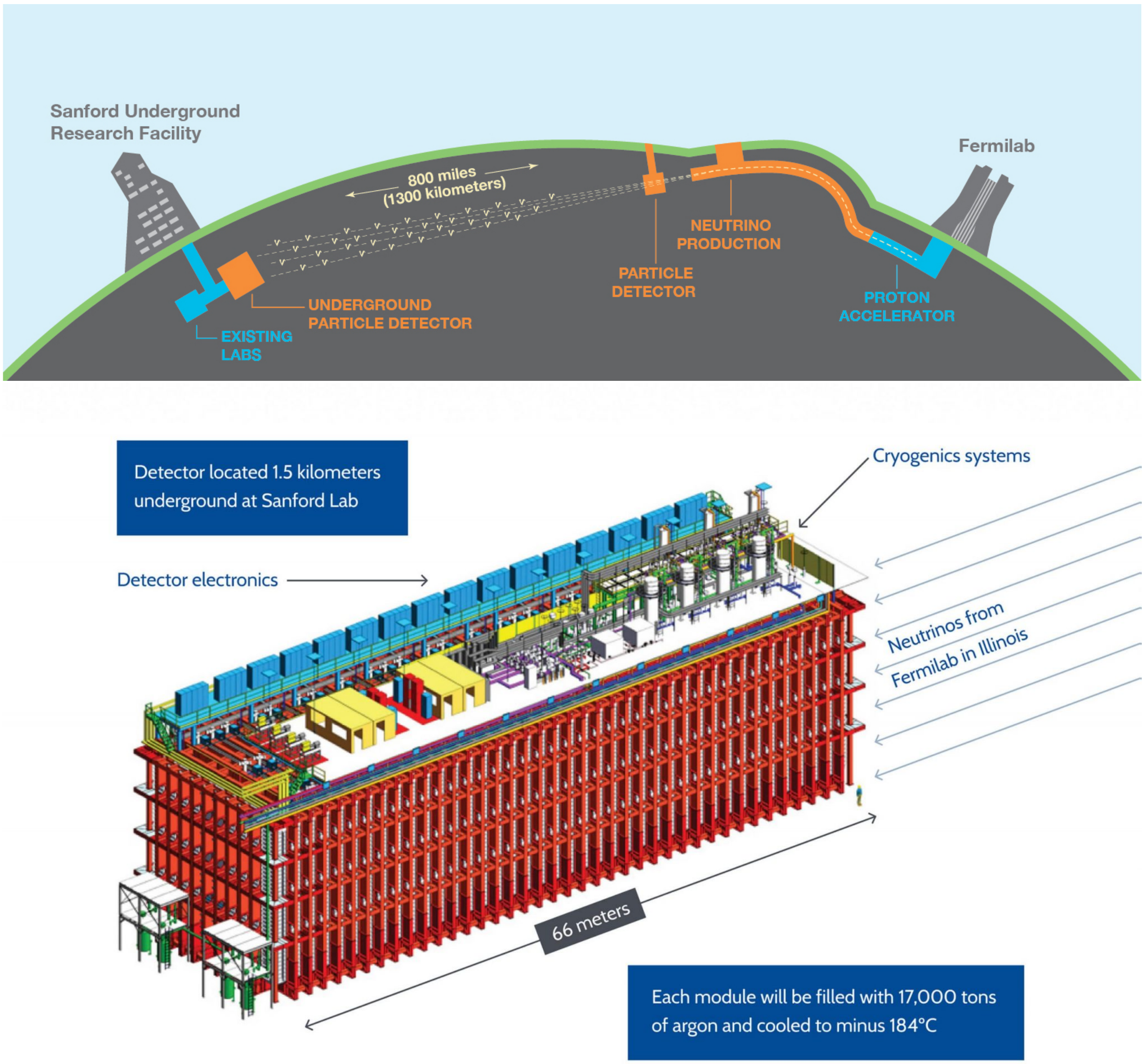

Figure 4.1: Top: An overview of the full DUNE experiment is shown. An accelerated proton beam spallates on a target at Fermilab, producing unstable particles (usually mesons) which in turn decay into neutrinos. The newly created neutrino beam then travels through the Earth some $1300\,\mathrm{km}$ to the Sanford Underground Research Facility in Lead, South Dakota, where the oscillated neutrinos are then measured within the detector modules. Bottom: An overview of a single $10\,\mathrm{kt}$ fiducial volume DUNE detector module. Taken from [396].

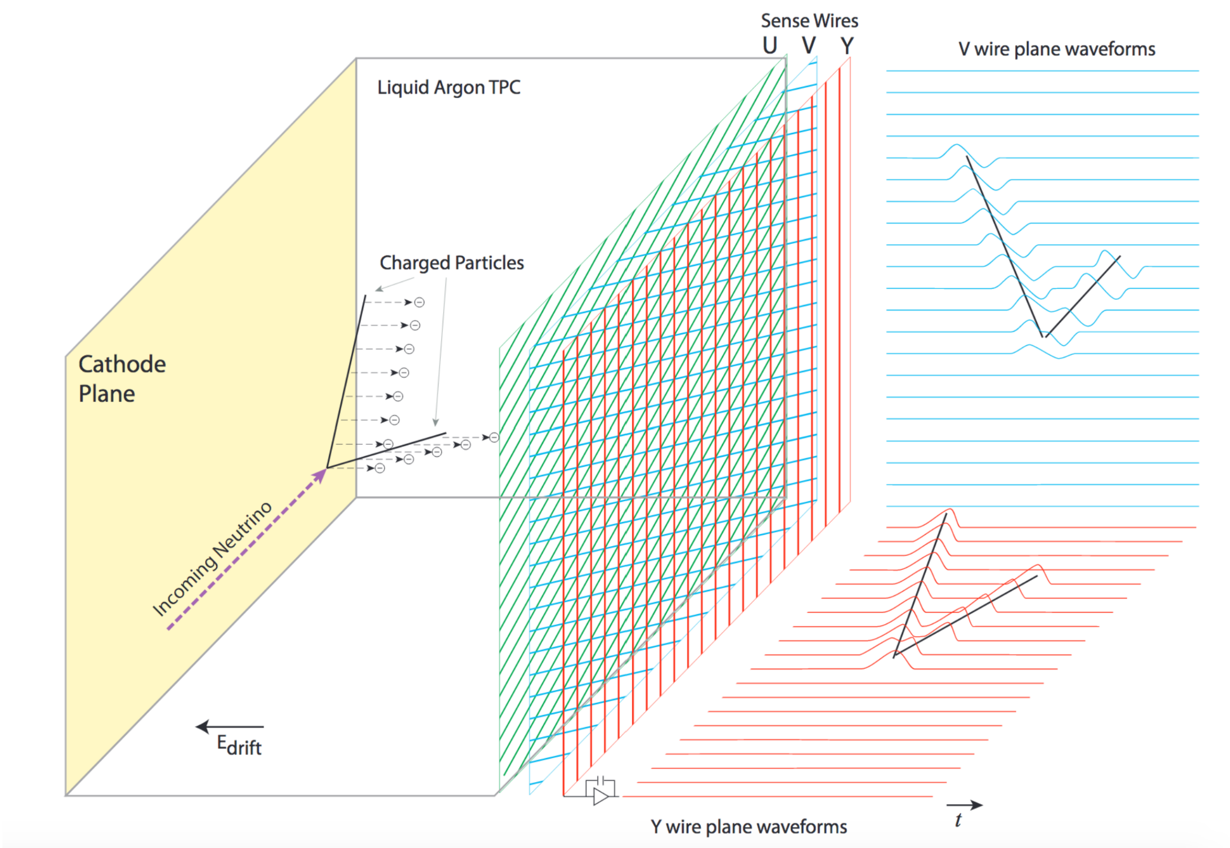

Figure 4.2: A schematic overview of a LArTPC is shown. Charged particles ionize the LAr medium, and the produced electrons are drifted to wires to produce three-dimensional images of the topology.

4.2 Atmospheric Neutrino Backgrounds

Atmospheric neutrinos play a critical role in shrouding beyond Standard Model signal events. Their continuous energy and momentum spectra can create effectively innumerable topologies which may be mis-identified as an $n \to \bar{n}$ event, either by producing multiple pions, or by other species (such as knock-out protons) being mis-construed as pions during reconstruction. However, it is expected that LArTPC's high spatial resolution will prevent much of this overlap given the unique semi-spherical topology an $n \to \bar{n}$ event. Automated analysis methods can in principle differentiate the visual characteristics and detector-generated physical observables between these. Here, I will discuss the new methods developed to begin studies of the effects for these backgrounds.

4.2.1 Brief Overview

Atmospheric neutrinos are generated via decay chains following high-energy cosmic ray interactions taking place in the upper atmosphere; here, unstable particles (muons, pions, etc.) can decay quickly, producing neutrinos and other species. It is assumed that the predominate species of neutrinos generated from such interactions are entirely of $\{\nu_\mu, \bar{\nu}_\mu, \nu_e, \bar{\nu}_e\}$ types. It is expected that their flux follows [291] a power law

$$\Phi_{\nu_\alpha} \sim E^{-3}\,, \tag{4.1}$$

for any given neutrino species α. Of course, neutrinos have mass, and thus oscillate [291, 218] in vacuum between any two species α and β as

$$P_{\nu_\alpha \to \nu_\beta}(L, E) = \sum_{k,j} U^*_{\alpha k} U_{\beta k} U_{\alpha j} U^*_{\beta j} \cdot e^{-i\frac{\Delta m_{kj} 2 L}{2E}}\,, \tag{4.2}$$

$$P_{\bar{\nu}_\alpha \to \bar{\nu}_\beta}(L, E) = \sum_{k,j} U_{\alpha k} U^*_{\beta k} U^*_{\alpha j} U_{\beta j} \cdot e^{-i\frac{\Delta m_{kj} 2 L}{2E}}\,, \tag{4.3}$$

where U_{mn} is the PMNS mixing matrix [218, 230]. In order to assess any experimental expectations as to their rates, one must consider oscillations through matter as they pass through the Earth. This is accomplished [230] via the transport equation

$$i\frac{d\vec{v}}{dt} = \frac{1}{2E}\left[U\mathrm{Diag}\left(0, \Delta m^2_{21}, \Delta m^2_{31}\right)U^\dagger \pm 2EV_m)\right]\vec{v}\,, \tag{4.4}$$

where $U = U(\theta_{12}, \theta_{13}, \theta_{23})$ is the PMNS mixing matrix, and Diag(a, b, c) represents a diagonal 3×3 matrix of first diagonal $(1, 1)$ element a, second diagonal $(2, 2)$ element b, and third diagonal $(3, 3)$ element c, and $V_m = \sqrt{2}G_F N_e \mathrm{Diag}(1, 0, 0)$ is the matter potential, where the Diag$(1, 0, 0)$ matrix picks out the electron component, thus permitting a coherent interaction of neutrinos with matter [218], and so inducing further interferences via oscillations[5].

4.2.2 Honda Fluxes, Coordinates, and Improvements to `GENIE`

The Honda [247] group has developed atmospheric neutrino flux models taking into account the multiphysics of their generation, including also the effects of air currents, temperatures and seasons, Earth's magnetic field, geographic factors, etc. Production height is also has a small but quantifiable contribution to these calculations, and though known, is currently ignored in these studies. Fluxes can also change slightly dependent upon the solar cycle (during a solar maximum or minimum). For the following work, a production height of 15 km is assumed, and the flux of neutrinos through the Homestake mine site (the future home of DUNE) at a solar maximum is considered.

From all these considerations, the Honda group produces large tables considering the flux of neutrinos through bins of a consistent solid angle, all logarithmically spaced in initial energy from 0.1-$10,000$ GeV; here, a conservative energy spectrum cutoff of 100 GeV is chosen for these background studies. Due to the logarithmic binning, there is quite low energy resolution; tools such as CAFAna [53] will resolve these issues in the coming years, with much input expected from this work and the numerical interpolations to follow. The Honda tables are by default unoscillated, and the four flavor types are read into `GENIE` during atmospheric event generation, taking account of their angular and kinematic correlations.

[5] Matter effects are generally introduced as a modification of the neutrino propagation with respect to the vacuum.

The coordinates used by the Honda group are known as “topocentric horizontal”, a right-handed Cartesian system, which is to say that the assumed z-axis points toward the zenith above a chosen flux calculation point (the Homestake site for us), the x-axis points toward geographic south, and the y-axis toward the geographic east. However, given the chosen coordinate system of DUNE relies on the neutrino beam direction, this implies that the coordinate systems are quite misaligned. These differences are explored visually in Fig. 4.3.

The coordinate system differences were initially resolved by W. Wu and colleagues [416] in 2018 using `GENIE`v2, which at the time was bugged by an outdated implementation of the atmospherics generator module and which had mistakenly used a left-handed coordinate system. However, upon adoption of `GENIE`v3 (used throughout this work), this bug was resolved; however, the coordinate transformations were not re-corrected within LArSoft, and so have been for this work.

Once the atmospherics generator had it’s coordinates corrected in `GENIE`v3, the rotations necessary become quite simple, as illustrated in the central schematic of Fig. 4.3. Effectively, $z_{Honda} \rightarrow z_{DUNE}$ via a $90°$ rotation about the x_{Honda}-axis to the plane of the earth, bringing with it and aligning $y_{Honda} \rightarrow y_{DUNE}$; this is then followed by a right handed rotation about the new zenith-directed y_{DUNE}-axis by a $-7.17°$ rotation. Note here that this only rotates *the coordinate system*, as the direction of the incoming atmospheric neutrinos are unchanged; thus, only the projections of the momentum components change, and the topology of the events themselves are not perturbed. Rather than later re-projected within LArSoft, this change is easily implemented in the `GENIE` generation stage via an Euler angle rotation flag command of `-R 0.125237636,-1.57079633,0.0`. This rotation was robustly validated[6] for consistency by studying reconstructed atmospheric samples originating from single Honda angular bins in the DUNE far detector, and was approved by the DUNE HEP Working Group.

In keeping with the current effort to assess and approximate the potential signal model uncertainties by iteration of nuclear model configurations, the same was pursued for background atmospheric neutrinos. `GENIE` provides a host of nuclear models which vary the assumptions made in the initial Fermi motion of the struck nucleon, and so too affect their cross sections. All nuclear models were utilized within `GENIE`v3.0.6, and new cross section splines calculated,

[6]Many thanks to V. Pěč for his collaboration on this work.

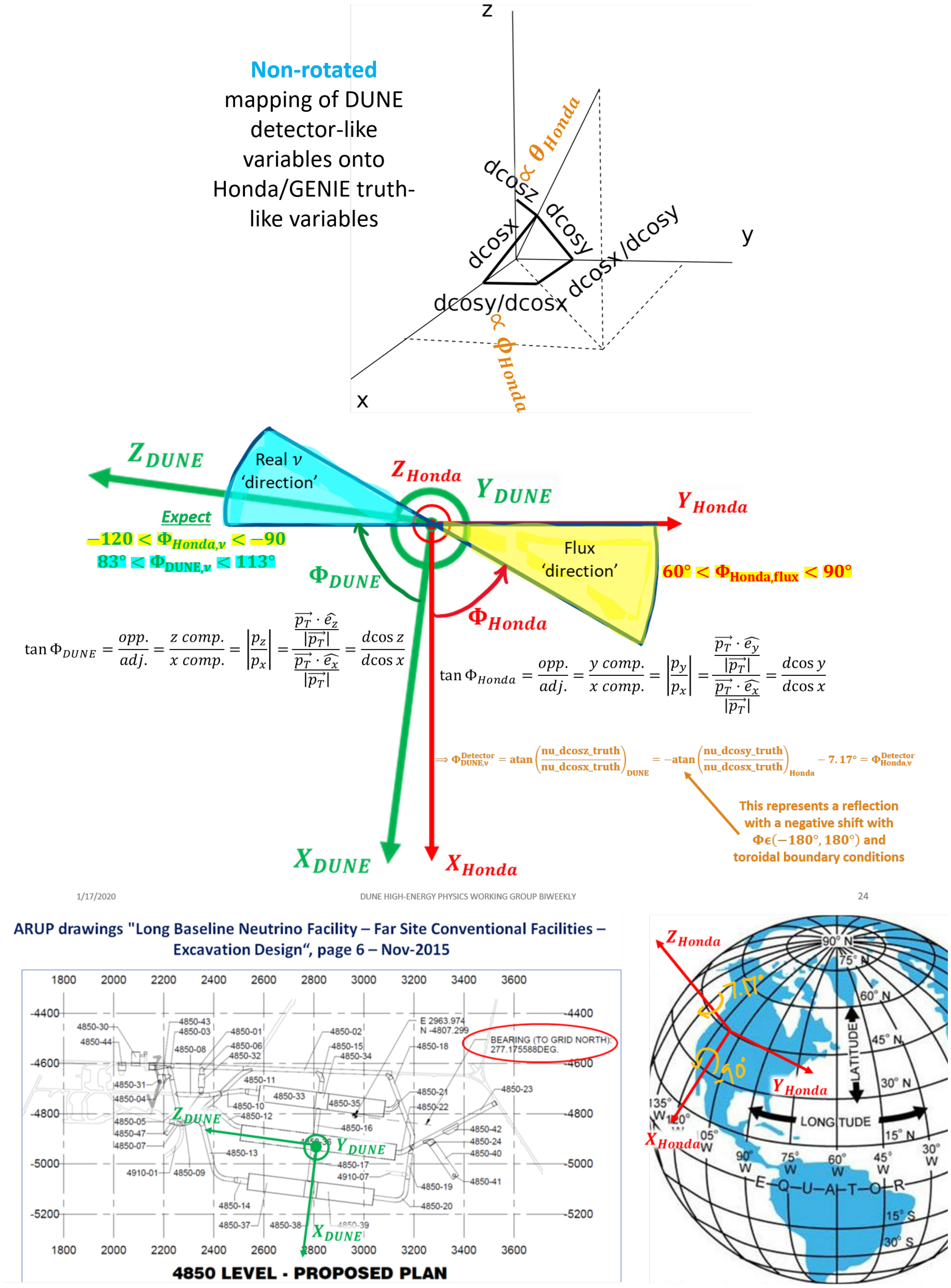

Figure 4.3: Top: DUNE coordinate system variables; illustration courtesy of V. Pěč. Middle: A visual explanation of atmospheric flux vs. neutrino direction within the DUNE detector coordinate system; events coordinate projections must be rotated to match. Bottom: The nominal Honda (topocentric horizontal) coordinate system is shown misaligned with the DUNE far detector coordinate system (aligned with the beam axis). A series of rotations must be completed to make sure the many directionally-dependent detector variables are properly transformed, while the topological objects of the neutrino interactions themselves are *not* rotated. This is completed within the GENIEv3.0.6 generation step.

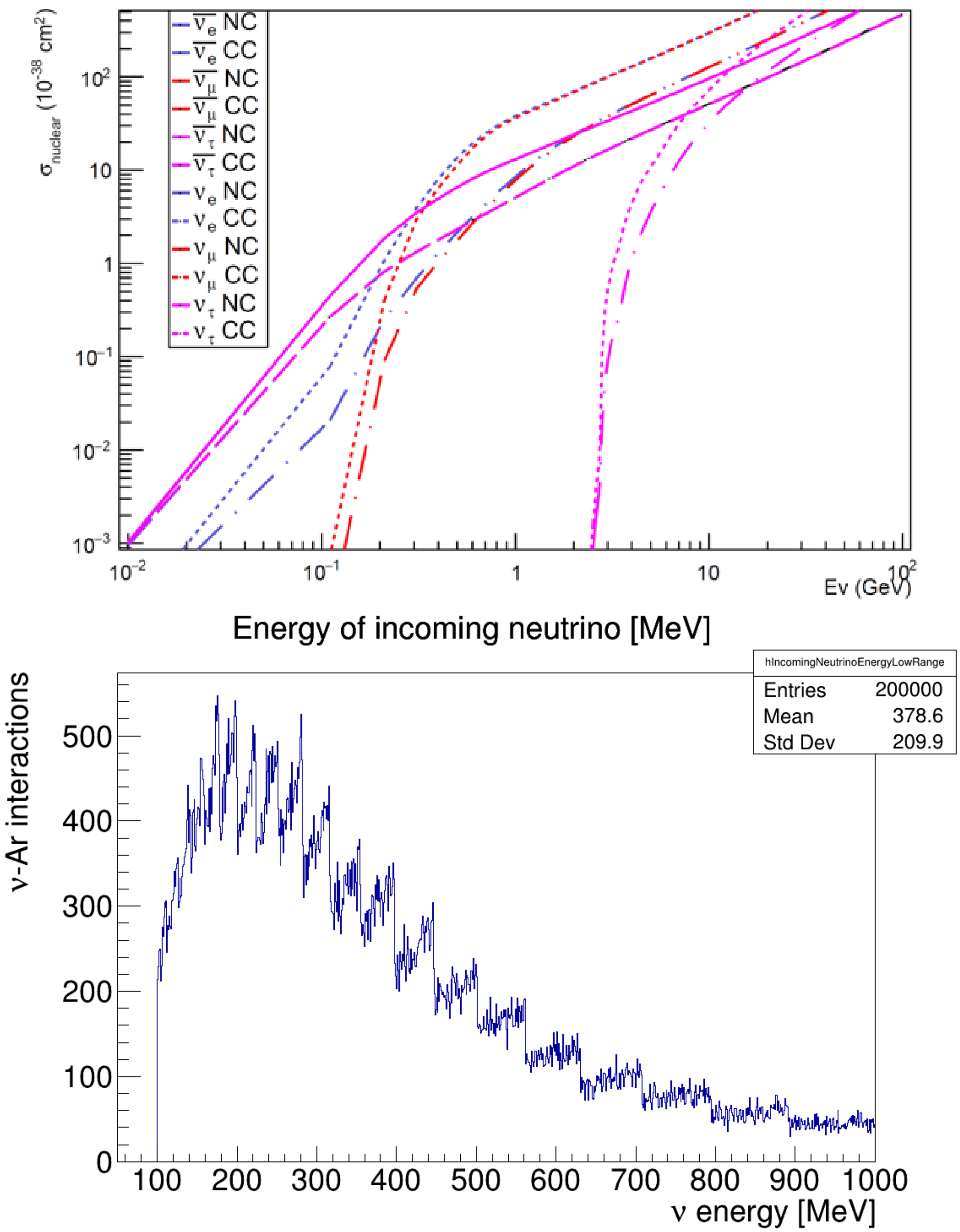

Figure 4.4: Top: Total neutral and charge current cross sections used within `GENIE`v3.0.6 using the default, relativistic, nonlocal Bodek-Ritchie nuclear model of Fermi motion with a phenomenological short-range-correlated tail, from the G18_10X tune. Other model configurations exist, and were all considered independently. All cross section splines have been recomputed for each nuclear model used in this work. Bottom: Previously unknown, a characteristic "stepping" of the atmospheric spectrum can be seen with high statistics and fine energy binning over a low initial energy range. This is due to the convolution of flat bins of logarithmically spaced energies from the Honda fluxes and an *approximately* linearly increasing cross section over the bins' widths. Such effects will be mostly smeared out in reconstruction.

as seen in Figs. 4.4. As an example, consider the approximate[7] formulation used in the current `QELEventGenerator` [40, 39] for quasielastic scattering interactions in `GENIE`:

$$\sigma \propto \int L_{\mu\nu} W^{\mu\nu} P\left(\vec{p}, E\right) d\Omega dE d^3\vec{p} \tag{4.5}$$

where leptonic and hadronic tensors are considered, along with the momentum distribution of the bound nucleon before scattering occurs, $P\left(\vec{p}, E\right)$. Thus, the assumed nuclear model of Fermi motion in principle partially dictates the behavior of the cross section, including both its overall shape and integral.

An as yet unresolved bug in `GENIE` was mutually discovered nearly simultaneously[8] through this work and other parallel ventures in Super-Kamiokande, and is illustrated in the right plot of Figs 4.4. When the atmospheric neutrino spectrum is considered at low energy under a high resolution,"stepping" appears. This is due to the effectively linearly increasing cross section of neutrinos (left plots of Figs. 4.4) when convolved with the flat, logarithmically spaced bins of the Honda flux tables. Though this bug still persists, development of a means of reshaping the spectrum to its appropriate form has begun locally within `GENIE` (though is not yet finished); other efforts are underway in parallel within the CAFAna [53] working group, of which this work is a future input. However, as the resolution of the energy reconstruction is not expected to be high at the low energies ($< 1\,\mathrm{GeV}$) shown here, this bug is not expected to vastly change any of the elements of the full $n \to \bar{n}$ analysis, which are primarily topological in nature. At higher energies, this effect is not easily visible. Reshaping the spectra using numerical methods will be pursued later in this section via interpolation.

With coordinates corrected and cross section splines computed for all nuclear model configurations, the next issue to address is the application of oscillations to the atmospheric neutrino fluxes. Originally, `GENIE` would begin with the four-type tables containing $\{\nu_\mu, \bar{\nu}_\mu, \nu_e, \bar{\nu}_e\}$ species over all angles and populated in logarithmically spaced energy bins. `GENIE` was modified to take in new inputs, instead containing six-type flux tables of all $\{\nu_\mu, \bar{\nu}_\mu, \nu_e, \bar{\nu}_e, \nu_\tau, \bar{\nu}_\tau\}$ over all angles and energies from 0.1-$10,000\,\mathrm{GeV}$.

[7]Many constants, kinematic variables, and energy conserving functions are not included here for simplicity.
[8]Many thanks to C. Marshall for discussions on this point.

Another change to GENIE meant to better estimate background rates for rare processes such as $n \to \bar{n}$ has been considered in this work. As illustrated in Fig. 4.5, it is known [130] from LEP data that, at particular energy transfers, rare multihadron final states can arise. Many of these, when produced via appropriate energy transfers from atmospheric neutrino interactions, including six-pion states, could *in principle* lead to extraneous backgrounds for intranuclear $n \to \bar{n}$ searches via similar topologies. Thus, a host (~ 100) rare yet known processes have been added to the internal PDG library of GENIE by hand; all values for these branching fractions were taken from the 2018 printed edition of the PDG [391]; if decays of resonances were observed but only an upper limit was derived, half of the published upper limit was taken as the branching[9]. All decays added to the internal PDG library were assumed to decay isotropically within GENIE's containerized PYTHIA build. Many of these branching ratios have values of 10^{-5}-10^{-10}, and are likely negligible; however, given the high statistics of the studies discussed here, they were thought important enough to add for multi-million event simulation samples.

[9]This will likely slightly overestimate any backgrounds, giving a more conservative approach to this work.

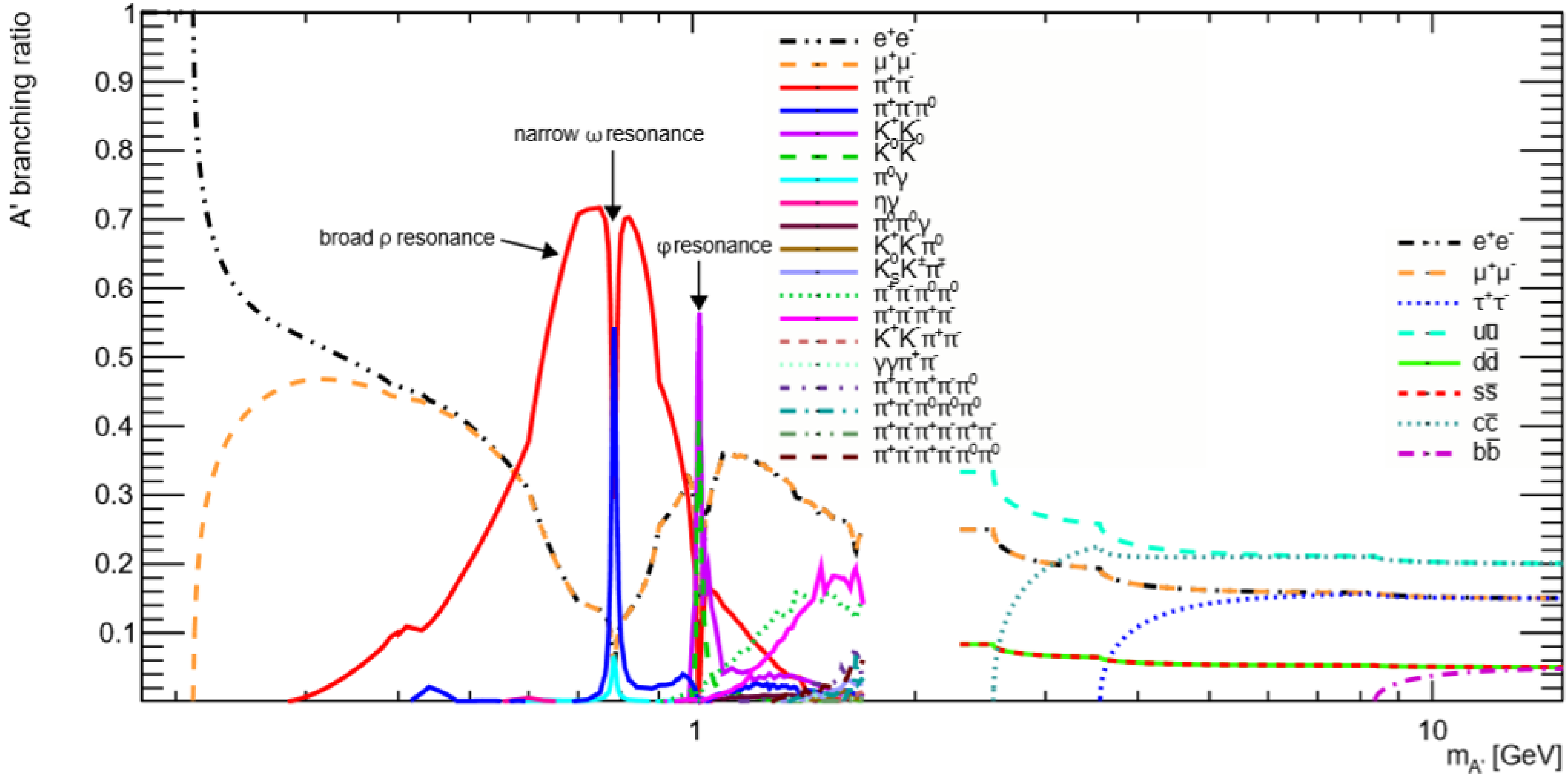

Figure 4.5: An illustrative plot is shown of branching ratios for a dark photon decay considered in [130] for contributions to measured standard processes. Many of these same resonances can be considered in terms of energy transfers rather than a dark photon mass, and can thus contribute to multihadron backgrounds for rare processes such as intranuclear $n \to \bar{n}$. Taken from [130].

4.2.3 Oscillation Parameters

With `GENIE` ready to receive new six-type inputs, one only needed to construct them. Oscillated fluxes are seen as especially important to $n \to \bar{n}$ searches, as τ decays can produce multiple hadrons in the final state which could mimic a signal event. The effects of oscillations were initially investigated by Hewes [243], where the addition of $\{\nu_\tau, \bar{\nu}_\tau\}$ species previously dropped signal efficiencies from $\sim 30\%$ to $\sim 20\%$; thus, in order to ascertain model theoretical uncertainties, they were added to this analysis.

Oscillations for the Homestake site were considered initially in [265], and this oscillation code was reworked to integrate well with the new six-type `GENIE` atmospherics driver. NuFit 4.1 [184] best fit parameters are utilized for these oscillation studies[10] from 0.1-100 GeV, and some of these probabilities can be viewed in Fig. 4.6. All angular correlations are preserved, and the atmospheric neutrino production height is assumed to be 15 km[11]. From these, new six-type neutrino flux tables are filled over the same angular and energy parameter space as the originals from Honda.

In the calculation of these new tables, hundreds of neutrino rays are thrown for each angular bin of $(\cos\theta, \phi)$[12], and then oscillated through the Earth an appropriate distance to the Homestake mine site. Regarding the Earth density profile, the PREM model [181] is utilized, dividing the Earth into 11 concentric layers. For each layer, the density (ρ) is given by a polynomial function in terms of the Earth radius, as shown in Fig. 4.7. Neutrino evolution through matter depends on the electron density (N_e) within; assuming the Earth density to be electrically neutral, N_e is then given by

$$N_e = \frac{\rho}{1 + r_{n/e}}, \tag{4.6}$$

[10] Many thanks to I. Martinez-Soler [291] for his collaboration on this work.

[11] Honda does provide tables of atmospherics production by altitude, though this was discovered after most of the development of this work. This is expected to be a small effect, especially for the background simulations in question. Future work can rather easily incorporate these dependencies, and will be necessary for any future atmospheric neutrino oscillations-focused sensitivity study (as with CAFAna [53]).

[12] The moniker used here actually represents a bin of a particular size; the widths of these bins in spherical coordinates within the Honda tables are $\Delta\cos\theta = 0.1$ and $\Delta\phi = 30°$.

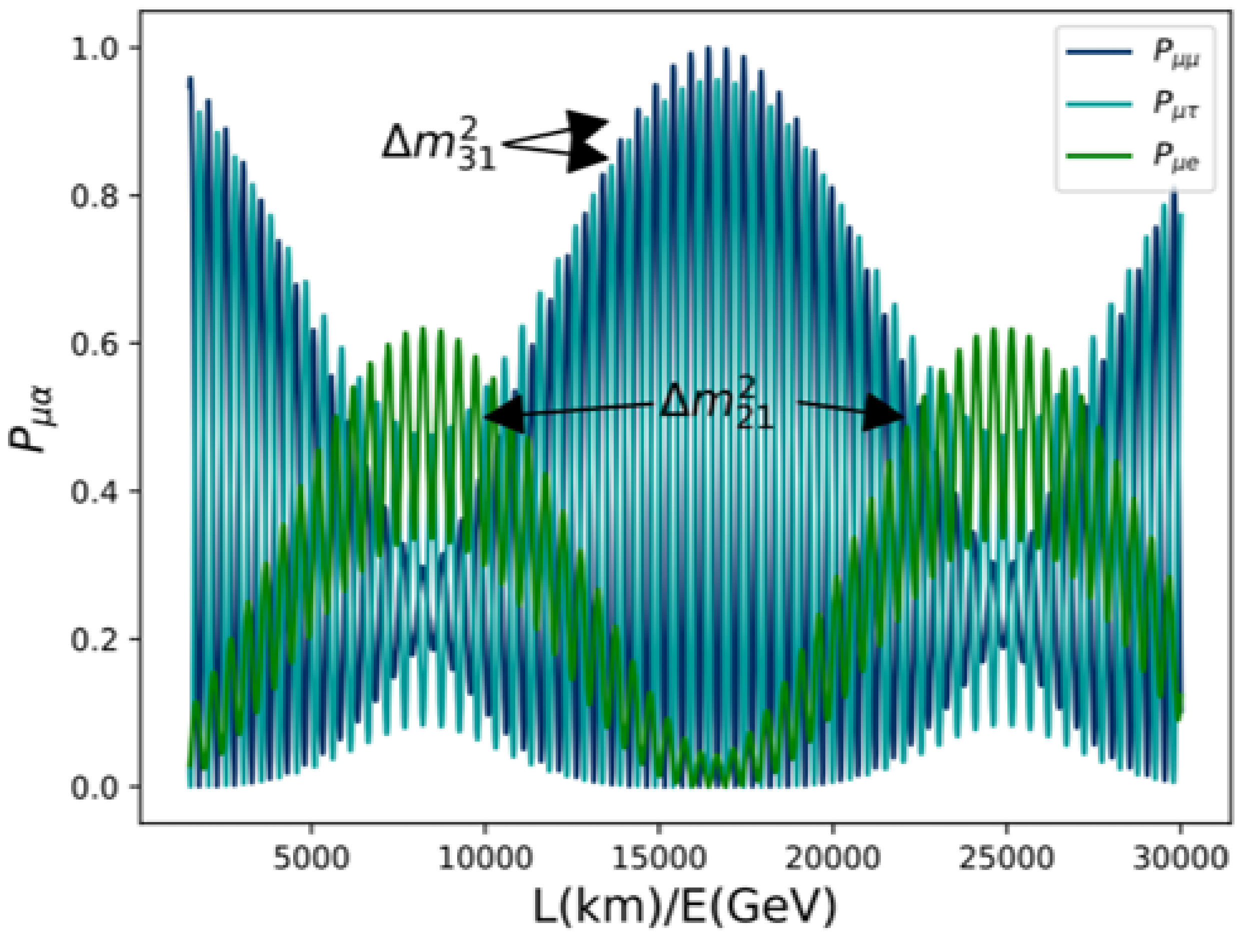

Figure 4.6: Oscillation probabilities as a function of L/E are shown for NuFit best fit results, and are used to estimate backgrounds for these particular studies. Courtesy of I. Martinez-Soler [291].

where $r_{n/e}$ is the neutron-to-electron ratio given by PREM, and takes on two distinct values: $\rho_{n/e} = 1.137$ for the Earth's core, and $\rho_{n/e} = 1.012$ for the Earth's outer layers. From hundreds of neutrino ray throws, one constructs an average effective oscillation probability bin-by-bin[13]:

$$\langle \Phi_{\nu_\beta} \rangle (\cos\theta, \phi, E) = \sum_\alpha \langle P_{\alpha\beta} \rangle (\cos\theta, E) \cdot \Phi_{\nu_\alpha}(\cos\theta, \phi, E)\,, \tag{4.7}$$

where[14]

$$\langle P_{\alpha\beta} \rangle (\cos\theta, E) = \frac{\int d\cos\theta P_{\alpha\beta}(\cos\theta, E)}{\int d\cos\theta}\,. \tag{4.8}$$

From these computations, and usage of the `GENIE`-generated cross sections, one is thus able to construct a final expected *oscillated* atmospheric neutrino spectrum at the DUNE Far Detector site in the Homestake mine.

4.2.4 Expected Oscillated Atmospheric Neutrino Spectra and Counts

In order to estimate the appropriate flux shape and expected count rates for each model configuration, despite the aforementioned bug in `GENIE`, interpolation is needed. Again refiguring codes developed within [265], this interpolation was accomplished using linear methods in a logarithmic energy basis, quite natural for Honda fluxes. Integrating over all directions, one can reconstruct the energy in new, small $1\,$MeV-spaced bins ($\Delta E = E - E_i$) for any energy E for any neutrino species α as

$$\log \Phi_\alpha(E) = \log \Phi_\alpha(E_i) + \frac{d\log\Phi_\alpha}{d\log E} \cdot (E - E_i)\ . \tag{4.9}$$

Upon this interpolation from 0.1-$100\,$GeV in energy across these very small bin widths, one reshapes the spectrum appropriately and so avoids any "stepping" effects; thus, one may utilize these new distributions within a proper reshaping technique during the generation step (to be implemented directly in `GENIE` and or via reweighting methods in CAFAna [53] at a later date). In any case, these new distributions can thus provide an accurate description of the expected neutrino

[13]Note that any dependence upon the distance traveled through the Earth, L, is encapsulated in the angular dependencies of the functions shown here.

[14]Note that the the probability is independent of ϕ, as the integral over the solid angle yields cancelling factors of 2π for both the numerator and denominator. Taking this into account, all neutrino rays thrown are by variation of $\cos\theta$.

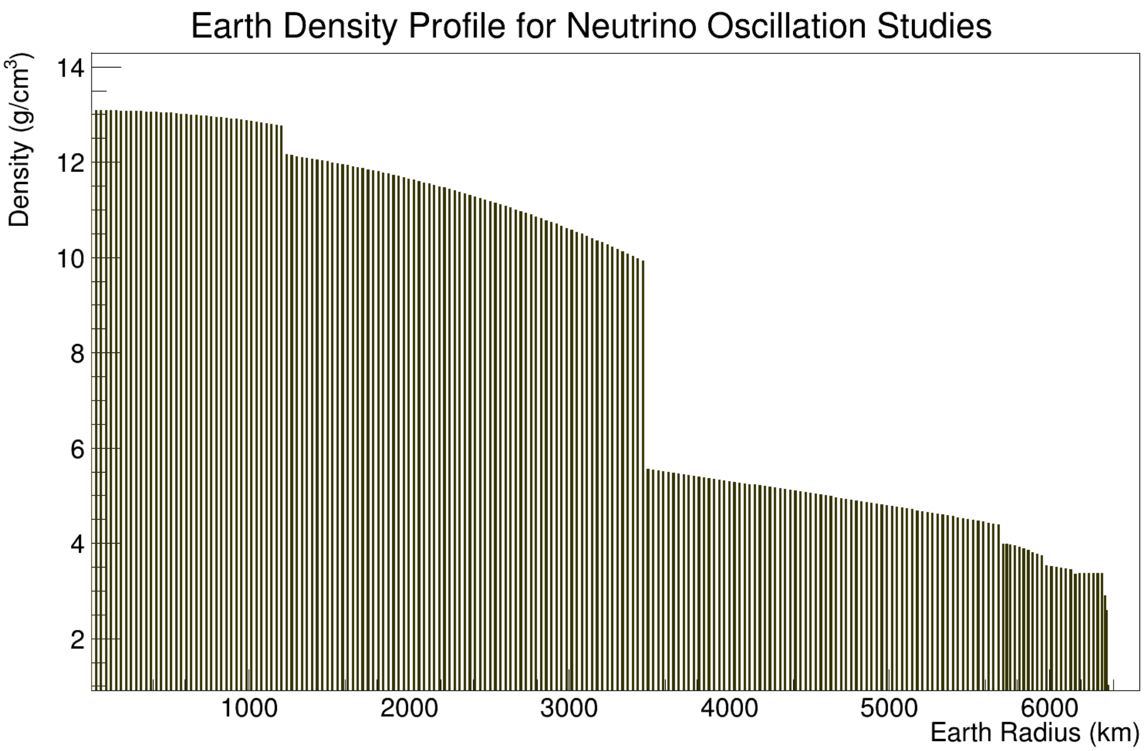

Figure 4.7: The density profile of the Earth, as used for the oscillations of neutrinos in this study.

spectra for all charged and neutral current processes, and can be seen in Figs. 4.8; when properly normalized, they also provide an estimated event rate, model configuration by model configuration.

An integration of these spectra (summation over bins) yields event counts via

$$N \sim \sum_{f=1}^{6} N_f \sim 40\,\text{kt of Argon} \times N_{\text{Avogadro}} \times \sum_{f=1}^{6} \sum_{E_i}^{E_m} \sigma\left(E_{i,f}\right) \cdot P_{\nu_f \to \nu_{f'}}\left(L, E\right) \cdot \Phi_{\text{Honda Interp.}}\left(E_{i,f}\right) , \tag{4.10}$$

for all six types of neutrinos (f) at all energies across $1\,\text{MeV}$ bins. With appropriate normalization factors for a $10\,\text{kt} \cdot \text{yr}$ run, this work yield counts per interaction type per model configuration, as shown in Tab. 4.1. Given the automated methods used for signal identification and background rejection (which utilize topological methods via the CNN), these counts[15] provide the normalization for this study's background rejection rate used in the final evaluation of $\tau_{n\bar{n}}$ lower limits.[16]

[15]Errors in these counts are not shown, but in principle depend on errors in the flux, cross section, and oscillation parameters. Parametrizations of the flux uncertainties as a function of energy are known; errors in NuFit parameters are of course known from measurements. Each of these are still being integrated now and will be shown in the final version of this table within [72].

[16]It should be noted here that this work implies that the DUNE Physics program could potentially access a total of ~ 800 $\{\nu_\tau, \bar{\nu}_\tau\}$ charged current appearance events for a $400\,\text{kt} \cdot \text{yr}$ exposure, ~ 500 of which would create visible τ hadronic decays with proper reconstruction [65].

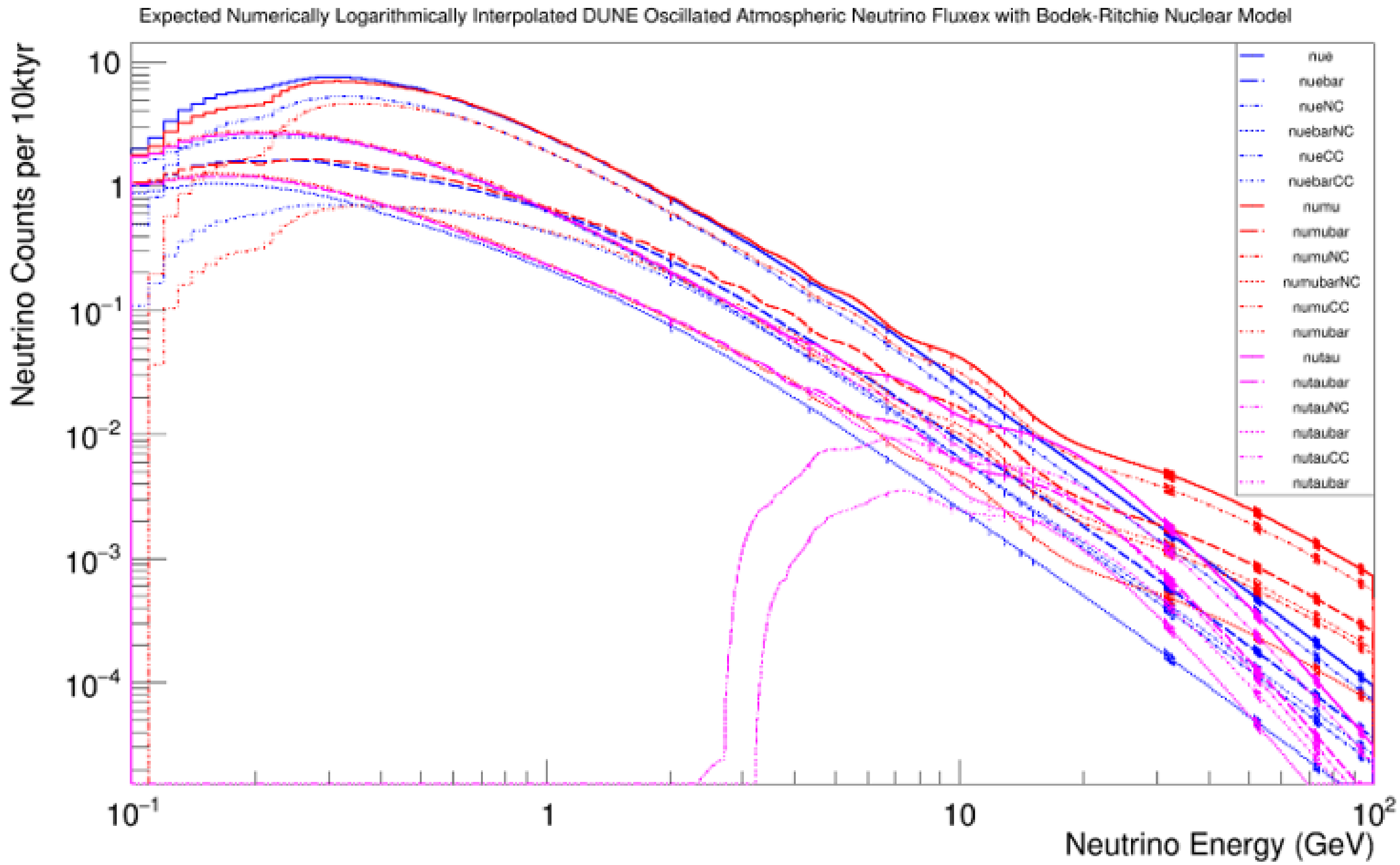

Figure 4.8: Expected oscillated total event count spectra per $10\,\mathrm{kt}{\cdot}\mathrm{yr}$, flavor-by-flavor, as a function of one of three available nuclear models in GENIEv3.0.6 G18_10X-derived proprietary tunes (other model configurations year rather similar plots). Here, a relativistic nonlocal Bodek-Ritchie nuclear model is shown. Others exist: a nonrelativistic local Fermi gas nuclear model, and a nonrelativistic nonlocal effective spectral function nuclear model. All predictions are within $\sim 10\%$ of one another. These curves can easily serve as the (pseudo)analytical distributions used within developing atmospheric oscillation sensitivity studies pursuing reweighting schemes such as CAFAna [53].

4.3 Iteration Across Nuclear Model Configurations in GENIE

Given the now standard DUNE automated analysis methods such as combined BDT and CNN deep learning techniques [257, 12, 243] (which shall be referred to as BDT(CNN) from here on) used to evaluate rare signal sensitivities via MC for processes like $n \to \bar{n}$, a question arises: How certain can one be in the BDT(CNN)'s ability to learn topological and kinematic features which are physically relevant? Though not entirely a "black box", this is a concern. Indeed, nuclear models of Fermi motion and intranuclear cascades can differ greatly, and many can be shown to have consistencies with lepton scattering data in particular areas of phase space [287, 323, 315]; however, generally, they all show inconsistencies with data [190, 164], even when the MC is tuned to data. Also, estimating true errors in the model configurations are quite difficult, as many of the configurations which are used are not technically reweightable to one another as certain correlations (such as momentum and radius) are not maintained[17]; this is only made worse with intranuclear cascade dynamics, which in the most realistic models (such as hA Intranuke 2018 in GENIE) are stochastic, and so again are not reweightable. Thus, in order to study the response of automated analysis techniques to varying models, one must compare them via entirely separate samples.

As discussed in Chap. 2, GENIE has several models of Fermi motion and intranuclear cascades which can be switched in and out of simulations. Fermi motion models include the Bodek-Ritchie nonlocal relativistic Fermi gas [109], and a nonlocal nonrelativistic effective spectral function [108] alongside the classic local nonrelativistic Fermi gas (see again the bottom plots of Fig. 2.25). Intranuclear cascades currently include the hA Intranuke 2018 model (which uses a reweightable table-based method to assess final states using a single effective intranuclear interaction), and the hN Intranuke 2018 model (using a full intranuclear cascade)[18]. These can all be combined via the model product

$$\{\text{hA}\,,\ \text{hN}\} \otimes \{\text{Bodek-Ritchie}\,,\ \text{Local Fermi Gas}\,,\ \text{Effective Spectral Function}\} \tag{4.11}$$

$$= \{\text{hA\_BR, hA\_LFG, hA\_ESF, hN\_BR, hN\_LFG, hN\_ESF}\}\,. \tag{4.12}$$

[17] See again Figs. 2.26 (bottom plots) for examples of this.

[18] See again discussions in Sec. 2.8.2.

Table 4.1: Total expected atmospheric neutrino event counts for $10\,\mathrm{kt} \cdot \mathrm{yr}$ of exposure for various nuclear model configurations at the DUNE Far Detector in the Homestake mine using logarithmically interpolated Honda fluxes and GENIEv3.0.6 G18_10X-derived model configurations. Total counts are important to assess uncertainties at particular exposures.

Bodek-Ritchie Nuclear Model	Total	CC	NC
ν_e	746.76	538.93	207.83
$\bar{\nu}_e$	188.833	113.893	74.9393
ν_μ	756.522	527.679	228.842
$\bar{\nu}_\mu$	216.493	126.104	90.3886
ν_τ	234.757	14.1756	220.581
$\bar{\nu}_\tau$	92.5186	5.14774	87.3709
Totals per $10\,\mathrm{kt} \cdot \mathrm{yr}$	2235.88	1325.93	909.953
Local Fermi Gas Nuclear Model	Total	CC	NC
ν_e	782.185	578.756	203.43
$\bar{\nu}_e$	197.509	124.602	72.9071
ν_μ	788.383	564.348	224.036
$\bar{\nu}_\mu$	224.443	136.450	87.9928
ν_τ	230.162	14.2033	215.959
$\bar{\nu}_\tau$	90.2157	5.16265	85.053
Totals per $10\,\mathrm{kt} \cdot \mathrm{yr}$	2312.90	1423.52	889.377
Effective Spectral Function Nuclear Model	Total	CC	NC
ν_e	711.738	503.908	207.830
$\bar{\nu}_e$	182.029	107.089	74.9393
ν_μ	725.050	496.208	228.842
$\bar{\nu}_\mu$	209.751	119.362	90.3886
ν_τ	234.699	14.1175	220.581
$\bar{\nu}_\tau$	92.5227	5.15187	87.3709
Totals per $10\,\mathrm{kt} \cdot \mathrm{yr}$	2155.79	1245.84	909.953

This set of nuclear model configurations[19] will be used to generate signal and background MC samples for tests of the BDT(CNN) response, and the distribution of $\tau_{n\bar{n}}$ lower limits. Considering the unknown nature of rare processes such as $n \to \bar{n}$, this is a good strategy[20].

The new model configurations enter GENIE as individual "tunes" concocted for each combination in Eq. 4.12. These new tunes were based on the public G18_10X tune (see the GENIEv3.0 manual and [39]). Here, the "18" refers to the year of development, the "10" refers to a local Fermi gas model of Fermi motion, and the "x" refers to a particular intranuclear cascade, where x=a implies use of the hA Intranuke 2018 model, and x=b the hN Intranuke 2018 model. The G18_10a tune contains slightly different fitted constants than the G18_10b tune to best reproduce known neutrino scattering data; these differences are therefore also present in $n \to \bar{n}$ modeling taking place within each public tune[21].

Changes were made to the $n \to \bar{n}$ generator module within GENIE [243] in order to accommodate these model configuration switches. Also, some general improvements to GENIE were made. In particular, a *local* definition of intranuclear nucleon scattering centers within the intranuclear cascade was implemented; previously, these scattering centers were presumed to have Fermi motion derived from a global Fermi gas (similar to the Bodek-Ritchie distribution, but with no short-range correlation tail). Once implemented[22], this made the overarching description of the nuclear environment more consistent for all nucleons involved in a given interaction. This change can create apparently softer final state proton spectra arising from intranuclear knockout events, as shown in Fig. 4.9. A full report of this change is being completed now within the GENIE collaboration, and will likely appear publicly within GENIEv3.4.

[19] Use of other generators, such as the one described in Chap. 2 and [229, 71], along with NuWro [222] and GiBUU [131], is forthcoming within DUNE; integration of new generators into the LArSoft framework is currently quite difficult, but progress is being made.

[20] This is *not* a good strategy for a neutrino cross section of oscillation analysis. However, the spread in oscillation parameters for neutrinos are not considered in this study, but only these effects on $\tau_{n\bar{n}}$ as dependent upon background simulations.

[21] See again Figs. 2.29 for GENIE simulations.

[22] Thanks to C. Alt for his collaboration on this work.

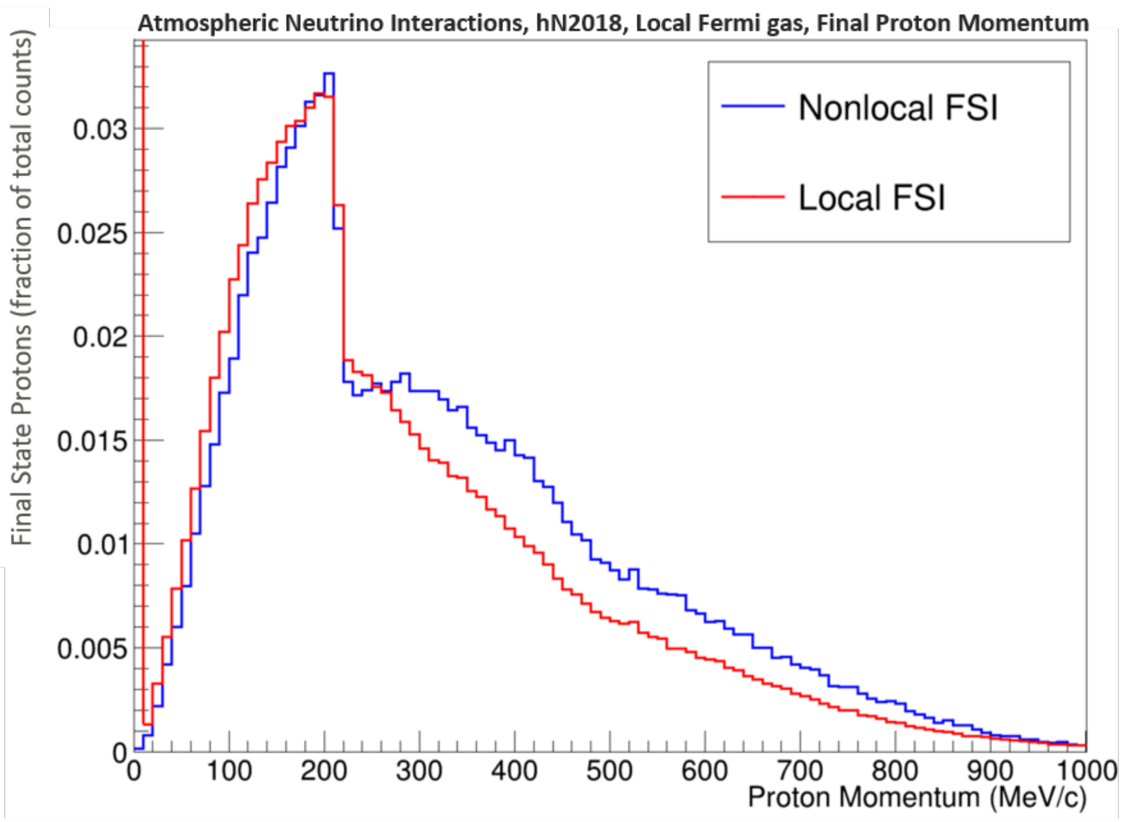

Figure 4.9: A plot of final state protons is shown for neutrino interactions on ^{40}Ar using a full intranuclear cascade and local Fermi gas (hA_LFG). When localization of intranuclear scattering centers is preserved, the harder blue spectrum is seen; when localization is turned on, the softer red spectrum appears.

4.3.1 Generation and Reconstruction of $n \to \bar{n}$ and Atmospheric Neutrino Samples

With most all changes to `GENIE`v3.0.6 made and new six-type oscillated atmospheric Honda fluxes created, event generation commenced on the FNAL grid for signal and background MC samples. In all, some 15.6 million events were produced across all available nuclear model configurations of Fermi motion and final state interactions for $n \to \bar{n}$ signal and background; see again Tab. 4.1 for atmospheric neutrino count predictions, and later Tab. 4.2 for individual sample sizes. All generated events were kept in the near universal `GHEP ROOT` file format. After generation, events were interfaced with `LArSoft` via the `AddGenieEventsToArt` module and placed uniformly across a 10 kt detector module[23], and from here the reconstruction chain for the samples could begin. Given the large statistics, this was accomplished with the aid of the DUNE Production team[24] using NERSC [303]; the full set of backgrounds was reconstructed over $\sim$ 2.5 months of computer time. All steps in the reconstruction chain, including `GEANT4`, detector simulation, and reconstruction were completed using collaboration standard setups in `dunetpc`v09_10_02[25]. Template `LArSoft .fcl` files were made and tested for each reconstruction step for both signal and background samples. An overview of all available reconstructed files is available for DUNE collaborators via [68]; all files are available on FNAL computing resources, and backed up on tape.

4.3.2 Some Example $n \to \bar{n}$ and Atmospheric Neutrino Event Displays

With samples made and reconstruction completed, event displays can now be made. In Fig. 4.10, a simulated intranuclear ^{40}Ar $n \to \bar{n}$ signal event using the hA_BR nuclear model configuration is shown with topology $n\bar{n} \to n\pi^0\pi^0\pi^+\pi^-$. The vertical axis is the "time to digital converter" (TDC) time value, measured with a sampling rate of 2 MHz; thus, one TDC time tick is 0.5 μs. The

[23] Given the scale of the Earth and associated oscillation distances from the atmosphere, the Homestake site is taken effectively as a point; thus, atmospheric neutrinos were generated uniformly across the full detector volume using a the `dune10kt_1x2x6` geometry. Of course, no detector position dependence is expected for rare proceeses.

[24] Thanks to K. Herner for his amazing collaboration on this work.

[25] This version of `dunetpc` was used due to issues which arose with τ-decays. From this and other parallel work, it was found that a bug in the `GEANT4` version used within `dunetpc`v8 produced unphysical energies in the multihadron decays of the τ. Upon fixing of these bugs, this work propelled the adoption of a new `dunetpc`v9 by LArTPC collaborations; this move greatly delayed the progress of this work by $\sim$ 4 months. Thanks to C. Alt for his collaboration and advocacy throughout this process. Thanks are also in order for R. Hatcher, T. Junk, E. Snider, and L. Garren for the many changes that had to be made to fix these issues.

horizontal axis is wire number. The bottom view is induction plane one, the middle is induction plane two, and the top is the collection plane. Hits associated with the back-to-back tracks of the charged pions are shown in red. The remaining hits are from the showers from the neutral pions, neutron scatters, and low-energy de-excitation photons. This topology was evaluated as "signal-like" by the automated BDT(CNN) analysis method detailed therein, and to be reviewed in Sec. 4.4. Now consider Fig. 4.11 showing a NC atmospheric neutrino event. Again, the vertical axis is the TDC value, and the horizontal axis is wire number and the plane configurations identical. This event mimics the $n \to \bar{n}$ signal topology by having multi-particle production and electromagnetic showers.

4.4 Nuclear Model Configuration Dependencies in Separation of Signal and Background for $\tau_{n\bar{n}}$

With all simulation samples now reconstructed, model configurations can be compared using automated analysis techniques. Currently, the full analysis is still under development within the DUNE High-Energy Physics Working Group and will be presented in full within [72]; despite this, some recent results using lower statistics MC samples will be presented alongside the DUNE TDR analysis [257, 12].

4.4.1 Automated Methods of Analysis

Hewes [243] originally developed techniques of visual discrimination between $n \to \bar{n}$ signal and atmospheric neutrino background topologies as reconstructed in the DUNE far detector in two-dimensional images of wire hits. Using a CNN, he was able to show good separation of signal and background via the visual uniqueness of the pion-star-like topology expected from an intranuclear $\bar{n}$ annihilation event. Given a set of training sample events from both signal and background, the deep learning technique is able to develop a "score" (s) for independently generated events as "signal-like" ($s \to 1$) or background-like ($s \to 0$). This work was built upon by Higuera and Jwa for the DUNE TDR analysis [257, 12] using a combined method of reconstructed physical variables from the DUNE far detector along with the same CNN score which were then inputted

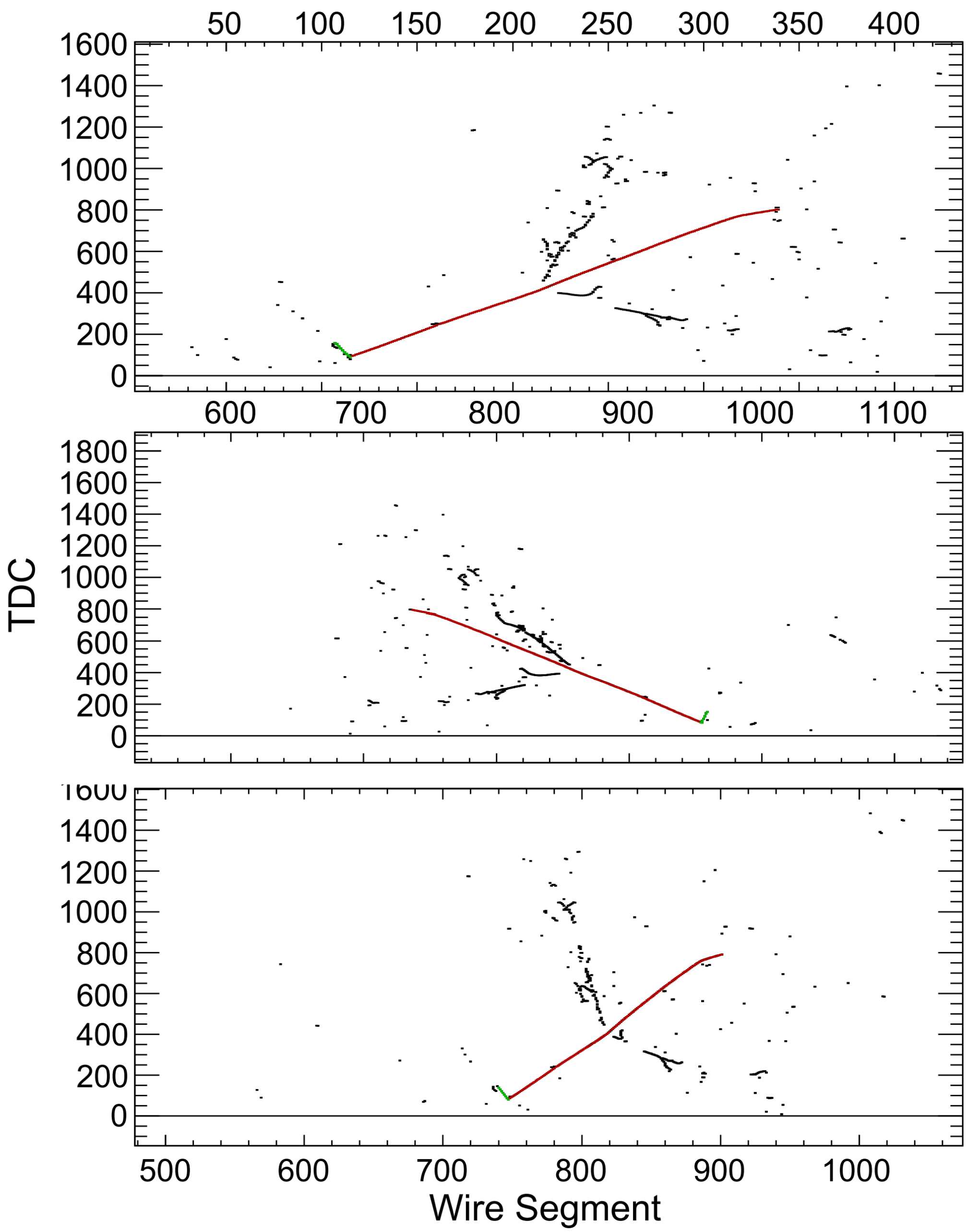

Figure 4.10: A simulated intranuclear ^{40}Ar $n \to \bar{n}$ signal event using the hA_BR nuclear model configuration is shown with topology $n\bar{n} \to n\pi^0\pi^0\pi^+\pi^-$. Made in collaboration with V. Pec and Y-J. Jwa for [12].

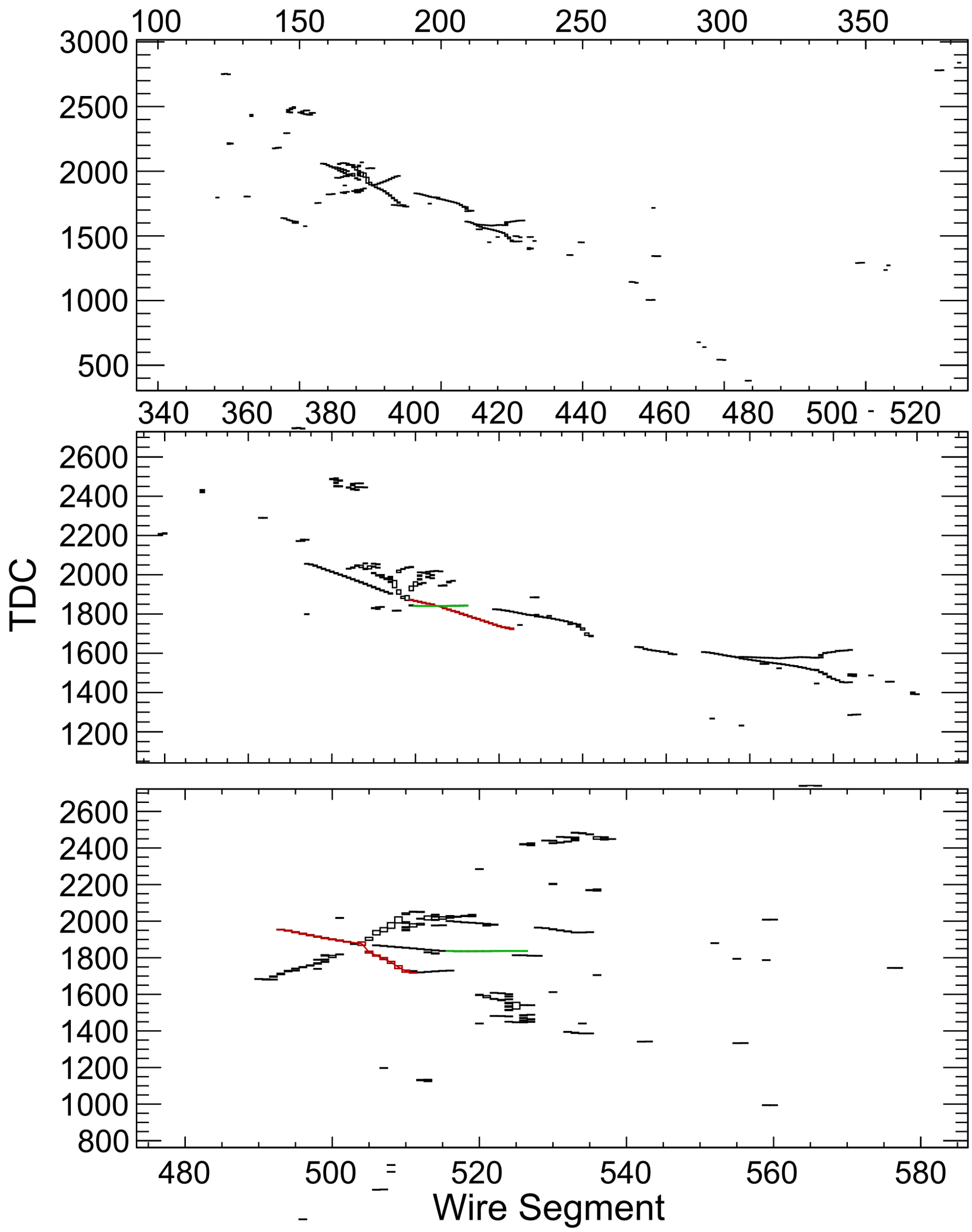

Figure 4.11: Event display for a NC DIS interaction initiated by an atmospheric neutrino. Made in collaboration with V. Pec and Y-J. Jwa for [12].

into a BDT to form a new BDT(CNN) method. The BDT(CNN) similarly produces a score, where higher numbers imply signal-like, and lower numbers background-like topologies. By optimizing the expected lower limit for $\tau_{n\bar{n}}$, one can derive cuts on each of the CNN and the BDT(CNN) scores. For the TDR analysis which used the `GENIE` default hA_BR nuclear model configuration, a TMVA CERN ROOT BDT framework [346] was used. The new analysis for a low statistics run of the hA_LFG nuclear model configuration presented here[26] now uses an XGBoost BDT [417], but the fundamental principles of each are the same. Effectively, rather than use visual techniques, a BDT surveys the full phase space of any set of inputted variables, separating hypervolumes within the multidimensional phase space recursively and optimizing these until some criteria is met. One can then cut through and select subportions of this reorganized volume via a score, allowing an emphasis of signal over background.

The input variables used within both model configuration analyses use identical BDT(CNN) schemes whose inputs are reconstructed variables from the full detector simulation, and currently include:

1. Total number of reconstructed tracks (DUNE PMA reconstruction)
2. Total number of reconstructed showers (DUNE reconstruction by the emshower algorithm)
3. Total track-like visible energy (DUNE PMA reconstruction and sum of track-like hits energy)
4. Total shower-like visible energy (DUNE PMA reconstruction and sum of electromagnetic-like hits energy)
5. Total visible energy (DUNE PMA reconstruction and sum of *all* visible energy deposited in hits)
6. Shower energy fraction of total energy
7. Longest track PID (DUNE PMA reconstruction inferred)
8. Longest track momentum (DUNE PMA reconstruction of momentum by range with reconstructed PID input)

[26] Thanks to Y-J. Jwa for her collaboration on this work.

9. dE/dx of most energetic electromagnetic shower (DUNE PMA reconstruction)

10. CNN score

Ongoing work [72] is actively expanding this list of inputs. Directly inferred particle identification (PID) is not very accurate, but a path forward will be highlighted later in Sec. 4.4.4. With an better handle on reconstructed PID, one can begin to estimate momentum of individual tracks more precisely, calculate the total momentum of a given event, compute the event's sphericity, count the number of pion candidates therein, reconstruct the event's invariant mass, etc. It is expected that such additions will greatly improve the performance of the full BDT(CNN) setup.

With these inputs, one can then begin to separate signal from background. The separation for the hA_BR model configuration is discussed in [12, 257], and so here I will discuss the separation for hA_LFG. Plots of some of the above mentioned variables inputted into the BDT are shown in the top and middle plots of Fig. 4.12, including the CNN score distribution. There is not great separation between these reconstructed quantities, though the visual differences elucidated by the CNN do show good separation.

The information the BDT(CNN) is learning about signal and background can be visualized by considering Figs. 4.13-4.14. Here, using truth-level quantities of total momentum and total invariant mass from final state pions, one can trace correlations in BDT(CNN) response to reconstructed quantities back to their original source. Figs. 4.13 shows the truth level pionic parameter space for signal (left), a shape now familiar from Chap. 2. When this space is weighted by the BDT(CNN) score using reconstructed quantities (bottom), one begins to see how the automated analysis method is learning about particular aspects of this parameter space. Note that the BDT(CNN) score ranges from $(0, 1)$, and so areas which do not change color much between each set of plots score highly[27].

Other final state truth-level variables can be considered as a function of the BDT(CNN) score, as shown in Figs. 4.14. Given the uniqueness of an $n \to \bar{n}$ signal producing $\sim$ 4-5 pions in the final state, the BDT(CNN) should be learning something about this multiplicity and contrasting it with the much lower multiplicities expected in backgrounds. As can be seen, the high scores in

[27]Future versions of these plots [72] will divide out any bin population dependencies, and show the score alone within this parameter space. Other plots showing where exactly signal and background are selected in the parameter space due to a high BDT(CNN) score *are available*, but the low statistics used for these plots ($\sim 30,000$ events) does not give much intuitive visual information worth considering here.

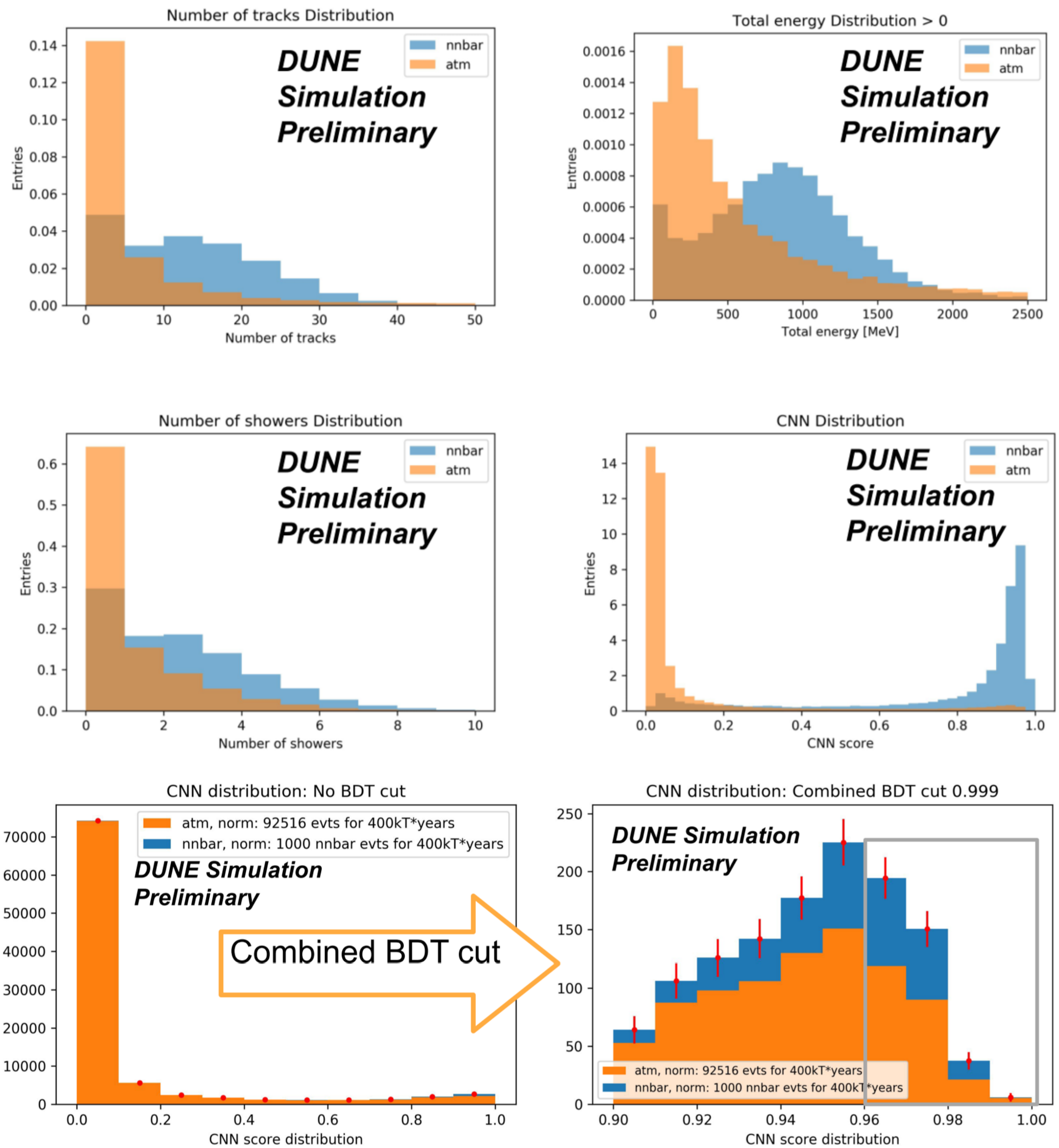

Figure 4.12: Top and Middle: A selection of BDT input variables are shown for signal and background events. Bottom: Separation of a small number of signal events is shown against a $400\,\mathrm{kt{\cdot}yr}$ exposure of atmospheric neutrinos; signal dominates at high CNN scores with a combined BDT score cut of $\gtrsim 0.999$, and a cut is made on the CNN score of $\gtrsim 0.97$. Courtesy of Y-J. Jwa.

the top plot for signal shows the network learning these high pion multiplicity topologies, while for low scores the atmospherics have opposite behavior at low pion multiplicity. Similarly, for the truth-level total invariant mass of pions (bottom), signal-like high scores have relatively high values of invariant mass from $\sim (1, 1.8)$ GeV/c^2, while background-like events cluster close to a scores of zero and one across all values of invariant mass. Again, these imply that the BDT(CNN) is largely learning what is wanted of it, related directly to hypothesized underlying topology and kinematics.

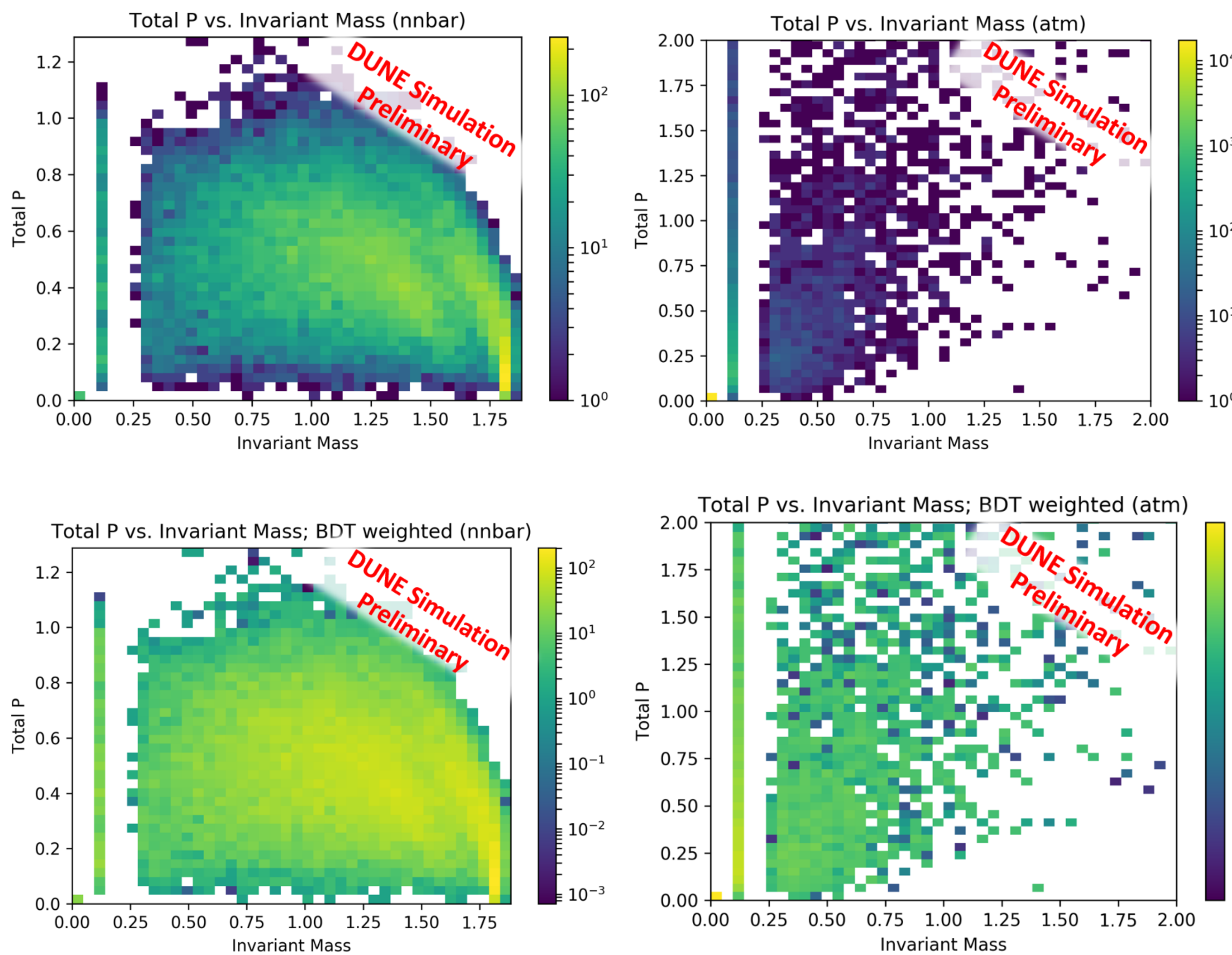

Figure 4.13: Top: The flat (unweighted) pionic parameter space is shown for the GENIE hA_LFG model configuration at truth level for signal (left) and background (right). Bottom: The BDT-score weighted plots of the same pionic parameter spaces are shown, again for truth level quantities. The BDT uses reconstructed quantities to generate a score. Plots made in collaboration with Y-J. Jwa.

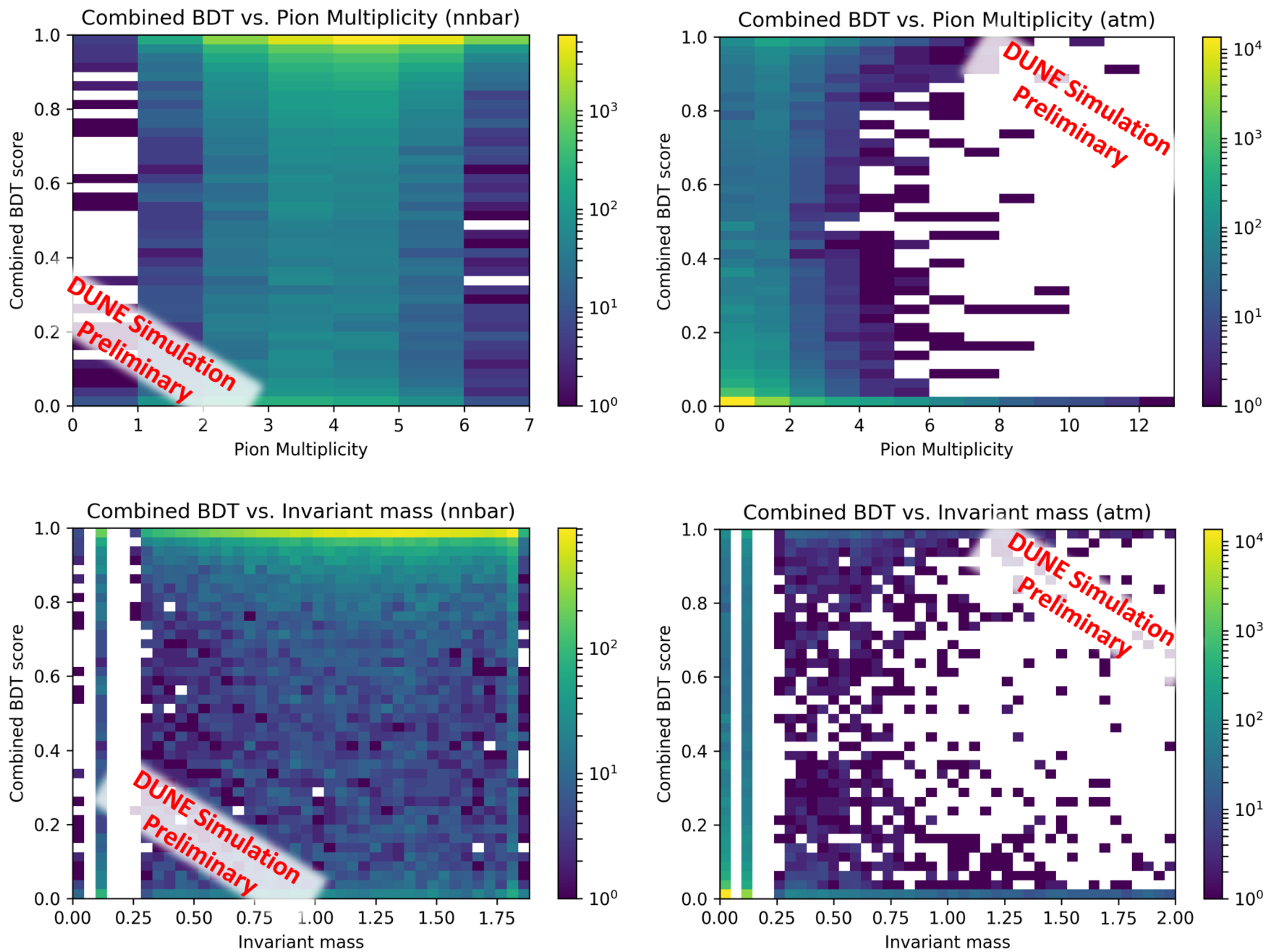

Figure 4.14: Top: The truth-level pion multiplicity of signal (left) and background (right) is shown versus the BDT(CNN) score using reconstructed quantities. Bottom: The total invariant mass of all final state pions is shown for signal (left) and background (right) versus the BDT(CNN) score. Plots made in collaboration with Y-J. Jwa.

4.4.2 Model Comparisons Using Automated Methods

With a signal and background separation technique established, one can begin to train and compare model configurations against each another. Again, this work is ongoing [72], but analysis plans can be discussed. Tab. 4.2 shows the available reconstructed sample sizes and planned sizes for BDT and CNN training, testing, and validation samples for each model configuration across signal and background. The validation samples will act as the "experiment" within [72], and their effective exposures in Mt·yr are shown.

Consider now Fig. 4.15 in the context of Tab. 4.2; training and validation can be considered in a pairwise fashion across all nuclear model configurations. Signal to signal (S:S) comparisons of relevant topological score or reconstructed detector variables can be made, and are expected to differ given various assumptions of Fermi motion and final state interaction models; the same can be done for atmospheric neutrino backgrounds (B:B). Of course, for each of these nuclear model configurations, the comparisons are not idempotent. However, comparisons between the responses of automated methods trained on one or another model of signal (or background) can thus yield many different potential values of $\tau_{n\bar{n}}$; the distribution and associated mean of these values thus informs the error band of any potential lower limits accessible to DUNE. This chapter has only considered two comparisons between signal and background: 1) for the hA_BR nuclear model configuration [257, 12] was trained and validated on itself, and 2) the hA_LFG nuclear model configuration was trained and tested on itself. Mixing between these and all other available BDT(CNN)'s trained on a given nuclear model configuration as priors will generate many values for $\tau_{n\bar{n}}$ lower limits, allowing an assessment of the stability of the signal as a function of the model. This agnostic method to the true physics that Nature employs for such rare signals is thus very encouraging.

Table 4.2: Overview of signal and background sample sizes generated using GENIEv3.0.6 G18_10X-derived nuclear model configurations. Reconstructed sample sizes for all signal and background atmospheric neutrino nuclear model configurations are shown. High statistics is necessary in order to make a definitive statement on DUNE's expected values of signal efficiency, background rejection rates, and associated lower limits on $\tau_{n\bar{n}}$. The hA_BR configuration is the default within GENIE, and so underwent higher statistical study here. Validation samples are used for actual analysis, and so yield signal efficiencies and background rejection rates; these also dictate the effective exposures of this study for each nuclear model configuration. These sample sizes will form the basis of the ongoing analysis to be considered in a forthcoming publication [72].

Nuc. Mod. Config.	$n \to \bar{n}$ **hX_XX**	ν_{atm} **hA_BR**	ν_{atm} **hN_BR**	ν_{atm} **hX_LFG**	ν_{atm} **hX_ESF**
$10\,$**kt · yr Counts**	—	2235.88	2235.88	2312.9	2155.79
Reconstructed Sample Size	$100,000$	$5,000,000$	$2,000,000$	$2,000,000$	$2,000,000$
Training Sample Size	$80,000$	$800,000$	$800,000$	$800,000$	$800,000$
Testing Sample Size	$10,000$	$100,000$	$100,000$	$100,000$	$100,000$
Validation Sample Size	$10,000$	$4,100,000$	$1,100,000$	$1,100,000$	$1,100,000$
Validation Exposure (Mt · yr)	—	18.34	4.92	4.76	5.10

S:S	hA_BR	hA_LFG	hA_E SF	hN_BR	hN_LFG	hN_ESF
hA_BR		Kinematic Distributions (BDT inputs)	…			
hA_LFG	Kinematic Distributions (BDT inputs)		⋱			
hA_ESF	⋮	⋱				
hN_BR						
hN_LFG						
hN_ESF						

S:B	hA_BR	hA_LFG	hA_ESF	hN_BR	hN_LFG	hN_ESF
hA_BR	$\tau_{n\bar{n}}$	…				
hA_LFG	⋮	⋱				
hA_ESF						
hN_BR						
hN_LFG						
hN_ESF						

B:B	hA_BR	hA_LFG	hA_E SF	hN_BR	hN_LFG	hN_ESF
hA_BR		Kinematic Distributions (BDT inputs)	…			
hA_LFG	Kinematic Distributions (BDT inputs)		⋱			
hA_ESF	⋮	⋱				
hN_BR						
hN_LFG						
hN_ESF						

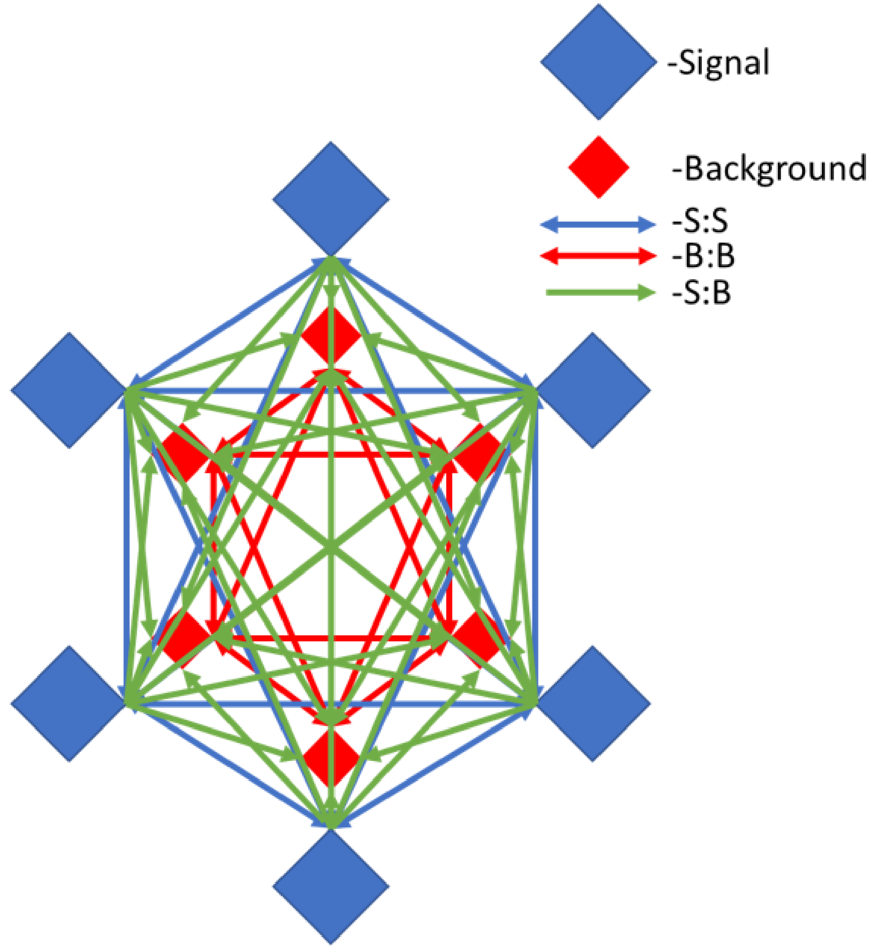

Figure 4.15: Illustrative tables and sample comparison flow diagrams are shown to explore potential theoretical model uncertainties of intranuclear $n \to \bar{n}$. Signal and background comparisons can be made model configuration by model configuration, and intermixed.

4.4.3 Current Intranuclear $\tau_{n\bar{n}}$ Lower Limit Calculations

Conditional Bayesian statistical methods can be used to describe the likelihood of a given observation. For a conditional probability of an event a given an event b, it is known that

$$P(a|b) = \frac{P(b|a)P(a)}{P(b)}\,, \tag{4.13}$$

where $P(a)$ and $P(b)$ are the probabilities of individual events a or b occurring. For most things, events occur via a Poissonian distribution

$$p(n, \lambda) = \frac{e^{-\lambda}\lambda^{n}}{n!}\,, \tag{4.14}$$

where n is the number of events observed of some type, and λ is an event rate. For a $n \to \bar{n}$ event, one can expect that the observed rate in a detector will follow from

$$\lambda = \Gamma E\epsilon + B \propto 1/\tau_{n\bar{n}}\,, \tag{4.15}$$

where Γ is the width of intranuclear $n \to \bar{n}$ (see again Chap. 2) and takes on units of $\Gamma = [\text{year}^{-1}]$, E is a total exposure for a given detector and has units of $E = [n\text{-years}]$ for a given number of neutrons within the detector medium, ϵ is the expected signal selection efficiency (inferred from MC studies), and B is the total expected background count rate over a given exposure time [28].

Preliminary sensitivities for DUNE using MC simulations can be assessed statistically [4] based on a given exposure, an evaluated $n \to \bar{n}$ signal efficiency computed from the automated analyses discussed in the preceding section, and an expected background count. The probability distribution for an intranuclear decay width Γ for $n \to \bar{n}$ can be evaluated for a given *count* ($C \equiv n$) of events "observed" in a virtual detector. Using the Bayesian methods outlined above, one can then construct individual probability distributions $P(E)$, $P(\epsilon)$, and $P(B)$ as gaussian priors; for each individual lower limit for $\tau_{n\bar{n}}$ for a given nuclear model configuration, the relative uncertainties (widths) of these distributions are taken as $\Delta E = 3\%$ and $\Delta\epsilon = \Delta B = 25\%$ [4]. From these, one can construct the conditional width distribution via substitution of Eqs. 4.14

[28] The general strategy within the DUNE collaboration is to assume that the number of expected event counts comes purely from an expected background count rate; in other words, one hypothesizes that no signal will be observed.

and 4.15 into Eq. 4.13, giving the integral

$$P(\Gamma|C) = A \int \frac{e^{-(\Gamma\epsilon E+B)}(\Gamma\epsilon E + B)^C}{C!} \cdot P(\Gamma)P(E)P(\epsilon)P(B)dEd\epsilon dB\,. \tag{4.16}$$

where A is a normalization constant. This integral can be completed numerically. For a particular value of $\Gamma \to \Gamma_{0.9}$ a full 90% of the total integral domain is covered, i.e.

$$0.9 = \frac{\int_{\Gamma=0}^{\Gamma_{0.9}} P(\Gamma|C)d\Gamma}{\int_{\Gamma=0}^{\infty} P(\Gamma|C)d\Gamma}\,, \tag{4.17}$$

and so represents the 90% confidence level for a given value of the intranuclear neutron lifetime limit (τ_m), where

$$\tau_m = \Gamma_{0.9}^{-1}\,. \tag{4.18}$$

From this, one can estimate the free neutron equivalent value via

$$\tau_{n\bar{n}} = \sqrt{\frac{\tau_m}{R}}\,, \tag{4.19}$$

where for ^{40}Ar one knows from [71] and Chap. 2 that $R = 5.6 \times 10^{22}\,\mathrm{s}^{-1}$.

With the automated BDT(CNN) analysis described previously, lower limits for $\tau_{n\bar{n}}$ for multiple model configurations can be constructed at a 90% C.L., as presented in Tab. 4.3. Note that the limits presented here, particularly the model configuration hA_BR used for the DUNE technical design report analysis [257, 12], do not necessarily have consistent atmospheric background calculations, as the developments presented earlier on precision oscillated atmospheric fluxes was not yet complete. The background counts for each model configuration which pass the same BDT(CNN) analysis cuts are presented in Tab. 4.4.

An estimation of the error in the total expected signal-like background counts (δB_S) is made via

$$\delta B = \frac{E_{\text{DUNE 10yr}}}{E_{\text{MC}}} \cdot \sqrt{B_S}\,, \tag{4.20}$$

where B_S is the background counts accepted as signal, E_{MC} is the equivalent exposure of the MC background sample analyzed via the BDT(CNN) method, and $E_{\text{DUNE 10yr}} = 400\,\text{kt}\cdot\text{yr}$ is the nominal $10\,\text{yr}$ full exposure for DUNE. Thus, the larger the MC exposure, the less error is presumed within the signal-like background estimate. Tab. 4.4 shows these signal-like background count rates and errors; an ideogram visualizing these two analyses is shown in Fig. 4.16.

Note that Fig. 4.16 is merely *instructive*. Once the full set of nuclear model configuration comparisons is complete [72], there will be many points filling this space, allowing a better assessment of expected background rates given an automated analysis. Furthermore, when atmospheric neutrino flux and oscillation parameter errors are introduced, the error bars will inflate. Similarly, there will be many values of $\tau_{n\bar{n}}$ which result from the many signal efficiencies and estimated background count rates, dependent upon what the chosen model configuration is for signal and background training and which are used for validation.

From these discussions and consideration of Tabs. 1.1, 4.3, and 4.4, one may hypothesize as to the the regions of $\tau_{n\bar{n}}$ parameter space probed by DUNE, alongside Super-Kamiokande and ESS NNBAR. In the context of post-sphaleron baryogenesis [50, 47] and Fig. 1.11, one can overlay the limits discussed in this chapter for comparison to other experiments and potential lower limits. A spread in the expected values of $\tau_{n\bar{n}}$ given various nuclear model configurations is *concerning*, especially as the underlying nuclear physics, though well constrained (see again Chap. 2), is not definitively known; however, more robust simulations are underway, and will be detailed in a future publication [72].

Table 4.3: A table of $\tau_{n\bar{n}}$ 90% C.L. lower limits from two models analyzed with the combined BDT(CNN) automated method. The TDR analysis [257, 12] does not list score cuts.

Model Analyzed	Exposure (10^{35} n-yr)	CNN Score Cut	BDT(CNN) Score Cut	ϵ	τ_m (10^{32} yr)	$\tau_{n\bar{n}}$ (10^8 s)
hA_BR	1.33	—	—	$\sim 8\%$	6.45	6.03
hA_LFG	1.33	~ 0.97	~ 0.999	$\sim 5\%$	2.01	3.36

Table 4.4: Background estimates are shown for signal-like atmospheric neutrino events. Note that the expected counts per 10 kt·yr for the hA_BR analysis [257, 12] used a different atmospheric neutrino flux.

Model Analyzed	MC Exposure (kt·yr)	Counts/10 kt·yr	Tot. ν_{atm} Counts	Bkgr. Acc. Rate	Res. Bkgr. Counts/400 kt·yr	Est. Bkgr. Count Error
hA_BR	200	2014	40280	0.02%	16.11	8.03
hA_LFG	400	2312.9	92516	0.06%	58.29	7.63

4.4.4 Promising Particle Identification via Semantic Segmentation Networks

A key contributor to the identification of rare signals is their final state observable particles. However, if detector reconstruction software is lacking in precision inference, these quantities may lead to misinterpretations of PID; this is largely the current reality within DUNE. However, new methods have been recently developed which allow for high fidelity particle identification at many energies using neural networks. Using a combination of truth-level training information and voxelized SpacePoints within LArTPCs, new semantic segmentation networks have shown great promise in ascertaining PIDs of many particles, including pions and highly ionizing particle ("hips") such a protons and kaons. For each voxel, a probability that a particular particle passed through can be assessed; the accuracy of these inferences can be seen in the confusion matrix shown in Fig. 4.18. From these probabilities, voxels can be grouped together into tracks, and each track given an averaged probability of being a particular particle type. Examples of this method are shown in Figs. 4.19 for atmospheric neutrinos in the hA_BR nuclear model configuration. Colors imply separated classes of particle types. Grouping these voxels into tracks and counting particle multiplicities directly offers hope for further background reduction; such a new reconstructed variable can be added to the full suite already present within the BDT(CNN), creating a new BDT(CNN,PID) framework [72].

4.5 Conclusions

In this chapter, I have discussed my furnishing of the first oscillated atmospheric neutrino background simulations using Honda fluxes for the DUNE collaboration; these will serve as a basis for further developments, including oscillation studies using the CAFAna framework [53]. I have estimated the background interaction counts in the DUNE far detector, and used these for simulated $n \to \bar{n}$ sensitivity studies alongside my colleagues within the DUNE HEP Working Group. A key contribution of mine has been the developing of a framework for the iteration of nuclear model configurations; this idea was initially spawned by me within the HEP Working Group, and was carried out by me in the context of GENIE. Integration of the independent model discussed in

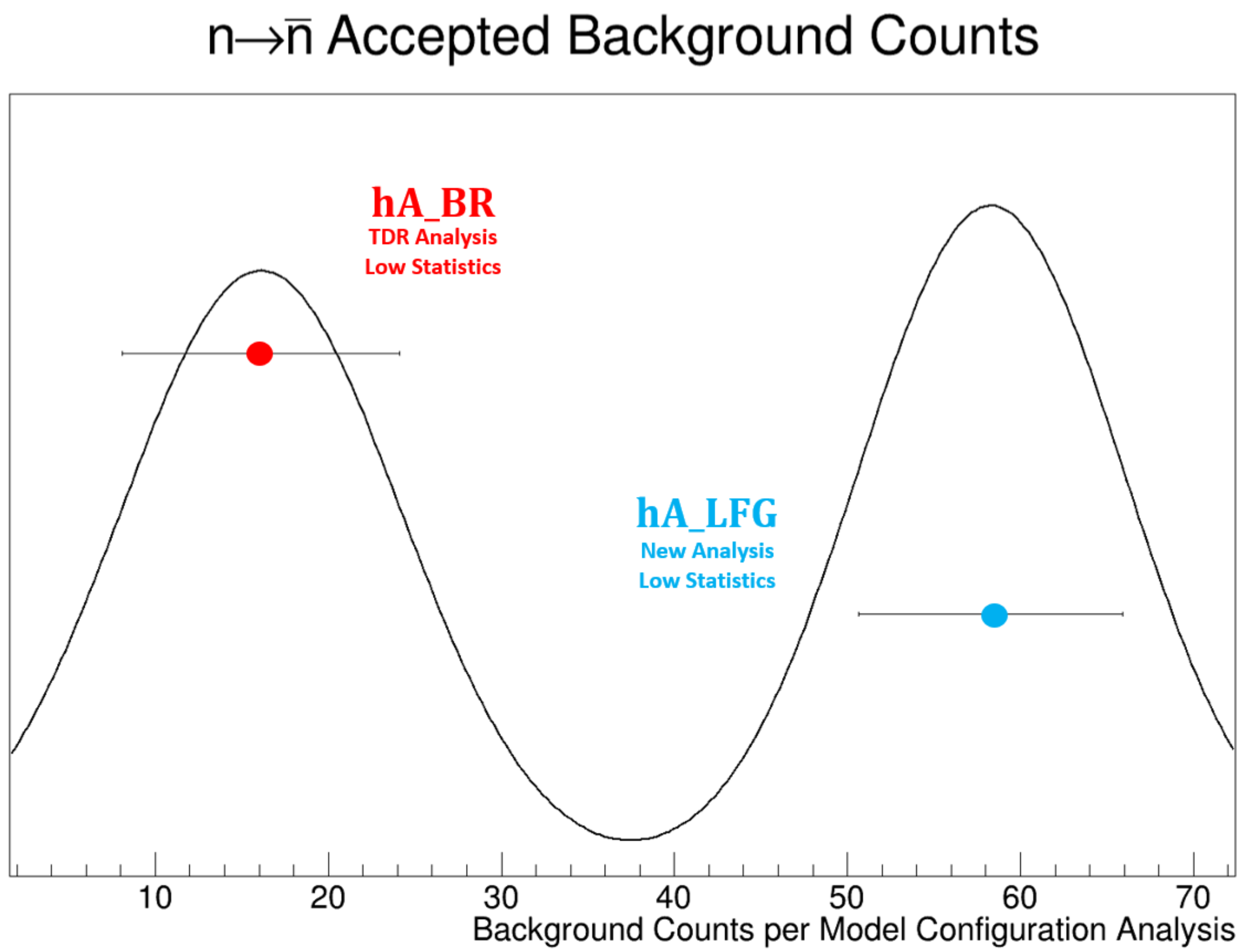

Figure 4.16: An ideogram shows the accepted background counts (appearing to be signal) for two model configuration analyses as shown in Tab. 4.4, including for the Bodek-Ritchie [109] used in the DUNE technical design report [257, 12] (red) and local Fermi gas models (blue), each using the hA Intranuke 2018 intranuclear cascade within `GENIE`. The y-axis scale and placement of model points is arbitrary; each count point is normalized for $400\,\mathrm{kt{\cdot}yr}$ of operation, with errors estimated via Eq. 4.20.

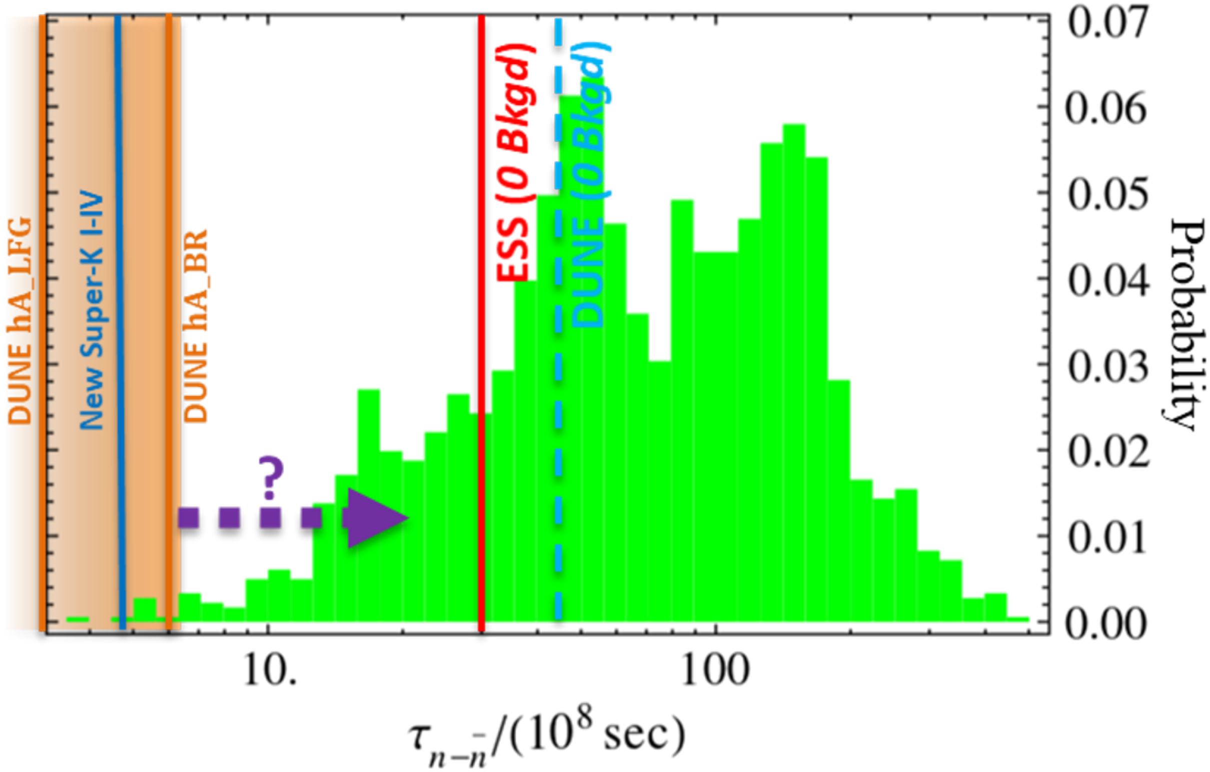

Figure 4.17: A reproduction of Fig. 1.11 is shown with new sensitivity overlays for DUNE using the low statistics simulations described in this chapter. It can be seen that their range largely overlays that of the Super-Kamiokande I-IV limit [6]. It is expected that new methods of particle identification, briefly discussed in Sec. 4.4.4, will increase these limits. Similarly, more robust oscillated atmospheric neutrino background simulations using new high statistics (Tabs. 4.1 and 4.2) will give these limits more credence.

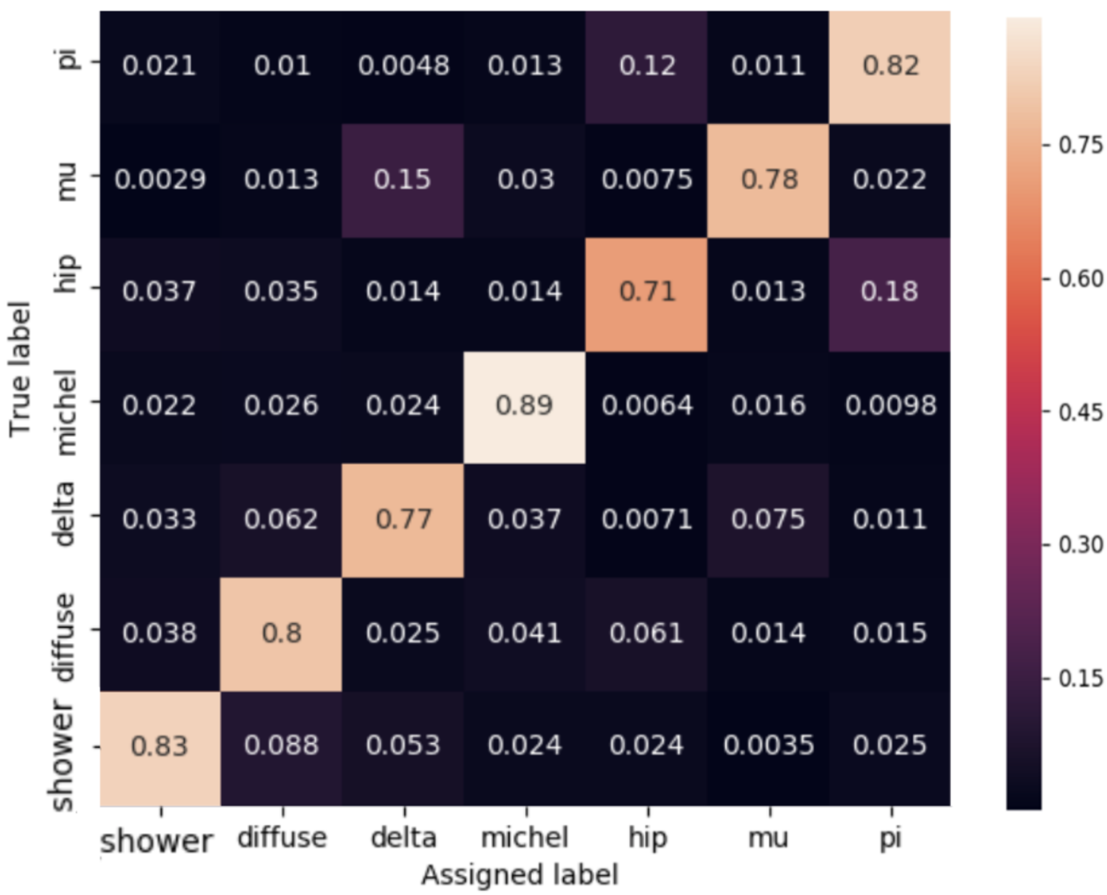

Figure 4.18: A semantic segmentation confusion matrix of truth vs. reconstructed ("assigned") PID is shown for various simulated particle types; note that "hip" stands for "highly ionizing particle" and "mu" is a muon. Correct inference capabilities are high along the diagonal, boding well for future combined analyses with a BDT(CNN,PID) using measured multiplicities as inputs to increase the signal to background ratio. Courtesy of C. Sarasty.

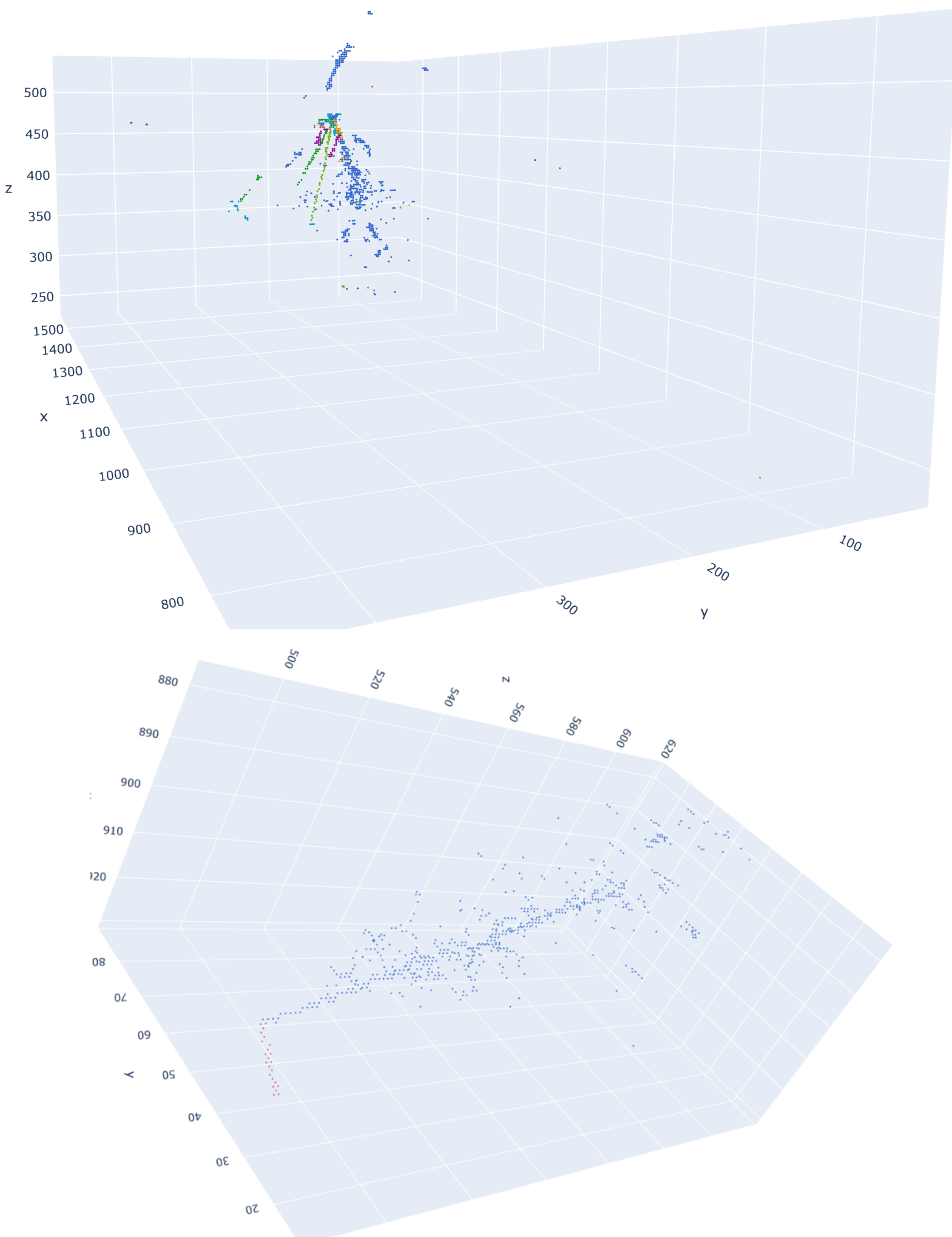

Figure 4.19: Top: A three-dimensional view of a well reconstructed charged current $\nu_{e,atm}$ event is shown via SpacePoints, where each colored point categorizes the particle which passed through a particular voxel. Dark blue represents showers, yellow is any diffuse activity, dark green are kaons, dark pink are Michel electrons, light blue are highly-ionizing particles, orange are muons (none to be seen), and light green are pions. Bottom: Another well reconstructed charged current $\nu_{e,atm}$ event is shown with a large electromagnetic shower (blue) and a single proton (red) being emitted. Courtesy of C. Sarasty.

Chap. 2 and [71] into LArSoft is forthcoming. In a future publication [72], I hope to explore with my colleagues the full projected range of lower limits attainable by DUNE across all possible nuclear model configurations (Fig. 4.15), thus robustly informing the modeling uncertainties which form the foundation of interpretability for any hopefully observed $n \to \bar{n}$ signal. A wide spread of model sensitivities (*potentially* illustrated by *only two points* shown in Fig. 4.17) would be concerning, emblematic of a need for still better modeling of the effectively unknown underlying (nuclear) physics at the heart of an intranuclear $n \to \bar{n}$ process.

Chapter 5

Electrons for Improved Neutrino Scattering Modeling

The usage of Monte Carlo neutrino event generators (MCνEGs) is a norm within the high-energy ν scattering community. The relevance of quasielastic (QE) energy regimes to ν oscillation experiments implies that accurate calculations of νA cross sections in this regime will be a key contributor to reducing the systematic uncertainties affecting the extraction of oscillation parameters. In spite of this, many MCνEGs utilize highly phenomenological, parameterized models of QE scattering cross sections. Moreover, a culture of validation of MCνEGs against prolific electron (e) scattering data has been historically lacking. In this chapter, new eA cross sections obtained from nuclear *ab initio* approaches are implemented in `GENIE`, the primary MCνEG utilized by the FNAL community. In particular, results from Quantum MC methods which solve the many-body nuclear problem in the Short-Time Approximation (STA) are utilized, allowing consistent retention of two-nucleon dynamics which are crucial to explain available nuclear electromagnetic (electroweak) data over a wide range of energy and momentum transfers. This new implementation in GENIE is fully tested against the world QE electromagnetic data, finding agreement with available data below $\sim 2\,\text{GeV}$ of beam energy with the aid of a scaling function formalism. The STA is currently limited to study $A \leq 12$ nuclei, however, its semi-inclusive multibody identity components are exportable to other many-body computational techniques such as Auxiliary Field Diffusion MC which can reach $A \leq 40$ systems while continuing to realize the factorization contained within the STA's multinucleon dynamics. Together, these developments promise to make future experiments such as DUNE more accurate in their assessment of MCνEG systematics, ν properties, and potentially empower the discovery of physics beyond the Standard Model.[1]

5.1 Introduction

5.1.1 Future ν Oscillation Study Requirements

There is great importance for the particle physics community in the difficult task of mapping experimentally observed final state neutrino (ν) properties and energies onto initial ν states given the presence of oscillations and the complexity of chosen target nuclear systems [34]. Indeed, whether these ν's originate in a beam or the atmosphere, any lack of capacity in the reconstruction of these quantities can lead to misinterpretations of the true physics of the system under study, potentially distorting future results of the global short- and long-baseline ν oscillation program. Many technicalities and their interrelations limit the interpretive certainty of any experiment's results, including the ν cross section model and its dependence on the assumed structure of the nuclear target with (or without) the inclusion of *multinucleon correlations and interference effects*, the ν flux and beam divergence model, the intranuclear cascade (final state interactions) model, and the detector's capability (response) in efficiently reconstructing the topology of a ν event at particular kinematics. Many of these can currently only be efficiently simulated using Monte Carlo ν event generators (MCνEGs), a popular candidate being `GENIE` [40], and experiments rely on these and other types of computation to simulate their ν beam, ν interactions, intranuclear cascade, and observable final state topologies given modeled detector responses. All of these tools are necessary components for precise measurements of ν properties such as CP-violation (δ_{CP}) and the ordering of the ν masses.

In this chapter, I will focus on one of the above-mentioned components: cross sections with complex nuclear structure and multinucleon interactions *intact*. To outline this chapter in brief:

[1] Many thanks to S. Gardiner, S. Pastore, M. Betancourt, and J. Carlson for their collaboration on this effort [69].

1. The *ab initio* methods used within the quantum Monte Carlo Short-Time Approximation (QMC STA) [318] are briefly explained, and how these can be applied in the calculation of electromagnetic nuclear response functions and response densities for light nuclei;

2. A new, holistic framework within GENIE is discussed based on calculated electromagnetic (electroweak) nuclear response functions and supplemented by interpolation schemes to compute double differential electron scattering cross sections;

3. Comparisons are shown of these responses and double differential cross sections against abundant electromagnetic scattering data to assess the validity of both the GENIE implementation and the theoretical nuclear response function inputs. Similar studies have recently been performed for existing GENIE cross section models by multiple groups [41, 316].

This is a foundational work where the framework is tested, verifying that the events generated by GENIE are fully consistent with the inputs provided by the underlying theoretical calculations of nuclear responses from the STA. More broadly, this work will construct a solid basis for future implementations of ν-nucleus responses in the MCνEG. When using a consistent microscopic model of V and $V - A$ lepton-nucleus interactions, these will allow scientists to better estimate the precision of ν scattering event samples produced by MCνEGs which in-turn are used to understand experimental ν cross sections and oscillation parameters; such increases in the precision of these measurements may permit the necessary resolution to discover physics beyond the Standard Model (BSM).

5.1.2 Quasielastic Scattering Overview

Quasielastic (QE) scattering, or when a particle probes a nucleus by transferring energy and momentum *primarily* to a single nucleon, is a key interaction process observed at both current electron-scattering facilities, *e.g.*, Jefferson Laboratory [256], as well as current and future short- and long-baseline ν oscillation experiments [397, 399, 395]. However, the majority of the models utilized by MC event generators in this energy regime are generally highly phenomenological. Typically, an effective single-nucleon cross section is implemented which inherently ignores important high Bjorken-x interactions visible as missing energy or momentum via two-nucleon short-range correlations [383, 198]. This implies that a large portion of the truly quantum behavior at play within the nucleus being probed is partially or entirely ignored, including interference terms and tensor forces which mediate two-body dynamics and can create observable two-nucleon topologies in detectors, independent of final state interactions (FSIs). Overlooking these important dynamical components can lead to a suppression of the cross sections, which can in turn make experimental measurements *appear* enhanced in strength, perhaps leading accidentally to interpretations of extraordinary physics.

The QMC STA [318], adopted in the present work, incorporates these nontrivial multinucleon dynamics directly within electromagnetic nuclear response *densities* and associated nuclear response functions. The latter are given as functions of the energy, ω, and three-momentum transfer, $|\mathbf{q}|$. Using precomputed tables of these responses, one can interpolate across $(\omega, |\mathbf{q}|)$ space to calculate inclusive double differential and total QE cross sections where effects from two-body physics and enhancements can be observed. Since a formalism involving these nuclear response functions is common to many models of lepton-nucleus scattering, a software framework which takes them as input and uses them to produce simulated events allows competing models to be compared easily within a MCνEG. Given the complexity of the codes generally utilized to solve the many-body nuclear problem, direct implementation of the most realistic calculations in a MCνEG is impractical. Tables of precomputed nuclear responses allow for efficient event generation while preserving the physics content of sophisticated inclusive cross section models [318, 69]. Though this work is focused on electromagnetic scattering on very light nuclei, QMC STA methods are *directly* extendable to include up to $A \leq 12$ nuclei for electromagnetic and electroweak scattering; other known QMC computational methods, such as Auxiliary Field Diffusion Monte Carlo [136], can similarly maintain the interference and two-body contributions at play within the QE cross section, while being exportable to the $A \leq 40$ systems most important for future experimental programs such as the Deep Underground Neutrino Experiment (DUNE) [395]. This further motivates the creation of a universal input framework for use by theorists to more easily incorporate their work into experimental MC event production and analysis chains.

As a *start* to this long-term computation, simulation, and validation program outside and within the `GENIE` collaboration, inclusive QE scattering of electrons on ${}^4_2$He will be considered; validation of the behavior of the QMC STA within the `GENIE` MC event generator will be checked across the

QE-regime on publicly maintained world inclusive QE electron scattering data [77, 163]. Further, some predictions of nn, pp, and np contributions to the cross sections can be offered, which can be useful for current and future electron scattering experiments, while also hinting a path forward for the ν community. In closing, I wish to emphasize that the main point of this chapter is to *validate* the framework discussed here. This will set a solid basis for future developments in the `GENIE` MCνEG.

5.1.3 Brief GENIE Overview

`GENIE` (Generates Events for Neutrino Interaction Experiments) [40] is a collaboratively written and maintained suite of MC event generator and model tuning [39] packages used by many ν experiments, including MINERvA [398], MicroBooNE [397], the Short-Baseline Near Detector [374], and DUNE [395, 10, 257, 258]. Within `GENIE`, lepton-nucleus interactions are modeled as a two step process using the impulse approximation; interactions occur on individual bound and moving nucleons, and outgoing hadrons resulting from the primary interactions propagate through the nucleus and are subject to FSIs. `GENIE` is an event generator which seeks to provide comprehensive modeling for all nuclear targets and leptons of all flavors from MeV to PeV energy scales [40]. Using C++, XML, and CERN ROOT [42], `GENIE` offers modularity in its configurations and code design, and the collaboration encourages scientists to contribute new model implementations using their platform in the form of "Incubators". The work described in this chapter springs from just such an Incubator.

As a means of benchmarking ν cross section models against electron scattering data, the `GENIE` interface for consuming nuclear response tables was recently generalized to handle generation of both neutrino and electron scattering events on an equal footing.

5.1.4 Quasielastic Inclusive Cross Sections

The QE inclusive-scattering cross section of electrons and νs on nuclei can be considered in terms of nuclear electromagnetic or electroweak response functions. Under the assumption that the lepton-nucleus interaction is dominated by the exchange of a single virtual photon which couples to the nucleus' electromagnetic charge and current, the electron-scattering cross section of interest in this chapter is given by [261, 139, 137, 52]

$$\frac{d^2\,\sigma}{d\,\omega d\,\Omega} = \sigma_M \, \left[v_L \, R_L(\mathbf{q},\omega) + v_T \, R_T(\mathbf{q},\omega) \right] \, , \tag{5.1}$$

where ω and $\mathbf{q}$ are the energy and three-momentum transfer, respectively, and σ_M is the Mott cross section defined as:

$$\sigma_M = \left(\frac{\alpha \cos\theta/2}{2\,\epsilon_i \sin^2\theta/2} \right)^2 \, . \tag{5.2}$$

In Eq. 5.2, α is the fine structure constant, θ the electron scattering angle, and ϵ_i the initial electron energy. The lepton's kinematic factors are defined as

$$v_L = \frac{Q^4}{|\mathbf{q}|^4} \, , \qquad v_T = \frac{Q^2}{2\,|\mathbf{q}|^2} + \tan^2\frac{\theta}{2}, \tag{5.3}$$

where $Q^2 = q^2 - m^2 = -q_\mu q^\mu$ is the negative of the four-momentum transfer. The two nuclear electromagnetic response functions, namely the longitudinal (L) and the transverse (T), are schematically given by

$$R_\alpha(q,\omega) = \overline{\sum_{M_i}} \sum_f \langle \Psi_i | O^\dagger_\alpha(\mathbf{q}) | \Psi_f \rangle \langle \Psi_f | O_\alpha(\mathbf{q}) | \Psi_i \rangle \times \delta(E_f - E_i - \omega) \, , \qquad \alpha = L, T \tag{5.4}$$

where $O_L(\mathbf{q}) = \rho(\mathbf{q})$ is the nuclear electromagnetic charge and $O_T(\mathbf{q}) = \mathbf{j}(\mathbf{q})$ is the nuclear electromagnetic current. Here, $|\Psi_i\rangle$ and $|\Psi_f\rangle$ represent, respectively, the initial ground state and final continuum state with energies E_i and E_f, and an average over the initial spin projections M_i of the initial nuclear state with spin J_i (indicated by the overline) is implied. Note that, as $\theta \to 180°$, the double-differential cross-section of Eq. 5.1 is dominated solely by the transverse response function.

The nuclear response functions defined above carry all the information on the nuclear dynamics at play during the scattering event. The electromagnetic charge and current operators are determined by the probe and exhibit dependence upon, *e.g.*, the orientation of the nucleons' spins and isospins. Nuclear wave functions, responses, and response densities are calculated within a microscopic model of the nucleus using QMC computational methods [136] to solve the many-body nuclear problem. Within this approach, static and dynamical nuclear properties emerge from the interactions (or correlations) among all the constituent nucleons. For example, nuclear responses result from the coupling of external leptonic probes with individual nucleons (described by one-body operators), and with pairs of interacting or correlated nucleons (described by two-body operators).

This scheme can be appreciated by rewriting the response of Eq. 5.4 as

$$R_\alpha(\mathbf{q},\omega) = \int_{-\infty}^{\infty} \frac{dt}{2\pi}\, \mathrm{e}^{i(\omega+E_i)t} \times \overline{\sum_{M_i}} \langle \Psi_i | O_\alpha^\dagger(\mathbf{q})\, \mathrm{e}^{-iHt}\, O_\alpha(\mathbf{q}) | \Psi_i \rangle \,, \tag{5.5}$$

where the sum over the final states has been replaced with a real-time propagator. In the equation above, the many-body nuclear Hamiltonian, H, consists of single-nucleon (nonrelativistic) kinetic energy terms, and two- and three-nucleon interactions, such that

$$H = \sum_i -\frac{\hbar^2}{2m}\nabla_i^2 + \sum_{i<j} v_{ij} + \sum_{i<j<k} V_{ijk}, \tag{5.6}$$

where v_{ij} and V_{ijk} are highly sophisticated potentials [136, 52] which correlate nucleons in pairs and triplets. In the set of calculations used in this chapter, the Argonne-v_{18} two-nucleon potential [415] was utilized in combination with the Illinois-7 three-nucleon force [329], this nuclear many-body potential is indicated by "AV18+IL7". The Argonne-v_{18} [415] is a highly sophisticated two-nucleon interaction, reflecting the rich structure of the nucleon-nucleon force, and is written in terms of operatorial structures involving space, momentum, spin and isospin nucleonic coordinates, predominantly arising from one- and two-meson-exchange-like mechanisms. The long-range part of the nucleon-nucleon interaction is due to one-pion-exchange; the intermediate-range component involves operatorial structures arising from multipion-exchange supported by phenomenological radial functions; the short-range part is described in terms of Woods-Saxon functions [139, 136, 415]. The Argonne-v_{18} has 40 parameters that have been adjusted to fit the Nijmegen pn and pp scattering data base [382], consisting of ~ 4300 data in the range of 0–350 MeV, with a χ^2/datum close to one. While fitting data up to 350 MeV, the Argonne-v_{18} reproduces the nucleon-nucleon phase shifts up to ~ 1 GeV, an indication that its regime of validity goes beyond the energy range utilized to constrain the adjustable parameters. This is also an indication that relativistic effects are largely embedded in the parameters entering the nucleon-nucleon interaction. The Illinois-7 [329] is the three-body force, supplementing the Argonne-v_{18}; its latest formulation involves five parameters constrained (in combination with the Argonne-v_{18}) to reproduce ~ 20 energy levels of nuclear ground and excited states.

Calculations based on the AV18+IL7 many-body nuclear Hamiltonian successfully explain, both qualitatively and quantitatively, many nuclear electroweak properties [52, 139, 136], including electromagnetic moments and form factors [136, 358, 308], low-energy transitions including beta decays [320, 213, 319, 321, 160, 322, 317, 268], and electron scattering [318].

The charge, $\rho(\mathbf{q})$, and current, $\mathbf{j}(\mathbf{q})$, operators are also written as sums of one- and two-nucleon terms [139, 52]

$$O_\alpha(\mathbf{q}) = \sum_i O_i^{(\alpha)}(\mathbf{q}) + \sum_{i<j} O_{ij}^{(\alpha)}(\mathbf{q}) + \cdots \, . \tag{5.7}$$

Here, up to two-body contributions are included, that is up to operators of the form $O_{ij}^{(\alpha)}(\mathbf{q})$, where i and j designate that the operator is acting on nucleons i and j. The one-body charge and current operators are obtained by taking the nonrelativistic limit of the standard covariant nucleonic currents [52, 139, 136], and are written in terms of the nucleonic form factors required to correctly reproduce fall-off at increasing values of three-momentum transfer. In the calculations used in this chapter, the dipole parameterization for the proton electric and magnetic is adopted, and neutron magnetic form factors, and the Galster form of the neutron electric form factor [371]. Other parameterizations or calculations of the nucleon form factors, for example the z-expansion [294], or calculations from lattice gauge theory [254, 236, 253, 373, 29, 242, 28] can be rather easily implemented within the QMC STA framework.

The two-body currents, $\mathbf{j}_{ij}(\mathbf{q})$, used in this chapter have been summarized in [52, 139, 136] and the references therein. They consist of model-independent and model-dependent terms, the former being constructed by requiring they satisfy the current conservation relation within the Argonne-v_{18}. In this sense, they are consistent with the nucleon-nucleon interaction, in that their behaviour at both short and long ranges is consistent with that of the potential, or, equivalently, of two-nucleon correlations. At large internucleon distances, where the nucleon-nucleon interaction is driven by one-pion-exchange, these currents include the standard seagull and pion-in-flight currents. In the seagull mechanism, the external electromagnetic field couples with a nucleon producing a pion which is reabsorbed by a second nucleon, whereas for the pion-in-flight contribution the external field couples to the pion actively being exchanged by two nucleons. The model-independent currents are longitudinal, *i.e.*, they are parallel to the direction of the three-momentum transfer $\mathbf{q}$. The model-dependent two-body currents are orthogonal to the external momentum transferred, and they therefore cannot be constrained using current conservation. The model-dependent dominant term is associated with the excitation of intermediate (virtual) Δ-isobars; in this type of contribution, the external probe excites the nucleon to a Δ which then decays, emitting a pion which is reabsorbed by another nucleon [289, 359]. The two-body charge operator, $\rho_{ij}(\mathbf{q})$, consists of contributions of one-pion range, which can be regarded as relativistic effects. The specific form of the operators are listed, *e.g.*, in [139, 289].

Calculations based on the AV18+IL7 two- and three-nucleon correlations in combination with one- and two-nucleon electromagnetic charge and current operators successfully explain available data over a wide range of energy and momentum transfers [52, 136]. In particular, these calculations highlight the importance of accounting for many-body dynamics—especially two-nucleon dynamics—to achieve agreement with the available experimental data. For example, corrections from two-body electromagnetic currents enhance the magnetic moments of ^{9}C by $\sim 40\%$ [321], and give a $\sim 20 - 40\%$ contribution to both electromagnetic transitions between low-lying nuclear states [321] and electromagnetic transverse response functions [318, 284]. It is important to emphasize that two-nucleon terms in both the interactions and currents—collectively indicated by "two-body physics"—are dominated by one-pion-exchange dynamics.

5.1.5 Semifinal States, the Short-Time Approximation, and Response Densities

Quantum Monte Carlo computational methods [136] have been developed for the past 30 years to exactly solve the many-body nuclear problem of strongly correlated nucleons. Inclusive response functions, induced by both electrons and νs, have been calculated in recent years for nuclei up to ^{12}C [139, 137, 138, 284, 286, 283, 285, 282]. In particular, one evaluates the Laplace transform of the response [139, 136] which results in an imaginary-time response of the type

$$\widetilde{R}_\alpha(\mathbf{q},\tau) = \overline{\sum_{M_i}} \langle \Psi_i | O_\alpha^\dagger(\mathbf{q})\, \mathrm{e}^{-(H-E_i)\tau}\, O_\alpha(\mathbf{q}) | \Psi_i \rangle \ , \tag{5.8}$$

where Green's function Monte Carlo (GFMC) methods can then be used to calculate the relevant matrix elements between ground-state wave functions [136]. Since the nuclear response in the QE region is fairly smooth as a function of ω, maximum entropy techniques are successful in inverting the Laplace transform to obtain the response function [286]. Within this scheme, one can fully account for the correlations in the initial state and the interaction effects induced by the imaginary time propagator into the final state, along with quantum interference effects. Interference between one- and two-body currents plays a crucial role in explaining the experimentally observed enhancement in the electromagnetic transverse responses function [137] and should not be neglected in calculations of nuclear responses.

While being extremely successful in explaining available scattering data, the GFMC approach is computationally costly, which is why it has been applied only to nuclei up to $A = 12$. To meet the demands of the next generation neutrino oscillation experiments that will be utilizing ^{40}Ar as active material in the detectors, one has to resort to approximated computational schemes to calculate the associated nuclear responses. The STA [318] has been developed to address this issue without losing the resolution acquired by the exact GFMC calculations, that is, without losing the important contributions from two-body correlations and electroweak currents. The STA is based on the factorization of the real time response given in Eq. 5.5 at short-times (high-energies). In particular, only one- and two-body terms in the Hamiltonian entering the real time propagator are kept. The STA then fully retains two-body physics from both the Argonne v_{18} and the associated electromagnetic one- and two-body currents, and resultant interference terms. The initial state wave functions are fully correlated, as in the GFMC case. When used to calculate response functions, the STA produces results that are in very good agreement with the GFMC calculations at high energy transfers, ω, and moderate to high values of momentum transfer, $\mathbf{q}$. The low energy behaviour induced by low-lying nuclear excitations and by collective excitations are not captured by the STA.

In this *foundational* work, only electromagnetic response functions are implemented within the generator. However, the STA, due to the factorization scheme, provides additional important information on the leptonic *and* hadronic "*semi*final" states–in particular, for two-nucleon semifinal states struck by the external probe via one- and two-body electroweak currents before transport through the nuclear medium[2]. This information is cast in nuclear response *densities*, $\mathcal{D}(e, E_{\text{c.m.}})$, which are expressed in terms of the relative (e) and center of mass ($E_{\text{c.m.}}$) energies of the struck nucleon pair (or equivalently in terms of the relative and center on mass momenta of the pair). Upon integration of the response densities, one recovers the response functions via

$$\begin{aligned} R_\alpha^{\text{STA}}(\mathbf{q}, \omega) &= \int_0^\infty de \int_0^\infty dE_{\text{c.m.}}\ \mathcal{D}_\alpha(e, E_{\text{c.m.}}) \\ &\times\ \ \delta\left(\omega + E_i - e - E_{\text{c.m.}}\right)\ , \end{aligned} \tag{5.9}$$

where for simplicity the Jacobian has been ignored.

The transverse response density induced by electrons scattering from ^{4}He is displayed in Fig. 5.1. The implementation of this semifinal hadronic state information at the interaction vertex within `GENIE` will be the subject of a further work currently in preparation.

5.2 GENIE Implementation

Steps have been taken within the `GENIE` collaboration to create a new suite of software tools to allow for external contributors to implement their inclusive cross section calculations in a universal way using tabulated nuclear responses. Interpolation of these responses allows for the calculation of double differential cross sections at various kinematics, permitting validation against experimental data. Given the usually large $|\mathbf{q}|$-spacing between known responses, the sensitivity of these cross sections to the interpolation method can be nontrivial, occasionally leading to discontinuous behavior; secondarily, given a particular calculation's legitimacy within certain energy regimes (and the limitations of computational time and tabulated data sets), one may not be able to continuously interpolate cross sections to *all* conceivable kinematic regimes. However, creating a fine grid over a legitimate QE kinematic regime permits one to reduce each of these unsavory effects. Here, some of these solutions are discussed in more detail.

[2]Strikingly, unlike current models within `GENIE`, a component not present in these STA response densities is any *explicit* dependence upon a *phenomenological* nuclear model of constituent nucleon Fermi motion. Indeed, given that the response density has a full semi-final momentum-based characterization of the vertex interaction between one or two nucleons and the leptonic probe, no nuclear model is required to understand Fermi motion within a generator. Though these quantities are implicitly present within the calculation (due the solving of the Schrödinger equation with realistic multibody potentials), they are quantistically preserved without any classical approximation.

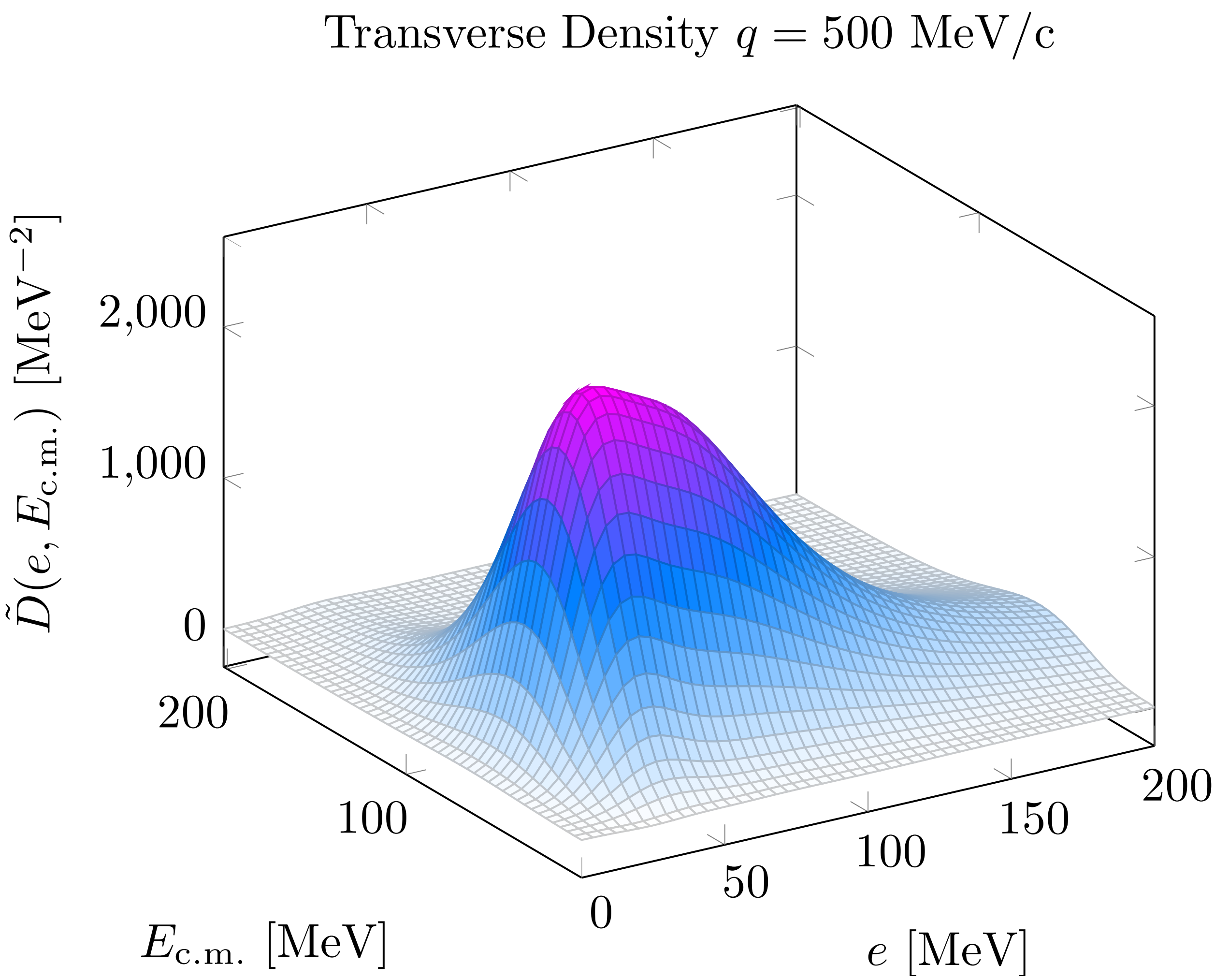

Figure 5.1: The ^{4}He transverse response density is shown for $\mathbf{q} = 500\,$MeV/c. The surface plot shows the response density as functions of relative energy e and center-of-mass energy $E_{\mathrm{c.m.}}$ of pairs of nucleons being actively scattered upon by the incoming electron, leading to microscopic knowledge of *semi*final states before intranuclear transport and final state interactions. Courtesy of S. Pastore.

5.2.1 Cross Section Calculation

To facilitate implementation of new lepton-nucleus cross section calculations, the GENIE collaboration has developed an interface for pre-computed nuclear responses to be used in event generation. The technique relies on the observation that the inclusive differential cross section can be written very generally in the form

$$\frac{d^2\,\sigma}{d\,\omega d\,\Omega} = \frac{\mathcal{C}}{\pi^2}\,\frac{|\mathbf{k}'|}{|\mathbf{k}|}\,L_{\mu\nu}\,W^{\mu\nu}\,, \tag{5.10}$$

where $\mathbf{k}$ ($\mathbf{k}'$) is the initial (final) three-momentum of the lepton, $L_{\mu\nu}$ ($W^{\mu\nu}$) is the leptonic (hadronic) tensor, and

$$\mathcal{C} \equiv \begin{cases} \frac{1}{2}\,G_F^2\,|V_{\mathrm{ud}}|^2 & \text{CC processes} \\ \frac{1}{2}\,G_F^2 & \text{NC processes} \\ \frac{\alpha^2}{Q^4} & \text{EM processes} \end{cases} \tag{5.11}$$

is a factor that contains the coupling constants appropriate for the scattering process of interest. For Standard Model processes, the leptonic tensor is well-known and given by a trace over Dirac matrices. The elements of the hadronic tensor may be computed in terms of nuclear response functions. Exploiting the Lorentz invariance of the tensor contraction $L_{\mu\nu}\,W^{\mu\nu}$, GENIE evaluates these in a frame in which the three-momentum transfer $\mathbf{q}$ points along the $+z$ direction. For electromagnetic scattering in such a frame, contributions from only two elements of $W^{\mu\nu}$ are nonvanishing:

$$W^{tt} = R_L, \tag{5.12}$$

$$W^{xx} = R_T, \tag{5.13}$$

where the nuclear responses R_L and R_T are defined as in Section 5.1.4.

Pre-computed tables of nuclear responses, evaluated on a two-dimensional grid in $(\omega, |\mathbf{q}|)$ space, may be provided to GENIE as a set of text files organized by target nucleus and interaction mode (e.g., a table may include only the one-body contribution). A simple nearest-neighbors bilinear interpolation scheme is used to evaluate the hadronic tensor elements $W^{\mu\nu}$ between the grid points. The numerical results obtained in this way are used to evaluate inclusive double differential cross sections using the standard form of the leptonic tensor $L_{\mu\nu}$. Further implementation details are available in [210].

The GENIE strategy described above for inclusive cross section calculations originated in work to implement the Valencia model [310, 232] for CCMEC interactions [361]. The treatment used therein was subsequently generalized and improved to allow for its application to other scattering processes (e.g., EM interactions). In addition to the model presented here, the same code framework was also recently used to add the SuSAv2 calculation [36, 170] of QE and MEC cross sections to GENIE for both neutrinos [169] and electrons [316].

5.2.2 Scaling and Interpolation Techniques

Given the computational difficulty in directly evaluating the STA nuclear responses on a finely-spaced ($\sim$ 1 MeV) grid in $(\omega, |\mathbf{q}|)$ space, one must employ some form of interpolation on the available sparse $\{R, \omega, |\mathbf{q}|\}$ surface [318]. For practical calculations in an event generator, the interpolation method must be fast and efficient while avoiding storage of very large tables in memory. The ability to handle input files for which the ω and $|\mathbf{q}|$ grid points are not regularly spaced is also highly desirable.

All of the above is accomplished within the GENIE MCνEG using a recently-developed "hadron tensor" interface [210], which computes cross sections using bilinear interpolation to obtain nuclear response values between grid points. For the ^{4}He EM responses used in this study, the input tables use a spacing of 2 MeV between ω grid points and 1 MeV between $|\mathbf{q}|$ grid points. The kinematic limits of the grid are 1 MeV $\leq |\mathbf{q}| \leq 2000$ MeV and 2 MeV $\leq \omega \leq 1800$ MeV.

Currently, to achieve such a high granularity on the $\{|\mathbf{q}|, \omega\}$ grid *with* good accuracy, an approximately $|\mathbf{q}|$-invariant object is chosen for use in the form of a nonrelativistic *scaling function*[3], to make thousands of *new* nonrelativistic total nuclear response functions at many *new* momentum transfers. These objects can be calculated from one among several existing nonrelativistic nuclear response functions [318], in-turn creating a single *average* nonrelativistic scaling function $\overline{f_{\alpha}^{nr}}[\psi^{nr}(|\mathbf{q}|, \omega)$ [174, 343, 345, 282] built up from any *set* of scaling functions,

[3]Thanks to S. Dytman, N. Rocco, and A. Lovato for many discussions on this point.

$f^{nr}_{\alpha,i}$, as follows:

$$f^{nr}_{\alpha,i}[\psi^{nr}(|\mathbf{q}_i| \in \widetilde{Q}, \omega)] = k_F \cdot \frac{R^{nr}_{\alpha}(|\mathbf{q}_i| \in \widetilde{Q}), \omega)}{G^{nr}_{\alpha}(|\mathbf{q}_i| \in \widetilde{Q})}, \tag{5.14}$$

$$\therefore \overline{f^{nr}_{\alpha}}[\psi^{nr}(|\mathbf{q}|, \omega)] = \frac{1}{N} \sum_{i=1}^{N} f_{\alpha,i}[\psi^{nr}(|\mathbf{q}_i| \in \widetilde{Q}, \omega)], \tag{5.15}$$

$$\longrightarrow R^{nr}_{\alpha}(|\mathbf{q}|, \omega) = \frac{1}{k_F} \cdot G_{\alpha}(|\mathbf{q}|) \cdot \overline{f^{nr}}[\psi^{nr}(|\mathbf{q}|, \omega)], \tag{5.16}$$

where $\psi^{nr} \equiv \psi^{nr}(|\mathbf{q}|, \omega)$ is a *nonrelativistic* scaling variable [174, 282], $R^{nr}_{\alpha}(|\mathbf{q}_i| \in \widetilde{Q}, \omega)$ is a known nonrelativistic nuclear response function for a particular component α from a known computed set [318] of momentum transfers $|\mathbf{q}| \in \widetilde{Q} = \{400, 450, \ldots, 750, 800, 1000\}$ MeV and where $\widetilde{Q}$ is of size N, $G^{nr}_{\alpha}(|\mathbf{q}|)$ can be any component-specific functional combination of single nucleon electric and magnetic form factors, and k_F is the nominal Fermi momentum of the system. The final $\{R_{\alpha}, |\mathbf{q}|, \omega\}$ surfaces resultant from this averaged scaling shown in Figs. 5.2 serve as the basis objects for all double differential cross section calculations in `GENIE`, and are displayed after subsequent sub-MeV bilinear interpolation on the tabulated grid.

Note that [282] shares a common theoretical basis with inputs used in this chapter [318], and also shows that good scaling behavior persists *even with the inclusion of two-body dynamics*. When comparing to the originally computed longitudinal nuclear response functions, this method *partially* removes some endemic contamination of the *elastic* scattering component, which would otherwise lead to over-estimations of longitudinal response function at low momentum transfers ($|\mathbf{q}| \lesssim 300$ MeV). However, as will be show, the use of an averaged scaling function takes away too much strength from the double differential cross section in some kinematics (particularly those of high outgoing angles). In particular, the averaging technique reduces the strength of *both* response functions at low $|\mathbf{q}|$—as shown in Fig. 5.5, indicating that this technique needs to be improved to achieve a good agreement with the data in the aforementioned kinematic regimes. See the next section for more details. In closing, it is worth pointing out that the elastic peak that is currently contaminating the longitudinal responses at low q can be removed directly within the QMC-STA calculations. Work along these lines is underway.

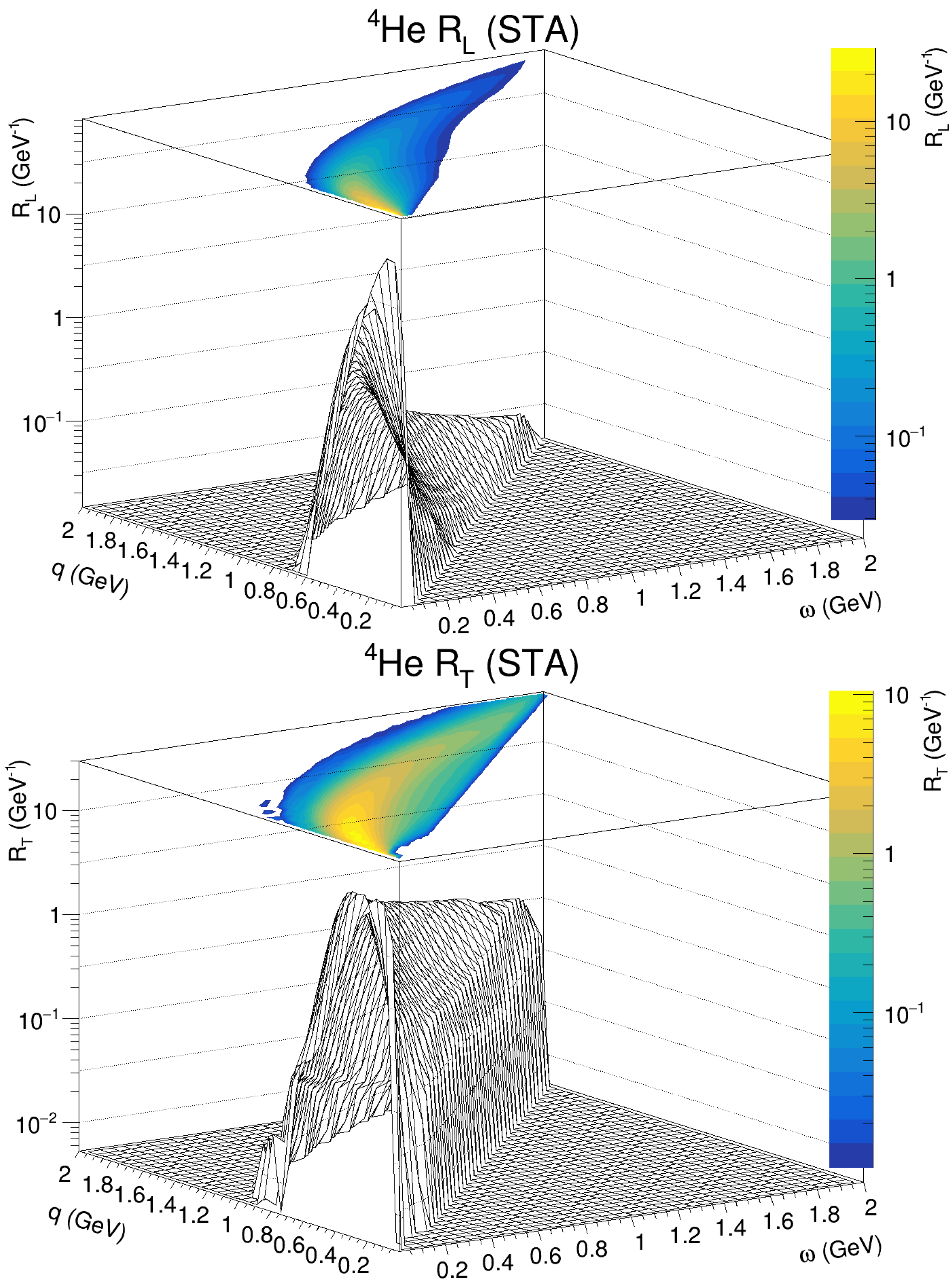

Figure 5.2: The interpolated nonrelativistic nuclear response surfaces $\{R_\alpha, |\mathbf{q}|, \omega\}$ are shown with sub-MeV grid-spacing. The underlying $\sim 1\,\text{MeV}$-spaced $\{|\mathbf{q}|, \omega\}$ grid forms the fundamental objects cast in tabulated form which `GENIE` then dynamically bilinearly interpolates upon to form all subsequent double differential cross sections for QE EM scattering. Lines along the surfaces serve as visual aides only.

5.3 Some Details

Here, some more technical elements of the interpolation techniques will be expounded upon, including the scaling and alignment behavior of the given nuclear response functions [318]. Studies of these properties in the QMC STA response functions can be completed utilizing the nonrelativistic formalisms within [345, 344, 343, 282, 174, 137]; this is appropriate, as relativistic effects on such responses (such as a broadening of the QE response distribution) have been shown previously to be rather small [345] in many QE-like kinematic regimes, and because the STA itself is currently conceived within a nonrelativistic framework.

5.3.1 Scaling Analysis and Densifying $\{R, |\mathbf{q}|, \omega\}$-space for Expansive Response Interpolation

It is critically important to understand the presence of scaling in the QMC STA response functions given the computational intensity behind the production of even a quite course $\{R, |\mathbf{q}|, \omega\}$ surface; if present, scaling allows for the (fast, cheap) construction of many finely spaced nuclear response functions, creating a more dense $\{R, |\mathbf{q}|, \omega\}$ surface which can then be easily interpolated across nearest neighbors to procure any necessary QE kinematic for comparison against empirical QE double differential cross sections. Such is the overarching purpose of the work shown in this section, while also serving to confirm expected similarities between the QMC STA and GFMC calculations which utilize the same many-body Hamiltonians, though differing in their computational methods.

The scaling analysis utilizes the *nonrelativistic* scaling variable ψ^{nr} [282]

$$\psi^{nr} \equiv \psi^{nr}(|\mathbf{q}|, \omega) = \frac{m_N}{|\mathbf{q}| k_F} \left(\omega - \frac{|\mathbf{q}|^2}{2m_N} - \varepsilon \right), \tag{5.17}$$

where m_N is the (weighted, nucleus-averaged) nucleon mass, k_F is the approximate Fermi momentum of the system (though this is a somewhat incomplete concept within *ab initio* methods), and ε is included to approximate the binding energy per nucleon of the system (or a corresponding energy shift). It can be conceived that both k_F and ε may be marginalized over as free parameters, and selected for their optimum scaling behavior; however, for the purposes of this work, values of

$k_F = 0.18$GeV/c and $\varepsilon = 0.015$GeV have been used, as was chosen in [345]; more enlightened efforts in the calculation of such constants from known QMC outputs are also possible. Note the particular form of Eq. 5.17 appears in discussions within [282], while previous discussions such as those in [343] did not take into account this small binding energy shift; removal of this shift does significantly change the scaling behavior.

The actual scaling functions $f_\alpha^{nr}(\psi^{nr})$ for a given nonrelativistic response $R_\alpha^{nr}(|\mathbf{q}|, \omega)$ can be considered in the nonrelativistic limit to take the form

$$f_\alpha^{nr}(\psi^{nr}) = k_F \cdot \frac{R_\alpha^{nr}(|\mathbf{q}|, \omega)}{G_\alpha^{nr}(|\mathbf{q}|)} \tag{5.18}$$

where $G_\alpha^{nr}(|\mathbf{q}|)$ can be any component-specific functional combination of single nucleon electric and magnetic Hohler form factors [244] of neutrons and protons, as shown in Fig. 5.3.

From these, and for *symmetric nuclei only a la* Rocco *et al.* [343], one may construct the scaling functions when evaluated at the approximate QE peak value of $\omega_{QE} = (\sqrt{|\mathbf{q}|^2 + m_N^2} - m_N)$ as

$$f_L^{nr} = \frac{k_F|\mathbf{q}|(Q^2 + 4m_N^2)}{4\mathcal{N}m_N^3} \cdot \frac{R_L^{nr}(|\mathbf{q}|, \omega)}{(G_{E,p} + G_{E,n})^2}, \tag{5.19}$$

$$f_T^{nr} = \frac{2k_F m_N}{\mathcal{N}} \frac{R_T(|\mathbf{q}|, \omega)}{|\mathbf{q}| \cdot (G_{M,p} + G_{M,n})^2 + k_F^2(G_{E,p} + G_{E,n})^2(1 - \psi^{nr})}, \tag{5.20}$$

where $\mathcal{N}$ is the number of neutrons or protons in the symmetric nucleus. Note the possibility of singularities within the transverse scaling function given higher values of $\psi^{nr} \gtrsim 4.5$, or $|\mathbf{q}| \gtrsim 400$. As seen in Figs. 5.4, these scaling formulations appear to (approximately) hold for *both* one-body diagonal and total response contributions across longitudinal and transverse components, showing many similarities to scaling analyses pursued within [343, 282] over a finite range of ψ^{nr}.

With confirmation of (approximate) scaling behavior ($\sim$invariant shape/alignment across many $|\mathbf{q}|$-values), one may begin to conceive of an interpolation scheme to create a more dense $\{R, |\mathbf{q}|, \omega\}$ grid. From a given set of fully computed responses with $|\mathbf{q}| \in \widetilde{Q}$ of size N, a general approximated strategy is to construct an *averaged* nonrelativistic scaling function (visible in total

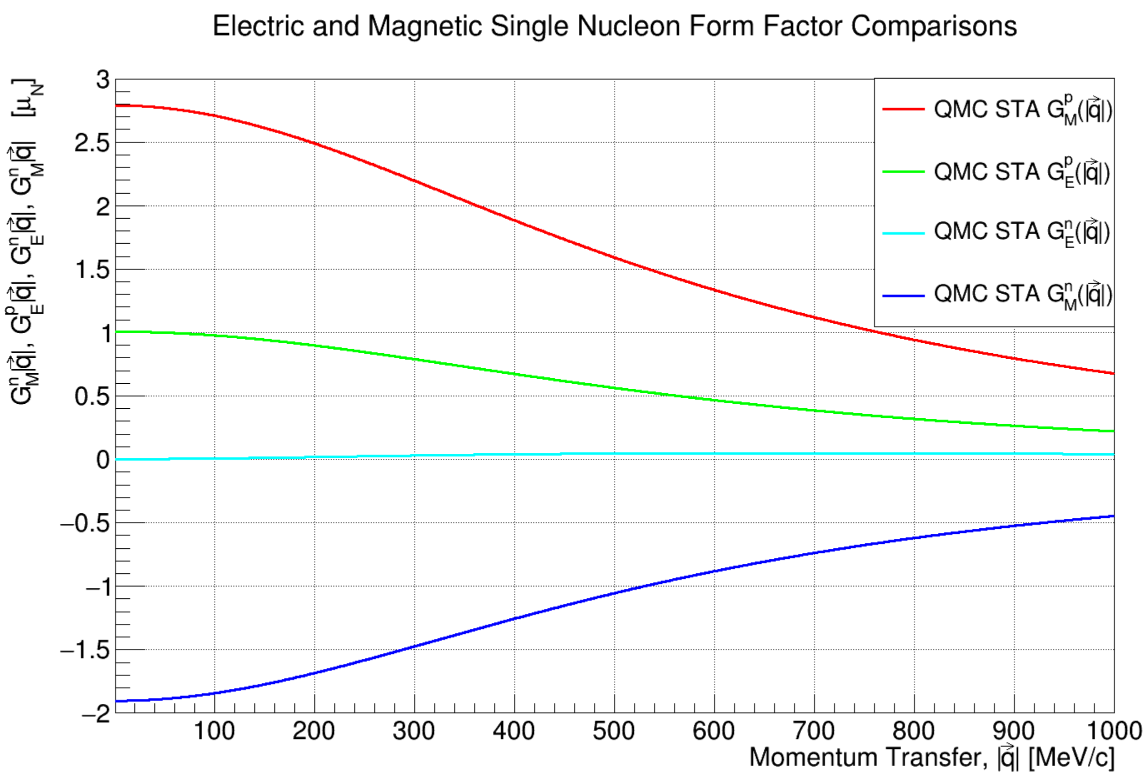

Figure 5.3: The shapes of the single nucleon electric and magnetic form factors [244] used in the QMC STA implementation are shown.

graphs of Figs. 5.4 by burgundy solid lines and labeled as 'Avg. Long.' and 'Avg. Trans.') as

$$\overline{f_\alpha^{nr}}[\psi^{nr}(|\mathbf{q}|,\omega)] = \frac{1}{N}\sum_{i=1}^{N} f_{\alpha,i}[\psi^{nr}(|\mathbf{q}_i|,\omega \in \widetilde{Q})], \tag{5.21}$$

such that one may invert Eq. 5.18 to extrapolate many responses from this single, $|\mathbf{q}|$-independent, averaged nonrelativistic scaling function using

$$R_\alpha^{nr}(|\mathbf{q}|,\omega) = \frac{1}{k_F}\cdot G_\alpha(|\mathbf{q}|)\cdot \overline{f^{nr}}[\psi^{nr}(|\mathbf{q}|,\omega)]. \tag{5.22}$$

The average scaling functions $\overline{f_\alpha^{nr}}(\psi^{nr})$ are calculated from individual components of the total response scaling functions by a simple unweighted average. Weighted averaging, or effectively choosing *which* scaling functions are best behaved, has not yet been investigated, though in principle could be done so to by marginalizing over some parameter(s) in the average's coefficients and comparing against experimental data in an automated way. The presence of scaling, or effective $|\mathbf{q}|$-invariance, permits an *expansive* formulation of new $R_\alpha^{nr}(|\mathbf{q}|,\omega \notin \widetilde{Q})$, and allows one to interpolate *between and beyond* the limited known response values at particular $|\mathbf{q}| \in \widetilde{Q}$, a critical component for QE event generation at many kinematics within `GENIE`.

Using this method, one can compare the *original* computed nuclear response functions [318] with those outputted from the average scaling function approach, as seen in Figs. 5.5 for

$$|\mathbf{q}| \in \widetilde{Q} = \{400, 450, \ldots, 750, 800, 1000\}\,\text{MeV}. \tag{5.23}$$

Overall agreement of the one-body diagonal longitudinal and transverse components are quite good, as expected from the studies of [343], especially at progressively higher momentum transfers where scaling behavior is maximized [174] and the presence of the elastic peak in the longitudinal response is absent.

Given the necessity of filling out the $\{R, |\mathbf{q}|, \omega\}$ surface (especially at higher $|\mathbf{q}|$-values) for more accurate active nearest-neighbors bilinear interpolation within `GENIE` to create double differential QE cross sections, thousands of these new responses are computed and collated to a form tabulated grid with a fine granularity. Here, a characteristic spacing of $\Delta|\mathbf{q}| = 1\,\text{MeV}$ is chosen over $|\mathbf{q}| \in \{1, 2000\}\,\text{MeV}$, and the characteristic spacing of $\Delta\omega = 2\,\text{MeV}$ over

$\omega \in \{2, 1800\}$ MeV, providing ample information for good predictions and validation against available world QE EM scattering data. The full sequence of all 4000 newly interpolated responses inhabiting the full $\{R, |\mathbf{q}|, \omega\}$ space from transverse and longitudinal components can be seen in Figs. 5.2. These are completed with average scaling input in 1 MeV spacing, and GENIE is allowed to bilinearly interpolate these on 0.5 MeV intervals (the example "thrown" energy for the QMC STA QE event generator).

This same method can be repeated on pairs of nucleons with known particle identities, such as pp and nn pairs [318]. This is especially possible for these pairs given the relative lack of two-body correlations present between them, allowing scaling behavior to more readily manifest. Average pp and nn scaling functions can be constructed from known $|\mathbf{q}| = \{500, 600, 700\}$MeV/c two-body particle identity-specific nuclear response functions. These will in principle grow in accuracy when a more complete set (perhaps $N > 7$) of response functions are computed with finer 50 MeV spacing. The current method leads to the curves seen in Figs. 5.10, but more can be seen in Figs. 5.6.

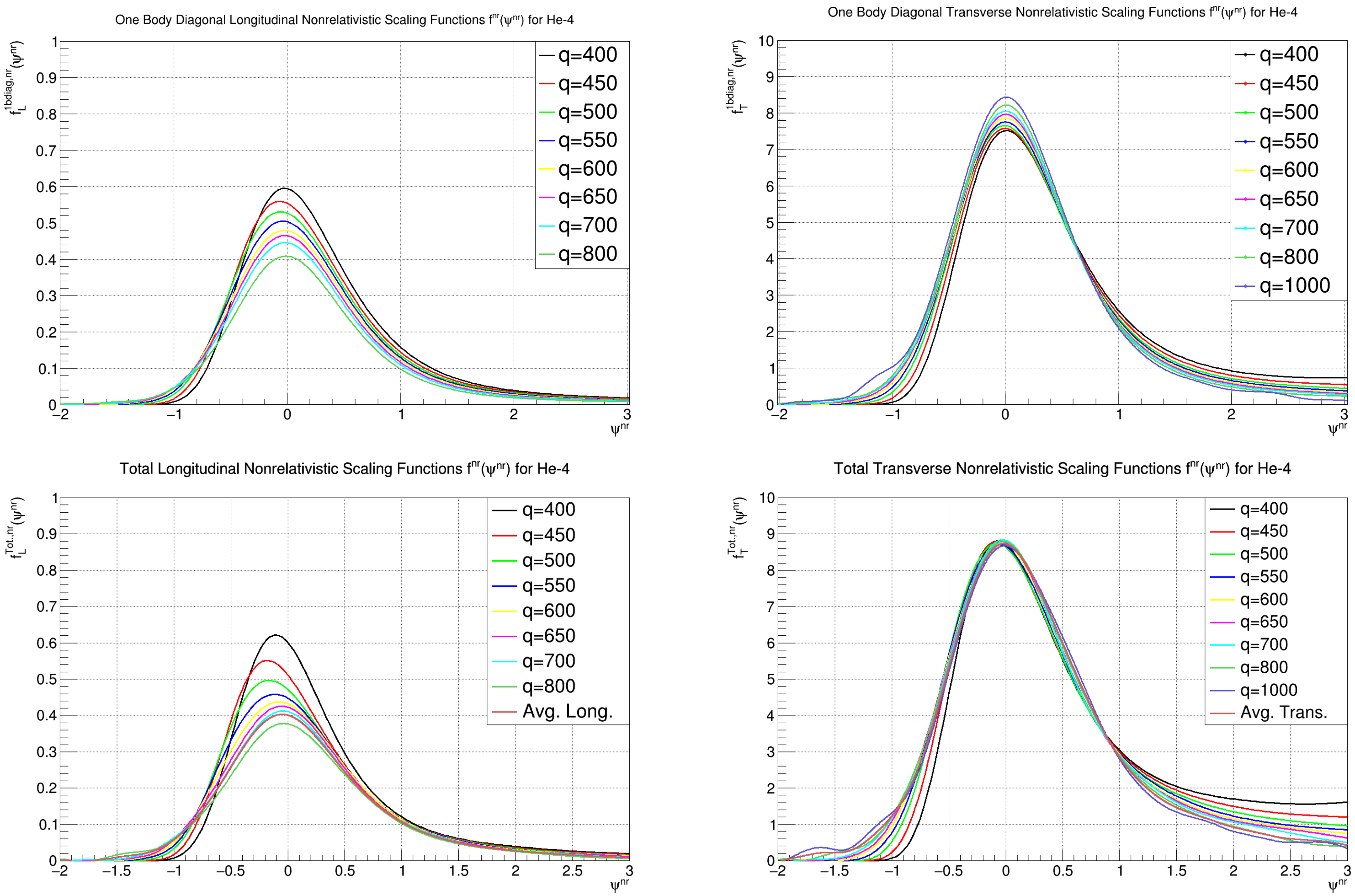

Figure 5.4: Approximate scaling is observed for both the one-body diagonal term ("1bdiag") and total ("Tot." = one body diagonal + one-body off-diagonal + interference + two-body) electromagnetic response contributions across longitudinal and transverse components; this appears particularly strong in the total transverse response. Note the respective (marginal) destructive and (strongly) constructive behavior of the longitudinal and transverse components when moving from a one-body diagonal to total response paradigm by adding additional interference and two-body terms. The average scaling function is calculated from all shown total responses. Though computed, responses for $|\mathbf{q}| = \{300, 350\}$MeV/c are currently not included in this analysis due to presence of the *elastic* peak, thus spoiling scaling across all components. The longitudinal component of $|\mathbf{q}| = 1000$MeV/c has not yet been computed.

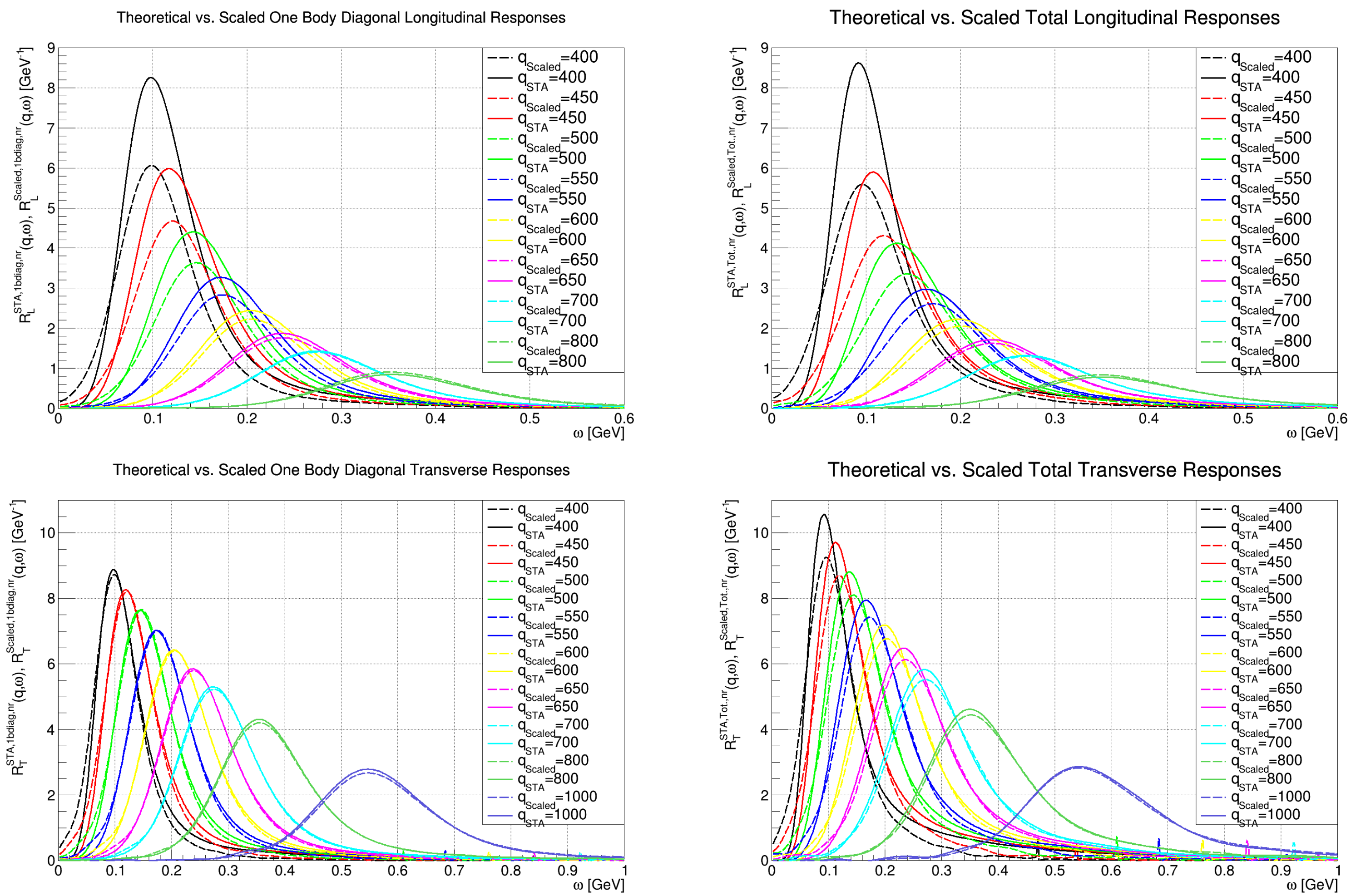

Figure 5.5: Comparisons between newly created scaled (dashed) and originally computed (solid) one-body diagonal and total nuclear response functions are shown. Note the excellent agreement of the transverse responses due to the lack of strength of the elastic peak in this particular component, while the reduced strength of the scaled longitudinal responses removes the elastic strength due to higher momentum transfer responses outweighing the average scaling function; however, too much strength is lost here due to the averaging scheme in both the longitudinal and transverse responses. Other methods may be pursued in future work.

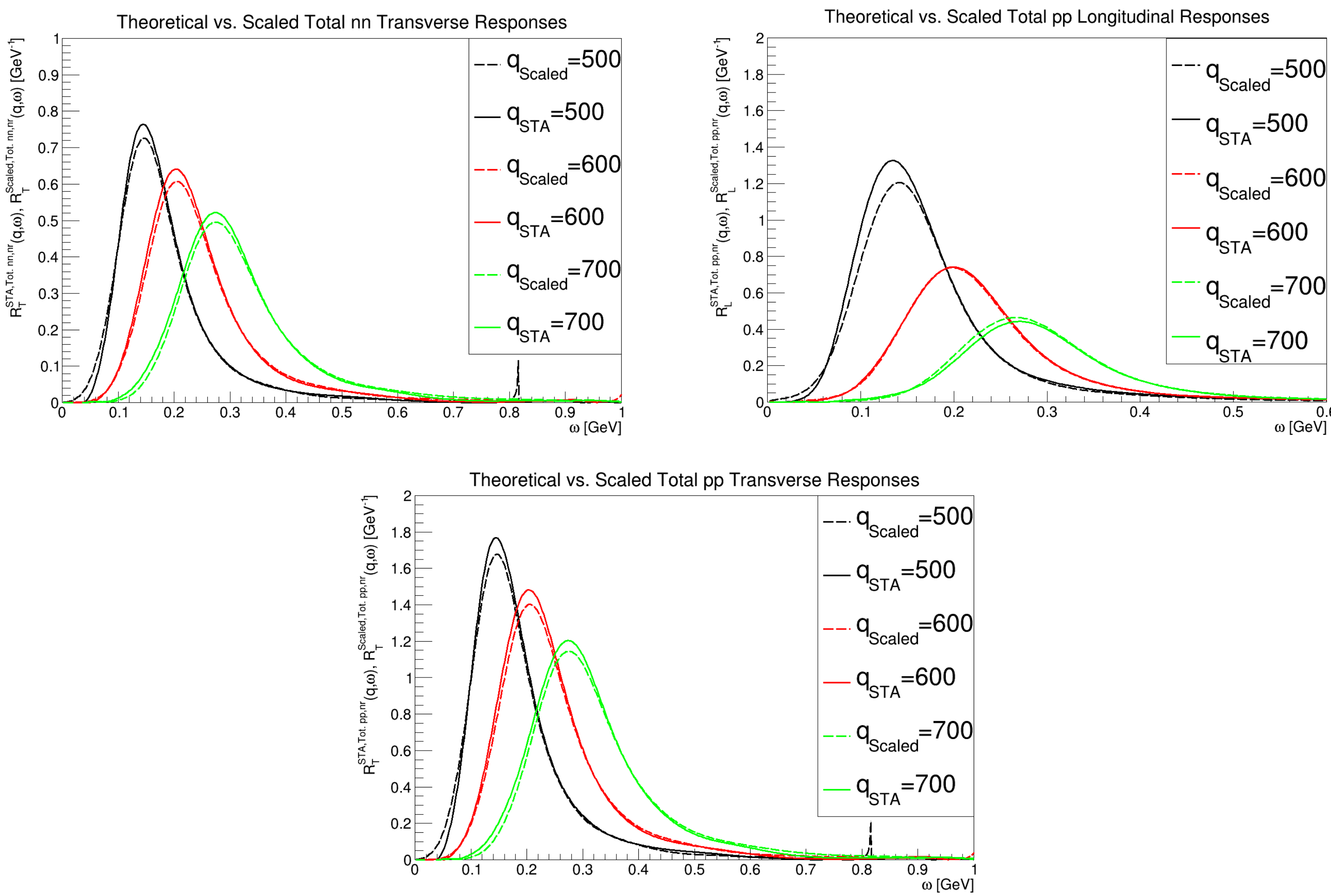

Figure 5.6: The original [318] and scaled two-body particle identity-specific nuclear response functions are shown for pp and nn pairs, mirroring Figs. 5.5. Only the $|\mathbf{q}| = \{500, 600, 700\}$MeV/c responses are shown here; in principle, the number of known responses can increase, allowing for better-behaved and *expansive* interpolation for a densifying of the two-body $\{R_{NN}, |\mathbf{q}|, \omega\}$-surface; from this, more robust double differential cross sections could be derived. Note the different ranges (strengths) of the different components of each channel due to differences in underlying pairing dynamics; the nn longitudinal responses are not shown due to low values.

5.3.2 Nuclear Responses in $\{R/G^2_{E,p}, |\mathbf{q}|, \psi^{'}\}$-space for Aligned, Interceding Response Interpolation

Another method for faster calculation of many responses at many different $|\mathbf{q}| \notin \widetilde{Q}$ is explored in [345] (drawing on previous works [27, 60, 343]), particularly with respect to Eq. (18) and Figs. 5 and 6 therein; reproductions of these from present work can be seen in Figs. 5.7, where response *alignment* occurs upon the variable transformation $\omega \to \psi^{'}_{nr}$; here, $\psi^{'}_{nr}$ takes the nonrelativistic *dimensional* form

$$\psi^{'}_{nr} = k_F \left(\frac{\omega - \varepsilon}{|\mathbf{q}|} - \frac{|\mathbf{q}|}{2m_N} \right), \tag{5.24}$$

and again one may choose that $k_F = 0.18$GeV/c and $\varepsilon = 0.015$GeV as in [345]. This allows one to transform the dimensional grids $\{R_{nr}, |\mathbf{q}|, \omega\} \leftrightarrow \{R_{nr}/G^2_{E,p}, |\mathbf{q}|, \psi^{'}_{nr}\} \equiv [GeV^2]$ for more accurate interpolation *between* aligned responses without loss of generality.

It should be noted that this interceding interpolation scheme will not have the ability to create as much phase space volume as the scaling method outlined above, as it critically does not rely $|\mathbf{q}|$-invariance to *expand* beyond the known response domain. Work to implement and compare behavior between this *interceding* interpolation and the previously discussed *expansive* interpolation is ongoing, and will be included in a future publication.

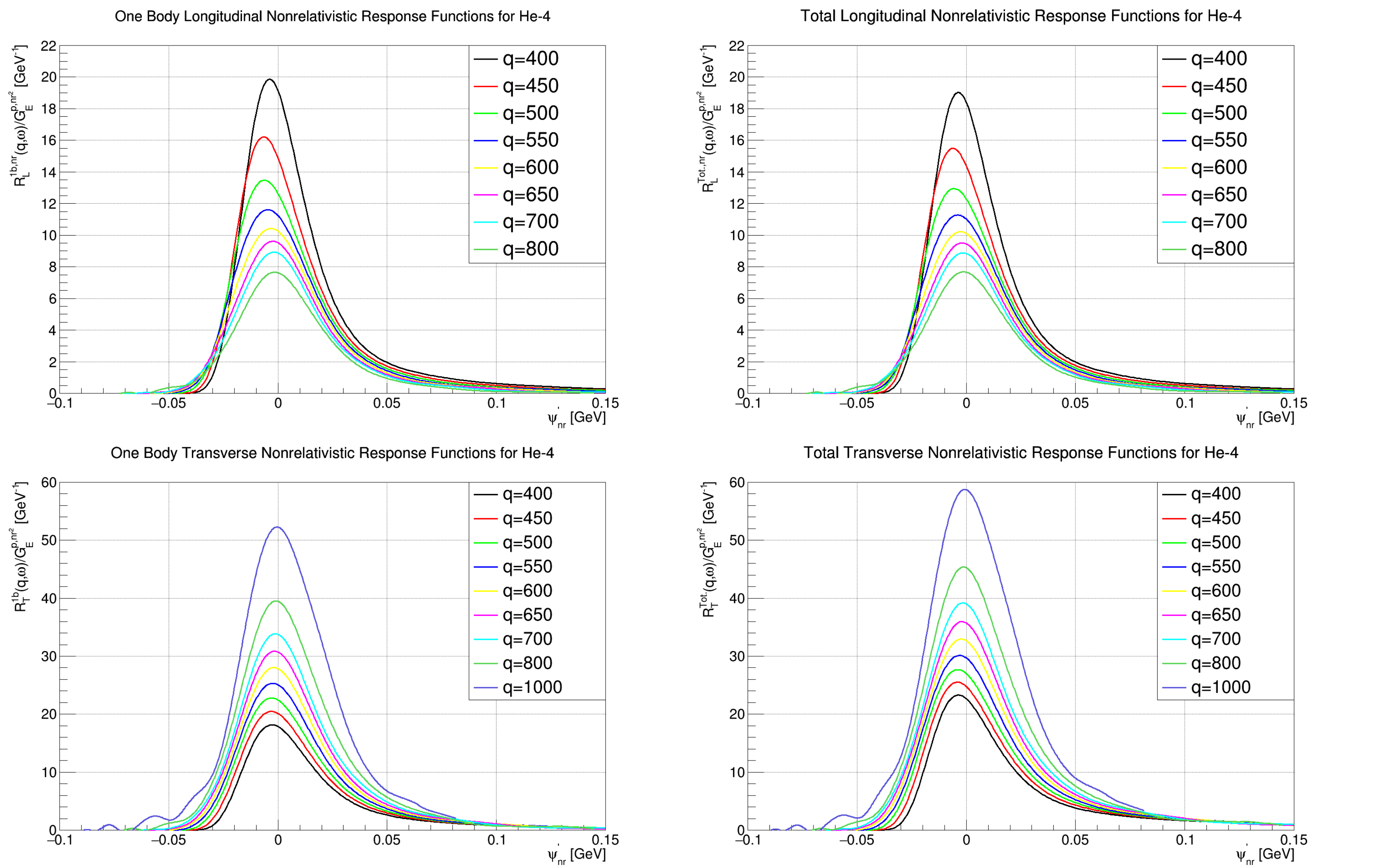

Figure 5.7: Alignment of form factor normalized response functions is shown when graphing against the nonrelativistic dimensional parameter ψ'_{nr}.

5.4 Validation Against e^4He Quasielastic Scattering World Data

5.4.1 Inclusive Electromagnetic Responses and Double Differential Leptonic Cross Sections

Transverse and longitudinal nuclear response functions [318] have been validated against available EM nuclear response data sets from Sick *et al.* [139] and von Reden *et al.* [405] where possible, as shown in Fig. 5.8 with excellent agreement without direct pion production. A tool utilizing `GENIE`'s hadron tensor framework completes bilinear interpolation of scaled nuclear responses across $|\mathbf{q}|$ and ω, allowing for calculation of double differential cross sections from scaled nuclear response inputs, and so one may compare to available world QE double differential cross section data sets [77, 163] for $^4_2$He. A small selection of these can be seen in Figs. 5.9. This simple technique shows good comparative power to data *despite* the use of the averaging interpolation techniques and the lack of explicit removal of the elastic peak, relativistic corrections, or on-shell π-production via Δ resonances, broadly matching the QE position and width up to around $2\,\mathrm{GeV}$ of electron beam energy (the highest scaled response $|\mathbf{q}|$-value utilized is $2\,\mathrm{GeV/c}$)[4]. Thus, as a purely QE theory [318], one observes MC-generated double differential cross sections beneath experimentally determined ones; this is in part thanks to scaling's effective removal of the elastic peak, but also due to the averaging scheme, which lowers the strength of the responses slightly too much at certain kinematics. Cross sections do remain consistent with experimental ones at moderate to high momentum transfers and moderate to high scattering angles, where the transverse response of the nucleus containing two-body dynamics plays a disproportionate role[5].

[4] The full statistical consistency of these model curves with data across all available angles and energies will be pursued in future work; comparison between various model predictions may also be pursued.

[5] Once coherent modules are complete for *simultaneous* event generation of leptonic and hadronic variables for the semifinal state at the interaction vertex, thus utilizing the STA response *densities*, it is planned that the scaled response function averaging scheme will be superseded by another nonlinear multidimensional interpolation technique [45]; comparisons with current techniques will follow in a future work.

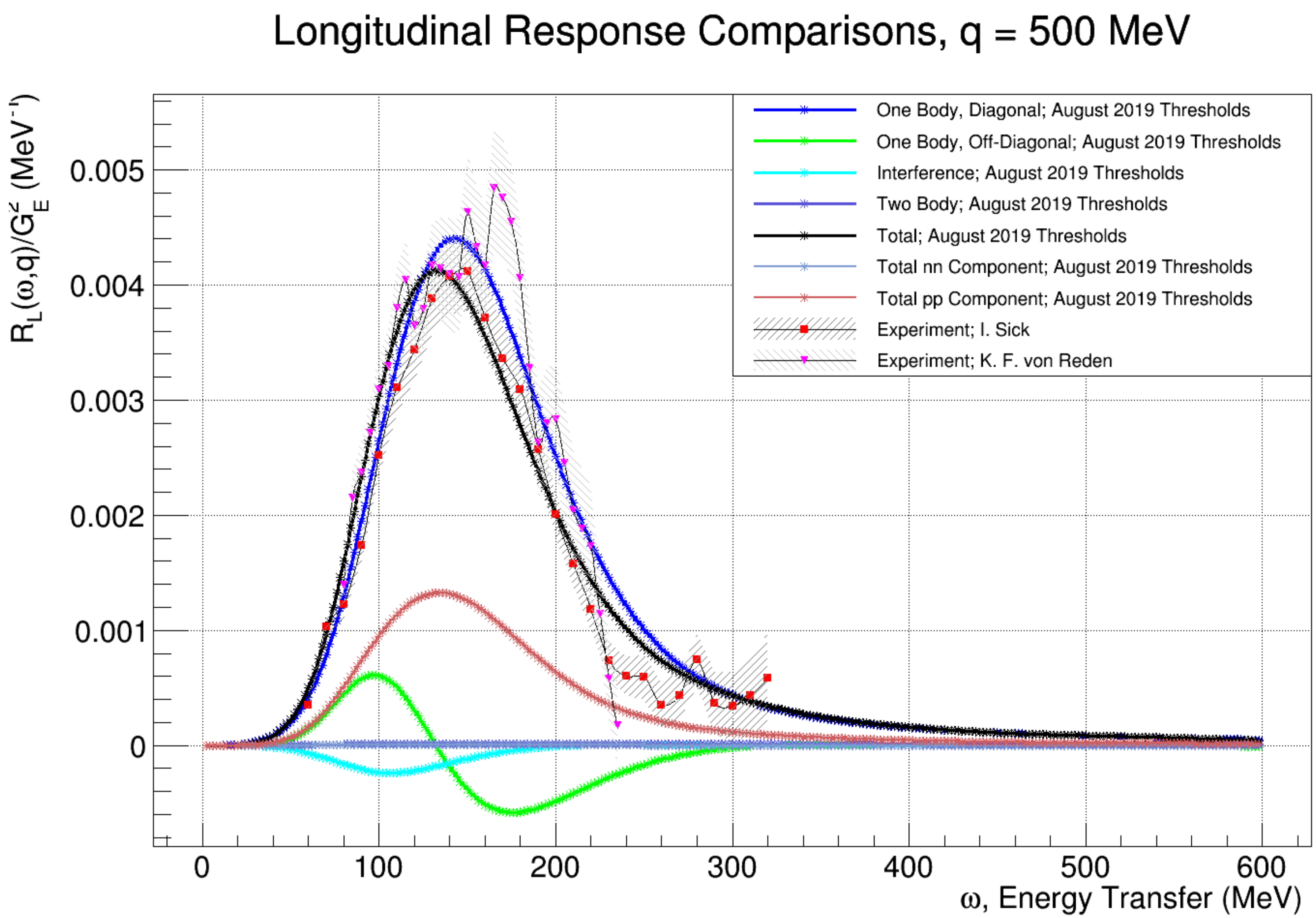

Figure 5.8: Longitudinal nuclear responses comparisons between QMC STA theory outputs [318] and available empirical data [405, 139]. Many response components are shown, including but not limited to *interference* and one-body *off-diagonal* terms, whose destructive qualities within particularly the longitudinal response limit the strength of the pure one-body contribution. Thresholds refer to a *small*, free shift-parameter which has been simplistically tuned in post-processing to better fit available response data. Transverse responses also show good agreement with data, and can be seen in [69].

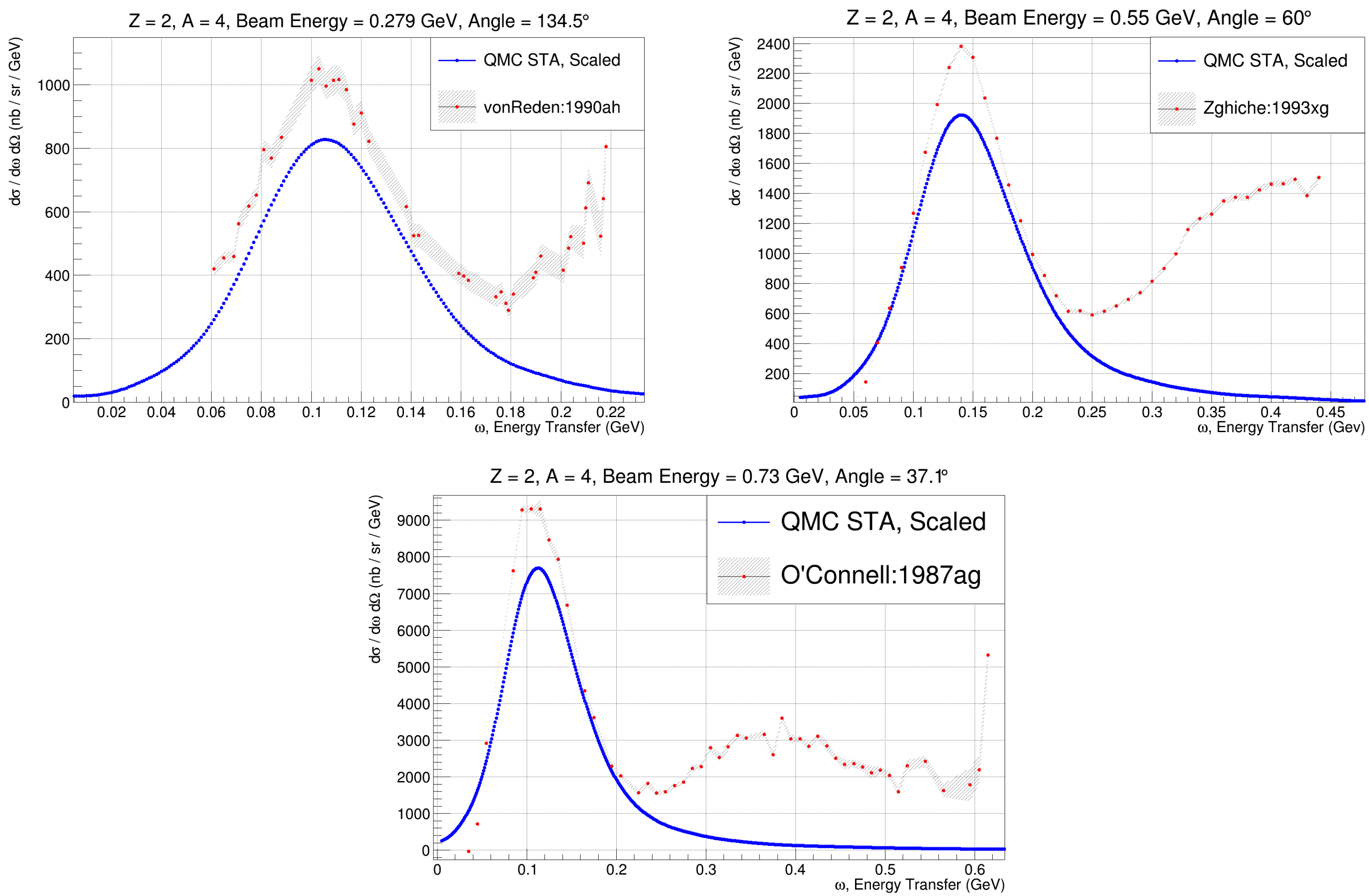

Figure 5.9: A series of ^{4}He double differential leptonic cross sections are shown for various beam energies and angles, derived from the scaled responses coming from the average scaling function. Behavior is good overall, with all curves properly and consistently undershooting the QE-peak due to lack of resonant production. This is especially true for beam energies $< 2\,\mathrm{GeV}$ and more forward angles, though even highly transverse cross sections appear quite consistent with data. However, one can see that strength is missing from the top-most plot at low energy and high angle, due to the current averaging scheme of scaled nuclear responses.

5.4.2 Double Differential Leptonic Cross Sections and Approximate Two-Body Final State Predictions

Using the QMC STA formalism, one may also consider total QE EM (reaction) double differential leptonic cross sections of individual components of the nuclear structure, giving one access to the one- and two-body contributions. In Figs. 5.10, the theoretical total QE EM double differential cross section (dark blue) is shown to match the shape and peak position of available data (red) quite well, while again properly under-predicting the total due to lack of π-production. Individual shapes of the cross sections for scattering from pp (pink) and nn (light blue) pairs can also be seen, including in a zoomed-in view (lower).

The pink and light blue curves shown are derived from an identical scaling method utilizing known $|\mathbf{q}| = \{500, 600, 700\}$ MeV/c particle identity-specific nuclear response functions. It should be stressed here that the (lower) plots in Figs. 5.10 are speaking to the final state lepton *only*; however, such a final state lepton indeed must be *approximately* commensurate with the appearance of pp and nn final states. This is approximate due to the nature of intranuclear FSIs, where multiple scattering can (generally) lead to reductions in the struck nucleons' kinetic energy to potentially below the Fermi energy; the resultant final state topology could then become $eNN \rightarrow eN$. Similarly, again *due* to FSIs, one may potentially have a true QE interaction, but multiple scattering may be such that two nucleons enter the final state, *i.e.*, $eN \rightarrow eNN$. The interference of these effects will be studied in greater detail in future work, where marriage between leptonic and hadronic components of the QMC STA will be mediated by correlated use of both QMC STA response *densities* and GENIE FSI models; once complete, two-nucleon final state data will be considered to validate (and *potentially* tune) the full generator module.

5.4.3 Generating GENIE Leptonic Events

Sampling of the lepton kinematic variables is handled by GENIE in the same way as for the SuSAv2 implementation [169]. An accept/reject approach is used to select a value of final lepton kinetic energy T_ℓ and its scattering cosine $\cos\theta_\ell$ in the lab frame from the probability distribution

$$P(T_\ell, \cos\theta_\ell) = \frac{1}{\sigma}\,\frac{d^2\sigma}{dT_\ell\, d\cos\theta_\ell} \tag{5.25}$$

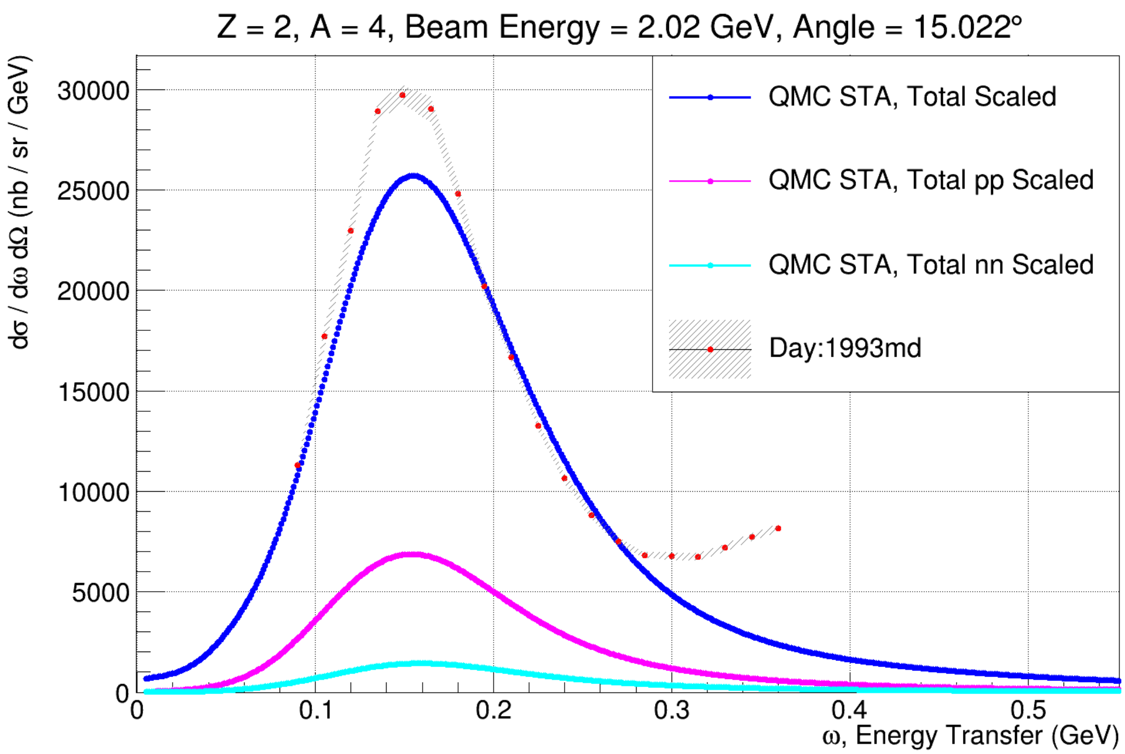

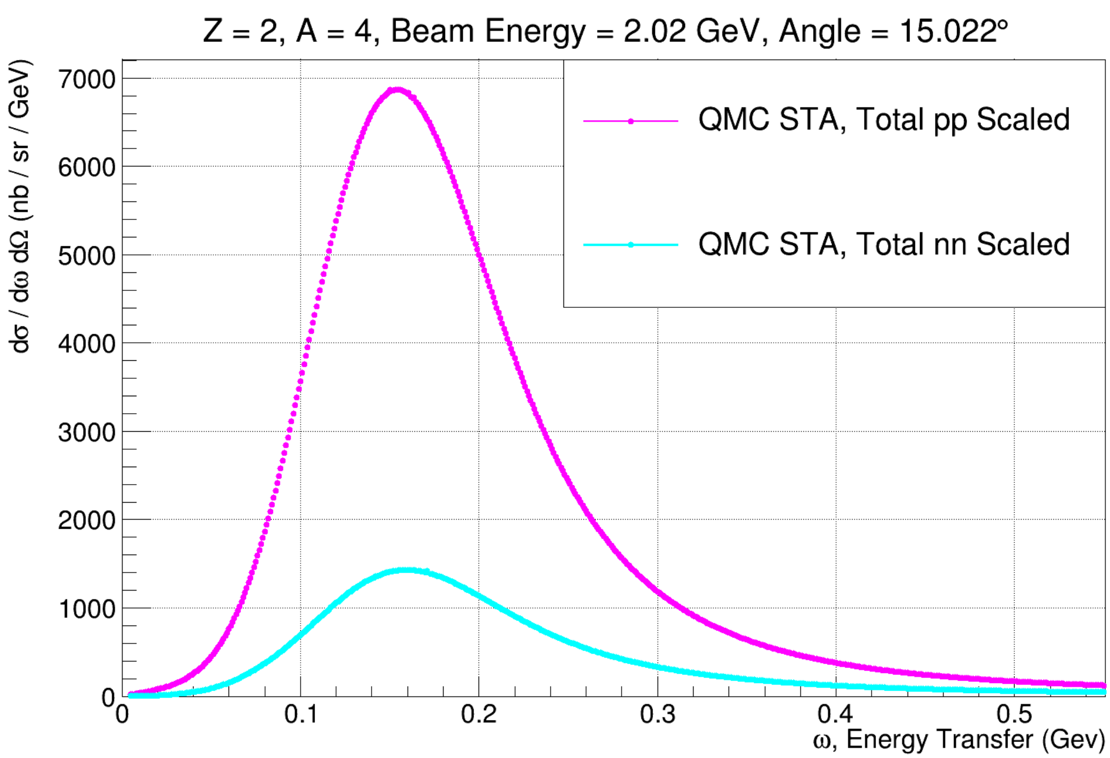

Figure 5.10: A prediction of total inclusive double differential electron scattering cross sections. The pp and nn channels are also shown.

where σ is the total cross section. The maximum value of the differential cross section in Eq. 5.25, which is needed for rejection sampling, is found via a brute-force scan over the two-dimensional phase space. After T_ℓ and $\cos\theta_\ell$ have been selected, a value for the azimuthal scattering angle ϕ_ℓ is chosen uniformly on the interval $[0, 2\pi)$.

In Fig. 5.11, the representative results from all of these efforts to validate `GENIE` simulations of inclusive electron-^{4}He scattering using the STA nuclear response functions [318] are shown. In each plot, the measured cross section [423, 163] at fixed scattering angle is drawn using red points, while the QMC STA calculation is shown by the blue curve. Cross sections computed using `GENIE` events (with the angular acceptance indicated in the plot title) are drawn as black histograms. Excellent agreement is seen between the generated events and the underlying STA calculation. Some expected strength can be seen to be missing from the lower plot, again due to the averaging scheme.

5.5 Outlook, Conclusions, and Some Next Steps

I have shown the formulation of a new quasielastic electron scattering module for final state leptonic variables conceived within the `GENIE` Monte Carlo event generator using scaled and tabulated nuclear response function inputs from quantum Monte Carlo Short-Time Approximation calculations. Importantly, the model implemented within the event generator module retains one-body, two-body, *and interference* physics in a fully quantistic manner within the quasielastic scattering regime, a unique and powerful addition to better understand experimental measurements. Despite the marked computational intensity to simulate the many-body problem, and the current contamination of the elastic peak in the calculated longitudinal response function at low momentum transfer ($|\mathbf{q}| \lesssim 300$ MeV), and thanks to the (approximated) average scaling analysis and proceeding interpolations, prodigious world data comparisons to `GENIE`-derived outputs over a large range of quasielastic momentum transfers show good agreement for both longitudinal and transverse angles, particularly in that no predicted double differential cross sections overshoot experimental data which contain resonant production. Going forward, the direct removal of the elastic peak from the Short-Time Approximation's longitudinal nuclear response functions and densities at low momentum transfer will be sought.

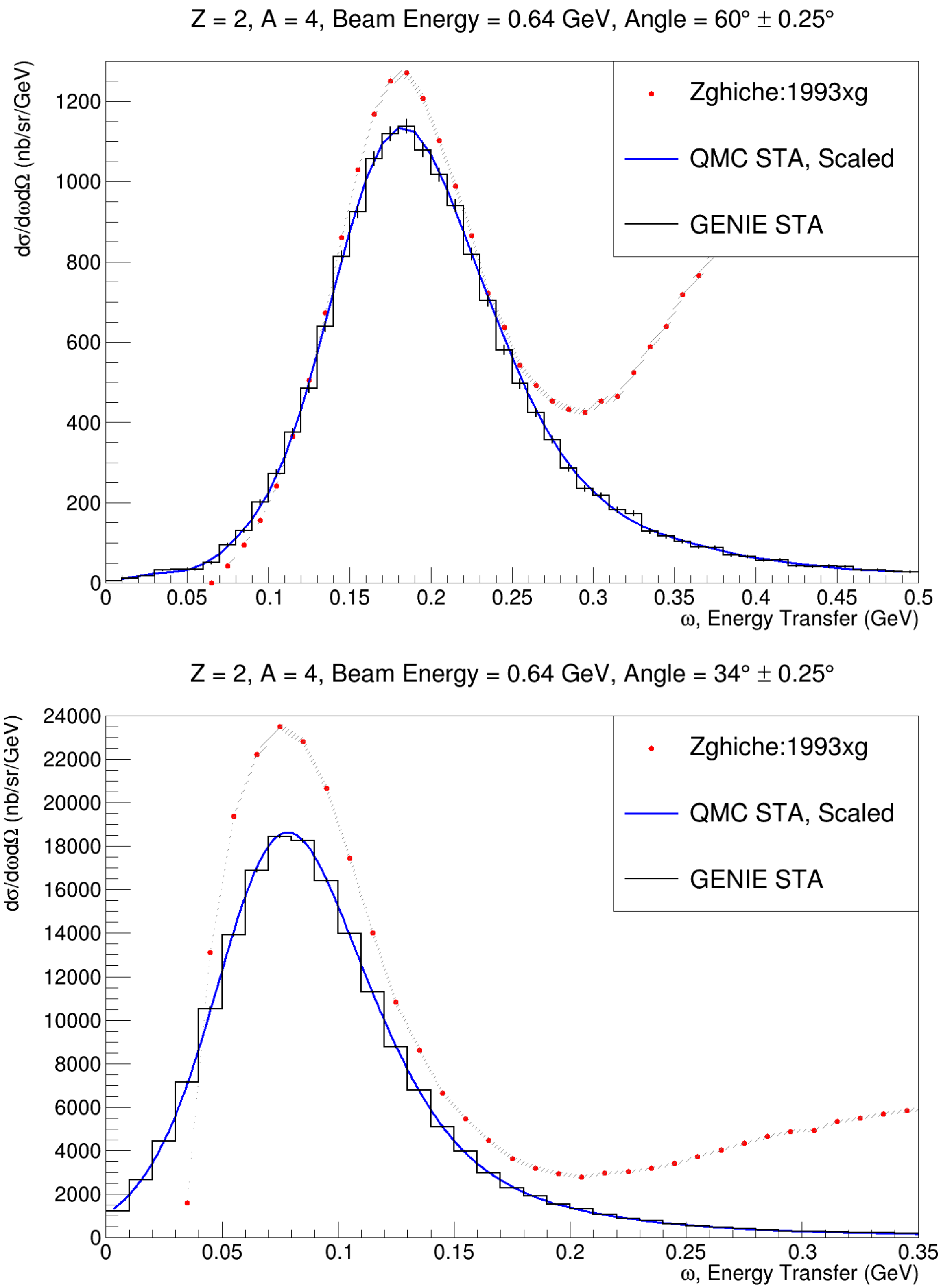

Figure 5.11: Two kinematics are shown for double differential cross sections showing data, scaled theoretical curves, and `GENIE` generator outputs. Great consistency in all three is observed throughout the QE regime. Courtesy of S. Gardiner.

I have hinted throughout this chapter on a more all-encompassing path beyond this thesis, where instead Short-Time Approximation nuclear response *densities* and their descriptions of intranuclear semifinal states will be eventually married to `GENIE` final state interaction models for intranuclear transport to assess simultaneous correlations between the outgoing lepton and one-or-two nucleons. The numerical interpolation [45] between and integration of these densities within `GENIE` itself, and comparison to *known* Short-Time Approximation outputs, will allow for robust validation amidst ongoing event generation. If this powerful method shows consistency between data and the resulting generated cross sections, it will be able to supersede the scaling analyses and interpolation schemes shown here, simultaneously generating correlated semifinal state behavior for *both* the lepton and hadrons moving out from the interaction vertex. None-the-less, optimization of scaling behavior for even stronger consistency with data will be pursued for the outgoing lepton, possibly by the use of weighted averaging and χ-square comparisons against data. Also, other nonlinear nearest-neighbor interpolation schemes can be pursued between scaled responses *and* nuclear densities for the creation of a still more accurate, dense $\{R, |\mathbf{q}|, \omega\}$ surface.

Furthermore, with the Short-Time Approximation supporting identical microscopic numerical simulation structures for *both* electromagnetic and electroweak interactions, multiple model predictions for electron and ν scattering can eventually be compared to assess overall validity of theory against experiment, allowing for better understanding of modeling systematics and their effects on interpretations of future ν measurements to take place within the quasielastic regime at future long- and short-baseline ν oscillation facilities. Such a program, in concert with many actively developing improvements across many simulation types and energy regimes within the broader community, may be able to better elucidate physics beyond the Standard Model; it can also provide definitive simulations for atmospheric neutrino simulations needed for BSM searches (see again Chap. 4). This is especially possible within the Short-Time Approximation formalism due to its extensible nature beyond light nuclei via Auxiliary Diffusion Monte Carlo methods up to ^{40}Ar. Alongside my collaborators[6], I plan to continue this work in the very near future beyond ^{4}He to include ^{3}He, ^{12}C, and possibly even ^{6}Li.

[6] Again, many, many thanks to S. Gardiner, S. Pastore, M. Betancourt, and J. Carlson for their collaboration on this work.

5.5.1 The Full Generator Module to Come with One-and-Two-Nucleon Final States

The only quasi-classical components involved with the eventual *full* `GENIE` implementation will likely be:

1. **Approximations of intranuclear interaction vertex position** One of the quantum mechanical limitations of this new momentum-based formalism, in contraversion to most event generators, is the seeming lack of definite angular/positional information in the nucleus: one cannot know a particle's location and momentum simultaneously. This means one must use other information to pass necessary but approximate event configurations to `GENIE`, such as single nucleon position and two-nucleon separation [327, 414] distributions to permit (semi-spherically degenerate) triangulation within the nucleus, as discussed within Fig. 5.12.

2. **(Randomized) approximations of the angular distribution of nucleons at the vertex** In concert with the tabulated nuclear response density information containing only nucleon pair total and relative momentum distributions for given values of momentum transfer, by assuming a uniform or gaussian two-body angular distribution, via Laws of Cosines, one can of course reconstruct the semi-final state of each individual nucleon in the nucleus before transport through the intranuclear cascade. More elegant formalisms *may* also be possible, and will be the subject of continued investigation. For instance, if one considers a geometric interpretation of the nuclear responses as expansions in the motional modes of the nucleus, say, as spherical harmonics, then two nucleons can be emitted from the nucleus along randomly chosen nodes while preserving momentum and angular correlations with the leptonic interaction plane. Both of these possibilities can be considered within the generator framework, and each would allow for study of overall consistency with experiment.

3. **A momentum threshold for nucleon emission** When striking a correlated nucleon pair, it is possible that only one nucleon receives most of the momentum transfer. This will be considered a free parameter and fitted to best match e scattering data [383, 77].

4. **The intranuclear transport of struck nucleons through the nucleus using `Intranuke hA/hN20XX`**

5.5.2 Conclusions

Once complete, a full validation of this generator on quasielastic (e,e'), $(e,e'N)$ and $(e,e'NN)$ scattering data will proceed. A goal of this comparison will be to understand dependence of two-nucleon final state multiplicities on initially correlated nuclear systems; this could directly constrain free parameters in the intranuclear cascade in GENIE. After this, once response densities become available, ν scattering comparisons in the quasielastic region will begin. The hope is that this more complete simulation can help clarify some controversial anomalies in certain experiments, possibly directly constraining nonstandard physics, and empower other BSM searches with precise background calculations. Altogether, I hope this will reduce the uncertainties throughout the technical points mentioned, aiding experimentalists in the precise reconstruction of ν properties.

The main thrust of my work within this chapter, beyond S. Gardiner's original development of the HadronTensor framework [210] within GENIE, has been the development of the interpolation scheme and data comparison methods. The average scaling function for *expansive* interpolation is my own original development[7], and seems to perform quite well within this work [69]. My application of these techniques to two-body response functions is entirely new, are rather surprising in their robustness, and allow for somewhat *exclusive* predictions to be made as to their relation to leptonic double differential cross sections. As discussed, I have also developed first steps in other *interceding* interpolation schemes, but these have not been completed to a point where double-differential cross section comparisons can be made. Otherwise, I have co-developed the scheme to determine the angular dependencies of the two-nucleon *semi-final* states before final state interactions, coining the term in the process.

[7] Thanks again to N. Rocco, A. Lovato, and S. Dytman for many discussions on this topic.

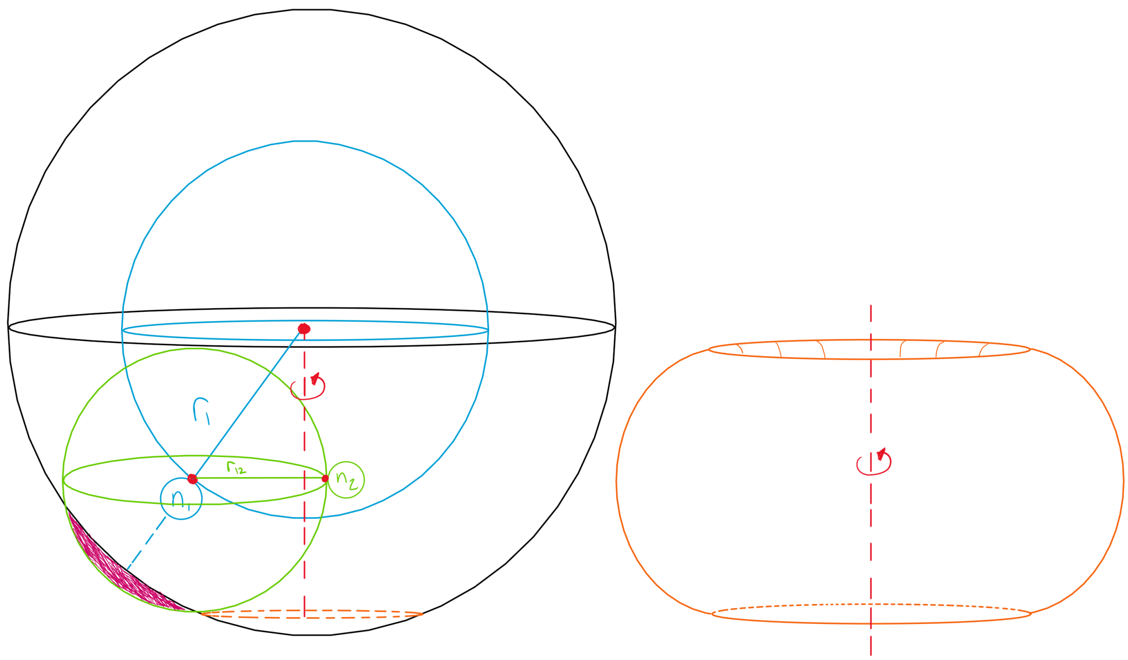

Figure 5.12: A spherical cow is shown (black) of a particular radius R. Though a pair of correlated cows (blue n_1 and green n_2) move about within the cow, it turns out that one can only track them with some form of geometric degeneracy. One can only utilize [414] by throwing from a one-body position distribution $P(r_1)$ first, followed by throwing from a two-body *separation* distributions $P(r_{12})$; thus, triangulation of these cows leads to a semi-toroidally degeneracy upon rotation (orange) of the separation sphere through space, unless broken by some other angular input. The pink region (lying outside the black cow) is disallowed, and would itself skin the torus (orange) with with a disallowed volume upon rotation.

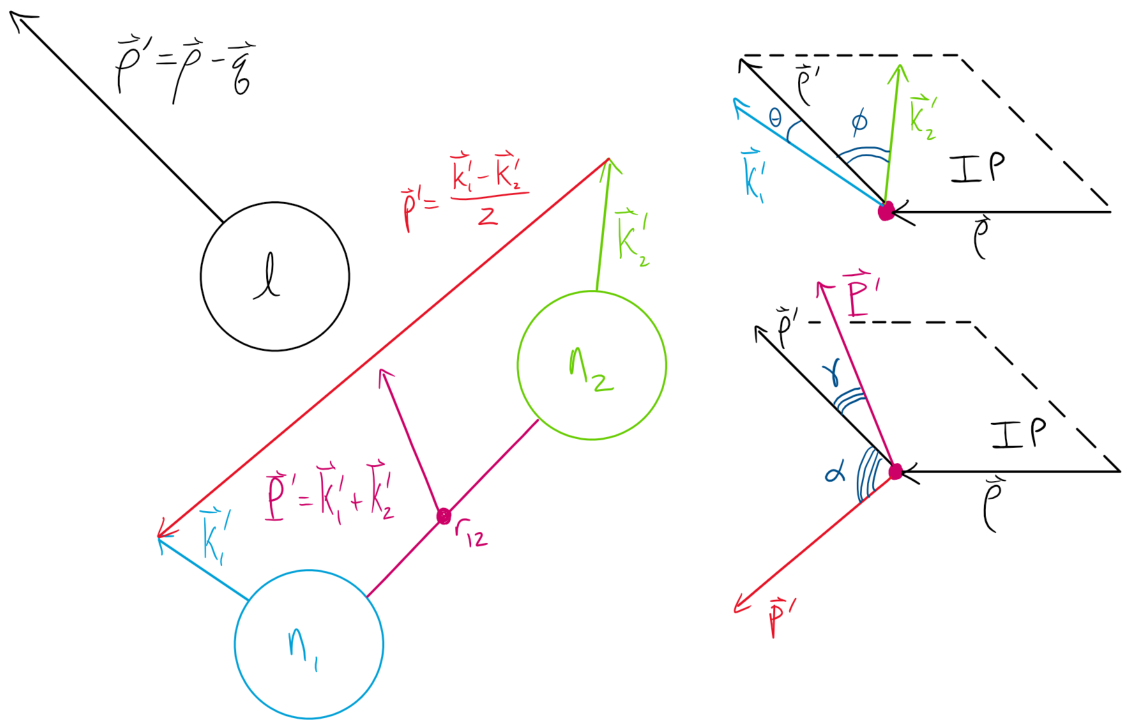

Figure 5.13: A simplified, classical view of the kinematics at play at the interaction vertex is shown. A lepton with initial momentum ρ is incident upon a pair of correlated nucleons with total momentum $\mathbf{P}'$ and relative momentum $\mathbf{p}'$ and transfers $\mathbf{q}$ of momentum to the pair, leaving the outgoing lepton with ρ'. Geometrically, the incoming and outgoing lepton momenta span the interaction plane (IP), from which the angles of all four nucleon pair relevant momenta are referenced; these can be mapped to each other by momentum conservation and Law of Cosines.

Chapter 6

Overarching Thesis Review and Summary of Scientific Contributions

Throughout this thesis, I have endeavored to update the community on recent work I have personally completed or been deeply involved with through the work of the NNBAR/HIBEAM and DUNE collaborations. Each of these experimental programs shows great promise for neutron-antineutron and neutron–mirror-neutron transformation searches. Each of these searches was motivated by a review of the pertinent theory.

Following this, my developments were discussed over the subsequent chapters of this thesis, and each can be broadly summarized as:

1. The further development of an independent antineutron annihilation Monte Carlo simulation for use in extranuclear antineutron-carbon and intranuclear antineutron-argon and antineutron-oxygen processes. Note this is the only widely used generator to have been tested and validated on available antiproton annihilation data [229]. Key among my contributions have been the suggestion, co-development, testing, and validation of multiple new parts of this independent simulation framework [229, 71, 70], including

    - The inclusion, evaluation and redistribution of the mesonic and pionic parameter spaces within the validation framework

    - General testing and validation of all simulations, and data comparisons where available

• The suggestion of the antineutron potential [71]

• The suggestion of the addition of photonic de-excitations of nuclear remnants, most pertinent to water Cherenkov detectors [70]

• Participating in and leading ongoing discussions of NNBAR/HIBEAM detector design requirements [67, 19]

• The implementation of the extranuclear antineutron-carbon annihilation signal in the NNBAR detector simulation [67]

2. The development of the first sensitivity calculations for neutron-antineutron and neutron–mirror-neutron transformations for the first stage HIBEAM experiment at the European Spallation Source's ANNI beamline at low power, useful for initial physics runs following beam commissioning. Particular contributions include:

   • Co-development of the experimental configurations for neutron–mirror-neutron disappearance and regeneration searches

   • First gravitational beam transport simulations for the HIBEAM experiment at ANNI using self-developed codes [19]

   • First neutron–mirror-neutron transformation sensitivities for both disappearance and regeneration style resonance searches using low magnetic fields at HIBEAM a la developments in [96] with the full ANNI beam simulation [19]

   • First neutron-antineutron transformation sensitivities at HIBEAM [19]

   • First developments to consider an ellipsoidal neutron reflector for increasing sensitivities at HIBEAM for neutron-antineutron transformations using self-developed codes

   • Integration of annihilation events' vertices within the NNBAR and HIBEAM detector simulations with positions derived from neutron transport calculations

3. The co-development of new [72] intranuclear neutron-antineutron sensitivity calculations in DUNE using full detector simulations of signal and oscillated atmospheric neutrino background. I developed methods of iteration across nuclear model configurations in order to assess the potential spread of statistical lower limits for $\tau_{n\bar{n}}$, a de facto appraisal of the

modeling uncertainties as a function of a automated analysis method involving boosted decision trees [257, 12] and convolutional neural networks [243] previously developed within the DUNE HEP Working Group. My contributions are:

- I co-developed the first background estimations for intranuclear neutron-antineutron transformation in the DUNE far detector by furnishing six-type oscillated atmospheric neutrino Honda fluxes [247] using NuFitv4.1 [184] oscillation parameters within `GENIE`

- I developed a logarithmic interpolation scheme to precisely determine oscillated atmospheric neutrino counts for all available nuclear model configurations in `GENIE`

- I co-developed rotational corrections of the atmospheric neutrino events to match the DUNE far detector geometry

- I developed changes within `GENIE` to allow for iteration across nuclear model configurations for intranuclear neutron-antineutron transformation signals in `GENIE`, and also co-corrected the nonlocality of intranuclear nucleon scattering centers within the `GENIE` intranuclear cascade model

- I generated large statistics samples of signal and background events, and developed and tested standard detector simulations for reconstruction of signal and background in the DUNE far detector

- I co-developed methods to check the automated analyses' understandings of critical topological variables

- I continue to lead an active research group within the DUNE HEP Working Group moving toward a publication [72] describing the effects of iteration over the available nuclear model configurations using automated analysis methods, including through the implementation of improved particle identification techniques

4. To improve future atmospheric neutrino predictions, precision cross section models and their implementations within event generators such as `GENIE` must be considered. In this vein, I made efforts to co-develop an implementation of the quantum Monte Carlo Short-Time Approximation [318, 69] within `GENIE`. The development is universally applicable to all

lepton scattering, though this proof of concept has focused on quasielastic electromagnetic scattering on ^{4}He for the time being. My contributions include:

- The development of methods for automatic double-differential cross section comparisons to simulations across all world data for all pertinent electromagnetic nuclear targets

- The development of an average scaling function for expansive interpolation across many values of momentum and energy transfers to form the full longitudinal and transverse nuclear response functions

- The co-development of a geometric method for assessing the angular dependencies of the semi-final state's two nucleons at the scattering vertex before intranuclear cascade

Throughout my graduate career, I have been lucky to write quite prodigiously about many of these topics, including in peer reviewed papers [229, 71, 69], conference proceedings [2, 3, 421, 121], reviews [19, 12], and most recently Snowmass Letters of Interest [66, 63, 64, 65] and associated forthcoming Snowmass White Papers. I have given many international talks on my work, and have even co-organized a highly successful Snowmass-official workshop on baryon-number violation physics [3], planning much of the timetable and talks.

All of this work, though on the surface quite dispersed, is actually incredibly synergistic. To achieve discovery of beyond Standard Model physics, such as through the neutron transformation searches discussed in this thesis, one must incorporate many areas of experiment and theory into one package: precision simulations of neutron-antineutron transformation signal and oscillated atmospheric neutrino backgrounds have been achieved; improvements have been made for better future neutrino background predictions via comparison to electron scattering; and other veins of beyond Standard Model physics, potentially related to dark matter and the neutron lifetime and a possible cobaryogenesis, have *all* been investigated. I hope this thesis serves as an arrow pointing forward to the horizon; toward the discovery of new physics, and, hopefully, with a bit of luck, Towards Neutron Transformations.

Bibliography

[1] (2018). The ESS instrument suite, a capability gap analysis. See here. 156

[2] (2019). *Neutrino Non-Standard Interactions: A Status Report*, volume 2. 294

[3] (2020). *$|\Delta\mathcal{B}| = 2$: A State of the Field, and Looking Forward–A brief status report of theoretical and experimental physics opportunities*. 10, 36, 294

[4] Abe, K. et al. (2015). The Search for $n - \bar{n}$ oscillation in Super-Kamiokande I. *Phys. Rev. D*, 91:072006. xviii, 14, 19, 20, 21, 30, 37, 63, 86, 87, 88, 95, 121, 122, 131, 140, 243

[5] Abe, K. et al. (2018). Hyper-Kamiokande Design Report. 36, 37

[6] Abe, K. et al. (2021). Neutron-Antineutron Oscillation Search using a 0.37 Megaton·Year Exposure of Super-Kamiokande. *Phys. Rev. D*, 103(1):012008. xiii, xviii, xxxv, 14, 19, 20, 21, 29, 30, 36, 37, 39, 86, 95, 121, 122, 154, 249

[7] Abel, C. et al. (2018). Statistical sensitivity of the nEDM apparatus at PSI to neutron mirror-neutron oscillations. In *International Workshop on Particle Physics at Neutron Sources 2018 (PPNS 2018) Grenoble, France, May 24-26, 2018*. 66

[8] Abel, C. et al. (2021). A search for neutron to mirror-neutron oscillations using the nEDM apparatus at PSI. *Phys. Lett. B*, 812:135993. xxi, 67, 206

[9] Abi, B. et al. (2017). The Single-Phase ProtoDUNE Technical Design Report. 209

[10] Abi, B. et al. (2020a). Deep Underground Neutrino Experiment (DUNE), Far Detector Technical Design Report, Volume I Introduction to DUNE. *arXiv preprint*. 257

[11] Abi, B. et al. (2020b). First results on ProtoDUNE-SP liquid argon time projection chamber performance from a beam test at the CERN Neutrino Platform. *JINST*, 15(12):P12004. 209

[12] Abi, B. et al. (2021). Prospects for Beyond the Standard Model Physics Searches at the Deep Underground Neutrino Experiment. *Eur. Phys. J. C*, 81(4):322. xv, xxxiii, xxxiv, 208, 226, 231, 232, 233, 235, 240, 244, 246, 248, 293, 294

[13] Ableev, V. et al. (1994). Annihilation cross-sections of anti-neutrons on C, Al, Cu, Sn and Pb at low momenta (180-MeV/c - 280-MeV/c) with the OBELIX spectrometer. *Nuovo Cim. A*, 107:943–953. 97

[14] Acciarri, R. et al. (2014). Detection of Back-to-Back Proton Pairs in Charged-Current Neutrino Interactions with the ArgoNeuT Detector in the NuMI Low Energy Beam Line. *Phys. Rev. D*, 90(1):012008. 209

[15] Acciarri, R. et al. (2019). Demonstration of MeV-Scale Physics in Liquid Argon Time Projection Chambers Using ArgoNeuT. *Phys. Rev. D*, 99(1):012002. 209

[16] Adams, C. et al. (2020). Calibration of the charge and energy loss per unit length of the MicroBooNE liquid argon time projection chamber using muons and protons. *JINST*, 15(03):P03022. 209

[17] Addazi, A., Berezhiani, Z., Bernabei, R., Belli, P., Cappella, F., Cerulli, R., and Incicchitti, A. (2015). DAMA annual modulation effect and asymmetric mirror matter. *Eur. Phys. J.*, C75(8):400. xxix, 38, 51, 56, 175

[18] Addazi, A., Berezhiani, Z., and Kamyshkov, Y. (2017). Gauged $B - L$ number and neutron–antineutron oscillation: long-range forces mediated by baryophotons. *Eur. Phys. J.*, C77(5):301. 32, 35, 56

[19] Addazi, A. et al. (2020). New high-sensitivity searches for neutrons converting into antineutrons and/or sterile neutrons at the European Spallation Source. xviii, xxix, xxx, 29, 30, 36, 37, 38, 49, 154, 156, 159, 173, 184, 197, 204, 292, 294

[20] Ade, P. et al. (2016). Planck 2015 results. XIII. Cosmological parameters. *Astron. Astrophys.*, 594:A13. 4, 6, 41

[21] Adler, R. J., Das, T., and Ferraz Filho, A. (1977). An Analytic Wave Function for the Deuteron D State. *Phys. Rev. C*, 16:1231. 66, 93

[22] Agnew, L. E., Elioff, T., Fowler, W. B., Lander, R. L., Powell, W. M., Segrè, E., Steiner, H. M., White, H. S., Wiegand, C., and Ypsilantis, T. (1960). Antiproton interactions in hydrogen and carbon below 200 mev. *Phys. Rev.*, 118:1371–1391. xxiv, 126

[23] Aharmim, B. et al. (2017). Search for neutron-antineutron oscillations at the Sudbury Neutrino Observatory. *Phys. Rev. D*, 96(9):092005. xviii, 14, 19, 35, 39

[24] Aitken, K., McKeen, D., Neder, T., and Nelson, A. E. (2017). Baryogenesis from Oscillations of Charmed or Beautiful Baryons. *Phys. Rev. D*, 96(7):075009. 12

[25] Ajzenberg-Selove, F. (1977). Energy levels of light nuclei A = 16–17. *Nucl. Phys. A*, 281:1–148. 97

[26] Akimov, D. et al. (2017). Observation of Coherent Elastic Neutrino-Nucleus Scattering. *Science*, 357(6356):1123–1126. 43

[27] Alberico, W., Molinari, A., Donnelly, T., Kronenberg, E., and Van Orden, J. (1988). Scaling in electron scattering from a relativistic Fermi gas. *Phys. Rev. C*, 38:1801–1810. 277

[28] Alexandrou, C., Bacchio, S., Constantinou, M., Finkenrath, J., Hadjiyiannakou, K., Jansen, K., Koutsou, G., and Vaquero Aviles-Casco, A. (2019). Proton and neutron electromagnetic form factors from lattice QCD. *Phys. Rev.*, D100(1):014509. 260

[29] Alexandrou, C., Constantinou, M., Hadjiyiannakou, K., Jansen, K., Kallidonis, C., Koutsou, G., and Vaquero Aviles-Casco, A. (2017). Nucleon electromagnetic form factors using lattice simulations at the physical point. *Phys. Rev.*, D96(3):034503. 260

[30] Allahverdi, R., Dev, P. S. B., and Dutta, B. (2018). A simple testable model of baryon number violation: Baryogenesis, dark matter, neutron–antineutron oscillation and collider signals. *Phys. Lett.*, B779:262–268. 13

[31] Altarelli, G. and Feruglio, F. (2010). Discrete Flavor Symmetries and Models of Neutrino Mixing. *Rev. Mod. Phys.*, 82:2701–2729. 68

[32] Altarev, I. et al. (2009). Neutron to Mirror-Neutron Oscillations in the Presence of Mirror Magnetic Fields. *Phys. Rev.*, D80:032003. xx, xxi, 49, 50, 60, 64, 67, 206

[33] Altarev, I. et al. (2015). A large-scale magnetic shield with 10^6 damping at mHz frequencies. *J. Appl. Phys.*, 117:183903. 179

[34] Alvarez-Ruso, L. et al. (2018). NuSTEC White Paper: Status and challenges of neutrino–nucleus scattering. *Prog. Part. Nucl. Phys.*, 100:1–68. 68, 254

[35] Amare, J. et al. (2021). Annual Modulation Results from Three Years Exposure of ANAIS-112. 45

[36] Amaro, J., Barbaro, M., Caballero, J., González-Jiménez, R., Megias, G., and Ruiz Simo, I. (2019). Electron- versus neutrino-nucleus scattering. *arXiv preprint*. 266

[37] Amsler, C. et al. (2003). Annihilation at rest of antiprotons and protons into neutral particles. *Nucl. Phys. A*, 720:357–367. xiii, 113, 114, 122

[38] Amsler, C. and Myhrer, F. (1991). Low-energy anti-proton physics. *Ann. Rev. Nucl. Part. Sci.*, 41:219–267. 92

[39] Andreopoulos, C., Barry, C., Dytman, S., Gallagher, H., Golan, T., Hatcher, R., Perdue, G., and Yarba, J. (2015). The GENIE Neutrino Monte Carlo Generator: Physics and User Manual. *arXiv preprint*. xiv, 68, 86, 87, 134, 135, 137, 140, 141, 146, 217, 228, 257

[40] Andreopoulos, C. et al. (2010). The GENIE Neutrino Monte Carlo Generator. *Nucl. Instrum. Meth.*, A614:87–104. 86, 217, 254, 257

[41] Ankowski, A. M. and Friedland, A. (2020). Assessing the accuracy of the genie event generator with electron-scattering data. *Phys. Rev. D*, 102:053001. 255

[42] Antcheva, I. et al. (2011). ROOT: A C++ framework for petabyte data storage, statistical analysis and visualization. *Comput. Phys. Commun.*, 182:1384–1385. 257

[43] Arnold, J. M., Fornal, B., and Wise, M. B. (2013). Simplified models with baryon number violation but no proton decay. *Phys. Rev. D*, 87:075004. 10, 13, 23

[44] Avdeyev, S. P. et al. (2002). Comparative study of multifragmentation of gold nuclei induced by relativistic protons, He-4, and C-12. *Nucl. Phys. A*, 709:392–414. 121, 147

[45] Baak, M., Gadatsch, S., Harrington, R., and Verkerke, W. (2015). Interpolation between multi-dimensional histograms using a new non-linear moment morphing method. *Nucl. Instrum. Meth. A*, 771:39–48. 279, 286

[46] Babcock, H. W. (1939). The rotation of the adromeda nebula. *Lick Observatory Bulletins*, 19:41–51. 41

[47] Babu, K., Dev, P. S. B., Fortes, E. C., and Mohapatra, R. (2013). Post-Sphaleron Baryogenesis and an Upper Limit on the Neutron-Antineutron Oscillation Time. *Phys. Rev. D*, 87(11):115019. xvii, xviii, 5, 12, 21, 23, 26, 28, 29, 30, 33, 37, 85, 180, 245

[48] Babu, K., Dev, P. S. B., and Mohapatra, R. (2009). Neutrino mass hierarchy, neutron - antineutron oscillation from baryogenesis. *Phys. Rev. D*, 79:015017. 12

[49] Babu, K. and Mohapatra, R. (2012). Coupling Unification, GUT-Scale Baryogenesis and Neutron-Antineutron Oscillation in SO(10). *Phys. Lett. B*, 715:328–334. 12

[50] Babu, K., Mohapatra, R., and Nasri, S. (2006). Post-Sphaleron Baryogenesis. *Phys. Rev. Lett.*, 97:131301. xvii, xviii, 5, 12, 23, 26, 28, 85, 180, 245

[51] Babu, K. and Mohapatra, R. N. (2016). Limiting Equivalence Principle Violation and Long-Range Baryonic Force from Neutron-Antineutron Oscillation. *Phys. Rev. D*, 94(5):054034. 32, 35

[52] Bacca, S. and Pastore, S. (2014). Electromagnetic reactions on light nuclei. *J. Phys.*, G41(12):123002. 258, 259, 260, 261

[53] Backhouse, C. (2017). Cafana for dune. Presentation to the DUNE LBL/ND Meeting can be found here; code for CAFAna can be seen at this GitHub. xxxiii, 208, 213, 217, 220, 222, 225, 247

[54] Balazs, C. (2014). Baryogenesis: A small review of the big picture. 7

[55] Baldes, I., Bell, N. F., Millar, A., Petraki, K., and Volkas, R. R. (2014). The role of CP violating scatterings in baryogenesis - case study of the neutron portal. *JCAP*, 11:041. 12

[56] Baldo-Ceolin, M. et al. (1994). A New experimental limit on neutron - antineutron oscillations. *Z. Phys.*, C63:409–416. xvii, xviii, 14, 17, 19, 20, 29, 30, 31, 33, 36, 39, 63, 159, 179, 185, 188, 197, 204

[57] Ban, G. et al. (2007). A Direct experimental limit on neutron: Mirror neutron oscillations. *Phys. Rev. Lett.*, 99:161603. xxi, 60, 64, 67

[58] Barashenkov, V. S., Ilinov, A. S., and Toneev, V. D. (1971). Further development of the intranuclear cascade model. *Yad. Fiz.*, 13:743–747. 115, 118

[59] Barashenkov, V. S. and Toneev, V. D. (1972). Interactions of high energy particles and atomic nuclei with nuclei; vzaimodeistviya vysokoenergeticheskikh chastits i atomnykh yader s yadrami. in Russian. 91, 105, 115, 118

[60] Barbaro, M., Cenni, R., De Pace, A., Donnelly, T., and Molinari, A. (1998). Relativistic y - scaling and the Coulomb sum rule in nuclei. *Nucl. Phys. A*, 643:137–160. 277

[61] Barrow, J., Bohm, C., Dunne, K., Makkinje, J., Meirose, B., Milstead, D., Oskarsson, A., Santoro, V., Silverstein, S., and Yiu, S.-C. (2021a). NNBAR-HIBEAM Detector Conceptual Design: Supporting Technical Note. Internal developing and preliminary technical note; available upon reasonable request. xxx, 130, 134, 186, 189, 192, 195, 198

[62] Barrow, J. et al. (2020a). Summary of Workshop on Common Neutrino Event Generator Tools. *arXiv preprint*. 68

[63] Barrow, J. L., Broussard, L. J., De Vries, J., Wagman, M., et al. (2020b). $|\Delta\mathcal{B}| = 2$: A State of the Field, and Looking Forward. See here. 10, 294

[64] Barrow, J. L., Broussard, L. J., Frost, M., Milstead, D., Santoro, V., et al. (2020c). Free Neutron-antineutron Transformation Searches at the European Spallation Source's Large Beamport. See here. 294

[65] Barrow, J. L. et al. (2020d). Atmospheric ν_τ Appearance in the Deep Underground Neutrino Experiment. See here. 224, 294

[66] Barrow, J. L. et al. (2020e). The Necessity of DUNE Intranuclear Baryon Minus Lepton Number-Violating Searches for a World-Leading, Complementary Physics Program. See here. 10, 294

[67] Barrow, J. L. et al. (2021b). A Computing and Detector Simulation Framework for theHIBEAM/NNBAR Experimental Program at the ESS. Accepted for publication to the 25th International Conference on Computing in High-Energy and Nuclear Physics; pending review and acceptance. Viewable upon request. xxx, 29, 130, 134, 186, 189, 192, 195, 198, 292

[68] Barrow, J. L. et al. (2021c). DUNE Wiki–High-E and Non-Accelerator Physics: Currently Available MC Samples. see here. 86, 230

[69] Barrow, J. L., Gardiner, S., Pastore, S., Betancourt, M., and Carlson, J. (2021d). Quasielastic electromagnetic scattering cross sections and world data comparisons in the GENIE Monte Carlo event generator. *Phys. Rev. D*, 103(5):052001. xxxvii, 81, 83, 254, 256, 280, 288, 293, 294

[70] Barrow, J. L., Golubeva, E. S., Botvina, A. S., Richard, J.-M., and Wan, L. (2021e). Preliminary title: A New Model of Intranuclear Neutron-Antineutron Transformations in $^{16}_{8}$O. Preprint in preparatory writing stages; available upon reasonable request to the authors. xiii, xxiii, 20, 85, 86, 88, 91, 102, 104, 110, 121, 129, 147, 291, 292

[71] Barrow, J. L., Golubeva, E. S., Paryev, E., and Richard, J.-M. (2020f). Progress and simulations for intranuclear neutron-antineutron transformations in $^{40}_{18}Ar$. *Phys. Rev. D*, 101(3):036008. xiii, xiv, xxiii, xxx, 14, 20, 21, 34, 35, 37, 38, 85, 86, 88, 91, 104, 110, 113, 120, 124, 129, 131, 154, 186, 198, 228, 244, 252, 291, 292, 294

[72] Barrow, J. L., Jwa, Y.-j., Sarasty, C., Hewes, J., Martinez-Soler, I., Pec, V., et al. (2021f). Preliminary title: A Systematic Study of Monte Carlo Theoretical Uncertainties for Intranuclear $p \to K^+\nu$ and $n \to \bar{n}$ Searches in the Deep Underground Neutrino Experiment Using Automated Analysis Methods. Preprint in preparatory writing stages; available upon reasonable request to the authors. xv, 38, 208, 224, 231, 235, 240, 241, 245, 247, 252, 292, 293

[73] Battistoni, G. et al. (1983). Nucleon Stability, Magnetic Monopoles and Atmospheric Neutrinos in the Mont Blanc Experiment. *Phys. Lett. B*, 133:454–460. xviii, 19, 39

[74] Belfatto, B., Beradze, R., and Berezhiani, Z. (2020). The CKM unitarity problem: A trace of new physics at the TeV scale? *Eur. Phys. J.*, C80(2):149. 56

[75] Belfatto, B. and Berezhiani, Z. (2019). How light the lepton flavor changing gauge bosons can be. *Eur. Phys. J.*, C79(3):202. 56

[76] Bellaize, N. et al. (2002). Multifragmentation process for different mass asymmetry in the entrance channel around the Fermi energy. *Nucl. Phys. A*, 709:367–391. 121, 147

[77] Benhar, O., day, D., and Sick, I. (2008). Inclusive quasi-elastic electron-nucleus scattering. *Rev. Mod. Phys.*, 80:189–224. 257, 279, 287

[78] Bento, L. and Berezhiani, Z. (2001). Leptogenesis via collisions: The Lepton number leaking to the hidden sector. *Phys. Rev. Lett.*, 87:231304. 40

[79] Berezhiani, Z. (1998). Unified picture of the particle and sparticle masses in SUSY GUT. *Phys. Lett.*, B417:287–296. 56

[80] Berezhiani, Z. (2004). Mirror world and its cosmological consequences. *Int. J. Mod. Phys.*, A19:3775–3806. 40

[81] Berezhiani, Z. (2008). Unified picture of ordinary and dark matter genesis. *Eur. Phys. J. ST*, 163:271–289. 40

[82] Berezhiani, Z. (2009). More about neutron - mirror neutron oscillation. *Eur. Phys. J.*, C64:421–431. 40, 55, 57, 59, 170

[83] Berezhiani, Z. (2016a). Anti-dark matter: a hidden face of mirror world. 57

[84] Berezhiani, Z. (2016b). Neutron–antineutron oscillation and baryonic majoron: low scale spontaneous baryon violation. *Eur. Phys. J. C*, 76(12):705. 19, 35, 40

[85] Berezhiani, Z. (2018). Matter, dark matter, and antimatter in our Universe. *Int. J. Mod. Phys. A*, 33(31):1844034. 38, 40, 57, 62

[86] Berezhiani, Z. (2019). Neutron lifetime puzzle and neutron–mirror neutron oscillation. *Eur. Phys. J.*, C79(6):484. xix, 48, 172

[87] Berezhiani, Z. (2020). A possible shortcut for neutron–antineutron oscillation. 40, 62, 63

[88] Berezhiani, Z. (2021). A possible shortcut for neutron–antineutron oscillation through mirror world. *Eur. Phys. J. C*, 81(1):33. 40

[89] Berezhiani, Z. and Bento, L. (2006a). Fast neutron: Mirror neutron oscillation and ultra high energy cosmic rays. *Phys. Lett.*, B635:253–259. 40, 49, 51, 53, 57, 62

[90] Berezhiani, Z. and Bento, L. (2006b). Neutron - mirror neutron oscillations: How fast might they be? *Phys. Rev. Lett.*, 96:081801. xx, 40, 53, 54, 56, 57, 58, 59

[91] Berezhiani, Z., Biondi, R., Geltenbort, P., Krasnoshchekova, I., Varlamov, V., Vassiljev, A., and Zherebtsov, O. (2018). New experimental limits on neutron - mirror neutron oscillations in the presence of mirror magnetic field. *Eur. Phys. J. C*, 78(9):717. xxi, 40, 60, 63, 64, 67, 206

[92] Berezhiani, Z., Biondi, R., Kamyshkov, Y., and Varriano, L. (2019). On the Neutron Transition Magnetic Moment. *MDPI Physics*, 1(2):271–289. 60, 176, 177

[93] Berezhiani, Z., Biondi, R., Mannarelli, M., and Tonelli, F. (2020). Neutron - mirror neutron mixing and neutron stars. 57

[94] Berezhiani, Z., Comelli, D., and Villante, F. L. (2001). The Early mirror universe: Inflation, baryogenesis, nucleosynthesis and dark matter. *Phys. Lett.*, B503:362–375. 40

[95] Berezhiani, Z., Dolgov, A. D., and Tkachev, I. I. (2013). Dark matter and generation of galactic magnetic fields. *Eur. Phys. J.*, C73:2620. 57

[96] Berezhiani, Z., Frost, M., Kamyshkov, Y., Rybolt, B., and Varriano, L. (2017). Neutron Disappearance and Regeneration from Mirror State. *Phys. Rev.*, D96(3):035039. xxi, 57, 64, 65, 66, 165, 167, 169, 170, 172, 292

[97] Berezhiani, Z. and Gazizov, A. (2012). Neutron Oscillations to Parallel World: Earlier End to the Cosmic Ray Spectrum? *Eur. Phys. J.*, C72:2111. 40, 57

[98] Berezhiani, Z. and Lepidi, A. (2009). Cosmological bounds on the 'millicharges' of mirror particles. *Phys. Lett.*, B681:276–281. 57

[99] Berezhiani, Z. and Nesti, F. (2012). Magnetic anomaly in UCN trapping: signal for neutron oscillations to parallel world? *Eur. Phys. J. C*, 72:1974. xxi, 40, 59, 60, 64, 67, 206

[100] Berezhiani, Z. and Vainshtein, A. (2018). Neutron–antineutron oscillation and discrete symmetries. *Int. J. Mod. Phys.*, A33(31):1844016. 31, 57

[101] Berezhiani, Z. and Vainshtein, A. (2019). Neutron–Antineutron Oscillations: Discrete Symmetries and Quark Operators. *Phys. Lett.*, B788:58–64. 31, 57

[102] Berezhiani, Z. G., Dolgov, A. D., and Mohapatra, R. N. (1996). Asymmetric inflationary reheating and the nature of mirror universe. *Phys. Lett.*, B375:26–36. 40

[103] Berger, C. et al. (1990). Search for Neutron - Anti-neutron Oscillations in the Frejus Detector. *Phys. Lett. B*, 240:237–242. xviii, 19, 20, 39

[104] Bergevin, M. (2010). *Search for Neutron Anti-neutron Oscillation at the Sudbury Neutrino Observatory*. PhD thesis, Guelph U. 20

[105] Beshtoev, K. (1972). *Joint Inst. for Nuc. Research Preprints and Comms.*, JINR P2-5480, P2-6337. 111

[106] Bhupal Dev, P. S., Millington, P., Pilaftsis, A., and Teresi, D. (2016). Flavour Covariant Formalism for Resonant Leptogenesis. *Nucl. Part. Phys. Proc.*, 273-275:268–274. xviii, 28

[107] Bitter, T. and Dubbers, D. (1985). Test of the quasifree condition in neutron oscillation experiments. *Nuclear Instruments and Methods in Physics Research Section A: Accelerators, Spectrometers, Detectors and Associated Equipment*, 239(3):461 – 466. 15, 17, 32, 179

[108] Bodek, A., Christy, M., and Coopersmith, B. (2014). Effective Spectral Function for Quasielastic Scattering on Nuclei. *Eur. Phys. J. C*, 74(10):3091. 226

[109] Bodek, A. and Ritchie, J. (1981). Fermi Motion Effects in Deep Inelastic Lepton Scattering from Nuclear Targets. *Phys. Rev. D*, 23:1070. xxxiv, 87, 137, 226, 248

[110] Bodek, K. et al. (2009). Additional results from the first dedicated search for neutron-mirror neutron oscillations. *Nucl. Instrum. Meth.*, A611:141–143. 60, 64

[111] Bolsterli, M., Fiset, E., Nix, J., and Norton, J. (1972). New Calculation of Fission Barriers for Heavy and Superheavy Nuclei. *Phys. Rev. C*, 5:1050–1077. 97

[112] Bondorf, J. P., Botvina, A. S., Ilinov, A. S., Mishustin, I. N., and Sneppen, K. (1995). Statistical multifragmentation of nuclei. *Phys. Rept.*, 257:133–221. 121, 147

[113] Botvina, A. B., Golubeva, Y. S., IIjinov, A. S., and Pshenichnov, I. A. (1992). Intranuclear-cascade mechanism in antinucleon-nucleus interactions. *Physics of Atomic Nuclei (English Translation); (United States)*, 55. 121

[114] Botvina, A. S. et al. (1995). Multifragmentation of spectators in relativistic heavy ion reactions. *Nucl. Phys. A*, 584:737–756. 121, 147

[115] Branco, G. C., Felipe, R. G., and Joaquim, F. R. (2012). Leptonic CP Violation. *Rev. Mod. Phys.*, 84:515–565. 68

[116] Breidenbach, M., Friedman, J. I., Kendall, H. W., Bloom, E. D., Coward, D. H., DeStaebler, H. C., Drees, J., Mo, L. W., and Taylor, R. E. (1969). Observed behavior of highly inelastic electron-proton scattering. *Phys. Rev. Lett.*, 23:935–939. 74

[117] Bressi, G. et al. (1989). Search for Free Neutron antineutron Oscillations. *Z. Phys.*, C43:175–179. 17, 33

[118] Bressi, G. et al. (1990). Final results of a search for free neutron antineutron oscillations. *Nuovo Cim.*, A103:731–750. 17, 33, 187

[119] Broggini, C., Giunti, C., and Studenikin, A. (2012). Electromagnetic Properties of Neutrinos. *Adv. High Energy Phys.*, 2012:459526. 57

[120] Broussard, L. et al. (2017). New Search for Mirror Neutrons at HFIR. In *Meeting of the APS Division of Particles and Fields*. 36, 66, 167, 170

[121] Broussard, L. et al. (2019). New search for mirror neutron regeneration. *EPJ Web Conf.*, 219:07002. 36, 66, 294

[122] Brown, M.-P. et al. (2018). New result for the neutron β-asymmetry parameter A_0 from UCNA. *Phys. Rev. C*, 97(3):035505. xix, 48

[123] Bruge, G. et al. (1986). Comparative Study of the Elastic Scattering of 178.4-{MeV} Antiprotons by the ^{16}O and ^{18}O Isotopes. *Phys. Lett. B*, 169:14–16. 97

[124] Brun, R. and Rademakers, F. (1997). ROOT: An object oriented data analysis framework. *Nucl. Instrum. Meth. A*, 389:81–86. 129

[125] Bryman, D. (2014). Two nucleon (B - L)-conserving reactions involving tau leptons . *Phys. Lett.*, B733:190–192. 19

[126] Buchoff, M. I. and Wagman, M. (2015). Neutron-Antineutron Operator Renormalization. *PoS*, LATTICE2014:290. 33

[127] Buchoff, M. I. and Wagman, M. (2016). Perturbative Renormalization of Neutron-Antineutron Operators. *Phys. Rev. D*, 93(1):016005. [Erratum: Phys.Rev.D 98, 079901 (2018)]. 33

[128] Bugg, D. et al. (1987). ANTI-P P TOTAL CROSS-SECTIONS BELOW 420-MEV/C. *Phys. Lett. B*, 194:563–567. 97

[129] Bunakov, V. (1980). Kinetic equations in nuclear reaction theory. *Fizika Ehlementarnykh Chastits i Atomnogo Yadra*, 11:1285–1333. 115

[130] Buschmann, M., Kopp, J., Liu, J., and Machado, P. A. N. (2015). Lepton Jets from Radiating Dark Matter. *JHEP*, 07:045. xxxiii, 218, 219

[131] Buss, O., Gaitanos, T., Gallmeister, K., van Hees, H., Kaskulov, M., Lalakulich, O., Larionov, A., Leitner, T., Weil, J., and Mosel, U. (2012). Transport-theoretical Description of Nuclear Reactions. *Phys. Rept.*, 512:1–124. 228

[132] Cabibbo, N. (1978). Time Reversal Violation in Neutrino Oscillation. *Phys. Lett. B*, 72:333–335. 68

[133] Calibbi, L., Ferretti, G., Milstead, D., Petersson, C., and Pöttgen, R. (2016). Baryon number violation in supersymmetry: n-nbar oscillations as a probe beyond the LHC. *JHEP*, 05:144. [Erratum: JHEP10,195(2017)]. 12

[134] Callan, Jr., C. G. and Gross, D. J. (1969). High-energy electroproduction and the constitution of the electric current. *Phys. Rev. Lett.*, 22:156–159. 78

[135] Carlson, E. D. and Glashow, S. L. (1987). Nucleosynthesis Versus the Mirror Universe. *Phys. Lett.*, B193:168–170. 56

[136] Carlson, J., Gandolfi, S., Pederiva, F., Pieper, S. C., Schiavilla, R., Schmidt, K. E., and Wiringa, R. B. (2015). Quantum Monte Carlo methods for nuclear physics. *Rev. Mod. Phys.*, 87:1067. 256, 258, 259, 260, 261, 262

[137] Carlson, J., Jourdan, J., Schiavilla, R., and Sick, I. (2002). Longitudinal and transverse quasielastic response functions of light nuclei. *Phys. Rev.*, C65:024002. 258, 261, 262, 269

[138] Carlson, J., Riska, D. O., Schiavilla, R., and Wiringa, R. B. (1990). Radiative neutron capture on 3He. *Phys. Rev.*, C42:830–836. 261

[139] Carlson, J. and Schiavilla, R. (1998). Structure and dynamics of few nucleon systems. *Rev. Mod. Phys.*, 70:743–842. xxxvii, 70, 258, 259, 260, 261, 279, 280

[140] Cassing, W. (2002). Anti-baryon production in hot and dense nuclear matter. *Nucl. Phys. A*, 700:618–646. 109

[141] Cerulli, R., Villar, P., Cappella, F., Bernabei, R., Belli, P., Incicchitti, A., Addazi, A., and Berezhiani, Z. (2017). DAMA annual modulation and mirror Dark Matter. *Eur. Phys. J.*, C77(2):83. 56

[142] Chamberlain, O. t. (1957). Experiments on antiprotons: Antiproton-nucleon crosssections. Technical report. 97

[143] Cherry, M., Lande, K., Lee, C., Steinberg, R., and Cleveland, B. (1983). EXPERIMENTAL TEST OF BARYON CONSERVATION: A NEW LIMIT ON NEUTRON ANTI-NEUTRON OSCILLATIONS IN OXYGEN. *Phys. Rev. Lett.*, 50:1354–1356. xviii, 19, 39

[144] Chetyrkin, K., Kazarnovsky, M., Kuzmin, V., and Shaposhnikov, M. (1980). Neutron - antineutron oscillations. *Pisma Zh. Eksp. Teor. Fiz.*, 32:88–91. 204

[145] Chetyrkin, K., Kazarnovsky, M., Kuzmin, V., and Shaposhnikov, M. (1981a). N anti-N OSCILLATIONS: HOW FAST COULD THEY BE? *Phys. Lett. B*, 99:358–360. 102

[146] Chetyrkin, K., Kazarnovsky, M., Kuzmin, V., and Shaposhnikov, M. (1981b). Neutron-Antineutron Oscillations: How Fast Could They Be? *Phys. Lett. B*, 99:358–360. 204

[147] Cheung, C. and Ishiwata, K. (2013). Baryogenesis with Higher Dimension Operators. *Phys. Rev. D*, 88(1):017901. 12

[148] Christenson, J. H., Cronin, J. W., Fitch, V. L., and Turlay, R. (1964). Evidence for the 2π Decay of the K_2^0 Meson. *Phys. Rev. Lett.*, 13:138–140. 6

[149] Chun, E. et al. (2018). Probing Leptogenesis. *Int. J. Mod. Phys. A*, 33(05n06):1842005. 25

[150] Chung, J. et al. (2002). Search for neutron anti-neutron oscillations using multiprong events in Soudan 2. *Phys. Rev. D*, 66:032004. xviii, 19, 20, 39, 95

[151] Clowe, D., Bradac, M., Gonzalez, A. H., Markevitch, M., Randall, S. W., Jones, C., and Zaritsky, D. (2006). A direct empirical proof of the existence of dark matter. *Astrophys. J. Lett.*, 648:L109–L113. 41

[152] Collaboration, T. D. (2021). The dama project. Retrieved from here. 43

[153] Collaboration, T. M. (2017). Proton track identification in microboone simulation for neutral current elastic events: Microboone-note-1025-pub. Public note retrieved from here. 147

[154] Condo, G. T., Handler, T., and Cohn, H. O. (1984). Λ^0 production from low energy antiproton annihilations in complex nuclei. *Phys. Rev. C*, 29:1531–1533. xxiv, 126

[155] Costa, G. and Kabir, P. (1983). Environmental Effects On Possible Neutron-Antineutron Transitions. *Phys. Rev. D*, 28:667–668. 33, 92

[156] Cottingham, W. and Greenwood, D. (2007). *An introduction to the standard model of particle physics*. Cambridge University Press. 6, 7

[157] Cuesta, C. (2020). Status of ProtoDUNE Dual Phase. *PoS*, EPS-HEP2019:381. 209

[158] D'Agostino, M. et al. (1996). Statistical multifragmentation in central Au + Au collisions at 35-MeV/u. *Phys. Lett. B*, 371:175–180. 121, 147

[159] D'Agostino, M. et al. (1999). Thermodynamical features of multifragmentation in peripheral Au + Au collisions at 35-A/MeV. *Nucl. Phys. A*, 650:329–357. 121, 147

[160] Datar, V. M. et al. (2013). Electromagnetic Transition from the 4+ to 2+ Resonance in Be8 Measured via the Radiative Capture in He4+He4. *Phys. Rev. Lett.*, 111(6):062502. 260

[161] Davis, E. D. and Young, A. R. (2017). Neutron-antineutron oscillations beyond the quasifree limit. *Phys. Rev.*, D95(3):036004. 32, 179

[162] Davoudi, Z., Detmold, W., Orginos, K., Parreño, A., Savage, M. J., Shanahan, P., and Wagman, M. L. (2020). Nuclear matrix elements from lattice QCD for electroweak and beyond-Standard-Model processes. 14

[163] Day, D. et al. (2015). Quasielastic Electron Nucleus Scattering Archive. See data library here. 257, 279, 284

[164] Delgado, M. A. R. (2021). MINERvA's Recent Results and Data Preservation Effort. Presented at the New Directions in Neutrino-Nucleus Scattering NuSTEC Workshop, viewable here. 226

[165] Demarteau, M. (2020). Neutrons at ORNL and ESS: A Synergistic Program. Presentation given at *Workshop on Theoretical Innovations for Future Experiments Regarding Baryon Number Violation, Part I*; see here. 36

[166] Detmold, W., Edwards, R. G., Dudek, J. J., Engelhardt, M., Lin, H.-W., Meinel, S., Orginos, K., and Shanahan, P. (2019). Hadrons and Nuclei. *Eur. Phys. J. A*, 55(11):193. 14

[167] Dev, B. (2020). Private communication. 33

[168] Dev, P. S. B. and Mohapatra, R. N. (2015). TeV scale model for baryon and lepton number violation and resonant baryogenesis. *Phys. Rev. D*, 92(1):016007. 12

[169] Dolan, S., Megias, G., and Bolognesi, S. (2019). Implementation of the SuSAv2-MEC 1p1h and 2p2h models in GENIE and analysis of nuclear effects in T2K measurements. *arXiv preprint*. 266, 282

[170] Dolan, S., Megias, G., and Bolognesi, S. (2020). Implementation of the SuSAv2-meson exchange current 1p1h and 2p2h models in GENIE and analysis of nuclear effects in T2K measurements. *Phys. Rev. D*, 101(3):033003. 266

[171] Dolgov, A. (1992). NonGUT baryogenesis. *Phys. Rept.*, 222:309–386. xvi, 4, 7, 8, 9

[172] Dolgov, A. (1997). Baryogenesis, 30 years after. In *25th ITEP Winter School of Physics*. xvi, 4, 5, 6, 7, 8, 9

[173] Dolgov, A. and Zeldovich, Y. (1981). Cosmology and Elementary Particles. *Rev. Mod. Phys.*, 53:1–41. xvi, 4, 7, 8, 9

[174] Donnelly, T. W. and Sick, I. (1999). Superscaling of inclusive electron scattering from nuclei. *Physical Review C*, 60(6). 266, 267, 269, 272

[175] Dover, C., Gal, A., and Richard, J. (1983). NEUTRON ANTI-NEUTRON OSCILLATIONS IN NUCLEI. *Phys. Rev. D*, 27:1090–1100. xviii, 21, 34, 35, 39, 92, 94, 95

[176] Dover, C., Gal, A., and Richard, J. (1985). LIMITS ON THE NEUTRON ANTI-NEUTRON OSCILLATION TIME FROM THE STABILITY OF NUCLEI. *Phys. Rev. C*, 31:1423–1429. 14, 21, 34, 37, 92, 94

[177] Dover, C., Gal, A., and Richard, J. (1995). Limits on the neutron - anti-neutron oscillation time from the stability of nuclei. *Phys. Lett. B*, 344:433–435. xviii, 39, 92

[178] Dover, C. and Richard, J. (1980). Elastic, Charge Exchange, and Inelastic anti-p p Cross-Sections in the Optical Model. *Phys. Rev. C*, 21:1466–1471. 21, 95

[179] Dover, C. B., Gal, A., and Richard, J. M. (1989). Neutron antineutron Oscillations in Nuclei. *Nucl. Instrum. Meth.*, A284:13. 34

[180] Dover, C. B., Gal, A., and Richard, J.-M. (1996). Neutron - anti-neutron oscillations at the surface of nuclei. In *International Workshop on Future Prospects of Baryon Instability Search in p decay and n —> anti-n Oscillation Experiments*, pages 241–243. 14, 87, 91, 92, 135

[181] Dziewonski, A. and Anderson, D. (1981). Preliminary reference earth model. *Phys. Earth Planet. Interiors*, 25:297–356. 220

[182] Efremov, S. and Parev, E. (1998). Subthreshold K+ meson production in proton - nucleus reactions. *Eur. Phys. J. A*, 1:99–114. 110

[183] Einstein, A. (1952). *The Collected Papers of Albert Einstein: The Berlin Years–The Foundation of the General Theory of Relativity*, volume 6. Princeton University Press. Retrieved from here. 40

[184] Esteban, I., Gonzalez-Garcia, M. C., Hernandez-Cabezudo, A., Maltoni, M., and Schwetz, T. (2019). Global analysis of three-flavour neutrino oscillations: synergies and tensions in the determination of θ_{23}, δ_{CP}, and the mass ordering. *JHEP*, 01:106. 220, 293

[185] Farrar, G. R. and Shaposhnikov, M. (1993). Baryon asymmetry of the universe in the minimal Standard Model. *Phys. Rev. Lett.*, 70:2833–2836. [Erratum: Phys.Rev.Lett. 71, 210 (1993)]. 7, 9

[186] Feng, J. L. (2010). Dark Matter Candidates from Particle Physics and Methods of Detection. *Ann. Rev. Astron. Astrophys.*, 48:495–545. 51

[187] Fermi, E. and Yang, C.-N. (1949). ARE MESONS ELEMENTARY PARTICLES? *Phys. Rev.*, 76:1739–1743. 95

[188] Feynman, R. (1996). *Feynman lectures on gravitation*. 40

[189] Fidecaro, G. et al. (1985). Experimental search for neutron antineutron transitions with free neutrons. *Phys. Lett.*, 156B:122–128. 17, 33

[190] Filkins, A. et al. (2020). Double-differential inclusive charged-current ν_μ cross sections on hydrocarbon in MINERvA at $\langle E_\nu \rangle \sim 3.5$ GeV. *Phys. Rev. D*, 101(11):112007. 226

[191] Flaminio, V., Graf, I. F., Hansen, J. D., Moorhead, W. G., and Morrison, D. R. O. (1979). *Compilation of cross-sections. 1. Pi- and pi+ induced reactions*. 118

[192] Fomin, A. (2017). Experiment on search for n-nbar oscillations using a projected UCN source at the WWR-M reactor. *PoS*, INPC2016:189. 37

[193] Fomin, A. et al. (2018). Project of NNbar Experiment at the WWR-M Reactor. *KnE Energ. Phys.*, 3:109–114. 37

[194] Fomin, A., Serebrov, A., Chaikovskii, M., Zherebtsov, O., Murashkin, A., and Golubeva, E. (2019a). Plan of NNbar experiment at the WWR-M reactor. *EPJ Web Conf.*, 219:07003. 37

[195] Fomin, A., Serebrov, A., Chaikovskii, M., Zherebtsov, O., Murashkin, A., and Golubeva, E. (2019b). Project on searching for neutron-antineutron oscillation at the WWR-M reactor. *J. Phys. Conf. Ser.*, 1390(1):012133. 37

[196] Fomin, A., Serebrov, A., Zherebtsov, O., Leonova, E., and Chaikovskii, M. (2017a). Experiment on search for neutron–antineutron oscillations using a projected UCN source at the WWR-M reactor. *J. Phys. Conf. Ser.*, 798(1):012115. 37

[197] Fomin, N. (2008). Inclusive electron scattering from nuclei at x $>$ 1 and high Q**2 with a 5.75-GeV beam. Other thesis. 70, 73, 74

[198] Fomin, N., Higinbotham, D., Sargsian, M., and Solvignon, P. (2017b). New Results on Short-Range Correlations in Nuclei. *Ann. Rev. Nucl. Part. Sci.*, 67:129–159. 74, 75, 80, 81, 256

[199] Foot, R. (2004). Mirror matter-type dark matter. *Int. J. Mod. Phys.*, D13:2161–2192. xx, 49, 52, 56

[200] Foot, R. (2014). Mirror dark matter: Cosmology, galaxy structure and direct detection. *Int. J. Mod. Phys. A*, 29:1430013. xx, 49, 52

[201] Friedman, E. and Gal, A. (2008). Realistic calculations of nuclear disappearance lifetimes induced by n anti-n oscillations. *Phys. Rev. D*, 78:016002. xiii, xviii, 14, 20, 21, 34, 39, 87, 92, 94, 95

[202] Friedman, E., Gal, A., and Mares, J. (2005). Antiproton-nucleus potentials from global fits to antiprotonic X-rays and radiochemical data. *Nucl. Phys. A*, 761:283–295. 110

[203] Friedman, J. I. and Kendall, H. W. (1972). Deep inelastic electron scattering. *Ann. Rev. Nucl. Part. Sci.*, 22:203–254. 78

[204] Frost, M. J. (2019). *Searching for Baryon Number Violation at Cold Neutron Sources*. PhD thesis, University of Tennessee. xviii, xxx, 29, 30, 38, 156, 159, 184, 188, 197, 198, 200, 204

[205] Frost, M. J. f. t. N. C. (2016). The NNBAR Experiment at the European Spallation Source. 36

[206] Fukuda, Y. et al. (1998). Evidence for oscillation of atmospheric neutrinos. *Phys. Rev. Lett.*, 81:1562–1567. 68

[207] Fukugita, M. and Yanagida, T. (1986). Baryogenesis Without Grand Unification. *Phys. Lett. B*, 174:45–47. xviii, 12, 25, 28, 68

[208] Galster, S., Klein, H., Moritz, J., Schmidt, K. H., Wegener, D., and Bleckwenn, J. (1971). Elastic electron-deuteron scattering and the electric neutron form factor at four-momentum transfers $5\mathrm{fm}^{-2} < q^2 < 14\mathrm{fm}^{-2}$. *Nucl. Phys. B*, 32:221–237. 74

[209] Gandolfi, S., Lonardoni, D., Lovato, A., and Piarulli, M. (2020). Atomic nuclei from quantum Monte Carlo calculations with chiral EFT interactions. *Front. Phys.*, 8:117. 14

[210] Gardiner, S. (2019). A generalized hadronic tensor framework for genie. https://genie-docdb.pp.rl.ac.uk/cgi-bin/ShowDocument?docid=137. GENIE docDB #137. 266, 288

[211] Gardner, S. and Yan, X. (2019). Processes that break baryon number by two units and the Majorana nature of the neutrino. *Phys. Lett. B*, 790:421–426. 13

[212] Gibin, D. (1996). A recent neutron antineutron search experiment at ILL. In *International Workshop on Future Prospects of Baryon Instability Search in p decay and n —> anti-n Oscillation Experiments*, pages 253–268. 88

[213] Girlanda, L., Kievsky, A., Marcucci, L. E., Pastore, S., Schiavilla, R., and Viviani, M. (2010). Thermal neutron captures on d and ^{3}He. *Phys. Rev. Lett.*, 105:232502. 260

[214] Girmohanta, S. and Shrock, R. (2019). Improved Lower Bounds on Partial Lifetimes for Nucleon Decay Modes. *Phys. Rev.*, D100(11):115025. 19

[215] Girmohanta, S. and Shrock, R. (2020a). Baryon-Number-Violating Nucleon and Dinucleon Decays in a Model with Large Extra Dimensions. *Phys. Rev. D*, 101(1):015017. 13

[216] Girmohanta, S. and Shrock, R. (2020b). Improved Upper Limits on Baryon-Number Violating Dinucleon Decays to Dileptons. *Phys. Lett. B*, 803:135296. 19

[217] Girmohanta, S. and Shrock, R. (2020c). Nucleon decay and n-$\bar{n}$ oscillations in a left-right symmetric model with large extra dimensions. *Phys. Rev. D*, 101(9):095012. 13, 19

[218] Giunti, C. and Kim, C. W. (2007). *Fundamentals of Neutrino Physics and Astrophysics*. 212, 213

[219] Glashow, S. (1980). The Future of Elementary Particle Physics. *NATO Sci. Ser. B*, 61:687. 10

[220] Glashow, S. L. (1986). Positronium Versus the Mirror Universe. *Phys. Lett.*, 167B:35–36. 56

[221] Gninenko, S. N. (1994). Limit on 'disappearance' of orthopositronium in vacuum. *Phys. Lett.*, B326:317–319. 56

[222] Golan, T., Sobczyk, J. T., and Zmuda, J. (2012). NuWro: the Wroclaw Monte Carlo Generator of Neutrino Interactions. *Nucl. Phys. B Proc. Suppl.*, 229-232:499–499. 228

[223] Golub, R. and Yoshiki, H. (1989). Ultracold antineutrons (UCN-bar). 1: The approach to the semiclassical limit. *Nucl. Phys.*, A501:869–876. 204

[224] Golubeva, E., Ilinov, A., and Kondratyuk, L. (1996). Antineutron annihilation event generator for n —> anti-n search experiment. In *International Workshop on Future Prospects of Baryon Instability Search in p decay and n —> anti-n Oscillation Experiments*, pages 295–305. 88, 89, 111, 135

[225] Golubeva, E., Ilinov, A., and Kondratyuk, L. (1997). Interaction of low-energy antineutrons with nuclei. *Phys. Atom. Nucl.*, 60:2006–2011. 135

[226] Golubeva, E., Ilinov, A., Krippa, B., and Pshenichnov, I. (1992). Effects of mesonic resonance production in annihilation of stopped anti-protons on nuclei. *Nucl. Phys. A*, 537:393–417. 88, 89, 111, 118, 122, 125, 135

[227] Golubeva, E. and Kondratyuk, L. (1997). Annihilation of low energy antineutrons on nuclei. *Nucl. Phys. B Proc. Suppl.*, 56:103–107. 14, 88, 89, 111, 135

[228] Golubeva, E. S. (1994). PhD thesis, The Institute for Nuclear Research, Moscow. 88

[229] Golubeva, E. S., Barrow, J. L., and Ladd, C. G. (2019). Model of $\bar{n}$ annihilation in experimental searches for $\bar{n}$ transformations. *Phys. Rev. D*, 99(3):035002. xiii, xiv, xxiii, xxiv, xxvi, xxx, 85, 86, 87, 88, 107, 108, 110, 112, 113, 114, 118, 120, 122, 123, 124, 125, 126, 127, 129, 131, 134, 135, 141, 146, 152, 154, 185, 186, 198, 228, 291, 294

[230] Gonzalez-Garcia, M. C. and Maltoni, M. (2008). Phenomenology with Massive Neutrinos. *Phys. Rept.*, 460:1–129. 213

[231] Gonzalez-Garcia, M. C. and Nir, Y. (2003). Neutrino Masses and Mixing: Evidence and Implications. *Rev. Mod. Phys.*, 75:345–402. 2, 68

[232] Gran, R., Nieves, J., Sanchez, F., and Vacas, M. J. V. (2013). Neutrino-nucleus quasi-elastic and 2p2h interactions up to 10 gev. *Phys. Rev. D*, 88:113007. 266

[233] Griffiths, D. (2008). *Introduction to elementary particles*. 69

[234] Grojean, C., Shakya, B., Wells, J. D., and Zhang, Z. (2018). Implications of an Improved Neutron-Antineutron Oscillation Search for Baryogenesis: A Minimal Effective Theory Analysis. *Phys. Rev. Lett.*, 121(17):171801. 12

[235] Gudkov, V., Nesvizhevsky, V., Protasov, K., Snow, W., and Voronin, A. (2020). A new approach to search for free neutron-antineutron oscillations using coherent neutron propagation in gas. *Phys. Lett. B*, 808:135636. 33, 36

[236] Gupta, R., Jang, Y.-C., Lin, H.-W., Yoon, B., and Bhattacharya, T. (2017). Axial Vector Form Factors of the Nucleon from Lattice QCD. *Phys. Rev.*, D96(11):114503. 260

[237] Gustafson, J. et al. (2015). Search for dinucleon decay into pions at Super-Kamiokande. *Phys. Rev.*, D91(7):072009. 19, 122

[238] Gustafson, J. D. (2016). *A Search for Baryon Number Violation by Two Units at the Super-Kamiokande Detector*. PhD thesis, Boston University. 88, 121

[239] Haidenbauer, J. and Meiσner, U.-G. (2020). Neutron-antineutron oscillations in the deuteron studied with NN and $\bar{N}N$ interactions based on chiral effective field theory. *Chin. Phys. C*, 44(3):033101. 13, 35, 95

[240] Hamatsu, R. et al. (1977). Inclusive Production of Nonstrange Mesons in anti-p p Annihilations. *Nucl. Phys. B*, 123:189. 113, 114

[241] Hammer, H.-W., König, S., and van Kolck, U. (2020). Nuclear effective field theory: status and perspectives. *Rev. Mod. Phys.*, 92(2):025004. 14

[242] Hasan, N., Green, J., Meinel, S., Engelhardt, M., Krieg, S., Negele, J., Pochinsky, A., and Syritsyn, S. (2019). Nucleon axial, scalar, and tensor charges using lattice QCD at the physical pion mass. *Phys. Rev.*, D99(11):114505. 260

[243] Hewes, J. E. T. (2017). *Searches for Bound Neutron-Antineutron Oscillation in Liquid Argon Time Projection Chambers*. PhD thesis, Manchester U. 34, 86, 87, 121, 122, 134, 141, 154, 208, 220, 226, 228, 231, 293

[244] Hohler, G., Pietarinen, E., Sabba Stefanescu, I., Borkowski, F., Simon, G., Walther, V., and Wendling, R. (1976). Analysis of Electromagnetic Nucleon Form-Factors. *Nucl. Phys. B*, 114:505–534. xxxvi, 270, 271

[245] Holdom, B. (1986). Two U(1)'s and Epsilon Charge Shifts. *Phys. Lett.*, 166B:196–198. 56

[246] Holstein, B. R. (1993). Anomalies for pedestrians. *American Journal of Physics*, 61:142–147. 7

[247] Honda, M., Sajjad Athar, M., Kajita, T., Kasahara, K., and Midorikawa, S. (2015). Atmospheric neutrino flux calculation using the NRLMSISE-00 atmospheric model. *Phys. Rev. D*, 92(2):023004. 68, 213, 293

[248] Hughes, V. W. and Kinoshita, T. (1999). Anomalous g values of the electron and muon. *Rev. Mod. Phys.*, 71:S133–S139. 68

[249] Hulthen, L. t. (1957). *Structure of Atomic Nuclei*. Springer-Verlab Berlin Heidelberg. 93

[250] Iazzi, F. et al. (2000). Antineutron proton total cross-section from 50-MeV/c to 400-MeV/c. *Phys. Lett. B*, 475:378–385. 97

[251] Ignatiev, A. Yu. and Volkas, R. R. (2000). Geophysical constraints on mirror matter within the earth. *Phys. Rev.*, D62:023508. 57

[252] Ilinov, A. S., Nazaruk, V. I., and Chigrinov, S. E. (1982). NUCLEAR ABSORPTION OF STOPPED ANTI-PROTONS: MULTI - PION - NUCLEUS INTERACTIONS. *Nucl. Phys. A*, 382:378–400. xxii, 90

[253] Ishikawa, K.-I., Kuramashi, Y., Sasaki, S., Tsukamoto, N., Ukawa, A., and Yamazaki, T. (2018). Nucleon form factors on a large volume lattice near the physical point in 2+1 flavor QCD. *Phys. Rev.*, D98(7):074510. 260

[254] Jang, Y.-C., Gupta, R., Lin, H.-W., Yoon, B., and Bhattacharya, T. (2019). Nucleon Electromagnetic Form Factors in the Continuum Limit from 2+1+1-flavor Lattice QCD. *arXiv preprint*. 260

[255] Jastrow, R. (1955). Many-Body Problem with Strong Forces. *Phys. Rev.*, 98:1479–1484. 80

[256] JLab (2021). Thomas Jefferson National Accelerator Facility. `https://www.jlab.org/`. 81, 255

[257] Jones, S. et al. (2020a). Deep Underground Neutrino Experiment (DUNE), Far Detector Technical Design Report, Volume II DUNE Physics. *arXiv preprint*. xv, xviii, xxxiv, 30, 36, 37, 38, 39, 154, 208, 226, 231, 235, 240, 244, 246, 248, 257, 293

[258] Jones, S. et al. (2020b). Deep Underground Neutrino Experiment (DUNE), Far Detector Technical Design Report, Volume IV Far Detector Single-phase Technology. *arXiv preprint*. 257

[259] Jones, T. et al. (1984). A Search for $N\bar{N}$ Oscillation in Oxygen. *Phys. Rev. Lett.*, 52:720. xviii, 19, 20, 39

[260] Jourdan, J. (1996). Quasielastic response functions: The Coulomb sum revisited. *Nucl. Phys.*, A603:117–160. 70, 83

[261] Jr., T. d. F. and Walecka, J. (1966). Electron scattering and nuclear structure. *Advances in Physics*, 15(57):1–109. 258

[262] Kaczmarek, A. and Radosz, A. (2019). Dark Matter within the Milky Way. See open access here. xix, 42

[263] Kamyshkov, Y. (2015). Anomalies and non-conservation of b, l in sm. Handwritten notes; lecture presented in Particle Physic II in Nielsen Physics Building, Knoxville, TN. 6, 7

[264] Kamyshkov, Y. (2020). Searches for neutron oscillations to sterile state $n \to n'$ and to antineutron $n \to \bar{n}$. Workshop presentation, Slide 20. xix, 48

[265] Kelly, K. J., Machado, P. A., Martinez Soler, I., Parke, S. J., and Perez Gonzalez, Y. F. (2019). Sub-GeV Atmospheric Neutrinos and CP-Violation in DUNE. *Phys. Rev. Lett.*, 123(8):081801. 220, 222

[266] Kerbikov, B. O. (2018). Lindblad and Bloch equations for conversion of a neutron into an antineutron. *Nucl. Phys. A*, 975:59–72. 33

[267] Kerbikov, B. O. (2019). The effect of collisions with the wall on neutron-antineutron transitions. *Phys. Lett. B*, 795:362–365. 204

[268] King, G., Andreoli, L., Pastore, S., Piarulli, M., Schiavilla, R., Wiringa, R., Carlson, J., and Gandolfi, S. (2020). Chiral Effective Field Theory Calculations of Weak Transitions in Light Nuclei. *arXiv preprint*. 260

[269] Klempt, E., Batty, C., and Richard, J.-M. (2005). The Antinucleon-nucleon interaction at low energy : Annihilation dynamics. *Phys. Rept.*, 413:197–317. xxiii, 113, 114, 123

[270] Klempt, E., Bradamante, F., Martin, A., and Richard, J. (2002). Antinucleon nucleon interaction at low energy: Scattering and protonium. *Phys. Rept.*, 368:119–316. 92, 97

[271] Klinkby, E., Batkov, K., Mezei, F., Schønfeldt, T., Takibayev, A., and Zanini, L. (2014). Voluminous D2 source for intense cold neutron beam production at the ESS. xviii, 30, 38, 156, 159

[272] Klinkby, E. and Soldner, T. (2016). Fundamental physics possibilities at the European Spallation Source. In *VI European Conference on Neutron Scattering (ECNS2015)*. 36

[273] Koch, V., Brown, G., and Ko, C. (1991). Mean field effects and apparent temperatures of nucleons and anti-nucleons. *Phys. Lett. B*, 265:29–34. 109

[274] Kohno, M. and Weise, W. (1986). Proton - Anti-proton Scattering and Annihilation Into Two Mesons. *Nucl. Phys. A*, 454:429–452. 95

[275] Kopeliovich, V. and Potashnikova, I. (2012). Restriction on the Neutron-Antineutron Oscillations from the SNO Data on the Deuteron Stability. *JETP Lett.*, 95:1–5. xviii, 39, 95

[276] Krishnaswamy, M., Menon, M., Mondal, N., Narasimham, V., Sreekantan, B., Hayashi, Y., Ito, N., Kawakami, S., and Miyake, S. (1986). Results From the Kgf Proton Decay Experiment. *Nuovo Cim. C*, 9:167–181. xviii, 19, 39

[277] Kuzmin, V., Rubakov, V., and Shaposhnikov, M. (1985). On the Anomalous Electroweak Baryon Number Nonconservation in the Early Universe. *Phys. Lett. B*, 155:36. xvi, 8

[278] Larionov, A., Pshenichnov, I., Mishustin, I., and Greiner, W. (2009). Anti-proton - nucleus collisions simulation within a kinetic approach with relativistic mean fields. *Phys. Rev. C*, 80:021601. 110

[279] Lawrence, D. J., Wilson, J. T., and Peplowski, P. N. (2021). Space-based Measurements of Neutron Lifetime: Approaches to Resolving the Neutron Lifetime Anomaly. *Nucl. Instrum. Meth. A*, 988:164919. 46

[280] Lee, T. and Yang, C.-N. (1956). Question of Parity Conservation in Weak Interactions. *Phys. Rev.*, 104:254–258. 49

[281] Levman, G., Singer, R., and Fields, T. (1980). Study of Prompt e^+e^-, Eta0, and Omega0 Production in Low-energy $\bar{p}p$ Annihilations. *Phys. Rev. D*, 21:1. 113, 114

[282] Lovato, A., Carlson, J., Gandolfi, S., Rocco, N., and Schiavilla, R. (2020). Ab initio study of (ν_ℓ, ℓ^-) and $(\overline{\nu}_\ell, \ell^+)$ inclusive scattering in ^{12}C: confronting the MiniBooNE and T2K CCQE data. *arXiv preprint*. 69, 81, 261, 266, 267, 269, 270

[283] Lovato, A., Gandolfi, S., Butler, R., Carlson, J., Lusk, E., Pieper, S. C., and Schiavilla, R. (2013). Charge form factor and sum rules of electromagnetic response functions in $^{12}\mathrm{C}$. *Phys. Rev. Lett.*, 111:092501. 261

[284] Lovato, A., Gandolfi, S., Carlson, J., Lusk, E., Pieper, S. C., and Schiavilla, R. (2018). Quantum Monte Carlo calculation of neutral-current $\nu -^{12} C$ inclusive quasielastic scattering. *Phys. Rev.*, C97(2):022502. 81, 261

[285] Lovato, A., Gandolfi, S., Carlson, J., Pieper, S. C., and Schiavilla, R. (2014). Neutral weak current two-body contributions in inclusive scattering from $^{12}\mathrm{C}$. *Phys. Rev. Lett.*, 112:182502. 261

[286] Lovato, A., Gandolfi, S., Carlson, J., Pieper, S. C., and Schiavilla, R. (2015). Electromagnetic and neutral-weak response functions of ^{4}He and ^{12}C. *Phys. Rev.*, C91(6):062501. 261, 262

[287] Lu, X. G. et al. (2018). Measurement of final-state correlations in neutrino muon-proton mesonless production on hydrocarbon at $\langle E_\nu \rangle = 3$ GeV. *Phys. Rev. Lett.*, 121(2):022504. 226

[288] Magas, V., Roca, L., and Oset, E. (2005). The phi meson width in the medium from proton induced phi production in nuclei. *Phys. Rev. C*, 71:065202. 110

[289] Marcucci, L. E., Viviani, M., Schiavilla, R., Kievsky, A., and Rosati, S. (2005). Electromagnetic structure of A=2 and 3 nuclei and the nuclear current operator. *Phys. Rev.*, C72:014001. 261

[290] Markisch, B. (2011). Experimental Status of Vud from Neutron Decay. 45

[291] Martinez-Soler, I. (2020). Oscillated atmospheric neutrino fluxes. Presented to the DUNE HEP Working Group, viewable here. xxxiii, 212, 220, 221

[292] Mcgaughey, P. et al. (1986). Dynamics of Low-energy Anti-proton Annihilation in Nuclei as Inferred From Inclusive Proton and Pion Measurements. *Phys. Rev. Lett.*, 56:2156–2159. xxiv, 125, 127, 128

[293] McKeen, D. and Nelson, A. E. (2016). CP Violating Baryon Oscillations. *Phys. Rev. D*, 94(7):076002. 12

[294] Meyer, A. S., Betancourt, M., Gran, R., and Hill, R. J. (2016). Deuterium target data for precision neutrino-nucleus cross sections. *Phys. Rev.*, D93(11):113015. 260

[295] Minor, E. D., Armstrong, T. A., Bishop, R., Harris, V., Lewis, R. A., and Smith, G. A. (1990). Charged pion spectra and energy transfer following anti-proton annihilation at rest in carbon and uranium. *Z. Phys. A*, 336:461–468. xiv, xxiv, 113, 114, 122, 124, 125, 128

[296] Mishustin, I., Satarov, L., Burvenich, T., Stoecker, H., and Greiner, W. (2005). Antibaryons bound in nuclei. *Phys. Rev. C*, 71:035201. 109

[297] Moffat, K., Pascoli, S., Petcov, S. T., Schulz, H., and Turner, J. (2018). Three-flavored nonresonant leptogenesis at intermediate scales. *Phys. Rev. D*, 98(1):015036. xviii, 28

[298] Mohapatra, R. and Pati, J. C. (1975). A Natural Left-Right Symmetry. *Phys. Rev. D*, 11:2558. 13

[299] Mohapatra, R. N. and Marshak, R. (1980). Local B-L Symmetry of Electroweak Interactions, Majorana Neutrinos and Neutron Oscillations. *Phys. Rev. Lett.*, 44:1316–1319. [Erratum: Phys.Rev.Lett. 44, 1643 (1980)]. 10, 13

[300] Mohapatra, R. N., Nasri, S., and Nussinov, S. (2005). Some implications of neutron mirror neutron oscillation. *Phys. Lett.*, B627:124–130. 57

[301] Mohapatra, R. N. and Senjanovic, G. (1980). Neutrino Mass and Spontaneous Parity Nonconservation. *Phys. Rev. Lett.*, 44:912. 68

[302] Multhopp, H. (1938). Die berechnung der auftriebsverteilung von tragflügeln. *Luftfahrtforschung*, 15:153–166. 94

[303] National Energy Research Scientific Computing Center (NERSC) (2020). 230

[304] Nelson, A. (2017). CP Violation, Baryon violation, RPV in SUSY, Mesino Oscillations, and Baryogenesis. Slide 4: http://www.int.washington.edu/talks/WorkShops/int_17_69W/People/Nelson_A/Nelson.pdf. 12, 21

[305] Nesvizhevsky, V., Gudkov, V., Protasov, K., Snow, W., and Voronin, A. (2020). Comment on B.O. Kerbikov, "The effect of collisions with the wall on neutron-antineutron transitions", Phys. Lett. B 795 (2019) 362. *Phys. Lett. B*, 803:135357. 36

[306] Nesvizhevsky, V., Gudkov, V., Protasov, K., Snow, W., and Voronin, A. Y. (2019a). Experimental Approach to Search for Free Neutron-Antineutron Oscillations Based on Coherent Neutron and Antineutron Mirror Reflection. *Phys. Rev. Lett.*, 122(22):221802. 198

[307] Nesvizhevsky, V., Gudkov, V., Protasov, K., Snow, W., and Voronin, A. Y. (2019b). Experimental Approach to Search for Free Neutron-Antineutron Oscillations Based on Coherent Neutron and Antineutron Mirror Reflection. *Phys. Rev. Lett.*, 122(22):221802. 204

[308] Nevo Dinur, N., Hernandez, O. J., Bacca, S., Barnea, N., Ji, C., Pastore, S., Piarulli, M., and Wiringa, R. B. (2019). Zemach moments and radii of ^{2,3}H and ^{3,4}He. *Phys. Rev.*, C99(3):034004. 260

[309] Nielsen, T. R., Markvardsen, A. J., and Willendrup, P. K. (2016). McStas and Mantid integration. 161

[310] Nieves, J., Simo, I. R., and Vacas, M. J. V. (2011). Inclusive charged-current neutrino-nucleus reactions. *Phys. Rev. C*, 83:045501. 266

[311] Nussinov, S. and Shrock, R. (2002). N - anti-N oscillations in models with large extra dimensions. *Phys. Rev. Lett.*, 88:171601. 13

[312] Nussinov, S. and Shrock, R. (2020). Using $\bar{p}p$ and e^+e^- Annihilation Data to Refine Bounds on the Baryon-Number-Violating Dinucleon Decays $nn \to e^+e^-$ and $nn \to \mu^+\mu^-$. 19

[313] Okun, L. (2007). Mirror particles and mirror matter: 50 years of speculations and search. *Phys. Usp.*, 50:380–389. 51

[314] Oosterhof, F., Long, B., de Vries, J., Timmermans, R., and van Kolck, U. (2019). Baryon-number violation by two units and the deuteron lifetime. *Phys. Rev. Lett.*, 122(17):172501. 13, 14, 35, 37, 92, 95

[315] Paley, J. (2020). Measurement of the Muon-neutrino Charged-Current Inclusive Cross Section in the NOvA Near Detector. Presented at the Fermilab Wine and Cheese Seminar, viewable here. 226

[316] Papadopolou, A., Ashkenazi, A., Gardiner, S., Betancourt, M., Dytman, S., Weinstein, L., Piasetzky, E., Hauenstein, F., Khachatryan, M., Dolan, S., et al. (2020). Inclusive electron scattering and the GENIE neutrino event generator. *arXiv preprint*. 255, 266

[317] Pastore, S., Baroni, A., Carlson, J., Gandolfi, S., Pieper, S. C., Schiavilla, R., and Wiringa, R. B. (2018). Quantum Monte Carlo calculations of weak transitions in $A = 6$–10 nuclei. *Phys. Rev.*, C97(2):022501. 260

[318] Pastore, S., Carlson, J., Gandolfi, S., Schiavilla, R., and Wiringa, R. B. (2020). Quasielastic lepton scattering and back-to-back nucleons in the short-time approximation. *Phys. Rev. C*, 101(4):044612. xxxvii, 69, 80, 81, 255, 256, 260, 261, 262, 266, 267, 269, 272, 273, 276, 279, 280, 284, 293

[319] Pastore, S., Girlanda, L., Schiavilla, R., and Viviani, M. (2011). The two-nucleon electromagnetic charge operator in chiral effective field theory (χEFT) up to one loop. *Phys. Rev.*, C84:024001. 260

[320] Pastore, S., Girlanda, L., Schiavilla, R., Viviani, M., and Wiringa, R. B. (2009). Electromagnetic Currents and Magnetic Moments in (chi)EFT. *Phys. Rev.*, C80:034004. 260

[321] Pastore, S., Pieper, S. C., Schiavilla, R., and Wiringa, R. B. (2013). Quantum Monte Carlo calculations of electromagnetic moments and transitions in A $\leq$ 9 nuclei with meson-exchange currents derived from chiral effective field theory. *Phys. Rev.*, C87(3):035503. 260, 261

[322] Pastore, S., Wiringa, R. B., Pieper, S. C., and Schiavilla, R. (2014). Quantum Monte Carlo calculations of electromagnetic transitions in ^{8}Be with meson-exchange currents derived from chiral effective field theory. *Phys. Rev.*, C90(2):024321. 260

[323] Patrick, C. (2016). *Measurement of the Antineutrino Double-Differential Charged-Current Quasi-Elastic Scattering Cross Section at MINERvA*. PhD thesis, Northwestern U. 226

[324] Pattie, R.W., J. et al. (2018). Measurement of the neutron lifetime using a magneto-gravitational trap and in situ detection. *Science*, 360(6389):627–632. xix, 46, 48

[325] Peggs, S. (2013). ESS Technical Design Report. 155

[326] Phillips, D.G., I. et al. (2016). Neutron-Antineutron Oscillations: Theoretical Status and Experimental Prospects. *Phys. Rept.*, 612:1–45. 10, 19, 36, 156, 159, 204

[327] Piarulli, M., Girlanda, L., Schiavilla, R., Kievsky, A., Lovato, A., Marcucci, L. E., Pieper, S. C., Viviani, M., and Wiringa, R. B. (2016). Local chiral potentials with Δ-intermediate states and the structure of light nuclei. *Phys. Rev.*, C94(5):054007. 287

[328] Pienkowski, L. et al. (2002). Breakup time scale studied in the 8-GeV/c pi-+ Au-197 reaction. *Phys. Rev. C*, 65:064606. 121, 147

[329] Pieper, S. C. (2008). The illinois extension to the fujita-miyazawa three-nucleon force. *AIP Conference Proceedings*, 1011(1):143–152. 259, 260

[330] Pignol, G. and Schmidt-Wellenburg, P. (2021). The search for the neutron electric dipole moment at PSI. 46

[331] Pokotilovski, Yu. N. (2006). On the experimental search for neutron —¿ mirror neutron oscillations. *Phys. Lett.*, B639:214–217. 46, 57, 59, 66

[332] Pshenichnov, I. A. (1997). PhD thesis, The Inistitute for Nuclear Research, Moscow. 112

[333] Rao, S. and Shrock, R. (1982). $n \leftrightarrow \bar{n}$ Transition Operators and Their Matrix Elements in the MIT Bag Model. *Phys. Lett. B*, 116:238–242. 33

[334] Rao, S. and Shrock, R. E. (1984). Six Fermion $(B-L)$ Violating Operators of Arbitrary Generational Structure. *Nucl. Phys. B*, 232:143–179. 13, 33

[335] Refregier, A. (2003). Weak gravitational lensing by large scale structure. *Ann. Rev. Astron. Astrophys.*, 41:645–668. 41

[336] Richard, J. (1992). The Nonrelativistic three-body problem for baryons. *Phys. Rept.*, 212:1–76. 94

[337] Richard, J. and Sainio, M. (1982). Nuclear Effects in Protonium. *Phys. Lett. B*, 110:349–352. 95

[338] Riedlberger, J., Amsler, C., Doser, M., Straumann, U., Truöl, P., Bailey, D., Barlag, S., Gastaldi, U., Landua, R., Sabev, C., Duch, K. D., Heel, M., Kalinowsky, H., Kayser, F., Klempt, E., May, B., Schreiber, O., Weidenauer, P., Ziegler, M., Dahme, W., Feld-Dahme, F., Schaefer, U., Wodrich, W. R., Ahmad, S., Bizot, J. C., Delcourt, B., Jeanjean, J., Nguyen, H., Prevot, N., Auld, E. G., Axen, D. A., Erdman, K. L., Howard, B., Howard, R., White, B. L., Comyn, M., Beer, G., Marshall, G. M., Robertson, L. P., Botlo, M., Laa, C., and Vonach, H. (1989). Antiproton annihilation at rest in nitrogen and deuterium gas. *Phys. Rev. C*, 40:2717–2731. xxiv, 126, 127

[339] Rinaldi, E., Syritsyn, S., Wagman, M. L., Buchoff, M. I., Schroeder, C., and Wasem, J. (2019a). Lattice QCD determination of neutron-antineutron matrix elements with physical quark masses. *Phys. Rev. D*, 99(7):074510. 13, 29, 33

[340] Rinaldi, E., Syritsyn, S., Wagman, M. L., Buchoff, M. I., Schroeder, C., and Wasem, J. (2019b). Neutron-antineutron oscillations from lattice QCD. *Phys. Rev. Lett.*, 122(16):162001. 13, 29, 33

[341] Riotto, A. and Trodden, M. (1999). Recent progress in baryogenesis. *Ann. Rev. Nucl. Part. Sci.*, 49:35–75. 7

[342] Rocco, N. (2019). Neutrino cross section. 69

[343] Rocco, N., Alvarez-Ruso, L., Lovato, A., and Nieves, J. (2017). Electromagnetic scaling functions within the Green's Function Monte Carlo approach. *Phys. Rev. C*, 96(1):015504. 69, 81, 266, 269, 270, 272, 277

[344] Rocco, N. and Barbieri, C. (2018). Inclusive electron-nucleus cross section within the Self Consistent Green's Function approach. *Phys. Rev.*, C98(2):025501. 81, 269

[345] Rocco, N., Leidemann, W., Lovato, A., and Orlandini, G. (2018). Relativistic effects in ab-initio electron-nucleus scattering. *Phys. Rev.*, C97(5):055501. 81, 266, 269, 270, 277

[346] ROOT Collaboration (2021). TMVA. See here. 234

[347] Roy, J. (1975). Inclusive Properties of anti-p d at Rest Annihilation Products. xxiv, 123

[348] Rubakov, V. and Shaposhnikov, M. (1996). Electroweak baryon number nonconservation in the early universe and in high-energy collisions. *Usp. Fiz. Nauk*, 166:493–537. 9

[349] Rubakov, V. and Shaposhnikov, M. (1998). Electroweak baryon number non-conservation in the early universe and in high-energy collisions. *AIP Conf. Proc.*, 419(1):347–412. xvi, 6, 7, 8, 9

[350] Rubin, V., Thonnard, N., and Ford, W.K., J. (1980). Rotational properties of 21 SC galaxies with a large range of luminosities and radii, from NGC 4605 /R = 4kpc/ to UGC 2885 /R = 122 kpc/. *Astrophys. J.*, 238:471. 41

[351] Rubin, V. C. and Ford, W.Kent, J. (1970). Rotation of the Andromeda Nebula from a Spectroscopic Survey of Emission Regions. *Astrophys. J.*, 159:379–403. 41

[352] Sakharov, A. D. (1967). Violation of CP Invariance, C asymmetry, and baryon asymmetry of the universe. *Pisma Zh. Eksp. Teor. Fiz.*, 5:32–35. [Usp. Fiz. Nauk161,no.5,61(1991)]. 6, 10

[353] Salvat, D. et al. (2014). Storage of ultracold neutrons in the magneto-gravitational trap of the UCNτ experiment. *Phys. Rev. C*, 89(5):052501. 46

[354] Salvini, P. et al. (2004). anti-p p annihilation into four charged pions at rest and in flight. *Eur. Phys. J. C*, 35:21–33. xiii, 113, 114, 122

[355] Santoro, V. et al. (2016). Neutronic design of the bunker. *ESS General Document, ESS-0052649*. 156

[356] Santoro, V. et al. (2020). Development of High Intensity Neutron Source at the European Spallation Source. In *Accepted by Journal of Neutron Research*. xxx, 36, 155, 186

[357] Scharenberg, R. P. et al. (2001). Comparison of 1-A-GeV Au-197 + C data with thermodynamics: The Nature of phase transition in nuclear multifragmentation. *Phys. Rev. C*, 64:054602. 121, 147

[358] Schiavilla, R., Baroni, A., Pastore, S., Piarulli, M., Girlanda, L., Kievsky, A., Lovato, A., Marcucci, L. E., Pieper, S. C., Viviani, M., and Wiringa, R. B. (2019). Local chiral interactions and magnetic structure of few-nucleon systems. *Phys. Rev. C*, 99:034005. 260

[359] Schiavilla, R., Wiringa, R. B., Pandharipande, V. R., and Carlson, J. (1992). Effects of Delta-isobar degrees of freedom on low-energy electroweak transitions in few-body nuclei. *Phys. Rev.*, C45:2628–2639. 261

[360] Schmidt, U., Bitter, T., El-Muzeini, P., Dubbers, D., and Scharpf, O. (1992). Long distance propagation of a polarized neutron beam in zero magnetic field. *Nuclear Instruments and Methods in Physics Research Section A: Accelerators, Spectrometers, Detectors and Associated Equipment*, 320(3):569 – 573. 15, 17, 32, 179

[361] Schwehr, J., Cherdack, D., and Gran, R. (2017). GENIE implementation of IFIC Valencia model for QE-like 2p2h neutrino-nucleus cross section. *arXiv preprint*. 266

[362] Senjanovic, G. and Mohapatra, R. N. (1975). Exact Left-Right Symmetry and Spontaneous Violation of Parity. *Phys. Rev. D*, 12:1502. 13, 68

[363] Senjanovic, G. and Tello, V. (2020). Parity and the origin of neutrino mass. *Int. J. Mod. Phys. A*, 35(09):2050053. 68

[364] Serebrov, A. et al. (2009a). Search for neutron-mirror neutron oscillations in a laboratory experiment with ultracold neutrons. *Nucl. Instrum. Meth. A*, 611:137–140. xxi, 46, 49, 53, 64, 67

[365] Serebrov, A. and Fomin, A. (2011). New evaluation of neutron lifetime from UCN storage experiments and beam experiments. *Phys. Procedia*, 17:199–205. xix, 48

[366] Serebrov, A., Fomin, A., and Kamyshkov, Y. (2016). Sensitivity of experiment on search for neutron–antineutron oscillations on the projected ultracold neutron source at the WWR-M reactor. *Tech. Phys. Lett.*, 42(1):99–101. 37

[367] Serebrov, A. P. et al. (2008a). Experimental search for neutron: Mirror neutron oscillations using storage of ultracold neutrons. *Phys. Lett.*, B663:181–185. 60, 64

[368] Serebrov, A. P. et al. (2008b). Neutron lifetime measurements using gravitationally trapped ultracold neutrons. *Phys. Rev. C*, 78:035505. 46

[369] Serebrov, A. P. et al. (2009b). Search for neutronmirror neutron oscillations in a laboratory experiment with ultracold neutrons. *Nucl. Instrum. Meth.*, A611:137–140. 60, 64

[370] Sharma, N., Dahiya, H., Chatley, P. K., and Gupta, M. (2010). Spin $\frac{1}{2}^+$, spin $\frac{3}{2}^+$ and transition magnetic moments of low lying and charmed baryons. *Phys. Rev.*, D81:073001. 57

[371] Shen, G., Marcucci, L. E., Carlson, J., Gandolfi, S., and Schiavilla, R. (2012). Inclusive neutrino scattering off deuteron from threshold to GeV energies. *Phys. Rev.*, C86:035503. 260

[372] Shimizu, H. M. (2017). Cold Neutron Reflective Optics for NNBAR. Presentation given at the INT Workshop on Neutron Oscillations, see here. 201

[373] Shintani, E., Ishikawa, K.-I., Kuramashi, Y., Sasaki, S., and Yamazaki, T. (2019). Nucleon form factors and root-mean-square radii on a (10.8 fm)^4 lattice at the physical point. *Phys. Rev.*, D99(1):014510. 260

[374] Short-Baseline Near Detector (2021). `https://sbn-nd.fnal.gov/`. 257

[375] Sibirtsev, A., Cassing, W., Lykasov, G., and Rzyanin, M. (1998). Reanalysis of anti-proton production in proton nucleus and nucleus-nucleus reactions at subthreshold energies. *Nucl. Phys. A*, 632:131–152. 109

[376] Siegel, E. et al. (2021). Goodbye, DAMA/LIBRA: World's Most Controversial Dark Matter Experiment Fails Replication Test. *Forbes Science*. 45

[377] Sirunyan, A. M. et al. (2020). Search for high mass dijet resonances with a new background prediction method in proton-proton collisions at $\sqrt{s} = 13$ TeV. *JHEP*, 05:033. 37

[378] Snow, W. M. et al. (2015). A slow neutron polarimeter for the measurement of parity-odd neutron rotary power. *Review of Scientific Instruments*, 86(5):055101. 167

[379] Soldner, T., Abele, H., Konrad, G., Märkisch, B., Piegsa, F. M., Schmidt, U., Theroine, C., and Sánchez, P. T. (2019). ANNI – A pulsed cold neutron beam facility for particle physics at the ESS. *EPJ Web Conf.*, 219:10003. xxvii, xxviii, 37, 159, 160, 161, 163, 164, 166, 200, 205

[380] Spieles, C., Bleicher, M., Jahns, A., Mattiello, R., Sorge, H., Stoecker, H., and Greiner, W. (1996). Anti-baryons in massive heavy ion reactions: Importance of potentials. *Phys. Rev. C*, 53:2011–2013. 109

[381] Sternheimer, R. M. (1970). Quadrupole polarizabilities of various ions and the alkali atoms. *Phys. Rev. A*, 1:321. 92

[382] Stoks, V. G. J., Klomp, R. A. M., Rentmeester, M. C. M., and de Swart, J. J. (1993). Partial wave analaysis of all nucleon-nucleon scattering data below 350-MeV. *Phys. Rev.*, C48:792–815. 259

[383] Subedi, R. et al. (2008). Probing Cold Dense Nuclear Matter. *Science*, 320:1476–1478. 81, 83, 256, 287

[384] Sumi, N. et al. (2021). Precise Neutron Lifetime Measurement Using Pulsed Neutron Beams at J-PARC. In *3rd International Symposium on Science at J-PARC*. 46

[385] Sussman, S. et al. (2018). Dinucleon and Nucleon Decay to Two-Body Final States with no Hadrons in Super-Kamiokande. 19

[386] 't Hooft, G. (1976a). Computation of the Quantum Effects Due to a Four-Dimensional Pseudoparticle. *Phys. Rev. D*, 14:3432–3450. [Erratum: Phys.Rev.D 18, 2199 (1978)]. 7, 66

[387] 't Hooft, G. (1976b). Symmetry Breaking Through Bell-Jackiw Anomalies. *Phys. Rev. Lett.*, 37:8–11. 6, 7, 9

[388] Takenaka, A. et al. (2020). Search for proton decay via $p \to e^+\pi^0$ and $p \to \mu^+\pi^0$ with an enlarged fiducial volume in Super-Kamiokande I-IV. *Phys. Rev. D*, 102(11):112011. 10

[389] Takhistov, V. et al. (2015). Search for Nucleon and Dinucleon Decays with an Invisible Particle and a Charged Lepton in the Final State at the Super-Kamiokande Experiment. *Phys. Rev. Lett.*, 115(12):121803. 19

[390] Takita, M. et al. (1986). A Search for Neutron - Anti-neutron Oscillation in a ^{16}O Nucleus. *Phys. Rev. D*, 34:902. xviii, 19, 20, 39

[391] Tanabashi, M. et al. (2018). Review of Particle Physics. *Phys. Rev.*, D98(3):030001. 64, 218

[392] *et al.* (Particle Data Group, P. A. Z. (2020a). Retrieved from here. xix, 43, 44

[393] *et al.* (Particle Data Group, P. A. Z. (2020b). Retrieved from here. xix, 47

[394] *et al.* (Particle Data Group, P. A. Z. (2020c). Retrieved from here. 45

[395] The DUNE Collaboration (2015). The Deep Underground Neutrino Experiment. `https://lbnf.fnal.gov/`. 86, 255, 256, 257

[396] The DUNE Collaboration (2020). The Deep Underground Neutrino Experiment. Retrieved from here. xxxii, 210

[397] The MicroBooNE Experiment (2021). `http://www-microboone.fnal.gov`. 255, 257

[398] The MINERνA Collaboration (2021). MINERνA. `https://minerva.fnal.gov/`. 257

[399] The NOvA Experiment (2021). `http://www-nova.fnal.gov`. 255

[400] Thompson, S., Moretto, L., Heunemann, D., Jared, R., Gatti, R., and Nifenecker, H. (1973). Study of a fission-like environment in reactions with very heavy ions. LBL-1966. 121

[401] Thomson, M. A. (2010a). Deep inelastic scattering. xxi, 74, 75, 76, 77, 78, 79, 80

[402] Thomson, M. A. (2010b). Electron-proton elastic scattering. xxi, 69, 70, 71, 72, 73, 74

[403] Totani, D. and Cavanna, F. (2020). First Calorimetric Energy Reconstruction of Beam Events with ARAPUCA Light Detector in ProtoDUNE-SP. *JINST*, 15(03):C03033. 209

[404] Vigo, C., Gerchow, L., Radics, B., Raaijmakers, M., Rubbia, A., and Crivelli, P. (2020). New bounds from positronium decays on massless mirror dark photons. *Phys. Rev. Lett.*, 124(10):101803. 57

[405] von Reden, K. F. et al. (1990). Quasielastic electron scattering and Coulomb sum rule in He-4. *Phys. Rev.*, C41:1084–1094. xxxvii, 279, 280

[406] Wade, M. and Lind, V. G. (1976). Ratio of antiproton annihilations on neutrons and protons in carbon for low-energy and stopped antiprotons. *Phys. Rev. D*, 14:1182–1187. xxiv, 126, 127

[407] Wagman, M. (2020). Private communication. 29, 33

[408] Wagner, T. A., Schlamminger, S., Gundlach, J. H., and Adelberger, E. G. (2012). Torsion-balance tests of the weak equivalence principle. *Class. Quant. Grav.*, 29:184002. 35

[409] Wan, L. (2020a). Neutron-antineutron oscillation search at Super-Kamiokande. Link here, and video here. xiii, xviii, 20, 30, 37

[410] Wan, L. (2020b). Neutron-Antineutron Oscillation Search at Super-Kamiokande & Prospect for SK-Gd and HK. Link here. xiii, xviii, 20, 30

[411] Wietfeldt, F. (2014). The Neutron Lifetime. In *8th International Workshop on the CKM Unitarity Triangle*. 45

[412] Wietfeldt, F. E. (2018). Measurements of the Neutron Lifetime. *Atoms*, 6(4):70. 46, 177

[413] Wiringa, R. (2019). Two-nucleon momentum distributions. Retrieved from here. 81

[414] Wiringa, R. B., Schiavilla, R., Pieper, S. C., and Carlson, J. (2014). Nucleon and nucleon-pair momentum distributions in $A \leq 12$ nuclei. *Phys. Rev.*, C89(2):024305. xxxviii, 81, 287, 289

[415] Wiringa, R. B., Stoks, V. G. J., and Schiavilla, R. (1995). An Accurate nucleon-nucleon potential with charge independence breaking. *Phys. Rev.*, C51:38–51. 259

[416] Wu, W., Hatcher, R., and Yang, T. (2018). Honda flux in genie. DUNE FD Simulation/Reconstruction Group Meeting, see presentation here. 214

[417] xgboost developers (2021). XGBoost R Package. See here. 234

[418] Yanagida, T. (1979). Horizontal gauge symmetry and masses of neutrinos. *Conf. Proc.*, C7902131:95–99. 68

[419] Yiu, S.-C. (2021). Updates on the full detector simulation. Presentation given to the HIBEAM/NNBAR Detector Simulation and Computing Working Group; available here. xxx, 190, 198

[420] Yoshiki, H. and Golub, R. (1992). Ultracold antineutrons (UC antineutrons). 2: Production probability under magnetic and gravitational fields. *Nucl. Phys. A*, 536:648–668. 204

[421] Young, A. and Barrow, J. (2019). Future searches for free and bound $n \to \bar{n}$ transformations. *EPJ Web Conf.*, 219:07005. 19, 38, 294

[422] Yue, A., Dewey, M., Gilliam, D., Greene, G., Laptev, A., Nico, J., Snow, W., and Wietfeldt, F. (2013). Improved Determination of the Neutron Lifetime. *Phys. Rev. Lett.*, 111(22):222501. 46

[423] Zghiche, A. et al. (1994). Longitudinal and transverse responses in quasielastic electron scattering from ^{208}Pb and ^{4}He. *Nucl. Phys. A*, 572:513–559. [Erratum: Nucl.Phys.A 584, 757–757 (1995)]. 284

[424] Zwicky, F. (1937). On the Masses of Nebulae and of Clusters of Nebulae. *Astrophys. J.*, 86:217–246. 41

Vita

Joshua Lawrence Barrow was born in , United States, outside Atlanta in to interventional radiologist Dr. Brent Barrow and health administrator and nurse Charlsie Sue “Susie” Ratledge. Following his father’s completion of residency and fellowship at Emory School of Medicine, he moved to , United States at age three. There, with the support of his many loving family members, he would go on to attend . His high school career began at the , where he would graduate with Cum Laude and National Honors Society distinctions, as well as several regional and state titles for crew (rowing), in 2010. There, he excelled in the sciences, particularly enjoying physics alongside literature and writing, winning the Argonaut Creative Writing Award in 2010.

He began to his collegiate studies at his family’s alma mater, Southern Adventist University, in Collegedale, Tennessee during the fall of 2010, initially seeking a degree in biochemistry with intent to pursue MD/PhD graduate work, hoping to specialize in antiretroviral drug research to combat HIV/AIDS. Feeling unfulfilled (and unchallenged) by the coursework, he switched his major to Physics in his second year, and would go on to graduate in 2015 with Summa Cum Laude honors through his ~ 170 hours of classwork toward two Bachelor of Science degrees in Physics and Mathematics, as well as minors in Chemistry and Biology. Through this time, he also tutored some 20 courses under Dr. Januwoina Nixon at the university’s Learning Support Services office. Though his combination of coursework was initially intended to maintain requirements for medical school and or a potential high school teaching career, he was encouraged to join Professor Emeritus Ray Hefferlin in his research on quantum chemistry and periodic systems in 2013; they would go on to work together for another two years before Hefferlin’s unexpected passing, writing several papers and proceedings together. Following this, Barrow lead several university faculty and students on to finish Hefferlin's work, resulting in the cover article of the July 2016 volume of the International Journal of Quantum Chemistry.

Encouraged by Hefferlin to further develop his scientific capacities, Barrow was accepted to five of the nine graduate schools to which he applied, and joined the University of Tennessee at Knoxville in 2015 after a wonderful visit. During this visit, he would meet his future advisor, Professor Yuri Kamyshkov, and became fascinated with his work. After passing the 2016 qualifying examination, Barrow joined Kamyshkov as a full research assistant and began his work on intranuclear and extranuclear $n \to \bar{n}$, as well as $n \to n'$, within the DUNE, NNBAR/HIBEAM, and UTK/ORNL Neutron Oscillation collaborations, respectively. During this time, Barrow was taken in by Elena Golubeva of the Institute for Nuclear Research, Moscow, Russia, and began working with her remotely to update and validate her model of $\bar{n}N$ annihilation in/on nuclei, going on to produce several exciting works, with others in development; these make up much of this dissertation. He was also given the opportunity to attend the 2017 Computational Physics Summer Workshop at Los Alamos National Laboratory to work on nuclear reactor simulations using MCATK.

After a lapse in Department of Energy funding in April 2018, Barrow joined Associate Professor Nadia Fomin part time From June- December 2018, beginning his fascination with lepton (electron) scattering. While mentoring several other undergraduate and graduate students within Fomin's group and working visits to Jefferson Laboratory Halls A an C, Barrow made some initial progress in calorimetry studies, yield and cross section analyses before winning the Department of Energy's Office of Science Graduate Student Research Award to Fermi National Accelerator Laboratory (Fermilab) for the full year of 2019.

At Fermilab, he continued to pursue his work on intranuclear $n \to \bar{n}$ and atmospheric neutrinos within the DUNE Collaboration. While there, he also began work with Saori Pastore, Steven Gardiner, and Minerba Betancourt on a new quasielastic electron scattering Monte Carlo event generator for the GENIE Collaboration; though currently focused on light nuclei and the quasielastic regime, its valid energy regime is not generally fixed to this region and its simulation techniques are portable to heavier nuclei. Barrow would continue this work under the Universities Research Association's Visiting Scholar Award throughout all of 2020, continuing to be based at Fermilab (and then remotely in Knoxville following the onset of the COVID-19 pandemic).

During this time, Barrow, along with Leah Broussard, was invited by Michael Wagman and Jordy de Vries to co-organize the Prospects for Baryon Number Violation by Two Units workshop at the Amherst Center for Fundamental Interactions. This would eventually become the American Physical Society Snowmass 2021 Planning Process: Rare Processes and Precision Frontier–Baryon and Lepton Number Violation Topical Group's Theoretical Innovations for Future Experiments Regarding Baryon Number Violation, Part 1, later resulting in several Letters of Interest and an accompanying short proceedings.

Upon graduation, Barrow joined Or Hen (the Massachusetts Institute of Technology) and Adi Ashkenazi (Tel Aviv University) jointly at Fermilab as a postdoctoral Research Associate, continuing his GENIE work alongside his colleagues as well pursuing new and exciting quasielastic (ν_l,$l + p$) double differential cross section measurements for the MicroBooNE Collaboration.